ISSN 1927-0542 (Print)
ISSN 1927-0550 (Online)

EARTH SCIENCE RESEARCH

Vol. 1, No. 2 August 2012

CANADIAN CENTER OF SCIENCE AND EDUCATION

Editorial Board

Contents

Contents

Earth Science Research; Vol. 1, No. 2; 2012
ISSN 1927-0542 E-ISSN 1927-0550
Published by Canadian Center of Science and Education

Intelligent Spatial-Clustering of Seismicity in the Vicinity of the Hellenic Seismic Arc

A. J. Konstantaras[1], E. Katsifarakis[1], E. Maravelakis[2], E. Skounakis[2], E. Kokkinos[3] & E. Karapidakis[4]

[1] Laboratory of Computational Intelligence and Software Engineering (CISE lab), Technological Educational Institute of Crete, Chania, Greece

[2] Design and Manufacturing Laboratory (DML), Technological Educational Institute of Crete, Chania, Greece

[3] Department of Electronics, T.E.I. Crete, Chania, Greece

Correspondence: A. J. Konstantaras, Laboratory of Computational Intelligence and Software Engineering (CISE lab), Technological Educational Institute of Crete, Romanou 3, Chania 73133, Greece. Tel: 30-282-102-3033. E-mail: akonstantaras@staff.teicrete.gr

Received: January 12, 2012 Accepted: January 29, 2012 Online Published: May 16, 2012

doi:10.5539/esr.v1n2p1 URL: http://dx.doi.org/10.5539/esr.v1n2p1

Abstract

This research paper discusses possible seismic cluster formation and evolution in the vicinity of the Hellenic seismic arc and proposes a graphical user-interface monitoring and analysis tool based on various commercial and self-developed clustering algorithms for cluster discrimination, evolution and visualization. Self-developed algorithms enable the processing of both a) all recorder earthquakes and b) main seismic events alone, excluding foreshocks and aftershocks, by incorporating dynamic filters in space and time. The user can also import external formulae for the computation of the total earthquake preparation time, aftershocks duration and radius of the sphere of earthquake preparation region, and can also select specific regions of interest as well as the entire seismic map. The seismic imaging tool also addresses the concept of topical seismic cluster formation. Seismological maps indicate the presence of several seismic swarms forming within the region of the Hellenic arc, which appear to be either distinct or interacting together in groups of two or more. The identification of the number of possibly individual seismic clusters in a seismological area is a very challenging task by itself, which becomes even more complicated when investigating their outer boundaries especially in the case of multiple interacting clusters. The proposed imaging tool incorporates clustering algorithms that allow the user to apply various techniques for cluster identification, such as density based functions, gradient descent, centre of gravity, evolutionary allocation, and even import expert knowledge regarding the number of individual seismic clusters present.

Keywords: seismic epicentre clustering, spatial distribution, distinct earthquake regions, intelligent clustering algorithms

1. Introduction

Seismic cluster discrimination is of outmost importance in seismology as it can provide valuable information regarding the topology of the seismic phenomenon in relation with underlying faults. In most cases, little detailed information is readily available regarding the underground structure of a seismogenic region of interest, which in terms of epicenter depth extends from a few meters to several tens of kilometers below sea level. What is made apparent is a distorted reflection of the underlying faults' network on the surface of the planet painted by numerous compact seismic swarms that extend all the way across all active tectonic regions. The fact that underground faults are rarely distinct and in most cases they tend to form large topical or extent interacting networks complicates the process of surface seismic cluster discrimination as it is very difficult to identify discrete cluster boundaries. To make matters even more complex interacting clusters penetrate well into the stronghold vicinity of their companion and vice versa which can result in faulty allocations of seismic events to a particular cluster.

To evaluate this problem this paper applies a number of state-of-the-art clustering algorithms on seismic maps and proposes an intelligent platform allowing clusters to compete for newly existing seismic data points. Seismic data are made available either as distinct points or grouped together in seismic sequences, i.e. foreshocks, main

earthquake and aftershocks, in which case the user can select to work with main earthquakes only. Work can be carried out upon the entire seismic map or within any user-specified orthogonal region of interest. State-of-the-art clustering algorithms, such as fuzzy C-means clustering (Dunn, 1973; Bezdek, 1981), density-based spatial clustering (Ester et al., 1996), quantum clustering (Horn et al., 2002; Horn et al., 2003) and a self-developed dynamic spatial clustering algorithm are then applied comparatively upon the seismic data deriving distinct clusters of various shapes and dimensions. Furthermore, an intelligent platform has been developed to simplify the processes of dynamic evolutionary clustering at the appearance of new earthquakes upon the seismic clustering map by using a semi-automated interface. The platform applies contours and labels initial clusters predefined by the aforementioned clustering algorithms and enables them to compete for cluster allocation of new seismic events presented upon the seismic map using the centre-of-gravity algorithm. This approach allows irregularly shaped clusters to blend together and potential interact with each other depending upon the topology of initial cluster formation and the location of newly emerging earthquakes.

2. Epicentre Clustering

In order to identify regions of increased seismic activity we have implemented in our software a series of advanced clustering algorithms to cluster in the spatial domain, earthquake events identified as main events with the dynamic spatial clustering method. Since all spatial clustering algorithms rely on distance calculations between points, our software uses an ellipsoidal earth projected to a plane formula to estimate distance between earthquake events based on their geographical coordinates. The data throughout the paper have been obtained by the National Observatory of Athens Institute of Geodynamics seismicity catalogue (available online: http://www.gein.noa.gr/services/cat.html) for the entire Greek vicinity during the year 2009.

2.1 Fuzzy C-Means Clustering

The Fuzzy C-Means algorithm (Dunn, 1973; Bezdek, 1981) requires a specific number of cluster centers to be provided on initialization and is implemented so that for each cluster k the grade of cluster membership u_k for each earthquake event x is related to the inverse of its distance from the cluster center (1):

$$u_k(x) = \frac{1}{d(center_k, x)'} \quad (1)$$

In our current implementation (Figure 1) each event is assigned to the cluster with the highest grade of membership but since cluster membership ambiguities occur quite often, future implementations could take advantage of partial membership grades.

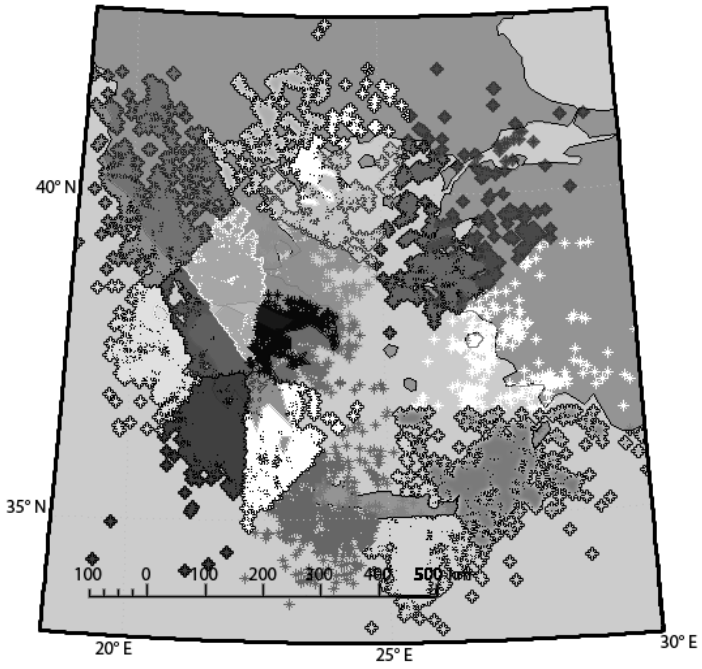

Figure 1. Spatial clustering indicative results using the Fuzzy C-Means algorithm with 15 cluster centres applied upon the entire dataset of earthquake events. Each colour indicates a distinct seismic cluster

2.2 Density-Based Spatial Clustering

The DBSCAN (Density-Based Spatial Clustering of Applications with Noise) algorithm (Ester et al., 1996) (Figure 2) does not require the number of clusters to be specified a priori as opposed to Fuzzy C-Means. Instead it clusters events spatially based on the notions of density reachability, density connectivity with respect to parameters Eps-neighborhood radius and the minimal number of objects considered as a cluster (MinPts). The *Eps neighborhood* of a point p, denoted by NEps(p), is defined by (2) :

$$\mathrm{NEps(p)} = \{q \in D \mid \mathrm{dist(p,q)} \leq \mathrm{Eps}\} \tag{2}$$

A cluster C is defined as a non-empty subset of a database of points D with respect to Eps and MinPts satisfying the following conditions:

a) $\forall$p, q: if p $\in$ C and q is density-reachable from p wrt. Eps and MinPts, then q $\in$ C.

b) $\forall$p, q $\in$ C: p is density-connected to q wrt. Eps and MinPts.

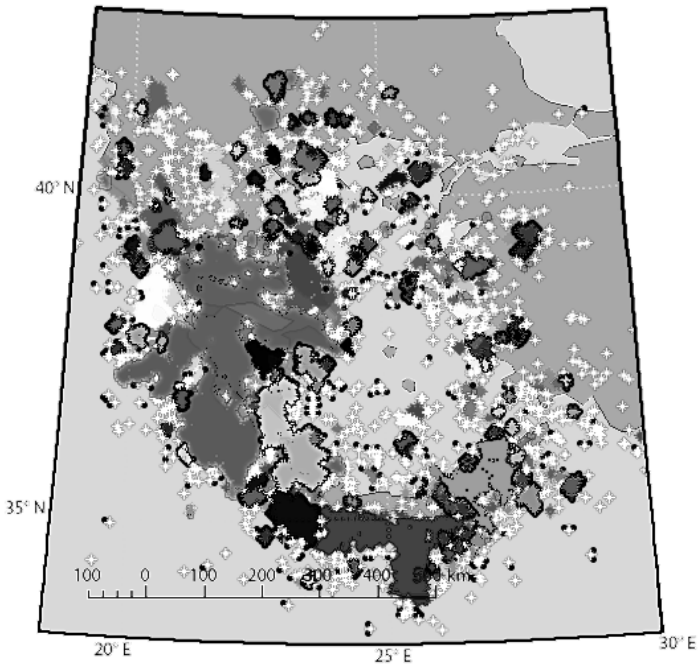

Figure 2. Spatial clustering indicative results using the DBSCAN algorithm applied upon the entire dataset of earthquake events. Yellow indicates noise - each other colour indicates a distinct seismic cluster

2.3 Quantum Clustering

The Quantum Clustering (QC) algorithm (Horn & Gottlieb, 2002; Horn & Axel, 2003) (Figure 3) starts out with a Parzen window approach assigning to each data-point a Gaussian of width σ which can be represented up to an overall normalization by the following Parzen-window estimator (3), $\psi(x)$:

$$\psi(x) = \sum_i e^{-\frac{(x-x_i)^2}{2\sigma^2}} \tag{3}$$

where x_i are the data points.

This can serve as a probability density function generating the data. One then proceeds to construct a potential function (4), $V(x)$:

$$V(x) = E + \frac{\frac{\sigma^2}{2}\nabla^2\psi}{\psi} \tag{4}$$

where

$$E = -\min + \frac{\frac{\sigma^2}{2}\nabla^2\psi}{\psi} \tag{5}$$

thus rendering V positive definite (5). In fact V has a global minimum at zero, and grows as a polynomial of second order outside the domain over which the data points are defined. Within this domain, V develops minima that are identified with cluster centres.

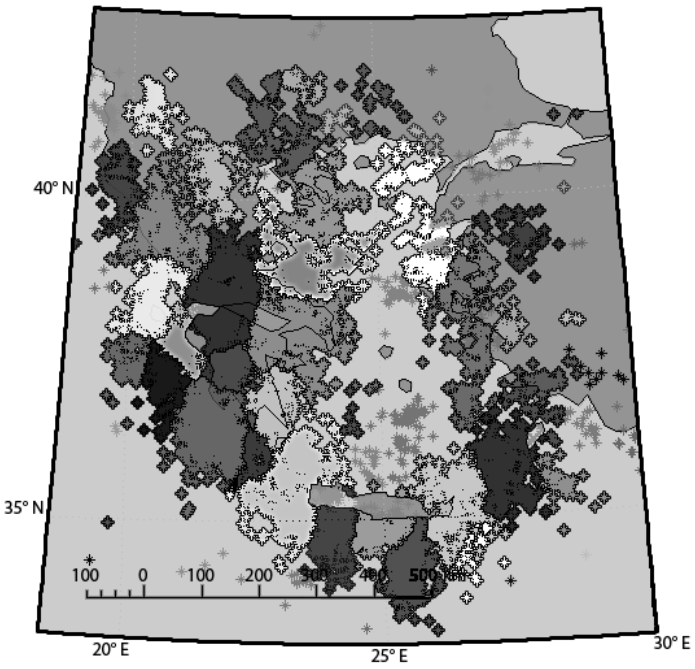

Figure 3. Spatial clustering indicative results using the Quantum Clustering algorithm applied upon the entire dataset of earthquake events. Each colour indicates a distinct seismic cluster

2.4 Dynamic Spatial Clustering

The self-developed dynamic spatial clustering algorithm is based on the concept of earthquake strain radii. The strain radius of an earthquake is defined as the radius of a hypothetical circle, centred at the epicentre of said earthquake, which encloses the zone of effective manifestation of the precursor deformations (Dobrovolsky et al., 1979).

Two different strain radius calculation methods (6, 7) have been implemented into the clustering solution using the following formulas based on event magnitude:

$$\text{a) } \rho = 10^{0.43\ M} \text{ km (Dobrovolsky et al., 1979)} \tag{6}$$

$$\text{b) } \rho = 10^{0.414\ M - 1.696} \text{ km (Dobrovolsky et al., 1989)} \tag{7}$$

where M is the event magnitude.

The time window can be a) either specified as a static period of days common to all events before and after the time of occurrence or b) dynamically calculated (Zubkov, 1987; Stein & Liu, 2009; Alden, 2009) for the time intervals before (8) and after (9) the main earthquake, respectively, where:

$$t_{before} = 10^{(0.5\ M\ -2.1)} * 365 \text{ days} \tag{8}$$

$$t_{after} = 10 \text{ years} \tag{9}$$

where tafter applies specifically to the current seismological region under investigation.

The dynamic spatial clustering algorithm works as follows:

1) Earthquake events are sorted in chronologically ascending order.

2) Events that do not belong to a cluster are processed individually, starting with the event that occurred first. That event becomes the currently processed event.

3) The strain radius and time window of the currently processed event are calculated. A new cluster is created and all events that occurred within the strain radius area and time window of the currently processed event are assigned to the new cluster.

4) The event with the greatest magnitude in the newly created cluster is determined. That event becomes the cluster's main event. If the main event is the currently processed event, the process advances, otherwise the cluster main event becomes the currently processed event. The process returns to step 3).

5) The next event in the dataset that does not belong to a cluster becomes the currently processed event and the process returns to step 5.

The above process is repeated until all events are assigned to a cluster.

Since expandability of the software solution was one of the key factors considered at the time of development, additional strain radius and time window calculation methods (Konstantaras et al., 2008) can be easily appended in the future. Furthermore a spatial filter capability is available to reduce large-territory datasets by processing only events in a smaller rectangular geographical region of interest, defined by its upper-left and lower-right corners' latitude and longitude (Figure 4).

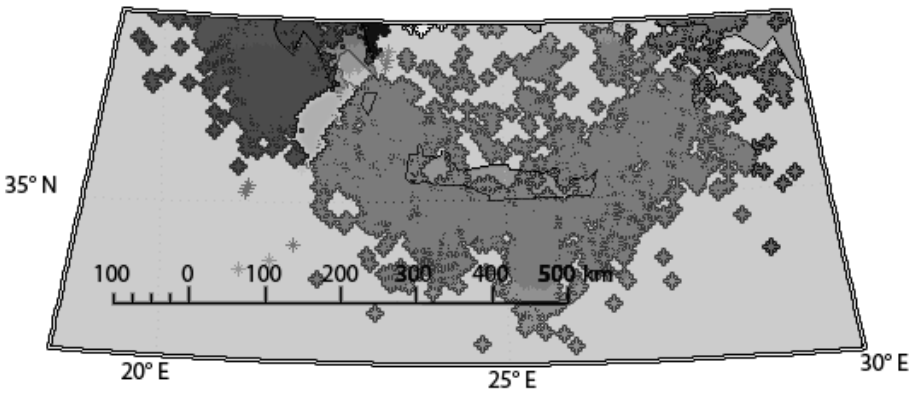

Figure 4. Dynamic spatial clustering applied upon a reduced version of the dataset using the spatial filter feature of our clustering software to focus on a smaller geographical region of interest ranging from 36°80"N, 20°50"E to 34°N, 29°20"E. Each colour indicates a distinct seismic cluster

The dynamic spatial clustering algorithm is an iterative agglomerative clustering algorithm. Initially, strain radius and time-window values are calculated for every event on the dataset and events are ordered by their time of occurrence and processed in the following manner: an unclustered event becomes the centre of a new cluster and all events within its strain radius and time-window become cluster members. At this point a competitive process begins where we look for the event with the highest magnitude within the newly-formed cluster. If that event is not the current cluster centre, a new cluster is formed and the aforementioned competitive process is repeated recursively. With the formation of a new cluster seismic events spatially and temporally located towards the far outer region of the initial cluster with respect to the new spatio-temporal cluster centre might not fall within the strain radius and/or the time window of the new cluster; therefore they remain as members of the initial cluster. Consequently, the dynamic spatial clustering algorithm forms irregularly-shaped seismic clusters allowing cluster interaction by enabling multiple clusters to occupy the same geographical area by exploiting time as an additional physical layer. Indicative results of our dynamic spatial clustering algorithm applied on the National Observatory of Athens Institute of Geodynamics seismicity catalogue (available online: http://www.gein.noa.gr/services/cat.html) throughout the Greek vicinity during 2009 using the first strain radius equation can be examined in Figure 5.

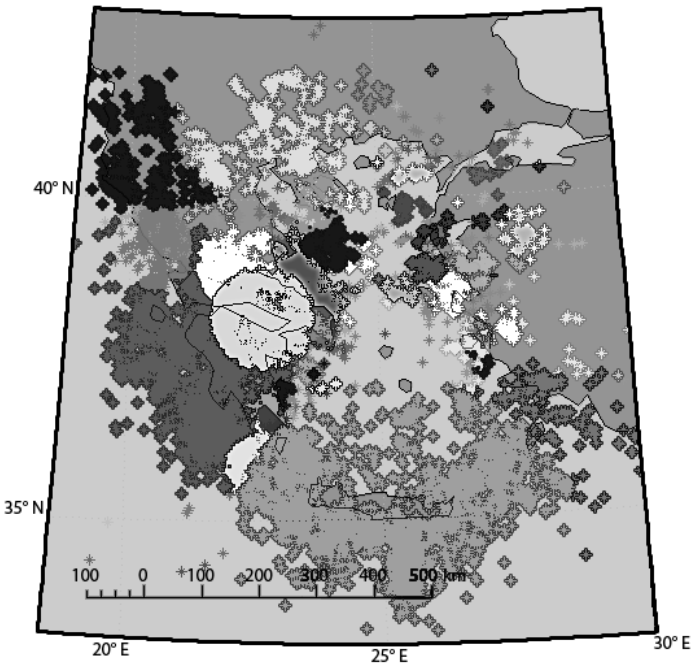

Figure 5. Dynamic spatial clustering applied upon entire dataset of earthquake events. Each colour indicates a distinct seismic cluster, cluster overlapping within the same region but at a different time frame is made apparent by the invasion of different colour data points well into the vicinity of compact clusters

3. Evolutionary Clustering Multifunctional Process

In order to identify and extract information from complex seismic images, we have developed the intelligent platform proposed below. This platform simplifies the processes of grouping and labelling several areas into a seismic image by using a semi-automated interface. The platform is based on the .NET framework architecture (available online: http://msdn.microsoft.com/en-us/kb/kb00829019.aspx) and can be used in any Windows-based computer with the .NET framework ver. 2.0 or later. However, .NET framework permits, in concept, the porting of the application in many other Linux based environments, using the Mono project (available online: http://msdn.microsoft.com/en-us/kb/kb00829019.aspx) functionality and libraries, so the user can run an application using the No-Touch Deployment (available online: http://msdn.microsoft.com/en-us/kb/kb00829019.aspx).

Three different phases explain the sequence of the processes shown in Figure 6 and Figure 7.

- **Phase 1**: The seismic data of an area which are depicted on a seismic data map are processed with several segmentation algorithms in order to produce seismic clustering maps such as the one shown in Figure 7 using quantum clustering. This procedure implemented by Phase 1 of the Seismic Monitor Organizer divides a given image into separate regions forming an initial set of clusters.
- **Phase 2**: The resulting seismic clustering map from the above procedure is loaded onto the platform for further analysis. By applying a fast multifunctional version of the classical region-growing segmentation algorithm, we can define precisely and apply contours and labels to various areas of interest.
- **Phase 3**: The region-growing algorithm is assigned to allocate new earthquakes to a particular cluster based upon the magnitude of the centre of gravity of the existing clusters; or create a new cluster if all centers of gravity are above a predefined by the user upper threshold point.

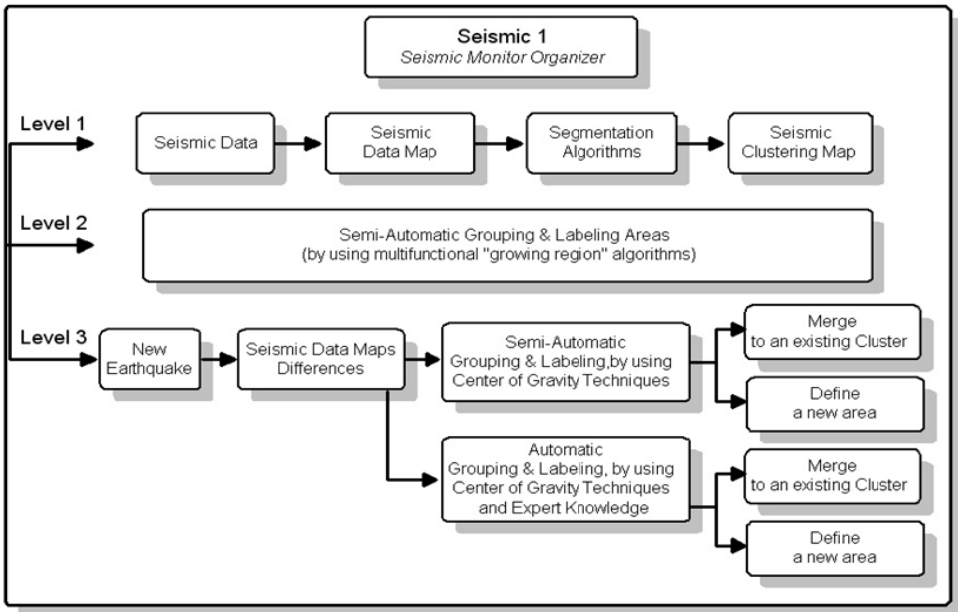

Figure 6. A schematic representation of the proposed platform

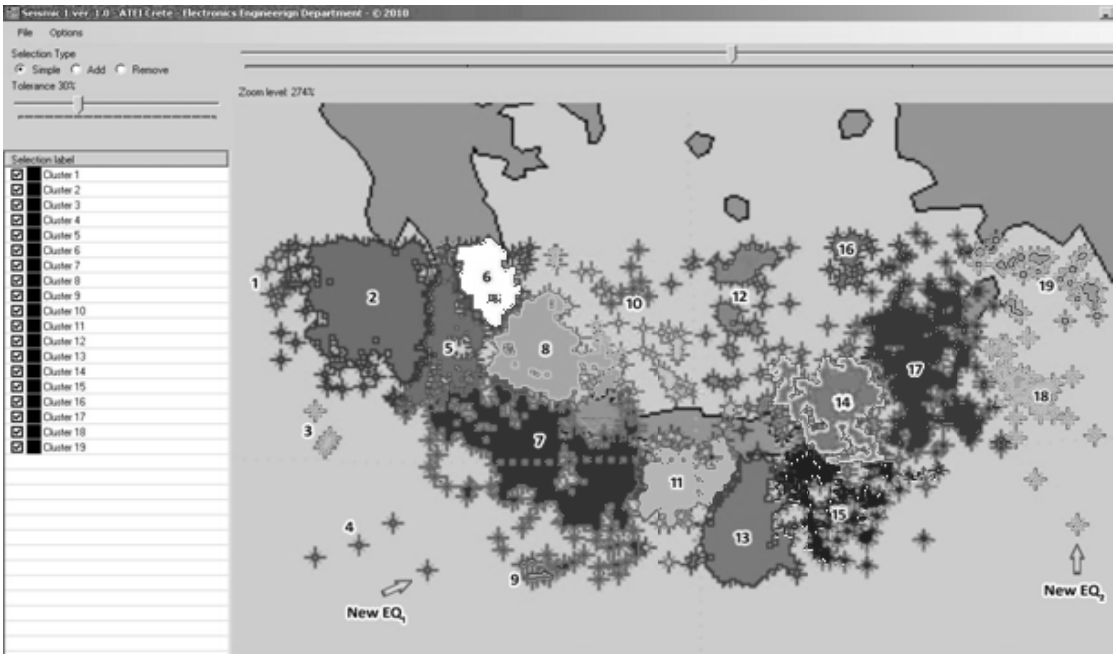

Figure 7. Example illustration of using the Centre of Gravity technique for the classification of newly introduced Earthquakes where New EQ_1 and New EQ_2 are being allocated to clusters "4" and "18", respectively

3.1 The Region-growing Algorithm

The function of the "Region-Growing Algorithm" is based on finding and selecting all the pixels around a pre-specified user-selected initial point that are similar in gray intensity. A tolerance value can also be set by the user to determine how closely to match colours (higher tolerance ends up in a larger selection) (Fujita & Fejri, 2006; Skounakis et al., 2009). All the points selected by the algorithm are automatically stored in an image mask of the same size as the original image. Each pixel in the image mask represents the position of the selected pixels in the original image and is used to label the delineated areas. To enhance its effectiveness, we have implemented a faster version of this algorithm which excludes all the pixels that have already been examined ensuring that the algorithm does not check them again.

When new points are being introduced into the seismic clustering map, e.g. after a new earthquake (see arrows in Figure 7), the platform allows for either their definition as new seismic clusters, or their mergence with one of the predefined seismic cluster. This can be achieved either semi-automatically, allowing for user interaction, or automatically by selecting the cluster with the minimum centre of gravity value for mergence or by defining a new cluster if the value of the centre of gravity exceeds a certain upper threshold induced by the user. The centre of gravity (CoG) of a region defines the centre of a region, and it is important in localizing that region. The centre coordinates r_G (10) and c_G (11) are given by:

$$r_G = \frac{1}{N} \sum_{r=0}^{Rows-1} \sum_{c=0}^{Columns-1} r \cdot f(r,c) \tag{10}$$

$$c_G = \frac{1}{N} \sum_{r=0}^{Rows-1} \sum_{c=0}^{Columns-1} c \cdot f(r,c) \tag{11}$$

r and *c* are the coordinates of the image, *N* represents the number of pixels of the region and *f(r,c)* is the image function. These formulae yield an '1' if the current pixel (*r*,*c*) falls within the region of a particular cluster, otherwise a'0' is obtained. The platform calculates the CoG of all the presented areas as well as the distances between the CoG of the new area and the existing ones automatically and presents a list of the proposed areas to be merged in, as shown in Figure 7.

3.2 Experimental Procedure

The experimental procedure comprises of six steps:

Step 1: The original "Seismic Data Map" is used to produce "Seismic Group Maps" by using several segmentation algorithms.

Step 2: A "Seismic Group Map" from the above procedure, is loaded on the platform.

Step 3: The right click on the list area of the platform enables the labelling (name & colour) of a newly introduced area on the "Seismic Group Map".

Step 4: The zoom and pan controls which are integrated in the platform allow a more detailed view of the region of interest on the map, and render its processing more efficient.

Step 5: The application of the region – growing algorithm to a region of interest on the "Seismic Group Map" leads to the definition of that area. The option to adjust the tolerance level of the gray-level differences is available during this process. The "add" and "remove" options can also be used to define more complex areas.

Step 6: A switch between "contour" and "area" of the selected areas is also available.

Steps 3 to 6 can be repeated to define new areas on the Seismic Group Map.

4. Results

The application of various clustering algorithms on seismic data produces a variety of results with several commons and some distinct differences. Larger seismic clusters appear to be depicted by most if not all of the clustering algorithms. Such an observation strengthens the possibility that these clusters in particular highlight a number of distinct seismic regions possibly baring a largely independent network of underground faults. In several cases there are more than one clustering algorithms depicting similar cluster boundaries at close proximity with one another, which, when applicable, gives a strong indication of the boarder region between neighbouring clusters. The opposite result provides a strong indication that the clusters involved are possible strongly interacting together at some part of their vicinity, which might be the result of inter-crossing underground faults at that particular region. Furthermore, if the clusters involved do not present a dense seismic swarm at some other part of their vicinity then it is possible that the clustering algorithms are at fault and what appears as individual seismic clusters might actually be parts of single broader seismic cluster.

Every clustering algorithm exhibits some particular distinct characteristics in terms of its operation and outcomes worth noting. The fuzzy c-means algorithm does not class any cluster point to a particular cluster. Instead it assigns to it various degrees of membership for a number of clusters. This principle provides a great means of identifying the extent of areas that are in dispute and claimed by various clusters as well as the undisputed strongholds that form the core of each cluster. The fuzzy c-means algorithm also allows for expert knowledge to

be imported in terms of the number of clusters present. The density based clustering algorithm does not necessarily class every cluster point to a particular cluster nor it creates a new cluster for every few scarce points throughout the seismic map. Instead it creates an open cluster to which, in effect, all un-classed seismic events are allocated. This principle reduces significantly the overall number of seismic clusters with respect to other clustering algorithms. The sophistication of the quantum clustering algorithm provides data clusters with more irregular shapes expanding towards areas that could well have been anticipated to belong to a neighbouring cluster. The self developed dynamic spatial clustering algorithm enables multiple clusters to occupy different seismic events located within the same geographical area by exploiting time as an additional physical layer.

The evolutionary clustering multifunctional process is an image processing interactive approach to the problem of cluster formation working in a genesis and growth manner. It relies on an existing clustering algorithm, e.g. quantum clustering, to create early seismic clusters at their infancy, i.e. containing few seismic events, and encompasses a region-growing algorithm to allocate new seismic data points to existing clusters. The region growing algorithm computes the centre of gravity of all existing clusters and measures their distance from the location of the next seismic event. That way the infant clusters compete for every new earthquake thereby growing in size and at various irregular directions. In the case where the distance from the nearest centre of gravity exceeds a maximum user-defined threshold point a new seismic cluster is formed.

5. Conclusions

Understanding the seismic phenomenon remains an open front in the scientific community. An insight on the environment that hosts the phenomenon could provide valuable information regarding its nature, genesis and propagation to the surface. Satellite images and Earth-based investigations of the Earth's interior have revealed the existence of an underground faults network almost throughout the most active seismic regions on the planet but they are all conducted at a distance from the source of interest. The work carried out on this paper acts complementary to these methods and aims to decode information carried through directly from the source to the surface of the planet via seismic waves. The numerous seismic events recorded on the surface of the planet form a distorted reflection of the underlying faults network. Perhaps working together these techniques could strengthen the validity of observations regarding the identification of the number of possibly individual or interacting together seismic clusters of various seismological regions as well as their outer boundaries and areas of interaction.

References

Alden, A. (2009). How long do aftershocks last. Retrieved from http://geology.about.com/b/2009/11/04/how-long-do-aftershocks-last.htm

Bezdek, J. (1981). *Pattern Recognition with Fuzzy Objective Function Algorithms*. New York: Plenum Press.

Dobrovolsky, I. P., Gershenzon, N. I., & Gokhberg, M. B. (1989). Theory of electrokinetic effects occurring at the final stage in the preparation of a tectonic earthquake. *Physics of the Earth and Planetary Interiors, 57*, 144-156. http://dx.doi.org/10.1016/0031-9201(89)90224-0

Dobrovolsky, I. P., Zubkov, S. I., & Miachkin, V. I. (1979). Estimation of the size of Earthquake Preparation Zones. *Pure and Applied Geophysics, 117*(5), 1025-1044. http://dx.doi.org/10.1007/BF00876083

Dunn, J. (1973). A fuzzy relative of the Isodata process and its use in detecting compact, well-separated clusters. *Journal of Cybernetics, 3*(3), 32-57. http://dx.doi.org/10.1080/01969727308546046

Ester, M., Kriegel, H., Sander, J., & Xu, X. (1996). A Density-Based Algorithm for Discovering Clusters in Large Spatial Databases with Noise. *Proceedings of 2nd International Conference on Knowledge Discovery and Data Mining* (KDD-96), 226-231.

Fujita, H., & Fejri, M. (2006). New trends in software methodologies, tools and techniques: How to create the magic wand?. *Proceedings of the Fifth SoMeT-06.* pp. 127.

Horn, D., & Axel, I., (2003). Novel clustering algorithm for microarray expression data in a truncated SVD space. *Bioinformatics, 19*, 1110-1115. http://dx.doi.org/10.1093/bioinformatics/btg053

Horn, D., & Gottlieb, A. (2002). Algorithm for Data Clustering in Pattern Recognition Problems Based on Quantum Mechanics. *Physical Review Letters, 88*(1), 18702. http://dx.doi.org/10.1103/PhysRevLett.88.018702

Konstantaras, A., Vallianatos, F., Varley, M. R., & Makris, J. P. (2008). Soft computing modelling of seismicity in the southern Hellenic arc. *IEEE Geoscience and Remote Sensing Letters, 5*(3), 323-327. http://dx.doi.org/10.1109/LGRS.2008.916069

Skounakis, E., Sakkalis, V., Marias, K., Banitsas, K., & Graf, N. (2009). DoctorEye: A multifunctional open platform for fast annotation and visualization of tumours in medical images. *IEEE Proceedings,* 3759-3762.

Stein, S., & Liu, M. (2009). Long aftershock sequences within continents and implications for earthquake hazard assessment. *Nature, 462*, 87-89. http://dx.doi.org/10.1038/nature08502

Zubkov, S. I. (1987). The appearance times of earthquake precursors. *Izv. Akad. Nauk SSSR Fiz. Zemli (Solid Earth), 5*, 87-91.

Earth Science Research; Vol. 1, No. 2; 2012
ISSN 1927-0542 E-ISSN 1927-0550
Published by Canadian Center of Science and Education

Spatial-Temporal Distribution and Characteristics of Internal Waves in the Lombok Strait Area Studied by Alos-Palsar Images

I Wayan Gede Astawa Karang[1, 2], Fumihiko Nishio[1], Leonid Mitnik[3] & Takahiro Osawa[2]

[1] Center for Environmental Remote Sensing, Chiba University, Yayoi, Inage, Chiba, Japan

[2] Center for Remote Sensing and Ocean Science (CReSOS), Udayana University, Denpasar, Bali, Indonesia

[3] V.I. Il'ichev Pacific Oceanological Institute FEB RAS, Vladivostok, Russian Federation

Correspondence: I Wayan Gede Astawa Karang, Center for Environmental Remote Sensing, Chiba University, 1-33 Yayoi-cho, Inage-ku, Chiba-shi 263-8622, Japan, Tel: 81-043-290-3836; Center for Remote Sensing and Ocean Science (CReSOS), Udayana University, PB Sudirman Street, Denpasar 80232, Bali, Indonesia. Tel: 62-361-256-162. E-mail: gede_karang@graduate.chiba-u.jp

Received: February 4, 2012 Accepted: February 15, 2012 Online Published: May 17, 2012

doi:10.5539/esr.v1n2p11 URL: http://dx.doi.org/10.5539/esr.v1n2p11

Abstract

Numerous packets of internal waves were revealed in Advanced Land Observing Satellite Phased Array L-band Synthetic Aperture Radar (ALOSPALSAR) images of the Lombok Strait area, and high-resolution and quick look images were used for their detection and analysis. The parameters of internal waves, such as the number of waves in a packet, crest length, and propagation velocity were estimated from the images. This paper describes the use of PALSAR imagery for internal wave frequency detection and presents the results of a survey that detected 90 internal wave occurrences with ScanSAR and Fine Mode PALSAR imagery over the period May 2006 to April 2011. The paper also discusses the spatial and temporal distribution of internal wave occurrences in the Lombok Strait area.

Keywords: ALOSPALSAR, internal waves occurrences, Lombok Strait, spatial and temporal distribution

1. Introduction

The ability of Synthetic Aperture Radar (SAR) to detect and measure oceanic internal waves has been widely proven since the launch of SEASAT in 1978 and launch of both the USSR Almaz-1 space station and the European Remote Sensing Satellite (ERS-1) in 1991. SAR observes the ocean surface waves within a broad swath with a spatial resolution from medium to high, which cannot be realized by in-situ measurements. SAR instruments, operating at wavelengths from 21 cm (L-band) to 3 cm (X-band), cannot measure internal waves directly because the depth of penetration of radar signals into saline seawaters does not exceed several millimeters. However, the variable currents associated with internal waves modulate the sea surface roughness, which in turn modulates the intensity of backscattered radar signals (Alpers, 1985; Mitnik & Alpers, 2000). Internal waves cause a pattern of converging and diverging current under the sea surface. These converging places causes the sea surface roughness increased and gives bright bands on SAR images. At diverging places the sea surface is smooth and gives dark bands on the SAR images. Internal waves occur in the World Ocean and are generated by an interaction of bathymetry, water stratification, and current flow. The evolution of internal waves may also make a significant contribution to internal oceanic mixing and, hence, have an important influence on climate change. For these reasons, the importance of scrutinizing the interaction of internal waves with the bottom topography is clear (Chen, 2012).

The use of SAR imagery for internal wave detection in the Lombok Strait area has been presented in several recent studies (Mitnik et al., 2000; Susanto et al., 2005; Mitnik, 2006; Karang et al., 2011). These studies demonstrated the utility of C-band SAR imagery acquired by the European Remote Sensing satellites (ERS-1, ERS-2, and Envisat) for the detection and parameter estimation of internal waves. From January 2006 to March 2011, numerous images over the Lombok Strait were acquired by L-band polarized SAR PALSAR onboard the ALOS satellite. PALSAR allows the study of dynamic oceanic phenomena, such as internal waves and fronts, in a broad range of spatial scales due to the availability of various regimes differing in swath width (70-350 km) and in ground resolution (from 7-10 to 100 m) (Rosenqvist et al., 2004). In this study, the ALOS-PALSAR

images of the Lombok Strait area with the surface imprints of nonlinear internal waves are considered, and the characteristics of their spatial-temporal variability are presented.

2. The Physical Oceanography of Lombok Strait

The Lombok Strait (Figure 1) separates the Bali Island and the Lombok Island. This strait is an important pathway for water transport from the Pacific Ocean into the Indian Ocean and is a part of the Indonesian throughflow (ITF). The length of the Lombok Strait is approximately 60 km, with a contrasting bathymetry along the strait from north to south. The depths in the north are typically between 800 and 1000 m. A shallow sill is found at the southern outlet, where the channel is divided in two by the small Nusa Penida Island. The channel at the western part of this island (Badung Strait) is shallower, with a depth less than 100 m. Right of this island is deeper and has an extremely irregularly shaped sill with a sill-crest depth of approximately 250 m (Susanto et al., 2005) and a length of 18 km, connecting islands of Nusa Penida and Lombok. Figure 2 shows a depth cross section of the Lombok Strait in the south to north direction. Depth increases from a minimal depth of 250 m at the sill to 1500 m in the Flores Sea. This sill is of great importance for the oceanographic behavior in the Lombok Strait. The highest current velocities are observed at the sill where a cross-sectional area of the strait, which bounds the transport of water through the strait, is minimal.

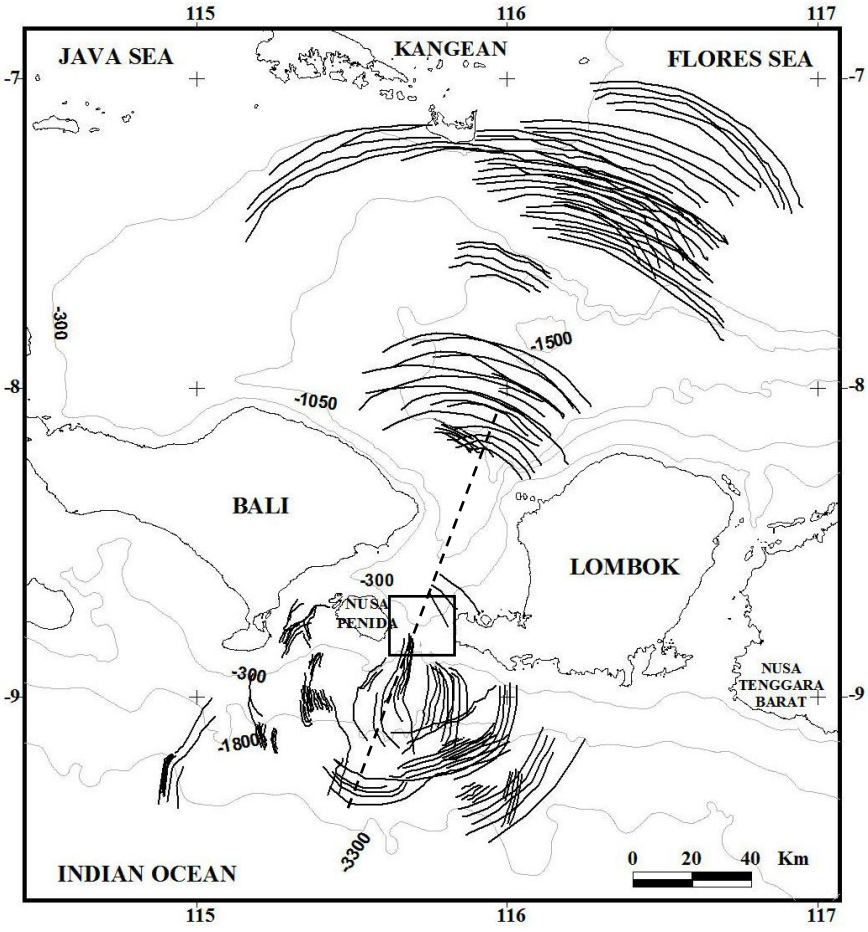

Figure 1. A map of the study area. The numbers on the isobaths are in meters. The bold lines represent crests of internal waves revealed on the PALSAR images. The rectangular box in the center defines an internal wave generation source region to be further analyzed in section 4. The dashed line is the south-north cross section shown in Figure 2

The ocean current pattern consists of the superposition of the main current flow and tidal currents. The tides in the Indonesian Seas are largely produced by tidal wave propagation from the Pacific and Indian Oceans (Schiler, 2004; Karang et al., 2010). Thus, the tide in the Lombok Strait is produced by tidal waves from the Indian Ocean.

The semi-diurnal tide, with a period of 12.4 hours, is predominantly at the sill, with a maximal tidal velocity of approximately ±3.5 m/s (Murray & Arief, 1988; Murray et al., 1990). On other side, that is, the northern part of the strait (approximately 50 km from the sill) the tidal velocity ranges from 0.2 to 0.5 m/s (Murray, 1988). The current velocity is also controlled by water column stratification. Sometimes the current velocity in the near surface even has an opposite direction to the current below or near the bottom, which is evidence of a division of the fluid in different layers. To the north of Lombok, the available density profiles show a large density gradient in the upper 300 m (Murray et al., 1990). The density difference between the upper and lower layers is caused by the difference in salinity and temperature. For example, two layers are observed in the Flores Sea: a high salinity layer at a depth of 150±20 m and a low salinity layer at 320-300 m (Murray at al., 1990). The interface of a two-layer fluid, the pycnocline, is defined by the normal modes of the fluid. This interface is usually defined at the place where the first internal mode has its maximal vertical velocity. In the northern area, this interface is located at a depth of 280 meters, where 1020 kg/m^3 (Figure 2) densities near the surface are observed. Because the water in the Indian Ocean is colder (Figure 2) than water in the Flores Sea, which comes from the Pacific, much higher values of the surface density (1022 kg/m^3) in the southward part of the Lombok Strait are observed. The warm upper layer, which enters the Indian Ocean over the sill, causes a much greater density difference south of the sill.

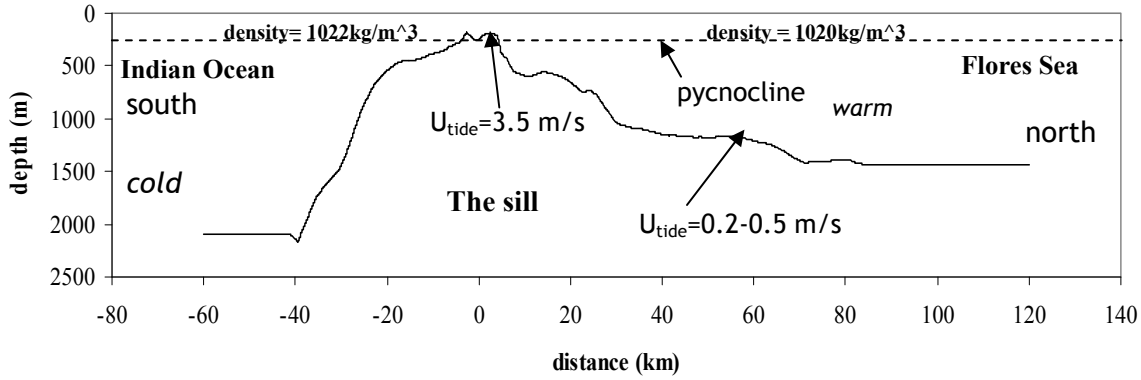

Figure 2. South-north cross section of the bottom topography of the Lombok Strait and water properties

Robertson and Ffield (2005) by numerical simulation show that Lombok Strait is suitable place for internal tides generation. By the narrow channel and shallow sill in the strait the current velocity rapidly increased causes the displacement of the pycnocline area for the generation of internal waves (Jackson, 2007). The nonlinear solitary waves were found to be generated by tidal current and topography interactions in the sill area with propagation velocity of 1.8-1.9 m/s, as estimated by the analysis of nonlinear wave packets revealed in ERS-1/2 SAR images (Mitnik et al., 2000). However by using the same SAR images combined with in-situ data the behavior of internal waves controlled by Lombok Strait water circulation also investigated (Susanto et al., 2005). They suggested that the emergence of internal waves and their propagation influenced by the variability of tides and water stratification associated with ITF circulation.

3. Dataset

The Phased Array L-band Synthetic Aperture Radar, PALSAR, is one of three instruments onboard the ALOS satellite. Having a steerable beam and scan modes with a choice of co-polarization (Horizontal-Horizontal, HH or Vertical-Vertical, VV) and cross-polarization (HV or VH), PALSAR is an advanced version of Japanese Earth Resources Satellite 1, JERS-1, SAR (Nemoto et al., 1991). PALSAR has the following three observation modes: Fine Mode, ScanSAR mode and Polarimetric Mode. The Fine Mode is the most commonly used under regular operation, and its maximum ground resolution of 7 m is among the highest, as SAR is loaded on a satellite (ERSDAC, http://www.ersdac.or.jp). The ScanSAR mode enables switching of the off-nadir angle from 3 to 5 times to cover a wide area from 250 km to 350 km with a ground resolution of 70 to 100 m. The Polarimetric Mode can simultaneously receive horizontal and vertical polarization per each polarized transmission. Table 1 provides an overview of the ALOS PALSAR characteristics (Shimada, 2002).

Table 1. PALSAR Characteristic

Mode	Fine		ScanSAR	Polarimetric
Center frequency	L-band (1270 MHz)			
Chirp bandwidth, MHz	28	14	14,28	14
Polarization	HH,HV	HH+HV, VV+VH	HH, HV	HH+HV+VH+VV
Incident angle, deg	8-60	8 - 60	18-43	8-30
Range resolution, m	7-44	14-88	100	24-89
Swath width, km	40-70	40-70	250-350	20-65
Bit length, bits	5	5	5	3 or 5
Data rate, Mbps	240	240	120,240	240

Fine Mode and ScanSAR images are used in the present study. The images, covering a period of five years, from May 2006 to April 2011, were collected by the Japan Aerospace Exploration Agency (JAXA, https://auig.eoc.jaxa.jp/auigs/top/TOP1000 lnit.do) and the Japanese Earth Remote Sensing and Data Acquisition Center (ERSDAC, http://www.ersdac.or.jp). The PALSAR images of the Lombok Strait were selected from the JAXA archive. Prominent SAR signatures of internal waves were found in the images and are discussed in detail in section 4.1 Statistical analysis of Lombok Strait images was mainly performed using the SAR browse archive maintained by ERSDAC.

4. Results and Discussion

4.1 Prominent PALSAR Signatures of Internal Waves

This section presents some of the clearest manifestations of internal waves propagating from the sill toward the north and south found in PALSAR images. The PALSAR ScanSAR and Fine mode images show that energetic and prominent internal solitary waves are identified in the Lombok Strait during the whole period (Figures 3-7). In particular, internal wave activity was observed on 21 February and 09 October 2007; on 29 August, 29 November, and 28 December 2010; and on 2 February 2011. The surface imprints of internal waves propagating northward in the Flores Sea (Figures 3-5), southward in the Indian Ocean (Figure 7) or in both directions (Figure 3) are clearly visible in the images. These waves are generated through the strong tidal flow over the sill in the south of Lombok Strait (Mitnik et al., 2000). The images show the interaction between sea surface waves and the current due to the internal waves activity.

Dark patches, bands and filaments can be observed in Figures 3-7. Dark features correspond to areas where the surface roughness is reduced due to the presence of surface active films both natural (biogenic) and anthropogenic (oil spills) damping the small-scale roughness, or due to weak wind speeds or wave-current interactions (Jackson & Aprl, 2004).

In the PALSAR image of 29 August 2010 (Figure 3a), two packets of internal waves was observed propagating northward into the Flores Sea. The distance between the first solitons of packets 1 and 2 is about $\Delta L = 77.8$ km. The averaged propagation velocity of 1.74 m/s was estimated from relationship $V = \Delta L/T$, where $T = 12.4$ hours is the semidiurnal tidal period. The length of the arc-like crest line of the leading wave exceeds 100 km, as also observed by Susanto et al. (2005). Packets 1 and 2 consist of approximately 9 and 5 solitons, respectively. The crest separation lengths or wavelengths of packet 1 decrease from the front to the rear from approximately 6 km to 4.1 km (see the backscatter values profile K to K' in Figure 3b). For packet 2, the wavelength between successive waves decreases monotonically from approximately 5.5 km to 3.4 km (see the backscatter values profile M to M' in Figure 3b). Also a smaller packet of internal waves south of Lombok Strait propagating into the Indian Ocean was observed on this image. Approximately 4 solitons are observed in packet 3; their wavelengths decrease from approximately 4 km to 1.5 km from the front to the rear (see the backscatter values profile N to N' in Figure 3b).

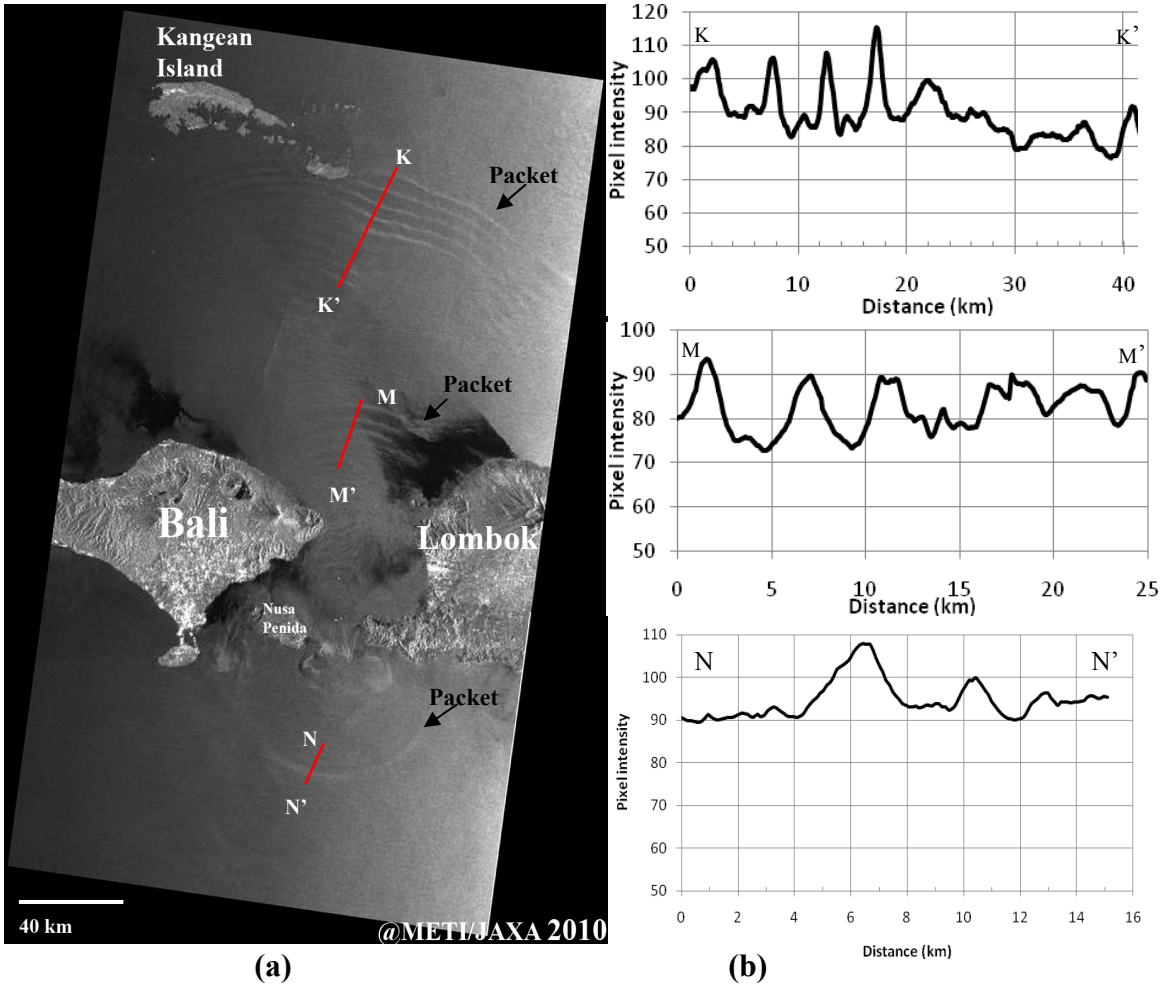

Figure 3. (a) SAR images of the Lombok Strait acquired on 29 August 2010 at 02:22:50 UTC (a) by the PALSAR ScanSAR mode. (b) Plot of cross profile along sections marked by a red line in KK', MM' and NN', respectively. In Figure 3a, three packets of internal waves are visible in the Lombok Strait area, two propagating north toward Kangean Island and one packet propagating south toward the Indian Ocean. Images © from the METI/JAXA

One clear packet of internal solitons in the Flores Sea was observed in the image acquired on 29 November 2010 (Figure 4a). Several waves of the packet reached the shallow water region around the Kangean Islands approximately 200 km from the sill where the coral reef is situated. Radar contrast of the individual waves in packet against the background depends on variations of sea surface currents accompanying of particular wave and on variations of the sea surface wind (sea surface roughness) which determine the brightness of the background. The first wave of the packet 1 is approximately 101.5 km away from the packet 2, and thus, the mean velocity is approximately 2.27 m/s. Unlike the unclear packet 2, packet 1 consists of 5 solitons. The waves of packet 1 are characterized by a narrow, bright band. Propagation of intense internal waves in the areas with weak winds (they look dark in SAR images) is accompanied by appearance of bands of steep surface waves, their breaking and foaming that explains their bright tone (Figure 4b). Pixel intensity profile between points O and O' (Figure 4c) illustrates high radar contrast of internal waves crests against the dark background. The average wavelengths of this packet are approximately 4.95 km. The internal wave packet which was generated by the next tidal wave in 12.4 h has the low contrast the gray-tone background that hinders the location of the first wave in this packet and estimate of the propagation velocity.

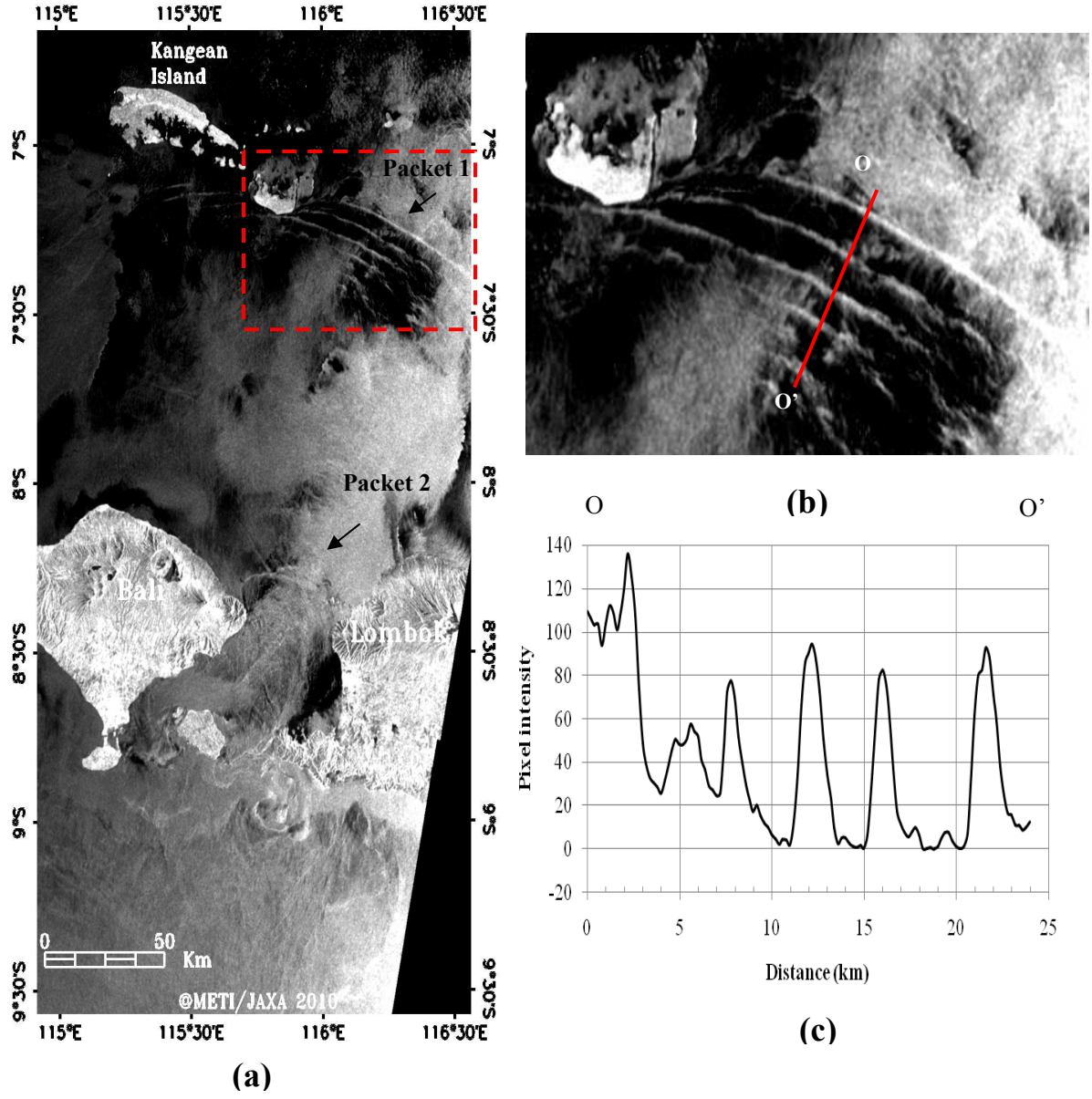

Figure 4. (a) PALSAR ScanSAR mode images of the Lombok Strait and adjacent area acquired on 29 November 2010 at 02:20:53 UTC; (b) enlarged fragment of the image shown by red rectangle in (a); (c) profile of radar backscatter along transect OO' indicated by a red line in the image. In Figure 4a, two packets of internal waves are propagating north toward the Kangean Islands. Images © from the METI/JAXA

In the PALSAR images taken on 28 December 2010, several solitons crossed the Kangean Island and some coral reefs. The southern part of the Lombok Strait is not observed in these PALSAR images. In Figure 5a, the northward-propagating waves contain two packets of solitons. The number of waves in Packet 1 reached 12; with wavelengths ranging from 0.5 km up to 5 km (see Figures 5b and 5c). Packet 2 consists of more than 25 solitons with a average wavelength of 4.5 km. Both packets have semi-circular patterns. The first wave of packet 2 is approximately 200 km from the sill reached a shallow topography eastward of the Kangean Islands.

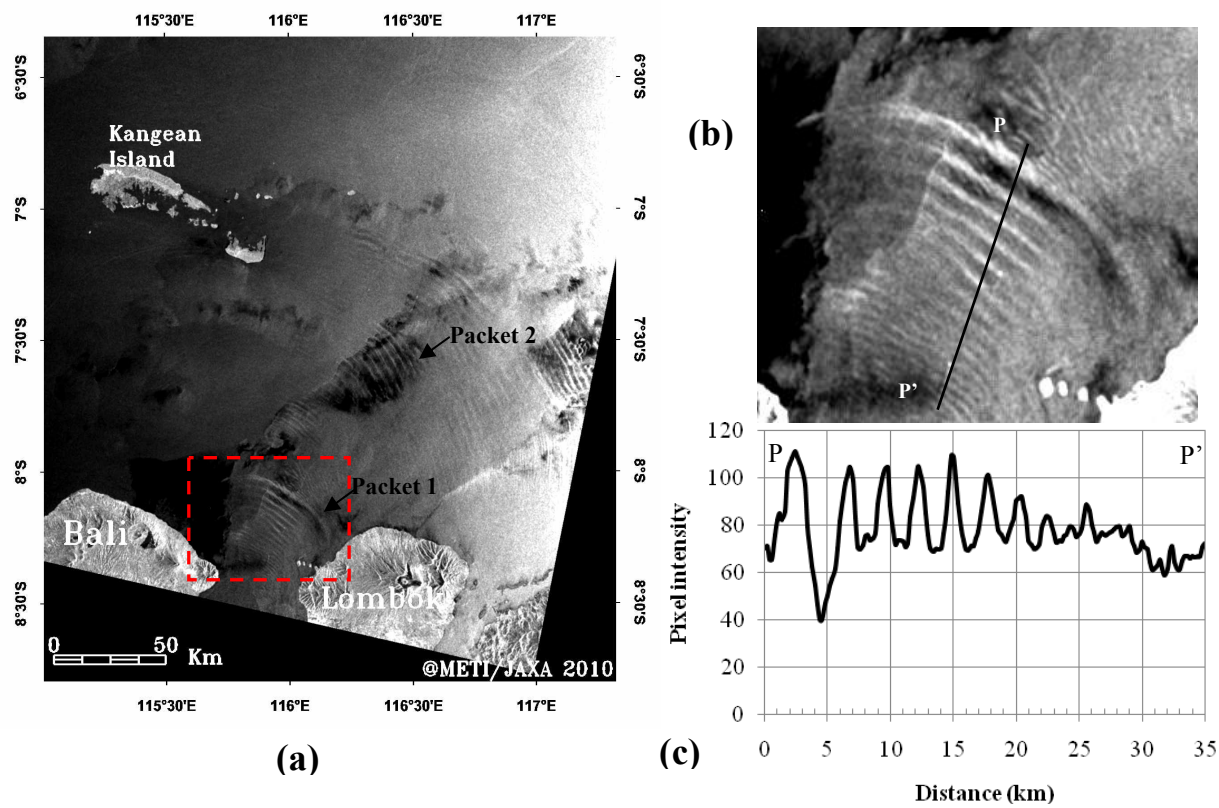

Figure 5. (a) PALSAR from ScanSAR mode images over the northern Lombok Strait acquired on 28 December 2010 at 02:15:27 UTC; (b) enlarged fragment of the image shown by a red rectangle in (a); (c) profile of radar backscatter along transect PP'. The internal waves of the two packets are visible north of the Lombok Strait in Figure. 5a. Packet 1 propagates to the north and the other packets to the northeast. Images © from the METI/JAXA

Figure 6a presents a weak radar signature of internal waves. This image was acquired on 2 February 2011 at 02:16:42 UTC and shows a weak-scale soliton. Five packets of internal waves are visible north of the Lombok Strait in Figure 6a. Three packets (packets 1, 2 and 3) with 1.5 to 5 km wavelength are originates from the Lombok sill and propagating to the north reached the Kangean Island and Flores Sea. Two packets (packets 4 and 5) propagating to the northwest are also visible in the image. The actual generation location and mechanism for these internal waves (packets 4 and 5) are still unknown, but we suppose that the generation of these packets is related to some local bathymetry-tides interaction in the Flores Sea. The surface imprints of the solitons from the succeeding tide are visible as low contrast semi-circular bands to the north of the Lombok Strait. The distance between the leading solitons in the two wave packets is approximately 84 to 104 km and, thus, the propagation velocity is approximately 1.8 to 2.3 m/s, respectively. The leading soliton of packet 3 is located at a distance of approximately 280 km from the sill, reaching the other two packets internal waves (packets 4 and 5 which propagating to the northwest).

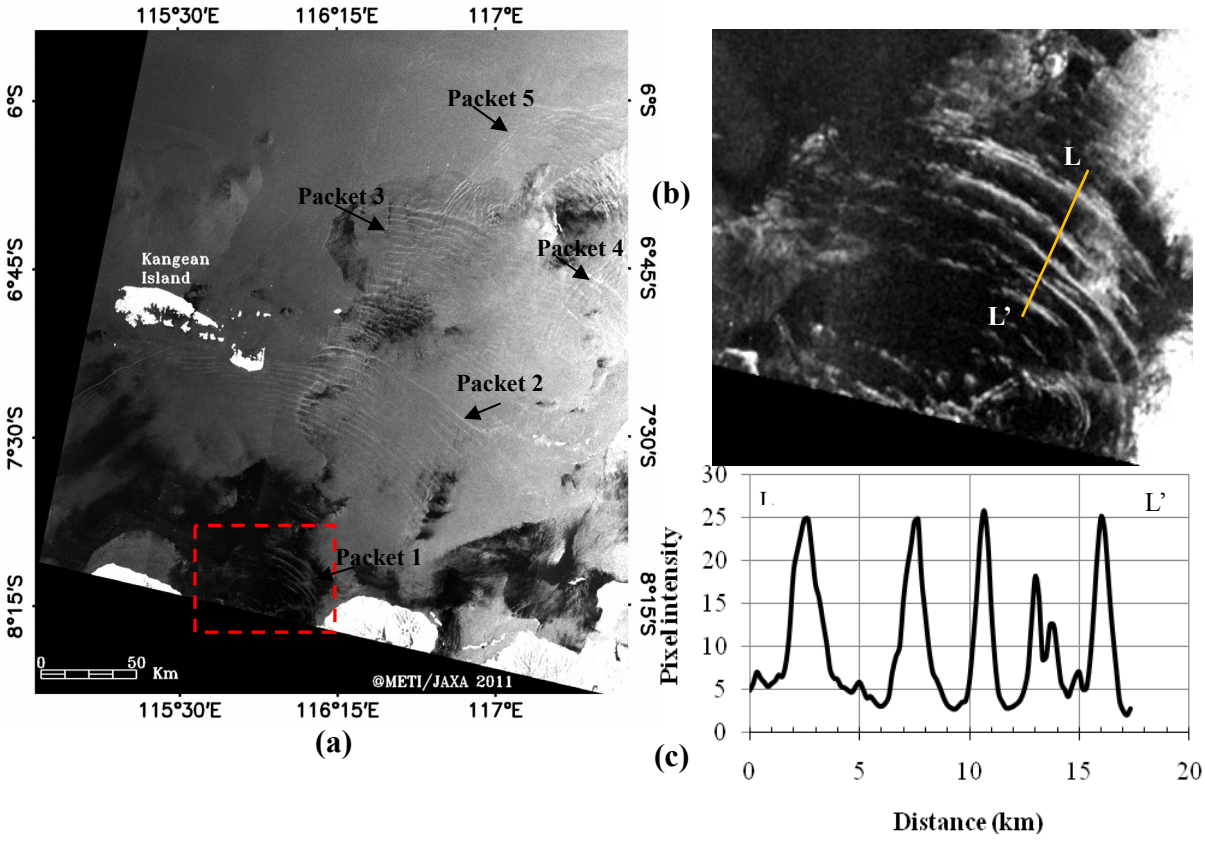

Figure 6. (a) PALSAR from ScanSAR mode images over the northern Lombok Strait area acquired on 2 February 2011 at 02:16:42 UTC; (b) the enlarged fragment of the image shown by a red rectangle in (a); (c) profile of the radar backscatter along transect LL' indicated by a red line in the image. Images © from the METI/JAXA

The sea surface manifestations of the irregular internal waves are also visible in the images taken in high spatial resolution from the PALSAR Fine Mode imagery. The images were taken in the middle of winter (21 February 2007 at 15:09:26 UTC, Figure 7a) and late of summer (09 October 2007 at 15:02:00 UTC, Figure 7b). In addition to an internal wave feature, well-developed thermal plume can be found in the image due to the intrusion of warm Pacific water from the Flores Sea into the Indian Ocean. This intrusion also corresponds to the measurements of the water transport of the Lombok Strait throughflow. The mean annual transport measured with current meters in 1985 was 1.7 Sv into the Indian Ocean (1 Sv $=10^6$ m^3/s). The maximum transport was observed during the summer months or south east monsoon (3.8-4 Sv) and a minimum of 1 Sv during the west monsoon in the spring (Murray et al., 1988). Thus, at 9 October 2007, approximately 3.8 milliard cubic meters per second of warm Pacific water was transported through the Lombok Strait.

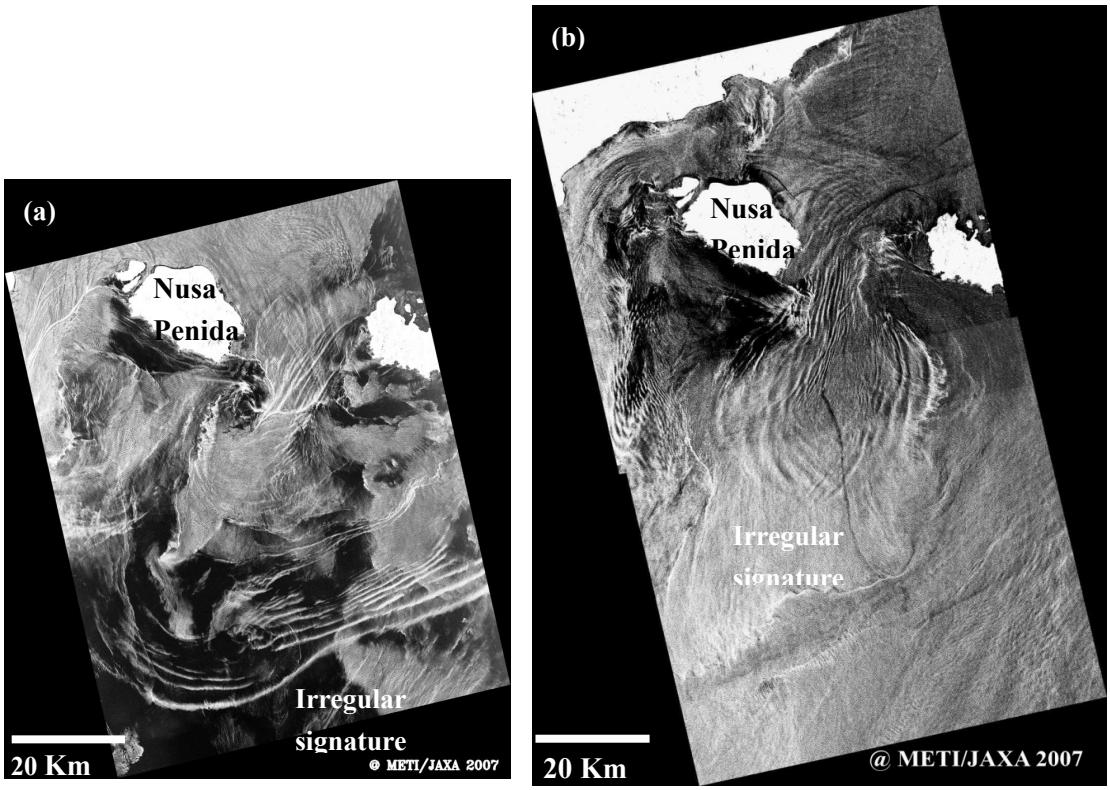

Figure 7. ALOS PALSAR images from Fine Mode acquired on 21 February 2007 at 15:09:26 UTC (a) and 09 October 2007 at 15:02:00 UTC (b). Images © from the METI/JAXA

4.2 Spatial Distribution of Internal Waves

A selection of 20 ALOS PALSAR images was obtained to study the spatial distribution of internal waves in the Lombok Strait area. The images span most calendar months and were spread out between 2007 and 2011. We created a spatial distribution map by placing all these internal wave packets at their corresponding locations (Figure 1). The results show that the internal wave packets are distributed in the north and south of the Lombok Strait and their origin is the shallow sill located between the Nusa Penida and Lombok islands. This result confirms the previous investigations showing that the internal waves in the Lombok Strait are generated through the strong flow over the sill in the south of Lombok Strait (Mitnik et al., 2000, Susanto et al., 2005 and Ningsih eta al., 2008). The internal solitary waves appear as circular bands frequently observed parallel to the sill with a northward direction. These circular internal waves penetrating to a depth of ~1000 meters and propagating away toward the Kangean Islands and the Flores Sea. The shallow topography of Kangean Island limits the region of activity of the internal solitary wave propagation from the north mouth of the Lombok Strait to approximately 7.1°S latitude.

4.3 Temporal Distribution of Internal Waves over Lombok Strait by PALSAR during 2006-2011

The ALOS-PALSAR quick look images were used as a baseline for the temporal variability of the Lombok Strait internal waves. The data covering a period of five years from May 2006 to April 2011 are collected from the ERSDAC, http://www.ersdac.or.jp. A total of 1013 scenes with different Granule ID were examined, of which 673 images were obtained by the Fine Mode and 340 images by the wider-swath ScanSAR mode. A total of 90 images taken on different days with visible internal wave imagery were collected. These records were compiled entirely ”by eye” and did not count individual wave packets but rather the distinct daytime wave activity visible in any given image.

For yearly distribution, the PALSAR-observed occurrence frequency is defined as

$$f_{iy} = \frac{N_i}{N_y} x100\% \quad (1)$$

where N_i is the number of total days on which the internal waves were imaged by PALSAR; here, *i(y)* represents the *i*th (*j*th) year. Tables 2 and 3 shows the PALSAR images distributed over Lombok Strait.

Table 2. Yearly distribution of PALSAR images over Lombok Strait

	2006	2007	2008	2009	2010	2011
No. of SAR data	13	41	48	27	55	17
No. of internal wave occurrence	7	22	17	11	28	5

Table 3. Monthly distribution of PALSAR images over Lombok Strait

	Jan	Feb	Mar	Apr	May	Jun	Jul	Aug	Sep	Oct	Nov	Dec
No. of SAR data	18	17	18	9	11	17	18	20	23	20	14	16
No. of internal wave occurrence	8	9	9	4	6	6	9	11	8	7	6	7

Figure 8 shows the yearly distribution of internal waves over the Lombok Strait. We can see that the results give an interannual variability of PALSAR-observed internal wave occurrence frequency in the Lombok Strait. The frequencies are higher in 2006, 2007 and 2010 than in other years. This interannual variability implies that there are long-term and large-scale processes that play a role in modifying internal wave occurrence frequency and SAR imaging in the Lombok Strait and adjacent areas. The ITF transports relatively warm water from the Pacific into the Indian Ocean, is important element that may influence the SAR-observed internal wave occurrence frequency in the Lombok Strait area. Previous investigations have found that the ITF is regulated by intraseasonal (Arief & Murray, 1996) and interannual (England & Huang, 2005) influences, with the latter a function of the El Niño Southern Oscillation (ENSO) (Mathews et al., 2011). These circulations directly contribute to the variations of the sea water condition from the surface to the bottom.

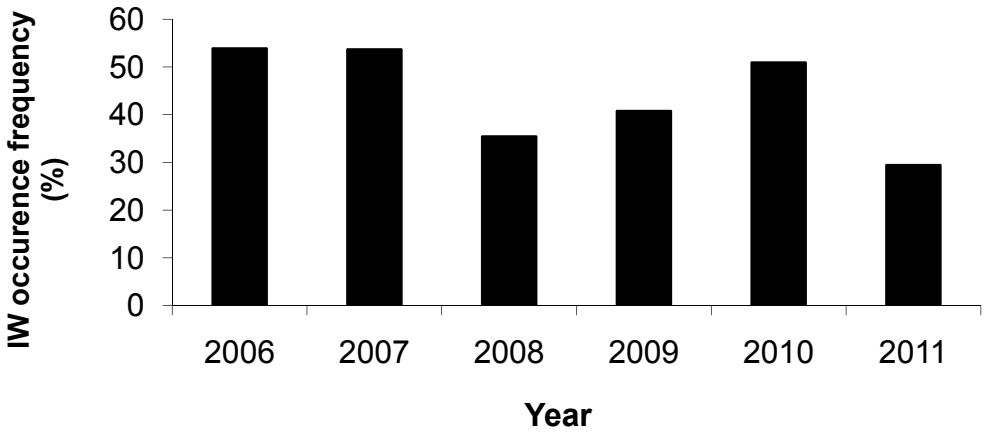

Figure 8. Yearly distribution of SAR-observed internal wave occurrence frequency in the Lombok Strait

For monthly distribution, the PALSAR-observed occurrence frequency is defined as

$$f_{im} = \frac{n_i}{n_m} x100\% \tag{2}$$

where n_i is the number of total days in the *i*th (*m*th) month of 6 years, at which the internal waves were acquired. The monthly distributions of the PALSAR-observed internal waves in the Lombok Strait are shown in Figure 9. We can see that the results give a seasonal variability. The high occurrence frequencies are distributed in February, May and August. The low occurrence frequencies are distributed in late summer, from September to October, and in June. The other months appear to be transition periods.

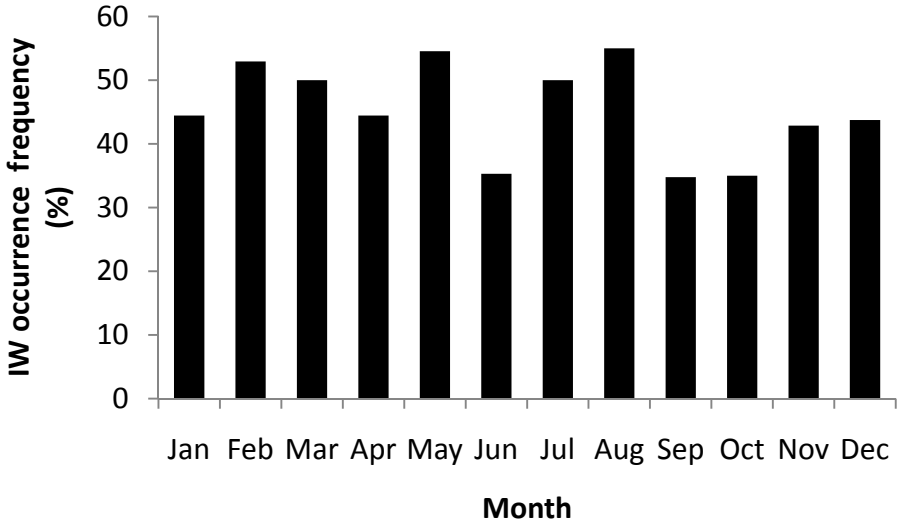

Figure 9. Monthly distribution of SAR-observed internal wave occurrence frequency in Lombok Strait

5. Summary

An attempt has been made to understand the characteristic of internal waves in the Lombok Strait area. The intense of internal waves generation in this area due to its geometry and the tidal flow associated with ITF. ALOS PALSAR, with its combined attributes of fine resolution, medium to large swath area, and ready image access (for quick look images) allowed a survey of spatial and temporal distributions of internal wave occurrences in the Lombok Strait. Analyses of the PALSAR images showed that the internal waves are generated in the central Lombok sill then propagate away into the north and south directions. Information on the type of modulation, wavelength, propagation velocity, direction of propagation and crest length of the internal waves can be immediately obtained from the images.

A survey of ScanSAR and Fine Mode PALSAR imagery acquired between May 2006 and April 2011 found 90 internal wave occurrences within a latitudinal band from 7.26^0 to 9.83^0S and a longitudinal band from 115.06^0 and 116^0E. The yearly distribution of SAR-observed internal wave occurrences indicates that the frequencies in 2006, 2007 and 2010 are higher than other years. This interannual variability reveals that there are great physical processes that play a role in modifying internal wave occurrence frequency in the Lombok Strait area. Interannual adjustments of thermocline structures in the Lombok Strait, as well as the behavior of the Indonesian throughflow, monsoons, and ENSO, are counted as great circulation processes. The monthly PALSAR-observed occurrence frequency shows that the high occurrence frequencies are distributed in February, May and August, with a maximum frequency of 55% in August. The low occurrence frequencies are distributed in June, September and October, with a minimum frequency of 34.8% in September. Because the visibility of internal waves on the SAR images depends on local environmental factors, there may be some external boundary conditions, such as wind speed and sea state, that will influence its appearance. Further dynamical analyses combined with *in situ* data are needed to clarify our investigations.

Furthermore, the data of the several remote sensing instruments in the last two decades offers the possibility of building a large database of internal wave activity in a broad area, though it is a great challenge to determine the detailed characteristics and mechanisms of internal wave activity associated with changing time and environmental conditions. Work on the examination of multisensor imagery for internal wave signatures in the Lombok Strait area is ongoing.

Acknowledgments

The authors would like to thank the JAXA and ERSDAC. The PALSAR scenes obtained from JAXA were provided by the CReSOS, Udayana University. We used the browser archives maintained by the ERSDAC. This research was supported by the Beasiswa Unggulan, Bureau for Planning and International Cooperation, Ministry of National Education and Culture of the Republic of Indonesia and from RFBR project 11-05-ophi-m-2011

References

Alpers, W. (1985). Theory of radar imaging of internal waves. *Nature, 314*, 245-247. http://dx.doi.org/10.1038/314245a0

Arief, D., & Murray, S. P. (1996). Low frequency fluctuations in the Indonesian through Lombok Strait. *J. Geophys. Res., 101*(C5), 12455-12464. http://dx.doi.org/10.1029/96JC00051

Chen, C. Yuan. (2012). A critical review of internal wave dynamics. Part 1 - Remote sensing and in-situ observations. *Journal of Vibration and Control, 18*(3), 417-436. http://dx.doi.org/10.1177/1077546310395971

England, M. H., & Huang, F. (2005). On the interannual variability of the Indonesian Throughflow and its linkage with ENSO. *J. Climate, 18*(9), 1435-1444. http://dx.doi.org/10.1175/JCLI3322.1

Jackson, C. R. (2007). Internal wave detection using the Moderate Resolution Imaging Spectroradiometer (MODIS), *J. Geophys. Res., 112*(C11012), 13.

Jackson, C. R., & Apel, J. R. (eds) (2004). Synthetic Aperture Radar (SAR) Marine User's Manual, NOAA NESDIS Office of Research and Applications, Washington DC.

Karang, I. W. G. A., & Nishio, F. (2011). Internal waves in the Lombok Strait revealed by ALOS PALSAR images. Proc. *IEEE Intern Geosci.Remote Sensing Symp. IGARSS 2011*. Vancouver, Canada. pp. 253-256.

Karang, I. W. G. A., Nishio, F., & Osawa, T. (2010). Estimation of tidal energy dissipation and vertical diffusivity in the Indonesian seas. *Int. J. Remote Sens. Earth Sci., 7*, 53-72.

Matthews, J. P., H. Aiki, S. Masuda, T. Awaji, & Y. Ishikawa. (2011). Monsoon regulation of Lombok Strait internal waves. *J. Geophys. Res., 116*(C05007), 14.

Mitnik, L. M. (2006). Dynamic phenomena in the Lombok Strait and surrounding waters: imprints on ERS and Envisat SAR images. *Earth Observations and Remote Sensing (Issledovanie Zemli iz Kosmosa), 6*, 83-92. (in Russian).

Mitnik, L. M. (2008). Advanced Land Observing Satellite PALSAR observations of the oceanic dynamic phenomena in the coastal zone.Proc. *IEEE Intern Geosci.Remote Sensing Symp. IGARSS 2008.* Boston, Ma, USA.

Mitnik, L., & W. Alpers. (2000). Sea surface circulation through the Lombok Strait studied by ERS SAR. Pp. 313–317 in *Proceedings of the 5th Pacific Ocean Remote Sensing Conference (PORSEC 2000)*, Vol. I, 5-8. Dec 2000, Goa, India.

Mitnik, L., W. Alpers, & H. Lim. (2000). Thermal plumes and internal solitary waves generated in the Lombok Strait studied by ERS SAR. Pp. 1-9 in ERS-Envisat Symposium: Looking down to Earth in the New Millenium, 16-20 October 2000. Gothenburg, Sweden. SP-461. European Space Agency, Publication Division, Noordwijk, The Netherlands.

Murray, S. P., & D. Arief. (1988). Throughflow into the Indian Ocean through the Lombok Strait, January 1985-January 1986. *Nature, 333*, 444-447. http://dx.doi.org/10.1038/333444a0

Murray, S. P., Arief, D., Kindle, J. C., & Hurlburt, H. E. (1990). Characteristics of circulation in an Indonesian Archipelago strait from hydrography, current measurements and modelings results. *Physical Oceanography of Sea Strait, 318*, 3-23.

Nemoto, Y., Nishio, H., Ono, M., Mizutamari, H., Nishioka, K., & Tanaka, K. (1991). Japanese earth resources satellite-1 synthetic aperture radar. *Proc. IEEE, 79*, 800-809. http://dx.doi.org/10.1109/5.90159

Ningsih, N. S., Rachmayani, R. Hadi, S., & Brodjonegoro, I. S. (2008). Internal waves dynamics in the Lombok Strait studied by numerical model. *Int. J. Remote Sens. Earth Sci., 5*, 17-33.

Robertson, R., & Ffield, A. (2005). M_2 baroclinic tides in the Indonesian seas. *Oceanography, 18*(4), 62-73. http://dx.doi.org/10.5670/oceanog.2005.06

Schiller, A. (2004). Effects of explicit tidal forcing in an OGCM on the water-mass structure and circulation in the Indonesian throughflow region. *Ocean Modeling, 6*, 31-49. http://dx.doi.org/10.1016/S1463-5003(02)00057-4

Shimada, M. (2002). User's Guide to NASDA's SAR Products Ver. 3 (NDX-000291). National Space Development Agency of Japan, Tokyo-To, Japan.

Susanto, R. D., Mitnik, L., & Zheng, Q. (2005). Ocean Internal Waves Observed in the Lombok Straits. *Journal of Oceanography, 18*(4).

Earth Science Research; Vol. 1, No. 2; 2012
ISSN 1927-0542 E-ISSN 1927-0550
Published by Canadian Center of Science and Education

Liquefaction Potential Variations Influenced by Building Constructions

Behnam Rahrou Khatibi[1], Mehdi Hosseinzadeh Sutubadi[1] & Gholam Moradi[1]

[1] Department of Civil Engineering, University of Tabriz, Tabriz, Iran

Correspondence: Behnam Rahrou Khatibi, Department of Civil Engineering, University of Tabriz, Iran. E-mail: behnam.rahro@gmail.com

Received: January 13, 2012 Accepted: January 29, 2012 Online Published: May 24, 2012

doi:10.5539/esr.v1n2p23 URL: http://dx.doi.org/10.5539/esr.v1n2p23

Abstract

In this paper, a sand deposit with liquefaction potential was simulated in *FLAC* using Finn constitutive model. Equivalent loads of 5, 10, 15 and 20-story buildings were applied to the deposit. As a cyclic loading, acceleration time history of Bam earthquake was used. To examine pore water pressure variations in the soil mass during the earthquake loading, parameter r_u (pore water pressure ration, which equals pore water pressure increment divided by the initial mean effective stress in the soil mass) was defined for the software by a Fish function. Static analyses show that by increasing the applied loading due to building construction, the values of effective and shear stress increase and it generally can be a factor to influence liquefaction potential. Furthermore, dynamic analyses show that there is a shallow longitudinal area beneath 15 and 20-story buildings in which liquefaction potential increases due to high confining effective stress.

Keywords: liquefaction potential, FLAC, pore water pressure ratio, standard penetration test, Finn constitutive model

1. Introduction

When saturated sandy soils are loaded by earthquake shaking, pore water pressure in the soil mass starts to progressively build-up leading to loss of soil shear strength. Liquefaction is the main consequence of this phenomenon. At the occurrence of soil liquefaction, the effective stress in the soil mass becomes zero and pore water pressure in the soil becomes equal to the initial static effective stress.

Most of the time, liquefaction phenomenon occurs at loose saturated sandy soils situated on regions which are prone to having earthquakes. When a saturated loose sand deposit is subjected to earthquake shaking, applied shear stress on the soil mass leads to reduce the volume of the soil mass and because the soil mass is saturated, this tendency to reduction of volume leads to an increase in pore water pressure. In these cases during dynamic loading, pore water pressure in the soil mass starts to progressively build-up and effective stress inclines to zero and the soil mass shows semi-liquid behavior and does not have enough shear strength.

A parameter named r_u (pore water pressure ratio) can be defined for examination of this process, equals the pore water pressure increment divided by the initial static mean effective stress in the soil. During cyclic loading in the loose saturated sandy soil, pore water pressure starts to progressively build-up and shear strain of the soil mass progressively increases and parameter r_u inclines to 1.0. In this situation, the soil mass might experience maximum shear strains and deformations because there is not enough shear strength.

Recently, some researchers have done examinations about the influence of external loading (such as building and embankments) on liquefaction potential. Most of the researches are classified in two major categories; the influence of building constructions on i) soil properties and ii) liquefaction potential, and they are discussed in the next part of the introduction.

1.1 The Influence of Building Constructions on Soil Properties

Rollins and Seed (1990) introduced three factors to evaluate the effect of overburden pressure on liquefaction potential. These factors are static shear stress, effective confining pressure and over consolidated ratio (OCR).

1.1.1 Initial Shear Stress

Overburden pressure and slope situation may induce anisotropy consolidated condition and cause initial static shear stress in the soil mass. According to related studies, static shear stress may affect soil liquefaction potential directly. Lee and Seed (1967) indicated that the liquefaction resistance of soil increases by increase of static

shear stress. Increase of initial static shear stress in the soil mass may lead to increase of soil settlement and compression and subsequently, it leads to increase of Cyclic Resistant Ratio (CRR).

$$CRR = \frac{\tau_{cy}}{\sigma'_{v0}} \quad (1)$$

where: τ_{cy}= cyclic shear strength, σ'_{v0}= vertical effective stress.

1.1.2 Effective Confining Pressure

Using the results of dynamic tri-axial testing, Peacock and Seed (1968) indicated that cyclic shear stress increases by increase of effective confining pressure, but Cyclic Resistance Ratio (CRR) is contrary. Mulilis et al. (1975) denoted that Cyclic Resistance Ratio (CRR) may slightly decrease by increase of effective confining pressure. Hynes and Olsen (1998) concluded that several factors such as method of deposition, stress history, aging effects and density may affect the influence of confining stress variations on the CRR.

1.1.3 Over-consolidation Ratio (OCR)

According to related studies, over-consolidation state is an important effect for soil liquefaction potential. If a soil mass has experienced stresses higher than its current state, it is an over-consolidated soil (OCR>1).

$$OCR = \frac{p_c}{p_0} \quad (2)$$

where: p_c=over consolidation stress, p_0=current existing stress.

Seed and Idriss (1971) showed that the liquefaction resistance increases by increase of the OCR values. Using cyclic torsion shear test, Ishihara and Takatsu (1979) showed the relations between OCR, K_0 and cyclic shear strength. As shown in their results, under constant K_0, the cyclic stress ratio increases by increase of the OCR value.

1.2 The Influence of Building Constructions on Liquefaction Potential

Using shaking table tests facilitates, Yoshimi and Tokimatsu (1978) denoted that soil liquefaction strength decreases beneath the building and liquefaction potential becomes more in this region. Whitman and Lambe (1986) also concluded the similar results by centrifuge model tests. Lopez and Modaressi (2008) preformed a numerical modeling about this issue and indicated that the pore water pressure distribution at the end of the earthquake motion is modified by the presence of the structure, even if the soil profile is far from it.

This study is about a general model ground and it is tried to determine the influence of building construction on liquefaction potential and consider pore water pressure distribution in the soil mass. For this aim, a sand deposit with liquefaction potential was simulated in *FLAC* using Finn constitutive model. Finn model unifies equations represented by Martin et al. (1975) and Byrne (1991) into the standard Mohr-Coulomb plasticity model. Parameter $(N_1)_{60}$ is the main factor for Byrne (1991) formula, so in the present study some parameters required for the Mohr-Coulomb plasticity model were defined for the program by equations which relate them with $(N_1)_{60}$. Considering effect of building construction on liquefaction potential, equivalent loads of 5, 10, 15 and 20-story buildings were applied to the deposit. Furthermore, as a cyclic loading, acceleration time history of Bam earthquake was used.

2. Finn Constitutive Model and Modeling Procedure

In this study, *FLAC* software which is a Finite Difference Method-based program (FDM) was used. According to *FLAC* guidance manual, there are several constitutive models that facilitate soil behaviors under static and dynamic loadings. Calculation of excess pore water pressure in the soil mass due to dynamic loading is the main factor in the modeling process of liquefaction phenomenon. *FLAC* has a constitutive model named Finn model which unifies equations represented by Martin et al. (1975) and Byrne (1991) into the standard Mohr-Coulomb plasticity model. Using this model, it is possible to calculate pore water pressure generation by calculating irrecoverable volumetric strains during dynamic analysis. The void ratio in this model is supposed to be constant, also it can be calculated as a function of volumetric strain and other parameters can be defined by void ratio.

Martin et al. (1975) described initially the effect of cyclic loading on increase of pore water pressure as a result of irrecoverable volume contraction in the soil mass. In these situations, because the matrix of grains and voids is filled by water, the pressure of pore water increases. Later, Byrne (1991) presented a simpler equation which corresponds irrecoverable volume change and engineering shear strain with two constants. In this model, a soil mass with liquefaction potential was modeled using $(N_1)_{60}$ parameter as a main factor to the Finn model, so all of the soil properties needed for the model were defined for the program by $(N_1)_{60}$.

2.1 Definition of Soil Mass and Mesh Model

In this study, the soil profile consists of two types: First type was assumed with 30 m height saturated loose sand and second type of the soil was assumed with 2 m height dry and relatively dense sand that overlies the loose sand, so water level is at depth of 2 m from the surface. Defining dense upper layer helps the model to be close to reality. Furthermore, the length of soil mass was assumed 400 m (how this length is selected will be discussed later). According to Figure 1, grid size in the middle region of this mesh was selected finer enough to satisfy the analysis exactness and equivalent load of the building was imposed on this area to examine the effect of it on liquefaction potential of the soil deposit.

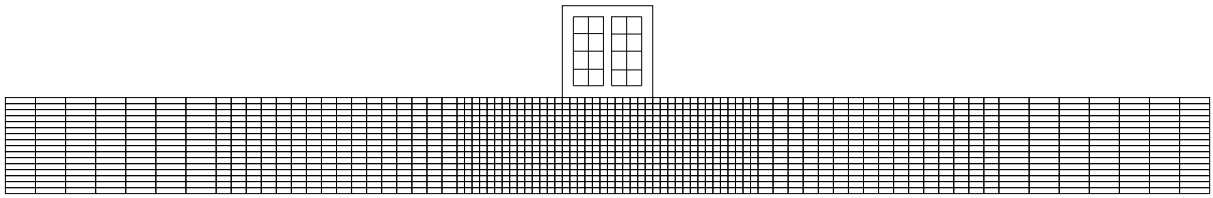

Figure 1. Physical schema of the soil mass mesh and location of loaded area

3. Imported Numerical Quantities for the Soil Mass

For the soil materials, based on the state of sandy soil density it was tried to define properties of materials according to their weight-volume relationships.

According to the Fish function written in *FLAC* program, for definition of liquefaction properties, Byrne (1991) formula was used.

$$\frac{\Delta\epsilon_{vd}}{\gamma} = C_1 \exp\left(-C_2\left(\frac{\epsilon_{vd}}{\gamma}\right)\right) \tag{3}$$

where: $\Delta\epsilon_{vd}$ is the increment of volume decrease and γ is cyclic shear-strain amplitude. This equation has two constants C_1 and C_2. Byrne (1991) notes that the constant, C_1, can be derived from normalized standard penetration test values, $(N_1)_{60}$,

$$C_1 = 8.7(N_1)_{60}^{-1.25} \tag{4}$$

C_2 is then calculated from $C_2 = 0.4/C_1$.

For determining the relative density (D_r) by $(N_1)_{60}$, Idriss and Boulanger (2004) was used

$$D_r = \sqrt{(N_1)_{60}/46} \tag{5}$$

According to ASTM-D2040 we determined e_{max} and e_{min} for several sandy soil specimens and the average values of them were: e_{max}=0.8 and e_{min}=0.25, so the quantity of "*e*" for each state of relative density according to Equation (6) was calculated.

$$D_r = (e\_max - e)/(e\_max - e\_min) \tag{6}$$

The values of "*e*" for each $(N_1)_{60}$ values can be calculated.

Table 1 summarizes above-mentioned soil properties.

Table 1. Numerical values of soil properties for the model

Soil condensation	Loose soil	Medium dense soil	Overlaid soil
$(N_1)_{60}$	8	15	30
D_r	0.417	0.571	0.81
γ_d (kN/m^3)	17	18	19.6
γ_{sat} (kN/m^3)	20	20.5	22.2
e	0.570	0.485	0.354

As mentioned in introduction, to examine the pore water pressure variations in the soil mass during the earthquake loading, the parameter r_u was defined for the software by a Fish function. Theoretically, if r_u inclines to 1.0, effective stress inclines to zero and liquefaction should occur. But r_u=1.0 is only theoretical definition for liquefaction occurrence. To make a valid comparison between in situ and laboratory pore pressure responses, Hazirbaba and Rathje (2004) carried out series of strain controlled- undrained cyclic simple shear tests on the soils which have same situations in the field. Results of the pore pressure generation show a smooth progressive pattern until the pore pressure ration reaches the value of about 0.9 and liquefaction occurs in that point. Therefore, lower boundary of r_u values which define liquefaction occurrence is 0.9 and if r_u reaches a value greater than 0.9 it is assumed that liquefaction happens.

3.1 Initial Conditions and Boundary Condition

The base boundary of the model was fixed along horizontal and vertical directions in both static and dynamic analyses. Right and left boundaries of the mesh were horizontally fixed for static analysis. In dynamic analyses, enough distance between the structure and right and left boundaries should be considered to prevent the reflection of waves contacting the boundaries. Choosing adequate dimensions for the model plays an important role in modeling process. For this aim, the length of mess was assumed 400m by trial and error method (data are not shown).

In *FLAC*, the dynamic input can be applied in one of the following ways: (a) an acceleration history; (b) a velocity history; (c) a stress (or pressure) history; or (d) a force history. In this study, for applying earthquake loading, acceleration time history of Bam earthquake with magnitude M=6.5 and maximum acceleration a_{max}=0.42 g was used. Duration of earthquake was chosen 37 seconds.

3.2 External Loading

Assuming both building and its foundation loading equal to 20 kPa per each m^2 for each story of building, numerical values of extended load applied to the soil surface for each above mentioned buildings are according to Table 2.

Table 2. Numerical values of applied extended loads for the model

Number of building stories	5	10	15	20
Equivalent load (kPa)	100	200	300	400

4. Results and Discussions

4.1 Examination of Results Due to Building Load on Soil Properties after Static Analysis

4.1.1 Shear Stress Distribution in the Soil Profile

In this stage, building construction loads were applied to loose sand with $(N_1)_{60}$=8 and medium dense sand with $(N_1)_{60}$=15. Figure 2 shows shear stress contours after applying static loading under 20-story building in soil with $(N_1)_{60}$=8. According to this figure, the values of shear stress start to expand from two edges of buildings and the influence of shear stress becomes wider by depth. The influence of shear stress distribution under the foundation due to weight of the building and its effect on liquefaction potential will be discussed.

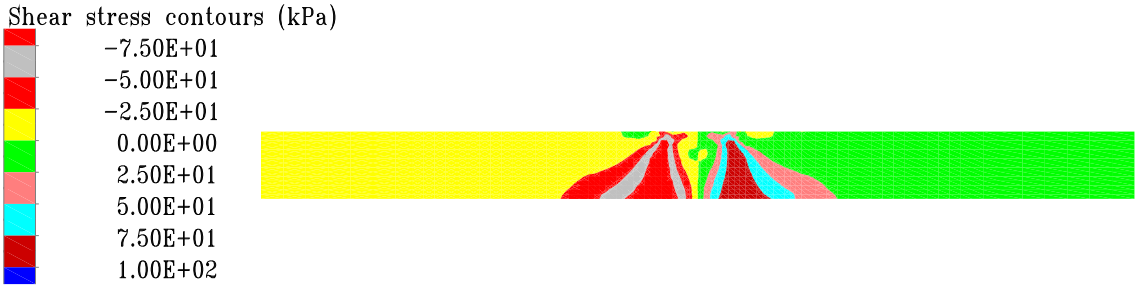

Figure 2. Shear stress distribution under 20-story building in soil with $(N_1)_{60}$=8

4.1.2 Confining Effective Stress Distribution in the Soil Profile

Figure 3 from top to bottom, shows confining effective stress contours in case $(N_1)_{60}$=8 related to 5-story building (Part(A)), 10-story building (Part (B)), 15-story building (Part (C)), 20-story building (Part (D)), respectively. According to Figure 3, parts C and D, applying heavy loads on the soil mass can lead to stress concentration on the edges of loaded area and increase of initial confining effective stress in this region. This process may lead to increase in growth potential of ΔU values in equation $r_u = \Delta U / \acute{\sigma}_0$ and therefore, liquefaction potential in the regions near foundation of tall buildings may increase.

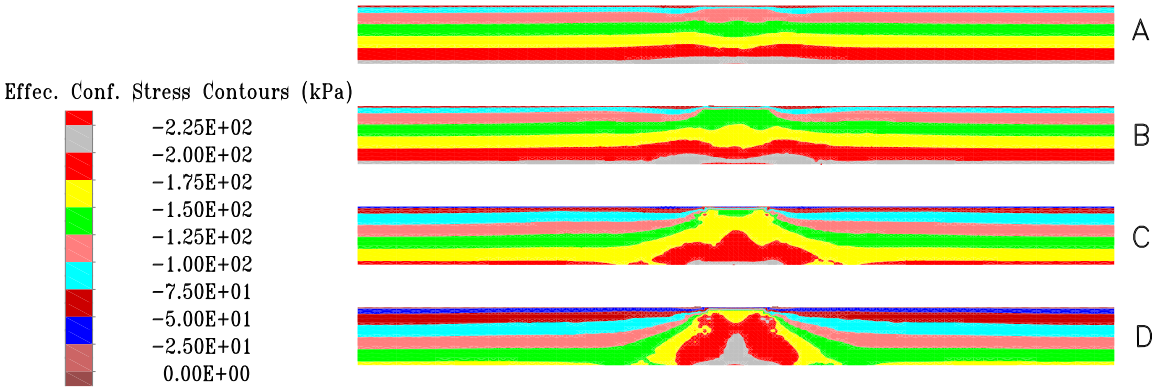

Figure 3. Confining effective stress contours in case $(N_1)_{60}$=8 before dynamic analyses

As described in the introduction, according to previous works preformed by several researchers, the influence of shear stress distribution and confining effective stress on liquefaction potential is contrary. Increase of these two parameters in the soil mass may affect the liquefaction resistance.

4.2 Examination of Results after Dynamic Analysis

After static analyses, as a dynamic loading, acceleration time history of Bam earthquake was applied into the model. Figures 4 and 5, from top to bottom, show maximum values of r_u related to 5-story building (Part(A)), 10-story building (Part (B)), 15-story building (Part (C)), 20-story building (Part (D)), respectively.

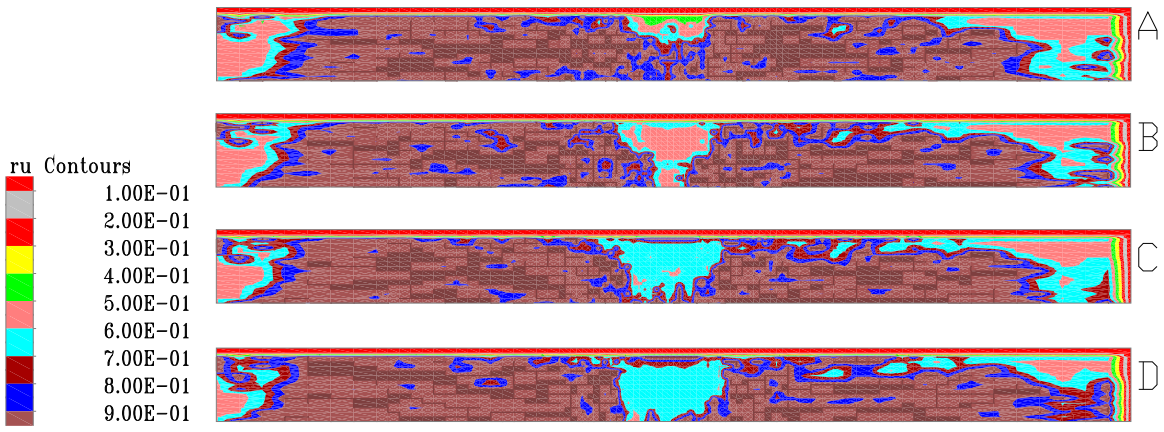

Figure 4. Maximum values of r_u in loose sand at presence of building loads induced by dynamic loading

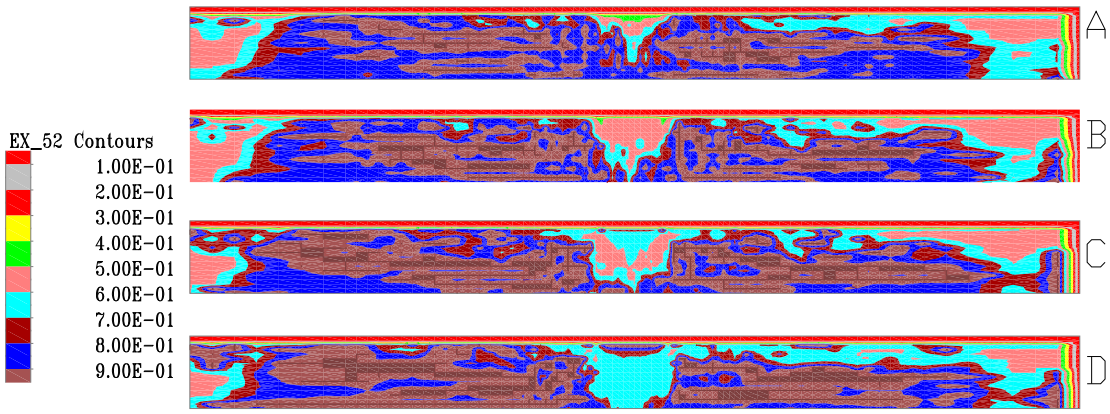

Figure 5. Maximum values of r_u in medium dense sand at presence of building loads induced by dynamic loading

According to Figures 4 and 5 in all cases, in general, construction loading leads to reduce maximum values of r_u in the underlying deposits. The main reason of this result is the influence of applied loading on the soil mass and increase of effective stress in the soil deposit before earthquake loading. This loading leads to an increase in both relative density and shear stress values in the soil mass. Also it can be seen that by increase of external loading values, safe area (regarding to occurrence of liquefaction phenomenon) becomes larger. Therefore, occurrence of liquefaction phenomenon under buildings is generally cancelled.

4.3. Discussion

According to Figures 4 and 5, building construction can be a reduction factor of liquefaction potential in the soil mass, but under 15 and 20-story buildings (parts C and D), there is a shallow longitudinal region under loaded area (marked by dark blue) in which the maximum values of r_u reach about 0.8 to 0.9. In this region, amount of effective stress increment due to external loading theoretically inclines to the overburden value. In this case, it should be elaborated that a change in soil mass mechanism is occurred and soil liquefaction strength (or CRR) decreases significantly beneath the building. The main reason of this phenomenon might be confining pressure built-up in upper layers due to heavy overburden pressure.

The influence of shear stress distribution and effective confining stress on liquefaction potential is inverse, so considering Figures 2 to 5, increase of liquefaction potential in upper layers due to higher confining stresses is dominant than decrease of liquefaction potential due to shear stress distribution in this layer and therefore, maximum values of r_u are close to 0.9 and liquefaction probability beneath tall buildings becomes more. Conversely, decrease of liquefaction potential in lower layers due to shear stress distribution is dominant than increase of liquefaction potential due to higher confining stresses and therefore, probability of liquefaction occurrence in lower layers of the soil mass becomes less.

5. Conclusions

Based on numerical results, the following conclusions can be obtained.

1). Results show that by increasing the applied loading due to building construction, the values of effective confining and shear stress in the soil mass increase and it generally can be a factor to influence liquefaction potential in the deposit. In general, overburden pressure due to building construction leads to reduction in maximum values of r_u in the underlying deposits.

2). One of the other effective factors about liquefaction phenomenon is generation of effective confining stress in the soil mass situated under loaded area with high overburden pressure. Due to external loading, the value of excess effective stress in upper layers inclines theoretically to the applied overburden loading. The increase of effective confining stress in this region may lead to an increase in growth potential of ΔU in upper layers. The increase of ΔU in equation $r_u = \Delta U / \acute{\sigma}_0$ may lead to an increase in r_{umax} values and therefore liquefaction potential in upper layers is high.

3). Generally, the stress concentration and high effective confining stress in upper layers of the soil mass can be named as the factors to increase of liquefaction potential due to building construction. Construction of tall buildings on the alluvium applies heavy load into the soil and changes soil mechanism due to stress concentration on two sides of loaded area. Therefore, liquefaction potential in the regions near foundation of building increases.

References

Byrne, P. (1991). A cyclic shear-volume coupling and pore-pressure model for sand. *Second International Conference on Recent Advances in Geotechnical Earthquake Engineering and Soil Dynamics. St. Louis, Missouri, 1*(24), 47-55.

Hazirbaba, K., & Rathje, E. M. (2004). A comparison between in situ and laboratory measurements of pore water pressure generation. *13th World Conference on Earthquake Engineering*, Vancouver, B. C., Canada, Paper No. 1220.

Hynes, M. E., & Olsen, R. (1998). Influence of confining stress on liquefaction resistance. *Proceedings of International Symposium on the Physics and Mechanics of Liquefaction*, Balkema, pp. 145-152.

Idriss, I. M., & Boulanger, R. W. (2004). Semi-empirical procedures for evaluating liquefaction potential during earthquakes. *Proceedings of the 11th International Conference on Soil Dynamics & Earthquake Engineering & 3rd International Conference on Earthquake Geotechnical Engineering.* Berkeley, California, pp. 32-56.

Ishihara, K., & Takatsu, H. (1979). Effects of over-consolidation and K_0 conditions on the liquefaction characteristics of sands. *Journal of Soils and Foundations, Japanese Society of Soil Mechanics and Foundations Engineering, 19*(4), 59-68.

Itasca Consulting Group Inc. (2000). FLAC manual, version 4.0. *Itasca Consulting Group Inc.,* Minneapolis, Minn.

Lee, K. L., & Seed, H. B. (1967). Cyclic stress conditions causing liquefaction of sand. *Journal of the Soil Mechanics and Foundations Engineering Division ASCE, 93*(1), 47-70.

Lopez, C. F., & Modaressi, F. R. A. (2008). Numerical simulation of liquefaction effects on seismic SSI. *Journal of Soil Dynamics and Earthquake Engineering, 28*(2), 85-98. http://dx.doi.org/10.1016/j.soildyn.2007.05.006

Martin, G. R., Finn, W. D. L., & Seed, H. B. (1975). Fundamentals of liquefaction under cyclic loading. *Journal of Geotechnic Division ASCE, 101*(5), 423-438.

Mulilis, J. P., Chan, C. K., & Seed, H. B. (1975). *The effects of method of sample preparation on the cyclic stress strain behavior of sands.* Environmental Engineering Research Council, Report No. 75-18.

Peacock, W. H. & Seed, H. B. (1968). Sand liquefaction under cyclic loading simple shear conditions. *Journal of Soil Mechanics and Foundations Engineering Division ASCE, 94*(3), 689-708.

Rollins, K. M., & Seed, H. B. (1990). Influence of building on potential liquefaction damage. *Journal of Soil Mechanics and Foundations Engineering Division ASCE, 116*(2), 165-185.

Seed, H. B., & Idriss, I. M. (1971). Simplified procedure for evaluating soil liquefaction potential. *Journal of Geotechnic Division ASCE, 97*(9), 1249-1273.

Whitman, R. V., & Lambe, P. C. (1986). Effect of boundary conditions upon centrifuge experiments using ground motion simulation. *Geotechnical Testing Journal, 9*(2), 61-71. http://dx.doi.org/10.1520/GTJ11031J

Yoshimi, Y., & Tokimatsu, K. (1978). Liquefaction of sand near structure during earthquake. *Proceeding Of the 4th Japan Earthquake Engineering Symposium*, Tokyo, pp. 439-446.

Earth Science Research; Vol. 1, No. 2; 2012
ISSN 1927-0542 E-ISSN 1927-0550
Published by Canadian Center of Science and Education

Factual Revelation of Temporal and Spatial Hierarchical Correlations by Structural Function Curvature Analysis Method

Grigory V. Vstovsky[1]

[1] "Energoavtomatika" Ltd., Moscow, Russia

Correspondence: Grigory V. Vstovsky, "Energoavtomatika" Ltd., 3/2, Ostapovsky Pr., 109316, Moscow, Russia. Tel: 7-495-981-0136. E-mail: vstovsky@yandex.ru

Received: March 1, 2012 Accepted: March 26, 2012 Online Published: May 24, 2012

doi:10.5539/esr.v1n2p30 URL: http://dx.doi.org/10.5539/esr.v1n2p30

Abstract

Basics of structural function curvature analysis method (SFCAM) are described shortly and three examples of SFCAM application are described: for revelation of earthquake predictors, surface relief analysis and surface relief evolution description. Discussion is carried out in terms of correlation times (CT) or correlation lengths (CL), respectively to the type of experimental data – time series or surface reliefs. CTs or CLs can be taken into account in two ways: by an order of their recognition, from the shortest to the greatest, or by separation over previously determined classes due to physical sense of investigated structure. On the whole, SFCAM represent a subtle enough tool for analysis of complex hierarchical systems.

Keywords: time series, surface relief, complexity, structural function, correlation time, correlation length

1. Introduction

This short review is to represent a new perspective tool for data processing in Earth's science: time series and surface reliefs. Time series are usually obtained when investigating the earthquakes, volcano activity and other natural phenomena producing vibrations that can be recorded in some digital form and then characterized quantitatively on the base of one or another mathematical apparatus. Surface reliefs are basic data for morphological analysis. They can be also scanned and recorded digitally to be visualized and mathematically processed and described. Most of modern quantitative description techniques for real data lean upon statistical analysis of measured values (the heights, sizes and other local or distributed parameters) giving their maximum, mean and minimum values, standard deviation, etc. – the parameters that can be easily calculated, but giving no information about 'internal structure" of the investigated object represented by the data under analysis. Meanwhile, all the real systems have, as a rule, highly organized hierarchical structures with internal correlations in time and space. And evolution of such systems, first of all, shows itself in changes and alterations of these correlations. A lot of general information on these topics can be found elsewhere, for example, Timashev (2011), where the basics of a so called Flicker Noise Spectroscopy (FNS) are described, from which the ideas described in this paper had grown.

Structural function curvature analysis method (SFCAM) offers a new tool of quantitative description of complex natural systems in terms of hierarchy of correlation times or lengths (CT, CL), first proposed in (Vstovsky, 2006). Of course, these values can't be calculated exactly for real "living" systems and we have to apply statistical methods to evaluate CTs and CLs, but these are statistics of hierarchy parameters. All these features are described below. First, the basic mathematical procedure is described, as shortly and simply as possible, applied to single series processing. Then application to time series analysis is described for revelation of earthquake precursor (Bornyakov & Vstovsky, 2010; Vstovsky & Bornyakov, 2010). Finally, application of SFCAM to surface relief analysis is demonstrated (Vstovsky, 2006). Surface reliefs, being more complex objects as compared with time series, require the use of additional statistical methods, because relief is treated as the set of spatial series, and one has to process each its series separately and then average out parameters of the series over all the relief. Nevertheless, as is shown below, such a complicated approach can be used even to follow relief evolution (Vstovsky et al., 2006).

2. SFCAM Basics

Structural function (SF) represents an effective tool in theoretical and experimental investigations of chaotic systems and processes, for example, in turbulence investigations (Frisch, 1995). For the series $\{h(t_k)\}$ SF of order p is calculated by formula

$$\Phi^p(\Delta) = \frac{1}{M}\sum_{k=1}^{M}\left|h(t_k) - h(t_k + \Delta)\right|^p , \quad (1)$$

where $h(t)$ – signal value in the series of N samples («points»), signal being given discretely in points (moments) $t_k = k\Delta t$ (Δt – discretization step) along coordinate t, $M = N - \Delta/\Delta t$, Δ - lag (argument) of SF equal to Δt, $2\Delta t$, $3\Delta t$, …, $(N_\Phi)\Delta t$, $N_\Phi = (0.5\text{-}0.8)N$, p – SF order. p=2 is used as a rule and this index will be omitted for this case. Otherwise p value is given explicitly. Figure 1 explains SFCAM. It shows examples of signal piece, its SF (in double logarithmic axes) and corresponding negative second derivative ("curvature") of smoothed double logarithmic SF. Extremuma positions of the latter give evaluations of CTs.

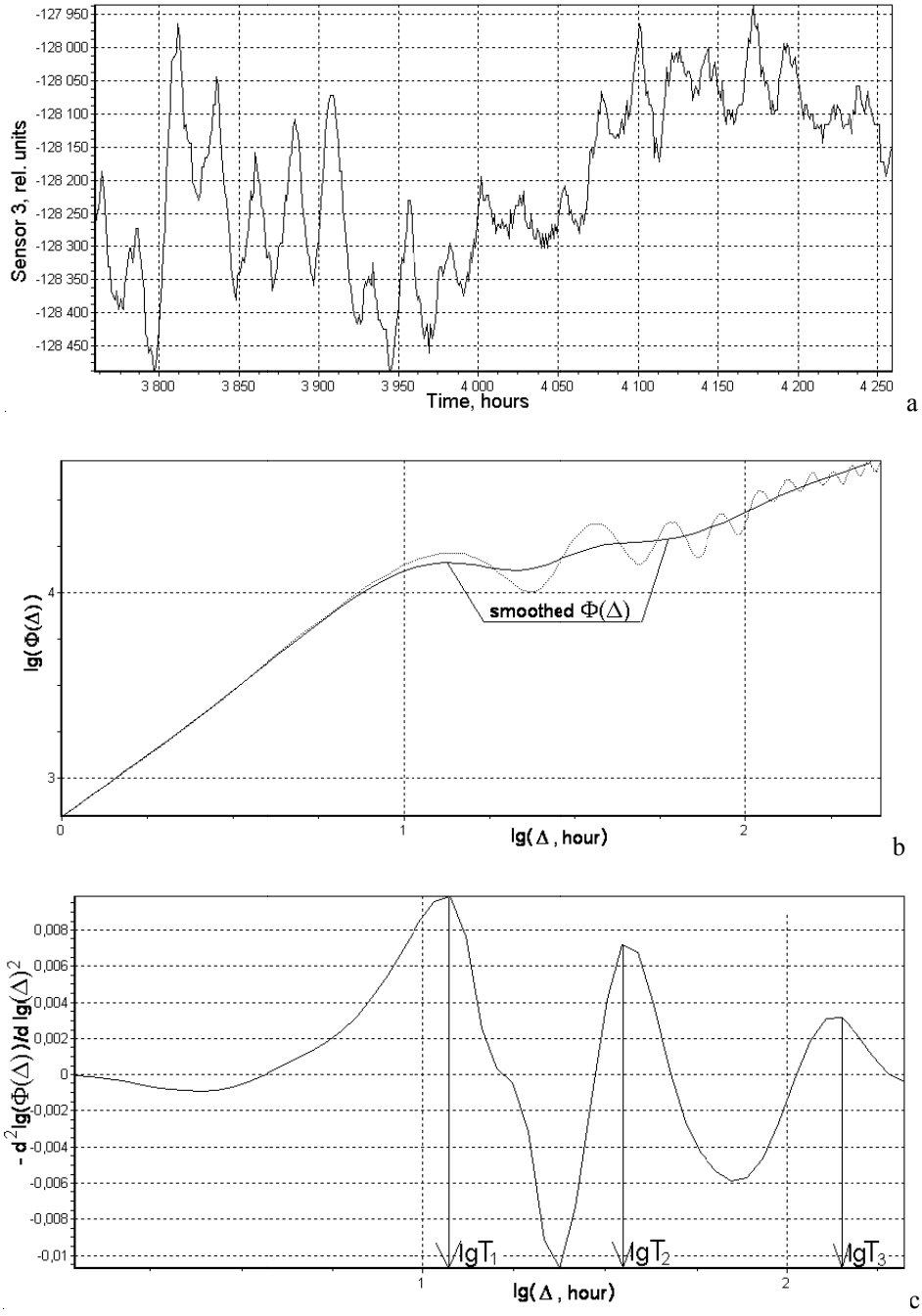

Figure 1. Piece of a signal (a), its double logarithmic SF and smoothed double logarithmic SF (b) and negative second derivative ("curvature") of smoothed double logarithmic SF (c) with indication of extremuma positions

Physical sense of SF is as follows. SF growth for small lags Δ, see Figure 1b, means that there are correlation links, interrelations, in the signal. Cessation of SF growth, saturation, for large lags means a failure (lost) of the interrelations. Conventional boundary of these scale regions (determined by one or another rule or algorithm) is called a correlation time (CT). In the simplest cases, when SF has only one "footstep", there is only one type of interrelation characterized by CT according to "footstep position" which can be determined by position of maximum of negative derivative of smoothed SF (under condition of positive first derivative) that was first proposed in (Vstovsky, 2006). That paper demonstrated effectiveness of such an approach in comparison with many parameter fitness (approximation) of SF. When SF has several "footsteps", corresponding to several different types of interrelations with different CTs, evaluation of SF's negative second derivatives extremuma positions enables to evaluate easily such CTs. So we can evaluate hierarchy of CTs. The case of SF with three "footsteps" is shown in Figure 1b, 1c. CTs are denoted by T_1, T_2, T_3,… starting with the smallest. This is a core of SFCAM.

Since real data are measured with finite accuracy, fluctuations, gaps and with other "defects", the calculated SFs are always imperfect, rough or deviating, one has to calculate CTs by a special multi-step algorithm including operations of reinterpolation of double logarithmic SF, smoothing it and then taking its second derivative. The used algorithms enable also to take into account the presence of data gaps (marked with a specified value) that is unique advance of the procedures used. These algorithms were coded in the program **SHIFT** (Scale Hierarchy Information Fertile Treatment) for time series analysis, and program **sm2FNS** for relief (atomic force microscopy) data processing. The results described below were obtained by these programs.

3. Time Series Processing

Processing of this data type is based on combination of SFCAM and sliding window method (SWM). The latter enables to present dynamical variable series as a sequence of values of one or another parameter calculated for each position of data window of given length. Window time coordinate is a position of its forward boundary. In such a way one can obtain the new time series of calculated parameters ascribing the parameters value to each window coordinate. For example, one can obtain the series of the parameters T_1, T_2, T_3, shown in Figure 1c, by sliding the window (piece), shown in Figure 1a, along a whole series of initial data.

This approach was used in refs (Bornyakov & Vstovsky, 2010; Vstovsky & Bornyakov, 2010; Vstovsky, 2008). The most demonstrative results obtained in such a way are shown in Figures 2, 3, 4. In (Vstovsky & Bornyakov, 2010) the results were reported for revealing the precursors of an intensive South-Biakal earthquake (M=6.3, at 09:31 on 27 August 2008). The logic of CT hierarchy analysis application to earthquake prediction is as follows. It is implied (Vstovsky, 2008) that, as the processes take place on/in the distributed self-organized system, the changes in the state of such a system must influence the course of the local processes. For instance, during the accumulation of deformation in the Earth's crust under external and internal factors, and as a consequence, the rearrangement of the crust space structure, CTs of local deformation processes can change. The registration and adequate interpretation of such changes can be an effective tool for the monitoring of the states of both the separate regions and the lithosphere as a whole to reveal and forecast the transition and critical states in the lithosphere evolution process. Several interesting results were reported in (Bornyakov & Vstovsky, 2010; Vstovsky & Bornyakov, 2010) about South-Biakal earthquake prediction, but the most significant are shown in Figures 2, 3, 4. Earthquake moment is marked with dotted line. CTs obtained with SF of second order, p=2, are shown in Figure 3, and the same values for p=4 (first reported here) are shown in Figure 4. One can see that more or less stable correlations with CTs about T_1=10, T_2=40, T_3=140 hours break apart, CTs decrease in more than 3 times, at 1700 hours (71 days) before the earthquake. Increase in SF order makes the precursor and earthquake indicator sharper.

The results were obtained for hourly data, and calculation time expenses are of order 1 second per one point (or lesser). So, the described mathematical apparatus represents a real tool for (or to be a part of) on-line monitoring of seismic activity, or other Earth crust processes.

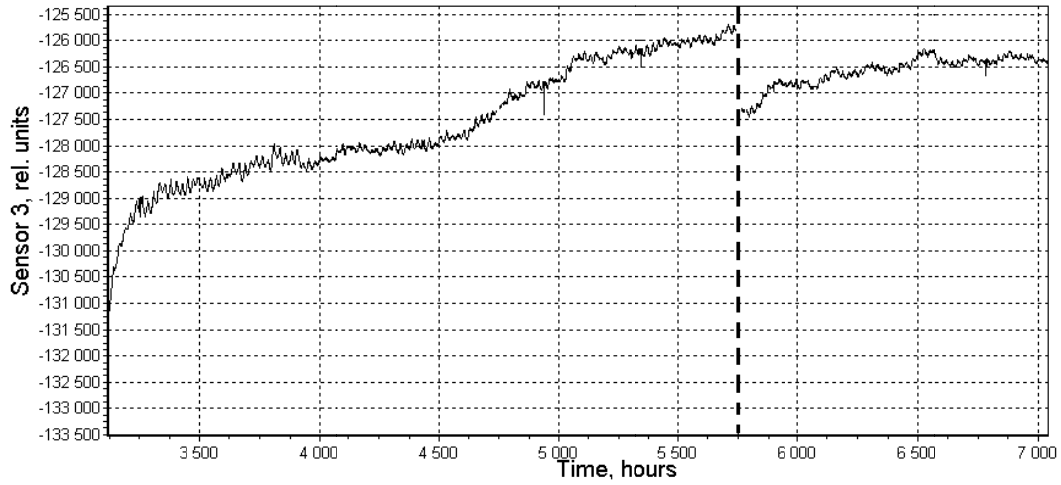

Figure 2. Recoded signal of vertical deformations in marblerock massive adit (Vstovsky & Bornyakov, 2010)

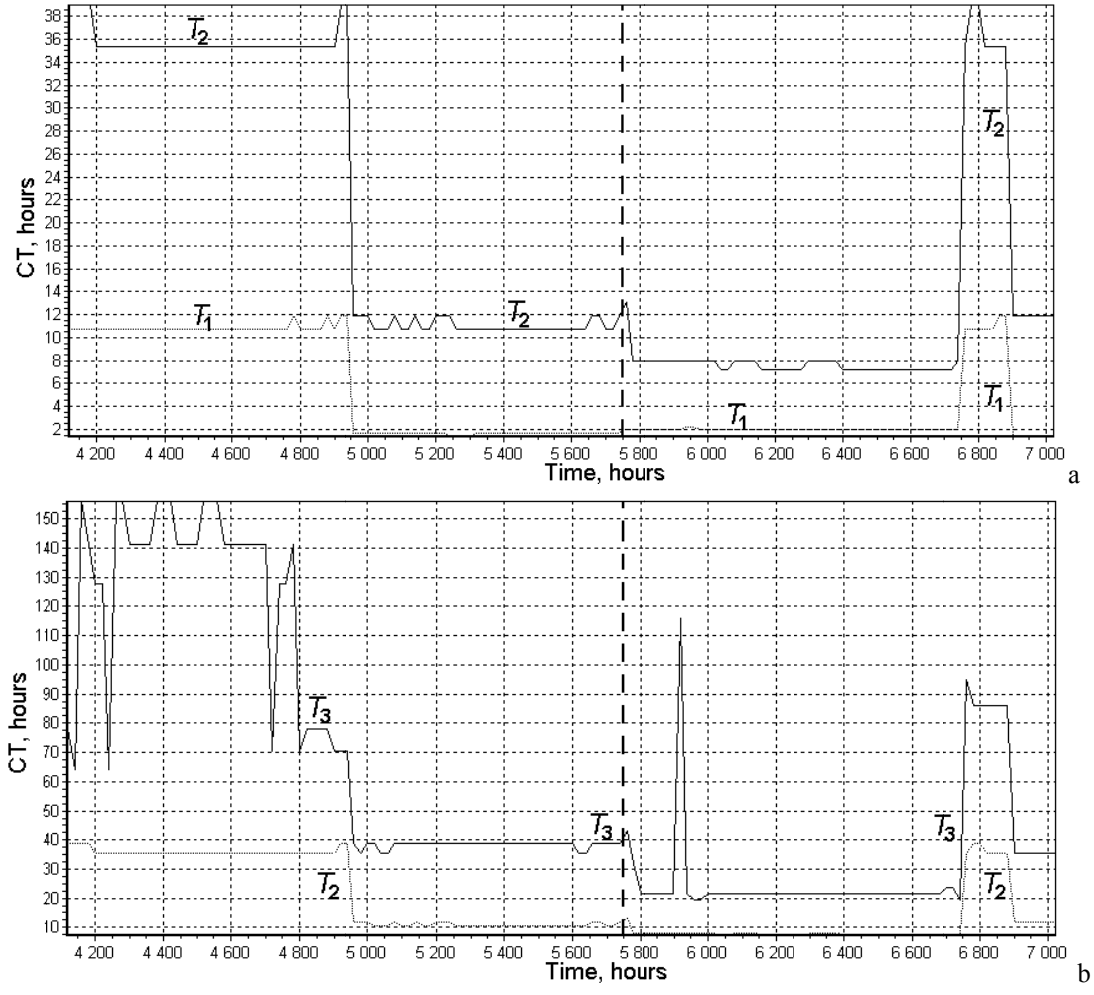

Figure 3. Results of calculation CTs T_1, T_2, T_3 for signal in Figure 2 for SF order p=2 and window size 1000 hours (Vstovsky & Bornyakov, 2010). Earthquake is marked by dotted line

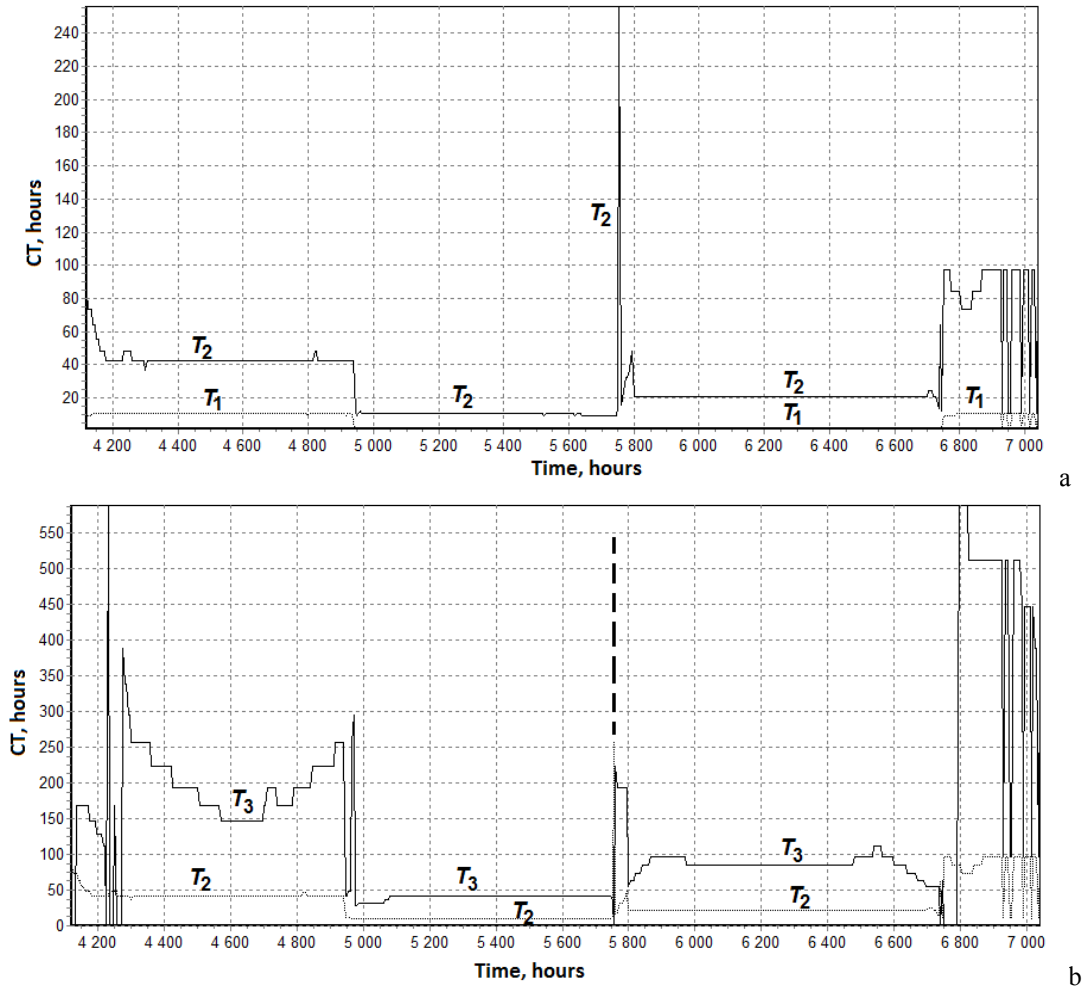

Figure 4. Results of calculation CTs T_1, T_2, T_3 for signal in Figure 2 for SF order p=4 and window size 1000 hours. Earthquake is marked by dotted line

4. Surface Reliefs

Application of SFCAM to relief processing is realized by processing the relief profiles in one or another direction, and following averaging the obtained profile parameters over relief. Two ways of averaging may be used, Figure 5, where "Curves" is for the SF and its negative derivative (other functions can be calculated also, for example, the Fourier power spectra). Below the results obtained by "Way 2" averaging are described.

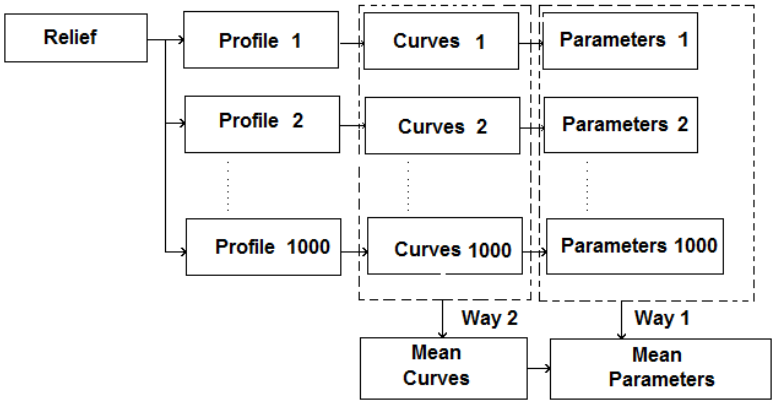

Figure 5. Two ways of obtaining average parameters for processing relief by SFCAM in "profile by profile" mode

This is easily realized for reliefs of 1000x1000 points size or about, and the smaller relief the less reliable CLs values. First application of SFCAM to relief processing was described in ref. (Vstovsky, 2006), where this method was proved to be valid being tried out for model objects with known CL values also. The experiments, described in ref. (Letnikova et al., 2001), were to investigate an influence of hydrogen treatment (by digester at high temperature and pressure) on the dissolution surfaces of LiF monocrystals. A mirror technique was used when monocrystal was cleaved into two pieces with mirror surfaces, then one piece was treated, but the other was kept as a reference sample. Atomic force microscopy (AFM) data (contact mode, 50x50 mcm, 1000x1000 points) were obtained for the samples dissolved in the water at temperatures 25-50 °C.

Typical relief view is shown in Figure 6. Typical views of the "curves" obtained for each relief are shown in Figure 7. These functions were averaged and parameters of average function were used to characterize the relief. More exactly, mean SFs were calculated for each relief and then CLs were obtained from their second derivatives. The arrows, indicating Cls L_1 and L_2 values, are given to explain the method. So, two CLs were revealed, Figure 8.

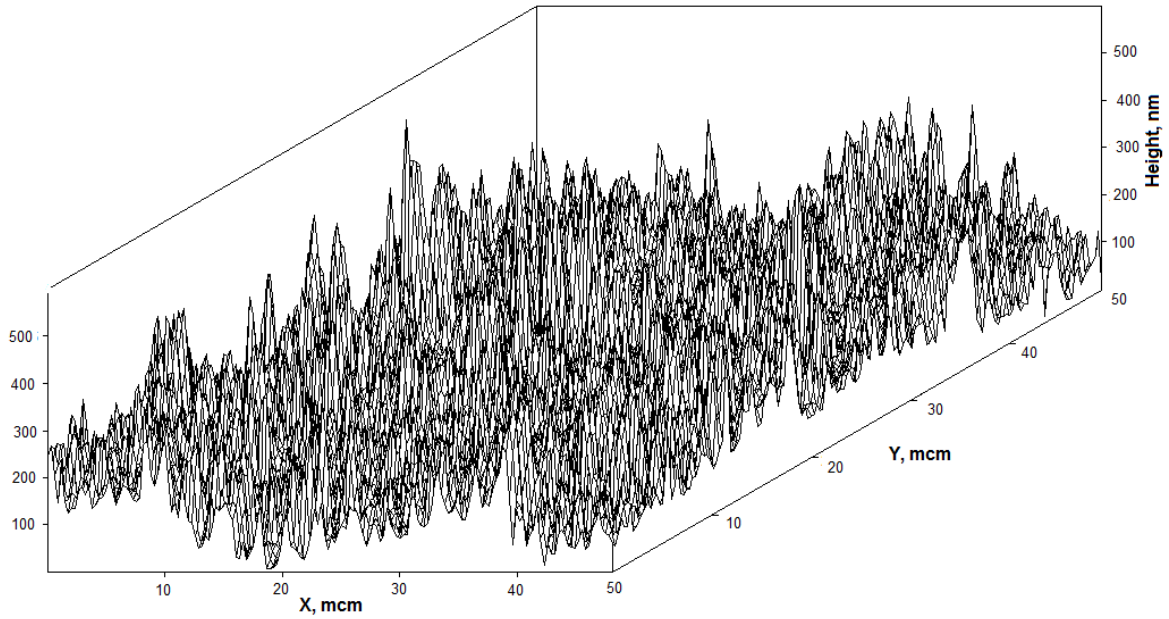

Figure 6. Typical view of LiF dissolution surface AFM relief (Each 6th point is shown for both the directions *x, y*)

The presence of two surface substructures is due to the way of monocrystal surfaces making – by cleavage generating the multiple crystal defects due to shear stresses. CL L_1 (300-800 nm) corresponds to the dislocation lodgments. CL L_2 (10-25 mcm) corresponds to extrusion-intrusion heterogeneities appearing as the "steps" and "crests" on dissolution surfaces (Letnikova et al., 2001). Surface anisotropy is due to the latters. Increase in dissolution temperature diminished effect of hydrogen treatment on extrusion-intrusion heterogeneities.

Thus, SFCAM enables to follow the subtle features of the objects under investigations. Here, this is demonstrated for the structures at micrometer scale, but the very method and its algorithms can be generally applied for processing digital relief data, representing the real objects of any required size or nature, including abstract reliefs, for example, distributions of insect populations, microbiological characteristics, ozone concentration, magnetic field intensity, or whatever else. "Profile-by-profile" application of SFCAM can be applied also to digital 3D distribution data - to reveal anisotropy, for example.

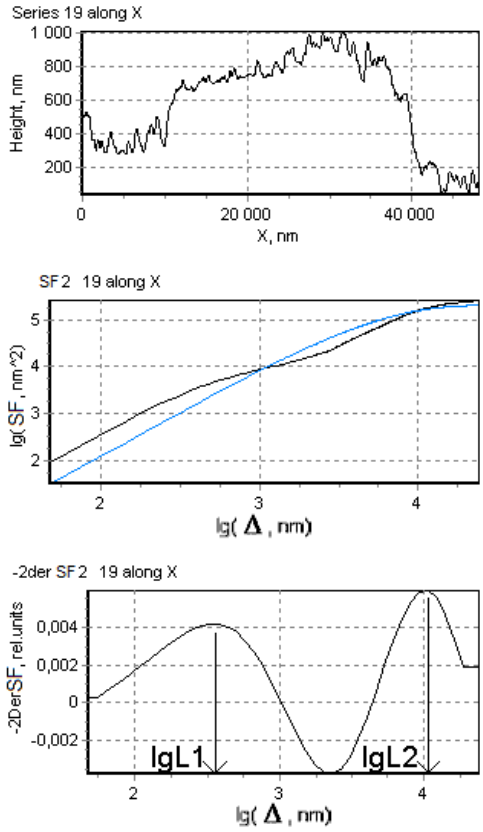

Figure 7. Typical views of SF and its negative second derivative which were calculated for each relief profile

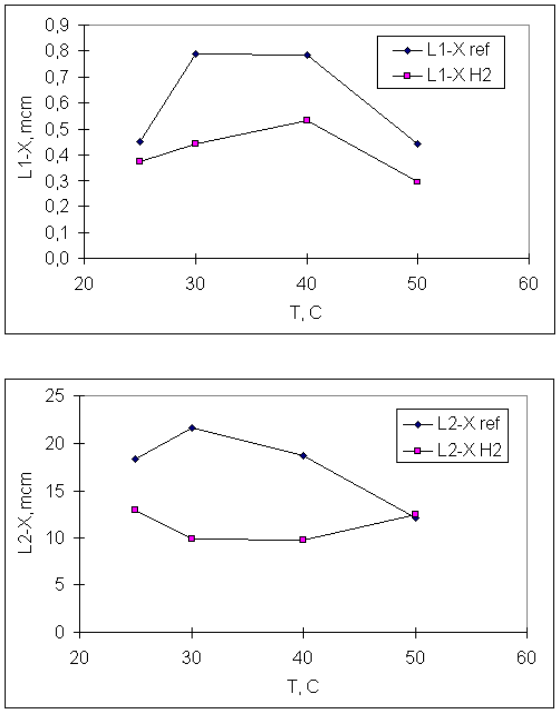

Figure 8. Dependence of CLs L_1 (a) and L_2 (b) on temperature for AFM data of ref. (Letnikova et al., 2001). "ref" (reference) is for initial crystal, "X" is for the direction of picked up profiles. Each value was obtained by SF averaged over 200 randomly picked up profiles and by averaging over 3-5 relief images

5. Surface Relief Evolution by Optical Microscopy Data

Above, the resulted CLs values were taken into account due to the order of their recognition - from the smallest to the greatest. But in some applications one has to analyze CLs statistically by separation them into several classes due to physical sense of CLs appearance. The case of such an approach is described in this section.

In ref. (Vstovsky et al., 2006) the mechanochemical polymer coverings of led shot were subject to fast chemical corrosion tests and their surfaces were investigated by optical microscopy with following data processing on the base of SFCAM. The proposed approach can be used to control the polymer and other coverings (of various geometry) both in laboratory conditions and real exploitation conditions.

The experiments were as follows. The 3 mm led balls were covered with high density polyethylene (HDPE) by mechanochemical method in ball mill, the coverings having grained structure (with about 30 mcm grains) due to the size of initial particles of HDPE dust introduced into the mill to form covering. Covering thickness was 50-100 mcm.

Then covered balls were subject to accelerated chemical tests: the obtained covered balls were put into solution of potassium dichromate in 0.1N hydrochloric acid, that will be referred to as chemical etching below. When covering solidness was destroyed, the insoluble lead chromate was produced, and potassium dichromate concentration decrease enabled to register corrosion process by subtle spectrophotometer method. In this case the effective destruction of coverings was observed after 7 days from tests start.

To conduct optical microscopy investigations, 3-5 balls were withdrawn from chemical solution for 3, 7, 8, 9, 10 days, then 15 730x730 mcm pictures were made with resolution 1024x1024 pixels by digital camera. The size was chosen in such a way to avoid effect of overall ball surface curvature on pixel brightness, and the surface pieces can be considered as plane fragments of rough surfaces. Typical photos are shown in Figure 9. Note, that there are no visual features in the photos that could enable to recognize the differences “by eye”.

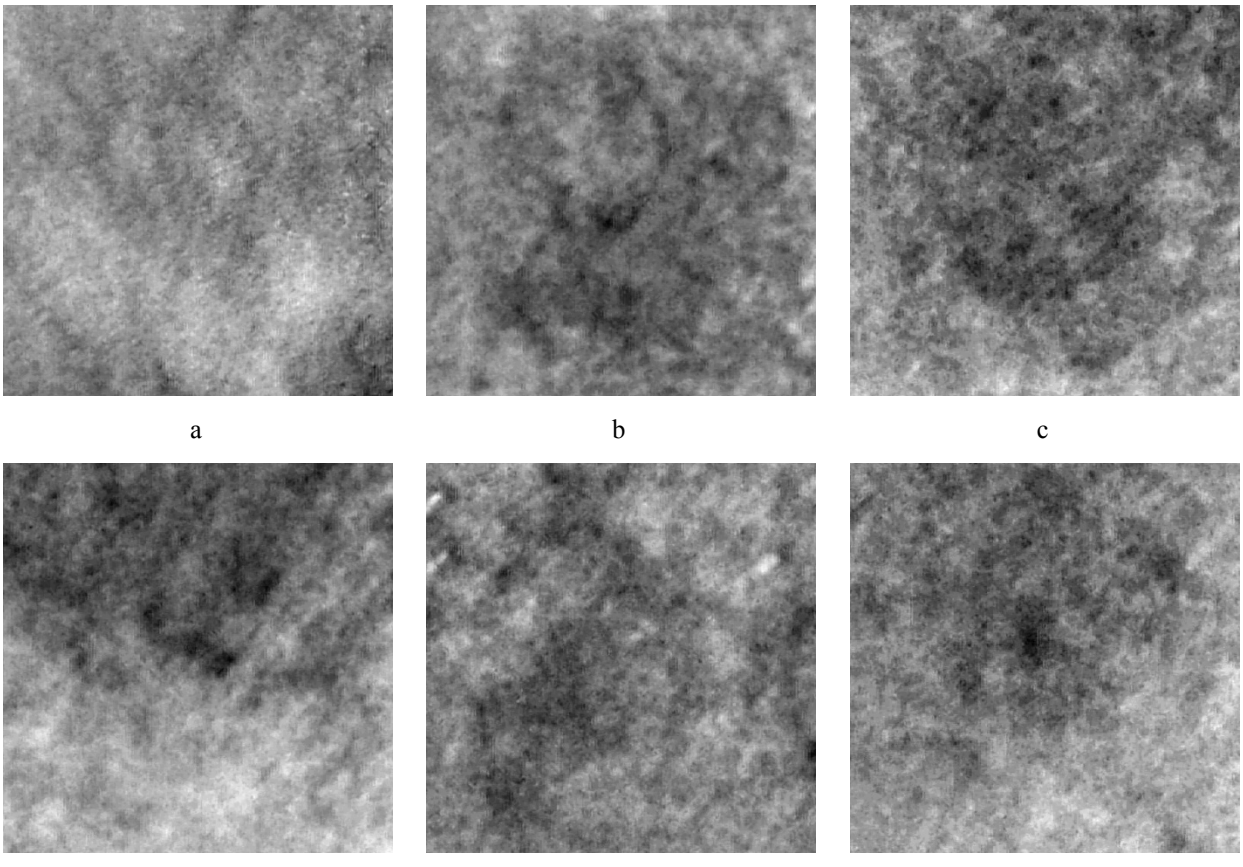

Figure 9. Examples of photos of led ball surface pieces 730x730 mcm: a) initial covering before etching (0 days), b-f) coverings after chemical test during 3, 7, 8, 9 and 10 days, respectively

The photos obtained were processed by a special program **FCP** (Formula for Chaos Processing) which enabled to represent photos as surface reliefs - the distributions of effective heights proportional to pixel brightness, set in the points respective to pixel positions in square matrix with discrete step 0.713 mcm in both directions. Typical view of such a relief is shown in Figure 10.

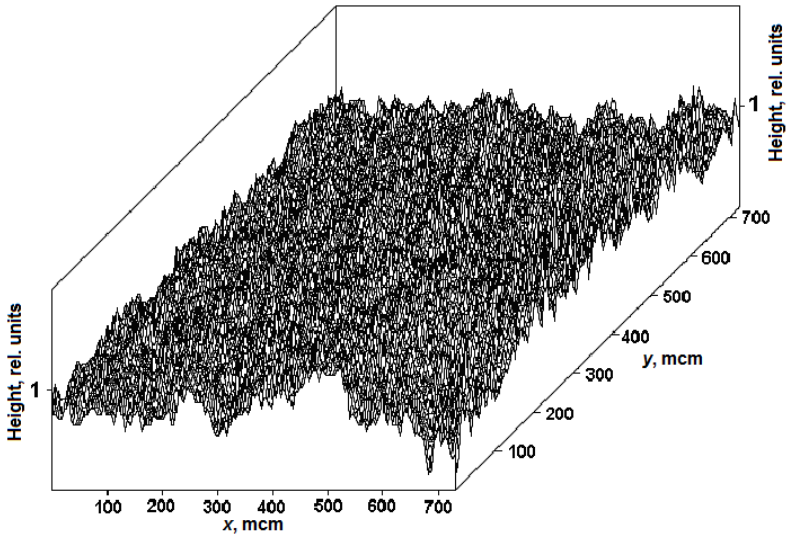

Figure 10. Relief view for the covering before etching, see Figure 9a (Each 6th point is shown for both the directions *x, y*)

The heights of such reliefs do not correspond to real roughness, but, as the pixel brightness correspond to local surface slope, reflecting the height gradients, then one can evaluate the scales of covering surface inhomogeneities using such effective reliefs, representing distribution of local reflecting ability of the surface, determined by surface roughness.

Then the reliefs were processed by **sm2FNS** program realizing SFCAM application to surface reliefs. Two examples of processed relief profiles are shown in Figure 11 for the cases of one and two CLs.

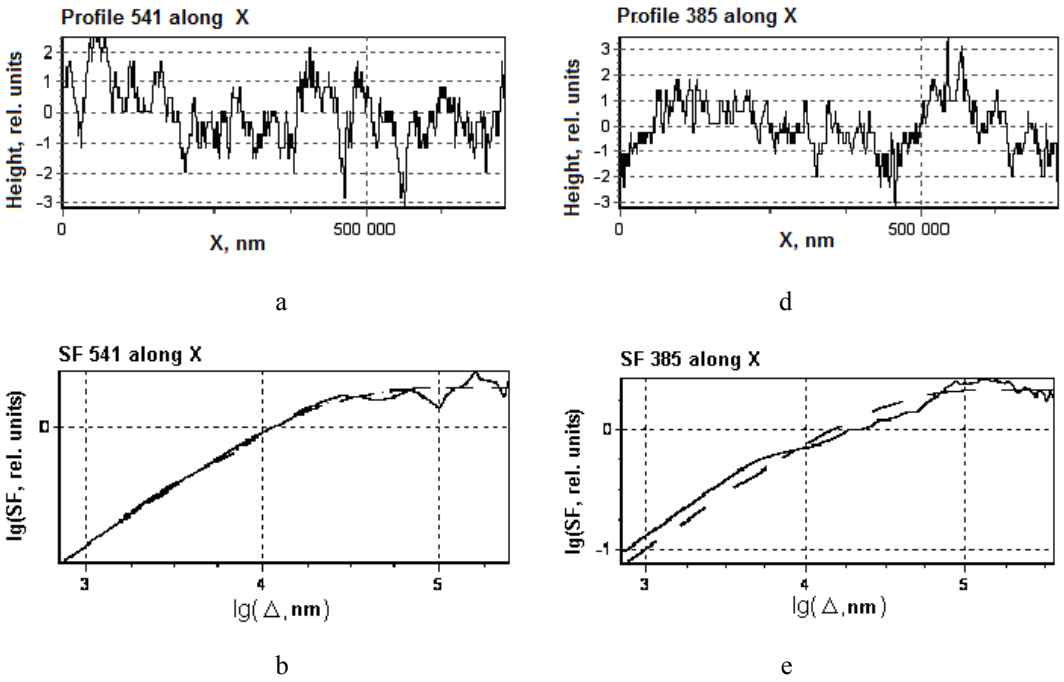

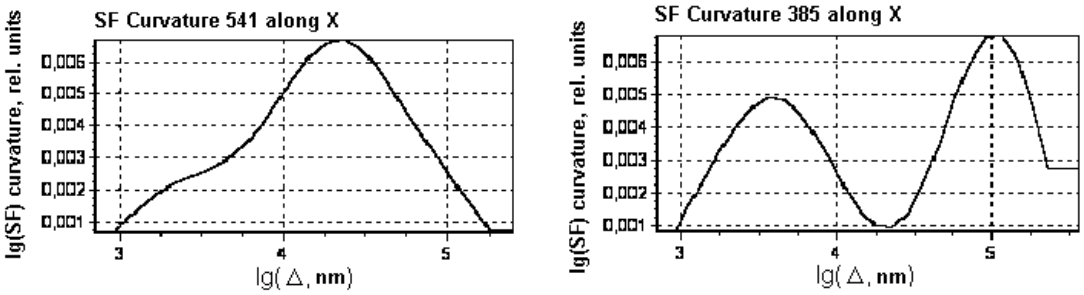

c f

Figure 11. Two different profiles of relief in Figure 10 (a, d), their SFs (b, e) and SF curvatures (c, e)

The obtained experimental data had shown that situation was not so simple as in the cases described above, because the individual SFs averaged over relief did not enable to reveal all the observed CLs. Analysis of calculated CLs had shown that the structures of obtained polymer coverings have CLs that can be separated into three classes. Variations of CLs into each class are due to real differences of surface pieces. So, one has to apply statistical methods to determine CLs as the means over registered relief pieces obtained for each etching time during the chemical test. To make the statistical procedure clearer, the results for 3 day etching are presented in Table 1. The maximum relative error of CLs determination can be taken equal to 30%, the CLs from neighboring classes differing by about one order, and so, CLs determination accuracy was sufficient to evaluate CL hierarchy.

Table 1. Summary of CLs obtained for polymer covering after 3 days etching

N photo	L_1, mcm	L_2, mcm	L_3, mcm
1	4,32	30,1	277
2	2,85	26,2	277
3	2,85	26,2	277
4	2,48	30,1	419
5	2,85	22,8	241
6	2,48	26,2	241
7	2,85	26,2	318
8		22,8	
9		13,1	277
10	4,96		69,2
11		22,8	241
12	1,88		69,2
13	3,28	22,8	241
14		19,9	
15	2,48	22,8	183
CL number	11	13	13
Mean CL, mcm	3,03	24,0	241
Standard deviation, mcm.	0,88	4,4	93,6

The mean CLs for each etching time were calculated in analogous way. The number of revealed CLs varied from 6 (rarely) to 15, see Table 2. The dependences of CLs on etching time are shown in Figure 12, Table 3.

Table 2. Numbers of revealed CLs by classes for each etching time

Time, days	*L*1	*L*2	*L*3
0	0	15	13
3	11	13	13
7	13	15	6
8	10	14	10
9	9	14	11
10	14	9	6
No covering	7	10	13

Table 3. Mean CLs values for each etching time

Time, days	*L*1, mcm	*L*2, mcm	*L*3, mcm
0		10,6	242
3	3,03	24,0	241
7	4,34	15,3	306
8	3,22	23,8	185
9	3,06	29,5	192
10	4,20	25,6	251
No covering	1,95	34,1	204

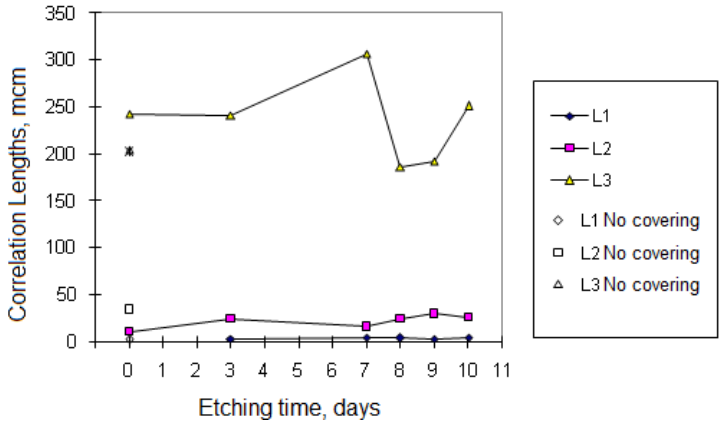

a

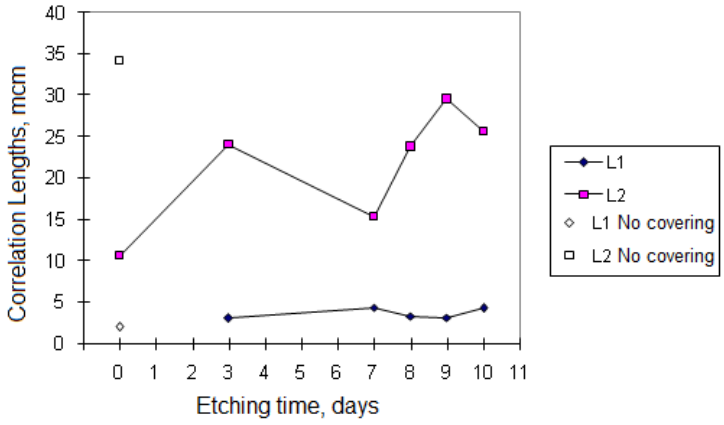

b

Figure 12. Dependence of CLs on etching time, b) being a magnified part of a) for the small CLs

The calculated results enable one to draw some conclusions about polymer covering surface evolution during the etching process. The greatest CLs L_3=250-300 mcm correspond to the craters, traces of ball collisions taking place during mechanochemical treatment in ball mill. It is seen that the structure of such craters was destructed after 7 days etching when the fast stage of covering destruction was starting. After longer etching the most dense covering fragments were stored on ball surface, that are the fragments corresponding to a skeleton of this structure characterized by CLs L_3=200-250 mcm.

CLs L_2=10-35 mcm corresponded to the grained structure of polymer covering due to grain size of initial polymer dust introduced into mill. During chemical etching, the covering destruction seemed to take place on grain boundaries. First, the finest blocks of size 10-15 mcm had removed from the covering that revealed the structure of the greater blocks (20-30 mcm) on covering surface. Destruction of the covering after 7 days etching revealed internal block structure of covering and its skeleton.

CLs L_1=2-5 mcm corresponded to the finest particles of matter independently of its nature (the metal, polymer, or graphite) and the finest craters on covering surface. As is well known, it is impossible to obtain the matter particles smaller than 1 mcm by simple blending using no special means, because the particles smaller than 1 mcm tend to stick together. This problem is solved by using the highly non-equilibrium conditions and special media. In our case the smallest particles were not revealed on the covering before chemical etching. This can be explained in such a way that they were aggregated just after mechanochemical treatment with aggregate size about 10 mcm and greater. During etching these aggregates were broken apart and the smallest particles could be discovered.

Thus, separation of CLs into classes enables to investigate the objects quantitatively on the base of fundamental knowledge about the system and it is most effective when not all the hierarchical levels of system structure can be easily registered by all the data samples. This situation is rather characteristic for natural systems and phenomena.

6. Conclusion

Three examples of SFCAM application above are to show that the proposed approach represents a rather subtle tool for investigation of complex systems on the base of various digital data types – time series or surface reliefs treated as the sets of space series. SFCAM, in combination with other well known methods like sliding window method or simplest statistical calculations, enables to register presence of hierarchical organization of the system under study and to evaluate the quantitative characteristics of this organization – the correlation times or correlation lengths. Taking them into account by an order of recognition, from the shortest to the greatest, can assist to reveal the main features of hierarchical structure, that can introduce new physical sense in concrete consideration. And more exact evaluation of hierarchical structures can be made on the base of statistical analysis of correlation characteristics taken into account by separation into classes on the base of general physical knowledge about investigated object. These correlation characteristics enable to evaluate the differences between the real objects due to environmental or experimental conditions, or to follow object's evolution. The proposed "series-by-series" application of SFCAM can be used for analysis of many dimensional objects also without any principal alterations. It should be noted also that SFCAM gave the correct values of half period for model periodic data (Vstovsky, 2006). So, one can obtain evaluations of "persistency lengths" for periodic or quasiperiodic systems. Note, that SF, being a difference moment, is less sensitive to presence of noise or systematic errors in measured data as compared with other processing methods, that is another advantage of SFCAM.

References

Bornyakov, S. A., & Vstovsky, G. V. (2010). First experience of seismodeformation monitoring of Baikal rift zone (by the example of South-Baikal earthquake of 27 August 2008). *Doklady RAS, Geophysics, 431*(4), 1-5.

Frisch, U. (1995). *Turbulence. The Legacy of A. N. Kolmogorov.* Cambridge Univ. Press.

Letnikova, A. F., Vstovsky, G. V., & Timashev, S. F. (2001). Formation of Anisotropic Fractal Structures during Dissolution of LiF Monocrystals. *Materials Science (Medziagotyra) (Kaunas), 7*(2), 98-103.

Timashev, S. F. (2011). Phenomenology of Complexity: Information in Chaotic Signals. *Russian Journal of General Chemistry, 81*(1), 220-233. http://dx.doi.org/10.1134/S1070363211010397

Vstovsky, G. V. (2006). Factual Revelation of Correlation Lengths Hierarchy in Micro- and Nanostructures by Scanning Probe Microscopy Data. *Materials Science (Medziagotyra) (Kaunas), 12*(3), 262-270.

Vstovsky, G. V. (2008). Revelation of spatial and temporal hierarchical structures in complex systems. In R. M. Yulmetev, A. V. Mokshin, S. A. Demin, & M. Kh. Salakhov (Eds.). *Fluctuations and Noise in Complex*

Systems of Living and Non-living Nature (pp. 441-454). Russia, Tatarstan Republic Ministry of Education and Science, Kazan City: "Shkola" Publishing Center.

Vstovsky, G. V. Solovieva, A. B. Timashev, S. F. Zarkhina, T. S. Timofeeva, V. A., & Netschadina, L. V. (2006). Revelation of hierarchical structure of mechanochemical polymer coverings of metal balls by optical microscopy data. *Zavodskaya Laboratoriya*, *N12*, 24-28. (In Russian)

Vstovsky, G. V., & Bornyakov, S. A. (2010). First experience of seismodeformation monitoring of Baikal rift zone (by the example of South-Baikal earthquake of 27 August 2008). *Nat. Hazards and Earth Syst. Sci., 10*, 667-672. http://dx.doi.org/10.5194/nhess-10-667-2010

Earth Science Research; Vol. 1, No. 2; 2012
ISSN 1927-0542 E-ISSN 1927-0550
Published by Canadian Center of Science and Education

Mathematical Model to Predict Conductive Properties of Contaminated Riverbed Sand in Ado-Odo Ota Local Government Area of Ogun State, Nigeria

Olukayode D. Akinyemi[1], Jamiu A. Rabiu[1], V. C. Ozebo[1] & O. A. Idowu[2]

[1] Department of Physics, University of Agriculture, Abeokuta, Ogun State, Nigeria

[2] Department of Water Resources Management and Agrometeorology, University of Agriculture, Abeokuta, Ogun State, Nigeria

Correspondence: Jamiu A. Rabiu, Department of Physics, University of Agriculture, Abeokuta, Ogun State, Nigeria. E-mail: jamoary@yahoo.com

Received: February 1, 2012 Accepted: February 14, 2012 Online Published: June 5, 2012

doi:10.5539/esr.v1n2p43 URL: http://dx.doi.org/10.5539/esr.v1n2p43

Abstract

The possibility of contamination is especially rising due to the increase in the number of industries in the Local Government Area. In this study, riverbed sands were collected from five major rivers in Ado-Odo Ota Local Government Area, and conductivity properties were determined after the samples have been treated with varying concentration of petrol, engine oil, diesel, caustic soda and H_2SO_4. HANNAN Electrical Conductivity Meter, KD2 Thermal Conductivity Meter and Constant Head Method were used to determine the electrical, thermal and hydraulic conductivities respectively. A mathematical model was developed that describes the effect of contaminants on the electrical (σ), thermal (λ) and hydraulic (k) conductivities of riverbed sand from the major rivers in Ado-odo Ota Local Government Area. The model equation incorporates the bulk density of the riverbed sand samples, as well as the concentration and conductivity of the contaminants as follows: $\lambda = 0.107x_1 + 0.10x_2 - 0.017x_3 + 1.673$, $\sigma = 1.911x_1 + 18.229x_2 - 0.015x_3 + 47.173$ and $k = 0.056x_1 + 0.381x_2 - 0.031x_3 + 0.162$, where x_1, x_2 and x_3 are bulk density of samples, conductivity and concentration of contaminants respectively. From interpolation analysis, sample from Ilogbo river contained about 30 ml/kg of engine oil, Mosafejo river contained about 10 ml/kg of caustic soda, Ijako river contained about 20 ml/kg of caustic soda, Iju river contained about 10 ml/kg of diesel and Igbogbo river contained 10 ml/kg of H_2SO_4, thus showing clearly how waste products from industries end up as contaminants in nearby rivers.

Keywords: mathematical model, riverbed sand, thermal conductivity, electrical conductivity, hydraulic conductivity, contaminants concentration

1. Introduction

Pollution of the soil environment with petroleum and refinery products is one of the factors expressing anthropopression. Due to its toxicity, widespread presence and complex nature, this type of pollution is a serious problem, one reason being that as the modern civilisation, urbanisation and mechanisation develop, the use of petroleum and petroleum-based products grows. Contamination of soils with crude oil and refinery products is becoming an ever-increasing problem, especially in the light of several breakdowns of oil pipelines and wells reported recently. Nonetheless, major points of soil pollution with refinery products are petrol stations, garages servicing cars and tractors, seaport areas (Michalcewicz, 1995). Other areas of concern are mining and distribution of petroleum-based products (Song & Barhta, 1990, Amadi et al., 1996, Jørgensen et al., 2000). Besides, heavy use of machinery in agriculture leads to higher consumption of diesel oil. Certain negligence when transporting, collecting or storing refinery products together with unsatisfactory care while disposing of old or used petroleum products lead to considerable pollution of the natural environment (Leahy & Colwell, 1990). Petroleum and refinery products penetrating soil cause its degradation (Sztompka, 1999). Once they enter an ecosystem, petroleum-based products initiate a series of processes, affecting both its biotic and abiotic elements (Małachowska-Jutsz et al., 1997). Crude oil and products derived from this raw material are composed of aliphatic, oleic, naphthenic and aromatic hydrocarbons (Chi & Krishnamurthy, 1995), which modify physical and chemical properties of soil and its structure. These compounds are largely responsible for changed fertility of

soil (Tyczkowski, 1993, Iwanow et al., 1994). Soil polluted by petroleum-based products loses its biological activity and may not be able to recover it over ten years (Sparrow & Sparrow, 1988, Racine 1993, Wyszkowska et al., 2001). Moreover, diesel oil has a negative effect on the biochemical and physicochemical characteristics of soils (Tyczkowski, 1993, Kucharski & Wyszkowska, 2001, Wyszkowska et al., 2002).

Since contamination of soil with refinery products deteriorates its biochemical and physicochemical properties, it also limits the growth and development of plants, whose nutritive and technological value can be low and often questionable. In this connection, the present study has been undertaken to determine the effect of soil contamination with Diesel oil, Engine oil, Petrol, Caustic soda and H_2SO_4 on thermal, electrical and hydraulic conductivities, and to determine the predictive mathematical models for the physical properties.

2. Study Area

The study was carried out on five major rivers in Ado-Odo/Ota Local Government Area of Ogun State. Ado-odo/Ota Local Government is one of the 20 Local Government areas of Ogun State located in the West Senatorial District. Geographically, it is situated within the tropical zone lying between 60^0 and 47^0 N of equator and 20.33^0E and 30.18^0 E of the Greenwich's Meridian and covers a land area of 1,263 square kilometers with a Terrain of 1,010.4 sq kilometer plain land and about 252.6 square kilometers. Terrain comprises of 16% riverine and 4% hilly regions. The Local Government has an estimated population of 527,242 people (Male 262,523 & Female 265,719) (2006 Census) with about four hundred and fifty (450) towns, villages and settlements. The map shown in Figure 1, illustrate the location of the sampling sites and the potential source of pollutants, which include agricultural wastes, industrial wastes, sewage, animal wastes, market wastes, etc. Three of the rivers (Ilogbo, Mosafejo and Ijako rivers) are located in the southern district of the area. While the remaining two (Igbogbo and Iju rivers) are located in the northern part of area. The Ijako and Ilogbo Rivers are particularly unique for several reasons. The Ijako community has undergone great economic development in recent years and is notably one of the fastest growing economically important communities in Ado-odo/ota L.G.A. which accommodates a considerable number of micro- industries (Coca-Cola Nig. Ltd, Sona Breweries plc, Universal Gas Ltd, Nigeria Foundries Ltd, 3Ace lnd. Ltd and Fine chemicals ltd.).The very popular market (Ilogbo market) and the timber business coupled with agricultural practices have drawn people from several cultural background in the country to make the settlement inter- tribal. This increase in anthropogenic activities surrounding the area has lead to an increase in environmental degradation. These multiple sources make it especially difficult to identify and isolate the risks associated with this contaminated water.

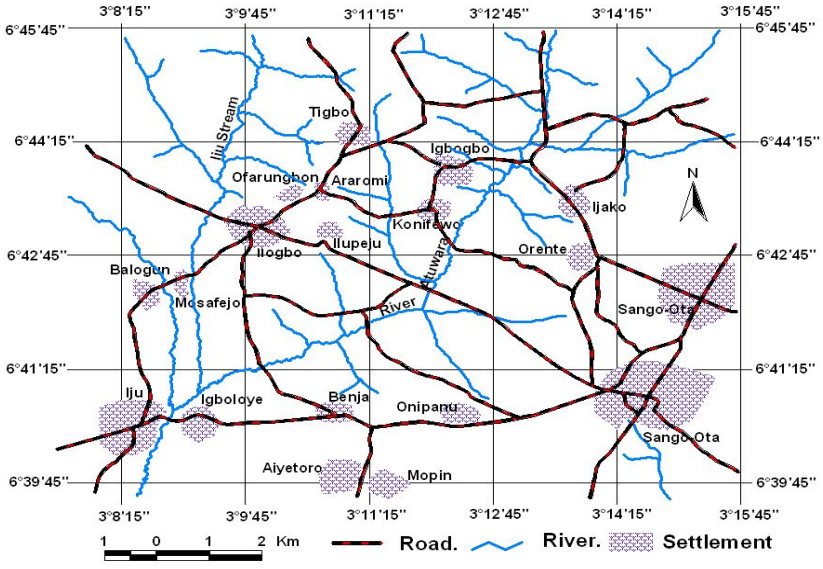

Figure 1. Map of study area

3. Materials and Methods

The equipments used in this work included Hannan electrical conductivity meter, KD2 thermal conductivity meter and Digital weight balance. Riverbed sands were collected from the five major rivers present in Ado-Odo

Ota Local Government Area of Ogun state. Surface sediment sample were collected manually from the rivers' bank, transferred into plastic containers, and transported to the laboratory (UNAAB). Samples collected were thoroughly washed to remove any hidden contaminant, air dried and sieved to ensure uniform grain size. 1.3g/cm^3 bulk density of each treated sample were moistened with uniform grain size of 0.2mm. Five readings of thermal conductivity and electrical conductivity were taken at different points in the cylinder in order to obtain the average values, after which the hydraulic conductivity was measured using constant head method. 5ml of each contaminant was added and mixed thoroughly.

4. Results and Discussion

Table 1. ANOVA Table for conductivity properties of Riverbed sands

Tests of Between-Subjects Effects

Source	Dependent Variable	Type III Sum of Squares	df	Mean Square	F	Sig.
Corrected Model	Thermal Conductivity	85.302[a]	60	1.422	32.359	.000
	Electrical Conductivity	291562.322[b]	60	4859.372	230.467	.000
	Hydraulic Conductivity	74.213[c]	60	1.237	29.020	.000
Intercept	Thermal Conductivity	518.814	1	518.814	11808.518	.000
	Electrical Conductivity	1440968.749	1	1440968.749	68341.241	.000
	Hydraulic Conductivity	125.521	1	125.521	2944.959	.000
Sample	Thermal Conductivity	7.236	4	1.809	41.175	.000
	Electrical Conductivity	1308.401	4	327.100	15.513	.000
	Hydraulic Conductivity	3.184	4	.796	18.678	.000
Contaminant	Thermal Conductivity	31.157	4	7.789	177.288	.000
	Electrical Conductivity	237296.004	4	59324.001	2813.577	.000
	Hydraulic Conductivity	55.921	4	13.980	328.004	.000
Concentration	Thermal Conductivity	1.881	4	.470	10.704	.000
	Electrical Conductivity	57.719	4	14.430	.684	.605
	Hydraulic Conductivity	6.144	4	1.536	36.039	.000
Sample * Contaminant	Thermal Conductivity	13.759	16	.860	19.573	.000
	Electrical Conductivity	6563.030	16	410.189	19.454	.000
	Hydraulic Conductivity	6.126	16	.383	8.982	.000
Sample * Concentration	Thermal Conductivity	1.068	16	.067	1.519	.121
	Electrical Conductivity	185.115	16	11.570	.549	.909
	Hydraulic Conductivity	1.320	16	.083	1.936	.033
Contaminant * Concentration	Thermal Conductivity	30.201	16	1.888	42.962	.000
	Electrical Conductivity	46152.053	16	2884.503	136.804	.000
	Hydraulic Conductivity	1.518	16	.095	2.226	.013
Error	Thermal Conductivity	2.812	64	.044		
	Electrical Conductivity	1349.434	64	21.085		
	Hydraulic Conductivity	2.728	64	.043		
Total	Thermal Conductivity	606.927	125			
	Electrical Conductivity	1733880.505	125			
	Hydraulic Conductivity	202.462	125			
Corrected Total	Thermal Conductivity	88.113	124			
	Electrical Conductivity	292911.756	124			
	Hydraulic Conductivity	76.941	124			

a. R Squared = .968 (Adjusted R Squared = .938)

b. R Squared = .995 (Adjusted R Squared = .991)

c. R Squared = .965 (Adjusted R Squared = .931)

From Table 1, thermal conductivity, electrical conductivity and hydraulic conductivity of different sand samples differ significantly at 5% ($p < 0.05$) level of significance. It is also observed from the table that these three properties differ significantly for the different contaminants used on the sand samples, but this is not the case for the different concentration of the contaminants. Rather it is seen that while the thermal and hydraulic

conductivities differ significantly at 5% level for the different concentration of contaminants used, electrical conductivity is not significantly different at 5% level.

Table 2. Mean values of the different conductivity properties for the different sand samples

2. Sample

Dependent Variable	Sample	Mean	Std. Error	95% Confidence Interval	
				Lower Bound	Upper Bound
Thermal Conductivity	Sample A	1.923	.042	1.839	2.007
	Sample B	2.024	.042	1.940	2.108
	Sample C	1.665	.042	1.581	1.749
	Sample D	2.207	.042	2.123	2.291
	Sample E	2.367	.042	2.283	2.451
Electrical Conductivity	Sample A	103.543	.918	101.708	105.377
	Sample B	107.550	.918	105.715	109.385
	Sample C	104.128	.918	102.293	105.963
	Sample D	109.484	.918	107.649	111.319
	Sample E	112.132	.918	110.297	113.967
Hydraulic Conductivity	Sample A	.765	.041	.682	.847
	Sample B	.968	.041	.885	1.050
	Sample C	1.262	.041	1.180	1.344
	Sample D	.974	.041	.892	1.057
	Sample E	1.042	.041	.959	1.124

Mean values of the different conductivities for the different sand samples used are shown in Table 2. It is seen that sample E has the highest thermal conductivity value (2.367), while sample C has the lowest thermal conductivity value (1.665).

Table 3. Mean values of the different conductivities properties for the different contaminants

3. Contaminant

Dependent Variable	Contaminant	Mean	Std. Error	95% Confidence Interval	
				Lower Bound	Upper Bound
Thermal Conductivity	Petrol	1.674	.042	1.591	1.758
	Diesel	2.297	.042	2.213	2.381
	Engine Oil	1.458	.042	1.375	1.542
	H2SO4	2.868	.042	2.784	2.952
	Caustic Soda	1.889	.042	1.805	1.973
Electrical Conductivity	Petrol	114.650	.918	112.815	116.485
	Diesel	54.580	.918	52.745	56.414
	Engine Oil	59.685	.918	57.850	61.519
	H2SO4	149.680	.918	147.845	151.515
	Caustic Soda	158.242	.918	156.408	160.077
Hydraulic Conductivity	Petrol	.708	.041	.626	.790
	Diesel	.420	.041	.338	.503
	Engine Oil	.446	.041	.363	.528
	H2SO4	1.230	.041	1.148	1.312
	Caustic Soda	2.206	.041	2.124	2.289

Table 3 shows the mean values of the different conductivities for the different contaminants used. It is seen that H2SO4 has the highest thermal conductivity value, (2.868) while Engine oil has the lowest thermal conductivity value (1.458).

Table 4. Mean values of the different conductivities properties for the different concentration of contaminants

4. Concentration of Contaminant

Dependent Variable	Concentration of Contaminant	Mean	Std. Error	95% Confidence Interval	
				Lower Bound	Upper Bound
Thermal Conductivity	5 ml	2.222	.042	2.138	2.306
	10 ml	2.093	.042	2.009	2.177
	15 ml	2.056	.042	1.972	2.140
	20 ml	1.952	.042	1.869	2.036
	25 ml	1.863	.042	1.779	1.947
Electrical Conductivity	5 ml	107.320	.918	105.485	109.155
	10 ml	106.869	.918	105.034	108.703
	15 ml	108.324	.918	106.489	110.158
	20 ml	107.890	.918	106.055	109.725
	25 ml	106.434	.918	104.600	108.269
Hydraulic Conductivity	5 ml	1.312	.041	1.230	1.395
	10 ml	1.168	.041	1.086	1.250
	15 ml	.997	.041	.914	1.079
	20 ml	.841	.041	.758	.923
	25 ml	.692	.041	.610	.775

It is observed from Table 4 that the thermal conductivity value is highest at 5ml concentration of the contaminants used while it is lowest at 25ml concentration of the contaminants used.

Table 5. Mean separation for thermal conductivity of different sand samples

Thermal Conductivity

Duncan [a,b,c]

Sample	N	Subset 1	2	3	4
Sample C	25	1.6652			
Sample A	25		1.9228		
Sample B	25		2.0240		
Sample D	25			2.2072	
Sample E	25				2.3672
Sig.		1.000	.093	1.000	1.000

Means for groups in homogeneous subsets are displayed.
Based on Type III Sum of Squares
The error term is Mean Square(Error) = .044.

a. Uses Harmonic Mean Sample Size = 25.000.

b. The group sizes are unequal. The harmonic mean of the group sizes is used. Type I error levels are not guaranteed.

c. Alpha = .05.

From Table 5, mean separation for thermal conductivity of the different sand samples. It was observed from the table that thermal conductivity of sample A is not significantly different from that of sample B, while thermal conductivity of all other samples are significantly different at 5% ($p < 0.05$) level.

Table 6. Mean separation for hydraulic conductivity of different sand samples

Hydraulic Conductivity

Duncan [a,b,c]

Sample	N	Subset 1	Subset 2	Subset 3
Sample A	25	.7648		
Sample B	25		.9676	
Sample D	25		.9744	
Sample E	25		1.0416	
Sample C	25			1.2620
Sig.		1.000	.238	1.000

Means for groups in homogeneous subsets are displayed.
Based on Type III Sum of Squares
The error term is Mean Square(Error) = .043.

a. Uses Harmonic Mean Sample Size = 25.000.

b. The group sizes are unequal. The harmonic mean of the group sizes is used. Type I error levels are not guaranteed.

c. Alpha = .05.

Table 6 shows the mean separation for hydraulic conductivity of the different sand samples. It was observed from the table that hydraulic conductivity of sample B and D are not significantly different from that of sample E, while the hydraulic conductivity of sample A is significantly different from that of sample C at 5% level.

Table 7. Mean separation for electrical conductivity of different sand samples

Electrical Conductivity

Duncan [a,b,c]

Sample	N	Subset 1	Subset 2	Subset 3
Sample A	25	103.54		
Sample C	25	104.13		
Sample B	25		107.55	
Sample D	25		109.48	
Sample E	25			112.13
Sig.		.654	.141	1.000

Means for groups in homogeneous subsets are displayed.
Based on Type III Sum of Squares
The error term is Mean Square(Error) = 21.085.

a. Uses Harmonic Mean Sample Size = 25.000.

b. The group sizes are unequal. The harmonic mean of the group sizes is used. Type I error levels are not guaranteed.

c. Alpha = .05.

Table 7 shows the mean separation for electrical conductivity of the different sand samples. It was observed from the table that electrical conductivity of sample A is not significantly different from that sample C, while the electrical conductivity of sample B is not significantly different from that of sample D, while electrical conductivity of sample E is significantly different from all other samples at 5% ($p<0.05$) level.

Table 8. Mean seperation for thermal conductivitiy of the sand samples for different contaminants used

Thermal Conductivity

Duncan[a,b,c]

Contaminant	N	Subset 1	2	3	4	5
Engine Oil	25	1.4584				
Petrol	25		1.6744			
Caustic Soda	25			1.8888		
Diesel	25				2.2968	
H2SO4	25					2.8680
Sig.		1.000	1.000	1.000	1.000	1.000

Means for groups in homogeneous subsets are displayed.
Based on Type III Sum of Squares
The error term is Mean Square(Error) = .044.

a. Uses Harmonic Mean Sample Size = 25.000.

b. The group sizes are unequal. The harmonic mean of the group sizes is used. Type I error levels are not guaranteed.

c. Alpha = .05.

Mean separation for thermal conductivities of the sand samples for different contaminants used as shown in Table 8. It is seen from the table that thermal conductivities of the sand samples differ significantly at 5% ($p<0.05$) level for the different contaminants used.

Table 9. Mean seperation for electrical conductivitiy of the sand samples for different contaminants used

Electrical Conductivity

Duncan[a,b,c]

Contaminant	N	Subset 1	2	3	4	5
Diesel	25	54.58				
Engine Oil	25		59.68			
Petrol	25			114.65		
H2SO4	25				149.68	
Caustic Soda	25					158.24
Sig.		1.000	1.000	1.000	1.000	1.000

Means for groups in homogeneous subsets are displayed.
Based on Type III Sum of Squares
The error term is Mean Square(Error) = 21.085.

a. Uses Harmonic Mean Sample Size = 25.000.

b. The group sizes are unequal. The harmonic mean of the group sizes is used. Type I error levels are not guaranteed.

c. Alpha = .05.

Electrical conductivities of the sand samples differ significantly at 5% ($p<0.05$) level for the different contaminants used as shown in Table 9.

Table 10. Mean seperation for hydraulic conductivitiy of the sand samples for different contaminants used

Hydraulic Conductivity

Duncan[a,b,c]

Contaminant	N	Subset 1	2	3	4
Diesel	25	.4204			
Engine Oil	25	.4456			
Petrol	25		.7080		
H2SO4	25			1.2300	
Caustic Soda	25				2.2064
Sig.		.668	1.000	1.000	1.000

Means for groups in homogeneous subsets are displayed.
Based on Type III Sum of Squares
The error term is Mean Square(Error) = .043.

a. Uses Harmonic Mean Sample Size = 25.000.

b. The group sizes are unequal. The harmonic mean of the group sizes used. Type I error levels are not guaranteed.

c. Alpha = .05.

It is seen from the Table 10 that, hydraulic conductivity of diesel is not significantly different from that engine oil at 5% ($p<0.05$) level for the different contaminants used. While hydraulic conductivities of other contaminants (petrol, H2SO4 and caustic soda) are significantly different at 5% level.

Table 11. Mean seperation for thermal conductivitiy of the sand samples at different concentration of contaminants used

Thermal Conductivity

Duncan[a,b,c]

Concentration of Contaminant	N	Subset 1	2	3	4
25 ml	25	1.8628			
20 ml	25	1.9524	1.9524		
15 ml	25		2.0560	2.0560	
10 ml	25			2.0932	
5 ml	25				2.2220
Sig.		.136	.085	.533	1.000

Means for groups in homogeneous subsets are displayed.
Based on Type III Sum of Squares
The error term is Mean Square(Error) = .044.

a. Uses Harmonic Mean Sample Size = 25.000.

b. The group sizes are unequal. The harmonic mean of the group sizes is used. Type I error levels are not guaranteed.

c. Alpha = .05.

It was observed that thermal conductivity of the sand samples when 25ml concentration of the contaminants used is not significantly different at 5% level from when 20ml concentration of the contaminant is used as shown in Table 11. Also the thermal conductivity does not differ at 5% level when 15ml concentration of the contaminant is used and when 20ml concentration of the contaminant is used, but that of 15ml differ significantly at 5% level from that of 25ml. also thermal conductivity at 10ml concentration does not differ significantly at 5% ($p<0.05$) level from that at 15ml, but it differs significantly from those at other concentrations. Thermal conductivity at 5ml concentration is observed to be significantly different at 5 % ($p<0.05$) from those at other concentrations.

Table 12. Mean seperation for electrical conductivitiy of the sand samples at different concentrations of contaminants used

Electrical Conductivity

Duncan[a,b,c]

Concentration of Contaminant	N	Subset 1
25 ml	25	106.43
10 ml	25	106.87
5 ml	25	107.32
20 ml	25	107.89
15 ml	25	108.32
Sig.		.202

Means for groups in homogeneous subsets are displayed.
Based on Type III Sum of Squares
The error term is Mean Square(Error) = 21.085.

a. Uses Harmonic Mean Sample Size = 25.000.

b. The group sizes are unequal. The harmonic mean of the group sizes is used. Type I error levels are not guaranteed.

c. Alpha = .05.

Table 12 shows the mean separation for the electrical conductivity of the sand samples at different concentrations of the contaminants used. It was observed that electrical conductivity of the sand samples are not significantly different at 5% ($p < 0.05$) level for the different concentration of contaminants used.

Table 13. Mean seperation for hydraulic conductivitiy of the sand samples at different concentration of contaminants used

Hydraulic Conductivity

Duncan[a,b,c]

Concentration of Contamina	N	Subset 1	2	3	4	5
25 ml	25	.6924				
20 ml	25		.8408			
15 ml	25			.9968		
10 ml	25				1.1680	
5 ml	25					1.3124
Sig.		1.000	1.000	1.000	1.000	1.000

Means for groups in homogeneous subsets are displayed.
Based on Type III Sum of Squares
The error term is Mean Square(Error) = .043.

a. Uses Harmonic Mean Sample Size = 25.000.

b. The group sizes are unequal. The harmonic mean of the group sizes error levels are not guaranteed.

c. Alpha = .05.

From Table 13, mean separation for the hydraulic conductivity of the sand samples at different concentrations of the contaminants used shown. It was seen from this table that the hydraulic conductivities of the sand samples differ significantly at 5% ($p < 0.05$) level for the different concentration of contaminants used.

Table 14. Regression analysis tables for thermal conductity of the sand sample

ANOVA[b]

Model		Sum of Squares	df	Mean Square	F	Sig.
1	Regression	7.219	3	2.406	3.599	.016[a]
	Residual	80.895	121	.669		
	Total	88.113	124			

a. Predictors: (Constant), Concentration of Contaminant, Contaminant, Sample

b. Dependent Variable: Thermal Conductivity

Coefficients[a]

Model		Unstandardized Coefficients		Standardized Coefficients	t	Sig.
		B	Std. Error	Beta		
1	(Constant)	1.673	.278		6.009	.000
	Sample	.107	.052	.181	2.073	.040
	Contaminant	.100	.052	.168	1.934	.055
	Concentration of Contaminant	-.017	.010	-.145	-1.661	.099

a. Dependent Variable: Thermal Conductivity

From the regression analysis results for thermal conductivity as shown in Table 14, it was observed that the thermal conductivity of the sand samples is significantly dependents at 5% level on the explanatory factors (concentration of contaminant, types of contaminant and sand sample) under consideration. These factors are responsible for 8.2% in the variation of the thermal conductivity of the sand sample. From the tables the regression equation as found to be y = 0.107x1 + 0.10x2 – 0.017x3 + 1.673 as shown in Table 14

Where:

y = Sample Thermal conductivity, x1 = Sample density,

x2 = Contaminant thermal conductivity, x3 = Concentration of contaminant

Table 15. Regression analysis tables for electrical conductity of the sand sample

Coefficients[a]

Model		Unstandardized Coefficients		Standardized Coefficients	t	Sig.
		B	Std. Error	Beta		
1	(Constant)	47.173	14.153		3.333	.001
	Sample	1.911	2.628	.056	.727	.468
	Contaminant	18.229	2.628	.533	6.936	.000
	Concentration of Contaminant	-.015	.526	-.002	-.029	.977

a. Dependent Variable: Electrical Conductivity

ANOVA[b]

Model		Sum of Squares	df	Mean Square	F	Sig.
1	Regression	83984.351	3	27994.784	16.213	.000[a]
	Residual	208927.4	121	1726.673		
	Total	292911.8	124			

a. Predictors: (Constant), Concentration of Contaminant, Contaminant, Sample

b. Dependent Variable: Electrical Conductivity

From the regression analysis results for electrical conductivity, it was observed that the electrical conductivity of the sand samples is significantly dependents at 5% level on the explanatory factors (concentration of contaminant, types of contaminant and sand sample) under consideration. These factors are responsible for 28.7% in the variation of the electrical conductivity of the sand sample. From the tables the regression equation y = 1.911x1 + 18.229x2 – 0.015x3 + 47.173 as shown in Table 15

Where:

y = Sample Electrical conductivity, x1 = Sample density,

x2 = Contaminant electrical conductivity, x3 = Concentration of contaminant

Table 16. Regression analysis tables for hydraulic conductity of the sand sample

ANOVA[b]

Model		Sum of Squares	df	Mean Square	F	Sig.
1	Regression	43.147	3	14.382	51.496	.000[a]
	Residual	33.794	121	.279		
	Total	76.941	124			

a. Predictors: (Constant), Concentration of Contaminant, Contaminant, Sample

b. Dependent Variable: Hydraulic Conductivity

Coefficients[a]

Model		Unstandardized Coefficients		Standardized Coefficients	t	Sig.
		B	Std. Error	Beta		
1	(Constant)	.162	.180		.901	.369
	Sample	.056	.033	.101	1.677	.096
	Contaminant	.381	.033	.686	11.388	.000
	Concentration of Contaminant	-.031	.007	-.282	-4.689	.000

a. Dependent Variable: Hydraulic Conductivity

From the regression analysis results for hydraulic conductivity, it was observed that the hydraulic conductivity of the sand samples is significantly dependents at 5% level on the explanatory factors (concentration of contaminant, types of contaminant and sand sample) under consideration. These factors are responsible for 56.1% in the variation of the hydraulic conductivity of the sand sample. From the tables the regression equation y = 0.056x1 + 0.381x2 – 0.031x3 + 0.162 as shown in Table 16

Where:

y = Sample Hydraulic conductivity, x1 = Sample density,

x2 = Contaminant hydraulic conductivity, x3 = Concentration of contaminant

5. Conclusion

In this work, results of electrical conductivity, thermal conductivity and hydraulic conductivity have been modeled to determine effects of contaminants (petrol, diesel, engine oil, caustic soda and H_2SO_4) on conductive properties of riverbed sands. Duncan results showed that, thermal conductivity of sample A is not significantly different from that of sample B, while thermal conductivity of all other samples are significantly different at 5% ($p< 0.05$) level. Electrical conductivity is not significantly different from that of sample C at 5% ($p< 0.05$) level, while hydraulic conductivity of samples B and D are not significantly different from that of sample E, but hydraulic conductivity of sample A is significantly different from that of sample C at 5% ($p< 0.05$) level.

Results from the coefficients of determination showed that concentration of contaminants, types of contaminants and sand samples are responsible for 8.2% in the variation of thermal conductivity, while these factors are also responsible for 28.7% and 56.1% in variation of electrical and hydraulic conductivities respectively.

References

Amadi, A., Abbey, S. D., & Nma, A. (1996). Chronic effects of oil spil on soil properties and microflora of rain-forest ecosystem in Nigeria. *Water Air Soil Pollut., 86*, 1-11. http://dx.doi.org/10.1007/BF00279142

Chi Yuan Fan, & Krishnamurthy, M. (1995). Enzymes for enhancing bioremediation of petroleum-contaminated soils: A brief review. *Air Waste Manage. Assoc., 45*, 453-460. http://dx.doi.org/10.1080/10473289.1995.10467375

Iwanow, W. N., Dylgierow, A. N., & Stabnikowa, E. (1994). Aktivnost niekatorych ekołogo-troficzieskich grup mikroorganizmow pri zagraznienii cziernoziema obyknowiennowo ygliewodorami niefci. *Mikrobioł. Zurn., 6*, 59-63.

Jørgensen, K. S., Puustinen, J., & Suortti, A. M. (2000). Bioremediation of petroleum hydrocarbon-contaminated soil by composting in biopiles. *Environ. Pollut., 107*, 245-254. http://dx.doi.org/10.1016/S0269-7491(99)00144-X

Joshua Paul Abrams. (2001). Mathematical modeling: Teaching the open ended application of mathematics

Leahy, J. G., & Colwell, R. R. (1990). Microbial degradation of hydrocarbons in the environment. *Microbiol. Rev. Sept., 54*, 305-315.

Małachowska-Jutsz, A., Mrozowska, J., Kozielska, M., & Miksch, K. (1997). Aktywność enzymatyczna w glebie skażonej związkami ropopochodnymi w procesie jej detoksykacji. *Biotechnol., 36*, 79-91.

Michalcewicz, W. (1995). Wpływ oleju napędowego do silników Diesla na liczebność bakterii, grzybów, promieniowców oraz biomasę mikroorganizmów glebowych. *Rocz. PZH, 46*, 91-97.

Neumaier, Amold. (2003). Mathematical modeling. Retrieved from http/www.mat.univie.ac.at/neum

Racine, Ch. H. (1993). Long-term recovery of vegetation on two experimental crude oil spills in interior Alaska black spruce taiga. *Can. J. Bot., 72*, 1171-1177. http://dx.doi.org/10.1139/b94-143

Song, H., & Bartha, R. (1990). Effects of jet fuel spills on the microbial community of soil. *Appl. Environ. Microb. Mar., 56*, 646-651.

Sparrow, S. D., & Sparrow, E. B. (1988). Microbial biomass and activity in a subartic soil ten years after crude oil spills. *J. Environ. Qual., 17*, 304-309. http://dx.doi.org/10.2134/jeq1988.00472425001700020024x

Sztompka, E. (1999). Biodegradation of engine oil in soil. *Acta Microb. Pol., 489*, 185-196.

Tyczkowski, A. (1993). Usuwanie zanieczyszczeń ropopochodnych z gleby i wód gruntowych metodami fizykochemicznymi i biotechnologicznymi. *Ekol. Techn., 3*, 10-13.

Wyszkowska, J., Kucharski, J., & Wałdowska, E. (2002). The influence of diesel oil contamination on soil enzymes activity. *Rostl. Výr., 48*, 58-62.

Wyszkowska, J., Kucharski, J., Jastrzębska, E., & Hłasko, A. (2001). The biological properties of the soil as influenced by chromium contamination. *Polish J. Environ. Stud., 10*, 37-42.

Earth Science Research; Vol. 1, No. 2; 2012
ISSN 1927-0542 E-ISSN 1927-0550
Published by Canadian Center of Science and Education

Three-Dimensional Modal Analysis of Brezina Concrete Arch Dam, Algeria

Amina Tahar Berrabah[1], Mohamed Belharizi[2], André Laulusa[3] & Abdelmalek Bekkouche[1]

[1] Department of Civil Engineering, Aboubekr Belkaid University, Tlemcen, Algeria

[2] Consultant, 37 impasse Armand, 92160 Antony, France

[3] Soditech Ingénierie, 1 bis Allée des Gabians, 06150 Cannes La Bocca, France

Correspondence: Amina Tahar Berrabah, Department of Civil Engineering, Aboubekr Belkaid University, 13000 Tlemcen, Algeria. Tel: 213-697-826-043. E-mail: tb_amina@hotmail.com

Received: January 29, 2012 Accepted: February 14, 2012 Online Published: June 5, 2012

doi:10.5539/esr.v1n2p55 URL: http://dx.doi.org/10.5539/esr.v1n2p55

Abstract

In this paper, modal responses of the Brezina concrete arch dam, Algeria, are determined using the finite elements commercial packages ANSYS. To study the effects of the foundation soil, three 3D models have been created, the dam alone without soil, the dam-massless soil and the dam-soil with soil mass model. Moreover, a parametric study of the viscous damping, in Raleigh form, has been conducted. It is found that the natural frequencies of either undamped or damped modes obtained from the dam-soil with soil mass model are drastically lower compared to that of the dam alone model, and are markedly lower than those obtained from the dam-massless soil model. Likewise, similar comparisons have been observed for the damping quantities, in absolute values, between the three models. An in-depth review of the literature reveals that the study carried out herein constitutes several elements of originality as only very few similar work have been undertaken.

Keywords: modal analysis, concrete dam, viscous damping, QR damped method

1. Introduction

The seismic response of an engineering structure is affected by the medium on which it is founded (Dimitri et al., 2008). It is now generally known that the foundation soil significantly affects the dynamic response of gravity dam during earthquakes (Bayraktar et al., 2005). Structural response is then governed by the interplay between the characteristics of the soil, the structure and the input motion. Soil-Structure Interaction (SSI), as this phenomenon has become known, has been of research interest for the past 30 years (Dimitri et al., 2008).

In the literature, there are four different modeling of the foundation soil: the standard rigid-base model, the massless-foundation model, the deconvolved-base-rock model, and the free-field dam-foundation interface model (Leger & Boughoufalah, 1989). In the massless foundation model, absence of mass makes the foundation rock as a spring, i.e., only the flexibility of the foundation rock is taken into account. Theoretically, to take advantage of the dam's geometrical characteristics and loading conditions, most structural analyses performed on the dam-foundation soil system are based on the 2D plane strain assumption.

The primary energy loss mechanism currently assumed in the analysis of concrete dams is viscous damping (Tepes et al., 2010). Equivalent viscous damping constants have been determined experimentally. Shaking tests using low-level excitations have been performed on concrete dams throughout the world, and damping ratio of 2 to 5 percent of the critical damping have been reported (Dreher, 1980). However, damping ratio as high as 10 percent of the critical damping has been measured during higher levels excitations. Therefore, a damping ratio of 2 to 10 percent appears reasonable for most concrete dams (Dreher, 1980).

It is well known that real modes, which are obtained assuming free natural vibrations without damping, can be used as a modal base in a modal superposition analysis, e.g. a spectrum analysis, where damping is small. However, for structures exhibiting significant viscous damping, for example a damping ratio of 5 percent, real modes might not be appropriate. In this case complex modes should be employed rather (Ansys theory manual, 2007).

In this paper, influence of the foundation soil on the modal response of the Brezina arch dam-foundation soil,

located in El Beyadh, Algeria, is investigated. Moreover, a parametric study of the damping ratio is conducted. Following this section, three dam-foundation soil finite element models are presented in Section 2. Undamped modal analysis results are reported in Section 3. Section 4 covers damped modal analysis results. Conclusions are offered in the last section of the paper.

2. Dam-foundation Soil Finite Element Models

Due to the arch shape of the Brezina dam, it is inappropriate to assume 2D plane strain conditions, see Figure 1. The dam is located in El Beyadh, in the west of Algeria. The dam is 60 m high, its maximum arch length is 78.5 m and its thickness varies from 5m at the crest to 36.3 m at the foundation level.

Figure 1. Brezina concrete arch dam

The dam-foundation soil structure is investigated using three 3D finite element models. The first model or dam alone, neglecting the soil, represents the dam only, which is clamped at its base on the soil, see Figure 2a. The second model or dam-massless soil, represents the dam and the adjacent soil but the soil's mass is neglected. The soil is also clamped at its base, see Figure 2b. Lastly, the third model or dam-soil with soil mass, is similar to the second one, except that the mass of the soil is taken into account (Figure 2b). These finite elements models are created using the finite element commercial package, ANSYS, with a mapped meshing (Ansys theory manual, 2007). The finesse of the mesh has been determined by performing a convergence analysis (mesh sensitivity). ANSYS is one of the leading commercial finite element programs in the world and can be applied to a large number of applications in engineering, it performs linear and nonlinear analyses; nevertheless it is not specialized for SSI analysis. Another objective of the present work is to orient this finite element code to the treatment of soil structure interaction problems.

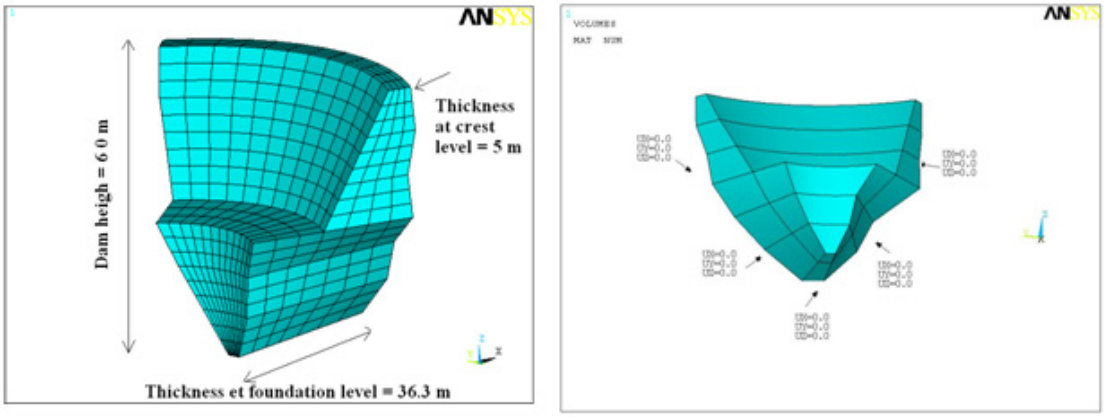

Figure 2a. 3D finite element model of Brezina arch dam without adjacent soil and boundary conditions

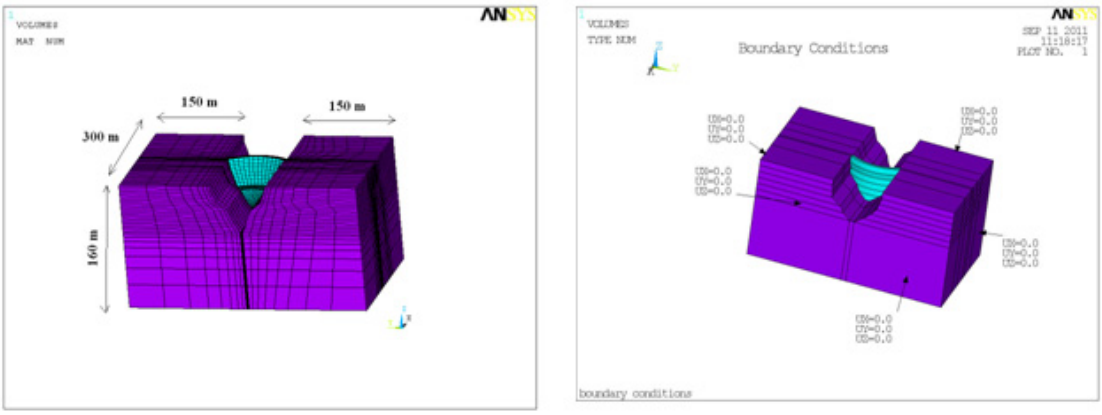

Figure 2b. 3D finite element model of Brezina arch dam with adjacent soil and boundary conditions

The first model, i.e., dam alone, possesses 972 quadratic solid elements (SOLID185) and 1378 nodes (Figure 2a). The second and third model (with the soil) exhibits 16252 quadratic solid elements and 19035 nodes (Figure 2b).

The length and width of the soil, along the global X and Y axis, respectively, are taken to be 150m, while its depth, along the Z direction, is taken to be 100 m. These sizes are chosen so that the applied boundary condition will not affect the modal responses of the dam.

The material properties for both the concrete arch dam and foundation soil are reported in Table 1. These characteristics are provided by a governmental organism in charge of the dam study and from the geotechnical rapport of Brezina dam site.

Table 1. Material properties of Brezina dam

Material	Young's Modulus (N/m^2)	Poisson's ratio	Density (kg/m^3)
Concrete dam	28.5e+09	0.2	2500
Foundation soil	14.5e+09	0.25	2100

3. Undamped Modal Analysis Results

This section covers undamped modal responses of the Brezina arch dam-foundation soil system. The modal responses are calculated using the Block Lanczos method (Ansys theory manual, 2007). Reported quantities are the first natural mode frequencies and the corresponding participation factor, Pfi along X direction, its ratio to the maximum participation factor, Ratio and effective mass, Mei. Table 2, Table 3 and Table 4 list these quantities for the dam alone, dam with massless soil, and dam-soil with soil mass, respectively (results are along X direction). The number of modes reported is such that the ratio of the cumulative effective mass to the total mass reaches a minimum of 0.9 along each of the three, X, Y and Z directions. Quantities along Y and Z direction are omitted herein.

The fundamental mode is defined as the one that involves the maximum mass, i.e., the most dominant mode having a ratio, Ratio of one for the direction considered (here along X direction).

As expected, the highest frequencies are obtained from the dam alone model (Table 2) while the lowest ones are due to the dam-soil with soil mass (Table 4). Qualitatively, these results can be explained with the single degree of freedom mass-spring system for which the circular frequency is:

$$\omega = \sqrt{\frac{k}{m}} \tag{1}$$

where k is the stiffness of the spring and m the mass (Shabana, 1995). With respect to the dam alone model, the dam-massless soil has the same total mass, but is globally less rigid since the soil's Young's modulus is almost half the value of that of the concrete dam (see Table 1), thus from Equation (1), lower frequencies are obtained from the latter model. Also, between the dam-massless soil and dam-soil with soil mass, the global stiffness is identical but the total mass is evidently larger for the dam-soil with soil mass, hence, again from Equation (1),

lower frequencies are obtained from the latter model. It is worth noting that the position of the fundamental mode is unchanged from the dam alone to the dam-massless soil model (mode number one of Table 2 and 3), while it switches to the fourth position when the mass of the soil is taken into account (Table 4).

Table 2. Dam alone first undamped natural frequencies in *X* direction

Mode	Frequency (Hz)	P_{fi}	Ratio	Mei (Kg)
1	12.42	5548.5	1.00000	0.3078e+08
2	18.56	-14.827	0.00267	219.850
3	24.83	-5402.2	0.97363	0.2918e+08
4	26.53	3259.9	0.58753	0.1062e+08
5	27.80	-195.93	0.03531	38388.0
6	30.37	-1909.8	0.34419	0.3647e+07
7	33.17	-143.98	0.02595	20730.7
8	35.86	190.59	0.03435	36323.9
9	38.56	4063.6	0.73238	0.1651e+08
10	44.41	-1961.4	0.35350	0.3847e+07
11	44.74	1253.8	0.22596	0.1571e+07
12	46.51	331.38	0.05972	109814.
13	48.04	1684.0	0.30349	0.2835e+07
14	49.02	-836.08	0.15068	699027.
15	51.22	160.33	0.02889	25706.9
16	51.46	-1437.2	0.25902	0.2065e+07
17	53.00	-2126.5	0.38326	0.4522e+07

Table 3. Dam with massless soil first undamped natural frequencies in X direction

Mode	Frequency (Hz)	P_{fi}	Ratio	Mei (Kg)
1	9.334	7712.6	1.00000	0.5948e+08
2	13.67	-29.543	0.00383	872.768
3	14.28	5749.5	0.74546	0.3305e+08
4	16.27	-243.47	0.031567	59275.8
5	16.78	-6195.4	0.8032	0.3838e+08

Table 4. Dam-soil with soil mass first undamped natural frequencies in X direction

Mode	Frequency (Hz)	P_{fi}	Ratio	Mei (Kg)
1	6.48	-3265.6	0.04513	0.10664e+08
2	6.90	-10.623	0.00014	112.840
3	7.40	184.01	0.00254	33858.1
4	7.83	72359.	1.00000	0.52358e+10
5	8.57	-40172.	0.55516	0.16137e+10
6	8.81	-493.93	0.00682	243963.
7	9.16	-36506.	0.50451	0.13327e+10
8	9.74	-12211.	0.16875	0.14911e+09
9	9.83	-941.21	0.01300	885870.
10	10.04	-4659.5	0.06439	0.21711e+08
11	10.065	-33267.	0.45975	0.11067e+10
12	10.57	-202.47	0.00279	40992.7
13	10.72	3511.3	0.04852	0.12329e+08
14	11.64	0.9712	0.00001	0.943311
15	11.70	10302.	0.1423	0.1061e+09
16	11.94	995.11	0.0137	990249.
17	12.15	33474.	0.4626	0.1120e+10

In terms of numerical values, the dam alone shows much higher frequencies than that of the dam-massless soil (12.42 Hz compared to 9.334 Hz for the first mode). This latter's frequencies, in turn, are also much higher than that of the dam-soil with soil mass (6.48 Hz for the first mode). These results are depicted for the first 5 modes in Figure 3. Table 5 summarizes the frequencies decrease between the three models for the first 5 modes. The calculations performed highlight the need to model the foundation soil as a deformable structure, and to take into account its mass.

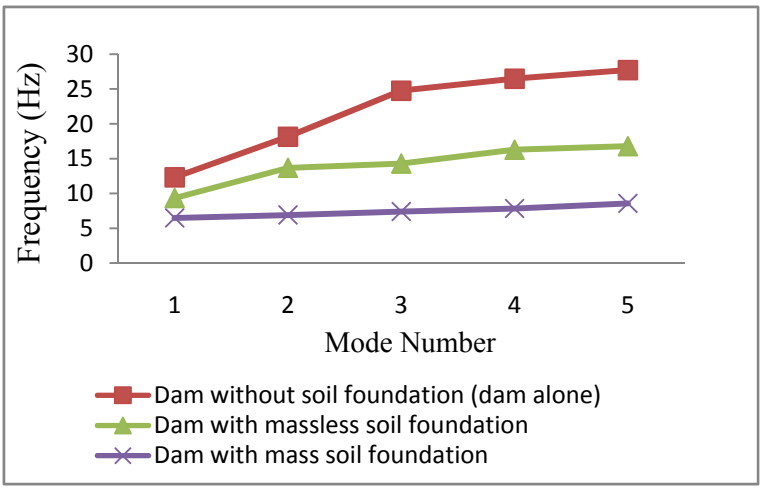

Figure 3. Undamped first 5 frequencies for the three models

Table 5. Frequencies decrease (%) between the three models

Mode	Dam-massless soil /Dam alone (%)	Dam-soil with mass soil /Dam alone (%)	Dam-soil with mass soil /Dam-massless soil (%)
1	24,85	47,80	30,54
2	26,30	62,79	49,52
3	42,46	70,18	48,18
4	38,64	70,45	51,84
5	39,62	69,15	48,91

4. Damped Modal Analysis Results

In this section, damped modal responses of the Brezina arch dam-foundation soil system are investigated. Recall that the free damped vibration equations (Reddy, 2002) are

$$M\ \ddot{x} + C\ \dot{x} + K\ x = 0 \tag{2}$$

where M, C and K is the mass, damping and stiffness matrix, respectively; $x, \dot{x}, \ddot{x}$ is the displacement, velocity and acceleration vector, respectively. Herein, viscous damping is assumed to be of the Raleigh form (Priscu et al., 1985):

$$C = \alpha\ M + \beta\ K \tag{3}$$

where α, β are constants referred to as mass and stiffness damping, respectively. From Eq. (3), the following relation can easily be established:

$$\xi_i = \frac{\alpha}{2\omega_i} + \frac{\beta\omega_i}{2} \tag{4}$$

where ξ_i is the viscous damping ratio to critical damping for mode i, and ω_i the corresponding circular frequency. The mass damping α, which is important for bodies resisting to wind or for submarine applications [6], is

neglected herein. Hence, assuming $\alpha = 0$, Eq. (4) is reduced to

$$\beta = \frac{2\xi_i}{\omega_i} \tag{5}$$

which yields β for given ξ_i and ω_i. Searching harmonic solutions, and making use of the Raleigh damping assumption Eq. (3) with $\alpha = 0$, Eq. (2) becomes

$$\left[(1 + j\omega\beta)K - \omega^2 M\right] x_0 = 0 \tag{6}$$

where j is the unit complex number, $j^2 = -1$ and x_0 the modal vector.

For the parametric study conducted herein, the viscous damping ratio ξ will be 2%, 5% and 10%, while ω_i will be the circular frequency of the fundamental mode (that involves the largest effective mass). The damped modal responses are calculated using the QR damped method [6]. Reported quantities are the first eigenvalues in terms of imaginary part, ω_i, and real part, σ_i, the corresponding participation factor along *X* direction, P_{fi}, the ratio to the maximum participation factor, *Ratio*, the effective mass, *Mei*, and the modal damping ratio, γ_i. Recall that the imaginary part ω_i of the eigenvalue ρ_i is the frequency whereas the real part σ_i of ρ_i is the damping related quantity for mode *i*. The modal damping ratio, γ_i, is

$$\gamma_i = \sigma_i / \sqrt{\sigma_i^{\,2} + \omega_i^{\,2}} \tag{7}$$

Table 6. Dam alone first natural damped frequencies, viscous damping ξ = 2%

Mode	Im part , ω_i (Hz)	R part, σ_i	P_{fi}	Ratio	Mei (kg)	γ_i
1	12,41	-0,251	19,267	0,01331	371,23	2,017E-02
2	18,55	-0,560	-0,071	0,00005	5,09E-03	3,015E-02
3	24,81	-1,002	-8,933	0,00617	79,804	4,034E-02
4	26,51	-1,143	-601,100	0,41524	361323	4,310E-02
5	27,77	-1,255	1447,600	1	2,10E+06	4,516E-02
6	30,34	-1,499	-1305,700	0,90195	1,70E+06	4,934E-02

Table 7. Dam with massless soil first natural damped frequencies, viscous damping ξ = 2%

Mode	Im part , ω_i (Hz)	R part, σ_i	P_{fi}	Ratio	Mei (kg)	γ_i
1	9,33	-0,188	1240,4	0,01337	1,54E+06	2,01E-02
2	13,67	-0,403	1,2709	0,00001	1,61521	2,95E-02
3	14,28	-0,440	-741,23	0,00799	549425	3,08E-02
4	16,27	-0,571	-50129	0,54016	2,51E+09	3,51E-02
5	16,78	-0,607	92804	1,00000	8,61E+09	3,62E-02
6	22,63	-1,107	-83822	0,90322	7,03E+09	4,88E-02

Table 8. Dam-soil with soil mass first natural damped frequencies, viscous damping ξ = 2%

Mode	Im part , ω_i (Hz)	R part, σ_i	P_{fi}	Ratio	Mei (kg)	γ_i
1	6,48	-0,107	4453,6	0,00055	1,98E+07	1,66E-02
2	6,90	-0,122	812,13	0,00010	659548	1,76E-02
3	7,40	-0,140	-1,20E+05	0,01493	1,45E+10	1,89E-02
4	7,84	-0,157	-8,05E+06	1,00000	6,49E+13	2,00E-02
5	8,57	-0,188	5,73E+06	0,71113	3,28E+13	2,19E-02

Table 6, Table 7 and Table 8 list these modal quantities for the dam alone, dam-massless soil, and dam-soil with soil mass, respectively. The input damping ratio ξ is 2% ($\xi = 0.02$). Firstly, these results show that the

frequencies are almost identical, but very slightly lower, as compared to that of the undamped modes for each model studied, e.g. 12.42 Hz from Table 2 and 12.41Hz from Table 6. These findings are not surprising. Consider the mass-damper-spring single degree of freedom system for which the circular frequency is

$$\omega = \frac{\sqrt{4km - c^2}}{2m} \tag{8}$$

where k is the stiffness of the spring, m the mass and c the damper (Reddy, 2002). It is assumed that the system is far from over damped so that in the above equation, $4km - c^2 > 0$. Eq. (8) shows that the frequency is always lower than that of the mass-spring system, and that the two frequencies are almost identical if the damping c is small enough, i.e., if the system is only moderately damped. This is obviously the case for the 3D dam-soil models under study. The second remark worth noting is the negative values of σ_i, indicating that the dam-soil system is stable. This is expected as the analogy can be made again with the simple system for which

$$\sigma = -\frac{c}{2m} \tag{9}$$

It should be noted that under the Raleigh damping assumption with $\alpha = 0$, the damping c, in the above mass-damper-spring system, becomes $c = \beta\ k$. Recall that σ and ω are the real and imaginary part, respectively, of the roots of the characteristic equation (Reddy, 2002). Lastly, Table 6 shows that adding damping to the dam-soil system switches the fundamental mode. For example, mode number five is now the fundamental mode for the dam alone (see Table 6) while without damping, the fundamental mode is number one (see Table 2).

For $\xi = 0.02$, Figure 4 depicts the frequencies decrease from the dam alone to the dam-soil with soil mass model for the first 5 modes, and Figure 5 illustrates the decrease of the damping related quantity α_i. Like the comments made in the preceding section, qualitatively, the frequencies decrease between the three models can be explained from Equation (8). Also, from Equation (9) and $c = \beta\ k$, the damping decrease, in absolute value, from the dam alone to the dam-soil with soil mass model is obvious. Finally, this decrease in percentage is summarized in Table 9 and Table 10.

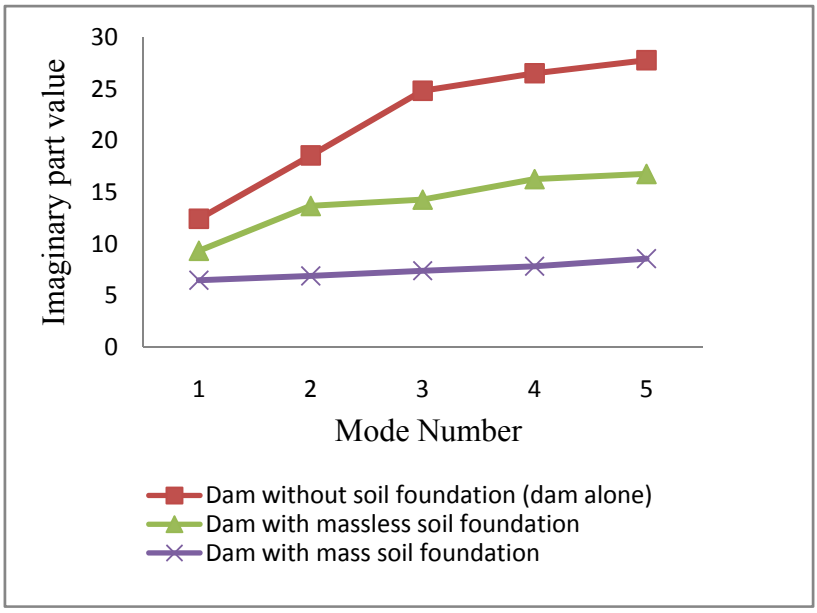

Figure 4. Damped first 5 frequencies for the three models, viscous damping ξ = 2%

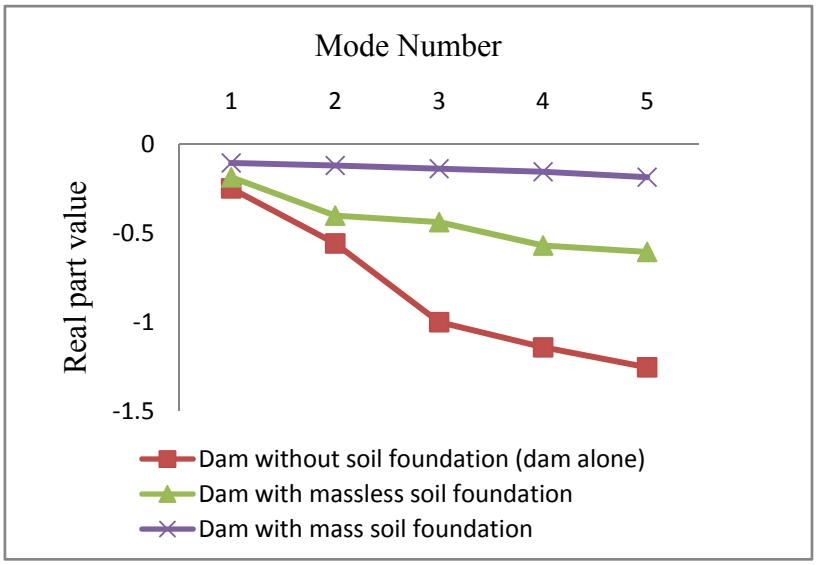

Figure 5. First 5 damping related quantities for the three models, viscous damping $\xi = 2\%$

Table 9. Frequencies decrease (%) between the three models, viscous damping $\xi = 2\%$

Mode	Dam-massless soil /Dam alone (%)	Dam-soil with soil mass /Dam alone (%)	Dam-soil with soil mass /Dam-massless soil (%)
1	24,85	47,80	30,54
2	26,30	62,79	49,51
3	42,44	70,17	48,17
4	38,62	70,43	51,83
5	39,60	69,13	48,89

Table 10. Damped related quantities in absolute values decrease (%) between the three models, viscous damping $\xi = 2\%$

Mode	Dam-massless soil /Dam alone (%)	Dam-soil with mass soil /Dam alone (%)	Dam-soil with mass soil /Dam-massless soil (%)
1	25,07	57,16	42,83
2	27,93	78,23	69,80
3	56,07	86,02	68,18
4	50,05	86,27	72,52
5	51,63	85,04	69,07

Similar results for the input damping ratio ξ of 5% and 10% are reported in Tables 11-13 and Tables 16-18, respectively. From these results, same comments as for $\xi = 2\%$ can be made although the differences in frequencies are slightly more pronounced with respect to that of the undamped modes: the larger the damping ratio, the bigger the differences. This is clearly supported by Equation (8). Figure 6, Figure 7, Figure 8 and Figure 9 depict the frequency and damping related quantity decrease between the three models for $\xi = 0.05$ and $\xi = 0.1$, respectively. Tables 14-15 and Tables 19-20 summarize theses evolutions in percentage.

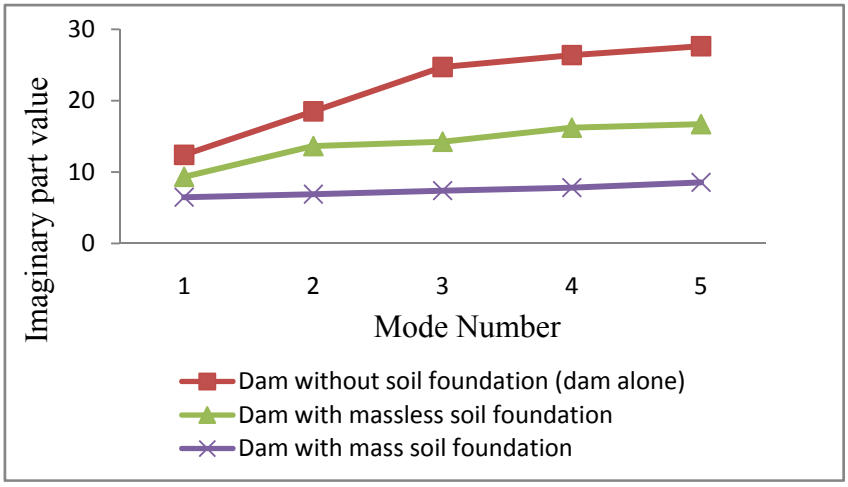

Figure 6. First 5 damped frequencies for the three models, viscous damping ξ = 5%

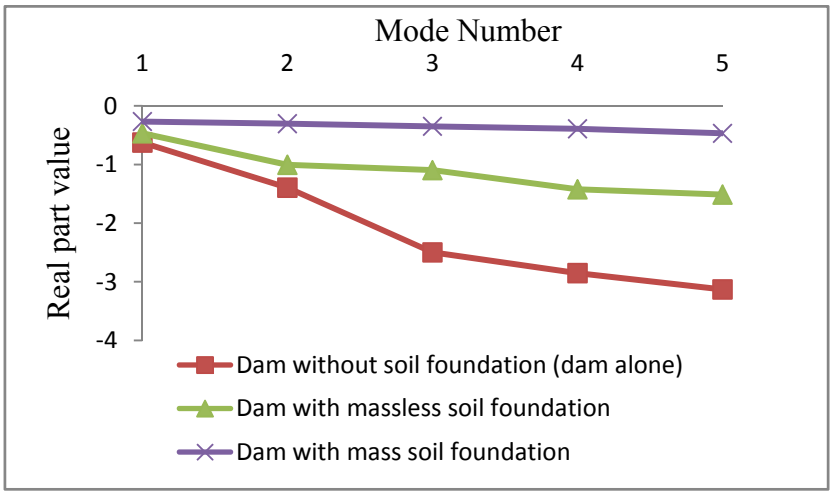

Figure 7. First 5 damped related quantities for the three models, viscous damping ξ = 5%

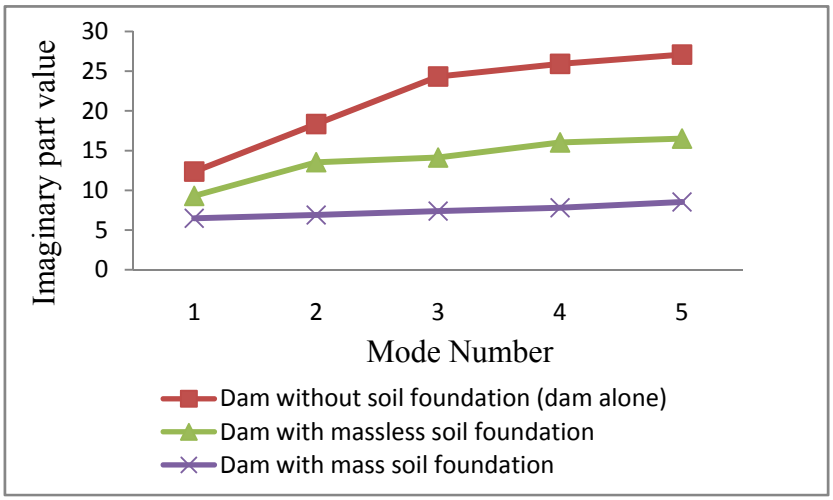

Figure 8. Damped first 5 frequencies for the three models, viscous damping ξ = 10%

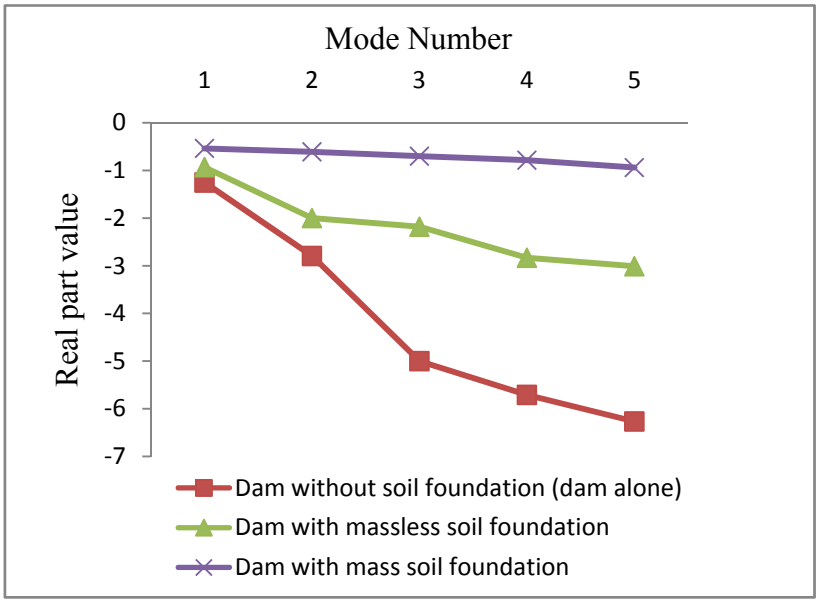

Figure 9. First 5 damped related quantities for the three models, viscous damping ξ = 10%

Table 11. Dam alone first natural damped frequencies, viscous damping ξ = 5%

Mode	Im part , ω_i (Hz)	R part, σ_i	P_{fi}	Ratio	Mei (kg)	γ_i
1	12.40	-0.625	-38.605	0.01331	1490.36	0.503e-01
2	18.50	-1.396	0.143	0.00005	0.204e-01	0.503e-01
3	24.70	-2.499	17.899	0.00617	320.386	0.752e-01
4	26.37	-2.853	1204.4	0.41524	0.145e+07	0.752e-01
5	27.62	-3.132	-2900.5	1.000	0.841e+07	0.100
6	30.14	-3.740	2616.1	0.90195	0.684e+07	0.100

Table 12. Dam with massless soil first natural damped frequencies, viscous damping ξ = 5%

Mode	Im part , ω_i (Hz)	R part, σ_i	P_{fi}	Ratio	Mei (kg)	γ_i
1	9.32	-0.468	457.64	0.01336	209432.	0.501e-01
2	13.64	-1.005	0.46888	0.000014	0.219844	0.734e-01
3	14.24	-1.096	-273.46	0.00798	74781.7	0.767e-01
4	16.21	-1.423	-18494.	0.54016	0.342e+09	0.874e-01
5	16.71	-1.513	34238.	1.00000	0.117e+10	0.901e-01
6	22.49	-2.758	-30924.	0.90322	0.956e+09	0.121

Table 13. Dam-soil with soil mass soil first natural damped frequencies, viscous damping ξ = 5%

Mode	Im part , ω_i (Hz)	R part, σ_i	P_{fi}	Ratio	Mei (kg)	γ_i
1	6.47	-0.268	229.81	0.0005	52811.6	0.413e-01
2	6.89	-0.304	41.906	0.0001	1756.11	0.440e-01
3	7.39	-0.349	-6204.3	0.015	0.3849e+08	0.472e-01
4	7.82	-0.391	-0.415e+06	1.000	0.1726e+12	0.499e-01
5	8.56	-0.469	0.295e+06	0.711	0.8733e+11	0.546e-01

Table 14. Frequencies decrease (%) between the three models, viscous damping ξ = 5%

Mode	Dam-massless soil /Dam alone (%)	Dam-soil with mass soil /Dam alone (%)	Dam-soil with mass soil /Dam-massless soil (%)
1	24,85	47,78	30,52
2	26,29	62,72	49,43
3	42,33	70,06	48,08
4	38,52	70,32	51,72
5	39,48	69,00	48,78

Table 15. Damped related quantities in absolute values decrease (%) between the three models, viscous damping ξ = 5%

Mode	Dam-massless soil /Dam alone (%)	Dam-soil with mass soil /Dam alone (%)	Dam-soil with mass soil /Dam-massless soil (%)
1	25,14	57,13	42,73
2	27,99	78,21	69,75
3	56,11	86,010	68,12
4	50,09	86,26	72,47
5	51,67	85,023	69,01

Table 16. Dam alone first natural damped frequencies, viscous damping ξ = 10%

Mode	Im part , ω_i (Hz)	R part, σ_i	P_{fi}	Ratio	Mei (kg)	γ_i
1	12.35	-1.250	-35.469	0.013	1258.08	0.10
2	18.34	-2.792	0.1314	0.00004	0.172e-01	0.15
3	24.32	-4.999	16.445	0.0061	270.452	0.201
4	25.91	-5.706	1106.6	0.4152	0.1224e+07	0.215
5	27.08	-6.264	-2664.9	1.000	0.71019e+07	0.225
6	29.44	-7.480	2403.6	0.901	0.57774e+07	0.246

Table 17. Dam with massless soil first natural damped frequencies, viscous damping ξ = 10%

Mode	Im part, ω_i (Hz)	R part, σ_i	P_{fi}	Ratio	Mei (kg)	γ_i
1	9.28	-0.930	-171.52	0.013366	29420.3	0.997e-01
2	13.53	-1.998	-0.17574	0.000014	0.308e-01	0.146
3	14.12	-2.181	102.49	0.007987	10505.1	0.152
4	16.03	-2.830	6931.6	0.540160	0.480e+08	0.173
5	16.51	-3.009	-12832.	1.00	0.164e+09	0.179
6	21.98	-5.485	11591.	0.903	0.134e+09	0.242

Table 18. Dam-soil with soil mass first natural damped frequencies, viscous damping ξ = 10%

Mode	Im part, ω_i (Hz)	R part, σ_i	P_{fi}	Ratio	Mei (kg)	γ_i
1	6.46	-0.536	-642.87	0.0005	413279.	0.826e-01
2	6.87	-0.608	-117.23	0.0001	13742.5	0.8807e-1
3	7.37	-0.699	17356.	0.0149	0.3012e+09	0.9444e-01
4	7.79	-0.783	0.11625e+07	1.0000	0.1351e+13	0.9998e-01
5	8.52	-0.938	-0.8267e+06	0.7111	0.6834e+12	0.1093

Table 19. Frequencies decrease (%) between the three models, damping ξ = 10%

Mode	Dam-massless soil /Dam alone (%)	Dam-soil with soil mass /Dam alone (%)	Dam-soil with soil mass /Dam-massless soil (%)
1	24,84	47,72	30,43
2	26,25	62,51	49,17
3	41,94	69,69	47,80
4	38,13	69,89	51,34
5	39,03	68,53	48,38

Table 20. Damped related quantities in absolute value decrease (%) between the three models, viscous damping ξ = 10%

Mode	Dam-massless soil /Dam alone (%)	Dam-soil with soil mass /Dam alone (%)	Dam-soil with soil mass /Dam-massless soil (%)
1	25,57	57,13	42,40
2	28,42	78,21	69,57
3	56,37	86,01	67,93
4	50,38	86,26	72,31
5	51,95	85,02	68,83

Influences of the viscous damping ratio ξ on the frequencies and the damping related quantity are summarized in Figures 10-11 and Tables 21-22 for the dam without soil model, Figure 12-13 and Tables 23-24 for the dam with massless soil model, and Figures 14-15 and Tables 25-26 for the dam-soil with soil mass model.

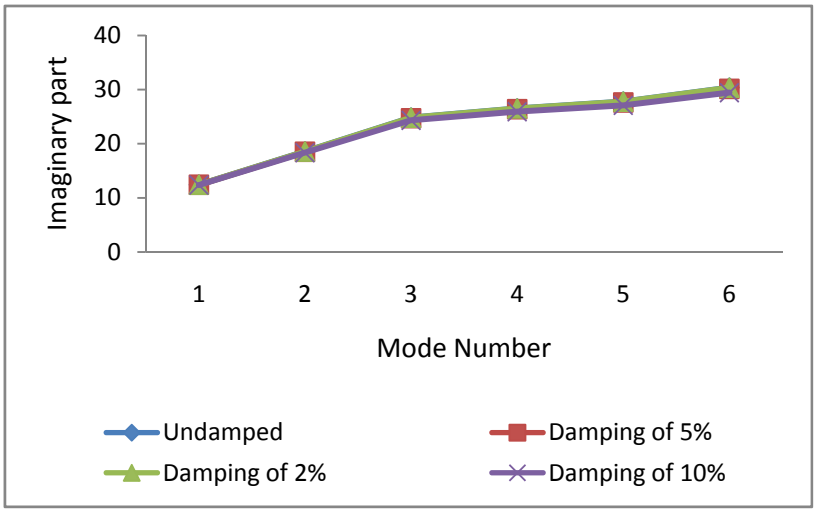

Figure 10. Influence of viscous damping ξ on the frequencies for the dam alone model

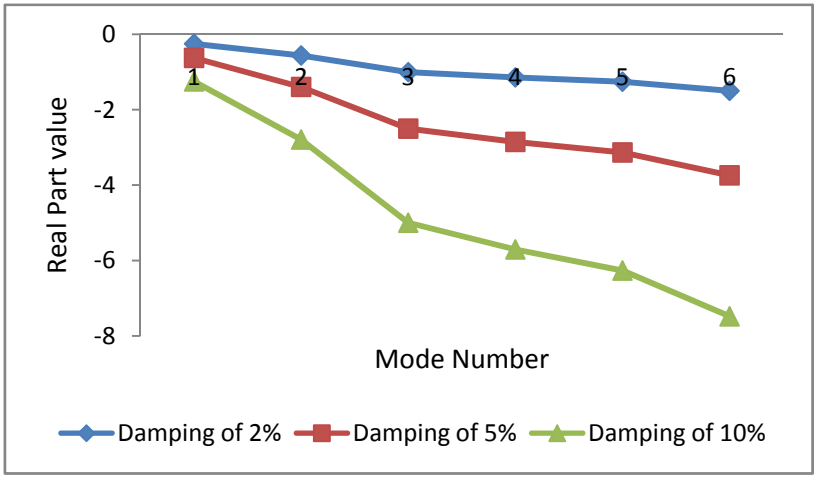

Figure 11. Influence of viscous damping ξ on the damping related quantities for the dam alone model

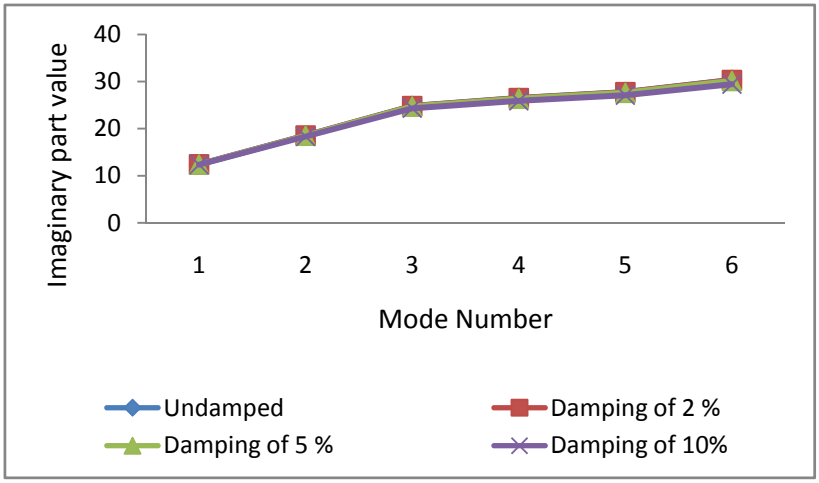

Figure 12. Influence of viscous damping ξ on the frequencies for the dam with massless soil model

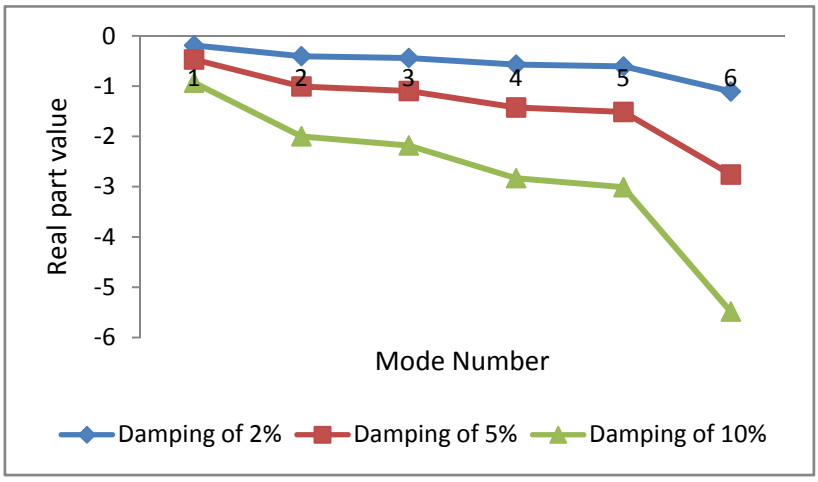

Figure 13. Influence of viscous damping ξ on the damping related quantities for the dam with massless soil model

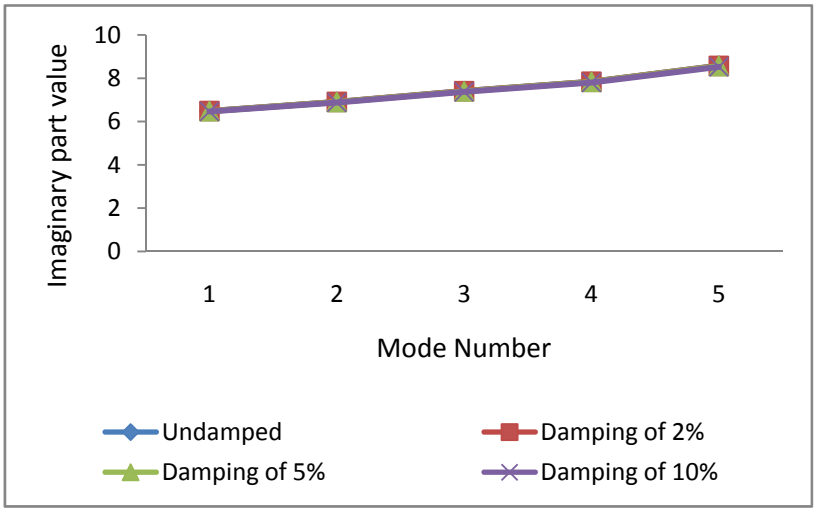

Figure 14. Influence of viscous damping ξ on the frequencies for the dam-soil with soil mass model

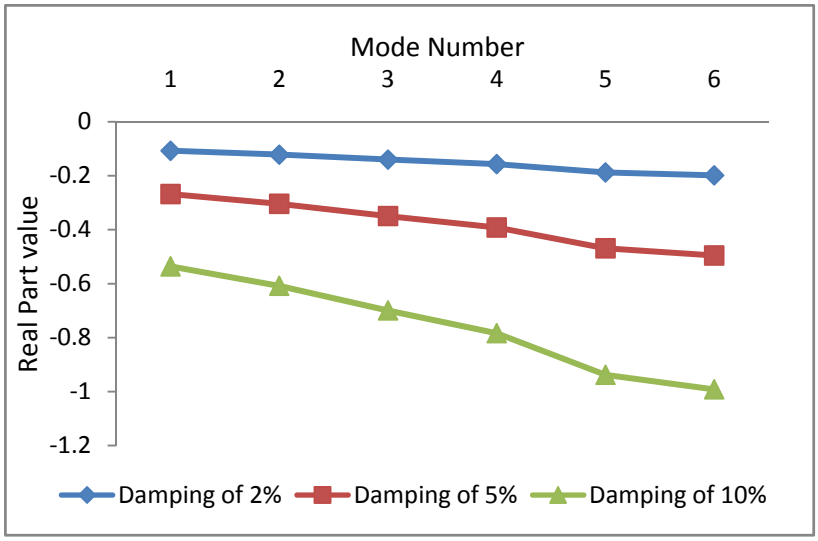

Figure 15. Influence of viscous damping ξ on the damping related quantities for the dam-soil with soil mass model

Table 21. Influence of viscous damping ξ on the frequencies for the dam alone model

Mode	Undamped	Damping of 2%	Damping of 5%	Damping of 10%
1	12,42	12,41	12,40	12,35
2	18,56	18,55	18,50	18,34
3	24,83	24,81	24,70	24,32
4	26,53	26,50	26,37	25,91
5	27,80	27,77	27,62	27,08
6	30,37	30,34	30,14	29,44

Table 22. Influence of viscous damping ξ on the damping related quantities for the dam alone model

Mode	Damping of 2%	Damping of 5%	Damping of 10%
1	-0,250	-0,625	-1,250
2	-0,559	-1,396	-2,792
3	-1,001	-2,499	-4,999
4	-1,143	-2,853	-5,706
5	-1,255	-3,132	-6,264
6	-1,499	-3,740	-7,480

Table 23. Influence of viscous damping ξ on the frequencies for the dam with massless soil model

Mode	Undamped	Damping of 2%	Damping of 5%	Damping of 10%
1	9,33	9,33	9,32	9,28
2	13,67	13,67	13,64	13,53
3	14,28	14,28	14,24	14,12
4	16,27	16,26	16,21	16,03
5	16,78	16,77	16,71	16,51
6	22,66	22,63	22,49	21,98

Table 24. Influence of viscous damping ξ on the damping related quantities for the dam with massless soil model

Mode	Damping of 2%	Damping of 5%	Damping of 10%
1	-0,187	-0,468	-0,930
2	-0,403	-1,005	-1,998
3	-0,440	-1,096	-2,181
4	-0,571	-1,423	-2,830
5	-0,607	-1,513	-3,009
6	-1,106	-2,758	-5,485

Table 25. Influence of viscous damping ξ on the frequencies for the dam-soil with soil mass model

Mode	Undamped	Damping of 2%	Damping of 5%	Damping of 10%
1	6,48	6,48	6,47	6,46
2	6,90	6,90	6,89	6,87
3	7,40	7,40	7,39	7,37
4	7,83	7,83	7,82	7,79
5	8,57	8,57	8,56	8,52

Table 26. Influence of viscous damping ξ on the damping related quantities for the dam-soil with soil mass model

Mode	Damping of 2%	Damping of 5%	Damping of 10%
1	-0,107	-0,268	-0,536
2	-0,121	-0,304	-0,608
3	-0,140	-0,349	-0,699
4	-0,156	-0,391	-0,783
5	-0,187	-0,469	-0,938
6	-0,198	-0,495	-0,991

Quantitatively, results reported in this section point out, again, the importance of taking into account the soil with its mass. For any of the damping ratio under study, the dam alone shows significantly higher frequencies than that of the dam-massless soil. This latter's frequencies are also much higher than that of the dam-soil with soil mass. The damping values calculated are also much lower in absolute value from the dam-soil with soil mass than that from the other two models. The results reported also show that adding only a small damping ratio, e.g. $\xi = 0.02,$ to the dam-soil model reduces the number of modes needed to obtain 90% of the system's total mass. For example, for the undamped dam alone model, 17 modes are needed to reach 91.73 % of the total mass, whereas for its damped counterpart with $\xi = 0.02,$ 6 modes are sufficient to reach 96.9 % of the total mass. This feature is of practical importance as it reduces the CPU time for a further analysis based on the modal superposition method such as a spectrum analysis or a modal superposition transient response analysis.

5. Conclusions

Modal responses of the Brezina dam-foundation soil system are calculated using the finite element software, ANSYS. The following conclusions are drawn based on the numerical experiments conducted herein:

1) For the study of the dam-soil system, the foundation soil should be modeled as a deformable structure with its mass taken into account. The natural frequencies of either undamped or damped modes are much lower from the dam-soil with soil mass than that from the dam alone, and significantly lower than that from the dam-massless soil model. Modeling the soil with its mass also affects the mode shape by changing the fundamental mode position.
2) Likewise, for any of the damping ratio under study, the damping related values calculated are significantly lower, in absolute value, from the dam-soil with soil mass than that from the dam-massless soil, and much lower than that from the dam alone model.
3) Adding only a small damping ratio of 2% to Brezina dam-soil model reduces the number of modes needed, as compared to the undamped model, to obtain 90% of the system's total mass. This is of practical importance as it reduces the CPU time for a further analysis based on the modal superposition method, such as a modal superposition transient response analysis, which will be undertaken following the present work.

References

ANSYS. (2007). ANSYS User's Manual, ANSYS Theory Manual. Version 11.0, 2007.

Bayraktar, A, Hancer, E., & Akkose, M. (2005). Influence of base-rock characteristics on the stochastic dynamic response of dam-reservoir-foundation systems. *Engineering Structures, 27*(10), 1498-1508. http://dx.doi.org/10.1016/j.engstruct.2005.05.004

Dimitris, P, Dietz, M., Wood, D. M., Clouteau, D., & Modaressi, A. (2008). Numerical simulation of dynamic soil-structure interaction in shaking table testing. *Soil dynamics and earthquake Engineering, 28*, 453-467. http://dx.doi.org/10.1016/j.soildyn.2007.07.011

Dreher, K. J. (1980). Seismic analysis and design considerations for Concrete dams. Proceeding of a Conference on Dams and Earthquake held at the Institution of Civil Engineers.

Leger. P., & Boughoufalah, M. (1989). Earthquake input mechanisms for time domain analysis of dam-foundation systems. *Engineering Structures, 11*, 37-46. http://dx.doi.org/10.1016/0141-0296(89)90031-X

Priscu, R., Popovici, A., Stematiu, D., & Stere, C. (1982). *Earthquake Engineering for Large Dams* (2nd revised ed.). Editura Academiei and John Wiley & Sons.

Reddy, J. N. (2002). *Energy Principles and Variational Methods in Applied Mechanics* (2nd ed.). New York: John Wiley & Sons.

Shabana, A. A. (1995). *Theory of Vibration – An Introduction. Mechanical Engineering Series* (2nd ed.). Springer.

Tepes, O. F., & Gelmambet, S. (2010). Evaluation of damping in dynamic analysis of structures. *International journal of mathematical models and methods in applied sciences, 2*(4), 124-131.

Earth Science Research; Vol. 1, No. 2; 2012
ISSN 1927-0542 E-ISSN 1927-0550
Published by Canadian Center of Science and Education

Engineering Properties of Lateritic Soils around Dall Quarry in Sango Area, Ilorin, Nigeria

Oladele A. Omotoso[1], Olusola J. Ojo[1] & Emmanuel T. Adetolaju[1]

[1] Department of Geology and Mineral Sciences, University of Ilorin, Ilorin, Nigeria

Correspondence: Olusola J. Ojo, Department of Geology and Mineral Sciences, University of Ilorin, Ilorin, Nigeria. E-mail: solafoluk@yahoo.com

Received: February 10, 2012 Accepted: February 28, 2012 Online Published: June 5, 2012

doi:10.5539/esr.v1n2p71 URL: http://dx.doi.org/10.5539/esr.v1n2p71

Abstract

Lateritic soils at the DALL Quarry in Ilorin metropolis (Sango area), southwestern Nigeria were investigated with respect to their geotechnical properties and their suitability as construction materials. The two samples collected fall within the basement complex and they overly the migmatite-gneiss complex rocks.

The grain size analysis shows that soil sample ADET 1 is silt-clayey, very gravelly sand while sample ADET 2 is gravelly, silt-clayey sand. Atterberg consistency limit test shows that ADET 1 has 40% liquid limit, 18.2% plastic limit, 21.8% plasticity index, 7.4% shrinkage limit and an activity of 0.95 (normal clay). ADET 2 has 46% liquid limit, 23.5% plastic limit, 22.5% plasticity index, 8.2% shrinkage limit and an activity of 0.63. The soil samples are above the activity (A) line in the zone of intermediate plasticity (CL) which means that they are inorganic soils. The samples contain inactive clay suggesting little or no swelling tendency and therefore good for construction material and this would prohibit foundation failure during foundation settlement. The California Bearing Ratio (CBR) values are 1-4 % (average = 2.5%) and 3-5% (average = 4%) in ADET 1 and ADET 2 respectively which means that they are good as sub-grade construction materials. The cohesion ranges from 60-100Kpa (average = 75%) and the angle of internal friction ranges from 31^o- 35^o with an average of 33^o.

The geotechnical analyses results show that the soils have high bearing capacity with little or no volume change and therefore can be used as construction materials in engineering works. Thus, the soil could support shallow foundation, dam construction, homogeneous embankments, slope stability and sub-grade materials in road constructions.

Keywords: sub-grade, settlement, Sango, shrinkage, laterite, gravel

1. Introduction

Engineering properties of soils play a significant role in civil engineering construction works particularly in road constructions, foundations, embankments and dams to mention a few. This made imperative, the testing of soil, on which a foundation or superstructure is to be laid. This would determine its geotechnical suitability as a construction material. In recent times, the alarming rate at which lives are being lost due to collapsed buildings and road failures calls for a solution. The solution could be brought by critical geotechnical testing of the engineering soil. The present area is situated within latitudes 8^o34'N and 8^o32'N and longitudes 4^o38'15''E and 4^o40'E (Figures 1 and 2). The rocks in the study area are mainly granite gneiss and banded gneiss with foliations.

Several authors have worked on the geotechnical properties of lateritic soils. Jackson (1980) reported that lateritic soils have been used successfully as base and sub-base materials in road construction. Vallerge et al. (1969) worked on laterite soil in connection with construction of road, highways and airfields. The engineering problems associated with lateritic soil were evaluated by Lyons et al. (1971). Balogun (1984) reported that the addition of lime to the soil increases its optimum moisture content, liquid limit, California Bearing Ratio (CBR) etc. Alao (1983) studied the engineering properties of some soil samples from Ilorin area and discovered that they could be stabilized by compaction and that the samples could yield maximum strength if they are compacted on the dry side of their optimum moisture content (omc). Ogunsanwo (1989) evaluated CBR and shear strength of some compacted lateritic soils from southwestern part of Nigeria. He reported CBR of 27% in un-soaked and 14% for soaked sample for laterite soils derived from Amphibolites. From mica schist, he

obtained 10% for unsoaked and 9% for soaked samples. As such it will be suitable as sub-base material but its linear shrinkage of 10% is greater than the 8% maximum suggested for sub base material.

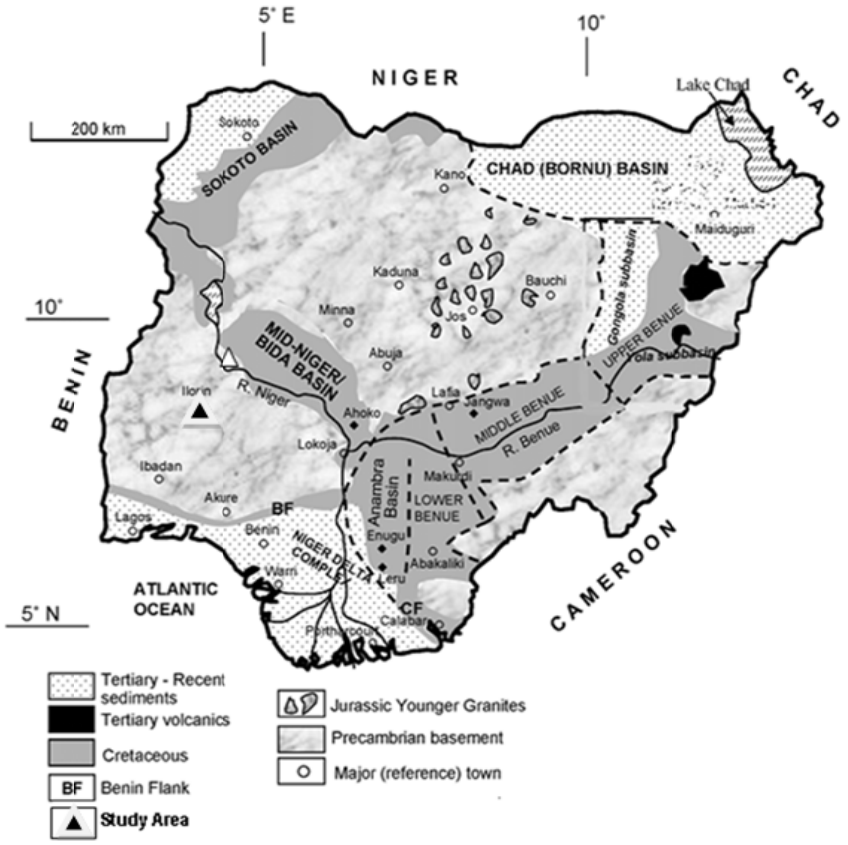

Figure 1. Geological Map of Nigeria showing the study area (Obaje et al., 2004)

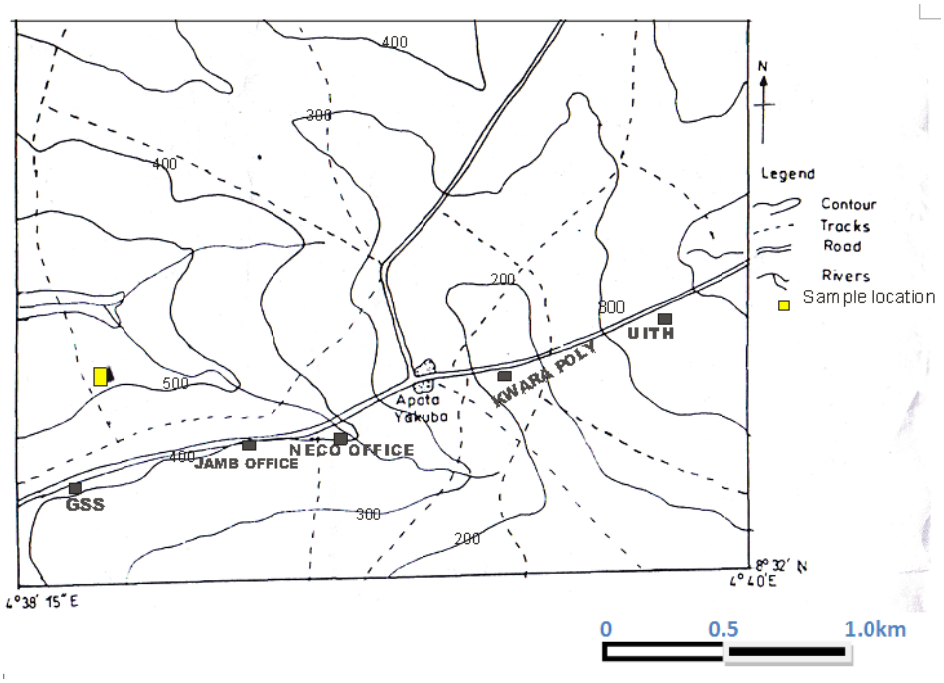

Figure 2. Sample location map showing sample locality

Ogunsanwo (1988) also studied laterite soil from Ojota area in Lagos state and obtained liquid limit of 49.5%, plastic limit of 21.8%, plastic index of 28.4% and linear shrinkage of 6.9%. On the basis of the geotechnical properties, he concluded that the soil is a good engineering construction material. Furthermore, Ogunsanwo (1989) performed CBR and shear strength tests on compacted lateritic soil from Benin sands. He then concluded that the compacted soil samples are suitable for use as sub-base materials in road construction as their CBR falls within the limits specified for this purpose (7-20%).

This paper examines the geotechnical properties around DALL Quarry (a laterite soil quarry) soil in Ilorin, Southwestern Nigeria around where road construction is on-going.

2. Materials and Methods

Two lateritic soils were sampled (ADET 1 AND ADET 2) and selected for the various testing techniques. Grain-size analyses were performed using the convectional coarse sieve and fine sieve methods. The compaction test was carried out by standard and modified proctor methods. For the standard and modified proctor compaction test, the following materials were used: mould dimension of 10cm by 5cm, weight of rammer=2.5kg, no of layers=5, no of blows=25 but 55 for modified proctor and height of rammer=11.5cm. The CBR tests (soaked CBR test and un-soaked CBR test) are determined using:

$$\text{CBR} = \frac{\text{test unit load}}{\text{Standard unit load}} \times 100$$

The analyses were carried out at the Civil Engineering Laboratory, University of Ilorin, Nigeria.

3. Results and Interpretations

3.1 Specific Gravity

The results of the specific gravity analysis of both soil samples, ADET 1 and ADET 2 are 2.68 and 2.63 respectively. Comparing these results with some standard results or values, ADET 1 could be required as sand and ADET 2 could be required as inorganic clay (Bowles 1979). Table 1 presents the typical values of specific gravity of soil particles.

Table 1. Typical values of specific gravity of soil particles (Bowles, 1979)

Soil type	Specific Gravity
Sand	2.65 – 2.68
Gravel	2.65 – 2.66
Clay(Inorganic)	2.52 – 2.66
Clay(organic)	2.68 – 2.72
Silt	2.65 – 2.66

3.2 Grain Size Distribution

The test is performed to determine the percentage of different grain sizes contained within the soil. The distribution of different grain sizes affects the engineering properties of soil which in turn influences their usability in construction works. The grain size distribution shows that ADET 1 is silty-clayey very gravelly sand, having 23% silt, 23% clay, 47% sand and 30% gravel compositions. Similarly, ADET 2 could be described as gravelly silt-clayey sand with 36% silt, 36% clay, 52% sand and 12% gravel compositions.

3.3 Atterberg Limits

The Atterberg consistency limit tests carried out on the soil samples show that ADET 1 has liquid limit of 40.0%, plastic limit of 18.2%, plasticity index of 21.8%, shrinkage limit of 7.4%, toughness index of 1.16 and activity of 0.95 while ADET 2 it has liquid limit of 46.0%, plastic limit of 23.5%, plasticity index of 22.5%, shrinkage limit of 8.2%, activity of 0.63 and toughness index of 0.82. The plots of plastic index against liquid limit on the plasticity chart show the Atterberg limits plots above "A" and it is in the zone of inorganic clayey silts, clays of low plasticity (CL) for both samples (Figure 3). This indicates Inorganic clays of low to medium plasticity, gravelly clays, sandy clay and silty clay. According to engineering use chart, the soil samples are impervious and inorganic clays useful for erosion resistance in canal constructions. They can also be useful in homogenous embankment in rolled earth dams because of their good to fair workability as construction materials and their fair shearing strength when compacted and saturated (Wagner, 1957). The values of activity (0.95 and 0.63

respectively) also indicate inactive clay content which means that volume change is minimal and not problematic in the samples (DAS, 2006). The values obtained could also be compared with the values obtained by Ogunsanwo (1988) who concluded that 'the soil should be good engineering construction materials when compacted'.

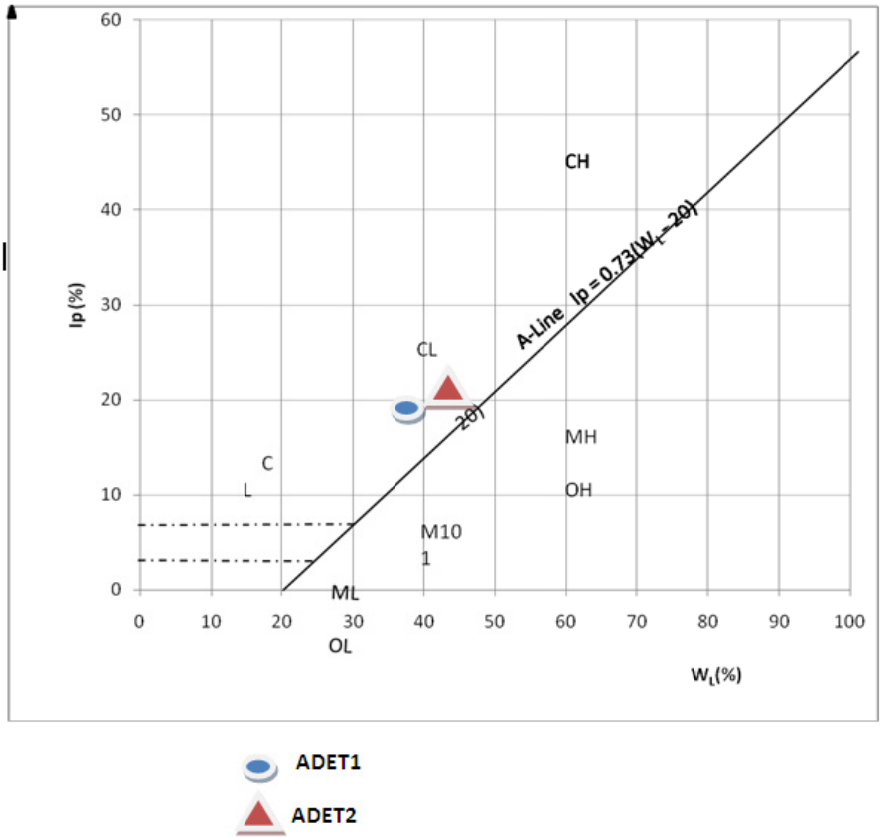

Figure 3. Plot of soil samples ADET 1 and ADET 2 on extended unified soil classification

3.4 Compaction Test

The standard proctor and modified proctor test variables, using 1000cm^3 moulds and the summary of compaction tests results are presented in Tables 2 and 3respectively. The compaction curves shows that dry density increases with increasing water content up to a maximum and later decrease. The maximum dry density (MDD) obtained for sample ADET1 is 1.85g/cm^3 at standard proctor and 1.84 g/cm^3 at modified proctor. For sample ADET 2, the maximum dry density is 1.84 g/cm^3 at standard proctor and 1.90 g/cm^3 for modified proctor (Figure 4). This falls within the observed range of 1.3-2.4 g/cm^3 obtained by Ogunsanwo (1989), Madu (1975) and Gidigasu (1972). There is slight decrease of maximum dry density down the profile in this study. The optimum water content for sample ADET 1 is 14.0% at standard proctor and 13% at modified proctor. For ADET 2 the optimum moisture content is 15% at standard proctor and 14% at modified proctor. The optimum moisture content (OMC) serves as guide to know the amount of water to add during construction.

Table 2. Specific for standard proctor and modified proctor test variables, using 1000cm^3 mould

	Standard Proctor	Modified Proctor
Weight of rammer (kg)	2.5	2.5
Height of rammer drop (cm)	11.5	11.5
Volume of mould (cm^3)	1000	1000
Number of layers	3	5
Number of blows	25	55

Table 3. Summary of compaction tests results

Sample	Standard Proctor		Modified Proctor	
Number	OMC (%)	MDD(g/cm^3)	OMC (%)	MDD(g/cm^3)
ADET 1	14.0	1.85	13.0	1.84
ADET 2	15.0	1.84	14.0	1.90

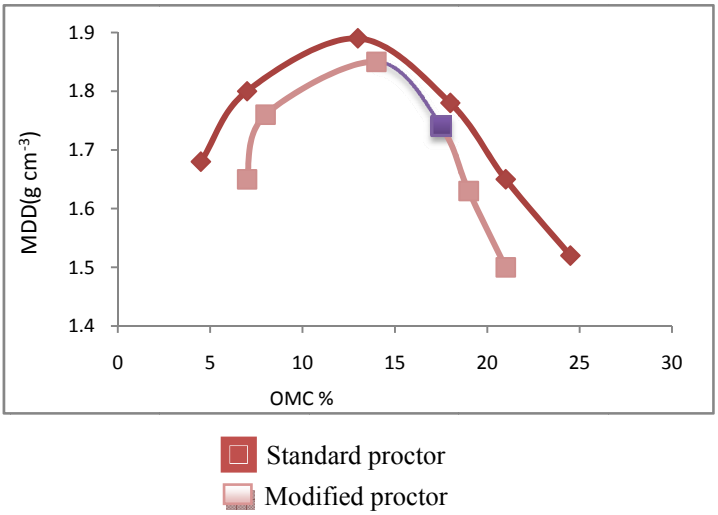

Figure 4. Compaction curve for soil sample ADET 1 standard and 1 modify

3.5 California Bearing Ratio (CBR) Tests

The results of the CBR and the interpretations are presented in Tables 4 and 5 respectively. For standard proctor unsoaked and soaked, ADET1 has 3% CBR and 1% CBR values respectively. ADET2 also has 4% CBR values respectively. Similarly, modified proctor unsoaked and soaked, ADET1 has 4% and 2% CBR values respectively and ADET2 has 5% and 3% CBR values respectively. Considering the values obtained, they fall within CBR value range of 0-3% and 3-7% respectively (Bowles, 1990), hence, the soils could be useful for slope stability, homogeneous embankment, core of roll earth dams and as sub-grade materials for road constructions.

Table 4. Summary of CBR tests results

Sample Number	Standard proctor %		Modified proctor %	
	Unsoaked %	Soaked %	Unsoaked %	Soaked %
ADET 1	3	1	4	2
ADET 2	4	4	5	3

Table 5. General rating of soil materials using CBR values (After Bowles, 1990)

CBR Value	General	Uses	Classification System
0-3	VERY POOR	Sub-grade	0H,CH,MH,OL
3-7	Poor-fair	Sub-grade	0H,CH,MH,OL
7-20	Fair	Sub-grade	OL,CL,ML,SC,SM,SP
20-50	Good	Base, Sub-grade	GM,GC,SW,SM,SP,GP
50	Excellent	Base	GW,GM

3.6 Direct Shear Tests

The direct shear test is used to determine the angle of internal friction of soil, the cohesion of the soil and the effective pressure. The test shows that soil sample ADET 1 compacted at standard proctor exhibits cohesion value of 70Kpa and angle of internal friction of 34^o, when compacted at modified proctor, the cohesion (C) is 100Kpa and angle of internal friction 32^o. Sample ADET 2 compacted at standard proctor has cohesion of 60Kpa

and internal friction of 35°. When compacted at modified proctor, the cohesion is 70Kpa and angle of internal friction is 31°. The graphical representation is shown in Figures 5-8. The shear box test revealed that the soils are of high strength having cohesion values ranging from 60Kpa to 100Kpa with an average of 75Kpa. Similarly, the angle of internal friction ranges from 31° to 35° with an average of 33°. Alao and Opaleye (2011) obtained an average value of cohesion, 65Kpa and an average value of angle of internal resistance, 26°. These values show that the soils have high bearing capacity as a result of their respective high cohesion and angle of internal friction values. It can therefore be deduced from the results of the test that the soil samples have a medium angle of internal friction which implies that the soils are hard according to the above references. Hence, the soils could support slope stability and shallow foundation.

Table 6a. ADET 1 standard proctor shear strength reading

Load(kg)	Shear Stress	Normal Stress
5	166	138.9
10	269	277.8
15	358	416.7
20	433	555.6

Cohesion=70Kpa, Angle of internal friction Φ = 340

Table 6b. ADET 1 modified proctor shear strength reading

Load(kg)	Shear Stress	Normal Stress
5	186	138.9
10	304	277.8
15	372	416.7
20	454	555.6

Cohesion= 100Kpa, Angle of internal friction Φ = 320

Table 6c. ADET 2 standard proctor shear strength reading

Load(kg)	Shear Stress	Normal Stress
5	160	138.9
10	269	277.8
15	359	416.7
20	433	555.6

Cohesion=60Kpa, Angle of internal friction Φ = 350

Table 6d. ADET 2 modified proctor shear strength reading

Load(kg)	Shear Stress	Normal Stress
5	153	138.9
10	231	277.8
15	320	416.7
20	428	555.6

Cohesion C=70Kpa, Angle of internal friction $\Phi = 31^0$

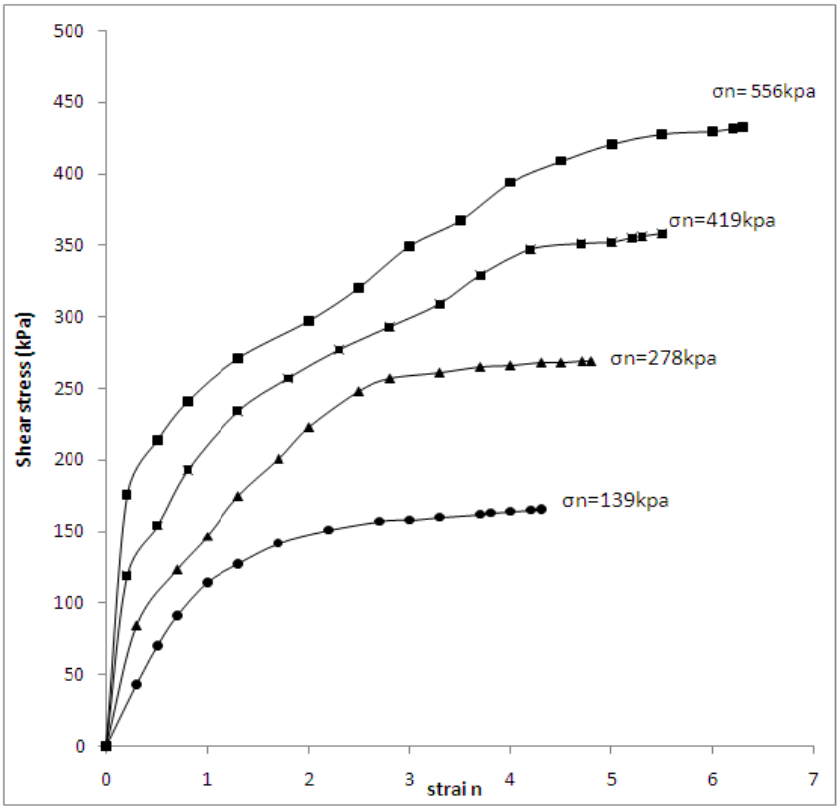

Figure 5a. Plots of shear stress (kpa) vs strain (%) for standard proctor compacted soil sample ADET 1

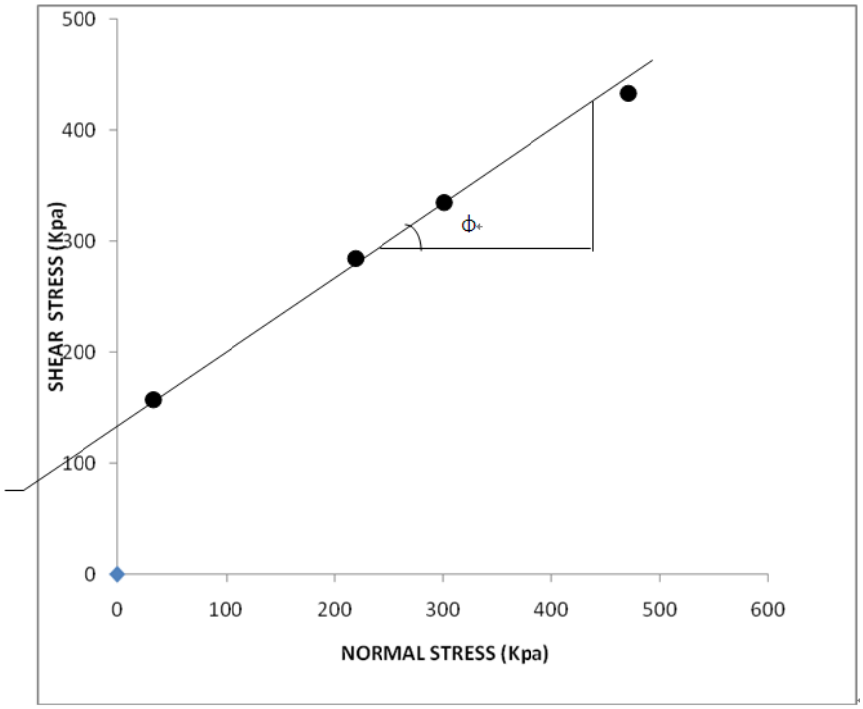

Figure 5b. Plot of shear stress (kpa) vs normal stress (kpa) for standard proctor compacted soil sample ADET 1

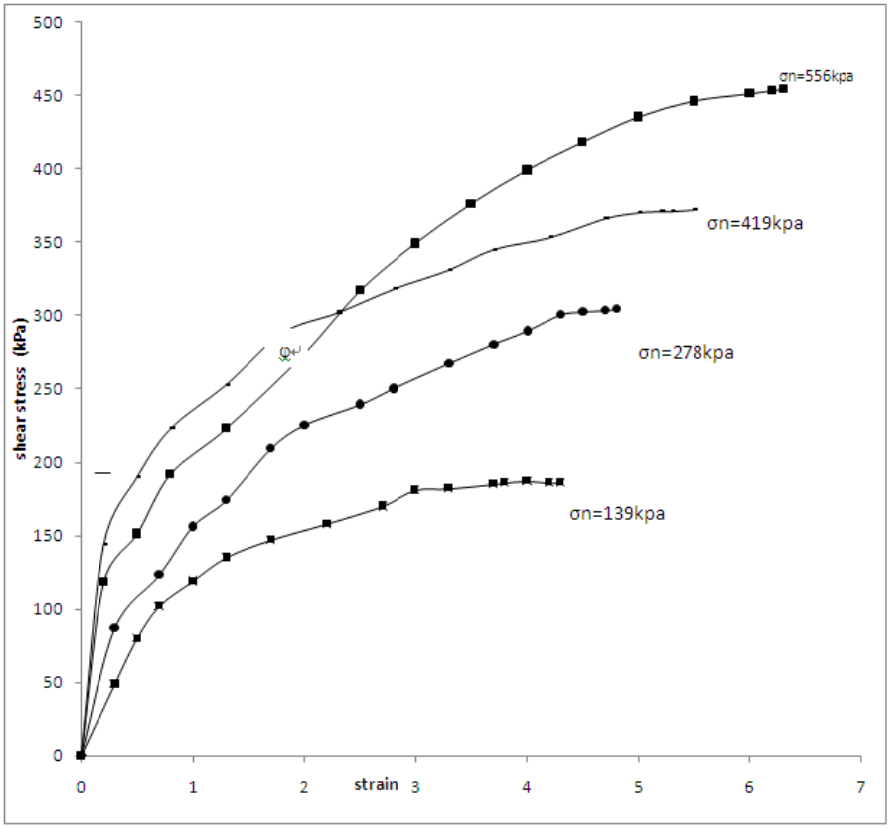

Figure 6a. Plots of shear stress (kpa) vs strain (%) for modified proctor compacted soil sample ADET 1

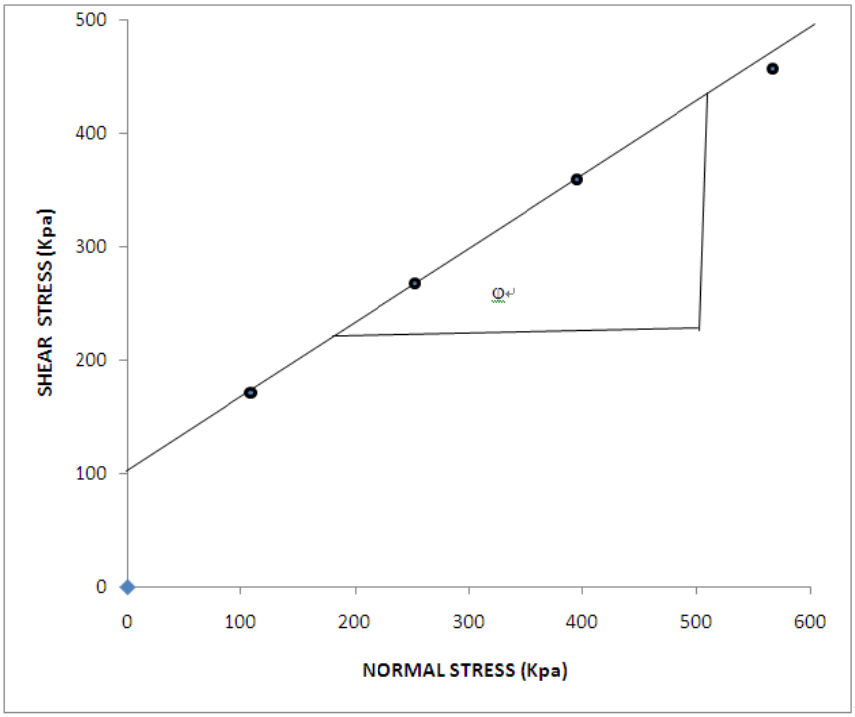

Figure 6b. Plot of shear stress (kpa) vs normal stress (kpa) for modified proctor compacted soil sample ADET1

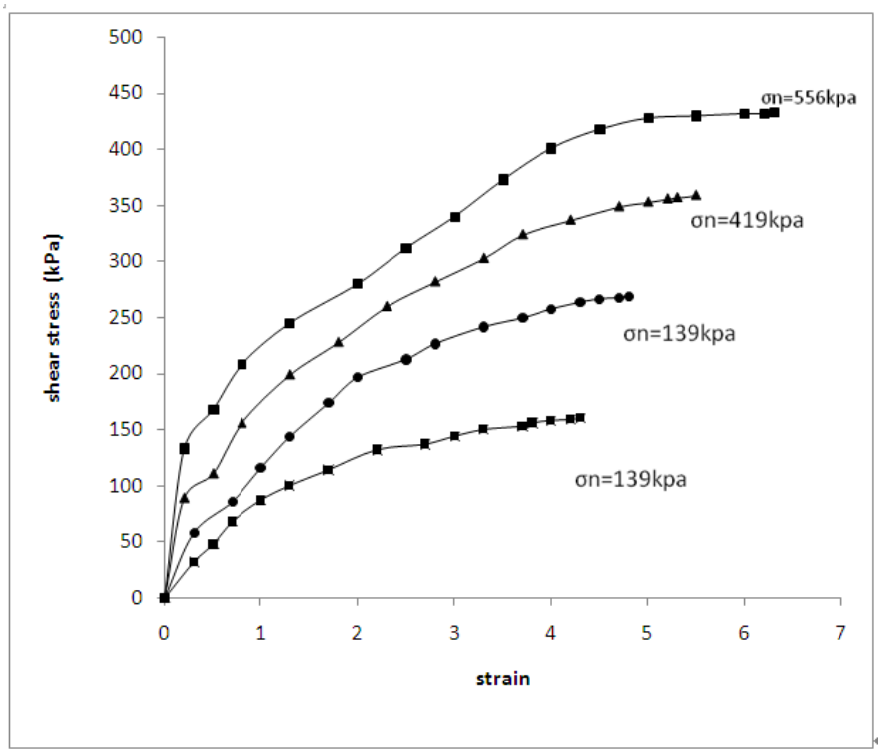

Figure 7a. Plots of shear stress (kpa) vs strain (%) for standard proctor compacted soil sample ADET 2

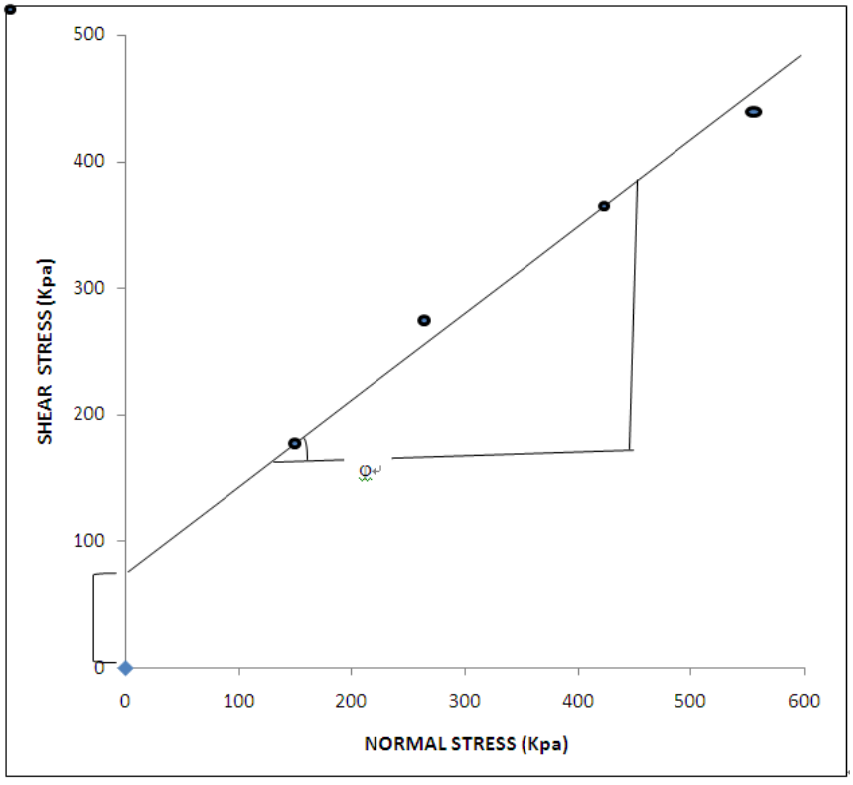

Figure 7b. Plots of shear stress (kpa) vs strain (%) for standard proctor compacted soil sample ADET 2

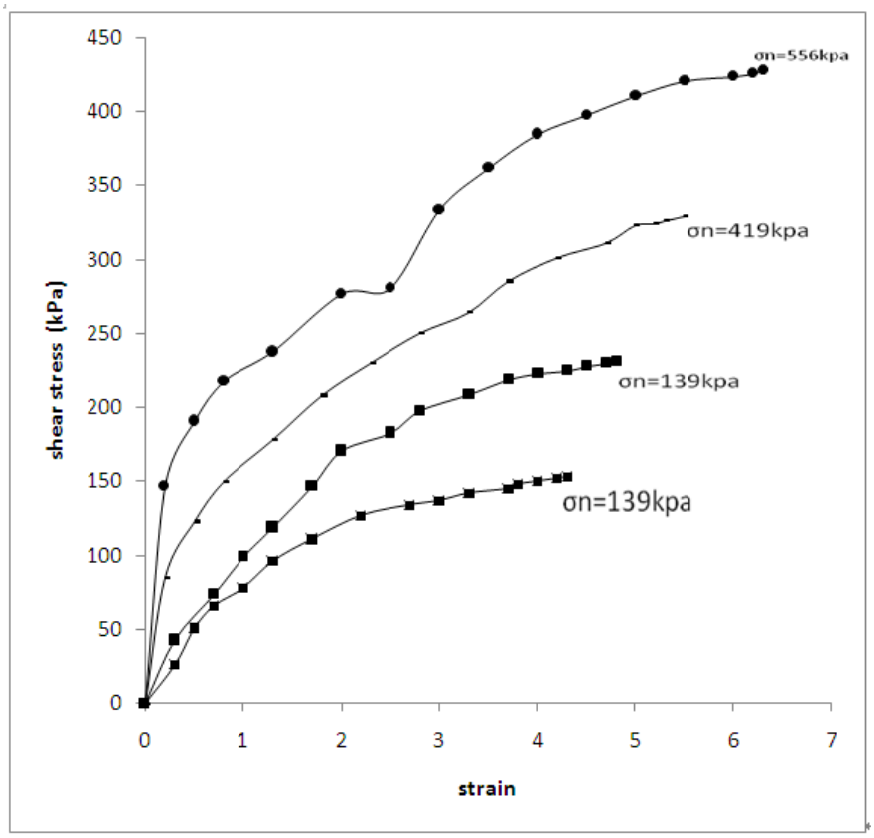

Figure 8a. Plots of shear stress (kpa) vs strain (%) for modified proctor compacted soil sample ADET 2

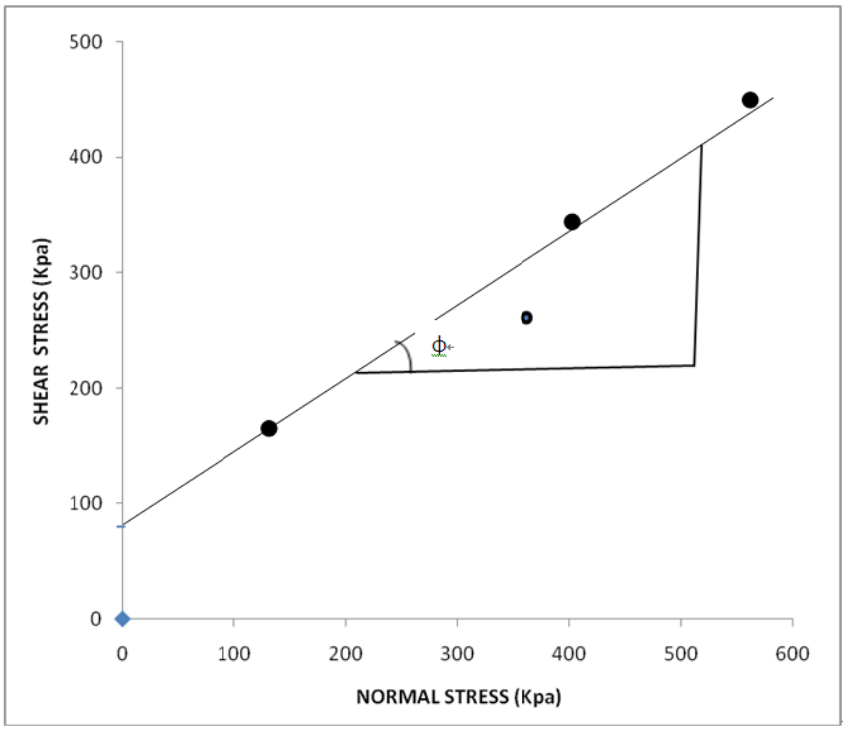

Figure 8b. Plot of shear stress (kPa) vs. normal stress (kPa) for modified proctor compacted soil sample ADET 2

4. Conclusions

Based on the grain size analysis, the soil sample ADET 1 is silt-clayey very gravelly sand (reddish brown colour) with 30% gravel, 47% sand, 23% silt and clay respectively. ADET 2 exhibits reddish brown colour and is characterized by 12% gravel, 52% sand, 36% silt and clay respectively.

Atterberge consistency limit test indicate that the soil samples are above the activity (A) line in the zone of intermediate plasticity clays (CL and there is negligible or no swelling of soils. Therefore they can be chosen as construction materials in buildings and foundations. The CBR values range from 1-5%. This may make it useful as sub-grade materials in road construction and could also be useful for slope stability.

The direct shear test results give an average value of 33^{o} for the angle of internal friction and average of 75Kpa for cohesion. These values are attributed to the high bearing capacity of the soils making them to be useful in slope stability. The foundation design of the area would be shallow foundation and could also support moderately steep slopes to a great height.

Based on the values obtained from the various tests carried out on the soil samples, it could be concluded that they are good road construction materials and can also be used for slope stability and dam constructions.

Acknowledgements

We appreciate the management of Dall Quarry for the permission granted us to sample the soil in the quarry for this study. Laboratory facility provided by the Civil Engineering workshop of the Department of Civil Engineering, University of Ilorin, Nigeria is gratefully acknowledged. This paper has benefited from valuable contributions from the two anonymous reviewers and we appreciate their efforts.

References

Alao, D. A. (1983). Geology and Engineering Properties of Lateritic Soil from Ilorin, Nigeria. *Engineering Geology, 19*, 111-118. http://dx.doi.org/10.1016/0013-7952(83)90029-7

Alao, D. A., & Opaleye, S. T. (2011). Geotechnical analysis of slope failure of a kaolin quarry at Kura, Jos North-Central. *Inter Jour. of Scientific Research, 1*(1), 87-102.

Balogun, L. A. (1984). Influence of geological origin on the geotechnical properties of lime-stabilized laterites. *Proc., 8th Regional Conf. for Africa on Soil Mechanics and Foundation Engineering. International Society for Soil Mechanics and Foundation Engineering, 1*, 355-362.

Bowles, J. E. (1990). *Physical and Geotechnical Properties of Soil* (2nd ed.). Mc Graw-Hill, Inc. p.478.

Das, B. M. (2006). *Principles of geotechnical engineering*. Stamford, CT: Thomson Learning College.

Gidigasu, M. D. (1972)**.** Mode of formation and geotechnical characteristics of laterite materials of Ghana in relation to soil forming factors. *Engineering Geology, 6*, 79-150. http://dx.doi.org/10.1016/0013-7952(72)90034-8

Jackson, M. O. (1980). The foundation failure in coastal plain sand of Nigeria. *Proceedings of the 7thRegional conference for Africa on soil mechanics and foundation Engineering. Institute of Civil Engineering Accra, 1*, 425-430.

Madu, R. M. (1975)**.** Some Nigerian residual lateritic soil, their characteristics and relative road building properties on Group Basis. *Proceedings of 6th Regional Conference for Africa Soil Mechanics and Foundation Engineering. Durban, South Africa*. *International Society for Soil Mechanics and Foundation Engineering, 1*, 121- 129.

Ogunsanwo, O. (1988). Basic geotechnical properties, chemistry and mineralogy of some Lateritic Soils from S.W. Nigeria. *Bulletin of Engineering Geology, 37*, 141-160.

Ogunsanwo, O. (1989). Some geotechnical properties of two Lateritic Soils compacted at different energies. *Engineering Geology, 26*, 261-269. http://dx.doi.org/10.1016/0013-7952(89)90013-6

Omotoso, O. A., Mamodu, M. O., & Ojo, O. J. (2011). Evaluation of Geotechnical Properties of Laterite Soils in Asa-Dam area, Ilorin, Southwestern Nigeria.

Vallergra, S. A., Shugter, J. A., Love, A. C. & Vantil, C. J. (1969). Engineering study of Laterite Soil in connection with construction of Roads, Highways and Airfields. *US AID, Report AID/CSD 1980*. 165p.

Wagner, A. A. (1957)**.** The Use of Unified Soil Classification System by the Bureau of Reclamation. *Proceedings, 4th International conference on soil mechanics and foundation engineering (London), 1*, p.125.

Earth Science Research; Vol. 1, No. 2; 2012
ISSN 1927-0542 E-ISSN 1927-0550
Published by Canadian Center of Science and Education

Novel Amphibole Geo-barometer with Application to Mafic Xenoliths

Alexander Simakin[1, 2], Olga Zakrevskaya[2] & Tamara Salova[2]

[1] Institute of Physics of the Earth, RAS, Moscow, Russia

[2] Institute of Experimental Mineralogy, RAS, Chernogolovka, Russia

Correspondence: Alexander Simakin, Institute of Experimental Mineralogy, Russian Academy of Science, Chernogolovka, Moscow region, 142432, Russia. Tel: 7-496-522-5853. E-mail: simakin@ifz.ru

Received: March 23, 2012 Accepted: April 10, 2012 Online Published: June 5, 2012

doi:10.5539/esr.v1n2p82 URL: http://dx.doi.org/10.5539/esr.v1n2p82

Abstract

Amphibole crystallization from hydrous high-magnesium andesite (Shiveluch volcano, Kamchatka) melt has been studied experimentally at pressures 2, 3, 5 kbar. Slightly subliquidus temperatures have been selected for amphibole crystallization. Amphiboles with close to the equilibrium composition have been obtained at low undercoolings in short 4 hours experiments. We select octahedral aluminium content and sum of high charged cations (Ti^{4+}, Fe^{3+}) all evaluated with the 13eCNK method as master parameters reflecting pressure of amphibole formation. Asymptotic maximum of Al^{VI} content at the sum $Ti+Fe^{3+}=0$ as a function of pressure was calculated following negative linear correlation trend for each run of the original and published experimental data sets. The derived novel Al^{VI} in amphibole barometer is calibrated in the pressure range of 2-12 kbar for andesitic and basaltic magmas. Reliability and validity of the new geobarometer were tested on the amphibolized ultramafic xenoliths from the Shiveluch Volcano (Kamchatka) and Dish Hill (California). In both cases our estimates appear to be equal within the uncertainty of the method to the predictions done by two-pyroxene geo-thermo-barometer (Putirka, 2008).

Keywords: amphibole, geobarometer, andesite

1. Introduction

The estimates of PT parameters and oxygen fugacity in the magmatic systems are necessary for the reconstruction of petrologic mechanisms of their formation. Pressure is the most important parameter for active magma chambers since it corresponds to their depth. Reliable assessment of the magma chamber depth is important for interpretation of geophysic and geodetic data in the areas of active volcanism and for the eruption prediction (e.g., Manley & Bacon, 2000). Oxygen fugacity and fluid composition are essential for ore generation potential of magmas (Moretti & Baker, 2008). In petrologic practice various mineralogical geo-thermo-barometers are used to determine PT parameters of water bearing magmas. Two-pyroxene (Putirka, 2008) and spinels composition based QUILF (Andersen et al., 1993) thermo-barometers are known as the most reliable ones.

Amphibole is a mineral typical for calk-alkaline magmas stable at water content above ca 2 wt.% in the pressure range 1.5-12 kbar or from the crustal to near Moho (crust-mantle boundary) depths. This phase composition reflects PT and f_{O2} of the parental melt and is used to calibrate solo amphibole (Schmidt, 1992; Anderson & Smith 1995) and amphibole-plagioclase (Blundy & Holland, 1990) geo thermo-barometers. Recently Ridolfi et al. (2010) have proposed empirical universal amphibole sensor to estimate of f_{O2} and PT parameters. However, most of the experimental data used for calibration of the above mentioned models relate to the low temperature amphiboles grown from dacitic and rhyolitic melts. The accumulation of the precise information on the equilibrium amphibole compositions in andesitic and basaltic systems is timely goal for the experimental study. Low viscosity of the hydrous basic melts complicates experimentation by easy secondary nucleation and low temperature overgrowth at quenching. Other factors, that can distort equilibrium composition are undercooling at growth and melt fractionation. At a large degree of crystallization nominally (initially) andesitic and basaltic melts get silicic composition. Therefore, a great fraction of the published analyses of the allegedly equilibrium amphiboles can't be used in the empirical calibrations. Furthermore, totally empirical calibrations (like in Ridolfi et al., 2010) lack a physico-chemical analysis of the isomorphism and cation exchange between amphibole and melt.

In our early study (Simakin et al., 2009) we find that at the fixed pressure inverse correlation exists between the sum of high valence cations (Fe^{3+}+Ti^{4+}) and the content of aluminum in octahedral coordination state in amphibole. In the highly oxidized melt Al^{VI} in amphibole is totally substituted with ferric iron, whereas in the highly reduced melt octahedral aluminium attains the maximum content. In this study we employ this correlation to derive novel Al^{VI} in amphibole geo-barometer while using new data of the experiments with hydrous andesitic melt at pressures 2, 3, 5 kbar. A new geo-barometer was applied to estimate equilibration pressure of mafic xenoliths from the Shiveluch volcano (Kamchatka) and Dish Hill (California).

2. Method

2.1 Starting Materials and Equipment

A high magnesium andesite of the Shiveluch volcano (Kamchatka) was used as a starting material (composition in the Table l). This andesite was from the Holocene extrusion Karan representing rock with high degree of crystallinity and uniform texture containing amphibole and plagioclase phenocrysts. Hydrous glass was prepared for the further use from the rock powder in IHPV device. Rock powder was placed in platinum capsules with water, welded and held at the pressure of the future experiments (2, 3, 5 kbar, respectively) and T=1300°C.

Table 1. Compositions of the starting glasses recalculated to the sum 100%. All glasses are water saturated and prepared at the same temperature T=1300°C.

run	P, kbar	Na_2O	MgO	Al_2O_3	SiO_2	K_2O	CaO	TiO_2	Cr_2O_3	MnO	FeO
An65	2	4.16	5.24	15.87	59.87	1.29	6.84	0.69	0.05	0.10	5.91
An68	3	4.24	5.45	16.34	59.70	1.30	7.11	0.71	0.05	0.14	4.96
An69*	5	3.19	4.34	16.67	60.48	0.92	7.86	0.77	0.00	0.20	5.49

* significant deviation of this composition reflects glass heterogeneity due to fast rates of diffusion and crystals growth and segregation at the quenching of the hydrous andesitic melt at P=5 kbar with low viscosity

Table 2. Conditions of experiments and their products

#	run	T (°C)	P (kbar)	Time (h)	Overheating	Phases
1	An 65	1300	2	8	na	gl (amph)
2	An 65-1	950	2	4	No	gl cpx, pl, amph (ol)
3	An 68	1300	3	8	na	gl (cpx , amph)
4	An 68-1	930	3	4	No	gl amph, pl
5	An 68-3	930	3	4	Yes	gl, cpx, amph, spl
6	An 68-2	965	3	4	No	gl, cpx, amph, spl
7	An 68-5	965	3	4	Yes	gl (cpx, amph, spl, pl)*
8	An 68-6	980	3	4	Yes	gl (cpx, amph, spl, pl)*
9	An 69	1300	5	8	na	gl (cpx, amph)
10	An 69-3	970	5	4	Yes	gl, cpx, amph, spl (pl)
11	An 69-4	980	5	4	Yes	gl (amph, spl)*
12	An 69-1	990	5	4	No	gl, amph, (cpx, pl)
13	An 69-2	1030	5	4	No	gl (amph)*

Phases abbreviations: gl - glass, amph - amphibole, cpx - clinopyroxene, spl - spinel, pl - plagioclase, quenching phases are in parenthesis, * tentatively interpreted as quenching phase based on its composition and morphology.

Oxygen fugacity at the glass preparation is controlled by high pressure vessel material on the level around NNO + 0.5. Even a small amount of air remaining in a capsule increases oxygen fugacity at the beginning of the run (Simakin & Salova, 2004). Therefore, at every stage before welding a capsule was flashed with high purity argon to remove air. This operation is especially effective at the arrangement of charges with compact pieces of

hydrous glass (not powder) for the final runs. The run lasted 4-6 hours. Iron loss into the capsule walls for this short time has an acceptable level (see Table 1) and as shown in our earlier studies iron oxidation state remains close to the initial one (Simakin et al., 2009). The summary of the run P-T-t conditions and a list of the produced phases for each run are in Table 2. The effect of the melt superheating prior main stage of the experiment on the amphibole growth and composition will be considered below using the obtained experimental data.

2.2 Method of Crystallochemical Calculations

We recalculate amphibole analyses at the treatment of the experimental data on the basis of the method recommended by IMA (classification IMA-97, Leake et al., 1997) for calcium amphiboles. As well established amphibole has general chrystallo-chemical formula $A_{0-1}M4_2M2_2M3_1M1_2(T_8O_{22})X_2$, where position A is occupied with large cations Na and K, T with tetrahedral Al and Si, X – anion position mainly filled with OH- and partially Cl^-, F^-, O^{2-}. Octahedral positions M1,2,3 are for divalent and high charge cations (mainly Mg^{2+}, Fe^{2+}, Al^{3+}, Fe^{3+}, Ti^{4+}). Distorted M4 position is mainly for Na and Ca. There is a cation ordering with preferable occupancy of pair (per formula unit) of M2 sites with high valence cations: Fe^{3+}, Al^{3+}, Ti^{4+} (Deer et al, 1997). IMA-97 method is known as 13eCNK (13 cations excluding Ca, Na, K) and implies that M1-3 and T sites are fully filled with tetrahedral and small cations while alkalies and calcium fill the rest of M4+A sites. The accuracy of these calculations can be reduced when some portion of small cations (Adam et al., 2007) would shift to M4 site.

Cation distribution and iron oxidation state calculated from microprobe analyses reflect amphibole state at the moment of crystallization from the parental melt with uncertainty related to analytical precision and model assumptions validity. Later on mineral dehydration and partial iron oxidation can occur in accordance with reaction (Popp et al., 1995):

$$Fe^{2+}(OH)^- + 1/4\ O_2 \rightarrow Fe^{3+}O^{2-} + 1/2H_2O,$$

This process disvalues the results of the direct (e.g. Mossbauer) determination of Fe^{3+}/Fe^{2+} ratio in amphibole and gives preference to crystallo-chemical calculations to reconstruct the as-grown amphibole state related to the parental magma properties. Large systematic work on the comparison of the results of the direct determination and calculation with different methods of the iron oxidation state in calcic amphiboles of the diverse origin was performed by Gualda and Vlach (2005). These authors found that the lowest measured ferric/ferrous ratios appeared to be close to the calculated ones while most of measurements were significantly higher than the results of the crystallochemical calculations by 13eCNK method as expected due to the post growth oxidation.

2.3 Composition Representation

The recalculated amphibole compositions were plotted in the coordinates [Fe^{3+}+Ti, Al^{VI}]. The selected analyses are presented in Table 3. These parameters reflect pressure and oxygen fugacity at the growth stage (Simakin et al., 2009). Octahedral aluminum content and the sum of high valence cations Fe^{3+}+Ti are linearly correlated. Intersection with ordinate gets maximum octahedral aluminum content Al^{VI}_{max} at given pressure while intersection with abscissa defines the maximum content of high valence cations (except aluminum) that is about 1.8 apfu for calcic magmatic amphiboles grown from the melt. Parameter Al^{VI}_{max} reflects pressure better than merely Al^{VI} content depending on the iron oxidation degree or oxygen fugacity at mineral growth.

Table 3. Chemical composition of experimental amphiboles

run P/T	Na_2O	MgO	Al_2O_3	SiO_2	K_2O	CaO	TiO_2	Cr_2O_3	MnO	FeO	Total
An68-2 3/965*	2.17	16.81	12.03	45.21	0.36	11.43	1.19	0.16	0.00	7.94	97.65
	2.23	15.36	11.63	42.19	0.32	11.51	1.02	0.12	0.31	8.85	93.77
	2.11	15.14	12.28	41.42	0.31	11.58	0.82	0.00	0.23	9.18	93.47
	2.20	15.20	12.35	42.46	0.40	11.64	0.88	0.05	0.27	9.16	94.92
An68-6 3/980	1.99	16.31	11.43	42.98	0.44	11.25	1.69	0	0.36	8.61	95.06
	2.03	15.98	11.66	42.68	0.32	10.37	1.25	0	0	8.38	92.67
	1.88	15.67	11.25	41.95	0.36	11.23	1.57	0	0	8.47	92.37
	2.2	14.95	11.4	41.36	0.45	10.34	1.12	0	0	8.33	90.14
	2.42	16.16	11.26	44.69	0.45	10.81	1.21	0	0.38	8.04	95.41
	2.01	16.36	11.25	43.15	0.39	11.19	1.46	0	0	8.29	94.1
	2.16	16.53	11.4	42.63	0.49	10.18	1.15	0	0	7.96	92.51

An69-1 5/990	2.14	14.71	11.74	44.07	0.34	11.69	0.84	0.14	0.19	9.3	95.36
	2.24	14.45	12.48	42.83	0.36	11.42	0.92	0.1	0.03	8.09	92.98
	2.15	14.54	12.07	42.68	0.44	11.41	1.23	0.21	0.33	8.98	94.11
	1.98	13.26	11.38	40.23	0.4	10.72	1.2	0.14	0.19	9.1	88.66
	2	14.34	11.68	42.17	0.39	11.25	1.09	0.06	0.27	8.54	91.84
	2.08	14.64	11.41	42.63	0.44	10.81	1.23	0.2	0.24	7.55	91.26
An69-3 5/970	2.47	17.34	12.91	46.04	0.37	11.67	1.72	0.00	0.00	6.02	98.54
	2.23	18.49	11.77	47.62	0.37	11.73	1.29	0.00	0.00	6.20	99.69
	2.45	17.76	12.74	47.17	0.63	11.75	1.47	0.00	0.00	7.11	101.09
	2.28	17.89	11.93	47.30	0.42	11.42	1.22	0.00	0.33	7.71	100.49
	2.13	18.18	11.75	47.51	0.44	11.54	1.30	0.00	0.00	7.38	100.23
	2.32	17.35	11.04	46.33	0.36	11.09	1.21	0.00	0.00	7.64	97.33
	2.35	17.93	12.67	46.16	0.44	11.20	1.12	0.00	0.00	7.05	98.91
	2.34	17.65	11.56	45.70	0.41	11.47	0.83	0.00	0.00	6.61	96.57
An65-1 2/950	2.22	15.21	11.11	45.10	0.34	11.38	1.38	0.35	0.33	9.61	97.03
	2.09	17.65	11.26	46.53	0.27	11.37	1.36	0.00	0.29	9.18	100.00

* pressure in kbar, temperature in ^{o}C

3. Results of Experiments

3.1 Ptotal=PH_2O=2 Kbar

At pressure 2 kbar and T=950^{o}C one experiment was performed to check the previously obtained results (Simakin et al., 2009). In this experiment no superheating was applied. Therefore, the sample contains a lot of quenching crystals of two kinds: formed at glass preparation and glass heating from the ambient temperature at the start of the experiment and appeared at the final quenching at the end of the run. In the Figure 1 compositions of the amphiboles obtained are displayed. They form "quenching array" approaching the extreme point with the coordinate [Al^{VI}, Fe^{3+}+Ti] = [2÷2.2, 0]. The points from the previous study are shown with the error bars with their linear approximation. Only several crystals of the largest size in a smaple section are considered as potentially grown at the main stage of the experiment at the lowest undercooling and pocessing the near-equilibrium composition. The average composition of such amphiboles from the run with duration of 6 hours is plotted with the open diamond. The good correspondence between the previously obtained and new data is demonstrated.

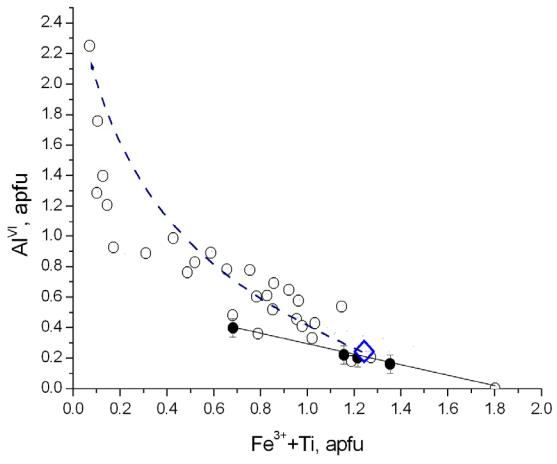

Figure 1. Compositions of amphiboles grown at T=950^{o}C and P=2 Kbar; open circles stay for data obtained in the given work, filled circles with error bars connected with continuous line represent data from (Simakin et al., 2009), diamond corresponds to the averaged composition of the selected on the size and habitus basis amphibole crystals of nonquenching origin (see text)

3.2 Ptotal=PH_2O=3 Kbar

At pressure 3 kbar the experiments have been performed at T=930, 965 and 980°C. Superheating applied in the runs An68-5 (T=965°C) and An68-6 (T=980°C) results in the effective melting of the quenching crystalline inclusions. During the main stage of the run An68-5 no crystallization occurs since homogeneous nucleation delay time was larger than 4 hours and only quenching phases form. On the Fe^{3+}+Ti - Al^{VI} plot amphibole analyses form typical quenching array as shown in Figure 1. At the same time the run An68-2 (T=965°C) was performed without superheating and sample observation demonstrates clots of amphibole crystals up to 20 mkm width, representing partially recrystallized and overgrown quenching phases (see Figure 2). Analyses of these amphiboles are plotted in Figure 3. The texture of the sample An68-3 (T=930°C) reflects two stage growth. Superheating also removes ceneters of heterogeneous nucleation. However, undercooling higher by 35°C than in the run An68-5 was sufficient for homogeneous nucleation of Cpx and amphibole crystals. Lower temperature leads to the larger degree of crystallization and melt fractionation. Amphibole compositions from this run form "dacitic bill" toaching abscissa in Figure 3. They had growing in the melt with progressively increasing silica content (decreasing Mg and Al^{VI} activity) and iron oxidation degree. Numerous tiny crystals grew at the quenching stage beyond diffusion zones.

Crystals formed in the run An68-6 (T=980°C) have equant morphology and relatively large sizes of quenching composition. This observation stands for the near liquidus temperature of the run An68-6 since strong superheating in the main stage of the experiment would lead to better homogenization and quenching crystallization at lower temperature with typical high supercooling morphologies. We tentatively set T_l=980-990 °C. Then T=930°C corresponds to the large undercooling ΔT=55-60°C able to shift Al^{VI} content significantly from the equilibrium one. For calibration we select the largest crystals from the run An68-2 formed in the near liquidus conditions. Their analyses are plotted with open squares in Figure 3. Rather small width of crystals implying possible matrix effect at microprobe analysis and probably incomplete equilibraiton results in significant data scattering. For this reason we approximate compositional trend by the line starting at the point [Fe^{3+}+Ti, Al^{VI}] = [1.8, 0] and passing through the middle of the cloud of the experimental points to the intersection with ordinate. The intersection point has coordinate [Fe^{3+}+Ti, Al^{VI}] = [0, 0.67].

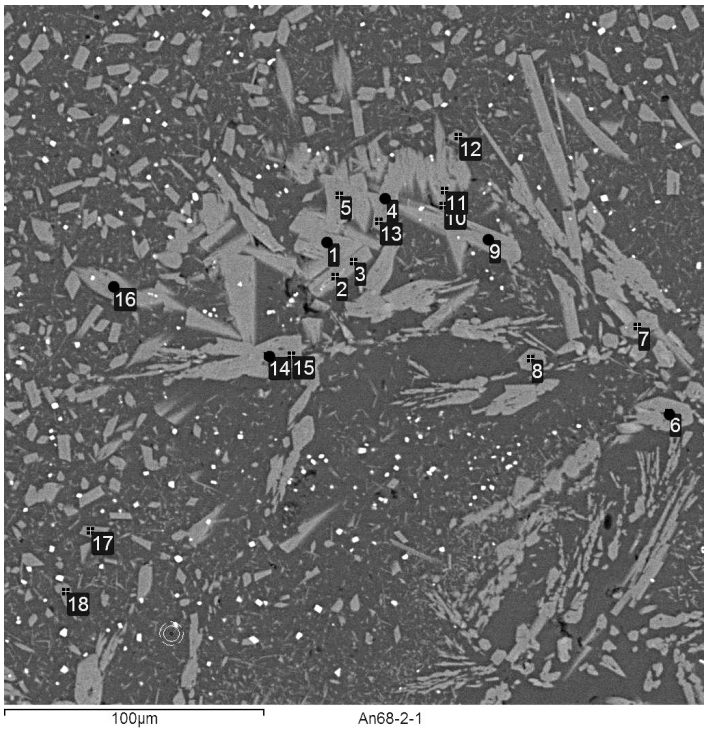

Figure 2. SEM image of the sample from the run An68-2 (see Table 2) with parameters T=965°C, P=3 kbar, no overheating. Amphibole crystals labeled with solid circles are probed for calibration

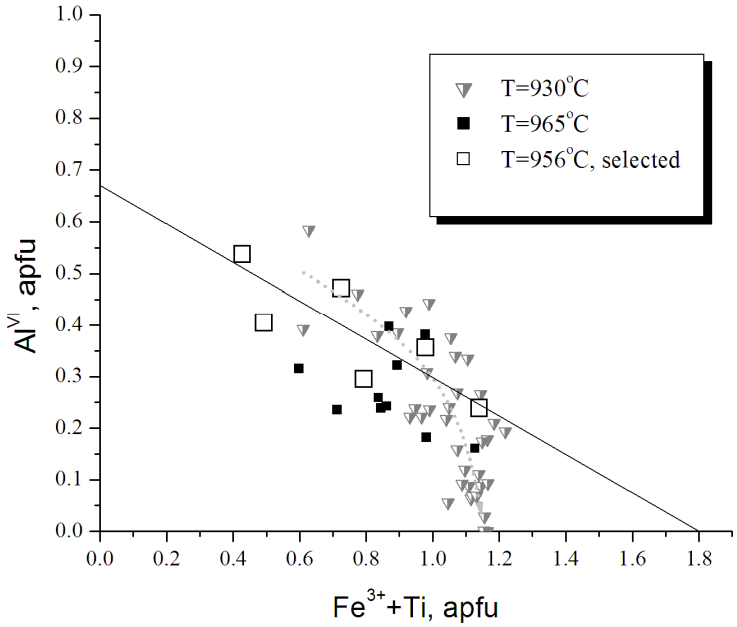

Figure 3. Parameterized compositions of amphiboles grown at pressure P=3 kbar at the different temperatures specified in the legend. At the lower temperature T=930°C (run An68-3) larger degree of crystallization and fractionation are attained resulted in the "dacitic bill" trend shown with dotted line. At T=965°C (run An68-2) crystals are recrystallized inherited from the starting glass and partially new ones grown near liquidus, open squares stand for the selected analysis of the largest amphiboles used for calibration. Continuous line depicts linear trend passing through point [1.8, 0] and analyses of the selected crystals (open squares)

3.3 Ptotal=PH_2O=5 Kbar

At pressure 5 kbar the experiments have been performed at temperatures T=970; 980 и 990 °C. In the run A69-3 (T=970°C) preheating was applied. In the main stage of the experiment homogeneous nucleation produces sparse centres of crystallization. Intergrowth of clinopyroxene and amphibole was observed (see Figure 4). Amphibole crystals gain the maximum sizes up to 150x30 mkm. Clinopyroxene might experience faster homogeneous nucleation. It starts to grow first becoming the centre of the later amphibole overgrowth. High water content at P=5 Kbar (about 8 wt.%) reduces homogeneous nucleation rate resulting in the low volume crystal population density and larger crystal sizes.

The charge in the run at T=980 °C (run An69-4) was also preheated (see Table 2). However, undercooling at the main stage of the experiment was too low to start homogeneous nucleation as in the run An68-5 at P=3 kbar. Homogeneous nucleation starts in the early moments of quenching (at the relatively low undercooling) and results in the formation of plenty of small lath –shape crystals uniformly distributed in the melt volume. Strike difference in the amphibole crystal morphology and sample texture was caused by such small run temperature difference as 10°C.

There was no preheating in the run performed at T=990°C (An69-1). Only a small fraction of amphibole crystals has a shape with low elongation among numerous quenching amphibole laths. When plotted (see Figure 5) isometric crystal compositions stay for the growth at a small undercooling. In Figure 5 one can notice that compositions of amphiboles from the run An69-1 follow a linear trend along pressure indicator line with small scattering and that this line comprises the exact upper edge of the analyses set of the run An69-3 (T=970°C). The experiments at T=1030°C without superheating yields crystals of quenching origin judging by their composition with the volume crystal density lower than that in the run at T=990°C. This observation demonstrates that T=1030°C is slightly above T_l. Therefore, we tentatively determine amphibole liquidus temperature at P=5 Kbar as 1005±5 °C. High water content in andesite melt at P=5 kbar enhances diffusion and thus recrystallization rate. Therefore, the experiments at this pressure provide the most accurate in this study estimate of Al^{VI}_{max} equal to 0.81.

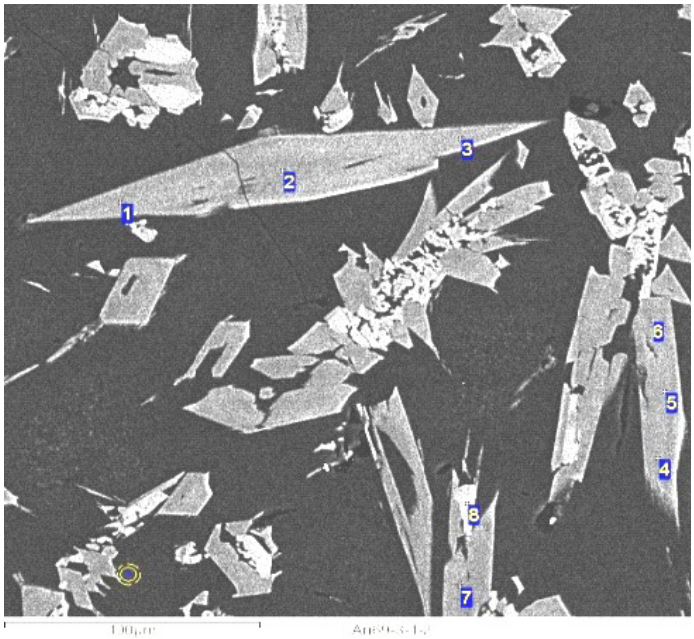

Figure 4. SEM image of the sample from the run An69-3 with parameters T=970oC, P=5 kbar, overheating. Dark crystals are amphiboles while bright ones are clinopyroxenes

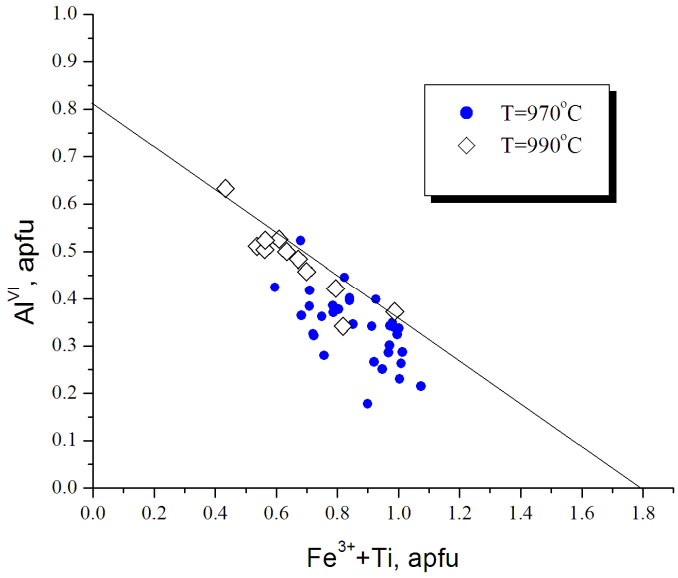

Figure 5. Compositions of amphiboles produced at P=5 kbar with temperatures of the runs shown in the legend. Crystals produced at T=990°C close to the liquidus follow linear trend almost perfectly and used for calibration. At 970°C amphiboles form large crystals along with clinopyroxenes causing appreciate melt fractionation reflected in the shift of amphibole compositions towards lower Al^{VI} contents

The above data demonstrate growing maximum asymptotic aluminium content in the octahedral positions of amphibole structure Al^{VI}_{max} with pressure increase. It is most important that in our experiments we take the influence of undercoolings on the crystal composition into consideration. This effect is much larger than a thermodynamic shift of equilibrium compositions to lower equilibrium temperatures (e.g., decrease of Mg# of minerals). Equilibration of nonequilibrium solids proceeds in experiments only through recrystallization since equilibration via the solid state diffusion in a crystal requires at least years (Pichavant et al. 2007).

Recrystallization is effective only for the crystals of submicron size (Cabane et al., 2005). It is especially sluggish at low water content in the melt and small melt fraction. We relied in our study on the tuning of the run temperature to provide small undercoolings. At such strategy small temperature step experiments are performed around T_l instead of using regular T-grid with a larger step.

4. Calibration of Dependence of Al^{VI}_{max} versus Pressure

The values of Al^{VI}_{max} evaluated from our experimental data at P=2, 3, 5 Kbar are well approximated as a linear function of pressure (see Figure 5a). Correlation Coefficient is 0.98. To extend model pressure range and to look how this correlation works for different melt compositions we use the published experimental data on magmatic calcic amphiboles.

Using published compositions raises the problem of data selection since practically all experimental studies were aimed on the melting diagram investigation and amphibole compositions were obtained as a byproduct. As mentioned above, there are two main sources of errors: large undercooling and melt fractionation. Only near liquidus amphiboles grown at moderate undercoolings and low total degree of crystallization reflect pressure and initial melt composition. Another source of inaccuracy is to present the average of several compositions in publications. The average of the crystallochemical formulas is preferable and not equal to that of the composition average.

First we include all available high temperature amphibole data into the data set for calibration (Adam et al., 2007; Allen and Boettcher, 1983; Alonso-Perez et al., 2009; Berndt et al., 2005; Grove, et al., 2003; Foden and Green, 1992; Moore and Carmichael, 1998; Parat et al., 2008; Sato et al., 2005). A cloud of data points becomes more diffusive and obeys linear regression with a smaller correlation coefficient r=0.89 (see Figure 5b). Then we exclude sources demonstrating maximum deviations from the linear trend (Adam et al., 2007, Foden and Green, 1992, Sato et al., 2005, Moore and Carmichael, 1998). Other data points were retained as more reliable. On instance we select two points from 63 runs reported in (Berndt et al., 2005). All the experiments of these authors were performed at P=2 kbar with a variable water contents and temperatures. We find that conditions $C_{H2O}\approx 2$ wt.% and T=950°C are rather close to amphibole liquidus. Improved data set defines a linear trend with the correlation coefficient r=0.99:

$$Al^{VI}_{max} = a + bP,\ a = 0.4871 \pm 0.0219;\ b = 0.0623 \pm 0.0029$$

We consider this regression as the Al^{VI} in amphibole geo-barometer for petrologic applications. Below we propose a theoretical explanation for the observed correlation based on pressure induced structural transitions in the alumino-silicate melt.

4.1 Aluminum Partitioning between Amphibole and Melt as a Basis for Al^{VI} in Amphibole Barometer

There were a lot of attempts to construct Al in amphibole geo-barometers based on a total content of aluminum (Hammarstrom & Zen, 1986; Johnson & Rutherford, 1989; Schmidt, 1992; Anderson & Smith, 1995; Ridolfi et al., 2010). Our choice of octahedral aluminum instead of total as a pressure indicator can be supported with considerations related to the structure of the parental alumino-silicate melt.

In general, aluminum can take network-forming (tetrahedral) structural position in the melt along with silica and be cation modifier coordinated with 5 and 6 oxygens like Mg^{2+}, Ca^{2+} and alkalies. As demonstrated by NMR concentration of five-coordinated aluminum is much higher than octahedrally coordinated one at a low pressure and becomes similar at high pressures of 4-6 GPa with totally about half aluminum in the high coordinated state (Kelsey et al., 2009). We assume that equilibrium fractionation of $Al^{(V+VI)}_{L}$ between melt and amphibole takes place.

Pressure has substantially higher influence on the octahedral aluminum content in amphibole since pressure range of amphibole growth in nature is from 2 to 15kbar while liquidus temperature for this mineral in adesites and basalts is in the range 930-1050 °C. We expect the increase of Al^{V+VI} fraction in the melt on 200-300% (Kelsey et al., 2009) and 10% (Stebbins et al., 2008) due to pressure and temperature variations, respectively.

Presence of aluminum in the cation-modifier form is unambiguously manifested by the easy nucleation of metastable corundum (Al_2O_3) from the melt of anorthite composition preceding homogeneous nucleation of stable triclinic $CaAl_2Si_2O_8$ (Abe et al., 1991). In accordance with Stebbins et al. (2008) Al^V fraction at T= 1500°C (near anorthite liquidus) attains the level of ca 18%. Similarly expanding of corundum field in the system An-Fo-Di at the expense of anorthite one at P=7 kbar reflects a structural transition Al^{IV}-> Al^{V+VI} in the melt (see e.g., Presnall et al., 1978).

Melt composition has also influence on the structural position of aluminum with the fraction of Al^{V+VI} markedly

increasing in the melts, rich in high-strength cations (strength is defined as a ratio of charge to the square of cation diameter $f=z/D^2$). Alkalies and calc-alkalies are ranged by strength as: Mg>Ca>Na>K (Kelsey et al., 2009). Generally Mg content is inversely correlated with silica one, therefore, fraction of Al^{V+VI} is minimal in the most differentiated granitic melt (Malfait et al., 2011) and maximum in high magnesium andesitic and basaltic melts (Neuville et al., 2008). Dependence of the aluminum structural state on the melt composition precludes universal Al^{VI} in amphibole geo-barometer. Fractionation effect was considered in our experimental data (see "dacitic bill" in Figure 3) above. In many publications experimental andesitic amphiboles due to this effect can be in equilibrium with dacitic and even rhyolitic melt. The inclusion of these minerals compositions into the data set for the calibration of geo-barometer for andesites and basalts (as probably in Ridolfi, 2010) would result in the weak and possibly erroneous correlation.

Aluminum in cation-modifier form has high activity not only in the least differentiated magmas, especially at high P but also in the fluid. Consideration of the amphibole composition in the [Al^{VI}, Fe^{3+}+Ti] coordinates permits to distinguish between magmatic (grown from the melt) and metamorphic (formed from the fluid phase) amphiboles. Compositional trends for magmatic amphiboles intersects with abscissa at Fe^{3+}+Ti (Cr^{3+}) =1.8-1.9 apfu. Plotting of the metamorphic amphibole compositions from (Imon et al., 2002) show that compositional trends are characterized by the higher Al^{VI} = 0.2-0.4 apfu at the maximum observed values of the sum Fe^{3+}+Ti = 2-2.2 apfu. This compositional feature may become a parameter to distinguish amphiboles formed from the melt in the complex systems from ones crystallized in the auto-metosomatic and metamorphic stages following magma solidification.

4.2 Influence of Water and Alkalies

According to the above model the content of Al^{VI} in amphibole may increase at depolymerization of alumino-silicate melt at the reaction with water. It was well established that dissolution of the first weight percents of water proceeds with the formation of hydroxyls and mainly break of Si-O-Si and to less extent Si-O-Al bonds (Xue & Kanazaki, 2006) with the expected detaching of some Al from network. Indeed with NMR method in the model andesitic Di62An38 system Xue and Kanazaki (2007) observed the increasing of Al^{V} and Al^{VI} fractions from 3.3 to 4.4 % and from 0 to 1.8% respectively at the incorporation of 1.7 wt.% of water into anhydrous glass. However, NMR study of hydrous rhyolitic glasses reveals even reducing of Al^{V}/Al_{total} with water content increase (Wim et al., 2011). There is no conclusive model of Al speciation in the hydrous alumino-silcate melts that can be used to predict the effect of water on amphibole composition.

Alkalinity rise leads to the formation of aluminates (e.g., $Na_2Al_2O_4$ (Simakin et al., 2010)) in the melt, where aluminum is network-forming component and thus, to the decreasing of Al^{V+VI} activity. Alkalinity influence may lead to pressure underestimation in the case of application of our geo-barometer to subalkaline and alkaline andesitic and basaltic hydrous magmas. The volume of the reliable experimental data on the amphibole crystallization from alkaline melts is too small to quantify this effect.

4.3 Strategy of Geo-barometer Application

Usually geo-sensors (geo-barometers, geo-thermometers, geo-oxygen barometers) are applied for each single analysis of the involved phase (one or several). The estimate by the set of values (P, T or f_{O2}) is taken to correspond to the maximum of histogram or its mean value. In our case while avoiding amphibole microlyths one will not encounter the effect of undercooling on mineral composition since phenocrysts usually grow at the near liquidus temperature. However, melt composition can vary due to the fractionation and mixing effects thereby reducing Al^{V+VI} activity in a magma and Al^{VI} in amphibole. Hence the desired pressure estimate can be obtained with the highest temperature amphiboles formed from the most primitive melt that can comprise only a fraction of all observed minerals. To solve this problem we plot analyses of amphiboles from nominally andesitic or basaltic magmas on the Fe^{3+}+Ti - Al^{VI} diagram and define the upper edge (towards higher Al^{VI} values) of the data points set. Pressure indicator line is drawn through this edge and predefined point – [Fe^{3+}+Ti, Al^{VI}]=[1.8,0] to the intersection with the ordinate defining $Al^{VI}_{max.}$ This parameter determines maximum pressure of growth for the amphibole crystal set in consideration. In some cases, e.g. for individual phenocryst (Simakin et al., 2009), data points on the master plot closely follow the pressure indicator line.

In the next section we consider the examples of the application of our Al^{VI} in amphibole geo-barometer to the well studied geological objects: to andesites of Shiveluch volcano (Kamchatka) and to mafic xenoliths in alkaline basalts from Dish Hill (California) characterized by independent methods.

5. Geologic Applications

5.1 Shiveluch Volcano

The Shiveluch volcano is located near the junction of Aleute and Kuril -Kamchatka subduction zones and marks a northern edge of the present day volcanic activity in Kamchatka. By total magma output it is the second and by andesites output it is the first among active volcanoes of Kuril -Kamchatka subduction zone (Gorbach & Portnyagin, 2011). The andesites of the Young Shiveluch are classified as adakites for their high MgO and Cr content and high Sr/Y ratio (Yogodzinski et al., 2001). They are also characterized by high water content and oxygen fugacity reaching NNO+2. Twice in Holocene eruptions of high magnesium basalts with low water content, low f_{O2} and presumably high CO_2 activity took place (7600 and 3600 BP) (Pevzner & Babansky, 2010). For pressure estimate we use the analyses of amphiboles from the samples collected by A. Babansky (described in Simakin et al., 2009), by authors in 2007 and published in (Bryant et al., 2007; Ferlito, 2011). The most important are amphiboles substituting Opx from the ultramafic inclusions. We study undated pyroxenite inclusion hosted in andesite from the western slope of the volcano.

In this ultramafic inclusion orthopyroxene was partially replaced by amphibole and eventually overgrown by amphibole (rim) corona. Amphibole compositions are plotted in Figure 6a. We interpret the observed distribution from Al^{VI} rich to Al^{VI} poor varieties towards the inclusion center as manifestation of concentration decrease of aluminum transported by diffusion from andesitic melt and consumed in the substitution reaction. We specify pressure indicator line passing through the point [Fe^{3+}+Ti, Al^{VI}]=[1.8, 0] and upper-right edge of xenolith points set. It intersects with the ordinate at Al^{VI}_{max}=0.98 with the corresponding equilibrium pressure P=7.9±0.8 kbar. Two-pyroxene geo-thermo-barometer (Putirka, 2008) gives us pressure estimate P=8.3±1.5 kbar and temperature T= 1013^{o}C. Ridolfi (2010) amphibole barometer yields P=3.4 kbar.

Bryant et al. (2007) described inclusions of amphibolized pyroxenites from the andesites of the Young Shieluch eruption of 1964 as mantle xenoliths transported from sub-Moho depths to magma chamber. The analyses of amphiboles from this paper and pressure indicator line are plotted in Figure 6b. A small number of analyses permits only approximate pressure estimate of P= 5.1±0.6 kbar. Two-pyroxene geo-barometer pressure estimate based on analyses published in (Bryant et al., 2007) is 5.6±1.1 kbar (at T= 931^{o}C). Amphibole analyses from (Bryant et al., 2007) also tell us that intrinsic oxygen fugacity of pyroxenites was much lower (Fe^{3+}+Ti =0.3-0.4) than that in the hosted andesitic magma (Fe^{3+}+Ti =1.1-1.2) exactly as concluded by authors of cited publication (Bryant et al., 2007).

However, while using Ca in olivine geobarometer Bryant et al. (2007) predicts much higher pressure of 1-2 GPa for the same samples. It is known that olivine grown from the melt contains a lot of calcium. Olivine is purified and releases CaO at the solid state recrystallization and equilibration with pyroxene. Ca in olivine geo-barometer can be used only for such aggregates. While used for magmatic olivine this tool may give highly erroneous results (Medaris et al., 1999). Pressure 6-8 kbar corresponds to the crustal magma chamber rather than sub-Moho mantle depths anticipated by Bryant et al. (2007). We can conclude that the Shiveluch hydrous andesites mix with basic dry reduced magma on the middle to low crust level. Ridolfi (2009) model provides quite lower value of pressure P=3 kbar. Summarizing ultramafic inclusions data we can conclude that our novel amphibole geo-barometer predicts pressure values confirmed by independent method while Ridolfi (2010) amphibole barometer strongly underestimates it.

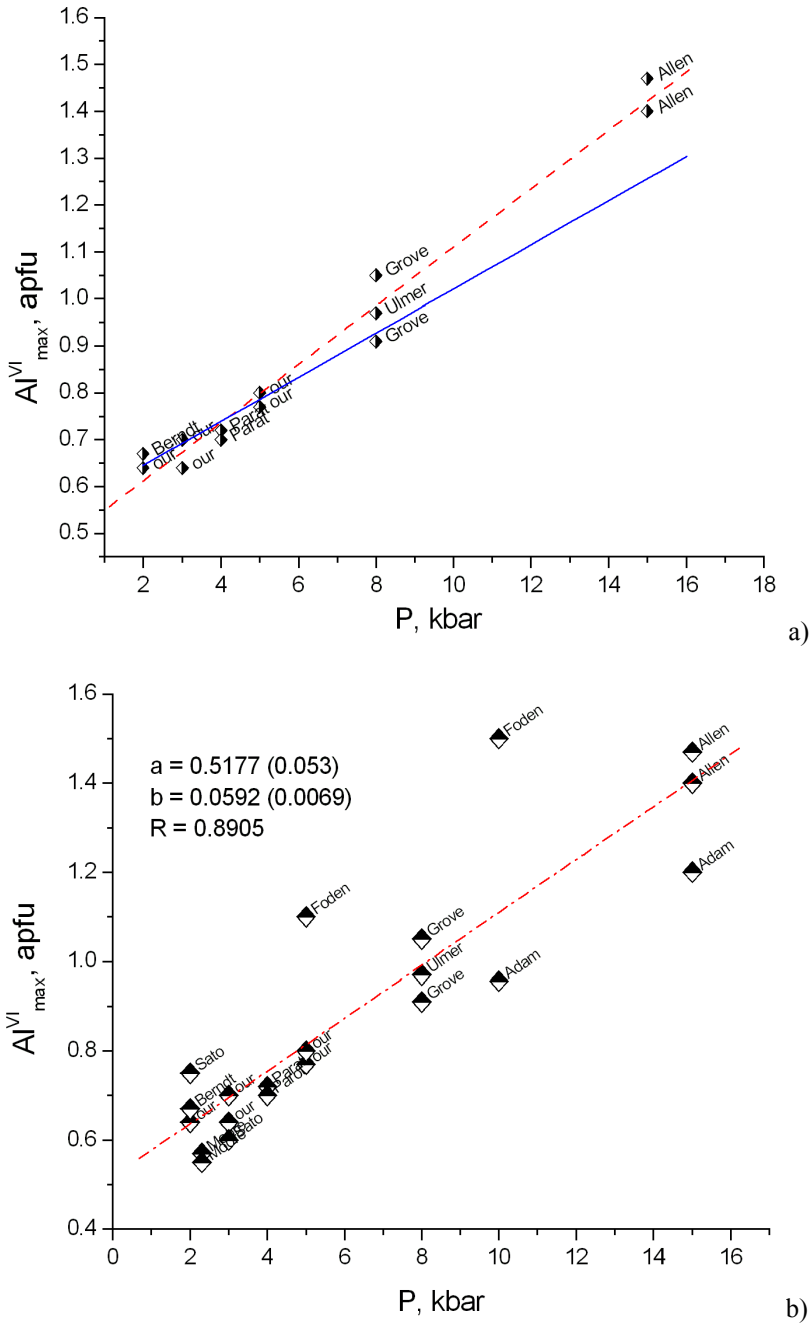

Figure 6. Calibration of Al^{VI} in amphibole geobarometer a) continuous line is linear regression of our experimental data obtained at P=2, 3, 5 kbar; dashed line represents linear regression of our data and selected published experimental results (points labeled with first names of the corresponding papers) b) regression of the more complete data set with inclusion of less precise points

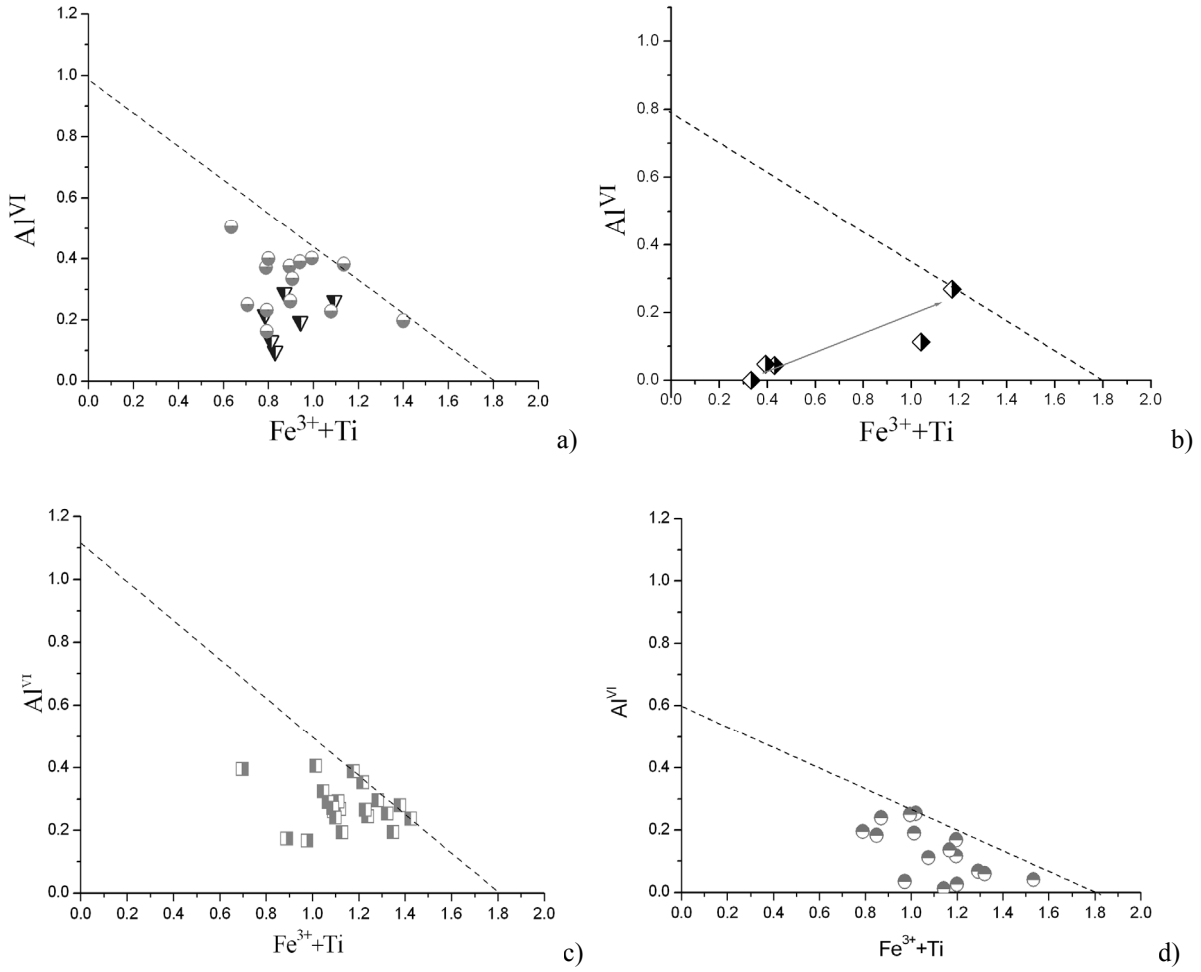

Figure 7. Compositions of amphiboles from Shiveluch volcano, Kamchatka a) mafic inclusion from the N-W flank of volcano b) amphibolized mafic inclusion from (Bryant et al., 2007), arrow demonstrates trend from reduced and Al deficit conditions in the center of xenolith towards oxidized rims equilibrated with andesitic magma, pressure indicator lines in all plots are depicted with dotted line c) phenocrysts from Holocene extrusions from the N-W flank of volcano d) amphiboles from andesitic lava rested in the shallow chamber before eruption

Amphiboles from the Holocene extrusions located along the western edge of Old Shivelush caldera have surprisingly high pressure of formation in accordance with our estimates. In Figure 7c we plot our data for amphiboles from the Karan extrusion. Most analyses specify an unequivocal position of pressure indicator line with the expected abscissa intersection point [Fe^{3+}+Ti, Al^{VI}] = [1.8, 0]. Pressure estimate for this sample is P=9.8±0.8 kbar approximately corresponding to the Moho depth of 33 km in NE Kamchatka (Levin et al., 2002). We get essentially the same high pressure around P=10 kbar at the consideration of the published analyses from Shiveluch extrusions found in (Gorbach & Portnyagin, 2011; Ferlito, 2011).

For comparison in Figure 6d we place amphibole diagram for undated andesitic lava slab sampled on the western slope of Shiveluch. It yields P=2.2±0.4 kbar. This points set indicates shallow magma chamber under volcano with the depth of about 5 km (plus 2-3 km of edifice load). The points on this diagram almost uniformly fill the sector between pressure indicator line and abscissa reflecting a close system fractionation of magma towards silicic compositions before and probably during the eruption.

5.2 Dish Hill Xenoliths

In the above example our geo-barometer was used for high magnesium andesite i.e. exactly within the composition field used for calibration. Further we consider a case of lherzolite xenoliths from the Pliocene basanite cones, Dish Hill (California). These ultramafic xenoliths with numerous interstitial amphiboles and

amphibole veins were described three decades ago (Wilshire et al., 1980) and since then have been intensively studied as a product of mantle metasomatose (Popp et al., 1995; Lamb & Popp, 2009). Calcic amphibole analyses from (McGuire et al., 1991) are plotted in Figure 7. Two sets of points correspond to two different samples of spinel lherzolite (WR and DH abbreviation from (McGuire et al., 1991)). A rather small spreading around well defined pressure indicator lines can be observed. Pressure estimates are P=8.1±0.8 kbar for WR and P=2±0.4 kbar for DH samples, respectively. Two-pyroxene geo-thermo-barometer gives the following estimates: P=9±0.3 kbar, T=1060^{o}C for WR and P=7.5±0.4 kbar, T=988^{o}C for DH samples. Pressure evaluations with both methods for WR samples are practically the same within uncertainty limits. DH sample amphiboles were formed at the significantly lower pressure than two-pyroxene aggregate. We can interpret these facts as amphibolization of WR sample in-situ in Upper mantle and in the shallow magma chamber in the case of DH sample. Pressure estimates made by two-pyroxene and amphibole geo-barometers are significantly lower than 2 GPa proposed by Lamb and Popp (2009) based on the thermodynamic modeling. Coordinated pressure guess for Dish Hill xenoliths of 8-9 kbar corresponds well to the Moho depths of 27-29 km obtained with seismic methods (Miller, 2009). Like in the Shiveluch case we anticipate that mantle generated magma was ponded first at the upper mantle – crust density interface. At the further ascend toward the surface magma carried fragments of the deep magma chamber walls as lherzolite xenoliths.

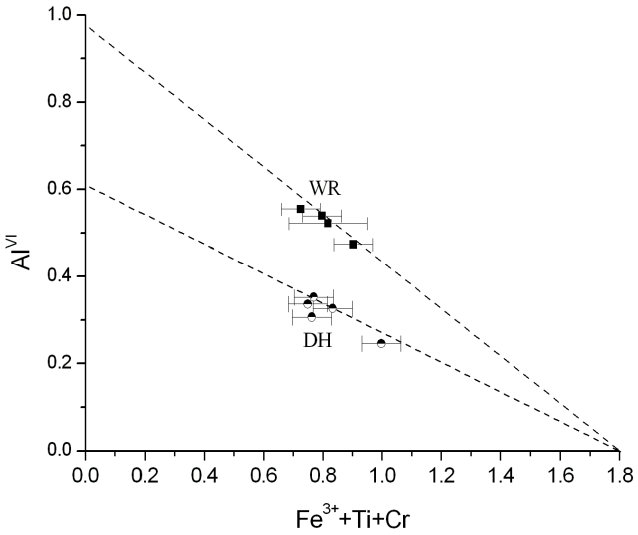

Figure 8. Amphiboles compositions of amphibolized mafic xenoliths from Dish Hill, California, source of data (McGuire et al., 1991). Upper pressure indicator line gives Moho depth pressure of xenoliths formation, lower data set corresponds to the pressure of the shallow magma chamber where DH sample was equilibrated before dyke intrusion

6. Conclusions

Amphibole is common phase crystallizing from hydrous magmas. This mineral composition can show a lot about physicochemical conditions of its formation. We perform experimental study of amphibole crystallization from high magnesium andesites (Shiveluch volcano, Kamchatka) at pressure of 2, 3 and 5 kbar. In our study we grow crystals at sufficiently low undercooling to minimize kinetic effect on the solid composition. The data obtained in this way permits calibration of Al^{VI} in amphibole geobarometer. To extend the dependence of the extrapolated maximum Al^{VI} content on higher pressures we additionally use the published experimental data that get linear regression $Al^{VI}_{max}(P)$ with correlation coefficient 0.99 after some reasonable selection. Our model is based on the assumption of the equilibrium distribution of the Al presented in the cation-modifier form in the melt and octahedral Al in amphibole. It is important that at the constant bulk composition a structural transition of the tetrahedral aluminum (network-forming form) into higher coordinated Al^{V} and Al^{VI} forms (detached from the network) is essentially pressure induced. It was shown that novel geobarometer pressure estimates are consistent with two-pyroxene ones (Putirka, 2008) for several amphibolized ultramafic xenoliths. This ensures application of our Al^{VI} in amphibole geobarometer for evaluation of hydrous magmas pressure of calc-alkaline andesitic to basaltic compositions.

Acknowledgements

Authors express their gratitude to Alexey Nekrasov for performing precise microprobe analyses and Michail Ivanov for technical assistance in the experiments on IHPV. Olga Mozgovaya is cordially acknowledged for language corrections of the manuscript.

References

Abe, T., Sukamoto, K., & Sunagawa, I. (1991). Nucleation, growth and stability of CaAl2Si2O8 polymorphs. *Physics and Chemistry of Minerals, 17*, 473-484.

Adam, J., Oberti, R., Cámara, F., & Green, T. H. (2007). An electron microprobe, LAM-ICP-MS and single-crystal X-ray structure refinement study of the effects of pressure, melt-H2O concentration and on experimentally produced basaltic amphiboles. *European Journal of Mineralogy, 19*, 641-655. http://dx.doi.org/ 10.1127/0935-1221/2007/0019-1750

Allen, J. C., & Boettcher, A. L. (1983). The stability of amphibole in andesite and basalt at high pressures. *American Mineralogist, 68*, 307-314. http://www.minsocam.org/ammin/AM68/AM68_307.pdf

Alonso-Perez, R., Muntener, O., & Ulmer, P. (2009). Igneous garnet and amphibole fractionation in the roots of island arcs: experimental constraints on andesitic liquids. *Contribution to Mineralogy and Petrology, 157*, 541–558. http://dx.doi.org/10.1007/s00410-008-0351-8

Andersen, D. J., Lindsley, D. H., & Davidson P. M. (1993). QUILF: a Pascal program to assess equilibria among Fe–Mg–Mn–Ti-oxides, pyroxenes, olivine, and quartz. *Computers & Geosciences, 19*, 1333-1350. http://dx.doi.org/10.1016/0098-3004(93)90033-2

Anderson, J. L., & Smith, D. R. (1995). The effects of temperature and fO2 on the Al-in-hornblende barometer. *American Mineralogist, 80*, 549-559. Retrieved from http://www.minsocam.org/msa/ammin/toc/Articles_Free/1995/Anderson_p549-559_95.pdf

Berndt, J., Koepke, J., & Holtz, F. (2005). An Experimental Investigation of the Influence of Water and Oxygen Fugacity on Differentiation of MORB at 200 MPa. *Journal of Petrology, 46*, 135-167. http://dx.doi.org/10.1093/petrology/egh066

Blundy, J., & Holland, T. J. B. (1990). Calcic amphibole equilibria and a new amphibole-plagioclase geothermometer. *Contribution to Mineralogy and Petrology, 104*, 208-224. http://dx.doi.org/10.1007/BF00306444

Bryant, J. A., Yogodzinski, G. M., & Churikova, T. G. (2007). Melt-mantle interactions beneath the Kamchatka arc: Evidence from ultramafic xenoliths from Shiveluch volcano. *Geochemistry, Geophysics, Geosystems, 8*, 1-24. http://dx.doi.org/10.1029/2006GC001443

Cabane, H., Laporte, D., & Provost, A. (2005). An experimental study of Ostwald ripening of olivine and plagioclase in silicate melts: implications for the growth and size of crystals in magmas. *Contribution to Mineralogy and Petrology, 150*, 37-53. http://dx.doi.org/10.1007/s00410-005-0002-2

Deer, W. A., Howie, R. A., & Zussman, J. (1997) *Rock-forming minerals, Chain Silicates*, 2B, (2nd ed.). The Geological Society, London.

Ferlito, C. (2011). Bimodal geochemical evolution at Sheveluch stratovolcano, Kamchatka, Russia: Consequence of a complex subduction at the junction of the Kuril Kamchatka and Aleutian island arcs. *Earth-Science Reviews, 105*, 49-69. http://dx.doi.org/10.1016/j.earscirev.2010.12.003

Foden, J. D., & Green, D. H. (1992). Possible role of amphibole in the origin of andesite: some experimental and natural evidence. *Contribution to Mineralogy and Petrology, 109*, 479-493. http://dx.doi.org/10.1007/BF00306551

Gorbach, N. V., & Portnyagin, M. V. (2011). Geology and Petrology of the Lava Complex of Young Shiveluch Volcano, Kamchatka. *Petrology, 19*, 134-166. http://dx.doi.org/10.1134/S0869591111020068

Grove, T. L. Elkins-Tanton, L. T., Parman, S. W., Chatterjee, N., Muntener, O., & Gaetani, G. A. (2003). Fractional crystallization and mantle-melting controls on calc-alkaline differentiation trends. *Contribution to Mineralogy and Petrology, 145*, 515-533. http://dx.doi.org/10.1007/s00410-003-0448-z

Gualda, G. A. R., & Vlach, S. R. F. (2005). Stoichiometry-based estimates of ferric iron in calcic, sodic-calcic and sodic amphiboles: A comparison of various methods. *Anais da Academia Brasileira de Ciências, 77*, 521-534. http://dx.doi.org/10.1590/S0001-37652005000300012

Hammarstrom, J. M., & Zen, E. A. (1986). Aluminum in hornblende: an empirical igneous geobarometer. *American Mineralogist, 71*, 1297-1313. http://www.minsocam.org/ammin/AM71/AM71_1297.pdf

Imon, R., Okudaira, T., & Fujimoto, A. (2002). Dissolution and precipitation processes in deformed amphibolites: an example from the ductile shear zone of the Ryoke metamorphic belt, SW Japan. *Journalof Metamorphic Geology, 20*, 297-308. http://dx.doi.org/10.1046/j.1525-1314.2002.00367.x

Johnson, M. E., & Rutherford, M. J. (1989). Experimental calibration of the aluminum-in-hornblende geobarometer with application to Long Valley caldera (California) volcanic rocks. *Geology, 17*, 837-841. http://dx.doi.org/10.1130/0091-7613(1989)017<0837:ECOTAI>2.3.CO;2

Kelsey, K. E., Stebbins, J. F., Singer, D. M., Brown, G. E., Jr., Mosenfelder, J. L., & Asimow, P. D. (2009). Cation field strength effects on high pressure aluminosilicate glass structure: Multinuclear NMR and La XAFS results. *Geochimica et Cosmochimica Acta, 73*(13), 3914-3933. http://dx.doi.org/10.1016/j.gca.2009.03.040

Lamb, W. M., & Popp, R. K. (2009). Amphibole equilibria in mantle rocks: Determining values of mantle aH2O and implications for mantle H2O contents. *American Mineralogist, 94*, 41–52. http://dx.doi.org/10.2138/am.2009.2950

Leake, B. E., Woolley, A. R., Arps, C. E. S., Birch, W. D., Gilbert, M. C., Grice, J. D., … Youzhi, G. (1997). Nomenclature of amphiboles: Report of the Subcommittee on Amphiboles of the International mineralogical Association, Commission on New Minerals and Mineral Names. *American Mineralogist, 82*, 1019-1037. http://www.minsocam.org/msa/ima/ima98(11).pdf

Levin, V., Park, J., Brandon, M., Lees, J., Peyton, V., Gordeev, E., & Ozerov, A. (2002). Crust and upper mantle of Kamchatka from teleseismic receiver functions. *Tectonophysics, 358*, 233-265. http://dx.doi.org/10.1016/S0040-1951(02)00426-2

Malfait, W., Xue, X., Verel, R., Ardia, P., & Sanchez-Valle, C. (2011). The speciation of hydrous aluminosilicate glasses and melts: a view from NMR, infrared and Raman spectroscopy. *Geophysical Research Abstracts, 13*, EGU2011-1404 http://meetingorganizer.copernicus.org/EGU2011/EGU2011-1404.pdf

Manley, C., & Bacon, C. R. (2000). Rhyolite thermobarometry and the shallowing of the magma reservoirs, Coso volcanic field, California. *Journal of Petrology, 41*, 149-174. http://dx.doi.org/10.1093/petrology/41.1.149

McGuire, A. V., Dyar, M. D., & Nielson J. E. (1991). Metasomatic oxidation of upper mantle peridotite. *Contribution to Mineralogy and Petrology, 109*, 252-264. http://dx.doi.org/ 10.1007/BF00306483

Medaris, G. L., Wang, H. F., Fournelle, J. H., Zimmer, J. H., & Jelínek, E. (1999). A cautionary tale of spinel peridotite thermobarometry: an example from xenoliths of Kozakov Volcano, Czech Republic. *Geolines, 9*, 92-96. http://geolines.gli.cas.cz/fileadmin/volumes/volume09/G9-092.pdf

Miller, M. S. (2009). Receiver Function Images of the Western U.S. Lithosphere Using Transportable Array Data. Retrieved from http://www.earthscope.org/es_doc/onsite/Su09_WUSRecFunc.pdf

Moore, G., & Carmichael, I. S. E. (1998). The hydrous phase equilibria (to 3 kbar) of an andesite and basaltic andesite from western Mexico: constraints on water content and conditions of phenocryst growth. *Contribution to Mineralogy and Petrology, 130*, 304-319. http://dx.doi.org/ 10.1007/s004100050367

Moretti, R., & Baker, D. R. (2008). Modeling the interplay of fO2 and fS2 along the FeS-silicate melt equilibrium. *Chemical Geology, 256*, 286-298. http://dx.doi.org/10.1016/j.chemgeo.2008.06.055

Neuville, D. R., Cormier, L., Montouillout, V., Florian, P., Millot, F., Rifflet J. C., & Massiot, D. (2008). Structure of Mg- and Mg/Ca aluminosilicate glasses: 27Al NMR and Raman spectroscopy investigations. *American Mineralogist, 93*, 1721-1731. http://dx.doi.org/10.2138/am.2008.2867

Parat, F., Holtz, F., & Feig, S. (2008). Pre-eruptive Conditions of the Huerto Andesite (Fish Canyon System, SanJuanVolcanic Field, Colorado): Influence of Volatiles (C-O-H-S) on Phase Equilibria and Mineral Composition. *Journal of Petrology, 49*, 911-935. http://dx.doi.org/10.1093/petrology/egn011

Pevzner, M. M., & Babansky, A. D. (2010). Age of Young Shiveluch volcano and evolution of its magmas composition. Magmatism and metamorphism in the Earth history. In: Magmatism and Metamorphism in the Earth History. Proceedings of XI All-Russian Petrographic conference, Ekaterenburg, II, 115-116

Pichavant, M., Costa, F., Burgisser, A., Scaillet, B., Martel, C., & Poussineau, S. (2007). Equilibration Scales in Silicic to Intermediate Magmas: Implications for Experimental Studies. *Journal of Petrology, 48*,

1955-1972. http://dx.doi.org/10.1093/petrology/egm045

Popp R. K., Virgo, D., Yoder, H. S., J. R., Hoering T. C., & Phillips, M. W. (1995). An experimental study of phase equilibria and Fe oxy-component in kaersutitic amphibole: Implications for the fH2 and aH20 in the upper mantle. *American Mineralogist, 80*, 534-548. Retrieved from http://www.minsocam.org/msa/ammin/toc/Articles_Free/1995/Popp_p534-548_95.pdf

Presnall, D. C., Dixon, S. A., Dixon, J. R., O'Donnell, T. H., Brenner, N. T., & Dycus, D. W. (1978). Liquidus phase relations on the join diopside-forsterite-anorthite from 1 atm to 20 kbar: Their bearing on the generation and crystallization of basaltic magma. *Contributions to Mineralogy and Petrology, 66*, 203-220. http://dx.doi.org/10.1007/BF00372159

Putirka, K. (2008). Thermometers and Barometers for Volcanic Systems. In: K. Putirka, F. Tepley, (Eds.), Minerals, Inclusions and Volcanic Processes. *Reviews in Mineralogy and Geochemistry, 69*, 61-120. http://dx.doi.org/10.2138/rmg.2008.69.3

Ridolfi, F., Renzulli, A., & Puerini, M. (2010). Stability and chemical equilibrium of amphibole in calc-alkaline magmas: an overview, new thermobarometric formulations and application to subduction-related volcanoes. *Contributions to Mineralogy and Petrology, 160*, 45-66. http://dx.doi.org/10.1007/s00410-009-0465-7

Sato, H., Holtz, F., Behrens, H., Botcharnikov, R., & Nakada, S. (2005). Experimental Petrology of the 1991-1995 Unzen Dacite, Japan. Part II: Cl/OH Partitioning between Hornblende and Melt and its Implications for the Origin of Oscillatory Zoning of Hornblende Phenocrysts. *Journal of Petrology, 46*, 339-354. http://dx.doi.org/10.1093/petrology/egh078

Schmidt, M. W. (1992). Amphibole composition in tonalite as a function of pressure: An experimental calibration of the Al-in-hornblende barometer. *Contribution to Mineralogy and Petrology, 110*, 304-310. http://dx.doi.org/10.1007/BF00310745

Simakin, A. G., & Salova, T. P. (2004). Plagioclase Crystallization from a Hawaiitic Melt in Experiments and in a Volcanic Conduit. *Petrology, 12*(1), 82-92.

Simakin, A. G., Salova, T. P., & Babansky, A. D. (2009). Amphibole Crystallization from a Water-Saturated Andesite Melt: Experimental Data at P = 2 kbar. *Petrology, 17*(6), 1-16. http://dx.doi.org/10.1134/S086959110906006X

Simakin, A. G., Salova, T. P., & Eremyashev, V. E. (2010). Mechanism of water solubility in silicate melts of the albite-nepheline system. *Mineralogy and Petrology, 99*, 279-285. http://dx.doi.org/10.1007/s00710-009-0107-9

Stebbins, J. F., Dubinsky, E. V., Kanehashi, K., & Kelsey, K. E. (2008). Temperature effects on non-bridging oxygen and aluminum coordination number in calcium aluminosilicate glasses and melts. *Geochimica et Cosmochimica Acta, 72*, 910-925. http://dx.doi.org/10.1016/j.gca.2007.11.018

Wilshire, H. G., Pike, J. E. N., Meyer, C. E., & Schwarzman, E.C. (1980). Amphibole-rich veins in lherzolite xenoliths, Dish Hill and Deadman Lake, California. *American Journal of Science, 280*, 576-593. http://earth.geology.yale.edu/~ajs/1980/ajs_280A_1.pdf/576.pdf

Xue, X., & Kanzaki, M. (2006). Depolymerization effect of water in aluminosilicate glasses: Direct evidence from 1H-27Al heteronuclear correlation NMR. *American Mineralogist, 91*, 1922-1926. http://dx.doi.org/10.2138/am.2006.2365

Xue, X., & Kanzaki, M. (2007). Al coordination and water speciation in hydrous aluminosilicate glasses: Direct evidence from high-resolution heteronuclear 1H– 27Al correlation NMR. *Solid State Nuclear Magnetic Resonance, 31*, 10-27. http:// dx.doi.org/10.1016/j.ssnmr.2006.11.001

Yogodzinski, G. M., Lees, J. M., Churikova, T. G., Dorendorf, F., Woerner, G., & Volynets, O. N. (2001). Geochemical evidence for the melting of subducting oceanic lithosphere at plate edges. *Nature, 409*, 500-504. http://dx.doi.org/10.1038/35054039

Earth Science Research; Vol. 1, No. 2; 2012
ISSN 1927-0542 E-ISSN 1927-0550
Published by Canadian Center of Science and Education

Characterization of Density and Porosity of Rocks Samples from Ogun State of Nigeria

Olukayode D. Akinyemi[1], Aderemi A. Alabi[1], Abimbola I. Ojo[1] & Oyewole E. Adewusi[1]

[1] Department of Physics, College of Natural Sciences, Federal University of Agriculture, Abeokuta, Nigeria

Correspondence: Aderemi A. Alabi, Department of Physics, College of Natural Sciences, Federal University of Agriculture, PMB 2240 Abeokuta, Nigeria. E-mail: derylab@yahoo.com

Received: March 12, 2012 Accepted: March 27, 2012 Online Published: June 19, 2012

doi:10.5539/esr.v1n2p98 URL: http://dx.doi.org/10.5539/esr.v1n2p98

Abstract

Knowledge of densities of rocks is essential in petrological and geological studies, interpretation of gravity anomalies and ground water exploration. Fifty samples were collected from Abeokuta, Sagamu, Odeda, Ewekoro, Ibese Yewa North Local Government, Ijebu East Local Government and Obafemi Owode in Ogun State and dry bulk density, saturated density, porosity and particle density were determined. Results showed that Ewekoro shale has the lowest mean density of 1.35g/cm^3 while Ibese, Yewa North Local Government limestone has the highest mean density of 3.9g/cm^3.Porosity ranges from 0.030 to 0.640 with the granite in Odeda local government having the highest porosity and the shale in Ewekoro local government having the lowest porosity. Mean porosity for all the rocks samples in the seven Local Government Areas was 0.34. Test of significance revealed that there is significant relationship in the values of density of rock samples within the state.

Keywords: dry bulk density, saturated density, particle density, porosity, groundwater exploration

1. Introduction

In geology, rock density has particular value as a theme that connects the properties of minerals and rocks to topics such as seismic velocity, isostasy and porosity (Robert and Robert, 2000). According to Caravaca et al. (2001) and Shrestha et al. (2007) study of bulk density, particle density, saturated density, porosity, organic matter content and size distribution of soil samples from an area reveal some vital soil physical properties of the area. Knowledge of densities of rocks is essential in petrological and geological studies and more so for a meaningful structural interpretation of gravity anomalies Ajakaiye (1975). It was also stated by Horgan (1996) that the gravity reduction is computed by taking the density as a constant (2.67g/cm^3) which represents the topographical density.

The effect of density on porosity follows a mixing law. The porosity, φ, is the fractional pore volume of a rock. The total mass of a volume of rock V_T is made up of the mass of the pore fluid, of densityρ_f, plus the mass of the matrix minerals of density ρ_{ma} the density measured is the bulk densityρ_h.

The total mass then becomes:

$$Total\ Mass = V_T\rho_h = \varphi V_T\rho_f + (1-\varphi)V_T\rho_{ma} \quad (1)$$

which gives a formula for the bulk density in terms of the porosity, pore fluid density and the matrix density. The mixing law for density is given as follows:

$$\rho_h = \varphi\rho_f + (1-\varphi)\rho_{ma} \quad (2)$$

From the mixing law we can then find the porosity via:

$$\emptyset = \frac{\rho_{ma}-\rho_h}{\rho_{ma}-\rho_f} \quad (3)$$

2. Geology of Study Area

Ogun State is entirely in the tropics, located in the Southwest Zone of Nigeria with a total land area of 16,409.26 square kilometers. It is bounded on the West by the Benin Republic, on the South by Lagos State and the Atlantic Ocean, on the East by Ondo State, and on the North by Oyo and Osun States. It is situated between

Latitude 6.2°N and 7.8°N, and Longitude 3.0°E and 5.0°E. The geology of Ogun state comprises of sedimentary rocks and basement complex rocks, which underlay the remaining surface area of the state. It also consists of intercalations at argillacous sediment. The rock is soft and friable but in some places cement by ferruginous on silicious material. It lies uncomfortably on the crystalline basement. The extensive Precambrian rocks are classified into three major groups: In Ogun state, the basement complex rock extends North western part to Ijebu-Igbo. They consist of rocks types like coarse – porhhyrrichornblerec – biotite – gramedicite, biotite granite, gneiss, pegmatite porphyroblashic granite anphibolite schist quartzite, quartz – schist and banuledgneissIloeje (1979).

The sedimentary rock unit of Ogun state consists of Abeokuta formation lying directly above the basement complex. This is in turn overlain by Ewekoro, Oshosun and llaroformations, which are themselves overlain by the coastal plain sands (Benin formation). The flood plains of the major rivers and streams are covered by the alluvial sands (Kehinde, 1992).

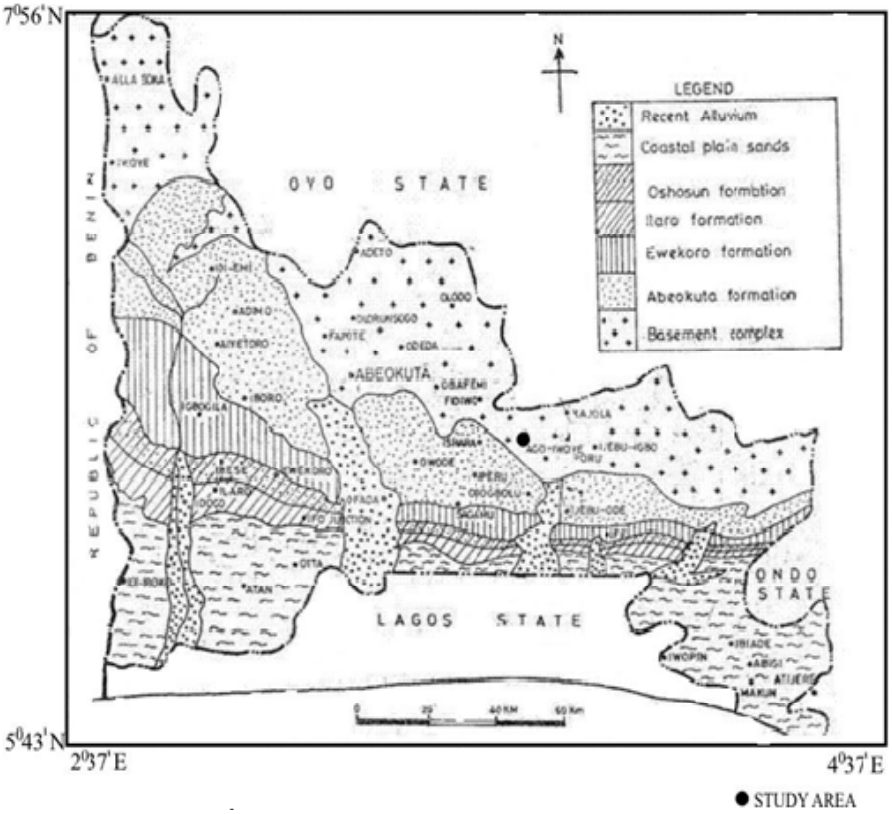

Figure 1. Geological Map of Ogun State

3. Methodology

Fifty rock samples were collected from Abeokuta North Local government and six other locations namely, Sagamu, Odeda, Ewekoro, IbeseYewa North Local Governments, Ijebu East Local Government and Obafemi-Owode in Ogun State. Samples were crushed into small grain size and later taken to the laboratory for analysis. Using an electronic weighing balance, 20g of rock samples were collected in 50 different crucibles and each crucible was labeled according to the sample description. The rock samples were heated in an oven at a temperature of 100°C for 18 hours and later weighed separately in air (w_d) and in water (w_w) (after adding 40ml of water to the samples). The samples were then saturated in water for 24 hours and weighed again in water (w_s) and in air (w_t).The weight in air after saturation (w_t) was measured by draining off the water remaining in the crucible and then weighing, using an electronic balance.

From the results obtained, that is, the value of W_d, W_w, W_t and W_s, the dry bulk density ($\boldsymbol{\rho_d}$), saturated density ($\boldsymbol{\rho_s}$) and particle or grain density ($\boldsymbol{\rho_g}$) for the fifty rock samples was calculated using the following mathematical expression (Ajakaiye, 1975).

$$\text{Dry Bulk Density, } \rho_d = \frac{W_d}{W_t - W_s} \quad (4)$$

$$\text{Saturated Density, } \rho_s = \frac{W_t}{W_t - W_s} \quad (5)$$

$$\text{Particle or Grain Density, } \rho_d = \frac{W_d}{W_t - W_s} \quad (6)$$

$$\text{Porosity, } \emptyset = \frac{Ws - Ww}{Wd - Ww} \quad (7)$$

4. Results and Discussion

4.1 Results

Table 1 shows the densities of the fifty rock samples collected from the different locations of the study areas. Table 2 is the Analysis of variance of studied parameters while Table 3 shows the mean densities and porosity of the rock samples.

The map of Ogun State within which the study areas located is shown in Figure 1. Figure 2 is the bar chart of the dry bulk density, saturated density, particle density and porosity of the rock samples taken from Odeda Local government area. The samples collected from Odeda local government area are pegmatite, granite and quartzite. Figure 3 is the bar chart of saturated density, dry bulk density, particle density and porosity of limestone being the only rock samples collected from Sagamu LGA. Figures 4, 5, 6, 7 and 8 are the bar charts showing the dry bulk density, saturated densities, particle density as well as porosity of rock samples respectively from Abeokuta North, Ewekoro, Yewa North ,Ijebu East and Obafemi-Owode local government area. Rock samples from Abeokuta North are quartzite, kaolin, feldspar and granite while limestone and granite were taken from Yewa North and Ijebu East Local Government Area. Also granite and kaolin were collected from Obafemi-Owode local government area and limestone and shale from Ewekoro Local Government Area.

Table 1. The densities of the fifty rock samples collected from the selected locations are given below

S/N	Sample Name	Sample Location	Dry bulk density (g/cm^3)	Saturated density (g/cm^3)	Particle density (g/cm^3)	Porosity
1	Pegmatite	OLG	1.83	2.2	3.66	0.309
2	Pegmatite	OLG	1.7	1.54	3.4	0.358
3	Pegmatite	OLG	1.71	1.22	3.42	0.355
4	Granite	OLG	1.74	3.5	3.48	0.343
5	Granite	OLG	1.72	2.07	3.44	0.351
6	Granite	OLG	1.55	1.9	3.1	0.415
7	Granite	OLG	1.86	2.25	3.72	0.298
8	Granite	OLG	1.82	2.26	3.64	0.313
9	Granite	OLG	1.99	2.4	3.98	0.249
10	Quartzite	OLG	1.88	2.43	3.76	0.291
11	Granite	OLG	7.6	7.61	7.63	0.64
12	Granite	OLG	3.08	3.09	3.09	0.4
13	Granite	OLG	2.82	2.95	3.24	0.08
14	Granite	OLG	2.22	2.22	2.22	0.12
15	Granite	OLG	3.12	3.12	3.12	0.44
16	Granite	OLG	1.99	2	2.02	0.09
17	Granite	OLG	1.85	1.85	1.85	0.08
18	Limestone	SLG	1.45	1.82	2.9	0.453
19	Limestone	SLG	1.96	2.31	3.92	0.261
20	Limestone	SLG	1.52	2.11	3.04	0.426
21	Limestone	SLG	1.58	2.02	3.16	0.404
22	Limestone	SLG	2.77	2.76	3.54	0.06
23	Quartzite	ANLG	1.61	1.93	3.22	0.392
24	Kaolitic clay	ANLG	1.3	1.94	2.6	0.509
25	Feldspar	ANLG	1.24	1.78	2.48	0.532
26	Granite	ANLG	1.76	2.17	3.52	0.336
27	Granite	ANLG	1.9	2.37	3.8	0.268
28	Limestone	ELG	1.72	3.4	3.44	0.351
29	Shale	ELG	1	1.61	4.96	0.623
30	Shale	ELG	1.23	2.19	2.46	0.536
31	Limestone	ELG	1.67	2.06	3.34	0.37
32	Limestone	ELG	1.56	2.02	3.12	0.41
33	Limestone	ELG	1.45	1.95	2	0.453
34	Shale	ELG	1.65	1.75	1.83	0.06
35	Shale	ELG	1.5	1.63	1.72	0.03
36	Limestone	YNLG	1.87	2.26	3.74	0.294
37	Limestone	YNLG	1.93	2.35	3.86	0.272
38	Limestone	YNLG	2.05	2.38	4.1	0.224
39	Granite	IELG	1.46	1.76	2.92	0.449
40	Granite	IELG	1.59	1.94	3.18	0.4
41	Granite	IELG	1.15	1.45	2.3	0.566
42	Granite	OOLG	1.59	3.13	3.18	0.4
43	Granite	OOLG	1.95	2.36	3.9	0.264
44	Granite	OOLG	1.89	2.3	3.78	0.287
45	Granite	OOLG	1.72	2.05	3.44	0.351
46	Granite	OOLG	1.85	2.26	3.7	0.302
47	Kaolin	OOLG	1.48	2.16	2.96	0.442
48	Granite	OOLG	1.69	2.07	3.38	0.362
49	Granite	OOLG	1.89	2.13	3.78	0.287
50	Granite	OOLG	1.93	2.23	3.86	0.272

OLG: Odeda Local government area
SLG: Sagamu Local government area
ANLG: Abeokuta North Local Government area
ELG: Ewekoro Local Government area
YNLG: Yewa North Local Government area
IELG: Ijebu East Local Government area
OOLG: Obafemi-Owode Local Government area

Table 2. Table of the analysis of variance of studied parameters

	Sum of Squares	df	Mean Square	F	Sig.
Saturated density Between Groups	3.598	6	0.6		
Within Groups	35.893	43	0.835	0.718	0.637
Total	39.491	49			
Dry bulk density Between Groups	6.87	6	1.145		
Within Groups	34.96	43	0.813	1.408	0.234
Total	41.831	49			
Particle density Between Groups	4.524	6	0.754		
Within Groups	36.183	43	0.841	0.896	0.506
Total	40.707	49			
Porosity Between Groups	0.12	6	0.02		
Within Groups	0.861	43	0.02	1.002	0.436
Total	0.982	49			

Table 3. The table below shows the mean densities of the rock samples

S/N	SAMPLE	Dry bulk density	Saturated density	Particle density	Porosity
1	Odeda granite	2.57	2.86	3.43	0.294
2	Odeda Pegmatite	1.75	1.65	3.49	0.341
3	Sagamu limestone	1.86	2.2	3.31	0.321
4	Ewekoro shale	1.35	1.8	2	0.312
5	Ewekoro limestone	1.6	2.36	2.98	0.396
6	Yewa North L.G limestone	1.95	2.33	3.9	0.253
7	Ijebu granite	1.4	1.72	2.8	0.472
8	Obafemi-Owode granite	1.81	2.32	3.63	0.316

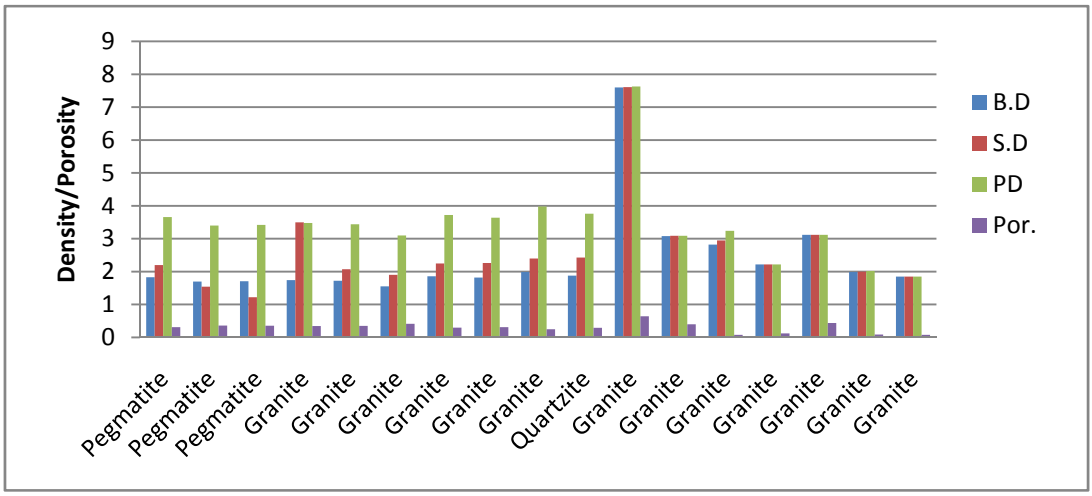

Figure 2. Bar chart of densities and porosity of samples from Odeda LG

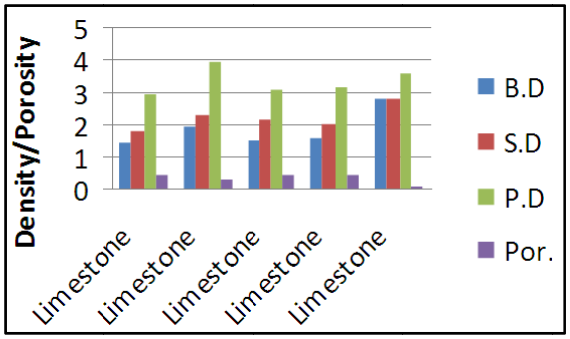

Figure 3. Bar chart of densities and porosity of samples from Sagamu LG

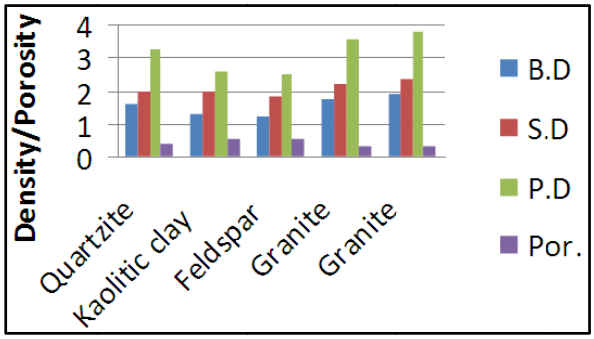

Figure 4. Bar chart of densities and porosity of samples from Abeokuta North LG

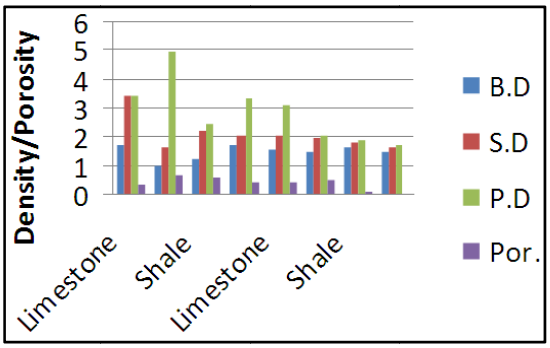

Figure 5. Bar chart of densities and porosity of samples from Ewekoro LG

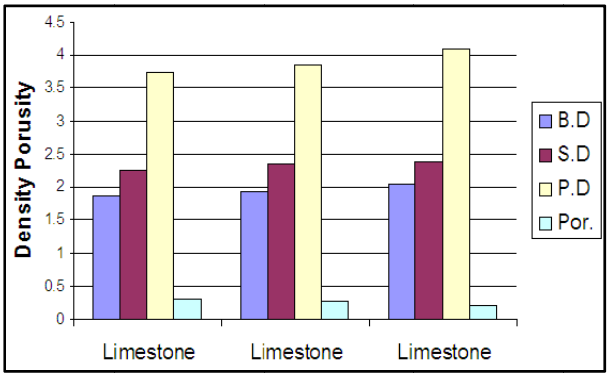

Figure 6. Bar chart of densities and porosity of samples from Yewa LG

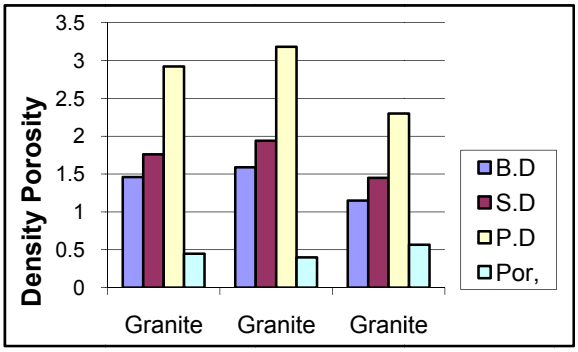

Figure 7. Bar chart of densities and porosity of samples from Ijebu East LG

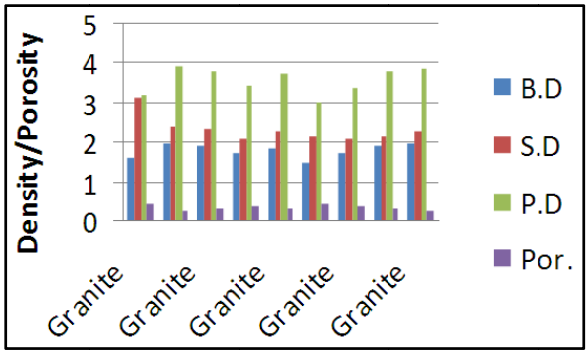

Figure 8. Bar chart of densities and porosity of samples from Obafemi-owode LG

4.2 Discussions

4.2.1 Dry Bulk Density

The only sample of quartzite from Odeda LGA has dry bulk density of 1.88g/cm. The dry bulk densities of granite and pegmatite from the same LGA range from 1.55g/cm^3 to 7.60g/cm^3 and from 1.70g/cm^3 to 1.83g/cm^3 respectively. The dry bulk density of the limestone from Sagamu LGA ranges from 1.45g/cm^3 to 2.77g/cm^3. Two rock types collected from Ewekoro LGA were limestone and shale and their dry bulk density range from 1.45g/cm^3 to 1.72g/cm^3, and from 1.00g/cm^3 to 1.65g/cm^3 respectively. Dry bulk density of limestone from Yewa North LGA ranges from 1.87g/cm^3 to 2.05g/cm^3 while bulk density of granite from Ijebu East LGA ranges from1.25g/cm^3 to 1.46g/cm^3. Two rock types samples were collected In Obafemi-Owode LGA, granite and kaolin. Dry bulk density of granites ranges from 1.48g/cm^3 to 1.95g/cm^3, while dry bulk density of kaolin in

Obafemi-Owode was 1.48g/cm^3. From Figures 2 and 3, granite in Odeda LGA has the highest dry bulk density (3.12 g/cm^3) among rocks samples while shale in Ewekoro LGA has the lowest dry bulk density (1.00 g/cm^3).

4.2.2 Saturated Density

Saturated density of granite from Odeda LGA ranges from 1.85g/cm^3 to 7.61g/cm^3 while the saturated density of pegmatite ranges from 1.22g/cm^3 to 2.20g/cm^3. Quartzite from Odeda has its saturated density determined to be 2.43g/cm^3, while the saturated density of the limestone from Sagamu ranges from 1.82g/cm^3 to 2.76g/cm^3. The saturated densities of limestone and shale in Ewekoro LGA range from 1.95g/cm^3 to 3.40g/cm^3,and from 1.61g/cm^3 to 2.19g/cm^{3}respectively. In Yewa North LGA saturated density of limestone ranges from 2.26g/cm^3 to 2.38g/cm^3, while granites from Ijebu East LGA have saturated density ranging from 1.45g/cm^3 to 1.94g/cm^3. Two rock types collected In Obafemi-Owode were granite and kaolin. The saturated density of granite in Obafemi-Owode ranges from 2.05g/cm^3 to 3.13g/cm^3, while for kaolin in the same Local Government, saturated density was determined as 2.16g/cm^3. Analysis of rock samples from Abeokuta North LGA shows that granite has the highest saturated density of 2.37g/cm^3 followed by quartzite, kaolitic clay and feldspar with 1.78g/cm^3. Figures 1 to 8 revealed that granite has the highest and lowest saturated density among all rock samples considered. Granite with highest saturated density (3.5 g/cm^3) was in Odeda LGA while the one with least value (1.45 g/cm^3) was found in Ijebu East LGA.

4.2.3 Particle Density

Particle densities of granite and pegmatite in Odeda LGA range from 1.85g/cm^3 to 7.63g/cm^3 and from 3.40g/cm^3 to 3.66g/cm^3 respectively, while particle density for quartzite in the same LGA was 3.76g/cm^3. The particle density of the limestone in Sagamu LGA ranges from 2.90g/cm^3 to 3.92g/cm^3, while the particle density of limestone In Ewekoro LGA ranges from 2.00g/cm^3 to 3.44g/cm^3. The particle density of shale from Ewekoro LGA ranges from 1.72g/cm^3 to 4.96g/cm^3, while particle density of limestone from Yewa North LGA ranges from 3.74g/cm^3 to 4.10g/cm^3. Particle density of granites from Ijebu East ranges from 2.30g/cm^3 to 3.18g/cm^3, while the particle density of granite from Obafemi-Owode ranges from 3.18g/cm^3 to 3.90g/cm^3. The particle density of kaolin for Obafemi-Owodewas 2.96g/cm^3. In Abeokuta North LGA, granite has the highest particle density of 3.80g/cm^3 followed by quartzite, kaolitic clay and feldspar with 2.48g/cm^3. Figures 1 to 8 revealed that particle density was consistently high for all rocks from the state. It also shows that granite from Obafemi-Owode LGA has the highest particle density (3.9g/cm^3) among all rock samples, while shale from Ewekoro LGA has the least particle density (1.72 g/cm^3).

4.2.4 Porosity

Mean porosity of granite from Odeda LGA was determined to be 0.341. For the pegmatite rock samples, the mean porosity was 0.302 while the mean porosity of all the rock samples in Odeda LGA was found to be 0.302. In Odeda LGA granite rock samples has the highest (0.640) and the lowest (0.088) porosity. The porosity of five samples of limestone rock from Sagamu LGA ranges from 0.060 – 0.453, while mean porosity was 0.321. The four different rock samples from Abeokuta North LGA are; Quartzite, kaolictic clay, feldspar and two granite rock samples with porosity of 0.392, 0.509, 0.532, 0.336 and 0.268 respectively. It is clearly seen that the granite samples have lowest porosity when compared to other rock samples for this area. The mean porosity for the local government area was 0.407. Mean porosity of limestone and shale from Ewekoro LGA was 0.354 while the mean porosity of limestone and shale rock samples was 0.396 and 0.312 respectively. The porosity of limestone rock samples ranges from 0.351 – 0.453 while that of shale ranges from 0.030 – 0.623. The highest and lowest porosity was recorded by shale in this local government area. The porosity of granite from Obafemi-Owode LGA ranges from 0.264 – 0.316. The mean porosity for the granite was 0.316; the porosity for the Kaolin rock sample was 0.442. The mean porosity of all the rock samples collected in this area was 0.330.

Considering the mean porosity of all the seven local government areas, the mean porosity ranges from 0.302 - 0.472. The lowest mean porosity (0.302) was in Odeda local government area while the highest porosity (0.472) was in Ijebu-East local government area. Figures 1 to 8 compared the porosity of the samples and place of origin, it can be deduced that granite from Odeda LGA has the highest porosity (0.64) while shale from Ewekoro LGA has the least porosity (0.03).

4.3 Test of Significance

To test the trend of the densities and porosity in seven selected local government areas, null hypothesis, Ho and alternative hypothesis, H1 were set for saturated density as follows:

Ho: There is no significant trend between saturated densities obtained from seven Local Government Areas

H1: There is significant trend between saturated densities obtained from seven Local Government Areas

From Table 2, F_{RATIO} (0.718) calculated for saturated density is greater than $F_{TABULATED}$ (0.637) at 5%, therefore suggesting that there is significant relationship between saturated densities obtained within the state.

Similarly for dry bulk density and particle density significant relationships exist between the dry bulk densities and also between the particle densities within the state. This is because F_{RATIO} (1.408) of dry bulk density is greater than $F_{TABULATED}$ (0.637) and also F_{RATIO} (0.896) of particle density is greater than $F_{TABULATED}$ (0.506).

Figure 2 also revealed that F_{RATIO} (1.002) calculated for Porosity is greater than $F_{TABULATED}$ (0.436) at 5% which suggests that there is significant relationship between porosity within the state.

5 Conclusion

The Limestone rock sample from Ibese, Yewa North Local Government area has the highest mean density value of 3.9g/cm^3 while the shale rock sample from Ewekoro has the lowest mean density of 1.35g/cm^3. The highest porosity was from granite in Odeda local government area with a value of 0.640 and the lowest porosity was from Shale in Ewekoro Local Government Area. The mean porosity of all the rock samples is 0.34 which shows that all the location does not have the same mean porosity when one location is compared with the other locations. It was observed that significant relationship exists between densities within the state, as well as between porosity within the state.

References

Ajakaiye, D. E. (1975). Densities of rocks in the Nigerian Younger Granite Province. In C. A. Kogbe (ed.), *Geology of Nigeria*. Elizebethan Publishing Co. Lagos, Nigeria, pp. 225-233.

Caravaca, F., Lax, A., & J. Albaladejo. (2001). Soil aggregate stability and organic matter in clay and fine silt fractions in urban refuse –amended semiarid soils. *Soil Science Society of America Journal, 65*, 1235-1238. http://dx.doi.org/10.2136/sssaj2001.6541235x

Horgan, G. W. (1996). *A Review of soil pore model.* Retrieved from http://www.bioss.sari.ac.uk/~graham/sprev.pdf

Kehinde Philips, O. O. (1992). Geological Map of Ogun State. In: Onakomaiya, S. O, Oyesiku, O. O., & Segede F. J. (eds). *Ogun State Map*. Rex Charles Publication, Nigeria, pp. 6-20.

lloeje, N. P. (1974). *A New Geography of West Africa.* London: Longman Group Limited.

Robert, S. N., & Robert, G. C. (2000). Rock – Density Exercises for Introductory - Level College Courses. *Journal of Geoscience Education, 48*, 400-442.

Shrestha, B. M., B. R., Singh, B. K. Sitaula, R. Lal, & R. M. Bajracharya. (2007). Soil aggregate- and particle-associated organic carbon under different land uses in Nepal. *Soil Science Society of America Journal, 71*(4), 1194-1203. http://dx.doi.org/10.2136/sssaj2006.0405

Earth Science Research; Vol. 1, No. 2; 2012
ISSN 1927-0542 E-ISSN 1927-0550
Published by Canadian Center of Science and Education

Internal Evolution of the Water-Rock System: Nature and Mechanisms

S. L. Shvartsev[1,2]

[1] Tomsk Division of Trofimuk Institute of Petroleum-Gas Geology and Geophysics of the Siberian Branch of the RAS, Tomsk, Russia

[2] National Research Tomsk Polytechnic University, Tomsk, Russia

Correspondence: S. L. Shvartsev, Institute of Natural Resourses, Tomsk Polytechnic University, Lenenave 30, Tomsk, Russia. Tel: 7-382-249-2163. E-mail: tomsk@igng.tsc.ru

Received: November 14, 2011 Accepted: November 28, 2011 Online Published: June 19, 2012

doi:10.5539/esr.v1n2p106 URL: http://dx.doi.org/10.5539/esr.v1n2p106

Abstract

Self-running internal evolution was thought for a long time to be possible in living systems only but, as the modern synergetic theory implies, it may occur in inorganic complex systems as well. The internal evolution in nonliving systems may be driven by formation of coherent atomic bonds in nonequilibrium conditions, though no material proofs for such a hypothesis has been available. The water-rock system investigated in this study evolves spontaneously due to its intrinsically contradictory equilibrium-nonequilibrium nature. Natural waters can never reach equilibrium with some mafic and ultramafic minerals they dissolve but are in equilibrium with the secondary phases they produce while reacting with the ambient rocks. This is the intrinsic nonequilibrium of water with mantle-derived aluminosilicates that maintains the global-scale evolution of the water-rock system. The evolution continues, without exterior controls, at any time and in any place as long as there are rocks and water, and gives rise to diverse secondary minerals associated with waters of certain compositions.

Keywords: evolution, water-rock interaction, self-organisation, equilibrium-nonequilibrium

1. Introduction

Equilibria in the water-rock system are commonly calculated using thermodynamic methods (Garrels & Christ, 1965), and results of such calculations can be found, for instance, in (Capuano & Cole, 1982; Reed & Spycher, 1984; Nesbitt, 1985; Drever, 1988; Rogers, 1989; Gislason & Arnorsson, 1993; Mohamed et al., 1993; Pawar, 1993; Apello & Postma, 1994; Zamana, 2000; Arnórsson et al., 2002; Gemici & Tarcan, 2004; Gumbardella et al., 2005; Gastrans & Chang, 2010). We have investigated the problem of water-rock equilibrium for years as well (Shvartsev, 1991, 1995a, 1998, 2001a, 2008a; Shvartsev & Dutova, 2001; Alekseev et al., 2005; Shvartsev et al., 2007), specifically, the equilibrium of diverse (fresh, brine, acidic, basic, oil, thermal, etc.) waters, including sedimentary formation water as old as millions of years, with main minerals in rocks.

Calculation of real equilibria in the water-rock system gave unexpected results. For instance, the brines of the Siberian Platform with a mineralization of 300-600 g/l, whose age is hundreds of millions of years and which are virtually immobile, did not come into equilibrium with anorthite, diopside, nepheline, grossular, prehnite, albite, phlogopite, forsterite, cordierite, wollasronite, etc. At the same time, they are in equilibrium with clay minerals, calcite, gypsum, halite, quartz, muscovite, paragonite, analcime, occasionally with albite, enstatite, laumontite, bischofite, tetrahydrite, etc. (Bukaty, 1999; Shvartsev, 2000a).

All of these have allowed us to prove that the water-rock system is an unusual dissipative structure which develops in far from equilibrium and has a number of fundamental properties, among which ability to evolution without participation of live matter. The purpose of the given paper is to show that the water-rock system is capable to internal, independent of external factors, evolution.

2. Equilibrium-nonequilibrium State of the Water-rock System

Analysis of ample published evidence together with our own results prompts that *the water-rock system is equilibrium-nonequilibrium everywhere in the crust* at natural conditions. Aqueous solutions never reach equilibrium with some minerals in igneous rocks (see below) but are, however, in equilibrium with certain secondary phases. Therefore, water can dissolve some minerals and form ever new secondary products. There are neither thermodynamic nor kinetic constraints for this evolution of the system, which is thus internally

consistent and capable of developing spontaneously and continuously for a long geologic time to generate basically new mineral phases and geochemical types of water (Shvartsev, 1991, 2008b; Shvartsev, Ryzhenko, et al., 2007).

Rather than being a particular or a local phenomenon limited in time or in space, water-rock interaction turns out to be a global process of directed changes in which the products have their structure and composition dramatically different from the original ones. For instance, feldspar may transform into montmorillonite, a clay mineral with different chemical and physical properties.

In this transformation, hydrolysis of aluminosilicate minerals is the leading mechanism (Keller, 1957). The compositions of new phases are controlled by the geochemical environment, with different minerals resulting from different processes, namely: mostly clay minerals from supergene alteration; zeolite, chlorite, or serpentine from hydrothermal metasomatism; kaolinite, chlorite, hydromica, or albite from catagenesis, etc. Thus, dissolution in hydrolysis causes transformation of one solid phase into another, the new phase being formed either exactly in the place of the disappearing mineral and replicating its structure (pseudomorphism) or somewhere away from it.

Anyway, two components-water and rock-produce a third one. The conclusion that hydrolysis of aluminosilicates leads to structure loss and system disintegration is partly true, as a new mineral phase forms while some primary mineral is being destroyed; the new phase, together with waters of different chemistries, gives rise to a more complex new structure thus imparting different properties to the evolving system. The new structure involves a new geochemical environment arising as waters uptake chemical elements from rocks and is more complex as it contains additional structural elements that are better adapted to the specific ambient conditions and represent an energetically advantageous state of the system. Therefore, the system proceeds to a more complex stationary state which then transforms, in its turn, into a still more complex one, and so on. This happens, for example, when a weathering profile forms.

The origin of a secondary phase is almost as important as biological reproduction, though the two processes are dissimilar in many ways. The key point is that in both cases a mother system changes dramatically its evolution course as daughter systems spring up. The geochemical environment controls the composition of the nascent secondary phase but changes itself as the latter forms. The changed environment further brings about another phase and again becomes subject to its influence, etc. Being leached, a rock chemically affects its ambience by reducing elements bound in the secondary phase (e. g., Si and Al when kaolinite forms). Thus, the ever changing geochemical environment provides links between the evolving system and its products (Shvartsev, 2009).

Water-equilibrium secondary minerals arise during the whole period of water-rock interaction, not being restricted to local equilibrium. This process is continuous, regional-scale, and nonlinear, this being common to synergetic systems. As the process develops, one association of water-produced secondary minerals grades into another, which corresponds to the known principle of stepwise mineral formation in metallogenic, hydrothermal, metasomatic, supergene, or other processes.

The origin and growth of secondary mineral phases in full accord with the environment is a self-running process going from disintegrated parts to integrity, which according to Ashby (1962) is the key property of self-organizing systems.

Yet, there are other things involved in the issue. Ground waters turn out to be unable of reaching thermodynamic equilibrium with some minerals of igneous (or less often metamorphic) rocks, especially basalt, such as low-silica plagioclase, olivine, and pyroxenes or Ca, Mg, and Fe aluminosilicates. Let us try to understand why.

The anorthite hydrolysis reaction is

$$CaAl_2Si_2O_8 + 3H_2O + 2CO_2 = Al_2Si_2O_5(OH)_4 + Ca^{2+} + 2HCO_3^- \quad (1)$$

with the equilibrium constant (K_1), at 25°C, being

$$K_1 = [Ca^{2+}][HCO_3^-]^2/P^2_{CO2} = 10^{5,4} \quad (2)$$

To compare, calcite dissolves as

$$CaCO_3 + H_2O + CO_2 = Ca^{2+} + 2HCO_3^- \quad (3)$$

with the constant (K_2), likewise at 25°C,

$$K_2 = [Ca^{2+}][HCO_3^-]^2/P_{CO2} = 10^{-6,0} \quad (4)$$

Thus, the equilibrium constants in the dissolution reactions for both minerals depend on the same components but, compared to calcite, the anorthite equilibrium requires (i) an eleven orders of magnitude greater constant and (ii) a squared partial pressure of CO_2. For this reason, the quotient in the reaction for anorthite is always smaller than that for calcite, even though the contents of elements in the solution are the same. One can compare the two quotients in quite a simple diagram for different groundwater types, as the constants in both reactions are a function of the same components. The dot product $[Ca^{2+}][HCO^-_3]^2$ can be estimated for each reaction at a certain value of P_{CO2}: it is $10^{-0.6}$ for K_1 and $10^{-9.0}$ for K_2 at $P_{CO2}= 10^{-3}$; $10^{1.4}$ and 10^{-8}, respectively, at $P_{CO2}= 10^{-2}$, etc. Thus, the saturation degrees of water with respect to two minerals (anorthite and calcite) are comparable in the same coordinates (Shvartsev, 1995b).

The estimates of $[Ca^{2+}][HCO_3^-]^2$ as a function of groundwater salinity (total dissolved solids, TDS) at different P_{CO2} are shown in Figure 1. See that fresh groundwater remains unsaturated with respect to calcite unless TDS becomes higher than 0.6 g/l. All saline waters and brines show equilibrium with calcite but calcite-laden waters are never anorthite saturated.

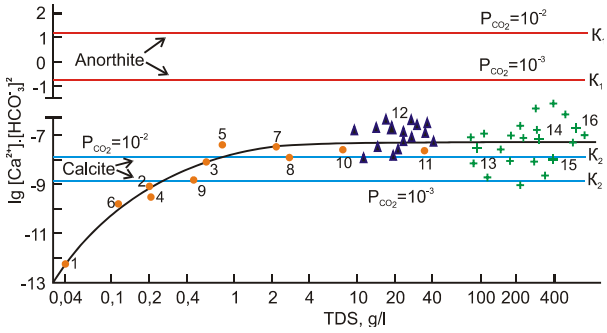

Figure 1. Saturation of groundwaters with respect to calcite and anorthite vs. TDS

K_1-K_2 are equilibrium constants (see text). Data points represent average compositions of waters from different regions and zones, namely: black circles *(1-10)* are for Guinea and Côte-d'Ivoir*(1)*, Siberian tundra *(2)*, Senegal *(3)*, zone of temperate climate, generally *(4)*, forest zone of Southern Siberia (5), Finland *(6)*, Central Asian steppes *(7)*, steppes of the USA *(8)*, zone of supergene alteration, generally *(9)*, steppes of the Donets Basin *(10)*; open circle is for ocean *(11)*; black triangles *(12)* correspond to waters in petroleum reservoirs of West Siberia; crosses *(13-16)* mark weak *(13)*, strong *(14)*, very strong *(15)*, and oversaturated *(16)* brines of East Siberia.

At TDS exceeding 1.0 g/l, the degree of water-anorthite equilibrium remains the same be the salinity 4 or 400 g/l. Moreover, saturation is impossible at normal conditions because calcite that binds Ca^{2+} and CO_3^{2-} acts as a chemical barrier on the way to equilibrium with anorthite. Equilibrium with anorthite is possible only at high $[Ca^{2+}]$ $[HCO_3^-]^2$ but it is never high because of calcite formation. Therefore, Ca carbonates prevent natural water from arriving at equilibrium with Ca-aluminosilicates.

Consider further an example of forsterite and magnesite dissolution. The reaction for forsterite is

$$Mg_2SiO_4+4H_2O+4CO_2 = 2Mg^{2+}+4HCO_3^-+H_4SiO_4 \quad (5)$$

with the constant at 25°C

$$K_3= [Mg^{2+}]^2[HCO_3^-]^4[H_4SiO_4]/P^4_{CO2} = 10^{-2.48} \quad (6)$$

or

$$[Mg^{2+}][HCO_3^-]^2[H_4SiO_4]^{0.5}/P^2_{CO2} =10^{-1.24} \quad (7)$$

For magnesite it is

$$MgCO_3+H_2O+CO_2 = Mg^{2+}+2HCO_3^- \quad (8)$$

and the constant at 25°C is

$$K_4 = [Mg^{2+}][HCO_3^-]^2/P_{CO2} = 10^{-5.52} \quad (9)$$

As in the case of calcite and anorthite, the equilibrium constants for both minerals likewise are controlled by the same components, and again K_3 is much greater than K_4 (four orders of magnitude) and the CO_2 partial pressure is squared in the former reaction. Therefore, the waters saturated with respect to magnesite never reach forsterite saturation. The latter is impossible in the crust because magnesite binds Mg^{2+} and CO_3^{2-} and thus becomes a barrier to water-forsterite equilibrium (Figure 2). Both figures show calcite (Figure 1) or magnesite (Figure 2) impeding equilibrium of groundwaters with magmatic minerals (anorthite and forsterite, respectively).

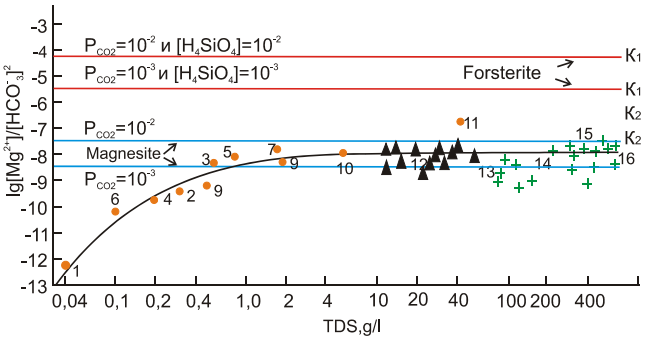

Figure 2. Saturation of groundwaters with respect to magnesite and forsterite vs. TDS

(Legend same as in Figure 1)

Therefore, equilibrium of groundwater with some minerals in igneous rocks is impossible because the leached elements give rise to secondary phases which bind the elements and thus impede the equilibrium. That is why groundwater remains not saturated with respect to these minerals for the whole time of interaction. There are hundreds of such minerals: oxides, hydroxides, silicates, aluminosilicates (clay minerals), carbonates, zeolite, chlorite, sulfates, phosphates, chlorides, etc. The most important Ca, Mg, and Fe minerals of this kind are listed in Table 1.

Table 1. Main minerals of basalt that are dissolved and generated in water-rock system

Element	Minerals continuously dissolved by water	Minerals continuously formed by water		
		Name	Chemical formula	lg dissolution constants at 25°C
Ca	anorthite, bitownite labradorite hedenbergite, diopside, etc.	calcite,	$CaCO_3$	-8.48
		dolomite,	$CaMg(CO_3)_2$	-17.1
		gypsum,	$CaSO_4 \cdot 2H_2O$	-4.58
		fluorite,	CaF_2	-10.6
		Ca-montmorillonite,	$Ca_{0,17}Al_{2,33}Si_{3,67}O_{10}(OH)_2$	-89.3
		lomontite	$CaAl_2Si_4O_{12} \cdot 4H_2O$	-98.9
Mg	forsterite, enstatite, etc.	magnesite,	$Mg\ CO_3$	-7.46
		dolomite,	$CaMg(CO_3)_2$	-17.1
		Mg-montmorillonite,	$Mg_{0,17}Al_{2,33}Si_{2,67}O_{10}(OH)_2$	-99.5
		talc, chlorite	$Mg_3Si_4O_{10}(OH)_2$	-60.7
			$Mg_6Si_4O_{10}(OH)_8$	-22.4
Fe	fayalite, ferrosilite, etc.	goetite,	FeOOH	-32.8
		hydroxide,	$Fe(OH)_3$	-36.0
		hematite,	Fe_2O_3	-83.6
		siderite,	$FeCO_3$	-10.9
		ferroglaucophane,	$Fe_3Al_2Si_8O_{22}(OH)_2$	-16.6
		daphnite	$Fe_5Al_2Si_3O_{10}(OH)_8$	-181
Al	anorthite, bitownite labradorite, diopside, etc.	gibbsite,	$Al(OH)_3$	-32.6
		kaolinite,	$Al_2Si_2O_5(OH)_4$	-79.4
		illite	$K_{0.38}Al_{2.38}Si_{3.62}O_{10}(OH)_2$	-108.7

The equilibrium-nonequilibrium state of the water-rock system is not local but general and ubiquitous. Water, wherever it exists, always dissolves some minerals and generates others. This intrinsically inconsistent state of the system never disappears with time but persists as long as there are rocks and waters. This property is indispensable for the existence of the water-rock system itself and is thus crucial to the evolution of inorganic matter.

Note that there are two evolution patterns in the water-rock system: one in the liquid and the other in solid components. Formation of a secondary mineral requires time for necessary elements to accumulate in the solution (e.g., Si and Al for kaolinite), which is a smooth and continuous process. Formation of minerals is, on the contrary, discrete, and each takes its specific time. Thus, the liquid and solid phases (water and rock) within the same system evolve in different ways: smoothly (continuously) in the former and discontinuously in the latter case.

The permanent nonequilibrium in the water-rock system causes a large-scale process in the upper crust in which water mobilizes chemical elements, transforms rocks into different rocks, and gives rise to new chemical types of water, new mineral phases, and new water-produced mineral associations. This process involving redistribution of chemical elements and formation of secondary minerals with quite different compositions (ores among them), eventually causes global changes to the mineral matter and water out of which our planet had originated, i.e., changes of Earth's crust as a whole (Shvartsev et al., 2007). Therefore, *water and rocks make up a unique system capable of long geological evolution*, even without biotic agents.

It is important that the idea of evolution in inorganic matter is consistent with the theory of synergetics (Prigogine & Stengers, 1984). Unlike cybernetics, nonequilibrium in synergetics makes basis for structure formation and pushes forward the evolution of the system rather than bringing it to collapse. This driving force of the system evolution transforms the irreversible energy (and material) fluxes that arise while evolving open systems are moving toward equilibrium.

Furthermore, they are the nonequilibrium systems that become nuclei of self-organization when new dissipative structures form in open nonlinear complex systems at the beginning of transition from chaos to order (Nicolis & Prigogine, 1977). Self-organization is a well-known phenomenon in the organic life and occurs also in nonliving matter (Shvartsev, 1995b, 2000b, 2001b, 2005, 2007, 2008b, 2009).

3. Internal Evolution of the Water-rock System

The evolution of geological systems has been traditionally assumed to have external controls, such as Earth's cooling, continental growth, reducing extent of tectonic activity, increasing oxidation, air composition changes, biotic effects, etc. (Garrels & Mackenzie, 1971, Ronov, 1980, Yanshin, 1993).

This is not nearly so yet. The water-rock system offers a prominent example of evolution that runs at any temperature or pressure, rock, water, or atmospheric compositions, magnetic field, size and configuration of continents, magmatic activity, etc. Everywhere and always, whichever be the forcing from outside, water dissolves minerals (more or less rapidly), changes the compositions of fluids producing new chemical types of waters, and gives rise to various secondary minerals and mineral assemblages.

External factors can never stop water-rock interaction, though they may influence its rate, intensity, duration, extent, or environment. No force in nature can ever forbid chemical reactions in the water-rock system and prevent water from dissolving primary minerals or from producing secondary phases. The reactions cannot stop unless all water escapes from rock but in this case, however, the system itself will disappear, as well as interaction within it.

This ability of the water-rock system to run by itself prompts the presence of some internal driving mechanisms that must maintain its integrity and isolation, of course on condition of matter and energy supply (the system is stationary and open) (Shvartsev, 2008b). These intrinsic mechanisms allow the system to develop following the thermodynamic laws and to control its own evolution paths and the rates, sequence, and stages of the formation of new products and their compositions, as well as the proportions of elements in the liquid and solid phases, substitutions, etc.

The very fact of running an inherently directed evolution depending on interaction within itself makes the water-rock system so particular and similar to a biological one. The specificity of its evolution (in nonliving matter) is due to geologic-scale duration, continuity of interaction, and impossibility for water to reach equilibrium with all primary minerals.

Geoscientists are well familiar with the results of this evolution, though the links with its intrinsic mechanisms remain unrecognized. The evident results are groundwaters of numerous chemical types, secondary minerals, ore

deposits, diverse formations (such as laterite, clay, loess, redbed, salt-bearing, hydrothermal, ore-bearing, pelagic, flysch, or other rocks), and – on a larger scale – the sedimentary, metamorphic, granite, etc. layers and, perhaps, the crust as a whole. The longer the water-rock interaction, the greater the amount and diversity of secondary products.

Each stage of rock interaction with water produces its own mineral association which gradually covers the geological space, becomes predominant, and defines the aspect of the environment (Shvartsev et al., 2007; Shvartsev, 2007, 2008b).

Let us look deeper into the mechanisms that sustain the internal evolution of the water-rock system. As it was noted above, the nonequilibrium of water with magmatic minerals is the principal driving force. Due to this nonequilibrium, the primary minerals are continuously leached and all chemical elements present in the rocks accumulate in the solution in the beginning of interaction. The rates of dissolution being different in different minerals (Alekseev et al., 2005; Kerrick et al., 1991) the relative percentages of elements always depart from those in the original rock.

While magmatic minerals are continuously being dissolved, the concentrations of elements in the solution are growing and saturation with Fe and Al hydroxides (Table 1) occurs at the initial interaction stage, according to the law of mass action. As the hydroxides precipitate, a part of elements passes from the solution to sediment, thus disturbing the original element partitioning. Iron and aluminum fall out the earliest while all others (including Si, Ca, Mg, etc.) keep accumulating. If the interaction continues, dissolved Si increases and, after some time, the system arrives at equilibrium with formation of kaolinite:

$$2Al^{3+}+2H_4SiO_4+6OH^- = Al_2Si_2O_5(OH)_4+5H_2O \quad (10)$$

the constant at 25°C being

$$K = 1/[Al^{3+}]^2[H_4SiO_4]^2[OH^-)^6 = 10^{79.4} \quad (11)$$

In this case the solution loses also Si besides Fe and Al, though all other elements preserve their ability to concentrate in water. Then there appears another feature of difference: Al is bound in gibbsite or böhmite prior to kaolinite saturation but becomes also bound in kaolinite afterwards. Thus, the setting is growing ever more complicated. The question arises which Al minerals will form in this case?

In order to answer the question, one has to compare the composition of kaolinite with those of the leached primary minerals. Namely, Si in igneous rocks is 3.7 times as high as Al, whereas kaolinite contains equal atomic and weight percentages of Al and Si. Therefore, once kaolinite precipitates, the solution becomes depleted more in Al than in Si, hence, kaolinite can form if water contains enough Si, otherwise gibbsite or böhmite will form.

Kaolinite binds all Al coming to the solution but it cannot bind all Si whose input is on average 3.7 times as high as Al, so dissolved Si increases on (Shvartsev et al., 2007; Shvartsev, 2008b). Thus, not every mineral that forms in the water-rock system can bind the whole amount of elements released from igneous rocks. This fact allows some important insights into the mechanisms of internal evolution in the water-rock system.

Meteoric water that falls on igneous rocks (e.g., basalt) dissolves all the constituent minerals. Although there is difference in dissolution kinetics, all chemical elements first enter the solution in approximately the same proportions as they existed originally in the rock. Anyway, the Si input is much greater than Al, though gibbsite forms before kaolinite because gibbsite precipitation begins at a lower activity of aluminum. For instance, at pH = 5.0 groundwater becomes saturated with respect to gibbsite as

$$Al^{3+}+3OH^- = Al(OH)_3 \quad (12)$$

already when the activity of $[Al^{3+}]$ is as low as $10^{-6.2}$, which is achieved quite soon for the interaction time T_1 (Figure 3). Inasmuch as water keeps interacting with the igneous rock, Si unlike Al progressively increases in the solution, which eventually brings the system to equilibrium with kaolinite according to reaction (10) when the activity of H_4SiO_4 reaches $10^{-4.7}$, at pH = 5.0.

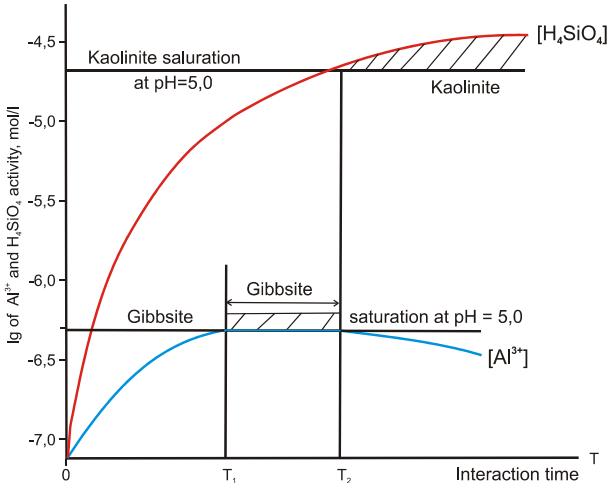

Figure 3. Deposition of gibbsite and kaolinite vs. time of interaction between groundwater and magmaticaluminosilicate minerals

Kaolinite thus precipitates later than gibbsite, after longer water-rock interaction for the time T_2. Since kaolinite does not bind all Si coming to the solution (see above), the activity of Al^{3+} cannot increase but rather decreases at the same pH, according to the constant of (11), which breaks the equilibrium with gibbsite and the latter, being unable to precipitate, gives place to kaolinite.

Therefore, *gibbsite and kaolinite are competing minerals: they contend for possessing Al supplied to the water from the leached igneous rock*. Gibbsite leads in the beginning of interaction but then lags behind kaolinite while the latter impedes further precipitation of gibbsite. The proof is evident in weathering profiles where gibbsite and kaolinite are always separated and kaolinite lies deeper than gibbsite because its deposition requires a longer interaction time (Keller, 1957; Ollier, 1969).

Interaction between fresh water and magmatic aluminosilicates produces secondary minerals in the following succession: no minerals form in the very beginning at $T_x<T_1$; at $T_1>T_x<T_2$ precipitation begins with gibbsite; kaolinite forms at $T_x>T_2$; then all other minerals appear in their order (Figure 4). Of course, the process in nature is still more complicated because pH actually changes (most often grows), and for this reason gibbsite neither forms at $T_x>T_2$ nor dissolves. What is important anyway, is that the nonliving water-rock system evolves being driven by its intrinsic mechanisms. Furthermore, *the internal evolution in the water-rock system complies with a single trend of dissolving aluminosilicate minerals and precipitation of ever later phases* (Figure 4).

The explanation of this postulate is as follows. When arriving at equilibrium, say, with calcite (point E in Figure 4) on interaction with the igneous rock it falls into, water will form calcite rather than any other mineral; as elements accumulate progressively in the solution, the latter moves forward to equilibrium with gypsum (point F) rather than back to the earlier equilibrium point of montmorillonite (D).

Thus, as the examples of gibbsite and kaolinite have demonstrated, *a water solution experiences chemical differentiation as partitioning of elements in newly formed minerals changes relative to that in the leached rock, this differentiation being an important indicator of internal evolution in the water-rock system*.

So, water continuously dissolves minerals in the rock it interacts with, and thereby changes its own composition and relative percentages of dissolved elements, also changes the environment, and creates conditions for the appearance of ever new mineral phases. This is the essence of internal evolution in the water-rock system, which lasts for thousands or millions of years.

Note again that this evolution gives rise to quite new minerals basically different from the leached ones (anorthite, labradorite, fayalite, forsterite, etc.), including those the Earth originally lacked, such as gibbsite, kaolinite, montmorillonite, calcite, magnesite, illite, lomontite, etc. (Table 1). This ability of the water-rock system is really striking.

In addition to new minerals, there appear waters of new geochemical types: each secondary mineral forms in water with its composition different from the previous one. For instance, gibbsite, kaolinite, and calcite precipitate from compositionally different waters. Following V. I. Vernadsky (2003), each of these water types

should be interpreted as a separate water mineral. Therefore, each solid secondary mineral must be associated with a certain liquid mineral, or with a certain chemical type of water. Thus, there is a profound genetic link and an intrinsic compositional unity of secondary minerals, waters, and their environment, which is indispensable for the very existence of all these materials. Altogether, they make up a single genetic unit which we suggest to call a *water-mineral formation*. This is *a genetically related association of mineral, organic, and dissolved compounds which are in equilibrium with the parent environment and result from the internal evolution of the water-rock system* (Shvartsev et al., 2007).

Each unit of this kind records a certain evolution stage of the system, which, like a smoothly running machine, produces a formation of a certain composition, for a geologically long time, e.g., laterite at one stage, kaolinite at another stage, and so on. Each new water-mineral formation is a qualitatively more complex system consisting of additional structural elements. Being perfectly ordered and adapted to the environment, they propagate from the local domain of their nucleation and cover ever new geological spaces. This is, for example, laterite in tropic zones of supergene alteration; clay weathering products in zones of temperate climate; iron-manganese concretions in seas and oceans; carbonate calcrete in steppes; redbeds, etc., or thick chloritization and illitization zones in sedimentary basins, or zones of hydrothermal and ore-related metasomatism.

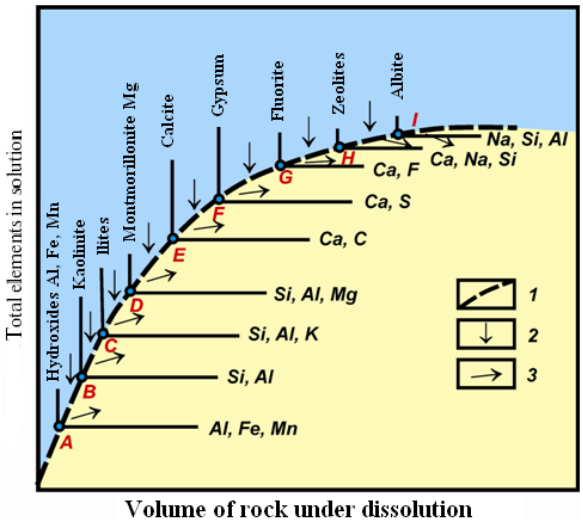

Figure 4. Successive precipitation of secondary minerals during evolution of water-rock system *(1)* new secondary phases: onset of precipitation, *(2)* zones of possible water input, and *(3)* possible cessation of water-rock interaction

Nucleation and propagation of a secondary mineral phase is a typical example of initiation of dissipative structures (Prigogine &Stengers, 1984). Not only the solid becomes more complex, but also its structure does, which is especially important. Progressive salinity increase, nonuniform distribution of elements, growing complexity of compounds and ion pairs, increasing number of minerals which the solution is in equilibrium with: they are all features of development and increasing diversity of structural bonds.

Thus, the water-rock system evolving in a domain far from equilibrium is a source of ordering, growing complexity, and formation of new more highly organized and intricate water-mineral systems, with interaction mechanisms more complex than those that form in equilibrium settings. That is why many geological processes that would seem degrading are not such actually. Chemical weathering, for instance, is commonly assumed to be degradation (disintegration) as it breaks up and thus simplifies structural bonds between minerals and chemical elements. Weathering is often compared with breakup, or at least transformation, of lattice overlooking the fact that it yields more complex new products, e.g., anorthite is weathered into montmorillonite with its structure much more complex than in the primary mineral.

Deposition of a secondary mineral is not just the appearance of a new solid phase, which is important by itself, but rather the origin of a new system “water-secondary mineral”. Moreover, as a mineral precipitates from water, the latter changes its composition and structure in its turn. In terms of synergetics, the onset of precipitation is the bifurcation point where the whole original system (especially water) changes. This happens at the molecular

level as molecules (ions) in water continuously create new structures (new water minerals according to Vernadsky, or new chemical types of water in our terminology).

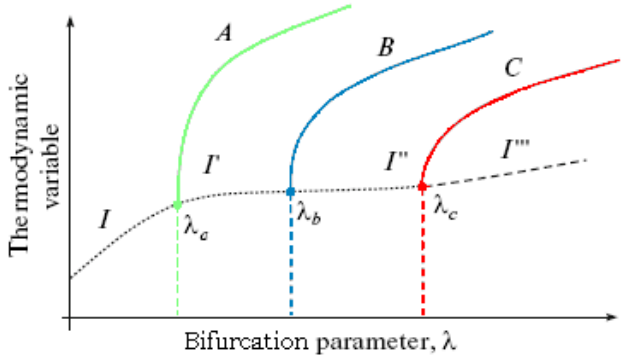

Figure 5. Evolution of a water-rock system in terms of synergetics: initial evolution (I) arrives at unstable state at critical points λ_a, λ_b λ_c (I^I, I^{II}, I^{III}) and changes trajectory at points A, B, and C (see text for explanation)

Once the solid phase begins nucleating, the water-rock system takes a different evolution path (trajectory) which ends in the formation of a secondary mineral, a new structure, and a new water composition. This is how one mineral successively gives way to others, which is well known as multistage mineral formation and successive substitutions of water types.

The process is infinite theoretically but finite in nature, at least because sooner or later water leaves the rock and the system disappears. The time when it happens depends on external factors (geology, geomorphology, climate, etc.), i.e., the environment can control the lifetime of the system but not its evolution trends.

Viewed in terms of Prigogine's theory (Prigogine, Stengers, 1984), the water-rock system (Figure 5) evolves in time as water chemistry and interaction patterns change though the primary rock remains the same. The slow but directed change in water composition leads to successive precipitation of minerals at the bifurcation points (gibbsite at A, kaolinite at B, montmorillonite at C, etc.), water chemistry being the govern parameter and equilibrium constant being the thermodynamic variable. Figure 5 images the succession in which secondary minerals actually form in nature (Figure 4).

Therefore, while interacting with igneous rock, water produces a new medium dramatically different from the previous one. First, this process shows up in water chemistry changes and appearance of new minerals dissimilar with the primary aluminosilicates: feldspar, olivine, and hornblend give way to kaolinite, montmorillonite, calcite, chlorite, gibbsite, goetite, etc. Later there come bacteria and new landscapes arise, to eventually create a new world (Shvartsev, 2010).

It is important that water forms the new world according to its composition, structure, and environment, and this world is thus *generated by water, in full harmony with the laws of its internal changes and its internal energy*. The water itself and the related chemical environment change under the effect of elements coming from the leached rock, and the structure and composition of the diverse new mineral compounds are defined by *water solutions*.

4. Conclusions

Thus, we have established for the first time the presence of internal, independent of external factors, evolution in lifeless dissipative structure to which the water-rock system belongs. According to Prigogine and Stengers «One of the most interesting aspects of dissipative structures is their coherence. The system behaves as a whole, as if it were the site of long-range forces. In spite of the fact that interactions among molecules do not exceed a range of some 10^{-8} cm, the system is structured as though each molecule were "informed" about the overall state of the system» (Prigogine & Stengers, 1984).

Coherent relations are especially characteristic for solutions. Therefore water, as the main solution of our planet, defines a direction of internal, so all of the global evolution.

Acknowledgements

This report is supported by grant Russian Foundation for Basic Research № 11-05-9311.

References

Alekseev, V. A., Ryzhenko, B. N., Shvartsev, S. L., Zverev, V. P., Bukaty, M. B., Mironenko, M. V., … Chudaev, O. V. (2005). *Geologic evolution and self-organization of the water-rock system.Book 1. The water-rock system in the earth's crust: interaction, kinetics, equilibrium and modeling*. Novosibirsk: SB RAS Publishers (in Russian).

Appelo, C. A. J., & Postma, D. (2005). Geochemistry, Groundwater and Pollution (2nd ed.). Taylor & Francis. http://dx.doi.org/10.1201/9781439833544

Arnórsson, S., Gunnarsson, I., Stefánsson, A., Andrésdóttir, A., & Sveinbjőrnsdóttir, A. E. (2002). Major element chemistry of surface- and ground waters in basaltic terrain, N-Iceland.: I. primary mineral saturation. *Geochimica et Cosmochimica Acta*, *66*(23), 4015-4046. http://dx.doi.org/10.1016/S0016-7037(02)00991-2

Ashby, W. R. (1962). *Principles of Self-Organization*. Oxford. Pergamon Press, 314-343.

Bukaty, M. B. (1999). Equilibrium between underground brines of the Tunguska basin and minerals of evaporate and terrigenousfacies. *Russian Geology and Geophysics*, *40*(5), 732-746.

Capuano, R. M., & Cole, D. R. (1982). Fluid – mineral equilibria in a hydrothermal system, Roosevelt hot springs, Utah. *Geochimica et Cosmochimica Acta, 8*, 1353-1364. http://dx.doi.org/10.1016/0016-7037(82)90271-X

Drever, J. T. (1988). *The geochemistry of natural waters* (2nd ed.). New Jersey: Prentice Hall

Garrels, R. M., & Christ, C. L. (1965). *Solutions, minerals and equilibrium*. N. Y.: Harper and Row

Garrels, R. M., & Mackenzie, F. T. (1971). *Evolution of sedimentary rocks*. N. Y.: Norton.

Gastrans, D., Chang, H. K., & Hutcheon, I. (2010). Groundwater geochemical evolution in the northern portion of the Guarani Aquifer System (Brazil) and its relationship to diagenetic features. *Applied Geochemistry, 25*(1), 16-33.

Gemici, U., Tarcan, G., Colak, M., & Helvaci, C. (2004). Hydrogeochemical and hydrogeological investigations of thermal waters in the Emet area (Kütahiga, Turkey). *Applied Geochemistry, 19*(1), 105-118. http://dx.doi.org/10.1016/S0883-2927(03)00112-4

Gislason, S. R., & Arnorsson, S. (1993). Dissolution of primary basaltic minerals in natural waters: saturation state and kinetics. *Chemical Geology*, *105*, 117-135. http://dx.doi.org/10.1016/0009-2541(93)90122-Y

Gumbardella, B., Marini, L., & Baneschi, I. (2005). Dissolved potassium in the shallow groundwaters circulating in the volcanic rocks of central-southern Italy. *Applied Geochemistry*, *20*(5), 875-898. http://dx.doi.org/10.1016/j.apgeochem.2004.12.001

Helgeson, H. C. (1968). Evolution of irreversible reactions in geochemical processes involving minerals and aqueous solutions. *Geochimicaet Cosmochimica Acta*, *32*(8), 853-877.

Keller, W. D. (1957). *The principles of geochemical weathering.* Columbia, Missouri: Lucas Brothers Publ.

Kerrick, D. M., Lasaga, A. C., & Raeburn, S. P. (1991). Kinetics of heterogeneous reactions. *Reviews in Mineralogy*, *26*, 583-671.

Mohamed, B. B., Bertrand, F., & Benoit, M. (1993). Diageneticalbitization of K-feldspar and plagioclase in sandstone reservoirs; thermodynamic and kinetic modeling. *Journal of Sedimentary Research, 8*, 1100-1109. http://dx.doi.org/10.1306/D4267CB2-2B26-11D7-8648000102C1865D

Nesbitt, H. W. (1985). A chemical equilibrium model for the Illinois Basin formation water. *American Journal of Science, 285*(5), 436-458. http://dx.doi.org/10.2475/ajs.285.5.436

Nicolis, G., & Prigogine, I. (1977). *Self-organization in nonequilibrium systems*. N. Y.: John Wiley and Sons.

Ollier, C. D. (1969). *Weathering.* Edinburgh: Oliver and Boyd.

Pawar, N. J. (1993). Geochemistry of carbonate precipitation from the ground waters in basaltic aquifers: An equilibrium thermodynamic approach. *Journal of the Geological Society of India, 41*(2), 119-131.

Prigogine, I., & Stengers, I. (1984). *Order out of chaos: man's new dialogue with nature*. Toronto, New York, London, Sydney: Bantam Books.

Reed, M., & Spycher, N. (1984). Calculation of pH and mineral equilibria in hydrothermal waters with application to geothermometry and studies of boiling and dilution. *Geochimica et Cosmochimica Acta, 48*(7), 1479-1492. http://dx.doi.org/10.1016/0016-7037(84)90404-6

Rogers, R. J. (1989). Geochemical comparison of groundwater in areas of New England, N. Y., and Pennsylvania. *Ground water*, *27*(5), 690-712.

Ronov, A. B. (1980). *Sedimentary cover of the earth*. M.: Nauka (in Russian).

Shvartsev, S. L. (1991). Interaction of water with aluminosilicate rocks: A review. *Soviet Geology and Geophysics*, *32*(12), 13-37.

Shvartsev, S. L. (1995b). The problem of self-organization of a water-rock geological system. *Russian Geology and Geophysics*, *36*(4), 17-24.

Shvartsev, S. L. (1995a). Equilibrium-nonequilibrium state of the water-rock system. *Proceidings of the 8th International Symposium on Water-Rock Interaction.* Rotterdam: Balkema.751-754.

Shvartsev, S. L. (1998). *Hydrogeochemistry of the hypergenesis zone* (2nd ed.). Moscow: Nedra (in Russian).

Shvartsev, S. L. (2000b). Equilibrium-nonequilibrium state of the water-rock system and its self-organization. *The International Journal of Hydrology Science and Technology, 1*(4), 171-180.

Shvartsev, S. L. (2000a). The chemical composition and strontium isotopes of brines from the Tunguska Basin: Implications for their formation. *Geochemistry International*, *38*(11), 1070-1083.

Shvartsev, S. L. (2001b). Evolution and self-organization of the water-rock system. *Proceidings of the 10th International Symposium on Water-Rock Interaction.* Lisse: Balkema, 2, 201-204.

Shvartsev, S. L. (2001a). The water-rock system synergy. *Earth Science Frontiers*, *1*, 36-46.

Shvartsev, S. L. (2005). Progressive self-organization in the water-rock system (in Russian). *Izv. Section Science of Earth RAEN, 13*, 139-152.

Shvartsev, S. L. (2007). Progressively self-organizing abiogenic dissipative structures in the Earth's geological history (in Russian). *Litosfera*, *1*, 65-89.

Shvartsev, S. L. (2008b). Basic Interaction Mechanisms in the Water-Rock System and its Internal Geological Evolution (in Russian). *Litosfera*, *6*, 3-24.

Shvartsev, S. L. (2008a). Geochemistry of fresh groundwater in the main landscape zones of the earth. *Geochemistry Intern*ational, 46(13), 1285-1398. http://dx.doi.org/10.1134/S0016702908130016

Shvartsev, S. L. (2009). Self-organizing abiogenic dissipative structures in the geologic history of the earth. *Earth Science Frontiers, 16*(6), 257-275. http://dx.doi.org/10.1016/S1872-5791(08)60114-1

Shvartsev, S. L. (2010). Where did global evolution begin? *Herald of the Russian Academy of Sciences*, *80*(2), 173-182. http://dx.doi.org/10.1134/S1019331610020097

Shvartsev, S. L., & Dutova, E. M. (2001). Hydrogeochemistry and mobilization of gold in the hypergenesis zone (Kuznetsk Alatau, Russia). *Geology of Ore Deposits*, *43*(3), 224-233.

Shvartsev, S. L., Ryzhenko, B. N., Alekseev, V. A., Dutova, E. M.,Kondratjeva, I. A., Kopilova, Yu. G., & Lepokurova, O. E. (2007). *Geologic evolution and self-organization of the water-rock system. Book 2, The water-rock system in the hypergenesis zone*. Novosibirsk: SB RAS Publishers (in Russian).

Vernadsky, V. I. (2003). *History of Natural Waters*. Moscow: Nauka (in Russian).

Yanshin, A. L. (1993). Evolution of geological processes: Origin of the problem. *Evolution of Geological Processes in the Earth's History*. Moscow: Nauka (in Russian).

Zamana, L. V. (2000). Calcium mineral equilibria of nitrogen-bearing springs of the rift zone of Lake Baikal. *Geochemistry International, 38*(11), 1059-1064.

Earth Science Research; Vol. 1, No. 2; 2012
ISSN 1927-0542 E-ISSN 1927-0550
Published by Canadian Center of Science and Education

Analysis of Physical Parameters of Limestone Deposits in Ewekoro Formation, Southwestern Nigeria

Oluwaseun T. Olurin[1], B. S. Badmus[1], O. D. Akinyemi[1], J. A. Olowofela[1], V. C. Ozebo[1] & S. A. Ganiyu[1]

[1] Department of Physics, University of Agriculture, Abeokuta, Ogun State, Nigeria

Correspondence: Oluwaseun T. Olurin, Department of Physics, University of Agriculture, Abeokuta, P.M.B 2240, Ogun State, Nigeria. Tel: 234-806-660-0703. E-mail: olurin@physics.unaab.edu.ng & stolurin@yahoo.com

Received: March 6, 2012 Accepted: March 21, 2012 Online Published: June 19, 2012

doi:10.5539/esr.v1n2p117 URL: http://dx.doi.org/10.5539/esr.v1n2p117

Abstract

Physical parameters of limestone in Ewekoro formation, south-western Nigeria were determined via direct laboratory method. The permeability and bulk density values obtained range from 1.47 to 7.99 ms^{-1} and 1.26 to 1.90 gcm^{-3} respectively. The resistivity values of the limestone samples collected from the study site were obtained by laboratory direct method and the result revealed that the resistivity values fall within 6 and 171 $k\Omega m$. These values correlate favorably with the results obtained from electrical resistivity method of geophysical prospecting of the study area. The two approaches showed a good degree of correlation in the resistivity value of the limestone and their varying qualities. This research work further showed the occurrence of vast deposit of limestone, which can be of economic importance in mining and for industrial purposes.

Keyword: bulk density, limestone, permeability and resistivity

1. Introduction

Mineral exploration work was carried out to analyse the physical parameters of limestone in Ewekoro formation. This geophysical exploration was carried out to map the limestone deposit of Ewekoro formation, southwestern Nigeria using direct laboratory method via direct current power supply. This direct method approach is to complement and compare the study carried out by Badmus and Ayolabi (2005) where limestone of Ewekoro formation was delineated using Schlumberger electrode array to map both vertical and lateral extents of the deposit (Figure 1). This approach would also confirm the accuracy of electrical resistivity method of geophysical prospecting for mineral exploration as well as characterizing the various litho-facies of Ewekoro limestone (Badmus & Ayolabi, 2005). Badmus et al. (2006) carried out geoelectric evaluation of mica schist deposit of Area J4, southwestern, Nigeria using the direct laboratory method to characterize the mica schist into different degrees of purity for both economic and commercial purposes. Several studies have also been carried out to evaluate the distribution of limestone deposits at Ewekoro quarry. Adegoke et al. (1970) subdivided the limestone deposits into three units. Omatosola and Adegoke (1981) then proposed a fourth unit. These units in stratigraphic order are: sandy biomcrosparite (bottom), shelly biomcrite, algal biosparite and red phosphate biomcrite (top). The sandy biomcrosparite forms the base of the formation and consists of a light brown sandy limestone with very few bioclassic fragments. Stratification is evident and is accentuated by variations in the quantity and grain size of the interbedded quartz and glauconite. The shelly biomcrite consists of pure limestone of about 4.5 to 6.0 m and constitute the bulk of the Ewekoro formation in the quarry. Limestone has abundant macrofossil content particularly gastropods, pelecypods, echinoderms and corals. The algal biosparite limestone overlies the shelly biomcrite unit. Resistivity is the only electrical characteristic of geoelectric property. Most rock forming minerals have conductivities spreading over a wide range and are semiconductors. However, these rocks are seen as insulators in their dried form. The amount of moisture contained in the rock depends on the structure especially the amount of pore space and cracks. Rocks and sediments contain space between grains (pore space) in fractures or in dissolved cavities (limestone), which may be filled with water. Isolating the drain from the atmosphere can lead to an increase of the partial pressure of carbon dioxide within the system and to an increase of the dissolution rate of calcite. More importantly, it also minimizes the potential for oxidation of Fe^{2+} (to Fe^{3+}) and the risk of precipitation of $Fe(OH)_3$ and of other related solids in the drain. Formation of these precipitates can result in premature drain failure due to limestone armouring, which can significantly reduce the

rate of calcite dissolution and affect the flow. The presence of Al^{3+} within the influent is also of concern; $Al(OH)_3$ is formed at a pH between 4 and 5 and it tends to accumulate in pores, thus potentially clogging the voids and consequently reducing the material hydraulic conductivity Poirier and Aubertin (2011). The porosity and chemical content of the water filling the pore spaces are more important in governing resistivity than conductivity of the mineral grains of which the rock is composed. The resistivity curves are deflected towards high levels with positive separation. The glauconite is prevailing in these intervals. The limestone of this formation is dolomitic, sandy and shaly in parts. In some limestone intervals, the glauconite is present. The marl is light gray, silty, calcareous and grading to limestone Ghorab (2010). Limestone is a raw material for the manufacturing of cement, asphalt filler, ceramics, flux in glass making, fertilizer filler, explosives to mention just a few. Jones and Hockey (1964) revealed Ewekoro limestone and the overlying Akinbo shale to be lateral equivalents of the Imo formation of eastern Nigeria. Other authors such as Omatsola and Adegoke (1991) and Oladeji (1992) have investigated the stratigraphy and depositional characteristics of limestone and clay/shale deposits in southwestern Nigeria. The West African Portland Cement Company also conducted extensive geological survey and commercial appraisal of Ewekoro limestone and shale beds for commercial cement production.

2. Study Area

The study area lies within Ogun State, which is bounded in the west by Benin Republic, in the south by Lagos State, in the north by Oyo and Osun States, and in the east by Ondo State. It occupies a total area of. Ewekoro is the host to West African Portland cement quarry and lies between longitude 3°05´E to 3°15´E and latitudes 6°40´N to 6°55´N (Figure 2).

3. Geology of the Study Area

The study area is located in the sedimentary area of southwestern Nigeria. Ewekoro formation belongs to tertiary-formed Palaeocene and Eocene; and the greater part of the depression is a potential artesian basin where ground water can be sourced. Adegoke et al. (1976) outlined the Albran and younger Palaeographic history of Nigeria and summarized the nature and extent of transgressive, regressive phases as well as the nature of the sediment. The geology of Ogun State comprises sedimentary and basement complex rocks, which underlie the remaining surface area of the state. It also consists of intercalations of argillaceous sediment. The rock is soft and friable but in some places cement by ferruginous and siliceous materials. The sedimentary rock of Ogun State consists of Abeokuta formation lying directly above the basement complex (Figure 2). Ewekoro, Oshosun and Ilaro formations in turn overlie this, which are all overlain by the coastal plain sands (Benin formation).

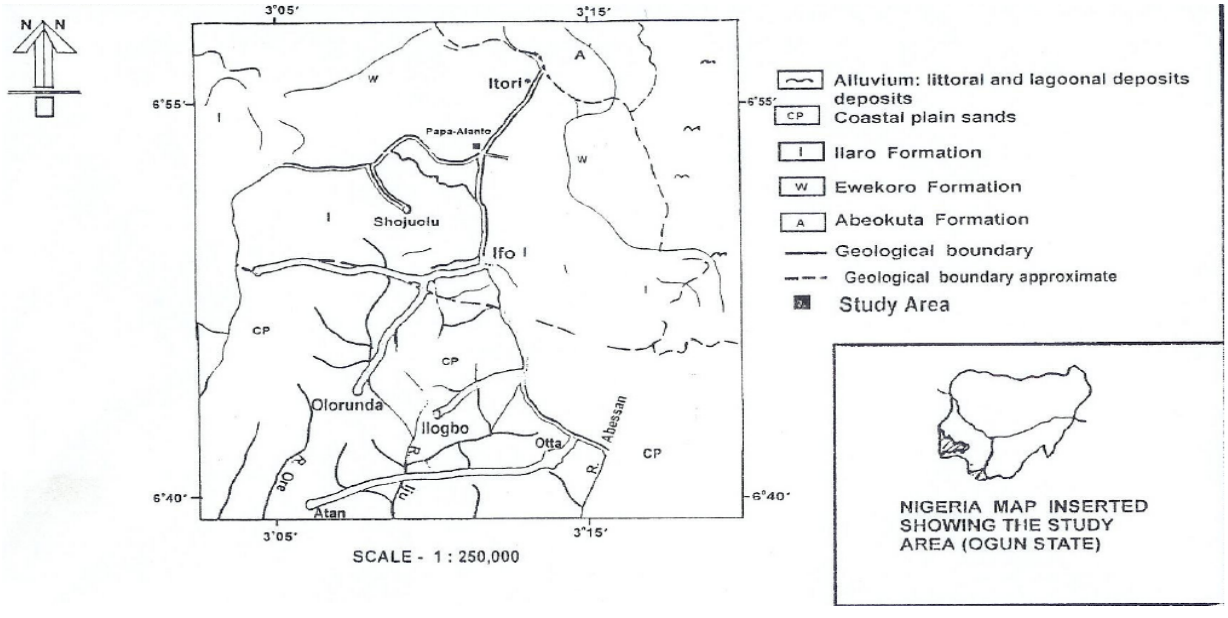

Figure 1. Geological map of Papa-Alanto and its environ (Bulletin: Geological Survey, Nigeria, No. 31, R. D. Hockey, H. A. Jones and J. D. Carter, 1957-61)

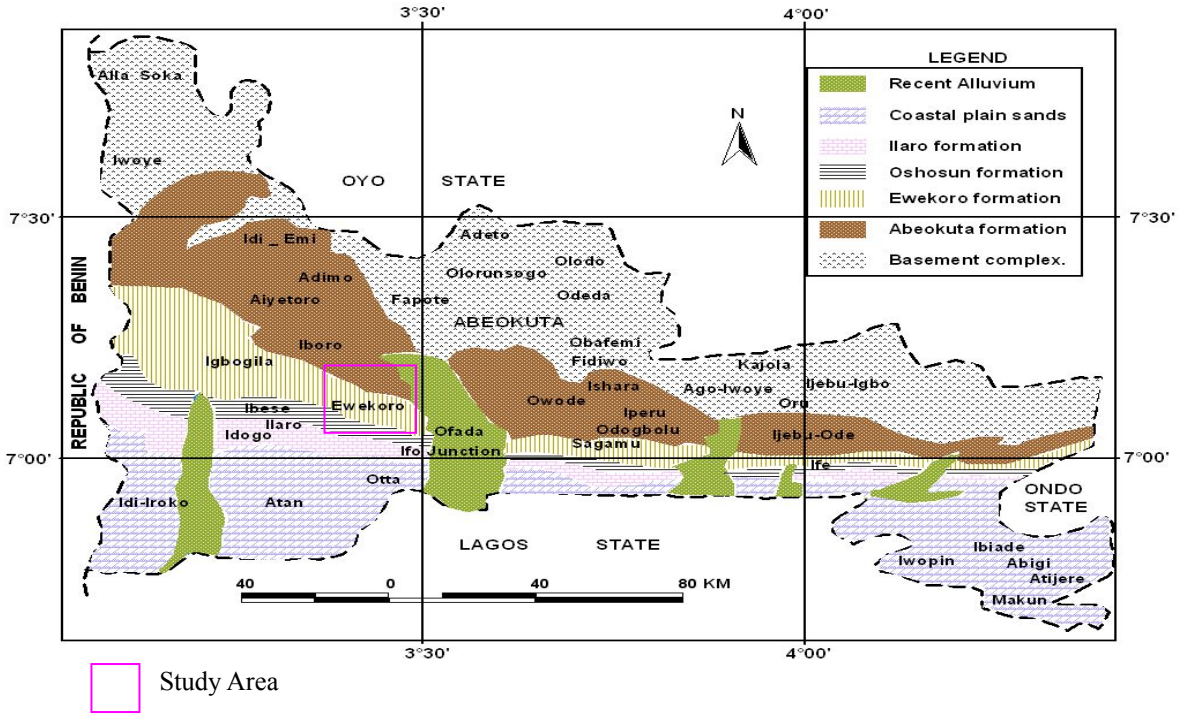

Figure 2. Geological map of Ogun State showing the study area

4. Methods

4.1 Direct Laboratory Measurement Using D.C Supply

Eight different samples were collected from different location from the study area. Resistivity of limestone sample collected from the study area were analysed using a simple laboratory experimental set-up (Figure 3). The limestone samples collected were packed into a core sampler of cylindrical shape and saturated hydraulically for 24 h. After which they were dried in the oven to remove completely the water content in the samples and were shaped into regular forms so as to make good contact with the pins (connecting wires) inserted into the samples. Direct current source was used to supply voltage across the two ends of the core sampler. Voltage was supplied at 12 and 24 V and the corresponding currents were recorded respectively (Table 1).

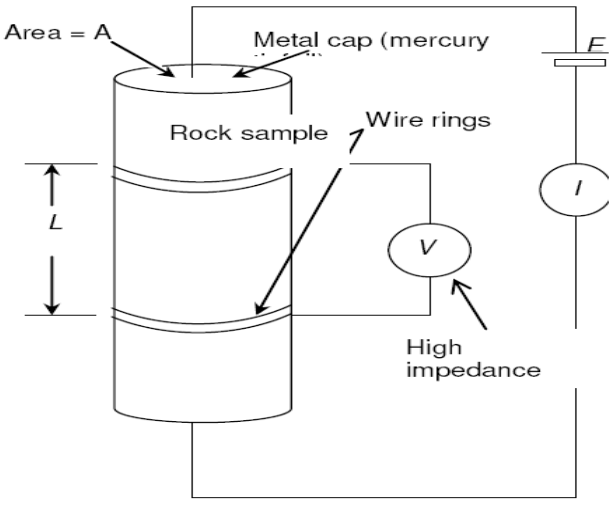

Figure 3. Direct method experimental setup

5. Results and Discussions

Table 1 and 2 shows the resistivity values, permeability values and bulk density as obtained from the simple laboratory direct measurement using a direct current supply of 12 and 24 V. The resistivity values range between $6.2k\Omega m - 171.2k\Omega m$ at 12 V supply and $6.2k\Omega m - 164.4k\Omega m$ at 24 V.

For the resistivity measurements, there is no significant difference between the values obtained for all the rock samples collected. However, all rock samples revealed a significant difference for both permeability and bulk density values. For hydraulic conductivity, the formula below was used:

$$K_{sat} = \frac{VL}{ATD}$$

Where:

$Area = \pi r^2$

r = radius of the core sampler

V = volume of water that passes the sample within 3 minutes

$D = L + H$

L = length of sample inside the core sampler

H = length of water from the top of the sample inside the core sampler

T = time of water run off

K_{sat} = Saturated hydraulic conductivity

Table 1. Resistivity obtained from direct laboratory measurement

Sample Type	Resistivity $(k\Omega - m)$ At 12V	Resistivity $(k\Omega - m)$ At 24V
A	15.41	15.62
B	97.60	97.40
C	171.23	164.38
D	11.82	12.33
E	14.90	14.79
F	6.10	6.10
G	35.62	35.78
H	44.18	43.97

Table 2. Results of Permeability and Bulk Density obtained from direct laboratory measurement

Sample Type	Permeability $(ms^{-1} \times 10^{-6})$	Bulk Density (gcm^3)
A	2.34	1.71
B	6.67	1.50
C	7.99	1.26
D	1.60	1.44
E	1.79	1.30
F	1.47	1.35
G	4.47	1.90
H	4.64	1.40

Badmus and Ayolabi (2005) already characterized the limestone into various litho-facies on the basis of resistivity variations; which is now correlated with the results obtained from the direct laboratory measurement. From this result, samples B and C are characterized as facie I because of their high values of permeability as well

as resistivity. Sample G and H belong to facie II, which revealed limestone with high compaction and of low economic quality (Table 1).

Samples A, D and E belong to facie III because the resistivity and permeability values revealed that the limestone here is porous with grains as confirmed by Badmus and Ayolabi (2005). While sample F belongs to facie IV with the lowest value of resistivity and highest value for permeability. The limestone here is confirmed to be highly porous with cracks of different degrees.

6. Conclusion

The resistivity values of limestone rock samples collected from different location within the study area has revealed by the simple laboratory set up using DC source of 12 and 24 V showed that the limestone of Ewekoro formation has various degrees of qualities as characterized by their resistivity and permeability values. This research work also showed to certain extents the accuracy of the electrical resistivity method of geophysical prospecting when compared with the results obtained in the work of Badmus and Ayolabi (2005). This research work further showed the occurrence of vast deposits of limestone, which can be of economic importance in mining and industrial purposes.

References

Adegoke, O. S., Dessauvagie, T. F. J., & Kogbe, C. A. (1972). Radioactive age determination of glauconite from the type locality of the Ewekoro Formation. *Conf. Afr. Geol. Ibadan* (1970), 277-280.

Adegoke, O. S., Dessauvagie, T. F. J., Kogbe, C. A., & Ogbe, F. G. A. (1971). Type section, Ewekoro Formation, biostratigraphy and microfacies. *4th African Micropal. Coll. Abidjan* (1970), 37-39.

Adegoke, O. S., Ogbe, F. G. A., & Jan Du Chene, R. E. (1976). Excursion to the Ewekoro quarry (Paleocene-Eocene). *Geol. Guide Nigerian Cretaceous-Recent Loc.*, 1-17.

Badmus, B. S., & Ayolabi, E. A. (2005). Litho-facies changes in Ewekoro limestone using Schlumberger geoelectric sounding techniques. *J. Appl. Sci. Technol., 10*(1&2), 42-52.

Badmus, B. S., Ayanda, J. D., & Popoola, I. O. (2006). Geoelectric evaluation of Mica Schist deposits in Area J4 of Southwest, Nigeria. *J. Appl. Sci. Technol., 11*(1&2), 39-43.

Ghorab, M. (2010). The Petrol characteristics and their effect on the reservoir for Mheiherrat formation at central part of the Gulf of Suez, Egypt. (Egyptian Petroleum Research Institute)

Jones, H. A, & Hockey, R. D. (1964). The geology of parts of Southwestern Nigeria. *Geol. Survey Nig. Bull, 31*, 22-24.

Kogbe, C. A. (1976). The Cretaceous and Paleogene sediments of southern Nigeria. In C. A. Kogbe (Ed.) *Geology of Nigeria*, 325-334.

Ojelabi, E. A., Badmus, B. S., & Salau, A. A. (2002). Comparative Analysis of Wenner and Schlumberger Methods of Geoelectric Sounding in subsurface delineation and groundwater exploration-a case study. *J. Geol. Soc. India, 60*, 623-628.

Oladeji, B. O. (1992). Environmental analysis of Ewekoro Formation at the Shagamu Quarry. *Nig. J. Min. Geol., 28*(1), 148-156.

Omatsola, M. E., & Adegoke, O. S. (1981). Tectonic Evaluation and cretaceous stratigraphy of the Dahomey Basin. *J. Min. Geol., 5*(2), 78-83.

Poirier, C., & Aubertins, M. (2011). A numerical investigation of physical parameters influencing saturated flow in limestone drains. Paper presented at Securing the future and 8th ICARD, June 23-26, 2009, Skellefteå, Sweden.

Earth Science Research; Vol. 1, No. 2; 2012
ISSN 1927-0542 E-ISSN 1927-0550
Published by Canadian Center of Science and Education

Formation Pressure Evolution in Lynedoch Fields, Northern Bonaparte Basin, Australia

Suliman Ahmed Hamid Fadul[1], Ye Jia Ren[1], Cao Qiang[1] & Liu Wenchao[1]

[1] Key Laboratory of Tectonics and Petroleum Resources, China University of Geosciences MOE, Wuhan, China

Correspondence: Suliman Ahmed Hamid Fadul, Key Laboratory of Tectonics and Petroleum Resources, China University of Geosciences MOE, Wuhan 430074, China. Tel: 86-132-7792-8597. E-mail: Nokkaa08@gmail.com

Received: January 18, 2012 Accepted: January 31, 2012 Online Published: June 19, 2012

doi:10.5539/esr.v1n2p122 URL: http://dx.doi.org/10.5539/esr.v1n2p122

Abstract

The Lynedoch Fields are located in the flanks of Calder Graben. Wells lynedoch-1, lynedoch-2 and Seismic line N11809 are selected to evaluate the pressure evolution history, investigate the mechanisms of overpressures generation and the timing of oil and gas generation from the potential hydrocarbon source rock. Three areas of pressure evolution were identified namely normal pressure, slight excess pressure and intense excess pressure. The pressure releases are consistent with the tectonic events increasing with depth and dissipating laterally. The peak of excess pressure generation, the peak sedimentation rates in wells Lynedoch-1 and Lynedoch-2 and the peak generation of oil and gas of the same wells were occurred during the Late Cretaceous at 65Ma. High sedimentation rates with rapid subsidence and oil and gas generation are the main favorable conditions for overpressure generation in the study area.

Keywords: overpressure mechanisms, high sedimentation rates, generation, expulsion, Lynedoch Fields

1. Introduction

Lynedoch Fields comprise two wells Lynedoch-1 and Lynedoch-2 (Figure 1). Lynedoch-1 was drilled in 1973 to test a low relief anticline within the flanks of the Calder Graben and terminated in Jurassic sediments at a total depth of 3967 m. The well Lynedoch-2 was drilled to a total depth of 4225mDF to test sands of Early to Middle Jurassic of Plover Formation with the Darwin Radiolarite as the secondary objective. Two-dimensional Seismic surveying conducted on the Lynedoch Fields based on the NT96 and NT97 surveys and the data was tied into the key wells in the immediate area. The succession penetrated at Lynedoch-2 was as expected from Lynedoch-1, with the exception of the presence of the Elang Formation and the absence of the Cleia Formation. The Fields offer opportunities for the delineation of structural and stratigraphic traps within the flanks of Malita and Calder Grabens and along their margins. No pressure measurements were conducted in well Lynedoch-1. At the well Lynedoch-2 the measurements of drill stem test (DST) were not run. However, the formation pressure tests and samples were taken in well Lynedoch-2 using RFT pressure measurements. A total 66 pressure readings were attempted and 14 readings were acquired in depth intervals of 3825.5m to 3906m. The maximum pressure value acquired was 51.73181MPa at depth 3883m, whereas the minimum pressure value recorded was 40.95MPa at depth 3826m. This study aimed to evaluate the pressure evolution history, investigate the mechanisms of overpressures generation and the timing of oil and gas generation from the potential hydrocarbon source rock.

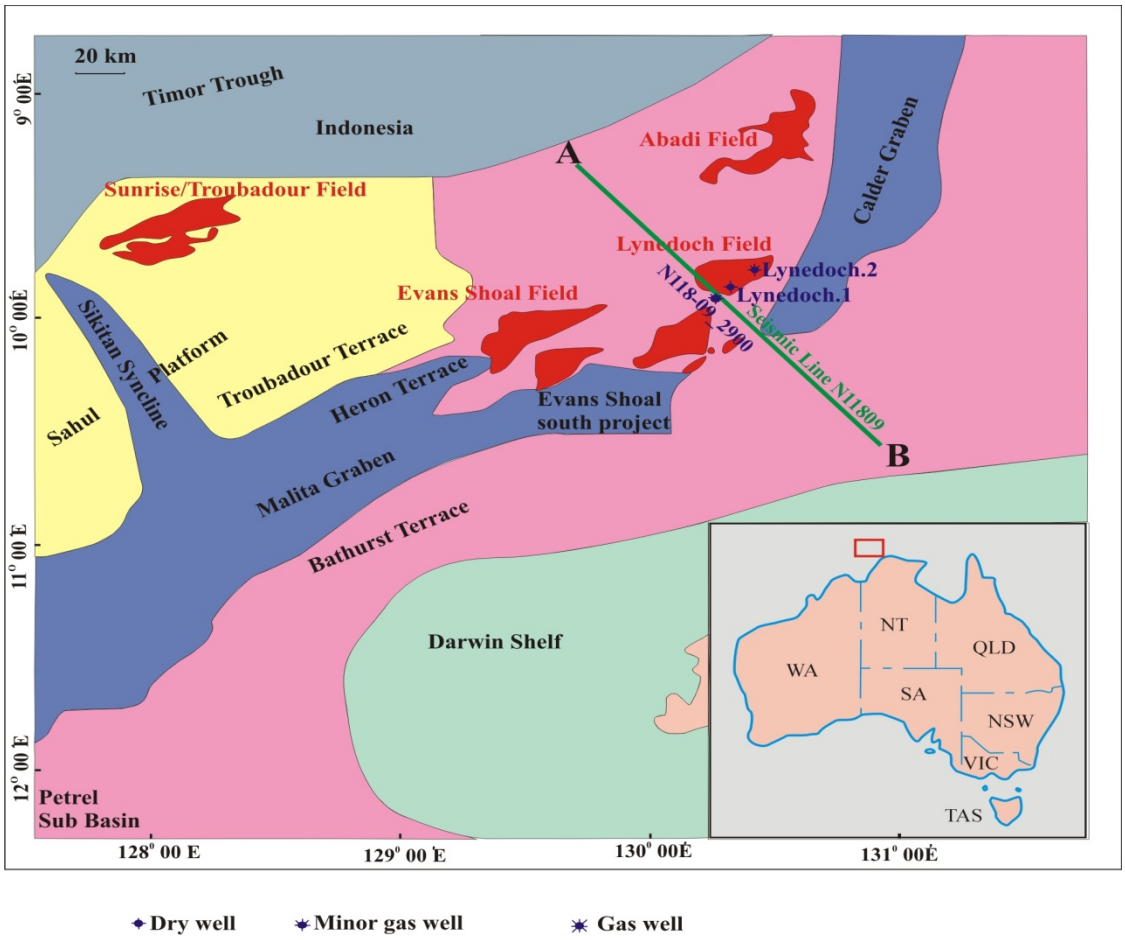

Figure 1. Location map of Lynedoch Fields showing wells Lynedoch-1, Lynedoch-2 and Seismic line N11809 passing over the virtual well N118-09_2900

2. Geological Settings

Lynedoch Fields lie within the north eastern portion of the Bonaparte Basin in the southern extent of the Calder Graben. The main tectonic events in the Northern Bonaparte Basin were formed by Mesozoic rifting which started at Late Triassic and continued throughout the Jurassic (Figure 2), which may be related to Gondwanan "break-up" along the northwestern margin of Australia. The northeast-southwest trending faults in the Northern Bonaparte Basin lead to rapid subsidence in the Malita and Calder grabens, which were developed as major Mesozoic depocentres in the basin. The major mappable seismic surfaces associated with "break-up" events are the Callovian Unconformity, intra-Valanginian Unconformity, and Aptian Unconformity. The main reservoirs in the Northern Bonaparte Basin occur in the Middle-Upper Jurassic Plover Formation. The Plover Formation is a regionally widespread predominantly fluvio-deltaic sequence, which grades into a tidal-estuarine/deltaic and marine shore face succession towards the Sunrise-Troubadour area in the northern part of the Sahul Platform. Post-rift subsidence of the Malita Graben resulted in the deposition of the Upper Jurassic to Lower Cretaceous Flamingo Formation, which varies in thickness across the northern Bonaparte Basin, however, the Flamingo Formation is absent in the wells of the Lynedoch Fields and thickens significantly towards the Malita Graben depocentre. The top of the Flamingo Formation occurs at the Intra-Valanginian Unconformity. The Cretaceous Bathurst Island Group, containing glauconitic claystone Formation is overlying the Intra-Valanginian Unconformity. The Aptian Unconformity marks the top of the Echuca Shoals which is characterized by a condensed radiolarian claystone /calcilutite section. The post-Albian sequence comprises a succession of marine shelf/slope sediments, which is dominated by carbonate deposits throughout the Paleocene to recent time (Figure 2).

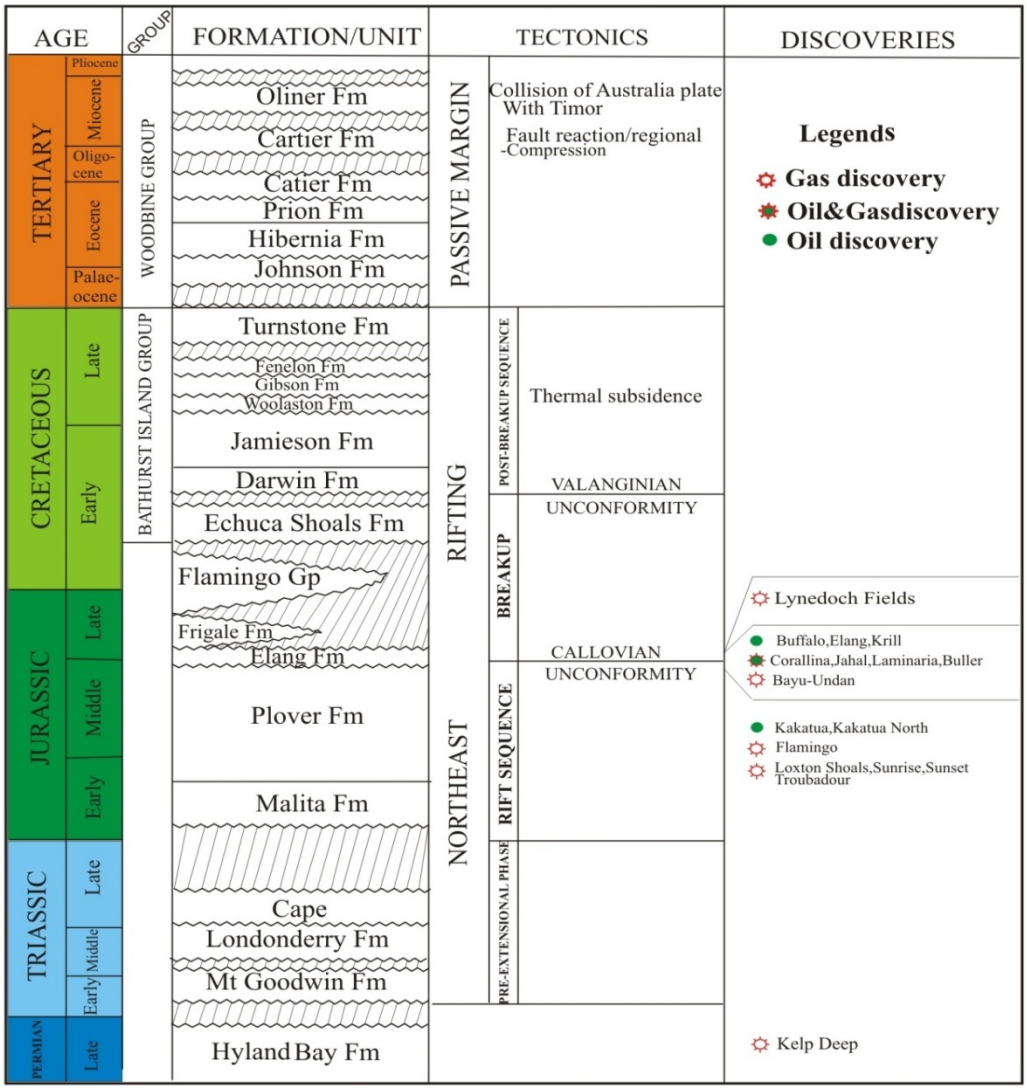

Figure 2. Stratigraphy, tectonics, and petroleum discoveries of Northern Bonaparte Basin, Australia

3. Materials and Methods

3.1 Methods

3.1.1 One-dimensional BasinMod

One-dimensional modeling of a single well location utilizing BasinMod 1D technique that uses mathematical method to reconstruct the burial history, thermal history and generation history determining the subsidence and sedimentation rates, excess pressure, and the maturation parameters, such as the time of onset, peak and end of oil generation according to the equations of backstripping and tectonic subsidence (Steckler & Watts, 1978) as follows:

$$Dt=\left[S\frac{(\rho m-\rho s)}{(\rho m-\rho w)}-\Delta SL\frac{\rho w}{(\rho m-\rho w)}\right]+(W_d-\Delta SL) \quad (1)$$

$$\rho s=\frac{\sum_i\left[\Phi_i\rho w+(1-\Phi_i)\rho_{sgi}\right]S_i}{S} \quad (2)$$

Where:

Dt = the amount of tectonic subsidence (water column (m) in past time).

S = the total stratigraphic thickness of the sediment column corrected for compaction (m).

ρ_s = the average density of the sediment stratigraphic column (g/cm^3).

W_d = the palaeo-water depth (m).

ΔSL = the relative increment for eustatic sea-level variation (m).

ρ_m = the density of asthenosphere (g/cm^3).

ρ_w = the density of water (g/cm^3).

Φ_i = the porosity of stratigraphic unit I (dimensionless).

ρ_{sgi} = the grain density of stratigraphic unit i (g/cm^3).

S_i = the thickness of stratigraphic unit i after compaction correction.

One dimensional BasinMod comprise the following models below:

1) Krevelen diagram (1961) after Peters et al. (2005):

   Characterization of kerogen by van krevelen diagram (1961) after Peters et al., (2005), utilizing the generative amounts of HC and CO_2 in Rock-Eval Parameters HI (hydrogen index) and OI (oxygen index), and vitrinite reflectance Ro to describe the OM types.

2) Coupled fluid flow Model:

   Coupled fluid flow calculation which based on the conservation law, which requires conservation of the mass in the fluid flow model (Huyakorn and Pinder, 1983; Aziz and Settari, 1979) is used as follows:

$$\frac{\partial}{\partial z}(\rho\phi) + q + \nabla\rho\upsilon = 0 \tag{3}$$

   Where: ρ is the density, υ is the velocity, ϕ is the porosity and q is the source term. Fluid flow calculation requires modeling of fluid transport in the sediments.

3) Darcy velocity:

   Darcy velocity is calculated using the Darcy's Law for modeling the movement of liquids using the equation of (Freeze & Cherry, 1979):

$$\upsilon = \frac{-k\rho g}{\mu}\frac{dh}{dl} \tag{4}$$

   Where: υ, k, ρ, g, μ and dh/d1 are represented by the Darcy velocity, permeability, density, gravitational acceleration, viscosity and hydraulic gradient, respectively.

4) The equation of the state by Bethke (1985):

   The equation of the state suggested by Bethke (1985) for the fluid flow fragments calculation is used to calculate the pressure and temperature relationship of the model as follows:

$$\rho = \rho_{sc}\exp\left[(P-0.1) - \alpha(T-25)\right]\text{kg/m}^3 \tag{5}$$

   Where: ρ is the density; ρ_{sc} is the density at standard surface conditions, P the pressure in MPa, T the temperature in ^{o}C, α is estimated as $5*10^{-4}C^{-1}$ and β is predicted as $3.4*10^{-4}MPa^{-1}$.

5) The viscosity as a function of temperature:

   The viscosity as a function of temperature can be expressed as (Lide, 1997) in the following equation:

$$\mu = 10^n$$
$$n = \left(\frac{1.3272(10-T) - 0.001053(T-20)^2}{T+105}\right) \tag{6}$$

Where μ is described as the viscosity which varies with temperature and T is the temperature in ^{o}C. The equations (5) and (6) are essential for modeling fluid flow in conjunction with pressure and temperature of sediments which are in close relation with density and viscosity.

6) The sediment compaction model:

The sediment compaction is modeled as a function of fluid pressure by the following formula:

$$\phi = f(P), \phi = \frac{e}{1+e}, e = e_A^* \left(\frac{P_f}{P_f^*} \right)^A \left(\text{fractionA} \right) + \left[e_B^* - B\left(P_f - P_{f^*} \right) \right] \left(\text{fractionB} \right) \quad (7)$$

Where e is the void ratio which is $\phi/(1-\phi)$, e_A^* is the initial void ratio of fraction A, e_B^* is initial void ratio of fraction B, P_f are the Frame, or matrix, pressure, P_{f^*} is the initial frame, or matrix pressure, A is the exponential compaction factor, B is the linear compaction factor, fraction A is the portion of lithology which compacts exponentially (all lithologies except sand), fraction B is the portion of lithology, which compacts linearly (sands) = 1-fraction A.

7) The fluid pressure algorithm of (Maubeuge & Lerche, 1993):

The fluid pressure algorithm of (Maubeuge & Lerche, 1993) which is responsible of handling the excess pressure calculation at each time step in comparison with calculated pressure for the next step is calculated using the following formula:

$$P_x = P_{overburden} - \left(P_{hydrostatic} - P_{frame} \right) \quad (8)$$

8) Transient heat flow Model:

The transient heat flow equation of 1D BasinMod is used to describe the thermal conduction and convection of the heat flow, assuming that the heat transfer in 1D is by vertical conduction and depends on Fourier's law of heat conduction coupled with the law of conservation which comprises a full differential equation and handles the thermal conductivity and heat capacities of different rock units while the instantaneous variations in the heat flow values are smoothed out over geologic time as a function of thermal conductivity and heat capacity, rather than resulting in sudden changes in the thermal profile as follows:

$$C_v \frac{\partial T}{\partial t} - \frac{\partial}{\partial x}\left(\lambda \frac{\partial T}{\partial x} \right) - Q = 0 \quad (9)$$

Where: where C_v is the volume heat capacity in J/m^3K, T is the temperature in Kelvin, λ is the thermal conductivity, t is the time and Q is the heat source term. Transient heat flow model could only be used with the fluid flow algorithm rather than mechanical compaction methods due to the necessity of calculating fluid flow dependent parameters.

9) The exponential equation (after Sclater & Christie, 1980):

The exponential equation (after Sclater & Christie, 1980) is used for porosity calculation:

$$P = P_0 \exp^{(-kz)} \quad (10)$$

Where: P is porosity (%), Po is initial porosity (%), k is compaction factor adjusted for varying compressibilities of different lithologies (m^{-1}) and z = depth (m).

10) Modified Kozeny-Carman equation is used to calculate permeability in 1D model:

$$K = \begin{cases} \dfrac{0.2\Phi^3}{S^2 o(1-\Phi)^2} & (\Phi \geq 0.1) \\ \dfrac{20\Phi^5}{S^2 o(1-\Phi)^2} & (\Phi < 0.1) \end{cases} \quad (11)$$

Where: K = permeability (md), Φ = porosity (dimensionless), S_O = specific surface area of the rock (m^2).

11) Maturation and hydrocarbon generation and expulsion model:

Predicted maturation and timing of hydrocarbon generation and expulsion are based on Lawrence Livermore National Laboratory (LLNL) vitrinite and kerogen kinetics.

3.1.2 Two-dimensional BasinMod

Two-dimensional BasinMod software package is used to reconstruct the maturation and generation histories, while the fluid flow Model of Bredehoeft et al.1994, Lee & Williams (2000) which was modified from the equation of Bethke (1989) in which the oil and gas generation are included as fluid source Terms ($q_{kerogen\text{-}oil}$ and $q_{oil\text{-}gas}$) is used for fluid flow and overpressure calculations as follows:

$$\varphi\beta\frac{P}{\partial t}=\frac{\partial}{\partial x}\left[\frac{K_x}{\mu}\left(\frac{\partial P}{\partial x}\right)\right]+\frac{\partial}{\partial z}\left[\frac{K_z}{\mu}\left(\frac{\partial P}{\partial z}-\rho g\right)\right]-\frac{1}{1-\varphi}\frac{\partial\varphi}{\partial t}+\varphi\alpha\frac{\partial T}{\partial t}+\left(q_{kerogen-oil}+q_{kerogen-gas}\right) \quad (12)$$

$$\alpha=\frac{1}{\rho}\frac{\partial\rho}{\partial T}\text{ and }\beta=\frac{1}{\rho}\frac{\partial\rho}{\partial P}$$

Where: subscript x refers to x-direction, and subscript z refers to z-direction; φ is porosity, P is the pore fluid pressure, T is temperature , t is time, K is permeability, ρ is density, μ is viscosity, α is fluid thermal expansibility , β is fluid compressibility and Q is pressure source. The equation (12) can be used to calculate the net pressure change resulting from various hydrologic and geological processes and the flow from the source beds acts to dissipate the pressure build-up in rocks, therefore the net pressure depends on rate of compaction (sedimentation), rate of hydrocarbon generation, the permeability of the reservoir and confining rocks and the rate of aquathermal expansion.

3.2 Materials and Input Parameters

The precision of basin modeling is greatly influenced by the effectiveness and accuracy of various inputs parameters. Data from boreholes, seismic surveys, well tests and geochemical analyses have been used in this study. The major input parameters comprise the stratigraphic thicknesses, burial depths, absolute ages of stratigraphic units that were interpreted from the regional stratigraphy using Geological Time Scale of (Haq et al., 1987) as a guide for generalized ages of stratigraphic units and ages of regional unconformities throughout the study area, whereas the ages at the system and series boundaries were adjusted to the (Harland, 1989) Geologic Time Scale. lithology of each stratigraphic unit, and the eroded thicknesses in the subsurface during the main uplift events, organic thermal indicators, include vitrinite reflectance values, heat flow values, the extrapolated bottom whole temperatures and the surface temperature, porosities, permeabilities, Rock-Eval pyrolysis parameters, RFT pore fluid pressure measurements from the well of the Lynedoch-2. Seismic line N11809 of the study area is also utilized to predict the pressure evolution which comprises eight key stratigraphic horizons as shown in (Figure 3). The initial porosity, matrix density, matrix thermal conductivity and matrix heat capacity, the densities and composition for water, crude oil and natural gas at the subsurface and the salinity of groundwater are adopted from the default values in BasinMod Software package.

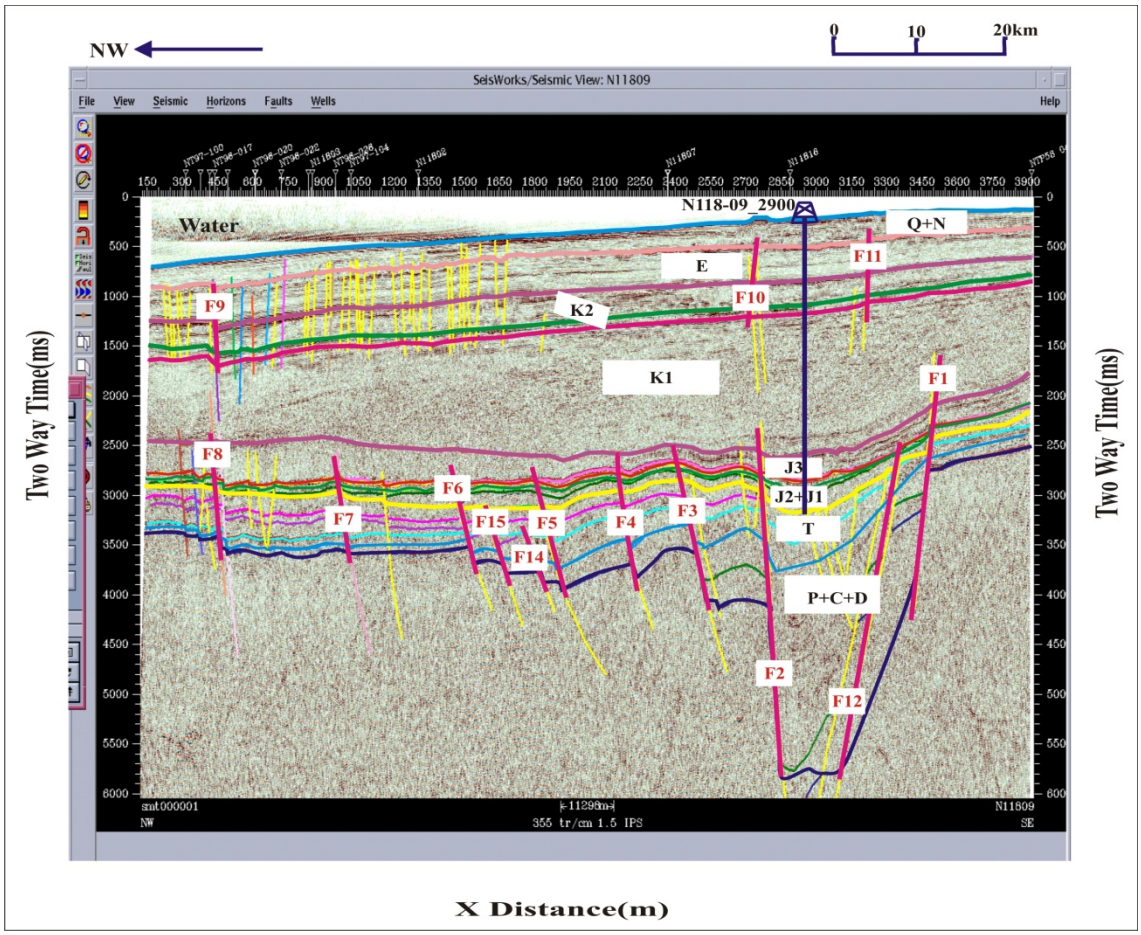

Figure 3. Two-Dimensional Seismic Section N11809 of Bathurst Terrace and passing through Calder Graben and Lynedoch Fields depicting the key Stratigraphic horizons denoted in black capital alphabets as follows: G+N = Oliver, Barracouta and Alaria formations, E = Cartier Formation, K2 = Turnstone and Hibernia formations, K1= Darwin, Jamieson ,Wangalu and Vee formations, J3 = Elang, Flamingo and Echuca Shoals formations, J2+J1=Plover Formation, T = Malita Formation and P+C+D=Pollard, Mt Goodwin and Hayland Bay formations, while the faults are segregated by red color of the letter F (F1 to F15)

4. Results

BasinMod one-dimensional that utilizes mathematical technique is used to analyze different geological scenarios for pressure evolution in Lynedoch Fields. The Seismic line N11809 that passes through the virtual well N118-09_2900 (Figure 3) was also used to predict the two-dimensional pressure evolutions in these Fields. The emphasis was to determine the pressure evolution and identify the causes of overpressure.

4.1 Pressure Evolution in the Lynedoch Fields

BasinMod 1D software is used to recover the formation pressures of single wells of Lynedoch-2 in Lynedoch Fields. Overpressure can, in principal, only be, calibrated if the water flow and water balance is adjusted correctly throughout the entire basin, therefore in overpressure modeling, the permeabilities of many layers, lithologies and rock types must be adjusted simultaneously. On average, the water flow is upward and therefore calibration should usually be performed from the top to down and from more to less permeable lithologies. The fluid pressures have been compiled from RFT performed in the well Lynedoch-2 and 14 pressure measurements were recorded. The results have shown that the onset of excess pressure was occurred at Early Cretaceous while the peak was occurred during the Late Cretaceous (Figure 4B). The maximum pressure value of 51.731MPa was measured at Echuca Shoals Formation. The plotted pressure data against the depth in the Echuca Shoals Formation has resulted in identification of depth intervals that are likely to contain overpressure (Figure 4A).

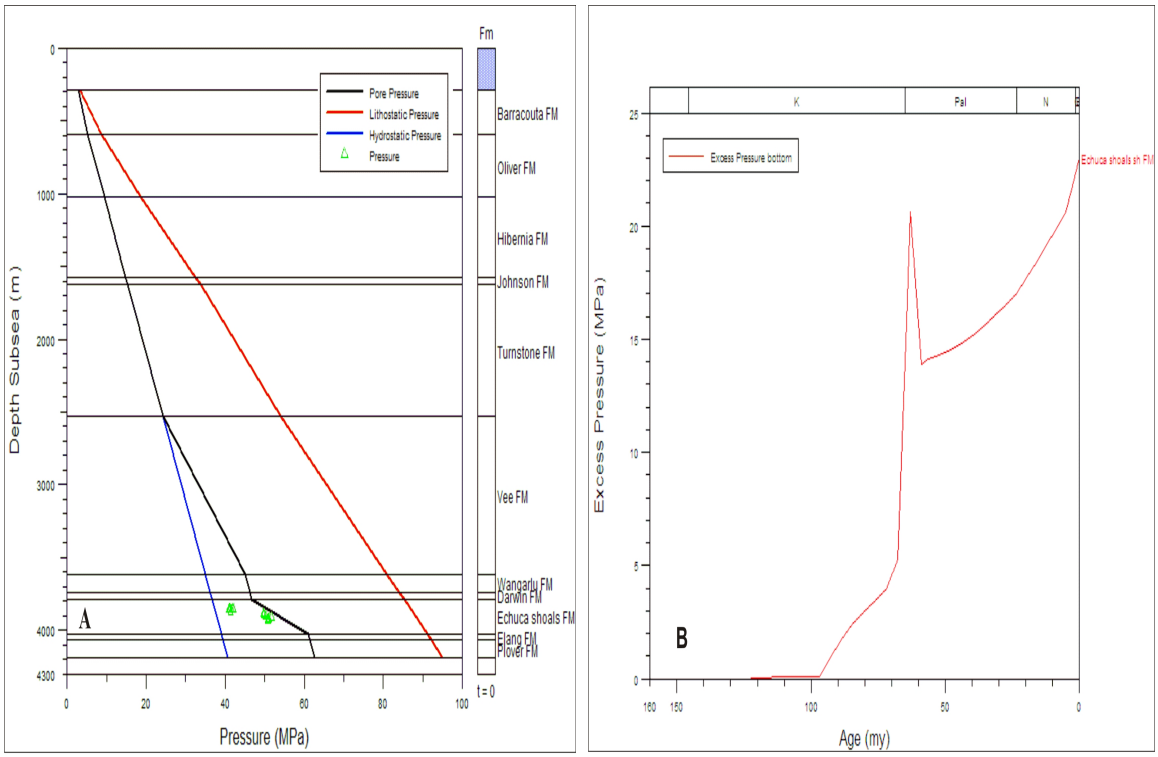

Figure 4. Schametic diagrams showing observed pressure data plots of well Lynedoch-2, **(A)** pressure profile (pressure versus depth), **(B)** excess pressure curve depicting its peak at (65Ma) Late Cretaceous, also indicated on the plot are reference lines of hydrostatic pressure, pore pressure and lithostatic pressure

The fluid pressure is also modeled based on eight key stratigraphic units of the seismic line N11809 (Figure 5). The modeling comprises the periods of depositional time from Late Carboniferous to the present-day under the assumptions that the bottom boundary is closed to fluid flow and subject to heat flow of 64mWm^2 based on the average geothermal gradient of the basin (3.62^{o}C/100m), the upper boundary is open to fluid flow and has a fixed temperature of 20^{o}C while the lateral boundaries are constants and are assumed to have zero heatflux taking into account the effects of disequilibrium compaction and oil and gas generation on overpressure development and the effects of relative permeability decrease on fluid overpressure have not taken into account in the calculations of the excess pressure. Based on the results of pressure evolution (Figure 5) the excess pressure generation can be interpreted as follows: the intensities of the excess pressure of the Fields is increased with depth, while its magnitudes decrease towards the margin of the Fields until the normal pressures are met. At 91Ma the excess pressure evolution was occurred at the J2+J1 and increased with depth and reached the maximum value of 30MPa at the Base of P+C+D and decreased laterally showing little continuity towards the margins until normal pressures are met at the faults F6 and F1 (Figure 5A). At 65Ma the evolution of excess pressure was occurred at the base of K1 and increased with depth and reached the base of P+C+D with maximum value of 37.5MPa, whereas it decreased laterally and exceeded beyond the fault F8 in NW direction and separated from the normal pressure by fault F1 in SE direction of the Fields (Figure 5 B). At 59Ma the evolution of excess pressure was occurred in the base of K1 and increased with depth and reached the base of the P+C+D with maximum of value of 40 MPa whereas it decreased laterally towards the margins (Figure 5 C). At 0Ma (present-day) the evolution of excess pressure occurred at the middle of the K1 and increased with depth and reached the base of P+C+D with maximum value of 51.7 MPa, whereas it decreased laterally but it is in greater amount than that of all above mentioned periods and has passed beyond the fault F8 in NW direction of the Fields as well as it exceeds the fault F1in the SE direction of the Fields (Figure 5 D). The pressure evolution profiles (Figure 5) can be categorized based on their intensities into normal pressures, slight excess pressures and intensive excess pressures and they are reliable pressure profiles.

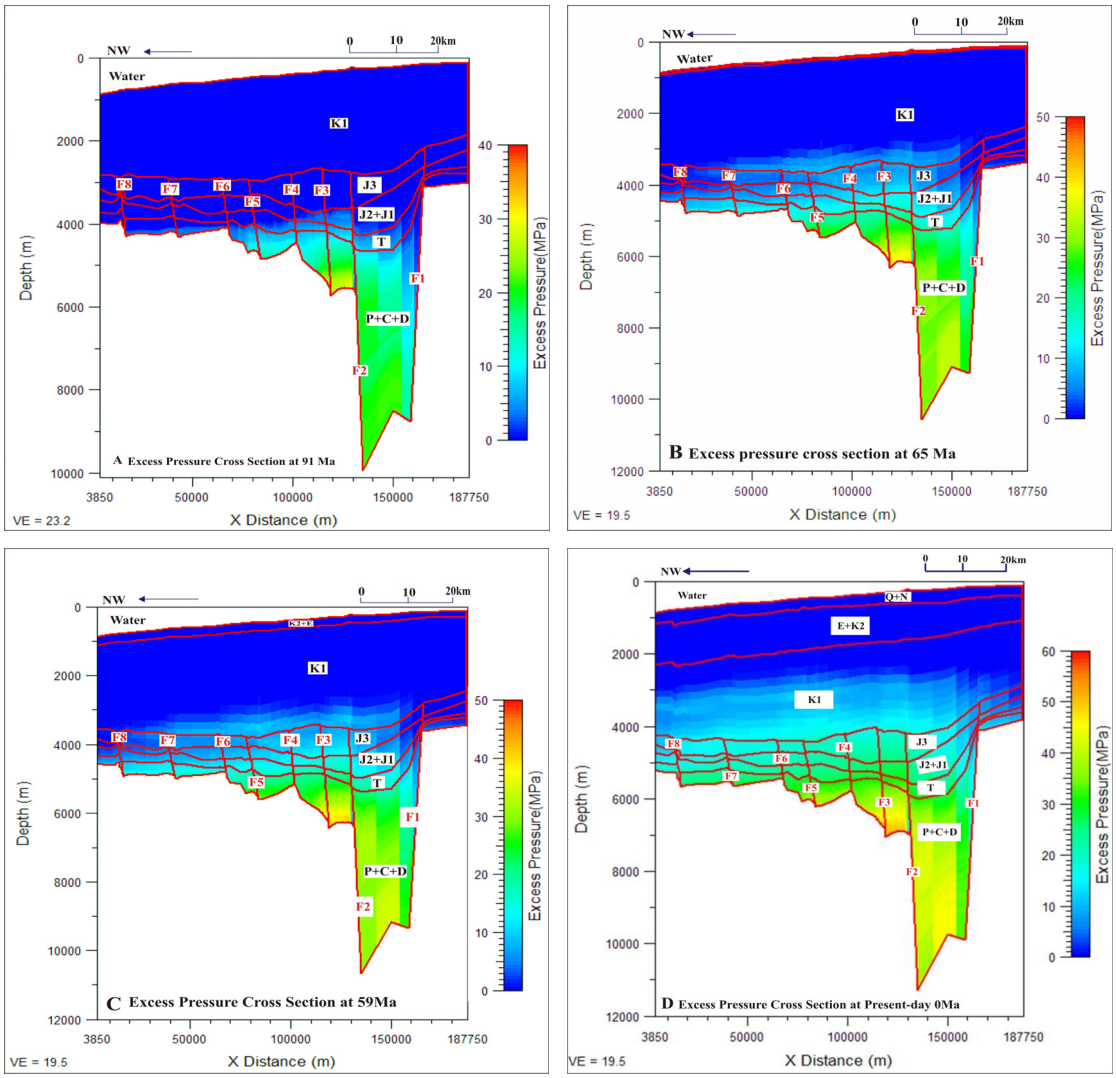

Figure 5. Schematic diagrams showing Excess Pressure evolution of Lynedoch Fields and the surrounding area along Seismic Line N11809. **(A)** At 91 Ma. **(B)** At 65Ma. **(C)** At 59 Ma. **(D)** At 0Ma. G+N = Oliver, Barracouta and Alaria formations, E = Cartier Formation, K2 = Turnstone and Hibernia formations, K1= Darwin, Jamieson, Wangalu and Vee formations, J3 = Elang, Flamingo and Echuca Shoals formations, J2+J1=Plover Formation, T = Malita Formation and P+C+D=Pollard, Mt Goodwin and Hayland Bay formations, while the faults are segregated by red color of the letter F (F1 to F8)

4.2 Mechanisms of Overpressure Evolution

Overpressure typically is defined as pore fluid pressure that significantly exceeds hydrostatic pressure of a column of water or formation brine (Dickinson, 1953). Overpressure, the difference between the pore pressure and hydrostatic and it directly controls fluid flow. Another way to view overpressure, in terms of the dynamics of subsurface fluid flow is the inability of formation fluids to escape at a rate which allows equilibration with hydrostatic pressure, the hydrostatic pressure gradient of 0.433psi/ft serves as a reference of pressure-depth ratios, greater than 0.433psi/ft represents overpressure conditions. The overpressure generation and expulsion during the evolution of the sedimentary basin have a close relationship with the large scale hydrocarbon generation and migration, the direction and concentration of which are controlled mainly by the formation pressure distribution (Ye et al., 2003; Vannucchi, 2001; Schegg et al., 1999). The analysis of models of overpressure suggests that three main mechanisms can result in the development of overpressure these are: sedimentation, hydrocarbon generation and vertical migration of fluids through faults. In this paper we concentrate on the effects of sedimentation and hydrocarbon generation on overpressure development in Lynedoch Fields.

4.2.1 Sedimentation and Porosity Reduction

The main factor which determines changes of pore space is compaction or decomposition of rocks under changing load. Sediment compaction is mostly a mechanical process resulting in the reduction of porosity by increases in vertical stress due to the loading on the sedimentary pile. Lateral deformation is commonly ignored. The temporal evolution of fluid pressure as a result of mechanical compaction is controlled by the relationship between sediment permeability and sedimentation rates. Sedimentation rates provide the time of the most pronounced periods of overpressure build-up due to the sediment loading. BasinMod1D and 2D are used to depict the mechanism of the overpressure generation and evolution in Lynedoch Fields through reconstruction of sedimentation rates and tectonic subsidence evolution of the wells Lynedoch-1 (Figure 6A) and Lynedoch-2 (Figure 6B) and compared with the results of 2D pressure evolution of the seismic line N11809 (Figure 5). Sedimentation and tectonic subsidence analysis (Figure 6) has shown three low periods of sedimentation and tectonic subsidence rates with one high period (peak sedimentation) at the Late Cretaceous (65Ma) in both wells. The sedimentation rates during the Late Cretaceous are 290m/Ma and 688.25m/Ma while the tectonic subsidence rates are 74.79 (m/Ma) and 92.20 (m/Ma) in wells Lynedoch-1 and Lynedoch-2 respectively.

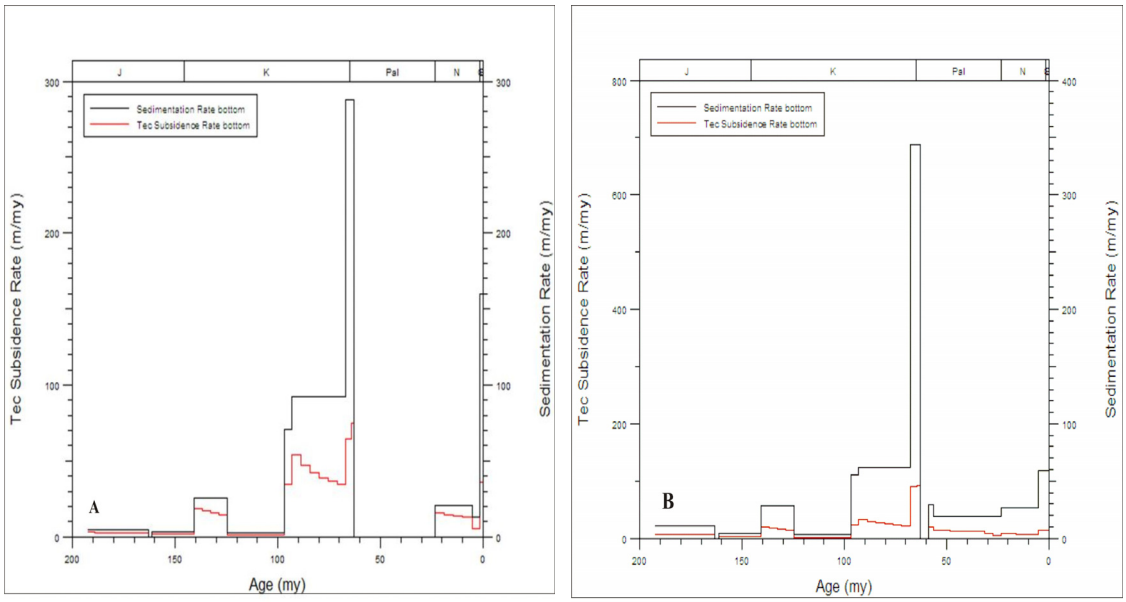

Figure 6. Schematic diagrams of sedimentation and tectonic subsidence rates in Lynedoch Fields, **(A)** well Lynedoch-1, (**B)** well Lynedoch-2

4.2.2 Hydrocarbon Generation

The generation of hydrocarbons involves the transformation of kerogen in organic matter into liquid and gaseous phase. It results in an increase of the fluid volume and a very small decrease in the volume of organic matter. The decrease of volume of the solid phase is insignificant. The increase of the fluid volume leads to the growth of formation pressure and related reduction of the effective stress. The wells Lynedoch-1and Lynedoch-2 and Seismic survey line N11809 were modeled to reconstruct burial, thermal and hydrocarbon generation histories of the Fields to assess the relationship between the excess pressures yielded in the Fields and the hydrocarbon generation from the source rock. The source rock and their present day maturities are identified using 1D and 2D BasinMod software. The present day thermal regime is obtained by calculating the heat flow in the wells Lynedoch-1 (53.4mWm^2), Lynedoch-2 (68.3mWm^2) and the Seismic Line N11809 (64 mWm^2). The source rock of Plover Formation in Lynedoch Fields was deposited during the Middle Jurassic and the TOC is variable from well to another (Table 1). In well Lynedoch-1 4 TOC readings were recorded with the average of 1.225 wt%. In well Lynedoch-2 4 readings of the TOC were recorded in the Plover Formation source rock with the average of 0.995; while the average TOC of the Plover Formation source rock from the horizons of Seismic Line N11809 is 2.20 wt %.

Table 1. Abundance of organic matter of the Lynedoch Fields, wells Lynedoch-1 and Lynedoch-2

Well name	Depth (m)	Formation	Lithology	TOC (wt %)	$HI_{(mgHC/gTOC)}$	$OI_{(mgCO2/gTOC)}$	(S_1+S) (mg/g)
Lynedoch-1	3911	Plover	Claystone	1.61	93.79	6.2	2.22
Lynedoch-1	3931.92	Plover	Claystone	0.69	37.68	73.91	0.41
Lynedoch-1	3950	Plover	Claystone	1.78	91.57	15.73	2.43
Lynedoch-1	3962.4	Plover	Claystone	0.82	40.24	92.68	0.49
Lynedoch-2	4050	Plover	Claystone	0.63	71.43	23.81	0.77
Lynedoch-2	4060	Plover	Claystone	0.88	59.09	6.82	0.91
Lynedoch-2	4130	Plover	Claystone	1.0	61	23	0.72
Lynedoch-2	4135	Plover	Claystone	1.31	49.62	19.85	0.82

TOC is total organic matter content (wt. %). (S1+S2) are the total amount of petroleum that might be generated from a rock. S1is free hydrocarbons (mg/g). S2 is the hydrocarbon generation potential of the source rock (mg/g)

Analysis of organic matter suggests that the Plover Formation source rock in Lynedoch Fields is a gas-prone source rock with OM type Π&ΙΙΙ kerogens dominantly (Figure 7). The generation of hydrocarbons from the wells of the Lynedoch Fields is demonstrated using 1-D BasinMod software through reconstruction of the burial, thermal, generation histories of Lynedoch-1 and Ly nedoch-2 (Figure 8). In well Lynedoch-1 the Plover Formation source rock entered oil widow at late Cretaceous and wet gas window at Early Neogene (Figure 8A), and the peak generation was recognized during late Cretaceous to early Paleogene (Figure 10). In well Lynedoch-2 the Plover Formation source rock also entered oil widow at late Cretaceous and wet gas window at Early Neogene (Figure 8B), and the peak generation was recognized during late Cretaceous to early Paleogene (Figure 11). The source rock maturation levels and hydrocarbon generation across the Lynedoch Fields were also conducted using Seismic Survey Line N11809 that passes through the Fields on the virtual well N118-09_2900.The maturity (Figure 9) is interpreted to have been initiated at a level of thermal maturity of 0.5%-0.7%Ro and concluded at a level of thermal maturity of 1.3%-2.0%Ro. The generation evolution history along this line can be described as follows: At 91 Ma the Plover Formation source rock entered mid-mature oil window at the center of Calder graben and early-mature oil window at the margins of Calder graben (Figure 9A). At 65Ma the Plover Formation entered mid-mature oil window at the margins of Calder graben and late-mature oil window at the center of Calder graben (Figure 9B). At 35.4Ma the Plover Formation entered mid-mature oil window at the margins of Calder graben and late-mature oil window at the center of Calder graben (Figure 9C). At the present-day (0Ma) the Plover Formation source rock entered late-mature oil window at the margins as well as the center of the Calder graben (Figure 9D). The modeling results are calibrated to the measured vitrinite reflectance values for the wells of the Lynedoch Fields and to the Seismic Line N11809. The correspondence between the simulated and the measured values is remarkably good, which indicates that the accuracy is relatively higher for both 1D and 2D modeling.

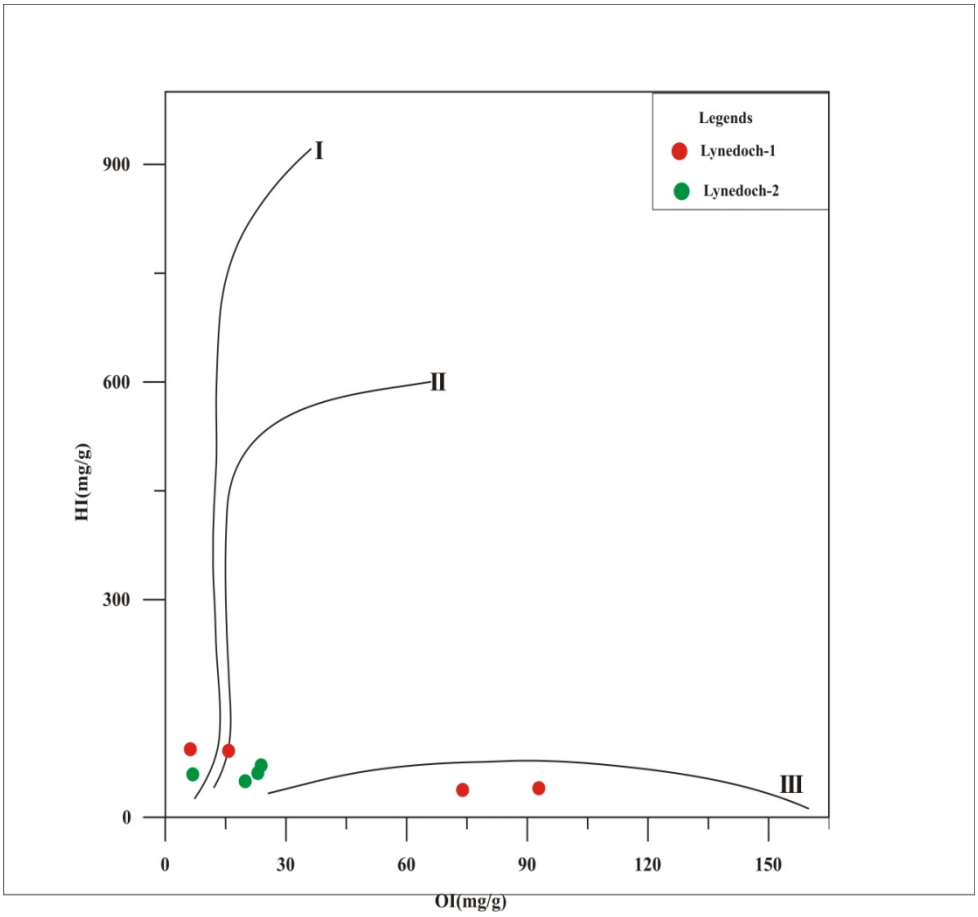

Figure 7. Organic Matter types of Plover Formation source rock in Lynedoch Fields

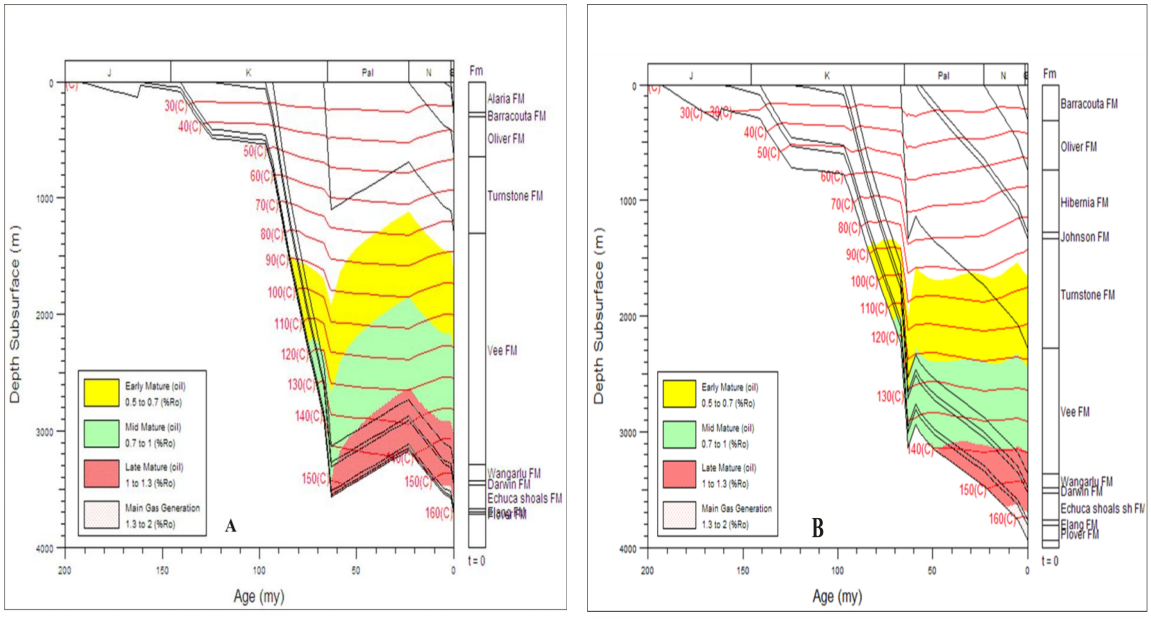

Figure 8. The burial history and isotherms of the wells of Lynedoch Fields, **(A)** The well Lynedoch-1, **(B)** The well Lynedoch-2

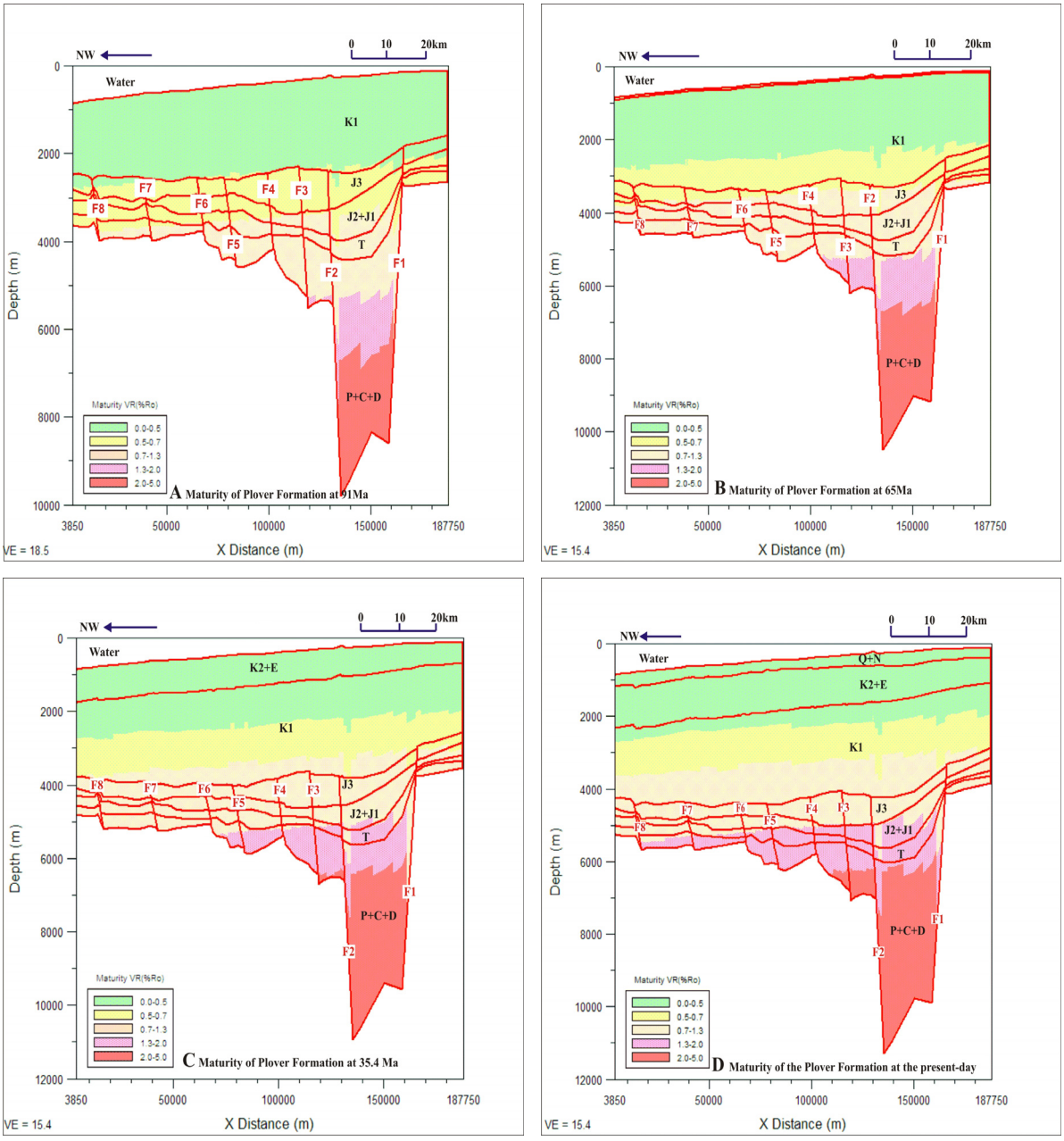

Figure 9. Schematic diagrams showing maturation evolution histories of the Plover Formation source rock along Seismic Line N11809. **(A)** 91 Ma. **(B)** 65Ma. **(C)** 35.4 Ma. **(D)** Present-day 0Ma. G+N = Oliver, Barracouta and Alaria formations, E = Cartier Formation, K2 = Turnstone and Hibernia formations, K1= Darwin, Jamieson, Wangalu and Vee formations, J3 = Elang, Flamingo and Echuca Shoals formations, J2+J1=Plover Formation, T = Malita Formation and P+C+D=Pollard, Mt Goodwin and Hayland Bay formations, while the faults are segregated by red color of the letter F (F1 to F8)

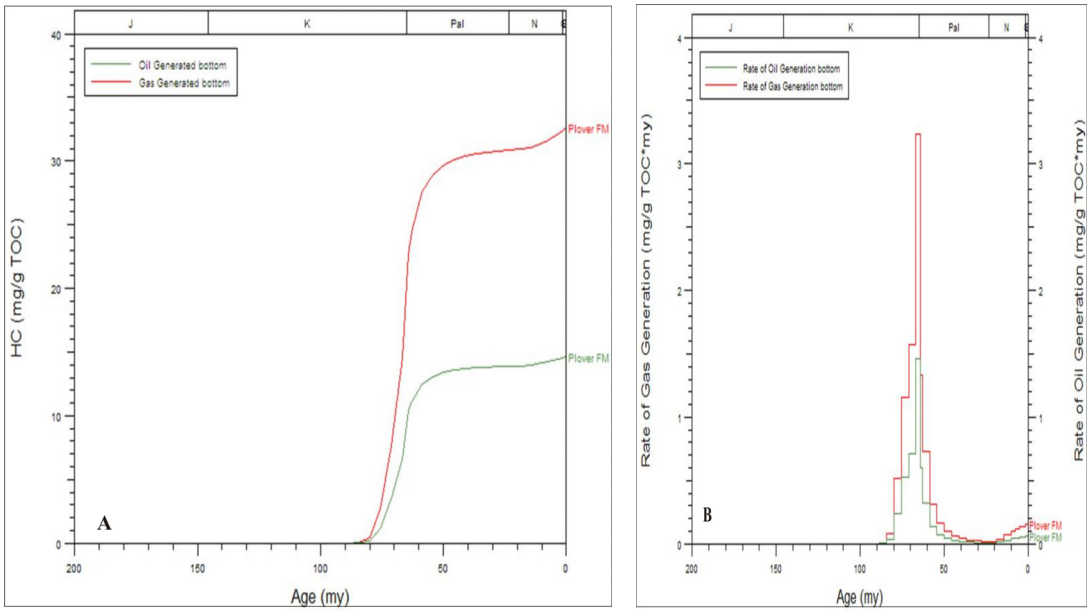

Figure 10. Generation of hydrocarbon history in well lynedoch-1, (**A)** hydrocarbon generating intensity, (**B**) the rate of generation (mg/g TOC.Ma)

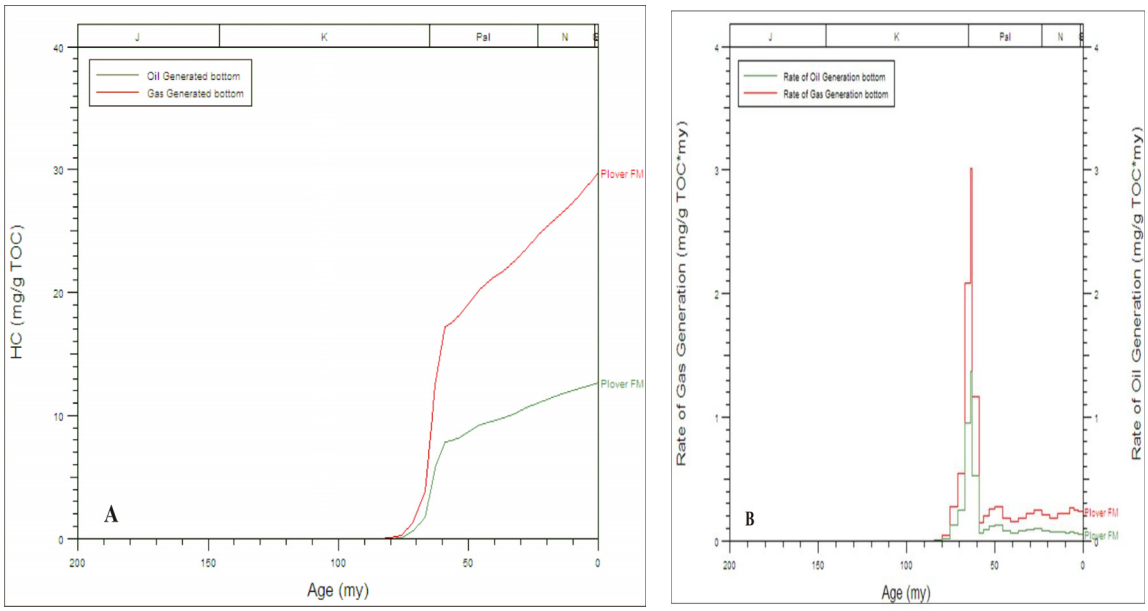

Figure 11. Generation of hydrocarbon history in well lynedoch-2, (**A)** hydrocarbon generating intensity, (**B**) the rate of generation (mg/g TOC.Ma)

5. Conclusions

The formation pressure evolution in Lynedoch Fields is modeled using wells Lynedoch-1 and Lynedoch-2 and Seismic line N11809. The resulted pressure profiles composed of normal pressures, slight excess pressures and intense excess pressures increasing with depth. The magnitude of the excess pressure decreases and dissipates laterally until it meets the normal pressures due to the faults activities (seismic line N11809). The pressure releases are consistent with the tectonic events of the study area and reached its peak during the Late Cretaceous (65Ma). The peak sedimentation and tectonic subsidence rates within the wells of the Lynedoch Fields were also occurred during the Late Cretaceous at 65 Ma. The peak sedimentation and tectonic subsidence rates are in coincidence with the peak oil and gas generation and also with peak of the excess pressure generation from the

same wells. Source rocks of Plover Formation in Lynedoch Fields entered oil window with OM types II&III dominantly and it is in wet-gas window at the present-day. The mechanisms that lead to generation of high excess pressures in the Felds are: 1) high sedimentation rates with rapid subsidence that accompanied low permeability sediments resulted in disequilibrium of the sediment compaction; 2) The hydrocarbon generation that resulted from the process of kerogen transformation into liquid hydrocarbons and cracking into gas. The correspondence between simulated and measured values of both pressure and maturity are significantly good and accurate for both 1D and 2D modeling.

Acknowledgements

We would like to acknowledge that the financial support provided by China University of Geosciences (Wuhan).

References

Burrus, J. (1998). Overpressure models for clastic rocks, their relation to hydrocarbon expulsion: a critical reevaluation, in Law, B. E., Ulmishek, G. F., & V. I. Slavin (ed.). Abnormal pressures in hydrocarbon Environments. *AAPG Memoir, 70*, 35-63.

Cadman, S. J., & Temple, P. R. (2003). *Bonaparte Basin, NT, WA, AC & JPDA, Australia Petroleum Accumulations Report 5* (2nd ed.). Canberra: Geoscience Australia.

Cao Qiang, Ye Jiaren, Wang Wei, Shi Wan Zhong, & Chen Chun Feng. (2009). Preliminary Prediction and Evaluation on Source Rock in Low Exploration Basin: A Case Study from the Northeast Depression, South Yellow Sea Basin, East China. *Journal of Earth Science, 20*(5), 836-847. http://dx.doi.org/10.1007/s12583-009-0070-8

David S. Gordon, & Peter B. Flemings. (1998). Generation of overpressure and compaction-driven fluid flow in a Plio-Pleistocene growth-faulted basin, Eugene Island 330, offshore Louisiana. *Basin Research, 10*, 177-196. http://dx.doi.org/10.1046/j.1365-2117.1998.00052.x

Gluyas, J., & Swarbrick, R. (2004). *Petroleum Geoscience*. (2nd ed.). Oxford, UK: Blackwell Science Ltd.

J, M. Verweij, H, J. Simmelink, R. T. Van Balen, & P. David. (2003). History of petroleum systems in the southern part of the Broad Fourteens Basin. *Netherlands Journal of Geosciences / Geologie en Mijnbouw, 82*(1), 71-90.

Ozkan Huvaza, Hasan Sarikayab, & Taner Isik. (2007). Petroleum systems and hydrocarbon potential analysis of the northwestern Uralsk basin, NW Kazakhstan, by utilizing 3D basin modeling methods. *Marine and Petroleum Geology, 24*, 247-275. http://dx.doi.org/10.1016/j.marpetgeo.2006.11.002

Salvin, V. I., & E. M. Smirnova. (1998). Abnormally high formation pressures: origin, prediction, hydrocarbon field development, and ecological problems, in Law, B. E., Ulmeshek, G. F., & V. I. Salvin (ed.). Abnormal pressures in hydrocarbon environments. *AAPG Memoir, 70*, 105-114.

Sheng He, & Mike Middleton. (2002). Heat flow and Thermal maturity modeling in the Northern Carnarvon Basin, North West Shelf, Australia. *Marine and Petroleum Geology, 19*, 1073-1088. http://dx.doi.org/10.1016/S0264-8172(03)00003-5

Suliman Ahmed Hamid Fadul, Ye Jia Ren, Cao Qiang, & Zhang Yang. (2011). Petroleum System of Evans Shoal Gas Field, northern Bonaparte Basin, Australia. *Journal of American Science, 7*(10), 36-48.

Swarbrick, R. E., & M. J. Osborne. (1998). Mechanisms that generate abnormal pressures: an overview in Law, B. E., Ulmishek, G. F., & V. I. Slavin (ends.) Abnormal pressures in hydrocarbon Environments. *AAPG Memoir, 70*, 13-34.

Thomas, H. A., & Kauerauf, I. (2009). *Fundamentals of Basin and Petroleum Systems Modeling* (2nd printing). Berlin: Springer.

Tissot, B. P., & Welte, D. W. (1978). *Petroleum Formation and Occurrence* (2nd ed.). Berlin: Springer. http://dx.doi.org/10.1007/978-3-642-96446-6

Ye Jiaren, Hairuo Qing, Stephen, L. Bend, & Huirong, Gu. (2007). Petroleum systems in the offshore Hihu Basin on the continental shelf of the East China Sea. *AAPG Bulletin, 91*(8), 1167-1188. http://dx.doi.org/10.1306/02220705158

Earth Science Research; Vol. 1, No. 2; 2012
ISSN 1927-0542 E-ISSN 1927-0550
Published by Canadian Center of Science and Education

Effects of Geometrical Properties of Rectangular Trenches Intended for Passive Isolation in Sandy Soils

Mehrab Jesmani[1], Arash Moghadam Fallahi[1] & Hamed Faghihi Kashani[1]

[1] Department of Civil Engineering, Imam Khomeini International University, Qazvin, Iran

Correspondence: Hamed Faghihi Kashani, Department of Civil Engineering, Imam Khomeini International University, Qazvin, Iran. Tel: 98-912-370-4837. E-mail: Hamed.faghihey@gmail.com

Received: May 2, 2012 Accepted: May 16, 2012 Online Published: June 19, 2012

doi:10.5539/esr.v1n2p137 URL: http://dx.doi.org/10.5539/esr.v1n2p137

Abstract

Wave barriers are placed actively and passively in the ground to reduce the transmission of vibration produced by industry, traffic, train, etc. They include open trenches, in-filled trenches and sheet piles, etc. In most recent studies, the researchers have worked on parameters such as depth, width, length of trenches and also, the distance between the source of vibration and trench in cohesive soils. Most researches are evaluation on screening induced by shallow foundation. In this study the passive isolation has been investigated with the help of open trenches screening against the vibration produced by deep foundations in sandy soils, and the effect of trench angle and radius have been studied. Moreover, the reasons for amplitude increasing before open trenches have been evaluated. Three dimensional finite element analyses (FEM) with ANSYS software are used to achieve an exact parametric study on passive screening. The assumed strains are less than 10^{-3}so the bilinear Elasto-Plastic behavior has been utilized.

Keywords: passive isolation, Rayleigh wave, pile foundation, ANSYS program, open trench, trench radius and trench angle

1. Introduction

It is obvious that vibration occurred by machines, structures, and dynamic systems is destructive; Firstly, because of their inculcating stresses and vibrations which can cause failure or fatigue on nearby structures and, Secondly because of the aggravating effect of vibration on the performance of vibration producer. So isolating structures against vibration created by traffic jam, machine foundations, explosion and earthquake has become an undeniable subject in engineering science.

Wave barrier is one of the solutions for this problem. Installing wave barriers near the sensitive structures is called passive isolation. Regarding to the literature of vibrations (Barkan, 1962) conducted an open trench screen to isolate a building against vibrations created by vehicle traffic and reported that screening is not a workable system for mitigating vibrations. In addition, he mentioned that open trench dimensions are related to the wavelength of the surface motion.

Woods (1967-1970) investigated the screening performance of trench's different parameters by conducting a series of field tests in active and passive isolation. Woods used rectangular open trenches for his research and also defined amplitude Reduction ratio (Arr). Furthermore, his research concluded that the thickness of the passive open trenches has an unimportant effect on their workability. In addition, Woods reported that effective trenches have a depth between $\frac{1}{2}$to$\frac{1}{5}$ times of the Rayleigh wavelength.

Wass (1972) presented that amplitude is reduced by screening when the frequency is high. Aboudi (1973) worked on the ground surface response of wave barriers affected by time-dependent loading in an elastic half-space with the help of finite difference method (FDM). Woods et al. (1974) evaluated the screening efficiency of hollow cylindrical piles as a passive system in a half-space model.

Haupt (1977) and G. Segol et al. (1978) investigated the effect of shape and trench dimension on amplitude reduction by the help of finite element method (FEM). Liao and Sangrey (1978) examined the effect of piles as a wave barrier against Raleigh waves with high wavelength. They announced that in the case of impractical trenches, piles are the best choice for reducing the wave amplitude. In addition, Fuykui and Matsumoto (1980)

considered the open trench efficiency on reduction of Rayleigh, P, SV and SH waves amplitude by using a two-dimensional method through finite difference method (FDM).

May and Bolt (1982) contemplated on the utilization of open trenches against compression and shear waves under the assumption of plane strain condition. Beskos et al. (1985-1991) worked on a complete series of numerical models which contains in-filled and open trenches isolation in continuously homogeneous and non-homogenous soils under the assumption of plane strain condition and by using boundary element method (BEM). They reported that if the depth of soil layer be less than 2.5 times that of Raleigh wavelength, the depth of trench must be at least2 times that of layer thickness.

Ahmad and Al-Hussaini (1991-2000) examined the effectiveness of active and passive isolation of circular open trenches. Besides, they investigated the effect of depth, width and location of the trenches by the usage of BEM method. Yeh et al. (1997) assessed the efficiency of open and in-filled trenches on reducing the vibration induced by train movement. This research showed that using trench barriers against vibration with low frequency is useless.

Kattis et al. (1999) examined the isolation of open trenches, in-filled trenches and pile barriers against the vibration produced by machinery foundations. Moreover, Shirvasta et al. (2002) explored the efficiency of open and in-filled trenches for screening Rayleigh waves by using 3D FE model.

Shen-Haw and Hung-Ta (2004) worked on the open and in-filled trenches as barriers for vibrations occurred by train movement. The results show that the adjacent building foundations have an important effect on vibration reduction.

Adam and Estroff (2005) deliberated the efficiency of open and in-filled trenches in reducing the six-storey building vibrations due to passing trains by using a two-dimensional FEM analysis. The results show that these barriers could reduce 80 percent of the vibrations. Also, they reported that open trenches are more effective in vibration reduction than in-filled trenches. El Nagger and Chehab (2005) conducted a numerical research using two-dimensional model to evaluate the screening effectiveness of open and in-filled trenches on reducing the pulse-induced waves of shallow foundations resting on an elastic half-space.

Celebi et al. (2006) with the help of finite element method (FEM) showed that using an open trench has an important effect on reduction of vibration amplitudes induced by passing trains. In addition, they presented two mathematical models and numerical techniques for solving problems related to wave propagation. Gaoet al. (2006) inspected the effect of pile barriers designed in rows as a passive screening by a three-dimensional model. The results show that piles with small diameter act like open trenches in reducing vibrations. Furthermore, they show that the distances between piles in a row are more important than the distances between rows of piles. Karlstorm and Bostrom (2007) investigated the opus of open trenches on reduction of wave amplitude induced by trains. They located these trenches in the both side of a railway and reported that these trenches could noticeably reduce the vibration amplitude especially at frequencies in the range of 2-8 Hertz.

Tsai et al. (2007) worked on active isolation provided by pile barriers against vibration induced by shallow foundations under vertical loading. They investigated the effect of pile dimensions, pile distances, pile materials and screening location. They reported that steel pipe is generally better than other solid piles, and a concrete hollow pile barrier can be ineffective because of its stiffness.

Jesmani et al. (2008) studied the effect of geometrical properties of an open trench intended for active isolation of deep foundations resting on a homogenous half-space cohesive soil by using a three-dimensional finite element method (FEM). In addition, Jesmani et al. (2011) conducted a research to evaluate the effect of geometrical properties of an open trench intended for passive isolation of deep foundation in sandy soils. Moreover, in this research the effect of soil properties and loading time has been investigated by using two-dimensional model in finite element method (FEM).

From the above review, most researches have focused on in-filled and open trenches as an active barrier against vibrations induced by shallow foundations. In addition, the effect of geometrical properties of trenches has been investigated such as depth, width, location, etc.

In this study, the ground passive isolation of deep foundations have been studied by open trenches in sandy soils and also the effect of two important parameters; trench radius and trench angle, have been evaluated.

2. Propagation and Attenuation Characteristics of Deep Foundation

The form of wave propagation is different in shallow foundations and deep foundations. Attewell and Farmer (1973) worked on wave propagation of deep pile foundations. Their results are depicted in Figure 1. The waves

which are induced by deep pile foundations in the ground are elastic waves in the form of shear waves, surface waves and compression waves. Each of these waves propagates differently; Shear and compression waves propagate radially in all directions from the pile toe on a spherical wave front, but Raleigh waves and surface waves propagate radially on a cylindrical wave front along the surface. Because of the geometrical damping, both body waves and Rayleigh waves decrease in amplitude by increasing the distance.

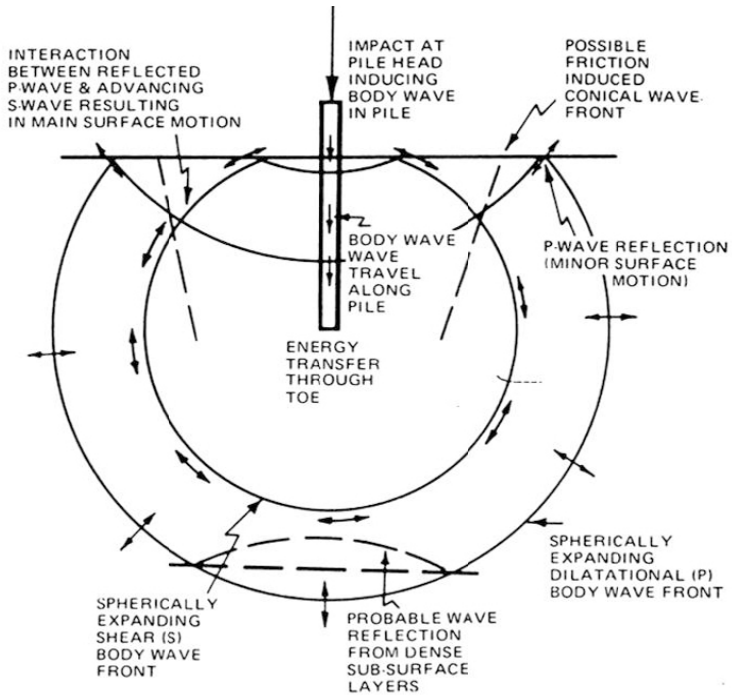

Figure 1. Wave propagation induced by deep foundation (Attewell & Farmer, 1973)

Wolf (1994) reported that the attenuation of ground vibrations in the far field is inversely related to the square of the area of the wave front; r^{-n} with r the distance and n the geometrical attenuation coefficient. The second parameter is equal to 0.5, 1 and 2 for surface waves propagating on a cylindrical wave front, body waves propagating on a spherical wave front and body wave propagating along the surface respectively.

3. Problem Definition, Assumptions, and Loading Condition

A rigid concrete (Table 1) foundation of height 1.5m and of radius 3.5 m (Rf), with 9 piles of diameter 70 cm, length D defined for this problem. Besides, this foundation is rested on a sandy soil layer (Tables 2 and 3) with a limited thickness of length Ls and thickness Hs, underlain by a hard stratum. This foundation is subjected to a harmonic (f=2HZ) compressive and concentrated load P0 sin (ωt) with P0=29430 Pa (or 0.3 kg/cm^2).

Table 1. Concrete properties

	Young's Modulus	Poisson's Ratio	Density	Material Damping
	E_s	υ	ρ	β_s
Concrete	$(\frac{N}{m^2})$	-	$(\frac{kg}{m^3})$	-
(1)	2E+10	0.2	2500	2%

An annular open trench of depth H and width w is located at the distance L which is the shortest distance from a point on the circumference of circular foundation and the annular trench. Moreover, the isolated building is located at the center of the annular trench with the radius of R and θ (the degree measure of the trench arc) (Figures 2, 3 and Table 4).

The foundation is assumed to be restrained against horizontal movement and the soil is under assumption of being isotropic and homogenous with linear soil behavior for low deformation.

Table 2. Static properties of the sandy soil

Static Properties	Young's Modulus	Poisson's Ratio	Specific Weight	Density	Material Damping	Soil Mechanical Parameters	
	E_s	υ	γ_s	ρ	β_s	C	φ
Soil	$(\frac{kN}{m^2})$	-	$(\frac{kN}{m^3})$	$(\frac{kg}{m^3})$	-	$(\frac{kN}{m^2})$	Degree
(1)	50 000	0.35	19	1936.80	5%	10	40

Table 3. Dynamic properties of the sandy soil

Dynamic Properties	G_s *Shear modulus*	V_s *Shear wave velocity*	K $V_r = K.V_s$	V_r *Rayleigh wave velocity*
Soil	$(\frac{kN}{m^2})$	$\frac{m}{s}$	-	$\frac{m}{s}$
(1)	33 333	131	0.936	123

Table 4. Geometric properties of the trench and deep foundation

Explanation	Value	Unit
Trench Depth(H)	20	m
Pile Length(D)	10	m
Trench Angle (θ)	90,120,150,180	°
Trench Width(w)	1	m
Trench Radius (R)	15,20,25	m
Trench Location(L)	R,2R,3R	----

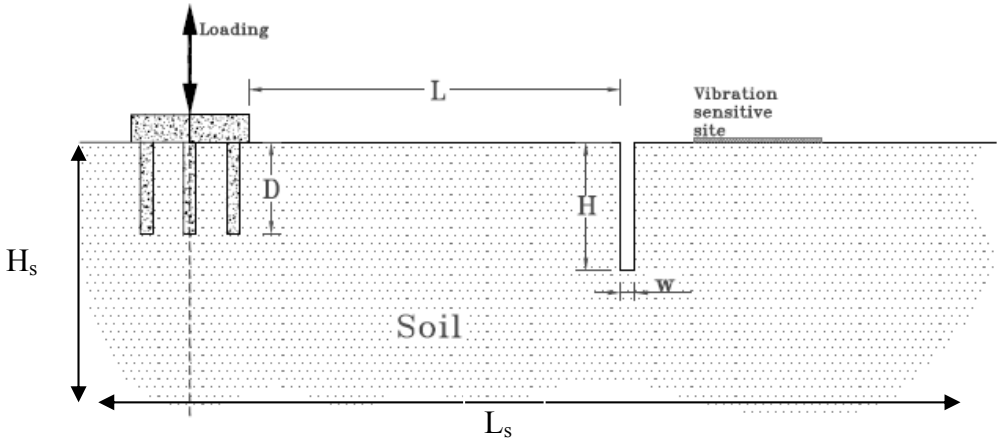

Figure 2. Problem definition – Section of passive isolation by open trench

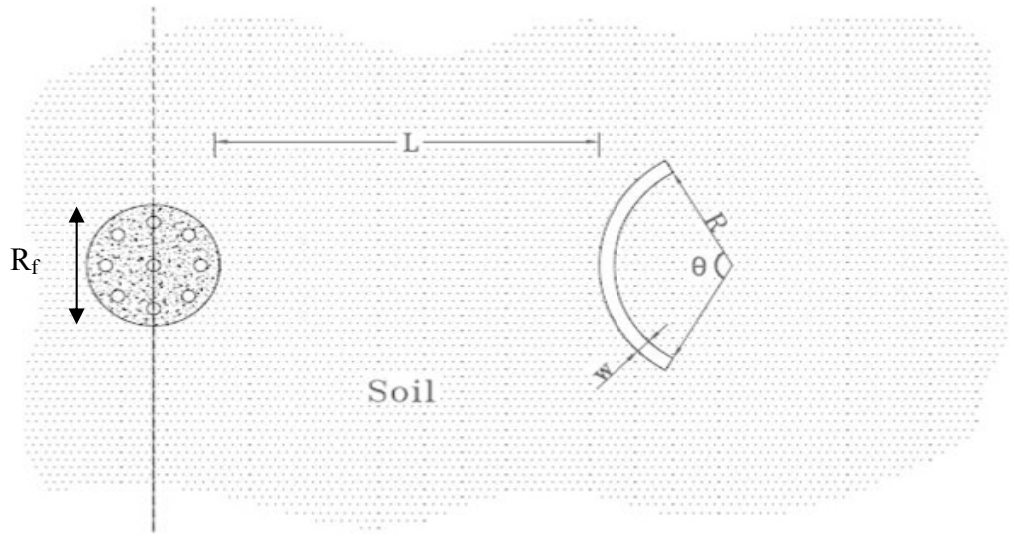

Figure 3. Problem definition – Plan of passive isolation by open trench

4. Geometric Model

For reduction in computation time, and with the help of axisymmetrey in plan, only $\frac{1}{4}$ of the actual model has been built in the model (Figure 4). In order to eliminate the effect of wave reflection, the depth of model has been taken more than 30 meter (Jesmani, 2008).

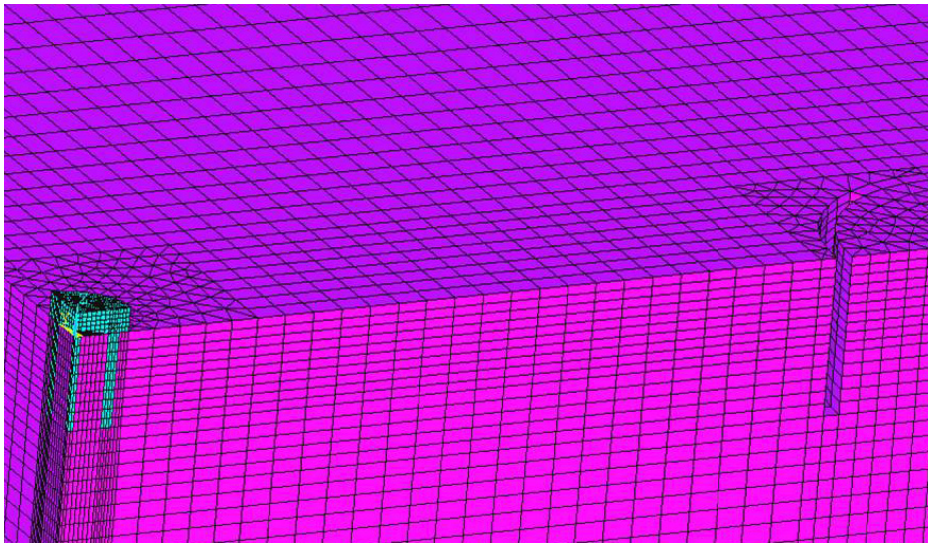

Figure 4. Model geometry of passive isolation by open trench

5. Finite Element Model

The most effective properties in evaluating wave propagation in low strains are damping, Poisson's ratio, stiffness and density. Because the predicted strains have been less than 10^{-3}, abilinear Elasto-Plastic model is applied to evaluate the soil behavior. In addition in this condition shear modulus is also an essential parameter (Figure 5) (Ishihara, 1996).

To investigate the behavior of the model such as sliding or any possible separation at the soil structure interface, three-dimensional surface-to-surface contact elements (TARGE 170, CONTA 174) have been employed. In the places with high concentration of stress or places needed to be focused for strains computation, such as foundation, three-dimensional elements Solid 95 (Figure 6) have been used. This element defined by twenty nodes having three degrees of freedom in the directions of x, y and z at each node.

Normal contact stiffness factor was assumed to be equal to 1 and 0.6 was taken to maximum contact friction coefficient. Solid 45 (Figure 7) is employed to model the soil in places that weren't play an important role in the results. This element is defined by eight nodes which have three degrees of freedom in each node.

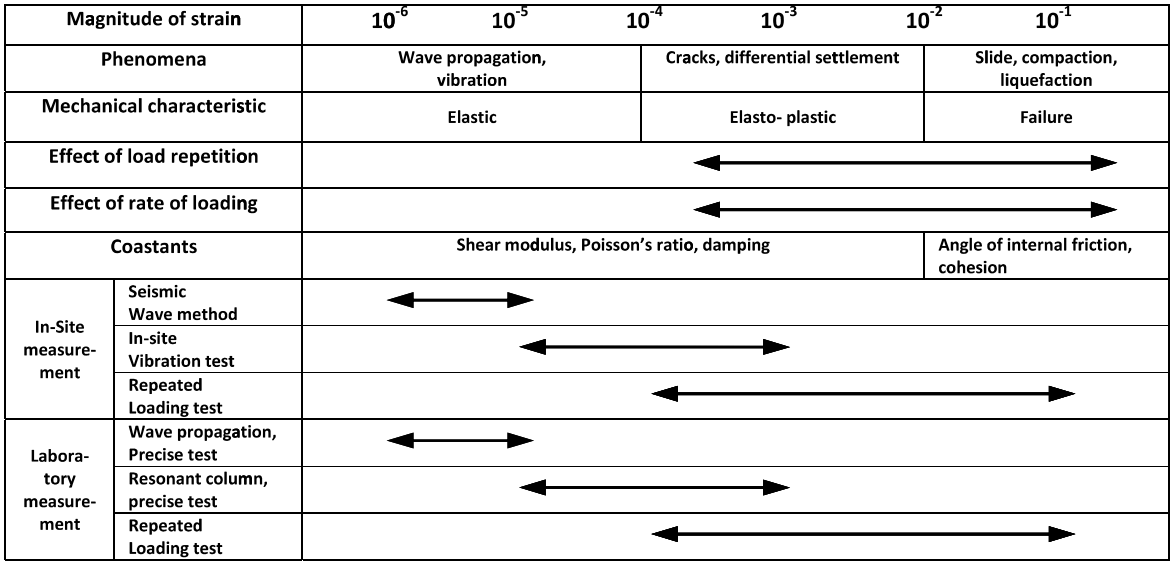

Figure 5. Soil behavior models in accordance with magnitude of strain (Ishihara, 1996)

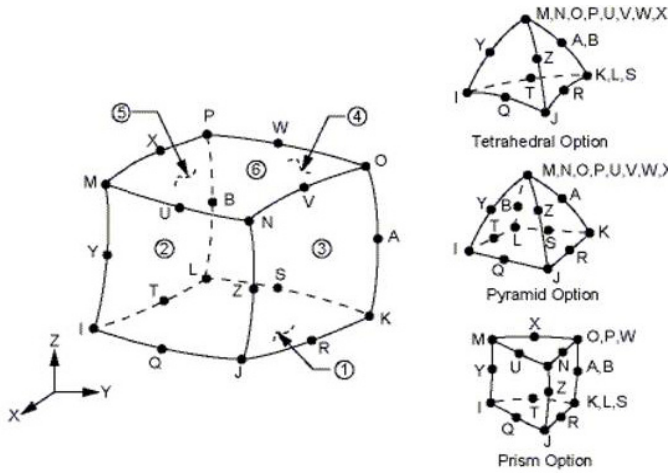

Figure 6. Twenty-node element (SOLID95)

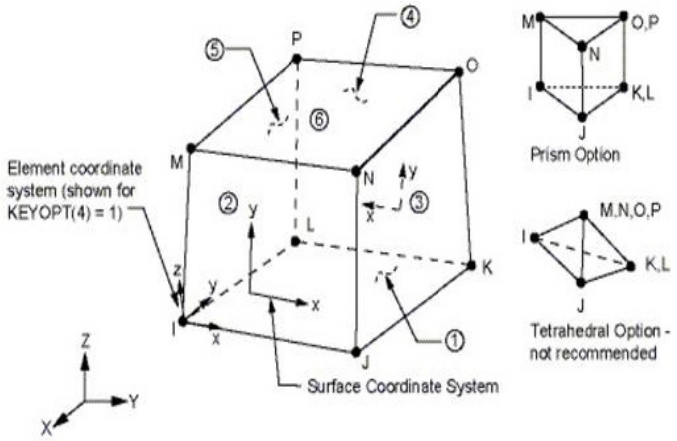

Figure 7. Eight-node Element (SOLID45)

6. Meshing and Boundary Condition

The mesh dimension has been taken 0.25 times of the shortest Rayleigh wavelength with loading frequency of 50HZ near the foundation. In addition, 1.5 meter length of element has been taken for the longest Rayleigh wavelength induced by low loading frequency of 2HZ.

The above range for the mesh dimension is between $\frac{1}{8}$ to $\frac{1}{35}$of Rayleigh wavelength, and in accordance with the suggestions of researchers this range is acceptable. By increasing the distance from the trench outer edge, the element size increases. The boundary nodes are restrained in X and Y directions. In accordance with the necessity of hard stratum underlaid the soil layer, it assumed to be restrained in three directions. The meshing model is shown in Figures 8 and 9.

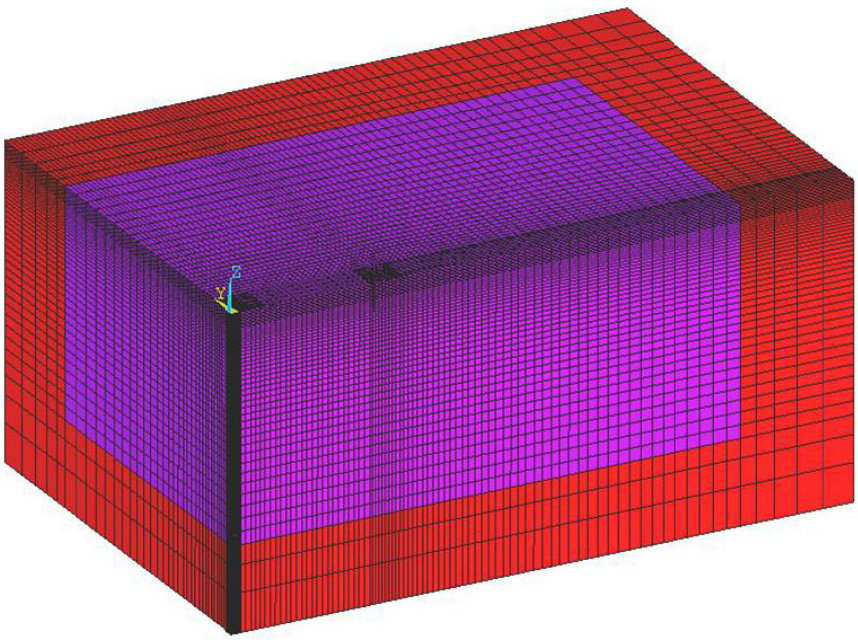

Figure 8. Meshing and boundary condition of model

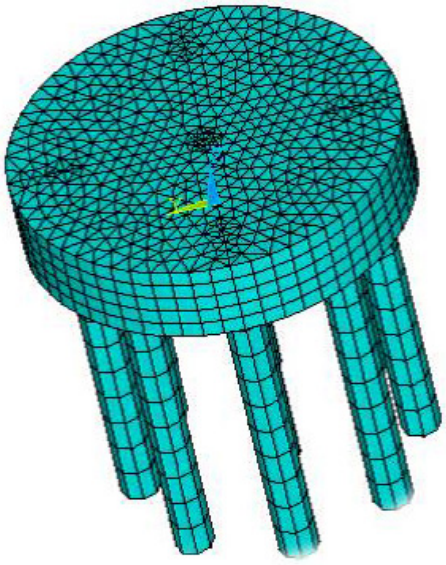

Figure 9. Meshing of the Deep Foundation

An amplitude reduction ratio, Arr, first proposed by Woods (1968-1969), to evaluate the trench effectiveness. Arr is the ratio of amplitude with trench and amplitude without trench.

$$Arr = \frac{\text{Amplitude with trench barrier}}{\text{Amplited without trench barrier}} \quad (1)$$

Aarr is the average of amplitude reduction ratio (Arr), and it is employed for investigating the screening effectiveness. Furthermore, Aarr is calculated along radial lines behind the trench and in the length of one Rayleigh wavelength.

$$Aarr = \frac{1}{n} l \int_{i=0}^{nl} Arrdi \quad (2)$$

i = is the distance between the trench and the outer edge of the foundation.

n = is the number of points along the distances

7. Model Verification

In order to investigate the validity of the obtained results from the current three-dimensional study, we compare the two-dimensional results of our study with the model of Beskoset al. (1986a) which was defined under the assumption of plain strain in two dimensional model by using BEM method and also, the researches of Ahmad and Al-Hussaini (1991) and EL Naggar and Chehab (2005) which have done by using ANSYS software (version 5.7). Finally, we developed this comparison for three-dimensional of current model. Figure 10exhibits an agreement between the current FEM model and the above researches.

The vertical and horizontal axis illustrates the Arr (Woods, 1968-1969) and trench location normalized by Rayleigh wavelength respectively.

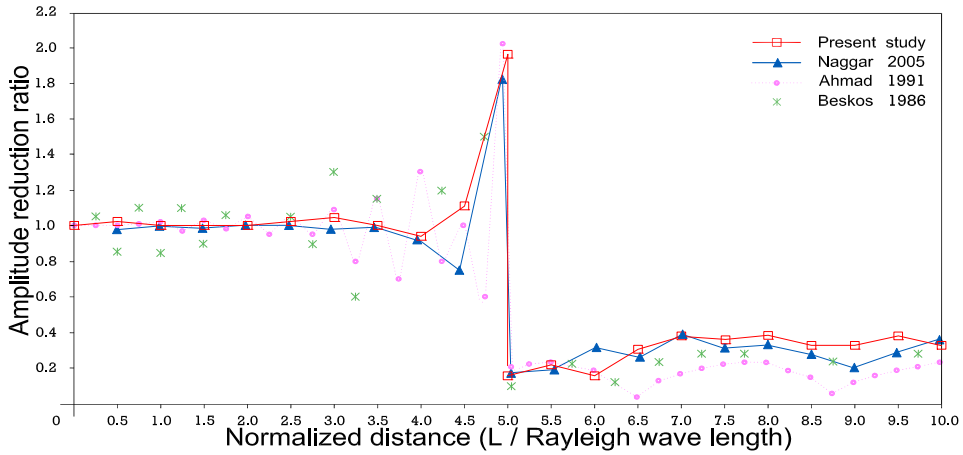

Figure 10. Comparative diagram

8. Results and Discussion

8.1 The Evaluation of Amplitude Increasing before Trench

As it can be seen in Figures 11 through 13, near the trench there is a dramatic increase in Arr. This result is caused by the following reasons:

1) When waves approach to an open trench which has an impedance coefficient equal to zero, they will be reflected with the same amplitude. This will emphasize the wave concentration near trench.

2) Excavating and removing the material from an open trench in actual situation causes a free movement for unrestrained trench edges because of its low stiffness. In conclusion, the wave amplitude near the trench edges increases in comparison with a model without open trench (Arr>1) (Jesmani et al., 2011).

In addition, as it can be seen in the Figures11 through 13, by increasing the trench angle, Arr increases. This issue is the result of increasing free nodes because of increase in trench dimension which increments the quantity of reflected waves.

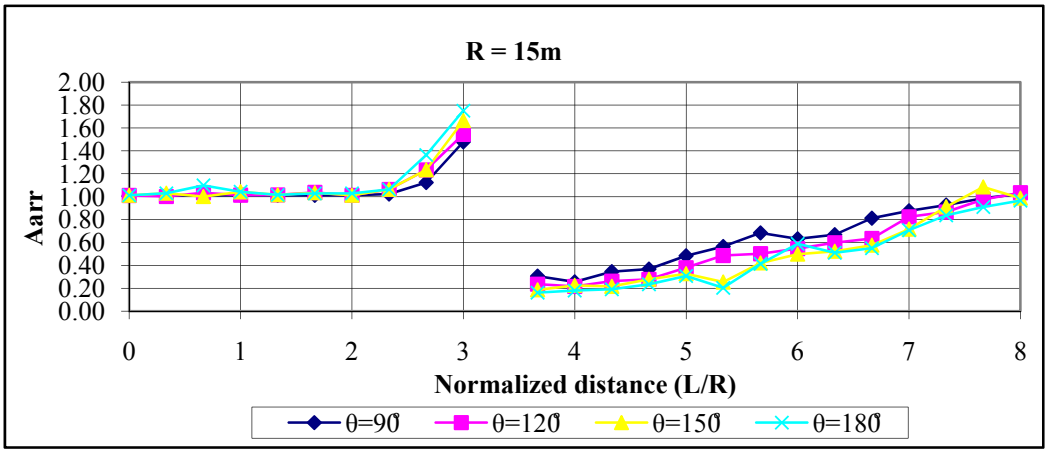

Figure 11. Amplitude Increasing before Trench (D=10m, H=20m, R=15m, Loading frequency=2Hz)

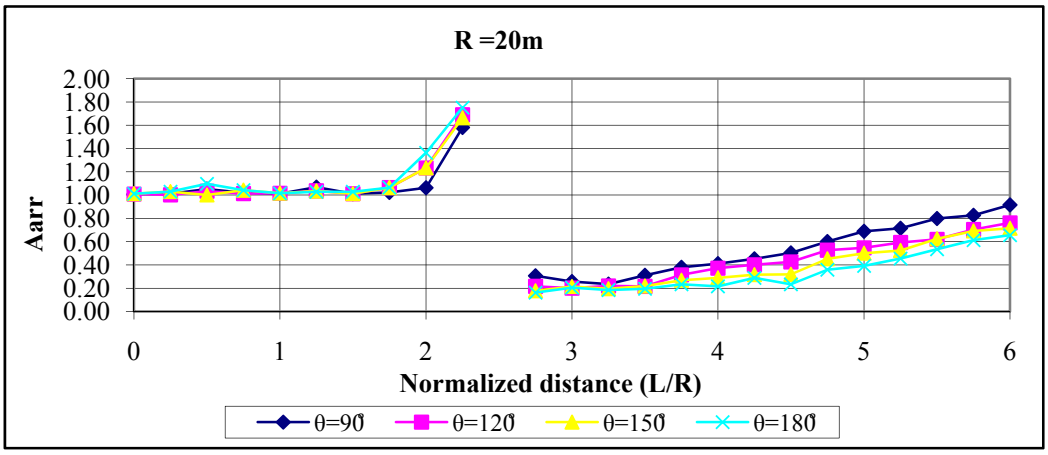

Figure 12. Amplitude Increasing before Trench (D=10m, H=20m, R=20m, Loading frequency=2Hz)

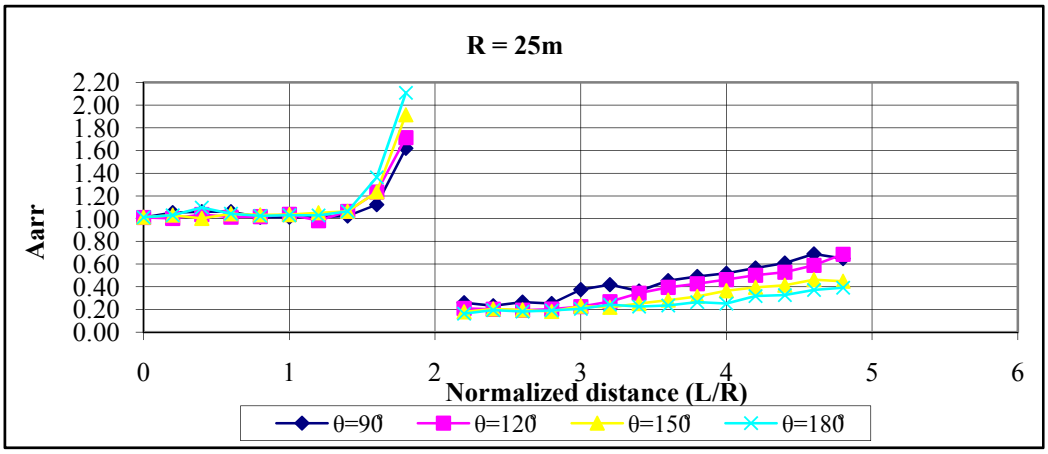

Figure 13. Amplitude Increasing before Trench (D=10m, H=20m, R=25m, Loading frequency=2Hz)

8.2 The Effect of Open Trench Angle

The effect of trench angle on Aarr is demonstrated in Figures14 through 16 for L= R, 2R and 3R middle distances. Generally, increasing the trench angle leads a decrease in Aarr. It also observed that the reduction rate in every curve decreases from the trench angle bigger than θ = 150°. Thus θ = 150° is highly recommended for the optimal open trench angles.Theequations that have been presented near curves (because of the low coefficient of x^2) approximately show a linear behavior between Aarr and trench angle. In addition, it is noticeable that increasing the trench angle has the most effect on the rate reduction of studied points in the distance of 2R from the vertex of the trench. However, this fact is in its lower value in the distance of R.

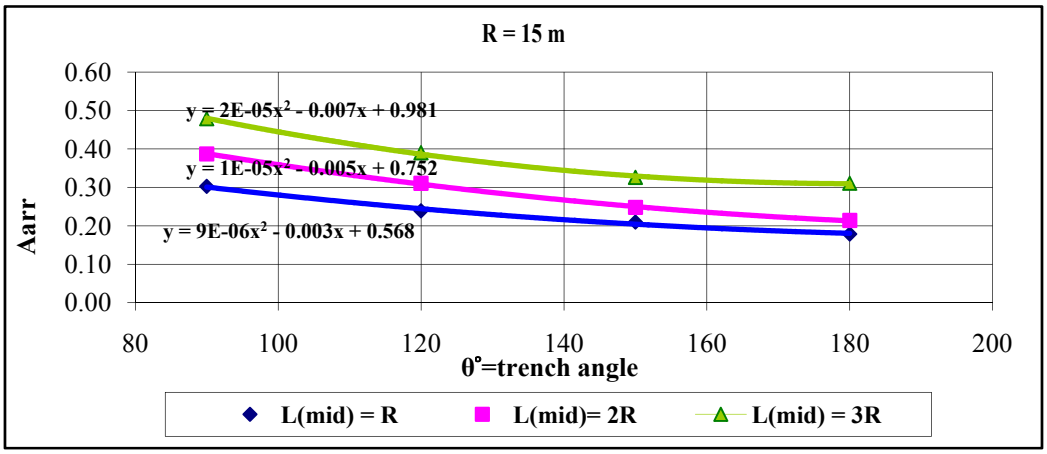

Figure 14. The Effect of Trench Angle (D=10m, H=20m, R=15m, Loading frequency=2Hz)

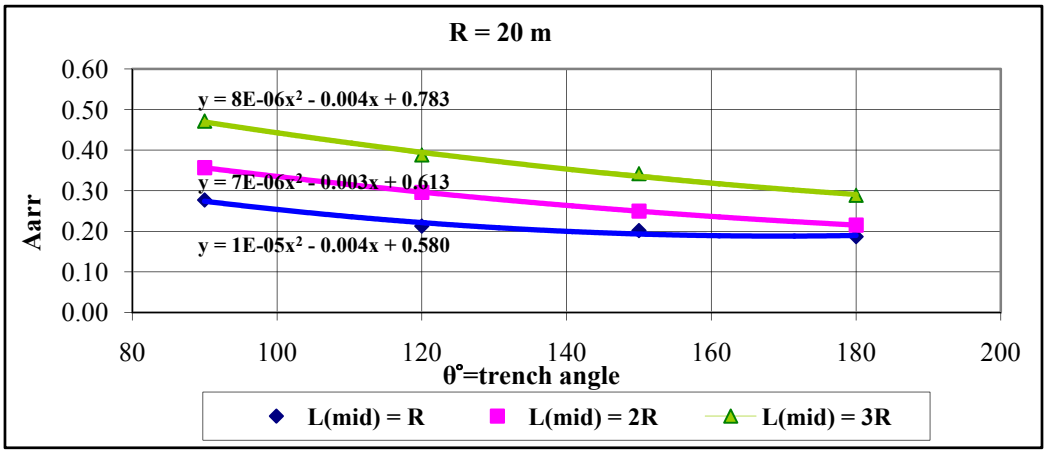

Figure 15. The Effect of Trench Angle (D=10m, H=20m, R=20m, Loading frequency=2Hz)

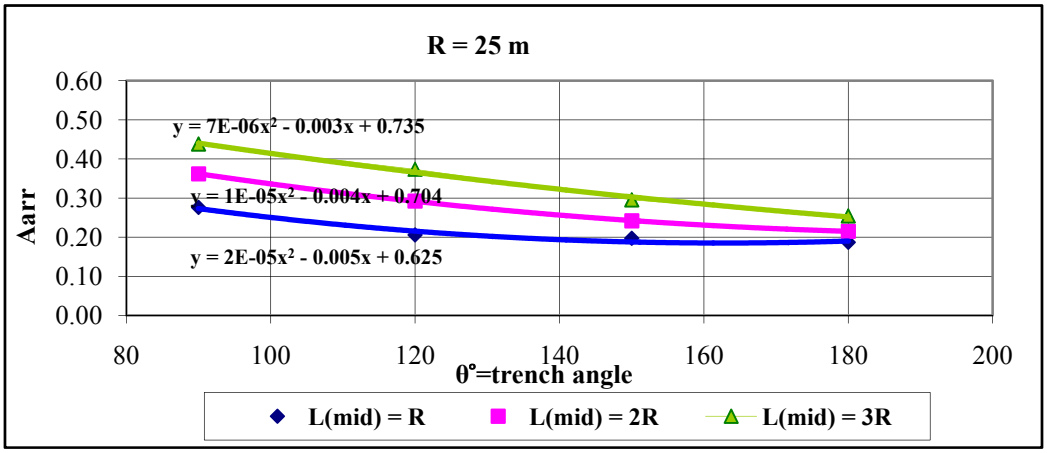

Figure 16. The Effect of Trench Angle (D=10m, H=20m, R=25m, Loading frequency=2Hz

8.3 The Effect of Open Trench Radius

The effect of trench radius on Aarr is illustrated in Figures 17 through 20 for L=R, 2R and 3R middle distances. As it can be seen in these figures, in a constant trench angle, increasing trench radius doesn't have an important effect on Aarr. Actually, in accordance with normalized distances by trench radius, the effect of trench radius

increasing has been omitted. It can also be inferred that by increasing the trench radius, longer length of wave path will be protected.

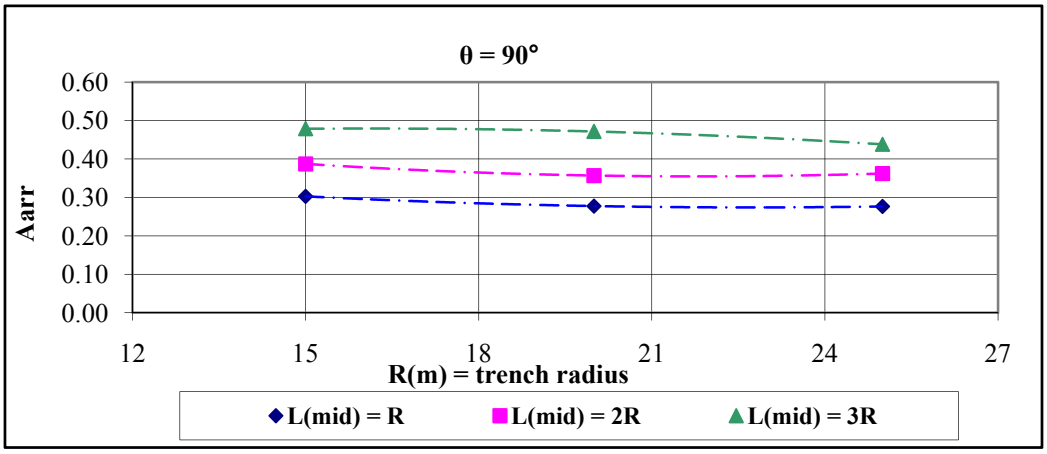

Figure 17. The Effect of Trench Radius (D=10m, H=20m, θ =90° , Loading frequency=2Hz)

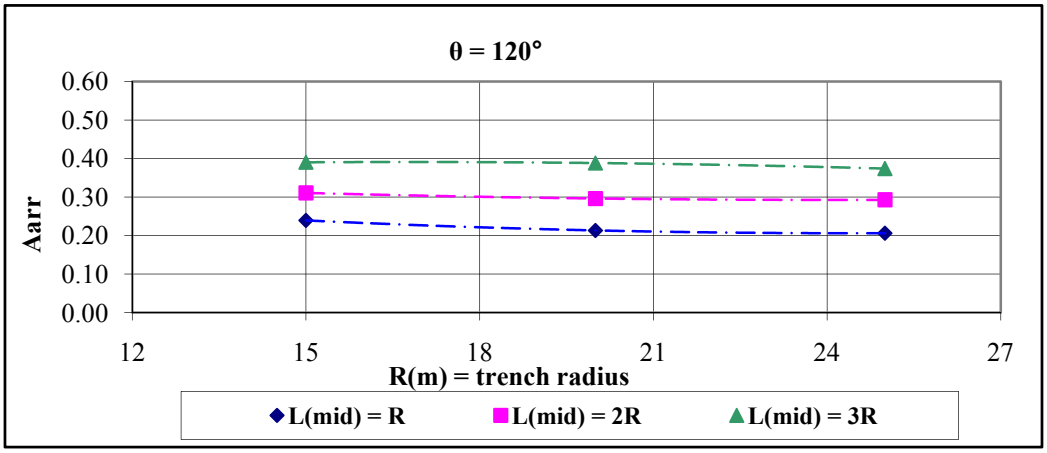

Figure 18. The Effect of Trench Radius (D=10m, H=20m, θ =120°, Loading frequency=2Hz)

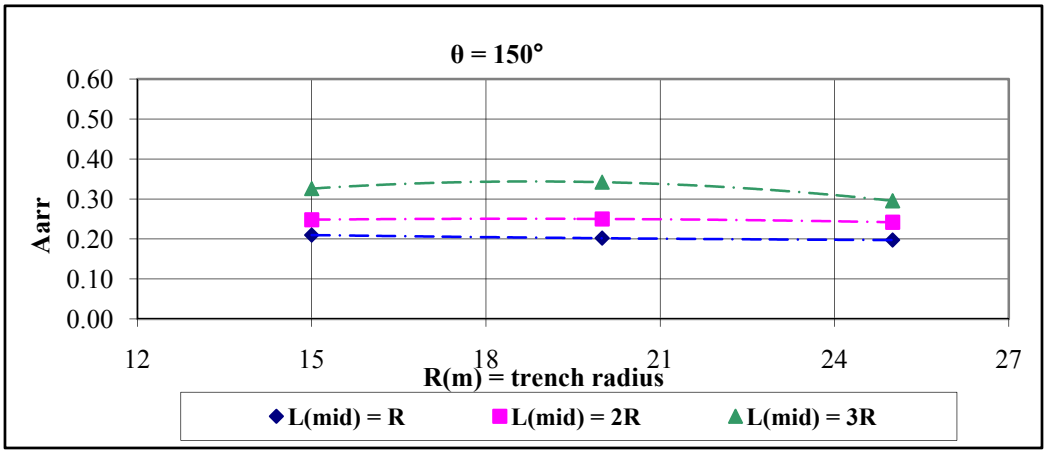

Figure 19. The Effect of Trench Radius (D=10m, H=20m, θ =150°, Loading frequency=2Hz)

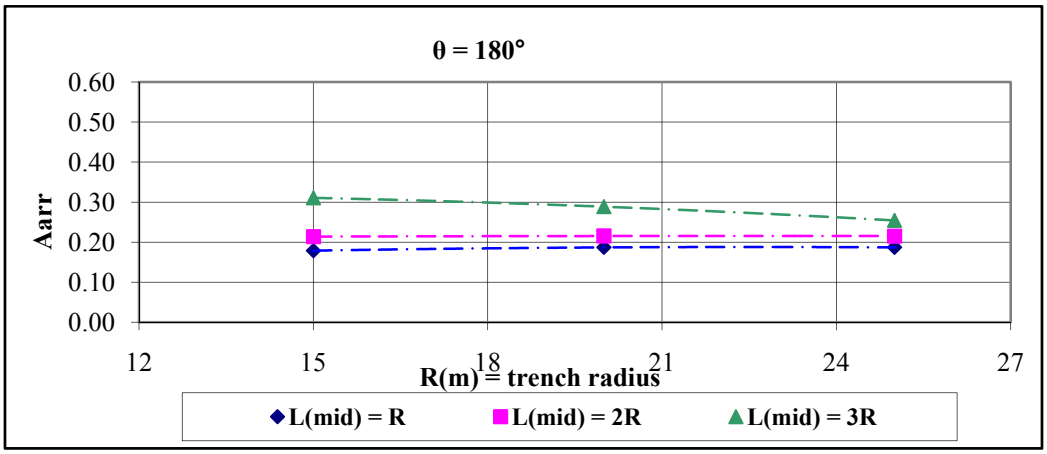

Figure 20. The Effect of Trench Radius (D=10m, H=20m, θ =180°, Loading frequency=2Hz)

9. Conclusions

A three-dimensional finite element analysis of a vibration of deep foundation has been taken in this research to evaluate the effects of passive isolation on the reduction of wave amplitude and the following conclusions can be extracted.

- Increasing the trench radius has a direct effect on the protected area. Hence, by increasing the trench radius a bigger area will be protected.
- By keeping the trench angle unchangeable, increasing in trench radius doesn't have a significant effect on wave amplitude reduction. Therefore, it is better to investigate the interaction of trench radius and angle simultaneously and put the responsibility of wave reduction to the height and geometric properties of trench related to the trench length.
- Generally, increase in trench angle cause a decrease in average amplitude reduction ratio (Aarr).
- Trench angle =150° is highly recommended for the optimal open trench angles.
- The behavior of wave amplitude reduction versus the increase of trench angle is approximately linear.

References

Aboudi, J. (1973). Elastic Waves in Half-Space with thin Barrier. *Journal of EngMech, ASCE, 99*(1), 69-83.

Adam, M., & Estorff, O. (2005). Reduction of Train-Induced Building Vibrations by Using Open and Filled Trenches. *Computers and Structures, 83*, 11-24. http://dx.doi.org/10.1016/j.compstruc.2004.08.010

Ahmad, S., & Al-Hussaini, T. M. (1991). Simplified Design for Vibration Screening by Open and In-Filled Trenches. *Journal of Geotechnical Engineering, ASCE, 117*(1), 67-88.

Ahmad, S., & Al-Hussaini, T. M. (1996b). Active Isolation of Machine Foundations by In-Filled Trench Barriers. *Journal of Geotechnical Engineering, ASCE, 122*(4), 288-294. http://dx.doi.org/10.1061/(ASCE)0733-9410(1996)122:4(288)

Ahmad, S., & Al-Hussaini, T. M. (2000). Numerical and Experimental Studies on Vibration Screening by Open and In-Filled Trench Barriers. International Workshop on Wave Propagation Moving Load and Vibration Reduction, Edited by Chouw, N., & Schemid, G. WAVE2000, Rotterdam, Balkema, 241-250.

Ahmad, S., Al-Hussaini, T. M., & Fishman, K. L. (1996a). Investigation on Active Isolation of Machine Foundations by Open Trenches. *Journal of Geotechnical Engineering, ASCE, 122*(6), 454-461. http://dx.doi.org/10.1061/(ASCE)0733-9410(1996)122:6(454)

Attewell, P. B., & Farmer, I. W. (1973). Attenuation of Ground Vibrations from Pile Driving. *Ground Engineering, 6*(4), 26-29.

Barkan, D. D. (1962). *Dynamics of Bases and Foundations*. New York, NY: McGraw-Hill.

Beskos, D. E., Dasgupta, G., & Vardoulakis, I. G. (1986a). Vibration Isolation Using Open or Filled Trenches. Part 1: 2D Homogeneous Soil. *Computational Mechanics, 1*(1), 43-63. http://dx.doi.org/10.1007/BF00298637

Beskos, D. E., Dasgupta, G., & Vardoulakis. I. G. (1985). Vibration Isolation of Machine Foundations. *Vibration*

Problems in Geotechnical Engineering, Edited by Gazetas, G., & Selig, E. T. ASCE, NY. 138-151.

Beskos, D. E., Leung, K. L., & Vardoulakis, I. G. (1986b). Vibration Isolation of Structures from Surface Waves in Layered Soil. Recent Application in Computational Mechanics, ASCE, NY. 125-140.

Beskos, D. E., Leung, K. L., & Vardoulakis, I. G. (1990). Vibration Isolation Using Open or Filled Trenches. Part 3: 2D Non-Homogeneous Soil. *Computational Mechanics, 7*(1), 137-148.

Beskos, D. E., Leung, K. L., & Vardoulakis, I. G. (1991). Vibration Isolation by Trenches in Continuously Non-Homogeneous Soil. By the BEM. *Soil Dynamics and Earthquake Engineering, 10*(3), 172-179. http://dx.doi.org/10.1016/0267-7261(91)90030-4

Celebi, E. (2006). Three-Dimensional Modeling of Train-Track and Sub-Soil Analysis for Surface Vibrations due to Moving Loads. *Applied Mathematics and Computation*, 1-22.

Celebi, E., Firat, S., & Cankayac I. (2006). The Effectiveness of Wave Barriers on the Dynamic Stiffness Coefficient of Foundations Using Boundary Element Method. *Applied Mathematics and Computation, 180*(2), 683-699. http://dx.doi.org/10.1016/j.amc.2006.01.008

EL Naggar, M. H., & Chehab, A. G. (2005). Vibration Barriers for Sock-Producing Equipment. *Canadian Geotechnical Journal, 42*, 297-306. http://dx.doi.org/10.1139/t04-067

Fuykui, M., & Matsumoto, Y. (1980). Finite Difference Analysis of Rayleigh Wave Scattering at a Trench. *BullSeismolSocAmer, ASCE*, 2051-2069.

G. Segol, P. C. Y. Lee, & J. F. Abel. (1978). Amplitude Reduction of Surface Waves by Trenches. *Journal of Soil Mechanics and Foundations Division, ASCE, 104*, 621441.

Gao, G. Y., Li, Z. Y., Qui, C. H., & Yue, Z. Q. (2006). Three-Dimensional Analysis of Piles as Passive Barriers for Ground Vibration Isolation. *Soil Dynamics and Earthquake Engineering, 26*, 1015-1027. http://dx.doi.org/10.1016/j.soildyn.2006.02.005

Haupt, W. A. (1977a). Isolation of Vibrations by Concrete Core Walls. Proceeding 9th International Conference on Soil Mechanics an Foundation Engineering, Tokyo, Japan, 2, paper no. 251.

Haupt, W. A. (1977b). Surface Waves in non-homogeneous half space Proc. *DMSR77 Karlsruhe 1*, 355-367.

Karlstorm, A., & A. Bostrom. (2007). Efficiency of Trenches Along Railways for Trains Moving at Sub or Supersonic Speeds. *Soil Dynamics and Earthquake Engineering, 27*, 625-64. http://dx.doi.org/10.1016/j.soildyn.2006.12.005

Kattis, S. E., Polyzos, D., & Beskos, D. E. (1999). Vibration Isolation by a Row of Piles Using a 3D Frequency Domain BEM. *International Journal for Numerical Methods in Engineering, 46*, 713-728. http://dx.doi.org/10.1002/(SICI)1097-0207(19991020)46:5<713::AID-NME693>3.0.CO;2-U

Liao, S., & Sangrey, D. A. (1978). Use of Piles as Isolation Barriers. *Proc., ASCE, 104*, 1139-1152.

M. Jesmani, A. Hamissi, M. Kamazare, & R. Sadehi Vileh. (2011). Optimum Geometrical Properties of Active Isolation. *Proceeding of the institution of civil engineering*, Vol. 164.

M. Jesmani, A. Moghadam Fallahi, & H. Faghihi Kashani. (2011). Study of Passive Isolation of Deep Foundation in Sandy Soil by Rectangular Trenches. *EJGE Journal, 16*, Bundle Q, 1297-1317.

M. Jesmani, M. R. Shafie & R. Sadeghi Vileh. (2008). Finite Element Analysis of Active Isolation of Deep Foundation in Clayey Soil by Rectangular Trenches. *EJGEJournal , 13*, Bundle E, 1-16.

May, T. W., & Bolt, B. A. (1982). The Effectiveness of Trenches in Reducing Seismic Motion. *Journal of Earthquake Engineering and Structural Dynamics, 10*(2), 195-210. http://dx.doi.org/10.1002/eqe.4290100203

Shen-Haw Jo, & Hung-Ta, Lin. (2004). Analysis of Train-Induced and Vibrations and Vibration Reduction Schemes Above and Below Critical Rayleigh Speeds by Finite Element Method. *Soil Dynamics and Earthquake Engineering, 24*, 993-1002. http://dx.doi.org/10.1016/j.soildyn.2004.05.004

Shirvasta, R. K., & Kameswara Rao, N. S. V. (2002). Response of Soil Media due to Impulse Loads and Isolation Using Trenches. *Soil Dynamics and Earthquake Engineering, 22*, 695-702. http://dx.doi.org/10.1016/S0267-7261(02)00060-X

Tsai, P. H. et al. (2007). Three-Dimensional Analysis of Screening Effectiveness of Hollow Pile Barriers for Foundation-Induced Vertical Vibration. *Computer and Geotechnics, 35*(3), 489-499.

http://dx.doi.org/10.1016/j.compgeo.2007.05.010

Wass, G. (1972). Linear Two-Dimensional Analysis of Soil Dynamics Problems in Semi-infinite Layered Media. Phd Dissertation. Uni. of California at Berkley.

Wolf, J. P. (1994).*Foundation Vibration Analysis Using Simple Physical Models*. Englewood Cliffs, NJ: Prentice-Hall.

Woods, R. D. (1967). Screening of Surface Waves by Trenches. Phd Dissertation. Uni. Of Michigan, Ann Arbor. Mich.

Woods, R. D. (1968). Screening of Surface Waves in Soils. *Journal of Soil Mechanics and Foundations Division, ASCE, 94*(4), 951-979.

Woods, R. D. (1970). *Vibration of Soils and Foundation*. New Jersey: Prentice-Hall.

Woods, R. D., Barnett, N. E., & Sagesser, R. (1974). Holography, a New Tool for Soil Dynamics. *Journal of Geotechnical Engineering, ASCE, 100*(11), 1231-1247.

Yeh, C. S., Liao, W. I., Tsai, J. F. & Teng, T. J. (1997). Train Induced Ground Motion and its Mitigation by Trench and WIB. Report of NCREE-97-009, NAT. Center of Research on Earthquake Engineering, Taipi, Taiwan, R.O.C.

Earth Science Research; Vol. 1, No. 2; 2012
ISSN 1927-0542 E-ISSN 1927-0550
Published by Canadian Center of Science and Education

Laboratory Study of Conductive Properties of Contaminated Riverbed Sands in Ado-Odo Ota Local Government Area of Ogun State, Nigeria

Olukayode D. Akinyemi[1], Jamiu A. Rabiu[1], V. C. Ozebo[1] & O. A. Idowu[2]

[1] Department of Physics, University of Agriculture, Abeokuta, Ogun State, Nigeria

[2] Department of Water Resources Management and Agrometeorology, University of Agriculture, Abeokuta, Ogun State, Nigeria

Correspondence: Jamiu A. Rabiu, Department of Physics, University of Agriculture, Abeokuta, Ogun State, Nigeria. E-mail: jamoary@yahoo.com

Received: January 29, 2012 Accepted: February 27, 2012 Online Published: June 19, 2012

doi:10.5539/esr.v1n2p152 URL: http://dx.doi.org/10.5539/esr.v1n2p152

Abstract

As industrial activities increase, the risk of contamination of rivers in Ado-Odo Ota Local Government Area of Ogun State in Nigeria is becoming higher. In this study, riverbed sands were collected from five major rivers in Ado-Odo Ota Local Government Area, and conductivity properties were determined after the samples have been treated with varying concentration of petrol, engine oil, diesel, caustic soda and H_2SO_4. HANNAN Electrical Conductivity Meter, KD2 Thermal Conductivity Meter and Constant Head Method were used to determine the electrical, thermal and hydraulic conductivities respectively. After treatment of the samples with different concentration of the contaminants, it was found that thermal, electrical and hydraulic conductivities of the samples were largely proportional to contaminants concentration in all the samples in general. However, with increase in concentration of caustic soda and H_2SO_4, increase in electrical and thermal conductivities of samples were observed, while increase in the concentration of other contaminants decreased the hydraulic conductivity of the samples.

Keywords: riverbed sands, thermal conductivity, electrical conductivity, hydraulic conductivity, contaminants concentration

1. Introduction

The disposal of wastes generated by human activities within a municipality is generally an urban problem. The recognition of the connection between human activities and pollution and need to protect human health, recreation and fisheries production led to the early development of water quality regulations and monitoring methods (Hem, 1985; Jenkins et al., 1996; USEPA, 2007). The need for socio-economic advancement has led to rapid expansion of the industrial sector in developing countries like Nigeria. These waste disposal sites are neither properly designed nor constructed. After some years a dumpsite undergoes biologically, chemically, geologically and hydro geologically mediated changes resulting in a weathering process and consequently it becomes point source for pollution of the aquiferous units close to them (Arienzo et al., 2001; Manjunatha et al., 2001; Awofolu et al., 2005; Wang & Zhuo, 2005; Adeniyi et al ., 2008).

Thermal conductivity (λ) is the amount of heat transferred in unit time through cross-sectional area, under a unit thermal gradient. This parameter has been investigated for a wide range of soil states, and a comprehensives review of the literature has been presented previously by Farouki (1986). The most common method for determining thermal conductivity in soil is the transient, thermal probe method (Steinmanis, 1982) which consists of a line heat source and temperature sensor. Once the probe has reached thermal equilibrium with the surrounding soil, the temperature of the heat source is rapidly increased and heat is allowed to dissipate into the surrounding soil. Thermal conductivity is a function of the rate of heat dissipation, and this can be determined from a theoretical solution of conductive heat flow from a line source through an infinite homogeneous medium (Carslaw & Jaeger, 1959).Soil thermal properties are required in many areas of engineering, agronomy, and soil science, and in recent years considerable effort has gone into developing techniques to determine these properties. Thermal properties of soils play an important role in influencing microclimate (Ghuman & Lal, 1985).

Electrical conductivity on the other hand is the ability of a material to carry electric current in a metallic conductor. When a voltage is applied between two inert electrodes immersed in a solution, any ions between them will be attracted by the electrode with the opposite charge. Ions will move between electrodes and produce a current depending on the electrical resistance of the solution. Electrical conductivity plays a determinant role in two complementary aspect of the exploration of the ground surface measurements and well-logging measurement. Furthermore the concept of electrical conductivity had found a very good use in Agriculture. The conductivity meters measure the number of ions that are mobile within a liquid and this is considered the most accurate way of determining the salinity of the soil which is indicative of the ability of the soil solution to carry an electric current. When an electrical potential difference is placed across a conductor, its movable charges flow giving rise to an electric current.

Hydraulic conductivity is one of the hydraulic properties of the soil; the other involves the soil's fluid retention characteristics. These properties determine the behavior of the soil fluid within the soil system under specified conditions. More specifically, the hydraulic conductivity determines the ability of the soil fluid to flow through the soil matrix system under a specified hydraulic gradient; the soil fluid retention characteristics determine the ability of the soil system to retain the soil fluid under a specified pressure condition. Hydraulic conductivity depends on the soil grain size, the structure of the soil matrix, the type of soil fluid, and the relative amount of soil fluid (saturation) present in the soil matrix. The important properties relevant to the solid matrix of the soil include pore size distribution, pore shape, tortuosity, specific surface, and porosity. In relation to the soil fluid, the important properties include fluid density ρ and fluid viscosity μ. For a subsurface system saturated with the soil fluid, the hydraulic conductivity, *K*, can be expressed as follows (Bear, 1972):

$$K = \frac{\kappa \rho g}{\mu}$$

where *k,* the intrinsic permeability of the soil, depends only on properties of the solid matrix, and g called the fluidity of the liquid, represents the properties of the percolating fluid.

Conductive properties of contaminated sands have been investigated sufficiently, but very little is found in literature on the combining electrical, thermal and hydraulic conductivities of contaminated porous media. The aim of the study therefore was to investigate the effect of contaminants on the combined conductive properties of riverbed sands.

2. Study Area

The study was carried out on five major rivers in Ado-Odo/Ota Local Government Area of Ogun State. Ado-odo/Ota Local Government is one of the 20 Local Government areas of Ogun State located in the West Senatorial District. Geographically, it is situated within the tropical zone lying between 60^0 and 47^0 N of equator and 20.33^0E and 30.18^0 E of the Greenwich's Meridian and covers a land area of 1,263 square kilometers with a Terrain of 1,010.4 sq kilometer plain land and about 252.6 square kilometers. Terrain comprises of 16% riverine and 4% hilly regions. The Local Government has an estimated population of 528,242 people (Male 262,523 & Female 265,719) (2006 Census) with about four hundred and fifty (450) towns, villages and settlements. The map shown in Figure 1, illustrate the location of the sampling sites and the potential source of pollutants, which include agricultural wastes, industrial wastes, sewage, animal wastes, market wastes, etc. Three of the rivers (Ilogbo, Mosafejo and Ijako rivers) are located in the southern district of the area. While the remaining two (Igbogbo and Iju rivers) are located in the northern part of area. The Ijako and Ilogbo Rivers are particularly unique for several reasons. The Ijako community has undergone great economic development in recent years and is notably one of the fastest growing economically important communities in Ado-odo/ota L.G.A. which accommodates a considerable number of micro- industries (Coca-Cola Nig. Ltd, Sona Breweries plc, Universal Gas Ltd, Nigeria Foundries Ltd, 3Ace lnd. Ltd and Fine Chemicals Ltd.). The very popular market (Ilogbo market) and the timber business coupled with agricultural practices have drawn people from several cultural background in the country to make the settlement inter- tribal. This increase in anthropogenic activities surrounding the area has lead to an increase in environmental degradation. These multiple sources make it especially difficult to identify and isolate the risks associated with this contaminated water.

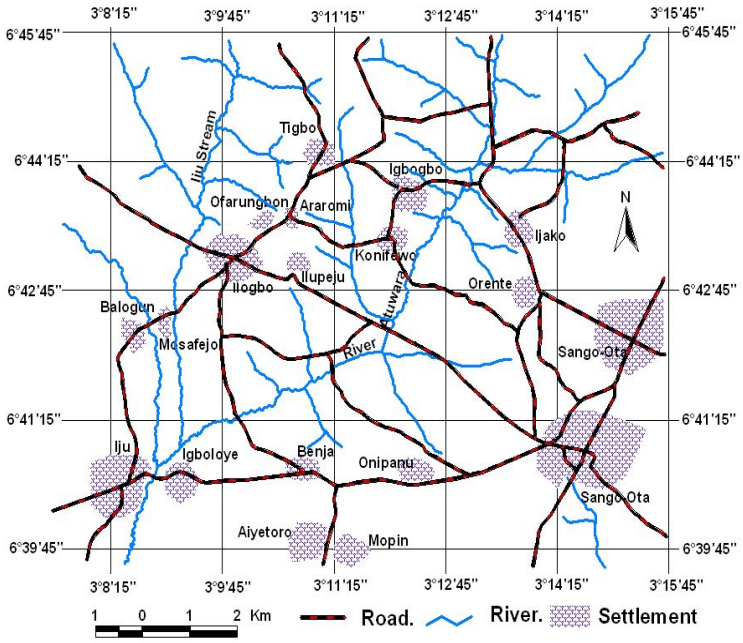

Figure 1. Map of the study area

3. Materials and Method

Laboratory tests were conducted to evaluate the conductivity properties at controlled room temperature (25^0C). Riverbed sands were collected from the five major rivers present in Ado-Odo Ota Local Government Area of Ogun state. Surface sediment samples were collected manually from the rivers' bank, transferred into plastic containers, and transported to the laboratory. Samples collected were thoroughly washed to remove any hidden contaminant, air dried and sieved to ensure uniform grain size. 1.3g/cm^3 bulk density of each treated sample were moistened with uniform grain size of 0.2mm. Five readings of thermal conductivity and electrical conductivity were taken at different points in the cylinder in order to obtain the average values, after which hydraulic conductivity was measured using constant head method. 5ml of each contaminant was added and mixed thoroughly, after which thermal, electrical and hydraulic conductivities were measured. The concentration of the contaminant was increased by the same volume at each experimental set-up until 25ml was achieved which is the fifth concentration. For each concentration, the corresponding conductivities were recorded. Thermal properties analyzer (KD2 Decagon Devices, Inc) was used to measure the thermal properties. Measurement was carried out by inserting the needle completely into the samples. The KD2 sensor needle contains both a heating element and a thermistor.

Constant head method was used to determine the hydraulic conductivity of the samples. Eight cylindrical pipes of same diameter (8.0cm) and hydraulic head (9.0cm) were used in a laboratory setting to determine hydraulic conductivity, while volume rate of flow was being measured. Hydraulic conductivity was determined using Darcy's equation which can be expressed as:

$$Q = KA \frac{\Delta h}{L}$$

where Q is the volumetric flow rate of water, K is the hydraulic conductivity, A is the cross-sectional area that the water flows through, Δh is the change in hydraulic head and L is the length of the porous medium.

3.1 Caustic Soda

Caustic soda is the major waste product generated from (Imperial roofing sheet industry) where different types of roofing sheet are being produced. Caustic soda easily mixed with soil and end up in streams and rivers. Available commercially in various white solid forms and as a solution of various concentrations in water, it is a highly corrosive and reactive. Caustic soda, as a 50% solution, is an odorless and colorless liquid. Upon adding it as a contaminant in the soil, increases the temperature of the soil causing an increase in conductivity of the soil. Caustic soda has a relatively very high conductivity, is soluble and very reactive with water.

3.2 Engine Oil

Engine oil is a part of the family of hydrocarbons; it is being generated as a waste product from almost all industries in the study area, especially those that make use of heavy machines. During servicing and repairing, engine oil easily mixed with soil and end up in streams and rivers. Melting point and boiling point are 34.4^0C and 360^0C respectively, like other hydrocarbons and the fact it is insoluble, it has a rather low conductivity and its concentrations in the porous media causes a reduction in the soil even in the presence of water in the soil.

3.3 Petrol

Petrol is a fuel derived from petroleum crude oil and used in spark-ignited internal combustion engines. Conventional gasoline is mostly a blended mixture of more than 200 different hydrocarbon liquids ranging from those containing 4 carbon atoms to those containing 11 or 12 carbon atoms (Speight, 2008). It has an initial boiling point at temperature of about 35^0Cand a final boiling point of about 200^0C. Octane rating, vapor pressure, sulfur content and storage stability are the properties that determine the performance of gasoline. It is important to note that petrol is covalent and made up of covalent bond.

3.4 Diesel

Like petrol, is also one of the major waste products generated from most industries in study area, diesel fuel contains varying amounts of various sulfur compounds which increase oil acidity. Legislation has reduced the sulfur content of highway fuel to 0.05% by weight. Off road fuel has an average of 0.29% sulfur by weight. By definition, aromatic content is characterized by the presence of the benzene family in hydrocarbon compound that occur naturally in the refining of diesel fuel. In the chemical make up of fuel, the heavier aromatic compounds toluene, xylene, and naphthalene are also present. Limiting these aromatic compounds has the effect of reducing temperature and thus NOx formation.

3.5 Battery Acid (Electrolyte)

An electrolyte is any substance containing free ions that make the substance electrically conductive. The most typical electrolyte generated as a waste product from (Universal Gas Ltd) situated very close to Ilogbo River is H_2SO_4. Electrolytes commonly exist as solutions of acids, bases or salts. Furthermore, some gases may act as electrolytes under conditions of high temperature or low pressure. Electrolytes solutions can also result from the dissolution of some biological (e.g., DNA. Polypeptides) and synthetic polymers (e.g., polystyrenesulfonate), termed polyelectrolytes, which contain charged functional group. Electrolyte solutions are normally formed when a salt is placed into a solvent as such as water and the individual components dissociate due to the thermodynamic interactions between solvent molecules, in a process called salvation. For example, when table salt, NaCl, is placed in water, the salt (a solid) dissolves into its component elements, according to the dissociation reaction. If a high proportion of the solute dissociates to form free ions, the electrolytes is strong, if most of the solute does not dissociate , the electrolyte is weak .the properties of electrolytes may be exploited using electrolysis to extract constituent elements and compounds contained within the solution.

4. Results and Discussion

Location and natural conductivity values of samples are discussed in Table 1, while Table 3 shows the decrease in Thermal, Electrical and Hydraulic conductivities of sample B as concentration of petrol, diesel and engine oil increased, while increase in conductivity properties were observed as the concentration of caustic soda and H_2SO_4 were increasing except the hydraulic conductivity which decreases as the concentration of all contaminants used increases. Table-4 shows decrease in conductivity properties of sample C as the concentration of contaminants such as petrol, diesel and engine oil increase. Increase in electrical and thermal conductivity was as a result of increase in concentration of caustic soda and H_2SO_4.

Table 1. samples location and natural conductivities values

Samples	Location	Thermal conductivity $(wm^{-10}c)$	Electrical conductivity $(\mu s/\ cm)$	Hydraulic conductivity (cm/ min)
A	Ilogbo River	1.26	42.30	0.34
B	Mosafejo River	1.37	126	2.64
C	Ijako River	1.52	137	2.59
D	Iju River	3.80	77	0.54
E	Igbogbo River	2.62	121	2.10

4.1 Conductivity against Concentration

Conductivities decreased with increase in concentration of petrol, diesel and engine oil, while increase in thermal and electrical conductivities was observed as the concentration of caustic soda and H_2SO_4 increased, except the hydraulic conductivity which decreases irrespective of contaminant used. This is due to fact that all the contaminants in porous media reduce its pore space, which resulted in flow rate reduction of water in porous media. Petrol and Diesel being a covalent hydrocarbon is a poor conductor of electrical current and heat. On the other hand, electrical and hydraulic conductivities increased with increase in concentration of Caustic Sodas and H_2SO_4 as shown in Table 2 for sample A. Caustic soda used in this study consist of Na, O, and H. Sodium hydroxide is a caustic compound which attacks organic matter. Upon adding it as a contaminant in the soil, it increases the temperature of the soil, causing an increase in conductivity of the soil. Caustic soda has a relatively very high conductivity, soluble and very reactive with water which has resulted in the observed conductivity trend.

Table 2. Values of thermal, electrical and hydraulic conductivity Vs Concentration of 5 contaminants for sample A

Concentration of contaminant in (ml)	Thermal conductivity of sample A ($Wm^{-1}{}^0C$)	Electrical conductivity of sample A (μ s/cm)	Hydraulic conductivity of sample A (cm/min)
Petrol (ml)			
5	2.81	148.0	0.51
10	2.42	135.0	0.42
15	1.94	128.0	0.36
20	1.52	100.0	0.30
25	*1.02*	*82.0*	0.28
Diesel (ml)			
5	2.50	70.0	0.48
10	2.15	58.12	0.42
15	1.95	46.52	0.37
20	1.48	40.0	0.30
25	1.05	35.55	0.25
Engine oil (ml)			
5	1.73	68.0	0.42
10	1.46	55.0	0.38
15	1.25	42.32	0.33
20	1.21	37.0	0.26
25	1.12	30.0	0.20
H_2SO_4(ml)			
5	1.80	100.0	0.67
10	2.05	125.0	0.88
15	2.75	154.0	1.05
20	3.12	177.0	1.30
25	3.82	190.0	1.75
Caustic soda (ml)			
5	1.25	130.0	2.01
10	1.52	140.0	1.92
15	1.80	155.0	1.65
20	2.05	167.05	1.41
25	2.30	175.01	1.20

4.2 Effect of Contaminants Concentration on Thermal Conductivity

Tables 2-4 show the thermal, electrical and hydraulic conductivity of treated samples with various concentrations of contaminants. From the data obtained, electrical conductivity has the highest values while hydraulic conductivity has the lowest values for various concentrations of the contaminants. Figure 2 shows the decrease in thermal conductivity of sample A as the concentration of petrol, diesel and engine oil increased. And increase in thermal conductivity was observed as the concentration of caustic soda and H_2SO_4 increased. In the same way Figure 3 shows the decrease in thermal conductivity of sample B, as the concentration of petrol, diesel and engine oil increased. But thermal conductivity of sample B increased as the concentration of caustic soda and H_2SO_4 increased. Figures 4, 5 and 6 also show the decrease in thermal conductivity of sample C, D and E respectively as the concentration of petrol, diesel and engine oil increased, while thermal conductivity increased with increase in caustic soda and H_2SO_4, hydraulic conductivity of all the samples decreased as the concentration of all contaminants increased.

Table 3. Values of thermal, electrical and hydraulic conductivity Vs Concentration of 5 contaminants for sample B

Concentration of contaminant in (ml)	Thermal conductivity of sample B ($Wm^{-1}{}^0C$)	Electrical conductivity of sample B (μ s/cm)	Hydraulic conductivity of sample B (cm/min)
Petrol (ml)			
5	3.0	150	*0.81*
10	2.75	142	*0.75*
15	2.45	135	*0.67*
20	2.20	128	*0.59*
25	*1.0*	*105*	*0.50*
Diesel (ml)			
5	2.85	80.0	*0.58*
10	2.50	68.05	*0.50*
15	2.20	58.15	*0.42*
20	1.87	50.0	*0.35*
25	*1.28*	*42.0*	*0.20*
Engine oil (ml)			
5	1.88	75.0	0.60
10	1.53	62.50	0.51
15	1.47	51.0	0.42
20	1.28	42.05	0.35
25	1.10	30.0	0.21
H_2SO_4(ml)			
5	1.72	100.0	1.70
10	2.08	129.0	1.34
15	2.42	158.0	1.10
20	3.05	168.0	0.88
25	3.19	188.0	0.68
Caustic soda (ml)			
5	1.35	125.0	2.65
10	1.55	133.0	2.43
15	1.78	149.0	2.20
20	1.95	155.0	2.00
25	2.15	165.0	1.75

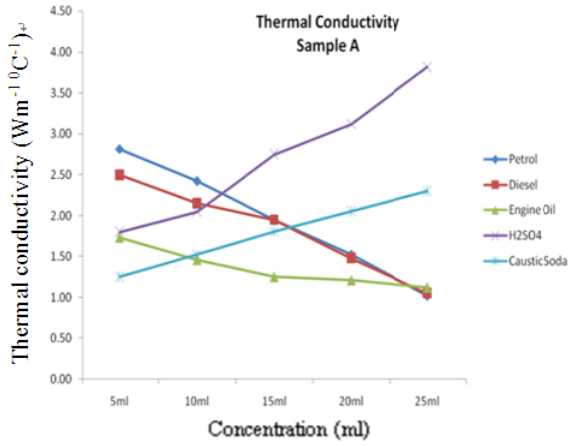

Figure 2. Effect of concentration of contaminants on thermal conductivity of sample A

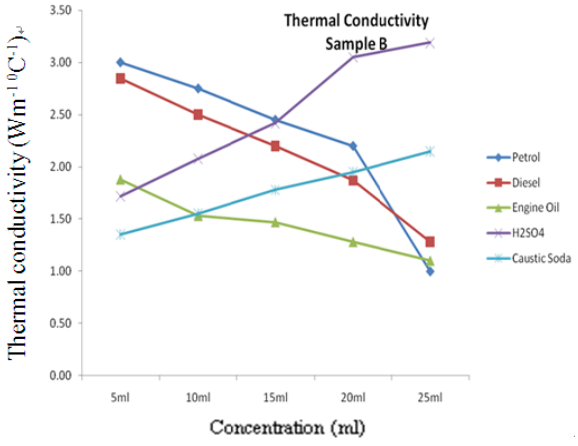

Figure 3. Effect of concentration of contaminants on thermal conductivity of sample B

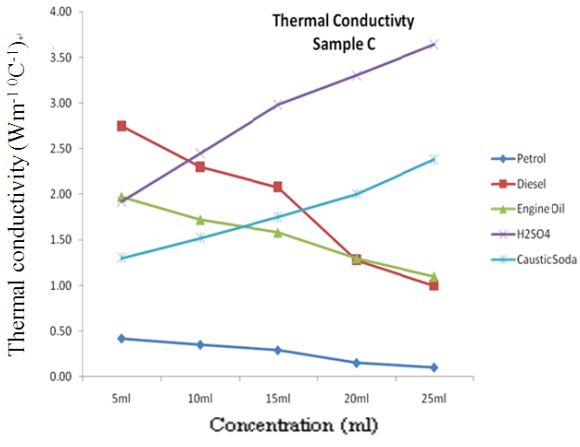

Figure 4. Effect of concentration of contaminants on thermal conductivity of sample C

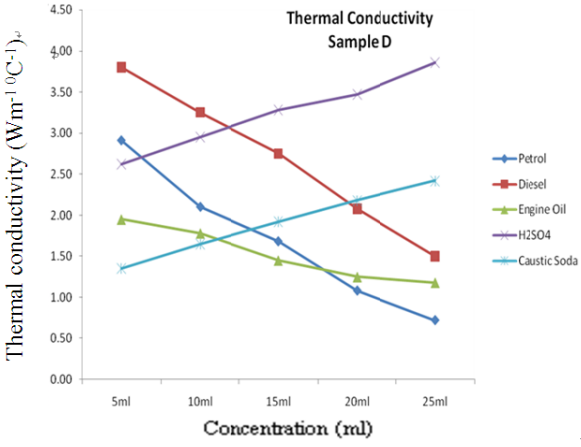

Figure 5. Effect of concentration of contaminants on thermal conductivity of sample D

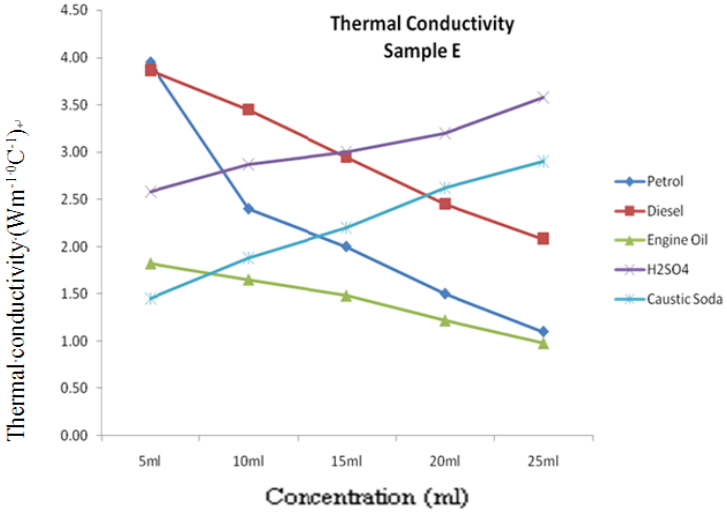

Figure 6. Effect of concentration of contaminants on thermal conductivity of sample E

4.3 Effect of Contaminants Concentration on Electrical Conductivity

Electrical conductivity of samples were determined by varying the concentration of contaminants. From the data obtained it can be seen that electrical conductivity has the highest values and the hydraulic conductivity has the lowest values for various concentration of the contaminants. Figures 7 and 8 show the decrease in electrical conductivity of samples A and B as the concentration of contaminants (Petrol, Diesel and Engine oil) increased, increase in electrical conductivity as the concentration of caustic soda and H_2SO_4 increased while Figures 9, 10 and 11 show the decrease in electrical conductivity of samples C, D and E respectively as concentration of Petrol, Diesel and Engine oil increased. However electrical conductivity of samples increased as the concentration of caustic soda and H_2SO_4 increased.

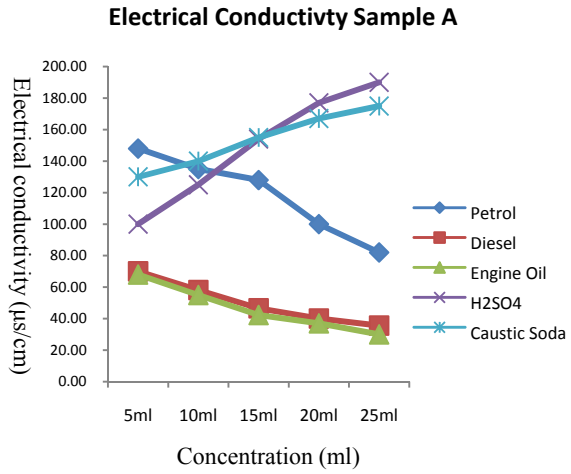

Figure 7. Effect of concentration of contaminants on electrical conductivity of sample A

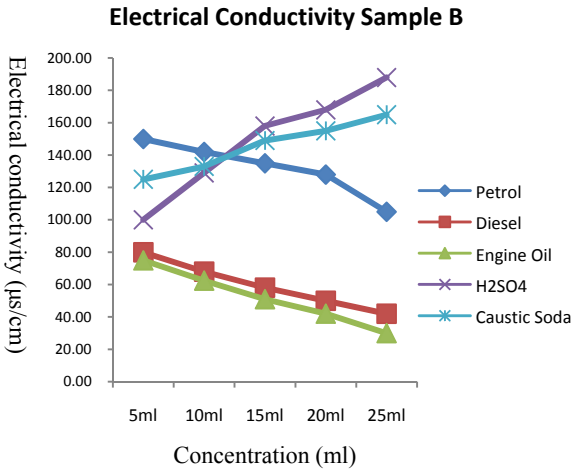

Figure 8. Effect of concentration of contaminants on electrical conductivity of sample B

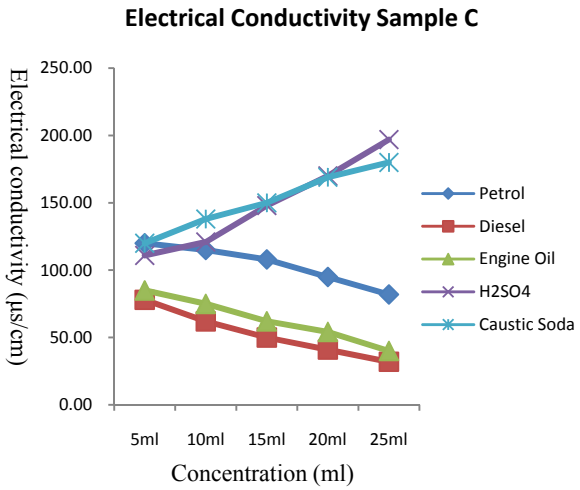

Figure 9. Effect of concentration of contaminants on electrical conductivity of sample C

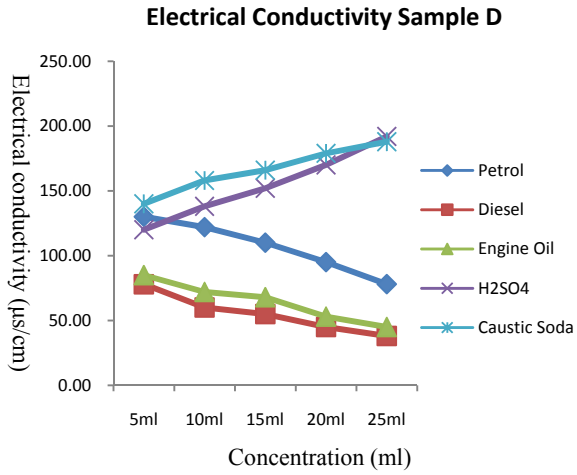

Figure 10. Effect of concentration of contaminants on electrical conductivity of sample D

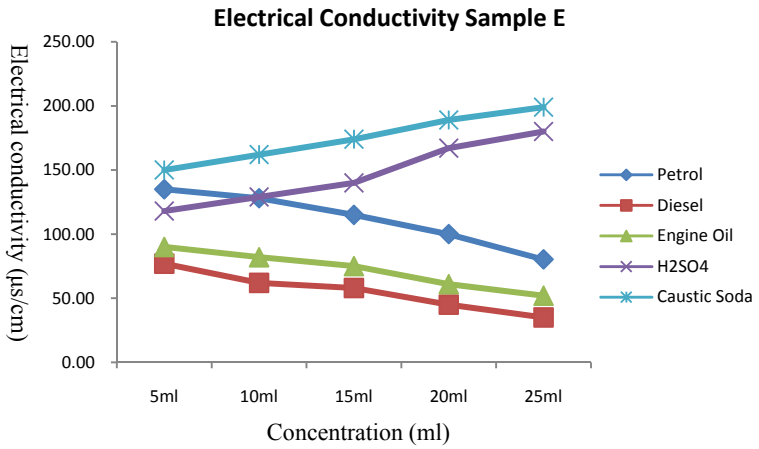

Figure 11. Effect of concentration of contaminants on electrical conductivity of sample E

4.4 Effect of Contaminants Concentration on Hydraulic Conductivity

Hydraulic conductivity of samples was determined by varying the concentration of contaminants. From the data obtained in Tables 2-4, hydraulic conductivity was plotted against the concentration of the contaminants. Figures 13, 14 and 15 show the decrease in hydraulic conductivity of samples B, C and D respectively as the concentration of all the contaminants used increased. It is clearly seen from the graphs that hydraulic conductivity of all the samples decreased with increase in the concentration of Petrol, Diesel, Engine oil and Caustic Soda. Although decrease rate of conductivity differs in different soils, hydraulic conductivity increased with increase in concentration of H_2SO_4 for sample A only, because sample A is the most porous sample.

Table 4. Values of thermal, electrical and hydraulic conductivity Vs Concentration of 5 contaminants for sample C

Concentration of contaminant in (ml)	Thermal conductivity of sample C ($Wm^{-1}{}^0C$)	Electrical conductivity of sample C (μ s/cm)	Hydraulic conductivity of sample C (cm/min)
	Petrol (ml)		
5	0.42	120.0	2.50
10	0.35	115.0	2.10
15	0.29	108.0	1.49
20	0.15	95.0	1.40
25	0.10	82.0	1.08
	Caustic soda (ml)		
5	1.30	120.0	2.85
10	1.52	138.0	2.60
15	1.75	150.0	2.39
20	2.00	169.0	2.28
25	2.38	180.0	2.10
	Diesel (ml)		
5	2.75	78.0	0.60
10	2.30	62.0	0.58
15	2.08	50.0	0.45
20	1.28	41.0	0.40
25	1.0	32.0	0.32
	Engine oil (ml)		
5	1.97	85.0	0.77
10	1.72	75.0	0.62
15	1.58	62.05	0.51
20	1.30	54.15	0.43

25	1.10	40.0	0.30
		H_2S0_4 (ml)	
5	1.92	111.0	1.80
10	2.45	121.0	1.48
15	2.98	148.0	1.15
20	3.30	170.0	0.85
25	3.64	197.0	0.50

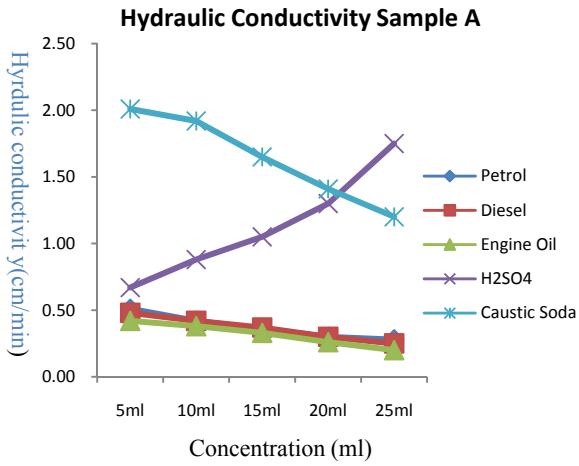

Figure 12. Effect of concentration of contaminants on hydraulic conductivity of sample A

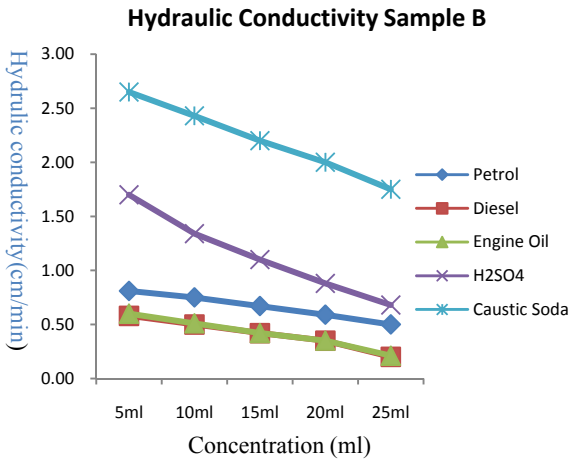

Figure 13. Effect of concentration of contaminants on hydraulic conductivity of sample B

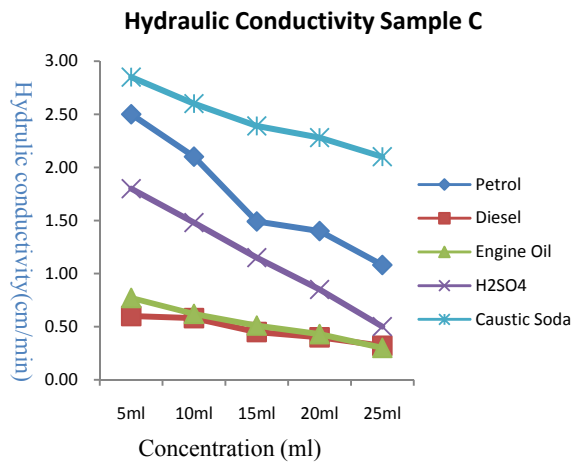

Figure 14. Effect of concentration of contaminants on hydraulic conductivity of sample C

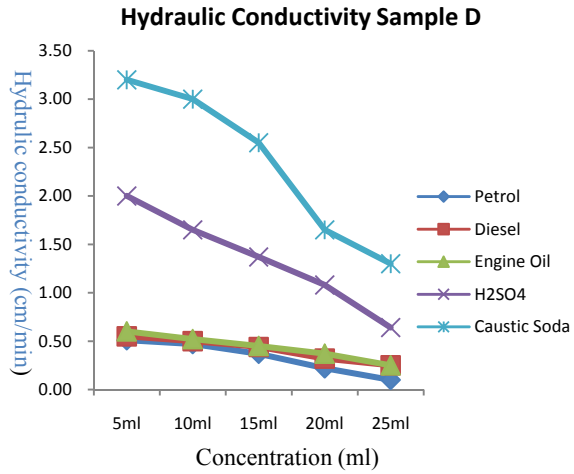

Figure 15. Effect of concentration of contaminants on hydraulic conductivity of sample D

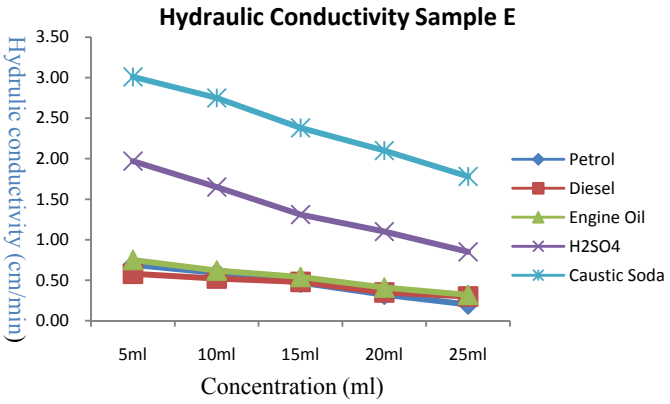

Figure 16. Effect of concentration of contaminants on hydraulic conductivity of sample E

5. Conclusion

General conductive properties of contaminated riverbed sands have been determined in this study to investigate variation with contaminants concentrations. Thermal, Electrical and Hydraulic conductivity varies with respect to contaminants present in porous media. Conductivity decreased with increase in the concentration of Petrol, Diesel and Engine oil. As observed in Table 4, electrical and thermal conductivities of sample C increased as the concentration of Caustic soda and H_2SO_4 increased. Hydraulic conductivity of sample C decreased as the concentration of all contaminants used in this study were increased. It was also already observed for all the samples investigated, conductive properties varied linearly with the increase in concentration. Presence of hydrocarbons in the riverbed sands reduces electrical and thermal conductivities.

Other contaminant such as Caustic Soda and Battery acid, if as a contaminant found in any porous media, increases electrical and thermal conductivity, but all contaminants investigated reduce hydraulic conductivity of porous media, due to the fact that contaminants reduce pore space, which directly reduced the rate of flow of water.

References

Adeniyi, A. A., Yusuf, O. O., & Okedeyi, O. O. (2008). Assessment of the exposure of two fish species to metals pollution in the Ogun river catchments, Ketu, Lagos, Nigeria. *Environ Monit Assess., 137*(1-3), 451-458. http://dx.doi.org/10.1007/s10661-007-9780-5

Arienzo, M., Adamo, P., Bianco, M. R., & Violante, P. (2001). Impact of land use and urban run-off on the contamination of the Samo river basin in southwestern Italy. *Water Air Soil Pollut., 131*(1-4), 349-366. http://dx.doi.org/10.1023/A:1011908019933

Awofolu, O. R., Du Plessis, R., & Rampedi, I. (2007). Influence of discharged effluent on the quality of surface water utilized for agricultural purposes. *Afr. J. Biotech., 6*(19), 2251-2258.

Awofolu, O. R., Mbolekwa, Z., Mtshemla, V., & Fatoki, O. S. (2005). Levels of trace metals in water and sediment from Tyume river and its effects on an irrigated farmland. *Water S. Afr., 31*(1), 87-94.

Carslaw, H. S., & Jaeger, J. C. (1959). *Conduction of heat in solids*. Oxford: Clarendon Press. p. 510.

Cremers, A., & Laudelout, H. (1965). Note on the 'Isoconductivity Value' of clay gels. *Soil Science, 100*, 298-299. http://dx.doi.org/10.1097/00010694-196510000-00012

Farouki, O. T. (1986). Thermal properties of soils. *Rock and Soil Mechanics*, Vol. 11, Trans Tech Publications, Clausthal-Zellerfeld, Germany. p. 1-136.

Ghauman, B. S., & R. Lal. (1985). Thermal conductivity, thermal diffusivity, and thermal capacity of some Nigerian soils. *Soil Sci., 139*(1).

Hem, J. D. (1985). Water supply paper. *Study and interpretation of the chemical characteristics of natural water* (3rd. ed.). University Press of the Pacific. P. 2254.

Steinmanis, J. E. (1982) Thermal property measurements using a thermal probe. *Underground cable thermal backfill*. New York: Pergamon Press. p 72-85.

USEPA. (2007). Recent recommended water quality criteria. United States Environmental Protection Agency.

Earth Science Research; Vol. 1, No. 2; 2012
ISSN 1927-0542 E-ISSN 1927-0550
Published by Canadian Center of Science and Education

Bacterial-Paleontological Study of Early Precambrian Weathering Crusts

Marina M. Astafieva[1] & Alexei Yu. Rozanov[1]

[1] A. A. Borisyak Paleontological Institute, Russian Academy of Sciences, Moscow, Russia

Correspondence: Marina M. Astafieva, A. A. Borisyak Paleontological Institute, Russian Academy of Sciences, Profsoyuznaya Str., 123, Moscow 117997, Russia. E-mail: astafieva@paleo.ru & aroza@paleo.ru

Received: November 29, 2011 Accepted: December 13, 2011 Online Published: June 19, 2012

doi:10.5539/esr.v1n2p163 URL: http://dx.doi.org/10.5539/esr.v1n2p163

Abstract

Existence of diverse microorganisms, bacteria (? Cyanobacteria) in the Early Precambrian (Archaean and Early Proterozoic) weathering crusts is determined. Presence of eukaryots can't be excluded also. So it is possible to speak about the colonization of land by microbes already at that time and about existence of single series from weathering crusts (primitive soils) to real soils.

Keywords: eukaryotes, prokaryotes, bacteria (? Cyanobacteria), Archaean, Proterozoic, Precambrian, weathering crust, paleosoles, Greenstone Belt

1. Introduction

The study of the origin and early evolution of life on Earth are fundamental scientific problems. These problems embrace investigation of ancient life both in marine and land conditions. The only reliable evidences of continental conditions existence are weathering crusts. Often they are the only source of information about exogenous processes and subsequently about conditions under which the development of biosphere occurred in Early Precambrian. Sediments, formed under the influence of weathering, are known from the earliest stages of the Earth geological development (Golovenok, 1975; Rozanov et al., 2008). Weathering profiles in all geological settings are reliable witnesses of continental regimes and in the Precambrian structures they often give unique information about continental features which led to biosphere development (Rozanov et al., 2008). Complex of diverse fossil microorganisms in ancient weathering crusts was discovered in result of electronic-microscope investigations, and conclusion about possibility of land colonization by microbes from the very beginning of geological annals was made (Rozanov et al., 2008; Rozanov & Astafieva, 2009; Astafieva et al., 2009).

The prokaryotic community that was the first to catalyze the system of biogeochemical cycles served as a basis for further evolution. It is possible to reconstruct the geobiological systems of the past using geochemical products of metabolism of prokaryotes that are preserved in the host rocks. The prokaryotic biosphere became a basis for the further evolution of life. Hence, the expansion of our knowledge on the evolution of the geo-biosphere in the Precambrian is a very important geological and biological task.

Most ancient organisms were found in rocks of 3.8 Ga age (Schidlowski, 1988, 2001) which means that even in the Archean age biomineralization was possible. The exact role of biota in autogenic mineralization is not clear. Clayey mineral formation is possible either with or without bacteria interaction. Modern investigations show that the final weathering product - clayey minerals, either biogenic or abiogenic, practically can't be recognized by structure and chemical composition (Tazaki, 1997; Kawano & Tomita, 1999). So, geochemical criteria of separation (division) of biogenic clayey minerals from abiogenic ones are absent.

Moscow Carboniferous basin white clays (collected by P. Kabanov) could be a nice example. These clays for a long time considered to be terrigenic. Bacterial-paleontological study of these clays (Figure 1) shows, that they are not terrigenic, but autigenic, i.e. most likely they were formed due to biological factor influence. The fact that core roundness, clearly seen on the picture, because of their small sizes (<<200 μm), cannot be due to rounding, serves as basis for such conclusion. We remind you that grains less 200 μm (0.2 mm) in sizes cannot become roundish under water influence, remaining angular. Our "balls" are about 5 μm in size. It means that their origin is biogenic, i.e. "balls" are fossilized coccoidal bacteria.

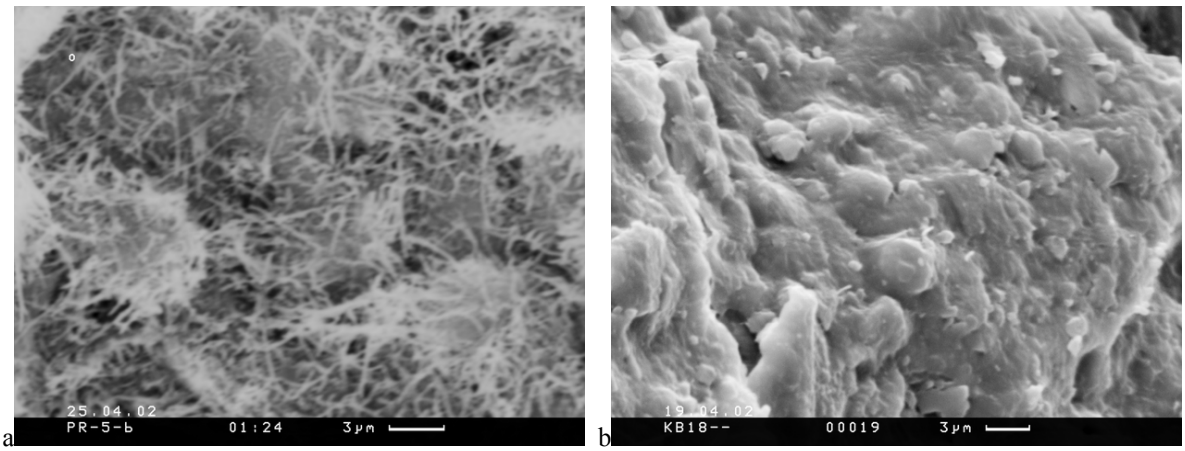

a b

Figure 1. Thread-like nannobacteria (? glycocalyx) surrounding coccoidal bacteria in the Lower Carboniferous clays of Moscow basin (a – quarry Priokskiy: specimen PIN, no. 5081/22, image 124; b – quarry Peski: specimen PIN, no. 5081/23, image 019)

Other evidence of bacterial participation in rock formation, earlier considered to be terrigenic, is siltstones with clay interlayers (illite) of Kola Peninsular (Imandra-Varzuga Greenstone Belt, Tominga Formation, collected by N.A. Alfimova and V.A. Matrenichev). Siltstones are known as classic terrigenous rocks. But rather numerous and diverse microfossils – threadlike, coccoidal, etc. forms – were found in studied siltstones (Figures 2-3). It is the evidence of biogenic factor (to some degree) in these siltstones formation.

It means that it is impossible to judge about rock genesis (including clayey ones) without bacterial-paleontological studies.

Earlier suggestions about life existence during the Early Precambrian cratons were made only on the basis of investigations of elemental and isotopic ratios of C, H, N and P in the rock matter. So it is confirmed the presence of microbial mat on the rock surface as far as 2.7-2.6 Ga (Watanabe et al., 2000; Sergeev et al., 2007). But fossil remains of the Precambrian land microorganisms have not been found yet.

This article aims at evaluation of bacteria role in an ancient weathering process.

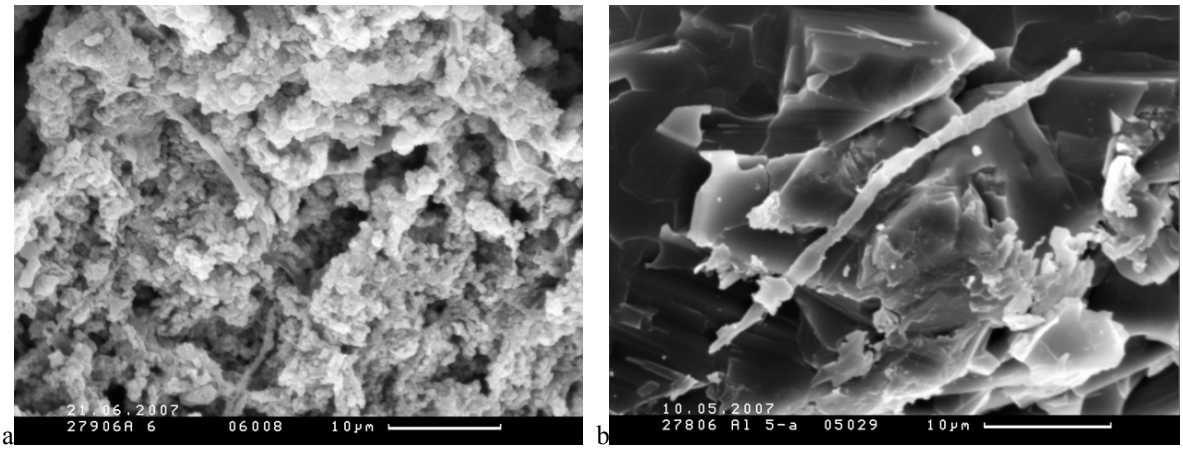

a b

Figure 2. Thread-like microfossils (a – threads submerged in glycocalyx) from Lower Proterozoic siltstones with clayer interlayers (illite) of Imandra-Varzuga (Kola Peninsular) Tomingskaya Formation (~2.0 Ga), specimen PIN, no. 5081/10, image 0608; b – single thread from Lower Proterozoic siltstones of Imandra-Varzuga (Kola Peninsular) Tomingskaya Formation (~2.0 Ga), specimen PIN, no. 5081/11, image 0529

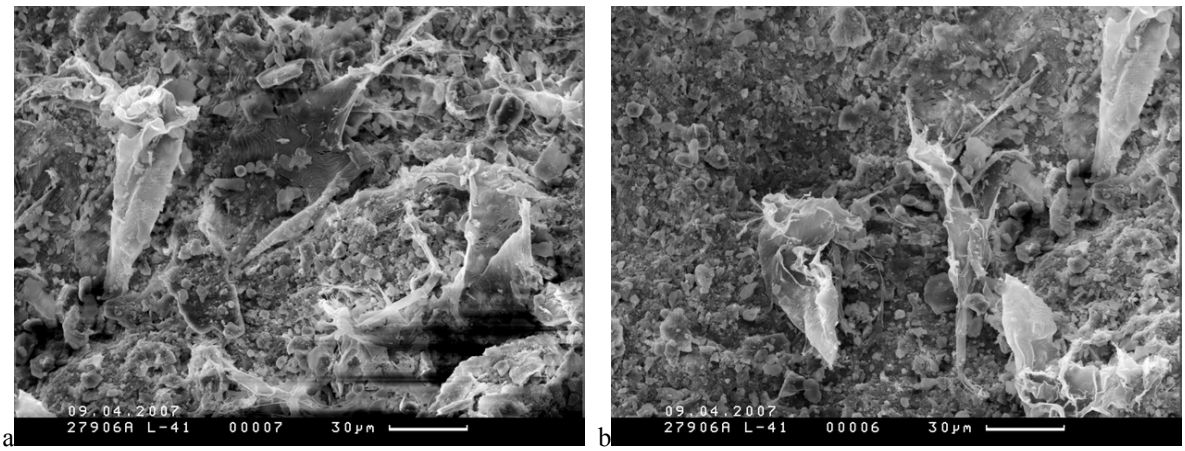

a b

Figure 3. a-b Flattened ?cyanobacterial sheaths from Lower Proterozoic siltstones with clayer interlayers (illite) of Imandra-Varzuga (Kola Peninsular) Tomingskaya Formation (~2.0 Ga). Specimen PIN, no. 5081/12, images 07, 06

2. Repository

Main objects of this paper are Early Proterozoic and Archaean weathering crusts of Karelia and Kola Peninsular (Plate 1, Figure 4). All samples are housed in the Paleontological Institute, collection number no. 5081.

Plate 1. Stratigraphic position of the studied weathering crusts (according to data by Akhmedov et al., 1996; Rozanov et al., 2008; Kheiskanen, 1990)

<table>
<tr><th colspan="4">General stratigraphic scale</th><th>Age Ga</th><th>Climate</th><th>Weathering crusts</th></tr>
<tr><td rowspan="6">PROTEROZOIC
PR</td><td rowspan="6">LOWER PROTEROZOIC
(KARELIAN)</td><td rowspan="5">Upper Karelian K_2</td><td>Jatulian</td><td>2.1</td><td>Nival</td><td><u>Jatulian</u>
Chapanshari Island,
Segozero Lake
(Centr. Karelia)</td></tr>
<tr><td rowspan="5">LowerKarelian K_1</td><td>Sariolian</td><td>2.3</td><td>Arid</td><td><u>Prejatulian</u>
Pechenga Green-stone Belt (Kola Peninsular);
Maly Janisyarvi Lake
(Northern Ladoga region)</td></tr>
<tr><td></td><td>2.4</td><td>Nival</td><td><u>Presariolian</u>
Vatulma Lake, Lekhta structure (Karelia);
Paanayarvi Lake
(Northern Karelia)</td></tr>
<tr><td>Sumian</td><td>2.45</td><td rowspan="3"></td><td><u>Sumian</u>
Imandra-Varzuga structure (Kola Peninsular)</td></tr>
<tr><td></td><td>2.5</td><td><u>Presumian</u>
Tsipringa structure
(Northern Karelia)</td></tr>
<tr><td>ARCHAEAN
AR</td><td>UPPER
ARCHAEAN
(LOPIAN)</td><td colspan="2">Upper Lopian L_3</td><td>2.8</td><td><u>Archaean</u>
Voronye Lake, Lekhta structure (Karelia);
Khizovaar structure
(Northern Karelia)</td></tr>
</table>

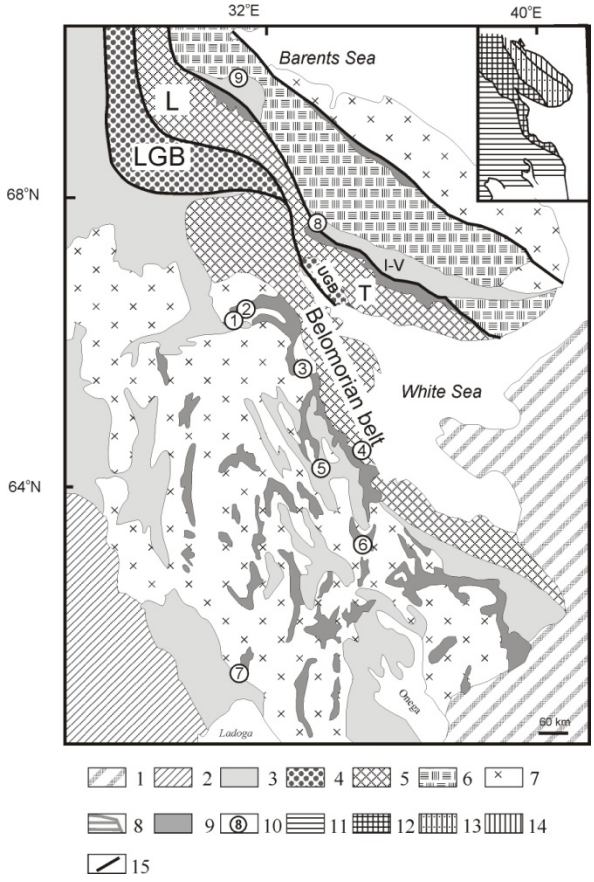

Figure 4. Geological scheme showing sample localities

Legend: 1 – Upper Proterozoic-Paleozoic Platform sheath; 2-5 – main Lower Proterozoic structures: 2 – svekophennids, 3 – sedimentary-volcanogenic structures (P – Pechenga, I-V – Imandra-Varzuga), 4 – Lower Proterozoic Laplandian (LGB)-Umbian (UGB) granulite belt, 5 – intermediate labile belts (Belomorian and Terrian-Lottian (T – Terrian, L – Lottian) fragments); 6 – Central-Kola granulite belt; 7 – granitoid (tonalite-trondhjemite-granodiorite, TTG) gneiss migmatite basement of granite-greenstone regions; 8 – Vodloserian block; 9 – greenstone belts; 10 – sample localities:1 – Paanayarvi Lake, Northern Karelia; 2 – Tsipringa structure, Northern Karelia; 3 – Khizovaar structure, Northern Karelia; 4 – Voronye Lake, Lekhta structure, Karelia; 5 – Vatulma Lake, Lekhta structure, Karelia; 6 – Chapanshari Island, Segozero Lake, Central Karelia; 7 – Maly Janisyarvi Lake, Northern Ladoga region, Karelia; 8 – Imandra-Varzuga structure (hole 1A) , Kola Peninsular; 9 – Pechenga Green-stone Belt, Kola Peninsular (hole 5A)

3. Methods

Bacterial paleontological studies have been done by CamScan-4 with microprobe Link-860. Only fresh chips of rocks were studied, selected samples were washed in spirit and were dried in muphel-stove.

4. Results

As a result of study of many rock samples, it was discovered that the absence of correlation between microfossil diversity and the abundance and the age of weathering crusts comprising these microbial remains. In all (for exeption of Khizovaar) weathering crusts it was revealed that the complex of diverse fossil remains of thread-like (filament), coccoidal (diameter up to 5 μm), larger ball-shaped (diameter > 10 μm) forms, fossil biofilms, etc. are present. Rather often rock fragments practically entirely consist from destroyed cocci, dumbbell-like forms and thread ravels (Figure 5).

1) Thread-like (filament) forms are the most abundant. Often they comprise whole organic rock (Figure 6).

2) By the most part threads are long diameter as a rule from 1 to 3 μm, sometimes up to 5-6 μm, some samples resemble crumpled sheaths of cyanobacteria Microcoleus (Zhegallo et al., 2000) (Figure 7).

3) Coccoidal forms are not so numerous. Discovered cocci have diameter about 2 μm (Figure 8). There are both single cocci and cocci met in clusters. Their surface often uneven and rough. Sometimes numerous traces of cocci are noted, probably the rock was literally comprised of coccoidal structures.

4) Rather large ball-shaped forms with diameter 15-30 μm with uneven rough surface (Figure 9). These structures are semidestroyed, but it is seen that they were heterogenous. The nature of construction and sizes allow to suppose possible reference of these forms to eukaryots. The possibility of these cocci accumulations to be a colony of small coccoidal bacteria associated by single envelope still exists.

5) Biofilms (Figure 10).

6) Peculiar rounded structures looking like cocci envelope (Figure 11). They situated close by each other.

Study of the youngest (2.1 Ga) weathering crusts among investigated - weathering crust of Chapanshari Island (Segozero Lake) – gave opportunity to trace microfossil distribution along different zones: quartz-sericite rocks, aleurites (siltstones) and amphibolites from contact zone of weathering crust and superposed rocks (dolomites).

Microfossils are rather abundant and diverse in these zones, filament forms dominate. But fossil bacteria met much more rarely in aleurites (siltstones) than in quartz-sericites and amphibolites. Fossil microbes are not found in the superposed dolomites. So revealing of distributional trends in different weathering crust zones is supposed subject for future study.

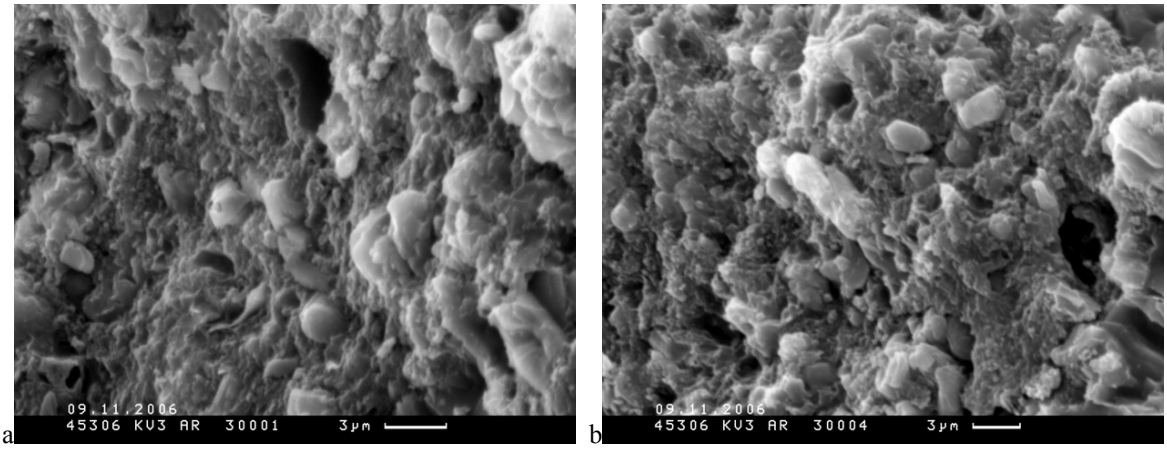

a b

Figure 5. a-b Presariolian, Paanajarvi Lake, microfossils comprising Precambrian weathering crusts. Specimen PIN, no. 5081/13, images 301, 304

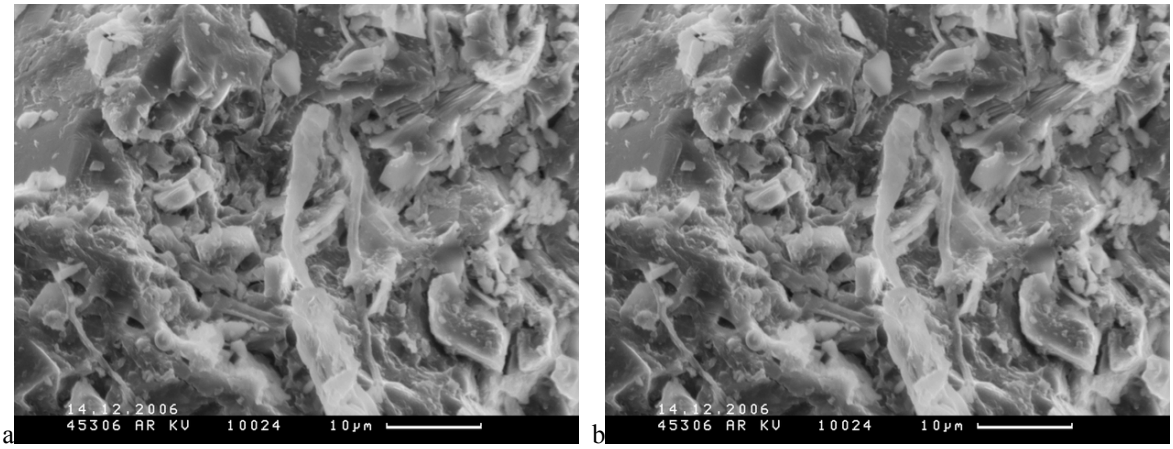

a b

Figure 6. Tread-like forms comprising weathering crusts almost entirely: a – Presariolian (Paanajarvi Lake: specimen PIN, no. 5081/14, image 124); b – Prejatulian (Maly Janisjarvi Lake: specimen PIN, no. 5081/15, image 1503)

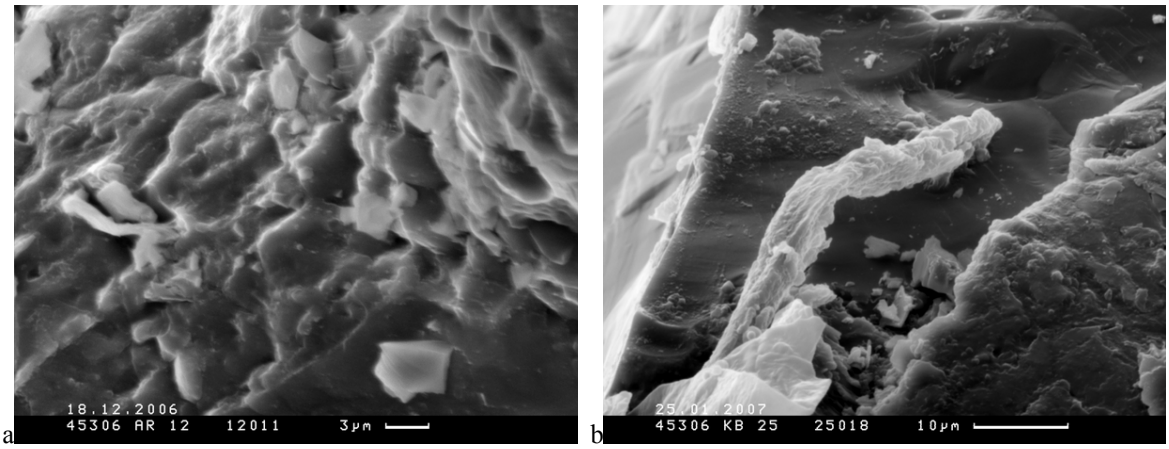

Figure 7. Presariolian (Paanajarvi Lake) filament microfossils: a - single filament: specimen PIN, no. 5081/16, image 1211; b - single filament looking like crumpled cyanobacteria Microcoleus envelope (Zhegallo et al., 2000). Specimen PIN, no. 5081/17, image 2518

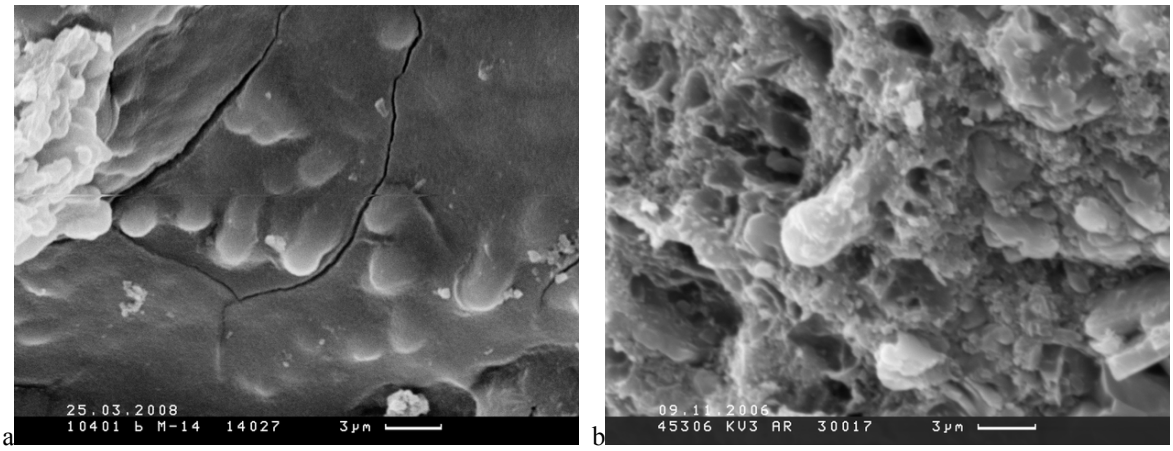

Figure 8. Cocci: a – numerous cocci in glycocalyx: Archaean weathering crust (Voronye Lake): specimen PIN, no. 5081/18, image 1427; b – coccoidal form with uneven surface, probably all the rock was covered by biofilm consisted from such cocci: Presariolian weathering crust (Paanajarvi Lake): specimen PIN, no. 5081/13, image 0317

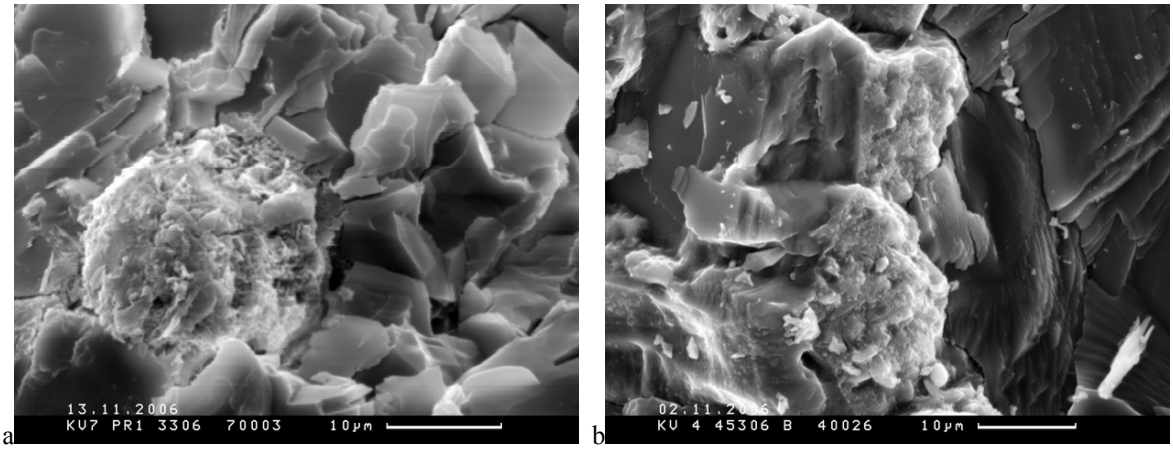

Figure 9. Large ball-shaped forms (diameter 15-30 µm) with uneven bumpy surface: a – Prejatulian weathering crust (Maly Janisjarvi Lake): specimen PIN, no. 5081/20, image 0703; b – Presariolian weathering crust (Paanajarvi Lake): specimen PIN, no. 5081/19, image 0426

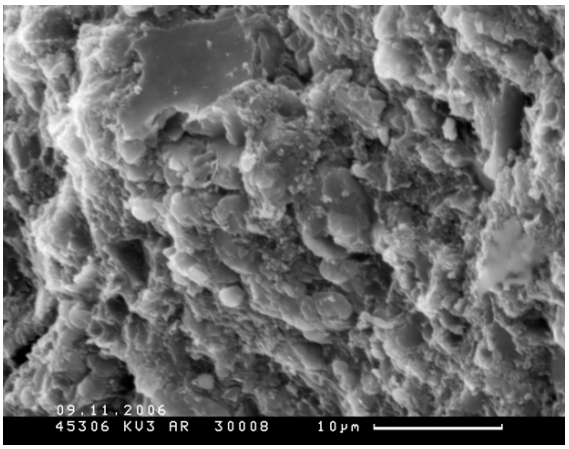

Figure 10. (?) Biofilm: Presariolian weathering crust (Paanajarvi Lake): specimen PIN, no. 5081/13, image 0308

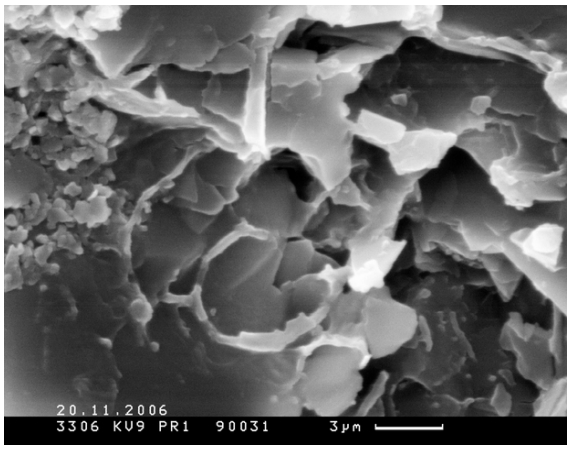

Figure 11. Peculiar rounded structures: Prejatulian weathering crust (Maly Janisjarvi Lake): specimen PIN, no. 5081/21, image 931

5. Discussion

Ancient weathering crust investigations are of higher priority for determination of continental sedimentation conditions during earliest stages of Earth development. At the same time climatic conditions dominated over the territory of the Baltic shield during formation of the objects under investigation were strictly different. Nival conditions of sedimentation are reconstructed on the basis of wide spreading of moraine rock associations for the interval 2.4-2.3 Ga (Akhmedov et al., 1996). Predominance of arid climatic conditions is suggested for Jatulian time (2.3-2.1 Ga) judging by presence of evaporates and red colored sediments in the sequences (Kheiskanen, 1990). Besides, some caliche are described for this period (Sochava et al., 1975), this fact also points to the arid climate conditions. According to the provided investigation, weathering crusts, formed both under nival and arid conditions, are characterized by the same peculiarities of geological structure and chemical composition. It causes doubts concerning leading role of climate for the process of formation of hypergene objects in the Early Precambrian.

Chemical composition of microfossils of the described complex in all cases is identical to the chemical composition of rock matrix and is represented by the main rock forming oxides of Si, Al, Fe, K and Mg. It serves as indirect confirmation, that microbiological complex is even-aged with the host rocks. More likely, microorganisms fixed in the rocks played role of catalyst – decay (decomposition) of minerals, comprising rocks, and their transformation into clayey minerals happened under bacterial participation (Rozanov et al., 2008). Perhaps, uncial weathering crusts of the Early Precambrian were formed due to interaction between peculiar specific composition of microorganisms and conditions of hypergene transformations.

6. Conclusions

As a result of investigations it is ascertained that the diversity of bacterial forms of life existed as early as the Early Precambrian. Bacterial founds in the objects of hypergene origin testify to the exogenous nature of studied objects.

In the Early Precambrian microorganisms, bacteria (? Cyanobacteria), and may be even eukaryots accompanied and promoted formation of weathering crusts. So it is possible to speak about colonization of land by microbes at this time and about existence of a single series from weathering crusts (paleosoles) to real soils.

Acknowledgements

The authors thank everybody, who helped us with valuable advice and discussion of the manuscript; geologists from Institute of Precambrian Geology and Geochronology, Russian Academy of Sciences (N. A. Alfimova, V. A. Matrenichev, A. B. Vrevsky, who vested us material and A. V. Kravtsev and L. T. Protasevich for the assistance with the CamScan-4 Scanning Electron Microscope.

The work was supported by the Program of Presidum of Russian Academy of Sciences “Origin of biosphere and evolution of geobiological systems” (subprogram II), Russian Foundation for Basic Research (project nos. 11-04-00129; 12-04-00102) and Scientific School: SS- 65493.2010.4.

References

Akhmedov, A. M., Travin, L. V., & Tikhomirova, M. (1996). Glaciation epoches and evaporitization in the Early Proterozoic and interregional correlation. *Regional geology and Metallogeny,* 5, 84-98.

Astafieva, M. M., Rozanov, A. Yu., Vrevsky, A. B., Alfimova, N. A., Matrenichev, V. A., & Hoover, R. B. (2009). Fossil microorganisms and formation of Early Precambrian weathering crusts. *Proceedings of SPIE, 7441*, 744107. http://dx.doi.org/10.1117/12.824535

Golovenok, V. K. (1975). Precambrian weathering crusts, their peculiarities and methods of lithological-geochemical studies. In *Precambrian weathering crusts* (pp. 16-27). Moscow: Nauka.

Kawano, M., & Tomita, K. (1999). Formation and evolution of weathering products in rhyolitic pyroclastic flow deposit, southern Kyushu, Japan. *The Journal of the Geological Society of Japan, 105*(10), 699-710. http://ci.nii.ac.jp/naid/110003012995/en

Kheiskanen, K. I. (1990). *Paleogeography of Baltic shield in Karelian time*. Petrozavodsk: Karelian Sc. Center AS USSR Press. 128 p.

Rozanov, A. Yu., & Astafieva, M. M. (2009). The Evolution of the Early Precambrian Geobiological Systems. *Paleontological Journal, 43*(8), 911-927. http://dx.doi.org/10.1134/S0031030109080103

Rozanov, A. Yu., Astafieva, M. M., Vrevskii, A. B., et al. (2008). Microfossils from the Early Precambrian Continental Crusts of Weathering of the Fennoscandian Shield. *National Geology, 3*, 83-90.

Schidlowski, M. (1988). A 3.800-Million year isotopic record of life from Carbon in sedimentary rocks. *Nature, 333*, 313-318. http://dx.doi.org/10.1038/333313a0

Schidlowski, M. (2001). Carbon isotopes as biogeochemical recorders of life over 3.8 Ga of Earth history: Evolution of a concept. *Precambrian Research, 106*, 117-134. http://dx.doi.org/10.1016/S0301-9268(00)00128-5

Sergeev, V. N., Semikhatov, M. A., Fedonkin, M. A., Veis, A. F., & Vorob'eva, N. G. (2007). Principal stages in evolution of Precambrian organic world: Communication 1. Archean and Early Proterozoic. *Stratigraphy Geological Correlation, 15*(2), 3-24. http://dx.doi.org/10.1134/S0869592X07020020

Sochava, A. V., Savelyev, A. A., & Shuleshko, I. K. (1975). In: *Caliche in the Middle Proterozoic sediments of Central Karelia. Leningrad: Proceedings of AS USSR, 223*(6), 1451-1454.

Tazaki, K. (1975). Biomineralization of layer silicates and hydrated Fe/Mn oxides in microbial mats: an electron microscopical study. *Clays and Clay minerals, 45*(2), 203-212. http://dx.doi.org/10.1346/CCMN.1997.0450208

Watanabe, Y., Martini, J. E. J., & Ohmoto, H. (2000). Geochemical evidence for terrestrial ecosystems 2.6 billion years ago. *Nature, 408*, 574-578. http://dx.doi.org/10.1038/35046052

Zhegallo, E. A., Rozanov, A. Yu., & Ushatinskaya, G. T. (2000). *Atlas of Microorganisms from Ansient Phosphorites of Khubsugul (Mongolia).* Huntsville, Alabama, USA: NASA.

Earth Science Research; Vol. 1, No. 2; 2012
ISSN 1927-0542 E-ISSN 1927-0550
Published by Canadian Center of Science and Education

Increase of Seismic Risk for Growth of a Large Metropolitan Area of Granada (Spain): Case Studies

I. Valverde-Palacios[1] & I. Valverde-Espinosa[1]

[1] Department of Building Construction, Escuela Técnica Superior de Arquitectura, University of Granada, Granada, Spain

Correspondence: I. Valverde-Palacios, Department of Building Construction, Escuela Técnica Superior de Arquitectura, University of Granada, Campus de Fuentenueva s/n 18071, Granada, Spain. Tel: 34-958-243-126. E-mail: nachoval@ugr.es

Received: January 16, 2012 Accepted: February 1, 2012 Online Published: July 6, 2012

doi:10.5539/esr.v1n2p171 URL: http://dx.doi.org/10.5539/esr.v1n2p171

Abstract

This paper analyzes the creation, consolidation, and growth of the metropolitan area of the city of Granada (Spain) from 1956 to 2007, using GIS and aerial photographs. In the last fifty years, the population of Granada and its metropolitan area has doubled. This has led to an increase in built-up land of approximately 4650 ha. Furthermore, the areas that have experienced the largest growth in population and built-up land are located less than 15 km from the city. The consolidation of the metropolitan area (MA) in Granada began in the 1970s. In 1950-2009, the overall population density (hab/km^2) rose 65%. This study has provided support to the main investigation to justify the increase of the exposed elements since the MA of Granada is the most active seismic zone in Spain. This primary research examines the foundations of buildings in static and dynamic conditions and the best direction of growth of villages taking into account the soil characteristics. It was found that seismic risk in this area has increased because of the significant growth of the elements exposed at risk (number of buildings as well as population). This study shows that in some cases the growth directions are not correct.

Keywords: Metropolitan Area (MA), Granada (Spain), built-up land, population, GIS, earthquakes, density, seismic risk

1. Introduction

This paper documents and analyzes the creation, consolidation and growth of the metropolitan area of the city of Granada (Spain) from 1956 to 2007 with GIS and aerial photographs (Figure 1). In the last fifty years, the population of Granada and its metropolitan area has doubled. This has led to an increase in built-up land of approximately 4650 ha. Furthermore, the areas that have experienced the largest growth in population and built-up land are located less than 15 km from the city.

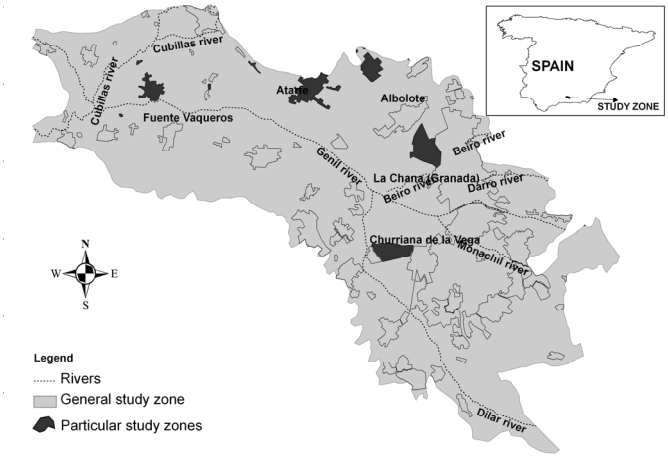

Figure 1. Location of the study zone

This purpose of this analysis was to verify the risk of seismic events since the area of study is the most active seismic zone in Spain, according to the Spanish seismic code (NCSE-02). In fact, seismic risk in this area has increased because of the significant growth in the number of buildings and population. This is despite the fact that buildings are now less vulnerable to earthquakes because of technical advances in construction, new materials, energy dissipation, and regulations to minimize and mitigate construction vulnerability (Valverde-Palacios, 2010).

Because of its morphological and productive characteristics, the region of La Vega in Granada has always been different from other neighboring areas. Since ancient times, its natural features and human activity have made it a unique agricultural space. At one time, its strategic position as a crossroads and its orographic singularity converged to transform it into the most important urban nucleus of Eastern Andalusia. However, it fell into decay because of the progressive migration of the population and economic activity towards coastal areas. The inland city of Granada has never been directly connected to the Mediterranean even though since ancient times the inhabitants have tried to devise an effective communication network, though with little success. It was necessary to wait until, the 20th century before these projects finally prospered. It was only then when a direct connection was established between the inland and the coastline. However, until the 20th century, Granada was economically isolated because it was located in an area of difficult accessibility, and thus, of low productivity. This was a major obstacle to the concentration of farming and agricultural activity that occurred between the 16th and 19th centuries to enrich other large cities in the region of Andalusia. Granada thus remained at the subsistence level.

After the Spanish Civil war, there was a period of economic stagnation that lasted for 25 years. In 1940-1960, the population of the city of Granada remained at 195,000 people. In contrast, the population of surrounding areas increased by 10,000 (from approximately 87,000 to 97,000 inhabitants). This ruralization process was inevitable because of the lack of supplies and urban jobs. Not surprisingly, in 1960 the province of Granada ranked fourth to last in national income per person. It was only surpassed by the provinces of Cordoba, Badajoz and Guadalajara (INE, 2009). Unwin (1996), Van Geffen (2003), Cooke and Marchant (2006), Boix (2007), Rozenfeld et al. (2008), Aguilera et al. (2009), and Storper (2010) also analyze the causes of the growth of metropolitan areas.

This organization of this article is as follows. Section 2 reviews the concept of metropolitan area (MA) from its origin in the United States (1850) to its appearance in Spain in 1960. Section 3 applies this concept to Granada, and provides a detailed justification of why Granada can be regarded as an MA. Section 4 explains the methodology used in the study, and section 5 presents the results of metropolitan growth in Granada, and analyzes the case studies of four municipalities. The final section gives the relevant conclusions that can be derived from this research.

2. The Concept of Metropolitan Area (MA)

The definition of metropolitan area (MA) is crucial to the study of urban growth. Evidently, the way that this concept is defined has a direct effect on the conclusions derived from the statistical distribution of urban activity. This term, *metropolitan area,* appeared for the first time in the USA in 1850, and is recorded in the 1910 census of the Federal Office. This office used the term in 1910 and 1920. Within the context of this definition, a metropolitan area was regarded as a large population nucleus of over 200,000 inhabitants, which was not included in the radius of influence of another large population. This area encompassed all territory within a distance of 10 miles from the core urban nucleus and with a minimum population density of 150 inhabitants per square mile (U.S. Census Bureau). This definition, however, is based solely on population criteria (Berry et al., 1968; Font, 1972, De Esteban, 1981).

This definition was subsequently modified to include new variables. This specification of the term permitted the elaboration of models based on an integrated system of functions. The concepts of *Standard Metropolitan Area* (SMA) and *Standard Metropolitan Statistical Area* (SMSA) appeared in 1950 and 1960, respectively. They have been the basic reference for many of the studies and analyses of metropolitan areas in North America and Europe (Nunes, 1986; Serra, 1991; Van Geffen, 2003).

According to Gohhen (1971), the criteria used to define metropolitan areas are the following: definitional criteria, population criteria, metropolitan criterion, and inclusion criteria. New criteria were proposed by Fox (1964), Friedman, et al. (1965), Berry (1973), Font (1972), Coombes, et al. (1978) and Hall and Hay (1980) which include economic and functional integration. Serra (1991) concludes that the definition of metropolis should be based on metropolitan intensity, i.e., a functional relationship between the main urban nucleus and secondary population nuclei.

Early studies that identify MAs in Spain date back to 1960 and 1967 (Boix, 2007), and are the work of the Spanish Ministry of Housing (1965). They used the following criteria, based on Davis (1959): (i) the existence of an urban nucleus of at least 50,000 inhabitants; (ii) economic and social links between the urban nucleus and peripheral municipalities such that the minimum population of the total area is 100,000.

In Spain, the Ministry of Housing has continued to define and specify metropolitan areas. The most recent samples of this work are the Atlases of 2000 and 2005, which define *metropolitan area* in terms of three basic criteria: (i) population size of the central urban nucleus; (ii) primacy of an open and diffuse urban nucleus; (ii) economic and social integration in a system of daily social interaction and relations. All of these aspects are ultimately an integral part of modern territorial dynamics.

3. Definition of Metropolitan Area of Granada (Spain)

In the region of Andalusia in southern Spain, the Andalusian Institute of Statistics defines an MA, as a polynuclear urban area that constitutes a unitary market of residence and work as well as a collective living space (Feria et al., 2005). For the specification of the boundaries of the metropolitan areas of Andalusia, the regional government uses the criterion of residence-work mobility, which includes the social and functional interdependence of the various towns that comprise it (Almoguera & Ríos, 2008).

The delimitation of the MA of Granada (Table 1) has been the focus of numerous studies (Fernández Avidad, 1999; Conde, 1999; Cañete et al., 2005; Sánchez González, 2005), given the wide range of criteria that can be considered. Authors such as Menor (1997) identify the region of Granada as an MA. This region meets a series of conditions and urban indicators that confirm the close relationship between Granada, the core urban nucleus, and various peripheral population centers. However, the authors of the *Plan de Ordenación del Territorio de la Aglomeración Urbana de Granada* (Spatial and Territorial Plan of the Urban Agglomeration of Granada) (POTAUG, 1999) examined a wide range of documents about the province of Granada, each of which gave a different specification of its metropolitan area.

Table 1. Summary of the number of municipalities that make up the metropolitan area of Granada and the region of Granada

	POTAUG, 1999	New POTAUG prevision	Sánchez González, 2005	Menor, 1997	Cañete et al., 2005	Fernandez Avidad, 1997	Conde, 1999
Metropolitan area	32	51	37	-	32	42	26
Region of Granada	-	-	-	33	-	-	-

After analyzing the documentation, the experts who elaborated the POTAUG (1999) decided that the following group of municipalities should be included within the urban agglomeration of Granada: Albolote, Alhendín, Armilla, Atarfe, Cájar, Cenes de la Vega, Cúllar Vega, Churriana de la Vega, Granada, Huétor Vega, Jun, Las Gabias, La Zubia, Maracena, Monachil, Ogíjares, Peligros, Pulianas, and Vegas del Genil. This area was subsequently expanded to encompass Güevéjar, Víznar, and Alfacar because of their radial relationship with Granada, the main urban nucleus. .Pinos Genil was included since it was located in the corridor to the Sierra Nevada ski resort. Gójar and Otura were also regarded as part of the metropolitan area, and Gojar itself, as the nucleus for other smaller population centers. The towns of Chauchina, Fuente Vaqueros, Pinos Puente and Santa Fe were added to the MA because of their central location in La Vega of Granada. Finally, Cijuela, Dilar, and Láchar were also included because of their functional relationship with the other municipalities in the metropolitan area.

Fernández Avidad (1997) defines, an MA, based on the criteria specified in Spanish Metropolitan Areas (Ministerio de Vivienda, 1960). According to these criteria, Granada can effectively be regarded as a metropolitan area.

Total population in the area of more than 100,000 inhabitants. There are 500,469 inhabitants in the MA of Granada (INE, 2009).

An industrial workforce of over 20,000 inhabitants in each municipality. In the city of Granada (and thus in the MA), there are more than 20,000 industrial jobs.

An active non-agricultural population in the area equal to or greater than 66 %. In the MA only 7.1% of the workforce is involved in farming activities (INE, 2009).

Gross population density exceeding 100 hab/km^2. The metropolitan area of Granada has a population density of 584 hab/km^2.

Interrelatedness. The MA of Granada forms a continuous area. The main urban nucleus is related to more peripheral population centers by direct contact or through municipalities that fulfill the preceding conditions.

Fernández Avidad (1997) concludes that the MA of Granada is composed of 42 municipalities, although he restricts the area to populated territorial fragments instead of expanding it to include the entire area.

Consequently, this clearly points to the existence of an MA in Granada. This area has gradually appeared as a large urban nucleus in which other radial areas are integrated. Other crucial elements are its geographical location and its functional relationship with the other municipalities of the metropolitan area, regarding employment, transportation, and commerce. The following section describes the methodology used to analyze the growth of this area.

4. Methodology

For the analysis of urban growth in the MA of Granada, the following sources were used to create a map of this area:

Topographic maps (auxiliary material)

Topographic Map of Andalusia (1995) 1:10,000 (Raster mosaic)

Topographic Map of Andalusia (1998) 1:10,000 (Vector)

Topographic Map of Andalusia (2001) 1:10,000 (Vector). (ideAndalucía) http://www.ideandalucia.es/#o1.

Topographic Map of Andalusia (2005) 1:100,000 (Vector). (ideAndalucía)

Aerial photographs and orthophotos (main material in the study)

1956. Set of black and white orthophotos at scale 1: 33,000 and resolution of 1 m. (ideAndalucía) produced by a U.S.A.F photogrammetric flight over Spanish territory

1978. Aerial Photography for Agriculture

1984. CNIG Aerial Photography

1994. Aerial photography made by the Junta Andalucía

2001. Aerial photography made by the Junta Andalucía

2007. Colour digital orthophoto of Spain, generated by a digital flight with a 0.90 m geometric resolution, Infrared RGB data at scale 1: 10,000. (ideAndalucía).

Other sources

Corine Land Cover

http://www.idee.es/clientesIGN/corineClient/index.html?lang=ES

Application of data regarding land use and geographic relief (IDEAndalucia)

Based on this information, the urban metropolitan area was digitized with a GIS software application for each year with available aerial photographs or orthophotographs (1956, 1978, 1984, 1994, 2001 and 2007). The following section presents the maps thus obtained. It also includes a table that summarizes the increase in built-up land in each location, and provides percentage graphs that justify the growth of the urban area in graphical and numerical form.

5. Results

In 1956-2007 there was an 84% increase in the built-up land in Granada and its metropolitan area (see Figures 2 and 3). This was also accompanied by a corresponding growth of the urban population. In fact, in 1956-1978, 32 municipalities experienced an increase in built-up land of more than 30%. The percentages for each town were the following:

(32%): La Zubia

(40-50%): Peligros, Monachil, Granada, Cijuela, Las Gabias, Güevéjar, Pulianas, and Fuente Vaqueros

(50-80%): Cúllar Vega, Albolote, Chauchina, Maracena, Armilla, Santa Fe, Dilar, Cájar, Otura, Churriana de la Vega, Jun, Viznar, Alfacar, Pinos Genil, Pinos Puente, Vegas del Genil, and Láchar

(over 80%): Huétor-Vega, Gójar, Cenes de la Vega, Alhendín, Ogíjares, and Atarfe.

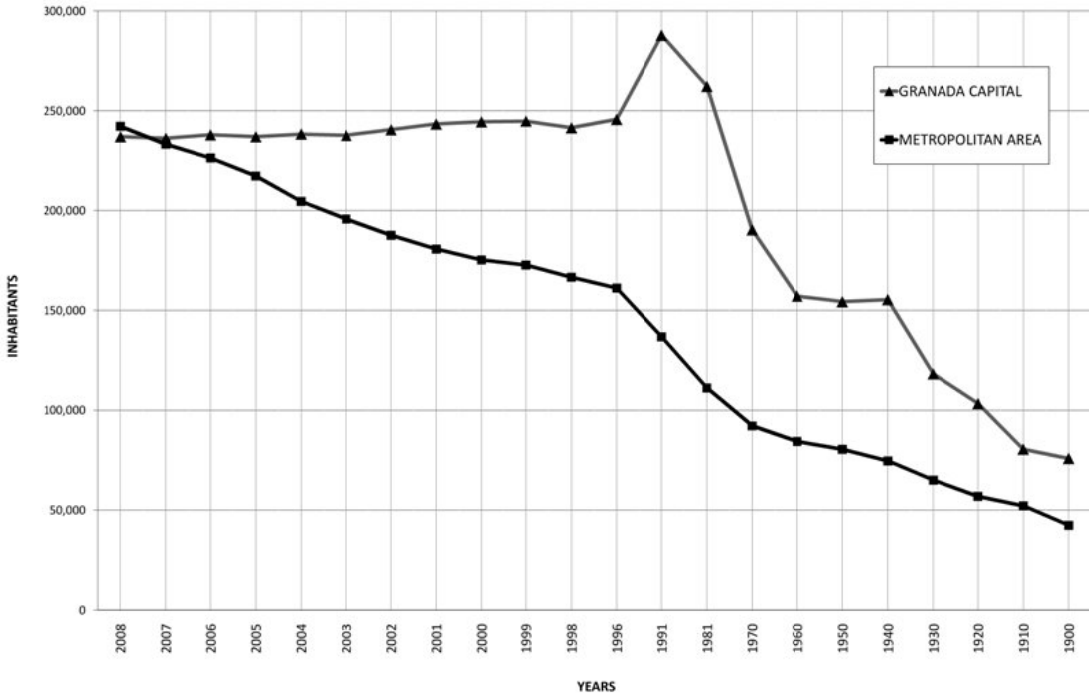

Figure 2. Evolution of the population in Granada city and towns nearby (Source: INE, 2009)

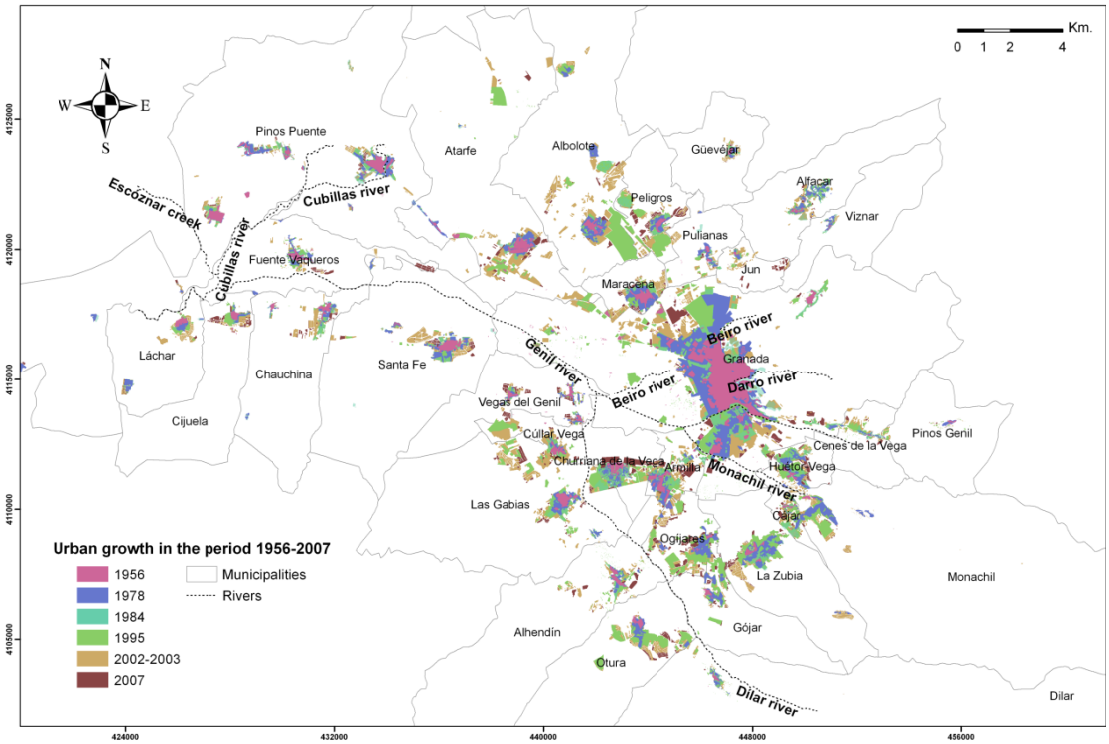

Figure 3. Urban growth in Granada and Metropolitan Area in the period 1956-2007

Regarding population growth, in 1970 the MA of Granada began to have a considerably greater number of inhabitants. This coincided with an enormous increase in built-up land. For example, in 1978 there was 57% more built-up land than in 1956.

5.1 Case Studies

The case studies presented in this paper focus on three towns in the west of Granada, Atarfe, Albolote, and Fuente Vaqueros, as well as one town in the south, Churriana de la Vega. Also included is La Chana (a district in the northwestern part of the city of Granada). The detailed maps, tables, and graphical summary that follow clearly reflect and justify the remarkable urban growth of the area, in which various conurbation processes can be observed.

Fuente Vaqueros (Figures 4 and 5) experienced a radial growth arising from the annexation of buildings that existed in 1956. This growth pattern runs parallel to the main roads (GR-NO-33, GR-NO-14, GR-NO-13) that start from the central plaza of the town (Plaza del Doctor Pareja). The entire area has an elongated shape, widening at the center. The direction of expansion is from NNW to SSE. The S sector has a hydrological boundary, the Genil River, which is the main river in La Vega of Granada. This village is in a dangerous zone taking into account the behavior of soil in seismic conditions, there are phenomenon of liquefaction and densification (Valverde-Palacios, 2010); as a result, the best direction of growth is to NNW instead of SSE.

Figure 4. Evolution of urban growth in Fuente Vaqueros for the period 1956-2007

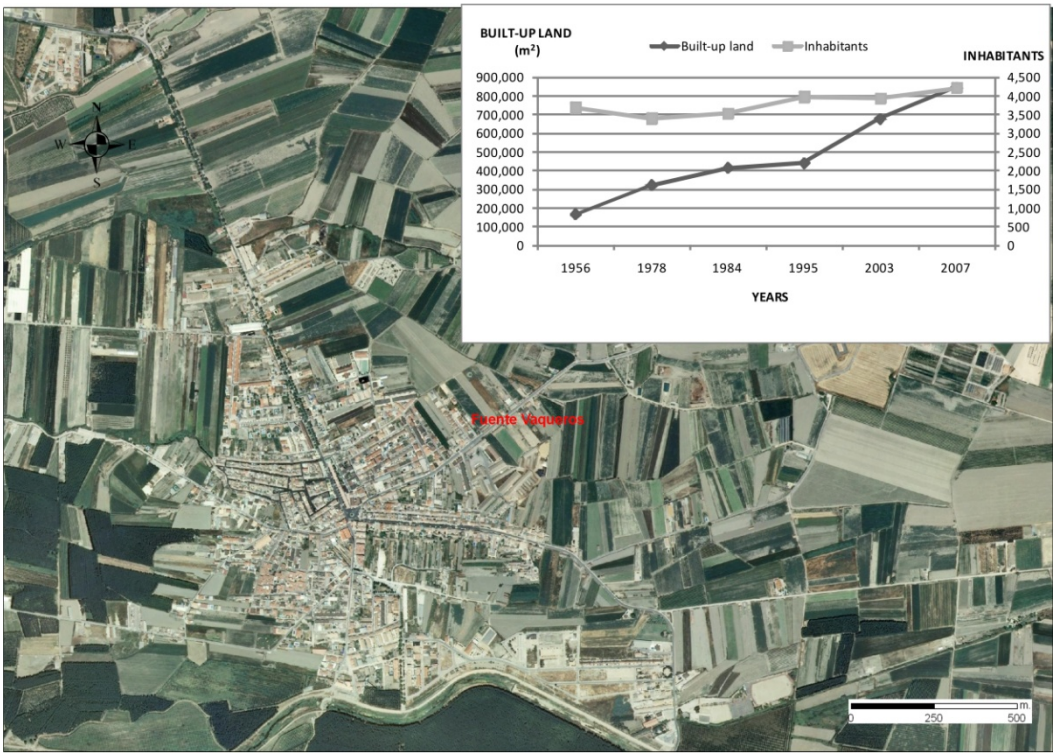

Figure 5. Fuente Vaqueros orthoimage for the year 2007 (source: IDEAndalucia. Junta de Andalucía). Graph of the evolution of urban growth and population for the period 1956-2007

In 1956-1978, the built-up soil in Fuente Vaqueros doubled, whereas in 1978-1984, it increased 22%. Subsequently, growth remained constant at 6% until 1995-2003, when it rose 34.9%. In 2003-2007, built-up soil increased 20%. Therefore, in the entire period from 1956 to 2007, Fuentevaqueros experienced an 80% increase in built-up land from 16Ha to approximately 85Ha. This increase was not accompanied by population growth since from 1950 to 2007, the population only increased by 526 inhabitants. The reason for the spectacular boom in built-up land with no significant population growth is that many of the new buildings were either second residences or factory installations in industrial parks.

Atarfe and Albolote (Figures 6-9) follow a model of multiple cores, which branch out from buildings that existed in 1956. In the case of Atarfe, growth is adjacent to the NE area, and in the case of Albolote, it is adjacent to the N-S and E-W areas. In addition, new population centers sprung up around existing buildings in the SW and WNW sectors of the towns. These growth patterns were further strengthened and consolidated by the important increase of built-up land in an important industrial park. Along with the industrial installations in Albolote-Peligros, both parks constitute an important link to the city Granada. Regarding relative growth, in 1956-1978, built-up land increased 40% in Atarfe and 70% in Albolote. In 1978-1984, even with the construction of housing developments, growth was slower in both towns (13.8% in Atarfe and 15.4% in Albolote). In 1984-1995 and 1995-2003, growth soared again because of the construction of industrial parks and housing developments (45% in Atarfe and 62% in Albolote), However, in 2003-2007, construction activity slowed significantly (7.2% in Atarfe and 3.1% in Albolote). The direction of growth is not the best in the case of Atarfe. In fact, the most suitable direction is SE and ESE, considering the effects of an earthquake in the soil (liquefaction).

Figure 6. Evolution of urban growth in Atarfe for the period 1956-2007

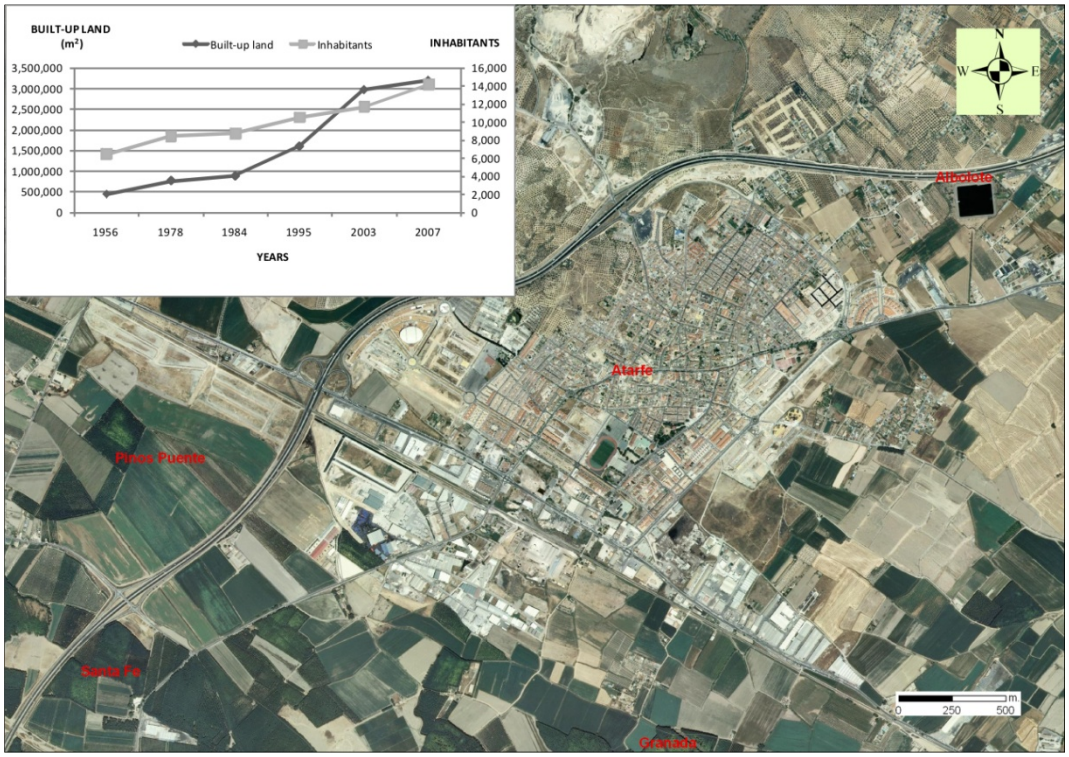

Figure 7. Atarfe orthoimage for the year 2007 (source: IDEAndalucia. Junta de Andalucía). Graph of the evolution of urban growth and population for the period 1956-2007

Figure 8. Evolution of urban growth in Albolote for the period 1956-2007

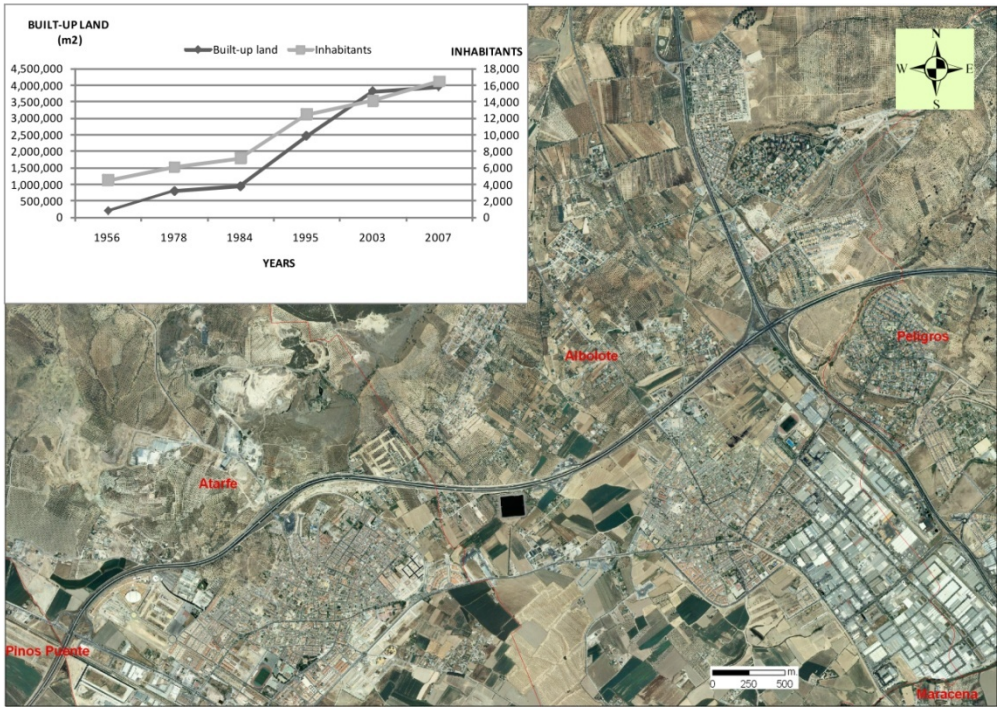

Figure 9. Albolote orthoimage for the year 2007 (source: IDEAndalucia. Junta de Andalucía). Graph of the evolution of urban growth and population for the period 1956-2007

The proximity of these towns to the city of Granada and their lower housing costs led to a population increase in both municipalities. According to the census figures of 1995-2007, the population of Atarfe increased by 7,689 inhabitants, and the population of Albolote by 11,963 inhabitants. These new residents occupied the newly built-up land, which increased by 86% during the same period. Atarfe experienced an increase in built-up land from 44Ha to about 320Ha, whereas Albolote experienced an increase of 18Ha to 390Ha. In this respect, Atarfe has become a major population nucleus for the first home of the population in the N sector of the metropolitan area.

The district of La Chana (Figures 11 and 12), in the city of Granada has also grown significantly. That is the result of Granada's expansion into the NW sector. This district is now linked to the town of Maracena town by the Cerrillo de Maracena, which reflects still another conurbation process. Built-up land in La Chana has increased by 90%, soaring from 17 Ha to approximately 175 Ha. Granada thus experienced a total increase of 1202 hectares in 1956-2007. Not surprisingly, the lower building costs in the surrounding areas near Granada have led to the exodus of the population towards these new urban nuclei. Accordingly, the population of the city of Granada has thus been decreasing since the 1980s. In this case and in Churriana de la Vega, there isn´t any problem with the behavior of the soil in dynamic condition.

Churriana de la Vega (Figures 12 and 13) reflects a longitudinal growth model expanding in an EW direction. This conurbation process has joined Churriana de la Vega to the town of Armilla, and practically to the city of Granada. A similar growth pattern is also reflected in the towns of Ogíjares, La Zubia, Gójar, and Cájar, where the boundaries of one municipality now seamlessly blend into those of another. The Armilla Air Force Base is one of the boundaries of Churriana de la Vega that limits urban growth to the south. Since the town has exhausted urbanizable land in the E and W sectors, its only alternative is to expand north into La Vega. At least for now, the partial urban plans only envisage single-family town houses. In 1956-2007, built-up land in Churriana de la Vega increased by 85.5% (from 15Ha to 170Ha). There was also a population growth of 70%. Along with Armilla, Ogíjares, La Zubia, Gójar and Cájar, Churriana de la Vega has become a new population nucleus for those building their first home in the S sector of the metropolitan area.

Figure 10. Evolution of urban growth in district of La Chana (city of Granada) for the period 1956-2007

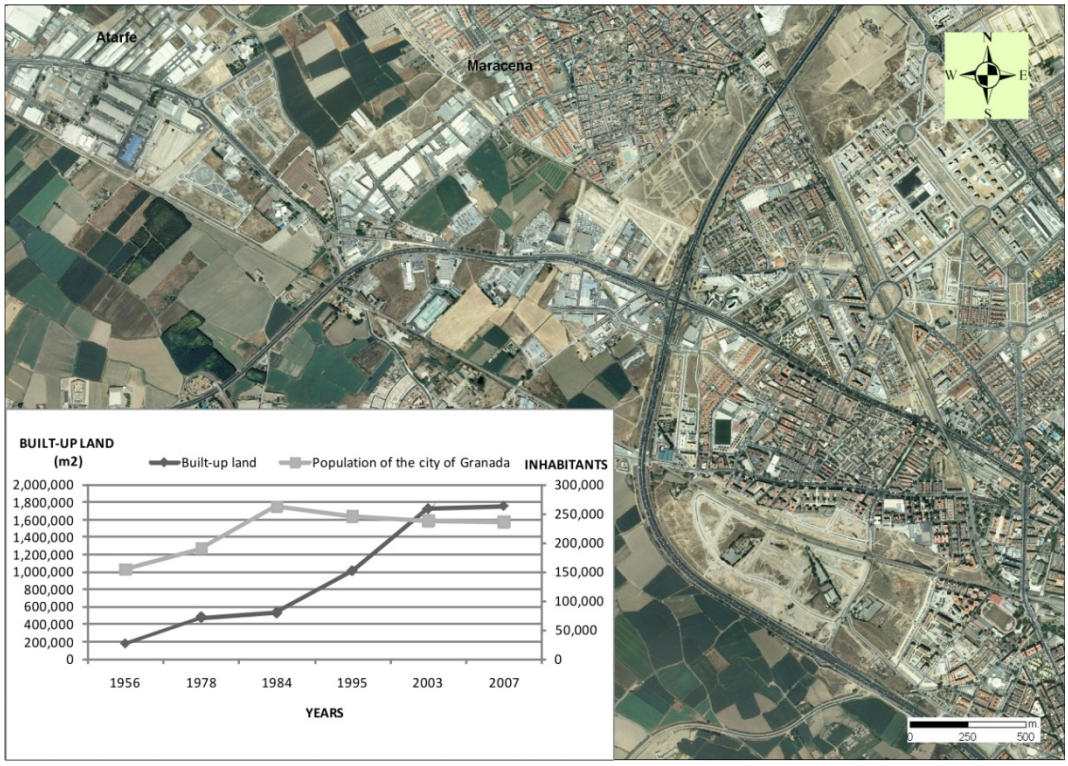

Figure 11. District of La Chana (city of Granada) orthoimage for the year 2007 (source: IDEAndalucia. Junta de Andalucía). Graph of the evolution of urban growth and population for the period 1956-2007

Figure 12. Evolution of urban growth in Churriana de la Vega for the period 1956-2007

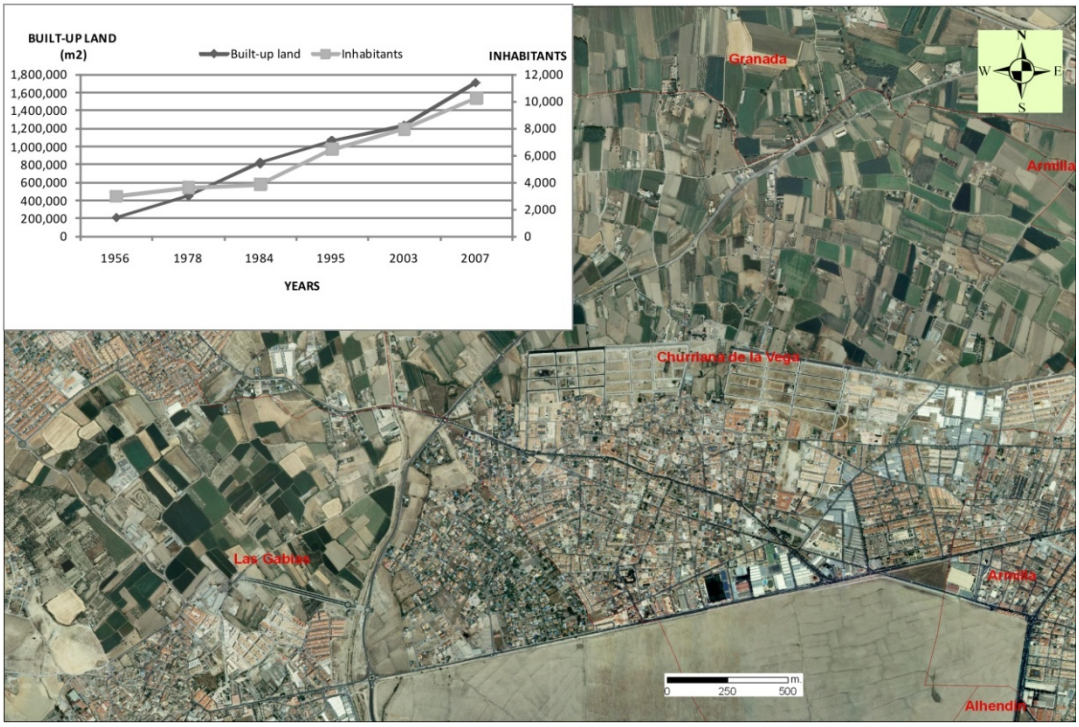

Figure 13. Churriana de la Vega orthoimage for the year 2007 (source: IDEAndalucia. Junta de Andalucía). Graph of the evolution of urban growth and population for the period 1956-2007

6. Conclusions

In the last fifty years, the population of Granada and its metropolitan area has doubled. This has led to an increase in built-up land of approximately 4650 ha. Furthermore, the areas that have experienced the largest growth in population and built-up land are located less than 15 km from the city.

In 1956-2007 there was an 84% increase in built-up land in Granada and its metropolitan area. In fact, in 1956-1978, 32 municipalities experienced an increase in built-up land of more than 30%. This was also accompanied by a corresponding urban population growth, which began in 1970 and lasted throughout the period.

Since the increase in built-up land and number of inhabitants has occurred in a moderate seismic hazard zone (NCSE-02), the risk from seismic events has become greater. This is despite the fact that buildings are now less vulnerable to earthquakes because of technical advances in construction, new materials, energy dissipation, and regulations to minimize and mitigate construction vulnerability.

The detailed study of urban growth in Albolote, Atarfe, Fuente Vaqueros, Churriana de la Vega and La Chana, together with analysis of soil dynamic behavior has established the optimal direction for the expansion of these municipalities (Valverde-Palacios, 2010). It is also important to consider urban growth scenarios as presented by Aguilera et al. (2011).

Finally, it is essential to take into account the seismic effects on the soil to plan urban growth.

This study shows that in some cases the growth directions are not correct, like in Fuente Vaqueros and Atarfe.

References

Aguilera, B. F., Plata, R. W., Bosque, S. J., & Gómez, D. M. (2009). Diseño y simulación de escenarios de demanda de suelo urbano en ámbitos metropolitanos. *Revista Internacional Sostenibilidad, Tecnologíay Humanismo, 4*, 57-80.

Aguilera, F., Valenzuela, L. M., & Botequilha-Leitão, A. (2011). Landscape metrics in the analysis of urban land use patterns: A case study in a spanish metropolitan area. *Landscape and Urban Planning, 99*(3-4), 226-238. http://dx.doi.org/10.1016/j.landurbplan.2010.10.004

Almoguera, S. M., & Ríos, V. M. T. (2008). Transformación de las áreas metropolitanas desde una perspectiva comparada: Sevilla y Gran Santiago de Chile. Implicaciones y respuestas desde la política de ordenación del territorio en la última década. Revista electrónica de Geografía y Ciencias Sociales, XII (270).

Berry, J. B., Gohhen, P. G., & Goldstein, H. (1968). *Metropolitan area definition: a reevaluation of concept and statistical practice*. Washington D.C.: U.S. Census Bureau.

Boix, D. R. (2007). *Concepto y delimitación de áreas metropolitanas: una aplicación a las áreas metropolitanas de España.* Seminario Las grandes áreas metropolitanas españolas en una perspectiva comparada. Centro de Estudios Andaluces. Junta de Andalucía. Seville. http://urban.uab.es/references/2007/07002.pdf

Cañete, P. J. A., Lozano, M. J. M., & Sáenz, L. M. (2005). Cambios demográficos en la aglomeración urbana de Granada y Plan de Ordenación del territorio. *Cuadernos Geográficos, 36*, 275-289.

Conde, F. (1999). Urbanismo y Ciudad en la aglomeración Urbana de Granada. Culturas e identidades urbanas. Sevilla: Junta de Andalucía. Consejería de Obras Públicas y Transportes. Empresa Pública del Suelo de Andalucía.

Cooke, T., & Marchant, S. (2006). The changing intrametropolitan location of high-poverty neighbourhoods in the US, 1990-2000. *Urban Studies, 43*(11), 1971-1989. http://dx.doi.org/10.1080/00420980600897818

Coombes, M. G. (1978). Towards a more rational consideration of census areal units: daily urban systems in Britain. *Environment and Planning, 10*, 1179-1185. http://dx.doi.org/10.1068/a101179

Davis, K. (1967). *La urbanización de la población humana*. In Scientific American: La Ciudad, Spanish translation, Madrid, Alianza Editorial.

De Esteban, A. (1981). Las áreas metropolitanas en España: Un análisis ecológico. Madrid: Centro de Investigaciones sociológicas. Colección Monografías.

Feria Toribio, J. M., Susino Arbucias, J., Casado Díaz, J. M., & Sardhina de Oliveira, G. (2005). *Movilidad por razón de Trabajo en Andalucía*. Sevilla: Instituto de Estadística de Andalucía.

Fernández, A. Á. (1997). Estructura de un espacio metropolitano. PhD thesis defended at the E.T.S. de Arquitectura, Granada: University Granada (Spain).

Font, A. (1972). La delimitación de las áreas metropolitanas: el caso de Barcelona. Cuadernos de Arquitecturay Urbanismo, 87.

Fox, K. A. (1964). Integrating National and Regional Models for Economic Stabilization and Growth. University of Pittsburgh.

Friedman, J., & Miller, J. (1965). The urban field. *Journal of the American Institute of Planners, 31*, 312-320. http://dx.doi.org/10.1080/01944366508978185

Gohhen, P. G. (1971). Metropolitan area definition: re-evaluation of concept and statistical practice. *Internal structure of the city reading on espace and enviroment*. Toronto: Oxford University Press.

Hall, P., & Hay, D. (1980). *Growth centers in the Urban Europ System*. London: Educational Books.

Instituto Nacional de Estadística. (2009). Retrieved February 12, 2009, from http://www.ine.es.

Junta de A., Consejería, de O., & Públicas, Y. T. (1999). Plan de Ordenación del Territorio de Aglomeración Urbana de Granada (POTAUG). Granada: Consejería de Obras Públicas y Transportes. Dirección General de Ordenación del Territorio y Urbanismo.

Menor, T. J. (1997). Transformaciones recientes en la Organización territorial de la Vega de Granada: del espacio agrario tradicional a la aglomeración urbana actual. *Estudios Regionales, 48*, 189-214.

Ministerio, de la V. (1960). Áreas Metropolitanas de España en 1960. Madrid: Dirección General de Urbanismo. Ministerio de la Vivienda.

Nunes, I., & Alonso, J. (1986). Aproximació a l´estructura de l´area metropolitana de Barcelona: les estructures d´intensitat diària. *Documents d´Anàlisi Geogràfica, 8-9*, 71-90.

Rozenfeld, H. D., Rybski, D., Andrade Jr., J. S., Batty, M., Stanley, H. E., & Makse, H. A. (2008). Laws of population growth. *Proceedings of the National Academy of Sciences of the United States of America, 105*(48), 18702-18707. http://dx.doi.org/10.1080/01944366508978185

Sánchez, G. D. (2005). El proceso de envejecimiento demográfico en Granada y su Área Metropolitana. *Cuadernos Geográficos, 37*, 185-199.

Serra, J. (1991). *La ciutat metropolitana delimitacions, desconcentracions, desequilibris*. Barcelona: Institut d`Estudis Metropolitans de Barcelona.

Storper, M. (2010). Why Does a City Grow? Specialisation, Human Capital or Institutions? *Urban Studies, 47*(10), 2027-2050. http://dx.doi.org/10.1177/0042098009359957

Unwin, D. J. (1996). GIS, spatial analysis and spatial statistics. *Progress in Human Geography, 20*(4), 540-551. http://dx.doi.org/10.1177/030913259602000408

Valverde, P. I. (2010). Cimentaciones de edificios en condiciones estáticas y dinámicas. Casos de estudio al W de la ciudad de Granada. PhD Thesis defended at the University of Granada (Spain). http://0-hera.ugr.es.adrastea.ugr.es/tesisugr/18877485.pdf

Van Geffen, J. (2003). Metropolitan Statistical Area Changes. Texas Labor Market.

Earth Science Research; Vol. 1, No. 2; 2012
ISSN 1927-0542 E-ISSN 1927-0550
Published by Canadian Center of Science and Education

An Environment-Friendly Conductive Concrete

Xin Tian[1,2], Hu Hu[1,2] & Bin Chen[1]

[1] Architecture Engineering School, Yunnan Agricultural University, Kunming, China

[2] Energy Saving and Reduction Inspection & Research Engineering Center, Yunnan Agricultural University, Kunming, China

Correspondence: Hu Hu, Architecture Engineering School, Yunnan Agricultural University, Kunming, China. Tel: 86-180-6486-4334. E-mail: 76huhu@163.com

Received: June 1, 2012 Accepted: June 21, 2012 Online Published: July 6, 2012

doi:10.5539/esr.v1n2p185 URL: http://dx.doi.org/10.5539/esr.v1n2p185

Foundation-supported program: The project of scientific research foundation of the Education Department of Yunnan Province (2010C231)

Abstract

This article describes that the author, through the continuous exploration of improving and optimizing the preparation method and process of conductive concrete, has found a kind of environment-friendly conductive concrete with high conductive property, simple preparation method and process, low cost and convenient application in the construction site.

Keywords: conductive concrete, preparation method and process, green and environment-friendly

1. Introduction

The property and mixed method of conductive concrete will vary with the conductive components (such as: graphite, steel slag, stainless steel fiber and carbon fiber) mixed in the concrete. The different conductive component, mixing proportion and preparation process not only determine the electric property of conductive concrete, but also affect the convenience and cost control in their late application. Today, with more and more attention to the green and environmental protection, account will be taken into the pollution of the materials mixed in the concrete to the environment. Otherwise, the conductive concrete, even it is of high property, will not be allowed to use.

The conductive property is decisive to the properties and application value of the conductive concrete. A simple preparation process will produce the convenience of application. Whether the conductive concrete is favorable for the green and environmental protection will reflect a responsible attitude to the nature and society. Therefore, high property, practicality and environmental protection has been the principle and direction the author adheres to his research and exploration of preparation method and process of conductive concrete.

2. Improving the Conductive Property of Concrete

The conductive property is the first element of conductive concrete. The material resistivity is an index which reflects the conductive property of the concrete. In order to obtain the resistivity as low as possible, the author experimented many different kinds of and different specifications of conductive materials, adopted different proportions and preparation processes, finally found a relatively reasonable optimization scheme after balancing the cost factors.

2.1 The Conductive Concrete with Graphite as Conductive Material

Graphite is a kind of good conductive material. It is widely used in the areas related to electric conduction and also a popular material used in the conductive concrete due to its good conductivity, stable property, wide material source and no pollution to environment. The author make some comparison tests in different proportions by taking respectively the soil shape common graphite samples with carbon content more than 80% and the flaky high grade graphite samples with carbon content more than 95% and fineness of 500 mesh. See Figure 1 Comparison of Different Graphite for the test result.

We can see from the figure, the conductive property of the high grade flaky graphite with high carbon content

and high fineness has the conductive property higher than that of the soil shape common graphite with low carbon content, and the conductive property of the concrete will improve with increase of the graphite proportion. However, the graphite inherent lubricity greatly decreases the strength of the concrete with high graphite proportion and the cost of the concrete greatly increases with increase of the graphite proportion. Obviously, it is not an ideal way to use the high price and high grade graphite and raise the graphite proportion in the concrete to improve the conductive property, the comprehensive property and economic result(it is not an ideal way to improve the conductive property, the comprehensive property and economic result by using the high price, high grade graphite and raising the graphite proportion in the concrete).

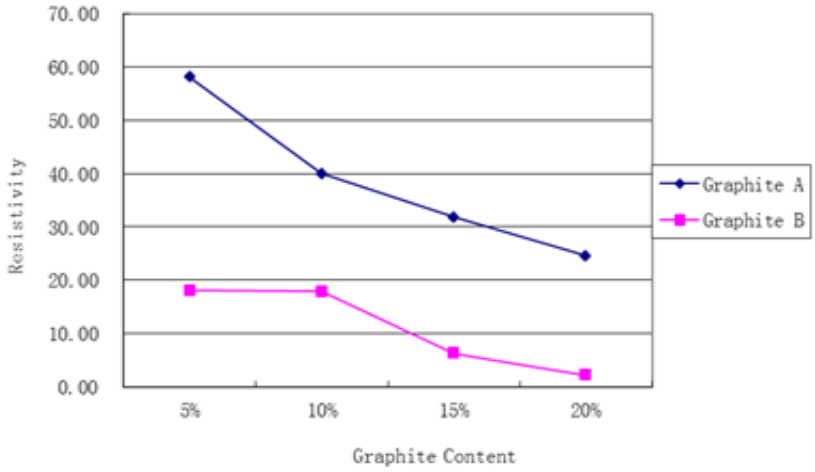

Figure 1. Comparison of Different Graphite

2.2 Composite Conductive Concrete with Carbon Fiber

The author tried to use the composite conductive concrete with a new conductive fiber material as the dominant material and other materials as the auxiliary ones for improving the conductive property of the conductive concrete since the conductive concrete mixed with pure graphite cannot get the satisfactory conductive property, strength and economic result. As it easily forms the conductive channel between the materials, the conductive fiber material can evidently improve the conductive property of the conductive concrete, as shown in Figure 2.

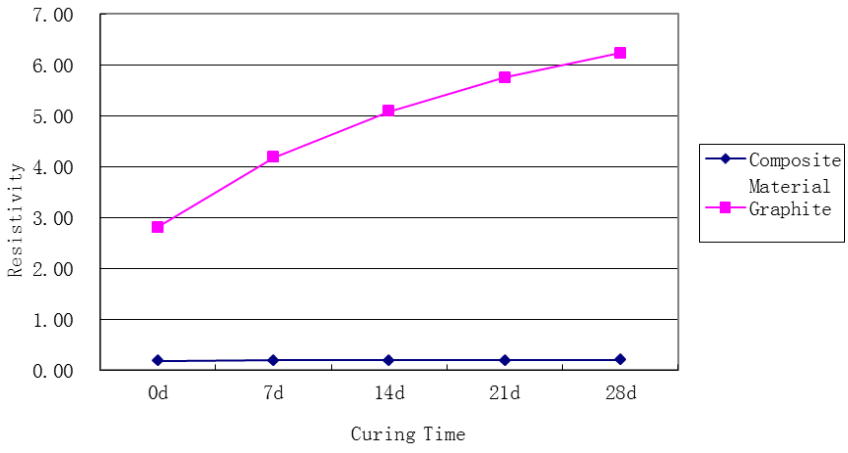

Figure 2. Comparison of Graphite and Composite

Figure 2 Comparison of Graphite and Composite Material shows, the graphite used for comparison is the high grade flaky graphite with 95% carbon content and in the proportion of 15%. According to the used material and its proportion, the conductive concrete is the very good graphite conductive concrete. But compared with the

composite conductive concrete, the conductive property of the graphite conductive concrete is evidently not in the same order of magnitude. Moreover, the resistivity of the graphite conductive concrete gradually will rise with the curing time extending, but the resistivity of the composite conductive concrete changes slightly and its conductive property is very stable. This is a big advantage of the composite conductive concrete, that is, the concrete already has a good and stable conductive property in its initial setting stage. Although the graphite conductive concrete has a relatively good conductive property in its initial setting stage, the conductive property will gradually decrease and finally reach a stable value as time goes on. When the conductive concrete is used as the resistance reducing agent, the composite conductive concrete can be used for the effect test soon after pouring. The test values measured in this stage are basically consistent with those measured after setting of concrete. This can not only improve the work efficiency and shorten the work cycle, but also increase the economic benefit.

3. Exploration on Improving Process and Practicality

Although the conductive fiber material can greatly improve the conductive property of the concrete, the original preparation process makes it very difficult to apply such fiber material in the construction site. In order to bring it into utmost play, the fiber material must be evenly distributed in the concrete, which needs to be accomplished by adding dispersant. The dispersant can be dissolved only in the high temperature water. It is not very difficult to solve the problem in the lab because it is a small-batch test. But in the construction site, to dissolve the dispersant in the high temperature water will be a Gordian knot. If this problem is not solved, the wide application of the fiber material in the engineering practice will be certainly limited.

Finally, the author has found a new conductive fiber material. Compared with the original material, the anti adhesive property of such new fiber material has been greatly improved. First, such fiber material is physically mixed with the superfine flake graphite and the lubricity and diffusibility of graphite will reduce the adhesive property among fibers to the minimum. During preparing the concrete, the stone powder material like silicon ash is also used for dispersing fiber again. The stone powder material has much lower cost than silicon powder and has wide sources. The author has finally solved the problems of fiber agglomeration and uneven distribution by using a physical dispersing method in place of the traditional chemical dispersing method, thus, has laid a good foundation for convenient application of such fiber material in the engineering practice.

4. Environment-friendly Resistance-reducing Material

In the grounding construction of the electric power system (such as substation and wind farm) and the special buildings (such as gas station), a number of resistance-reducing agent is used to reduce the grounding resistance because of high requirement of grounding resistance. Both the traditional chemical resistance reducing agents and the physical resistance reducing agents widely used now have a problem that themselves are not able to solidify and then run off, thus it cause great harm to environment. Firstly，these resistance reducing agents contain heavy metal and other chemical components harmful to environment. They will flow to the deeper soil with water in the soil to pollute the soil and water sources. Secondly, the running off of resistance reducing agent makes the soil which originally wraps the grounding electrode superseded by general soil, so severely reduces the resistance reducing effect. In this case, the grounding resistance value will rebound year after year and cannot reach the design standard. In addition, the traditional chemical resistance reducing agents have certain corrosion to the grounding electrode, which will make the grounding electrode out of action due to rusting at last, and make grounding not to be up to standard.

The composite conductive concrete prepared by the author has reached and even exceeded many resistance reducing agent materials in the aspect of conductive property (The conductive property of the composite conductive concrete prepared by the author has reached and even exceeded those of resistance reducing agent materials) (According to the national standard, the resistivity of the resistance reducing agent is $< 5\Omega\cdot m$ and the resistivity of composite conductive concrete prepared by the author is $< 0.5\Omega\cdot m$.) and at the same time, the greatest advantage lies in the environmental protection. No materials used in the composite conductive concrete contain the substance harmful to environment. This is particularly important today when the state energetically promotes the policy of environmental protection. Due to its own setting property, such conductive concrete does not run off in the soil as time goes on, does not corrode but protect the grounding body and can play a long and stable role in reducing resistance and also reduce the cost of its later use and maintenance. So it is an ideal green and environment-friendly resistance reducing material.

5. Conclusion

1) High carbon content and high fineness flaky graphite is favorable for improving the conductive property of the conductive concrete.

2) The composite conductive concrete which takes new conductive fiber as the dominant material and other materials as the auxiliary material has much higher conductive property and more stable performance than the graphite conductive concrete.

3) The adoption of the new materials and the new process is an important guarantee for convenient application of the conductive concrete in the engineering practice.

4) Whether the conductive property or the environmental property, the new type conductive concrete is a very ideal resistance reducing material. It can be used in the grounding system in place of the traditional resistance reducing agent.

In the process of preparation and exploration of the conductive concrete, a great number of data and also a satisfactory result have been obtained through both continuous adjustment of materials and mixing proportion and continuous process improvement. The good conductive property and environmental property of the new type conductive concrete has laid solid foundation of its future application in many areas.

References

Chen, B., Wu, K. R., & Yao, W. (2002). Studies on Electrical Conductivity of Fiber Reinforced Concrete and its Application. *CONCRETE, 7*, 23-27.

Cheng, L. H., Meng, H. R., & Xi, Y. L. (2006). Application of short carbon fibers in concrete. *CONCRETE, 4*, 29-31.

Deng, S. C., & Li, S. C. (2003). Studies and analyses on concrete electric resistance oefficient. *CONCRETE, 3*, 10-12.

Farhad, R., Gordon, B. B., Jerry, A. Y., & Jong, S. L. (2001). Volumeelectrical Resistivity of Carbon Fiber CementComposites. *ACI Materials Journal, 98*(1), 25-35.

Jiang, Z. W., Sun. Z. P., & Wang, X. Y. (2000). Conductive Concrete Technology. *CONCRETE, 9*,55-58.

Li, G. J., Zheng, X. M., & Wang, B. (2006). Experimental Study on Electrical Conductivity of Carbon Fiber Reinforced Concrete. *Journal of Jiamusi University (Natural Science), 3*, 457-459.

Lu, Z. H., & Zhang, Y. F. (2009). Study on the Compressive Strength and Electrical Conductivity of Carbon Fiber-slag Concrete. *Science Technology and Engineering, 9*, 2510-2512.

Mao, Q. Z., Zhao, B. Y., Shen, D. R., & Li, Z. Q. (1996). Study on the Compression Sensibility of Cement Matrix Carbon Fibre Composite. *Acta Materiae Compositae Sinica, 4*,8-11.

Park, S. B., Lee, B. I., & Llim, Y. S. (1991). Experimental study on the engineering properties of carbon fiber reinforced cement composites. *Cement and concrete research, 21*(4), 589-600. http://dx.doi.org/10.1016/0008-8846(91)90110-4

Shen, G., & Dong, F. Q. (2004). Performance Research on Carbon Fiber Conductive Concrete. *HIGHWAY, 12*, 178-182.

Sherif, Y., Christopher, Y. T., David, F., & Bing, C. (2000). Conductive Concrete Overlay for Bridge Deck Deicing Mixture Proportioning, Optimization, and Properties. *ACI Materials J., 97*(2), 172-181.

Sun, J. G., Yang, W. D., & Zhang, B. (2007). Research of Electrical Conductivity of Carbon Fiber Reinforced Concrete Based on Uniform Design. *Journal of Dalian Nationality College, 1*, 20-23.

Toutanji, H. A., EI –Torehi, T., & Tatz, R. N. (1994). Strength and reliability of carbon - fiber- reinforced cement composites. *Cement and concrete composites, 16*(1), 15-21. http://dx.doi.org/10.1016/0958-9465(94)90026-4

Xin, T., & Hu, H. (2012). Test and Study on Electrical Property of Conductive Concrete. 2012 International Conference on Structural Computation and Geotechnical Mechanics.

Zhang, W. F., Ma, C. H., Zhao, W. Y., Cai, Y. J., & Zhu, D. R. (2009). Electrical Conductivity of Graphite Conductive Concrete. *Journal of Daqing Petroleum College, 1*, 72-77.

Earth Science Research; Vol. 1, No. 2; 2012
ISSN 1927-0542 E-ISSN 1927-0550
Published by Canadian Center of Science and Education

Study on the Impact of Varying Degrees of Underground Accidental Explosions on Underground Pipes by Simulation

Akinola Johnson Olarewaju[1]

[1] Civil Engineering Department, School of Engineering, Federal Polytechnic, Ilaro, Ogun State, Nigeria

Correspondence: Akinola Johnson Olarewaju, Civil Engineering Department, School of Engineering, Federal Polytechnic, Ilaro, P.M.B. 50, Ilaro, Ogun State, Nigeria. Tel: 234-803-244-6036. E-mail: akinolajolarewaju@yahoo.com

Received: January 13, 2012 Accepted: January 31, 2012 Online Published: July 6, 2012

doi:10.5539/esr.v1n2p189 URL: http://dx.doi.org/10.5539/esr.v1n2p189

The research is financed by Ministry of Science, Technology and Innovation (MOSTI) Malaysia e-science grant No. 03-01-10-SF0042 at SKTM, Universiti Malaysia Sabah, 88999 Kota Kinabalu, Sabah, Malaysia (Tel: 60-102-453-947 & 60-148-728-131).

Abstract

Underground accidental explosions are caused by the detonation of explosive materials (solid, liquid or gas) stored below the ground surface. In this study, response of underground pipes due to varying degrees of underground accidental explosions was studied using ABAQUS code. Pipes buried in loose sand, dense sand and undrained clay at 1m depth below the ground surface were modelled. The material properties as revealed by several researchers were used. Pipe and soil materials were limited to linear, elastic, homogeneous and isotropic. The observed parameters are displacement, pressure, stress and strain at the crown, invert and spring-line of underground pipes. The results showed that irrespective of the ground media, displacement increases linearly as the loading wave velocity increases. Even though there is wide variation in the results due to dilations and compressions caused by the transient stress pulse of compression wave, observed parameters increases as the loading wave velocity increases.

Keywords: underground accidental explosion, pipes, structures, response, loading wave velocity, observed parameters

1. Introduction

Underground accidental explosion normally occur when an explosive material (solid, liquid or gas) explodes below the ground surface. Underground explosion can take place, broadly speaking, in sand as well as undrained clay with varying degrees of impact on underground structures. Depending on the mass and depth of burial of explosive charge as well as the geotechnical property of the ground medium, the consequence of underground accidental explosion is tremors which could be felt tens and hundreds of kilometres away from the point of burst of the buried explosive materials (Eric & Shino, 2011). The load emanating from the blast wave is termed loading wave velocity. It denotes the blast load which the buried explosive charge delivered to the buried structures. The underground accidental explosion loads in terms of loading wave velocity reduce to seismic velocity of soil at less than 10m from the source for explosive range of 10kg TNT to 250kg TNT buried in soils and undrained clay (Olarewaju et al., 2010b; 2010d; 2010h). Seismic velocity is a term describing the rate of propagation of an elastic wave through the earth due to disturbance in the earth caused by explosion or earthquake and it depends on the density and elasticity of the ground medium (Robert, 2002).

Due to complexity in accurately determining the mass of the explosive materials (i.e., solid, liquid and gas) that will produce the explosive loads on underground structures, there is need to study the consequences of these complexity. This is with a view to determining the extent and magnitude of the responses of underground structures like pipes due to varying degrees and impact of underground accidental explosions. Underground structures are divided into fully buried structures partially buried structures which can be any structure of diverse shapes such as, shelters, basement structures, underground mall facilities, underground parking spaces, silos, storage facilities, retention basins, shafts, tunnels, pipes, underground railway, metro stations, to mention a few.

Pipes are underground installations which are used to convey petroleum products, sewage, industrial and domestic wastes, liquid gas, acid, gas in petrol-chemical industries, atomic reactor, means of transportation in underground, means of access in mining industries, storage facilities, piling for jetties berths and foundations, caissons, surface and underground main lines for irrigation and drainage, penstocks for hydro-electric projects, etc. Due to huge investment involved in the construction of underground pipes and tremendous usage across the world, there is need to study the responses of underground installations (like pipes) due to underground accidental explosions. This is with view to providing design information and guidelines for underground pipes to resist the effects of underground accidental explosions. Explosion-load-evaluation of underground structures at low depth of burial is important in designing explosion-resistant underground structures like pipes. This study is aimed at determining by simulation, the impact of varying degrees underground accidental explosions on underground pipes.

2. Background Study

Explosive materials (solid, liquid or gas), are stored above the ground surface, on the ground surface and below the ground surface depending on the volatility and proximity to the surrounding settlement. This is mostly carried out at: military formations where defensive weapons like war heads, bombs, grenades, etc are stored; filling stations where fuels and other crude oil derivatives are stored; manufacturing industrial sites where propane are stored underground; etc. Explosion loads could be evaluated using empirical, semi-empirical and numerical techniques as the case may be (Unified Facilities Criteria, 2008; Peter & Andrew, 2009; Olarewaju et al., 2010a; 2010b; 2010d; 2011a; 2012). According to Unified Facilities Criteria (2008), explosive materials for underground explosions, confined and unconfined for surface explosions are expressed in kilogram (kg) trinitrotoluene (TNT) equivalent for an explosive. This is the mass of TNT that would give the same blast performance as the mass of the explosive in question.

Soil-pipe interaction due to short discontinuous events like underground accidental explosions depends mainly on stiffness of the constituents rather than strength (Liang-Chaun, 1978; Olarewaju et al., 2010c; 2010g). Underground explosions (nuclear or otherwise) could be carried out for different purposes such as earthmoving mechanisms and crater formation, even though it may have spiral effects. When explosive material (i. e. nuclear weapon, bombs, etc) explodes under the ground, a sphere of extremely hot, high-pressure gases, including vaporized weapon residues, soil and rock, is formed. This is the equivalent of the fireball in an air or surface burst. The rapid expansion of the gas bubble initiates a ground shock wave which travels in all directions within the ground medium away from the burst point. When the upwardly directed shock (mainly compression) wave reaches the earth's surface, it is reflected back as a rarefaction (or tension) wave. If the tension exceeds the tensile strength of the surface material, the upper layers of the ground will split off into more-or-less horizontal layers (The Effects of Nuclear Weapons, 1977).

A plowshare program test was conducted on the 6th July 1962 at the Nevada test site for the promotion of underground nuclear explosion to develop peaceful usage for the atomic energy. In this test, explosive of $104x10^3$ tons displaced $12x10^6$ tons of soil and released seismic energy of 4.75 Richter scale equivalents (United States Department of Energy, 2000; AubreyJ.org, 2006 - in public domain). The impacts of underground accidental explosions are mostly felt at grater distance from the source of the explosion (Robert, 2002; Eric & Shino, 2011). The United States of America has conducted a lot of deep underground tests, especially since September 1961 according to The Effects of Nuclear Weapon (1977).

3. Methodology

In this study, 1m diameter pipes buried in loose sand, dense sand and undrained clay at 1m depth below the ground surface were modelled using ABAQUS software (finite element numerical code). According to Olarewaju et al. (2012), it is more necessary to evaluate the explosion resistance of underground structures at lower depth of burial. This is because the inter-atomic bonds of the material yield more at lower depth of burial than those buried at grater depth. The contact between the soil and pipe was defined for 'no slip' condition. Therefore it is assumed that perfect bond exist between the soil and the pipe. The soil and pipe materials were assumed to be linear, homogeneous and isotropic. As a result, the material properties as revealed by various researchers and pipe manufacturers were used (Craig, 1994; Kameswara, 1998). In line with Geotechnical Modelling and Analysis with ABAQUS (2009), boundary conditions were defined with respect to global Cartesian axis.

In line with ABAQUS Analysis Users' Manual (2009) and ABAQUS/Explicit: Advanced Topic (2009), analysis were carried out on simulated models by solving the governing equation of motion of the system shown in

Equation 1 (with the initial conditions) using the time integration technique of the finite different scheme in ABAQUS/Explicit (Olarewaju et al., 2010c; 2010h; 2011c).

$$[m][\ddot{U}] + [c'][\dot{U}] + [k][U] = [P] \quad (1)$$

where *m, c', k, U* and *P* are the global mass matrix, global damping matrix, global stiffness matrix, displacement and load vectors respectively while dot indicate their time derivatives (Kameswara, 1998; ABAQUS Analysis User's Manual, 2009; ABAQUS/Explicit: Advanced Topic, 2009).

The observed parameters are displacement, pressure, stress and strain at the crown, invert and spring-line of pipes buried in loose sand, dense sand and undrained clay as shown in Figure 1 (Olarewaju et al., 2010a; 2010g; 2011c). Underground accidental explosions were assumed to have taken place outside the vicinity of the buried pipes and as a result, explosion loads for explosives range of 10kg TNT and 250kg TNT were represented by the loading wave velocities for sand and undrained clay as shown in Figures 2 and 3 respectively.

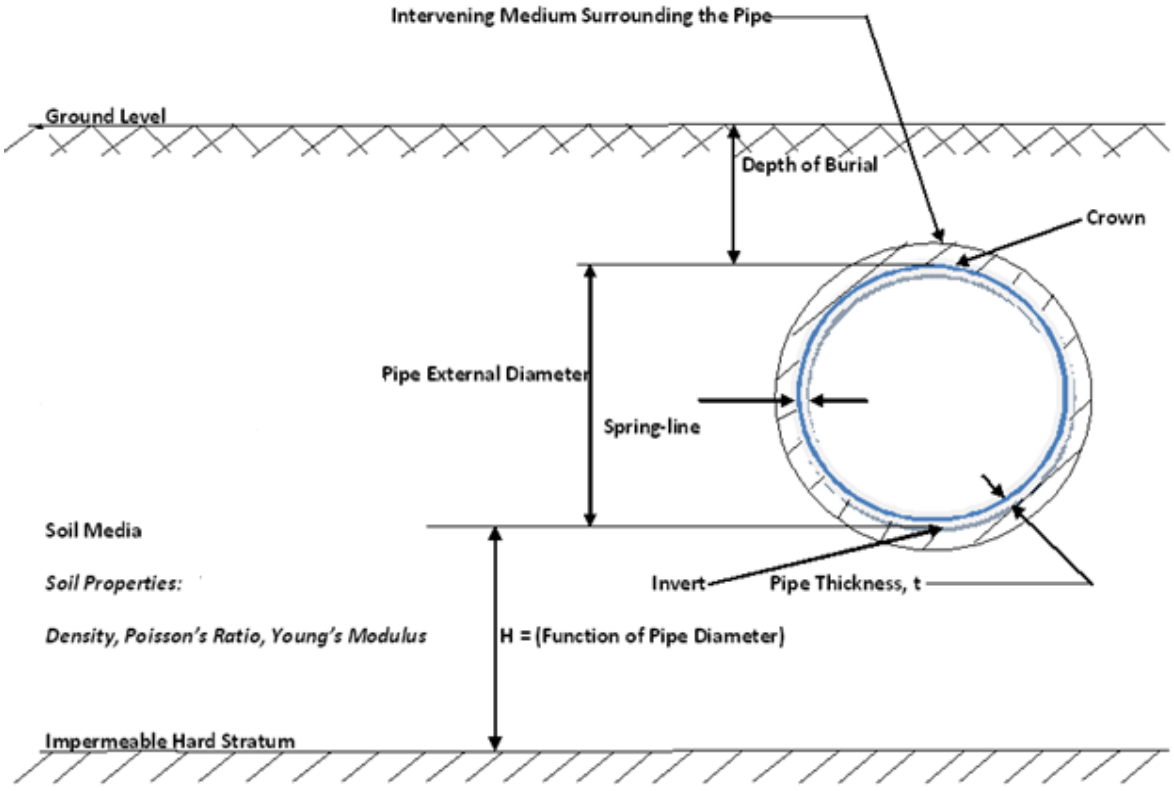

Figure 1. Problem definition for the response of underground pipe due to varying degree of impact of underground accidental explosions (Olarewaju et al., 2010a; 2010g; 2011c)

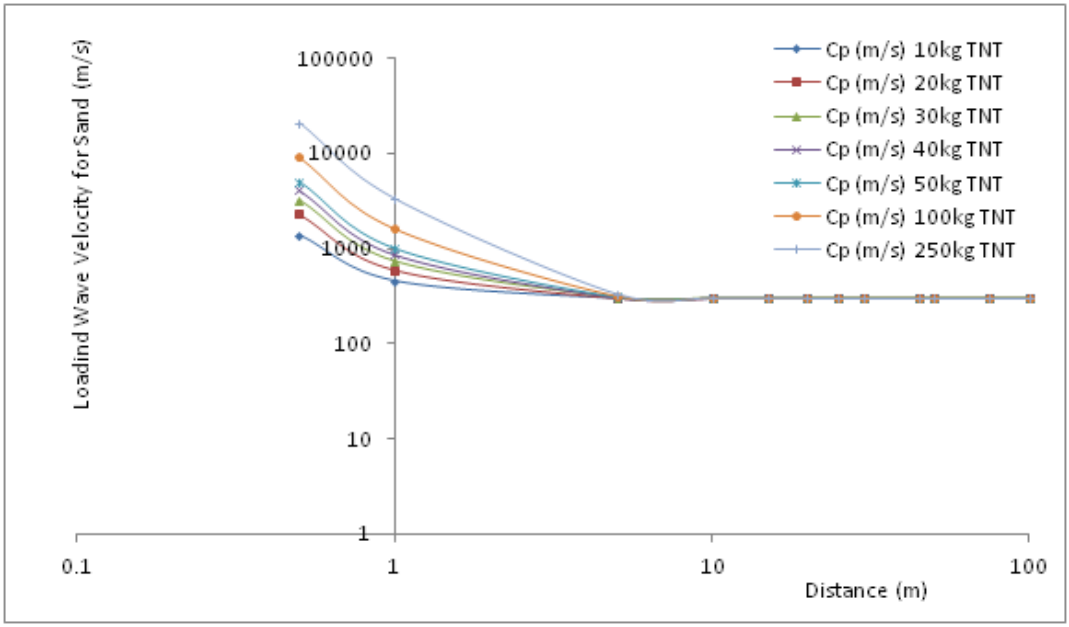

Figure 2. Loading wave velocity for sand at stand-off distance for varying weight of explosives (Olarewaju et al., 2010d; 2010e; 2010f; 2010h; Olarewaju et al., 2012)

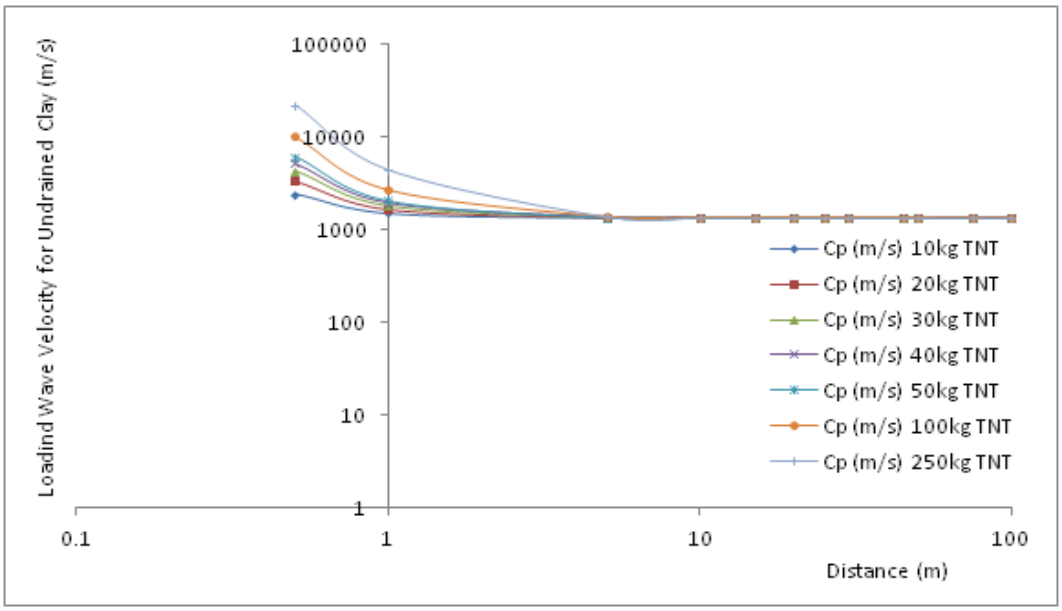

Figure 3. Loading wave velocity for undrained clay at stand-off distance for varying weight of explosives (Olarewaju et al., 2010d; 2010e; 2010f; 2010h; Olarewaju et al., 2012)

4. Results and Discussion

The results of loading wave velocities for explosives ranging from 10kg TNT to 250 kg TNT in sand and undrained clay due to underground accidental explosions, as obtained from Olarewaju et al. (2010d, 2010e; 2010f; 2010h) and Olarewaju et al. (2012) are presented in Figures 2 and 3 respectively. In addition to this, due to underground accidental explosions, the result of displacement at the crown, invert and spring-lie of pipes buried in loose sand, dense sand and undrained clay are presented in Figures 4, 5 and 6 respectively. Furthermore, due to underground accidental explosions, the result of pressure at the crown, invert and spring-line of pipes

buried in loose sand, dense sand and undrained clay are presented in Figures 7, 8 and 9 respectively. Due to underground accidental explosions, the result of stress at the crown, invert and spring-line of pipes buried in loose sand, dense sand and undrained clay are presented in Figures 10, 11 and 12 respectively. Finally, due to underground accidental explosions, the result of strain at the crown, invert and spring-line of pipes buried in loose sand, dense sand and undrained clay are presented in Figures 13, 14 and 15 respectively.

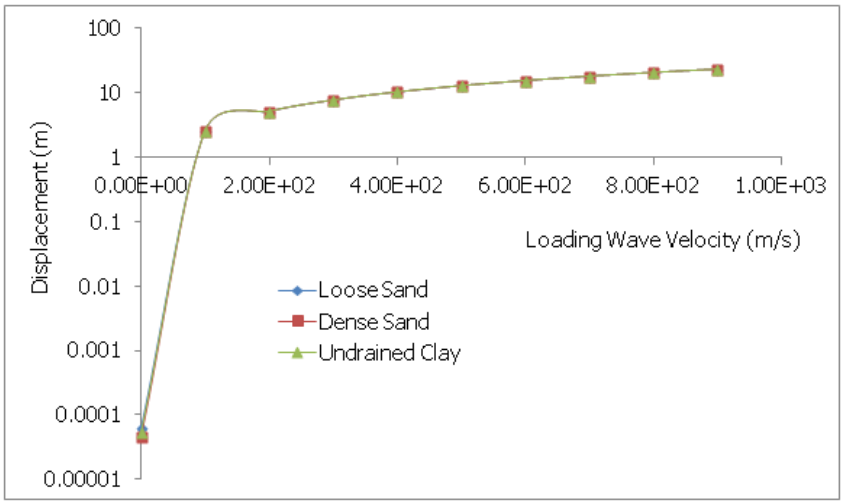

Figure 4. Displacement at the crown of underground pipes due to varying underground accidental explosions

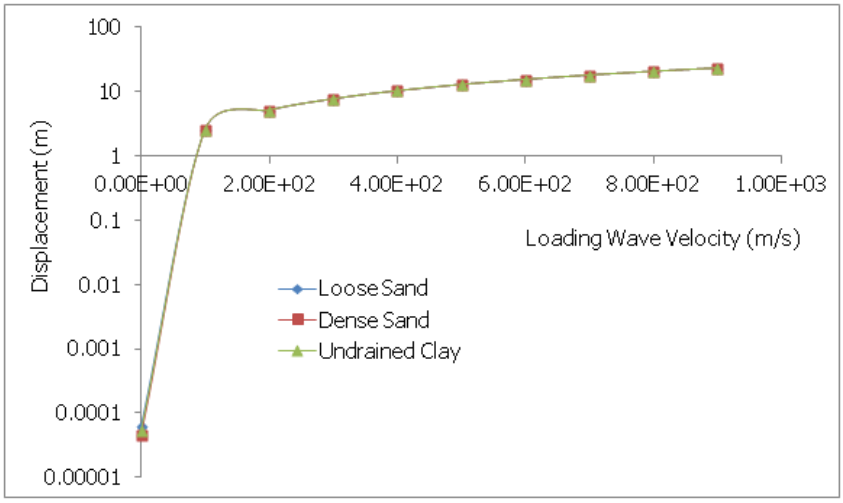

Figure 5. Displacement at the invert of underground pipes due to varying underground accidental explosions

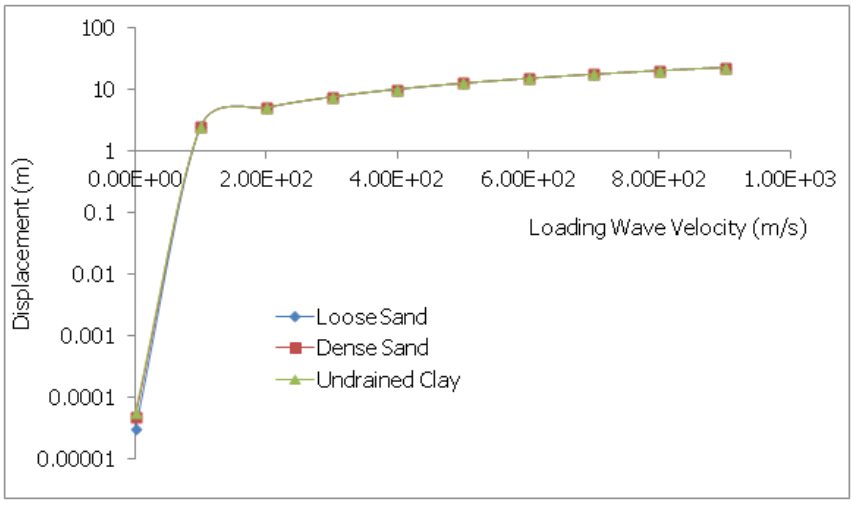

Figure 6. Displacement at the spring-line of underground pipes due to varying underground accidental explosions

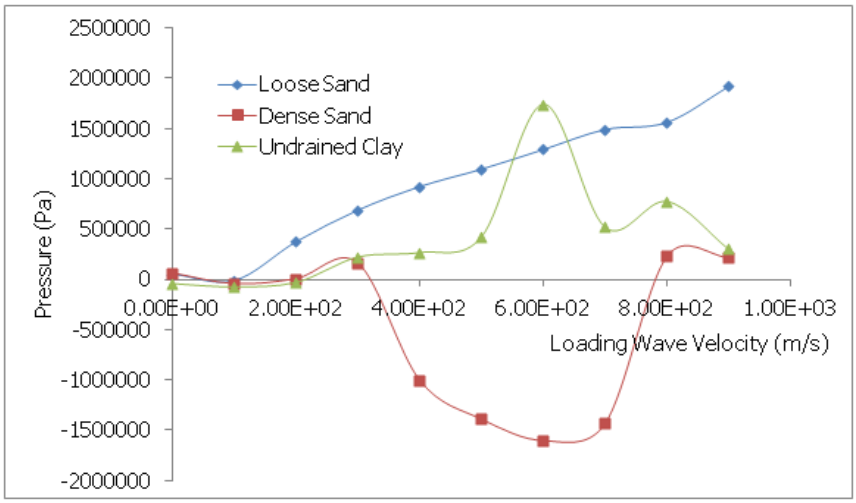

Figure 7. Pressure at the crown of underground pipes due to varying underground accidental explosions

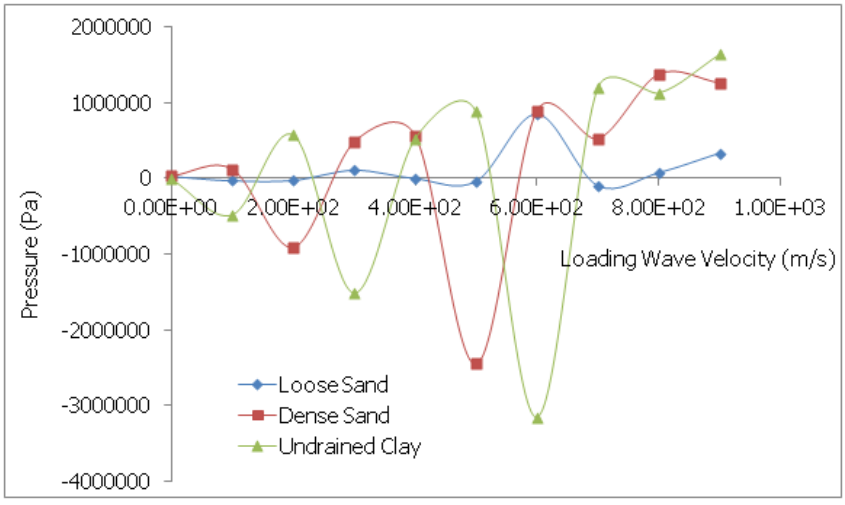

Figure 8. Pressure at the invert of underground pipes due to varying underground accidental explosions

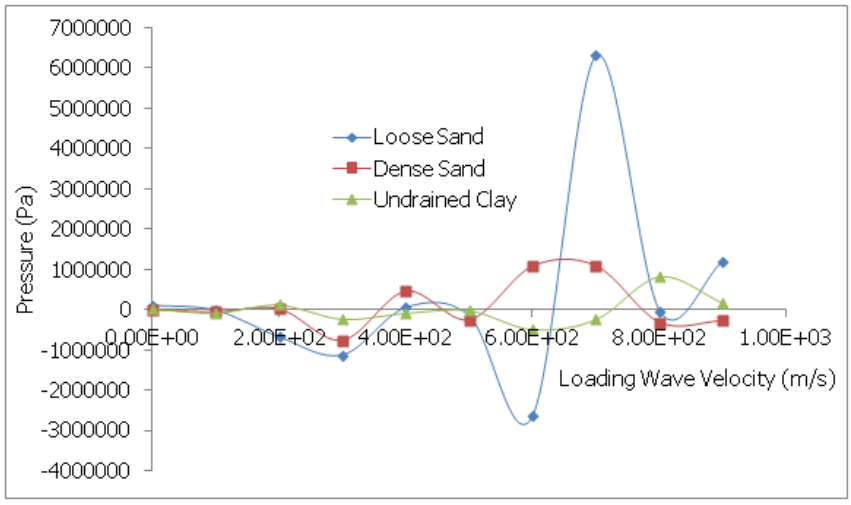

Figure 9. Pressure at the spring-line of underground pipes due to varying underground accidental explosions

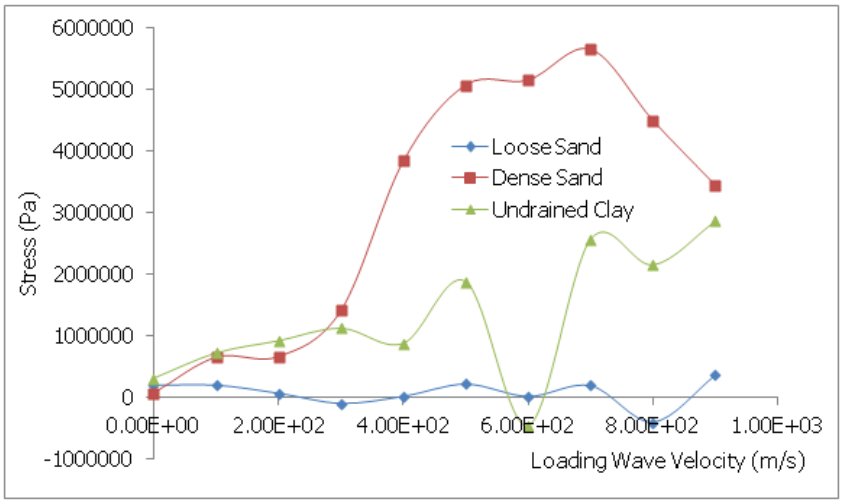

Figure 10. Stress at the crown of underground pipes due to varying underground accidental explosions

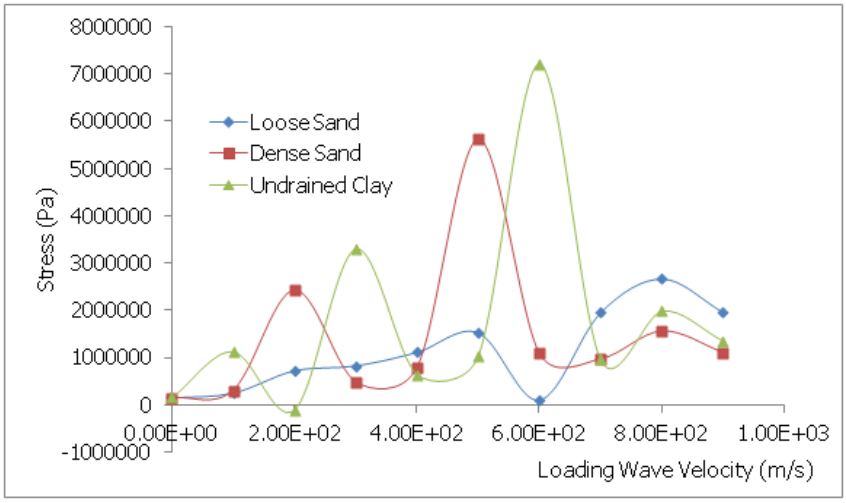

Figure 11. Stress at the invert of underground pipes due to varying underground accidental explosions

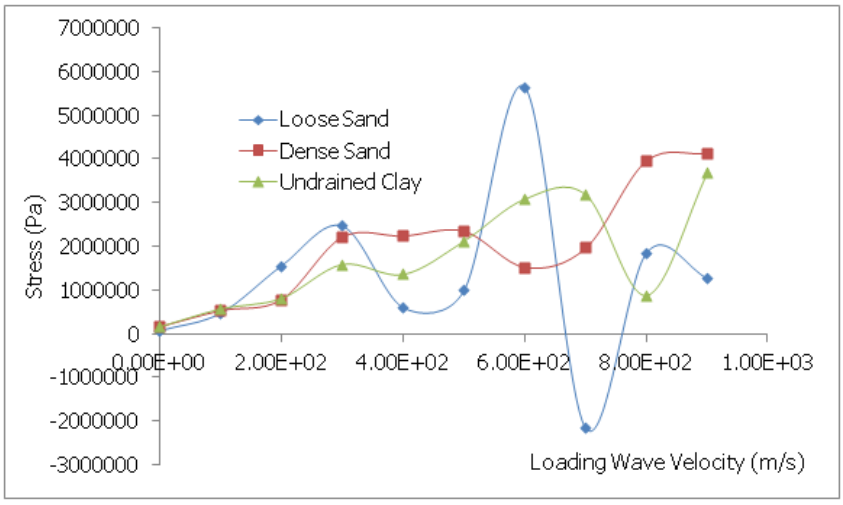

Figure 12. Stress at the spring-line of underground pipes due to varying underground accidental explosions

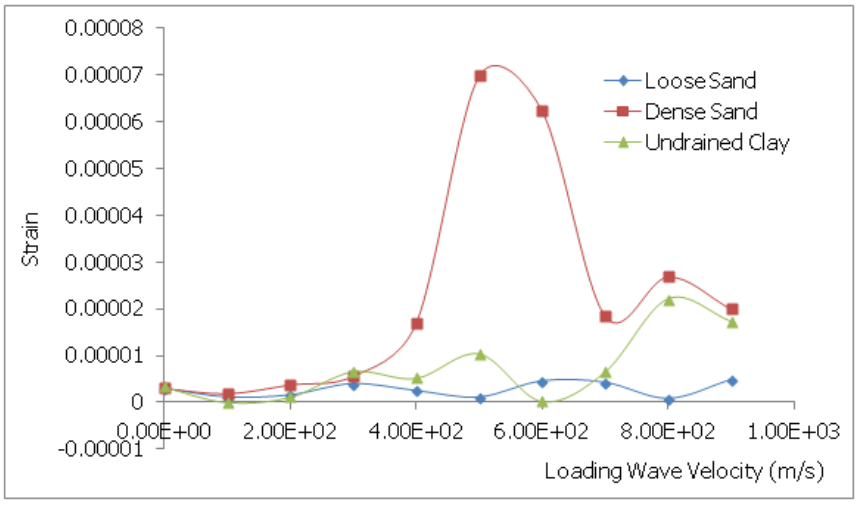

Figure 13. Strain at the crown of underground pipes due to varying underground accidental explosions

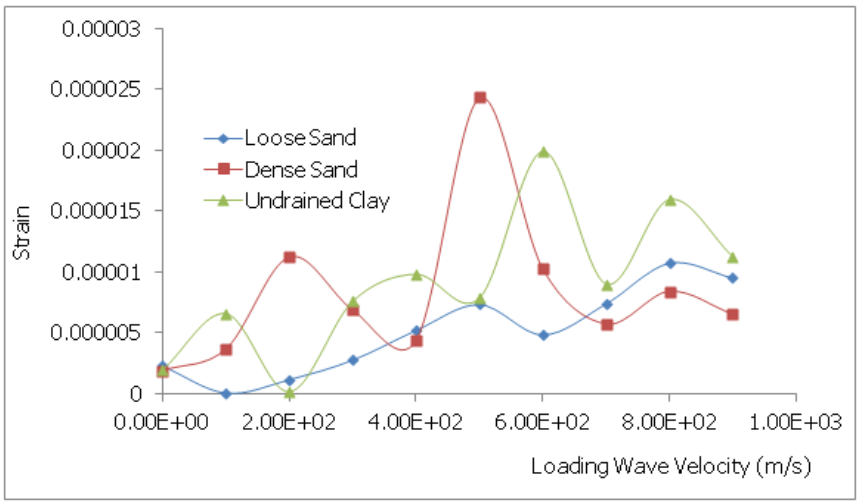

Figure 14. Strain at the invert of underground pipes due to varying underground accidental explosions

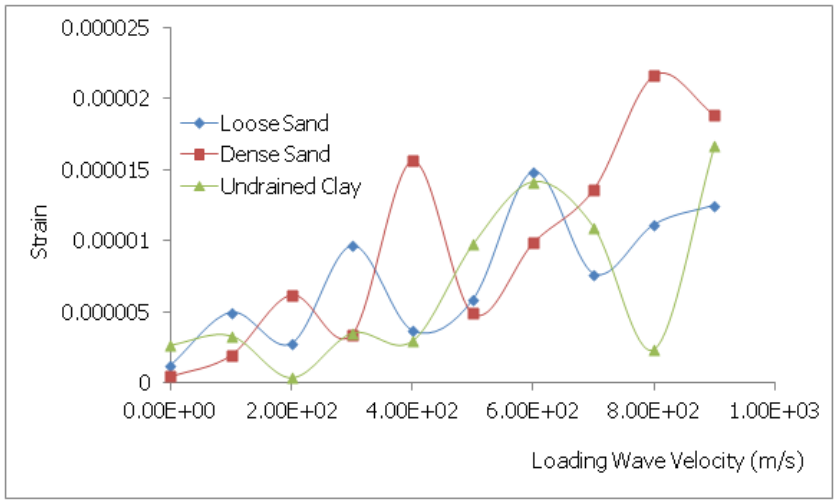

Figure 15. Strain at the spring-line of underground pipes due to varying underground accidental explosions

For the weight of explosives considered (i.e., 10kg TNT to 250kg TNT), loading wave velocity in sand and undrained clay reduces to seismic velocity of soil at a distance of less than 10m from the point of burst of underground accidental explosions as shown in Figures 2 and 3 respectively. This is because much of the energy from the explosive yield is spent in heating, melting, fracturing and plastically deforming the soil matrix around and within the vicinity of the source of underground explosion (Olarewaju et al., 2010i). The remaining energy is released to the ground medium in the form of seismic velocity. For the loading wave velocities investigated, the maximum pressure observed at the crown, invert and spring-line of pipes buried in loose sand, dense sand and undrained clay are 1.8 Mpa (N/mm^2), 3.3 Mpa and 6.2 Mpa as shown in Figures 7, 8 and 9 respectively. In addition to this, as shown in Figures 10, 11 and 12, the maximum stress at the crown, invert and spring-line of pipes buried in loose sand, dense sand and undrained clay are 5.7 Mpa, 7.2 Mpa and 5.5 Mpa respectively. Finally, the maximum strain at the crown, invert and spring-line of pipes buried in loose sand, dense sand and undrained clay are 0.00007, 0.000024 and 0.000022 as shown in Figures 13, 14 and 15 respectively.

Displacement at the crown, invert and spring-line of pipes buried in loose sand, dense sand and undrained clay increases linearly as the loading wave velocity increases as shown in Figures 4, 5 and 6 respectively. Irrespective of the ground media, displacement in the pipes is linear. In addition, as shown in Figures 7, 8 and 9, pressure changes from positive to negative in the buried pipes in all the ground media considered due to dilations and compressions caused by the transient stress pulse of compression wave from the underground accidental explosion. Furthermore, even though there is wide variation in the result due to dynamic nature of the load, as the loading wave velocities from underground accidental explosions increases, pressure shown in Figures 7, 8 and 9, stress shown in Figures 10, 11 and 12 as well as strain shown in Figures 13, 14 and 15 at the crown, invert and spring-line of pipes buried in loose sand, dense sand and undrained clay, respectively, increases. This study has shown that displacement is the most important criteria to be given priority in the design of underground pipes to resist effects of underground accidental explosions. It shows that as the displacement increases linearly due to increased loading wave velocity from underground accidental explosions, moment and stress induced in underground pipes will also increase and may eventually lead to material failure if the yield limit is exceeded.

5. Conclusion

In this study, the impact of varying degrees of underground accidental explosions on buried pipes has been examined. Pipes are generally laid (i. e. buried) at varying depth of burial depending on application, geotechnical properties of the ground media, etc. With time, due to hydraulic erosion, wind erosion, and other forms of erosion, the topmost part of the soil cover that forms the overburden on the underground structures like pipes is washed away. As a result of this, there is need for accidental explosion resistant evaluation of underground installations like pipes in order to have an optimal design of underground structures like pipes that would resist the effects of underground accidental explosions. This is imperative most especially around military formations where defensive and explosive weapons are stored underground, filing stations where automotive gas oil (AGO), premium motor spirit (PMS), dual purpose kerosene (DPK) are stored underground, manufacturing industrial areas where propane are stored underground, etc.

It is important to note that due to less overburden, structural materials yield more easily at lower depth of burial due to underground accidental explosions, whereas at grater depth of burial, due to confinement, response of underground structures such as pipes is minimal (Olarewaju et al., 2010f; 2011c; 2011d). In designing underground installations like pipes to resist effects of unpredictable varying magnitude of underground accidental explosions, displacement is one of the paramount factors to be given priority compared to other observed parameters (i. e. pressure, stress and strain). This is because displacement (i. e. with respect to given distances) of underground installations like pipes results in moments and stresses that will be induced. If the moment and stress induced in underground pipes due to displacement is large and it approaches the yield stress of the material of underground installations (i.e. pipes), invariably it would result to material failure. This study has demonstrated that higher loading wave velocity would result to higher displacement which invariably would result to higher induced moment and stress if multiplied by the corresponding distances (Liang-Chaun. 1978).

References

Abaqus Inc. (2009). Abaqus Analysis User's Manuals – Documentation, Version 6.7- and 6.8-EF, D'S Simulia, Providence, Rhode Island, USA.

Abaqus Inc. (2009). Abaqus/Explicit: Advanced Topics, D'S Simulia, Providence, Rhode Island, USA.

Abaqus Inc. (2009). Geotechnical Modelling and Analysis with Abaqus, D'S Simulia, Providence, Rhode Island, USA.

AubreyJ.org. (2006). United States Department of Energy, All in Public Domain. Retrieved from http://www.doe.gov.bridge

Craig, R. F. (1994). *Soil Mechanics* (5th ed.). GB: Chapman and Hall Press.

Eric, T., & Shino. (2011). Stricken Japan nuclear plant rocked by 2nd blast. Fukushima Dai-Ichi Nuclear Plant Plagued By Cooling Issues. The Associated Press, 14th March.

Kameswara, R. N. S. V. (1998). *Vibration Analysis and Foundation* (1st ed.). New Delhi: Wheeler Publishing Co. Ltd.

Liang-Chaun, P. (1978). *Soil-pipe interaction: Stress analysis methods for underground pipelines* (pp, 67-76). AAA Technology and Specialties Co. Inc., Houston, Pipeline Industry.

Olarewaju, A. J., Kameswara Rao, N. S. V., & Mannan, M. A. (2010a). Response of Underground Pipes due to Blast Load. *Proceedings of 3rd International Earthquake Symposium Bangladesh*, Bangladesh University of Engineering Technology, Dhaka, 165-172, Mar. 5th-6th.

Olarewaju, A. J., Kameswara Rao, N. S. V., & Mannan, M. A. (2010b). Blast Effects on Underground Pipes. *Electronic Journal of Geotechnical Engineering,* May*, 15*(F), 645-658.

Olarewaju, A. J., Kameswara Rao, N. S. V., & Mannan, M. A. (2010c). Behaviors of Buried Pipes due to Internal Explosion. *Malaysia Construction Research Journal,* 9(2).

Olarewaju, A. J., Kameswara Rao, N. S. V., & Mannan, M. A. (2010d). Blast Prediction and Characteristics for Simulating the Response of Underground Structures. *Proceedings 3rd International Conference of Southeast Asian on Natural Resources and Environmental Management*, Universiti Malaysia Sabah, Malaysia, Aug. 5th - 6th. 384-391.

Olarewaju, A. J., Kameswara Rao, N. S. V., & Mannan, M. A. (2010e). Design Hints for Buried Pipes to Resist Effects of Blast. *Proceedings of Indian Geotechnical Conference, Indian Institute of Technology, India*, Macmillan Press, Dec. 16th-18th, 881-884.

Olarewaju, A. J., Kameswara Rao, N. S. V., & Mannan, M. A. (2010f). Guidelines for the Design of Buried Pipes to Resist Effects of Internal Explosion, Open Trench and Underground Blasts. *Electronic Journal of Geotechnical Engineering, 15*(J), 959-971.

Olarewaju, A. J., Kameswara Rao, N. S. V., & Mannan, M. A. (2010g). Response of Underground Pipes due to Blast Loads by Simulation–An Overview. *Electronic Journal of Geotechnical Engineering, 15*(G), 831-852.

Olarewaju, A. J., Kameswara Rao, N. S. V., & Mannan, M. A. (2010h). Response of Underground Pipes Due to Underground Blast. *Proceedings of the International Agricultural Engineering Conference, China*, Sept. 17th - 20th, pp. (I) 321-329.

Olarewaju, A. J., Kameswara Rao, N. S. V., & Mannan, M. A. (2011a). Blast Effects on Underground Pipes Using Finite Element Method. *Proceedings of 12th International Conference on Quality in Research*, Faculty of Engineering, University of Indonesia, Bali, Indonesia, 4th-7th July, 2511-2518.

Olarewaju, A. J., Kameswara Rao, N. S. V., & Mannan, M. A. (2012). Chapter 20: Response of Underground Pipes to Blast Loads, Book Title: *Earthquake-Resistant Structures - Design, Assessment and Rehabilitation, Abbas Moustafa (Ed.), ISBN: 978-953-51-0123-9, Geology and Geophysics, InTech Publisher, University Campus STeP Ri, Slavka Krautzeka 83/A 51000 Rijeka, Croatia, Europe,* February, 507-524,

Olarewaju, A. J., Kameswara Rao, N. S. V., & Mannan, M. A. (2011c). Simulation and Verification of Blast Load Duration for Studying the Response of Underground Horizontal and Vertical Pipes Using Finite Element Method. *Electronic Journal of Geotechnical Engineering, 16*(G)**,** 785-796.

Olarewaju, A. J., Kameswara Rao, N. S. V., & Mannan, M. A. (2011d). Dimensionless Response of Underground Pipes Due to Blast Loads Using Finite Element Method. *Electronic Journal of Geotechnical Engineering, 16*(E), 563-574.

Peter, D. S., & Andrew, T. (2009). Blast Load Assessment by Simplified and Advanced Methods, Defence College of Management and Technology, Defence Academy of the United Kingdom, Cranfield University, UK.

Robert, W. D. (2002). *Geotechnical Earthquake Engineering Handbook*. NY: McGraw-Hill.

The Effects of Nuclear Weapons. (1977). Chapter II: Description of Nuclear Explosions – Underwater and Underground Blast. Trinity Atomic Web Site, Nuclear Weapons: History, Technology, and Consequences in History Documents, Photos, and Videos.

Unified Facilities Criteria. (2008). Structures to Resist the Effects of Accidental Explosions, UFC 3-340-02, Department of Defense, US Army Corps of Engineers, Naval Facilities Engineering Command, Air Force Civil Engineer Support Agency, USA.

United States Department of Energy. (2000). United States Nuclear Tests July 1945 through September 1992, Nevada Operations Office Las Vegas, Nevada DOE/NV--209-REV 15, 1-162.

Earth Science Research; Vol. 1, No. 2; 2012
ISSN 1927-0542 E-ISSN 1927-0550
Published by Canadian Center of Science and Education

Unmixing and Target Recognition in Airborne Hyper-Spectral Images

Amir Averbuch[1], Michael Zheludev[1] & Valery Zheludev[1]

[1] School of Computer Science, Tel Aviv University, Tel Aviv, Israel

Correspondence: Amir Averbuch, School of Computer Science, Tel Aviv University, Tel Aviv 69978, Israel. Tel: 972-54-569-4455. E-mail: amir@math.tau.ac.il

Received: May 25, 2012 Accepted: June 16, 2012 Online Published: July 6, 2012

doi:10.5539/esr.v1n2p200 URL: http://dx.doi.org/10.5539/esr.v1n2p200

Abstract

We present two new linear algorithms that perform unmixing in hyper-spectral images and then recognize their targets whose spectral signatures are given. The first algorithm is based on the ordered topology of spectral signatures. The second algorithm is based on a linear decomposition of each pixel's neighborhood. The sought after target can occupy sub- or above pixel. These algorithms combine ideas from algebra and probability theories as well as statistical data mining. Experimental results demonstrate their robustness. This paper is a complementary extension to Averbuch & Zheludev (2012).

Keywords: hyper-spectral processing, target recognition, sub- and above pixel, unmixing, dimensionality reduction, diffusion maps

1. Introduction

1.1 Data Representation and Extraction of Spectral Information

We assume that a hyper-spectral signature of a sought after material is given. In many applications according to Winter (1999), a fundamental processing task is to automatically identify pixels whose spectra coincide with the given spectral shape (signature). This problem raises the following issues: How the measured spectrum of a ground material is related to a given "pure" spectrum and how to compare between them to determine if they are the same? Spatial and spectral sampling produce a 3D data structure referred to as a data cube. A data cube can be visualized as a stack of images where each plane on the stack represents a single spectral channel (wavelength). The observed spectral radiance data, or the derived surface reflectance data, can be viewed as a scattering of points in a K -dimensional Euclidean space $\mathbb{R}^K$ where K is the number of spectral bands (wavelengths). Each spectral band is assigned to one axis. All the axes are mutually orthogonal. Therefore, the spectrum of each pixel can be viewed as a vector $x=(x_1,\ldots,x_K)$ where its Cartesian coordinates x_i are either radiance or reflectance values at each spectral band. Since $x_i \geq 0, i=1,\ldots,K$, then the spectral vectors lie inside a positive cone in $\mathbb{R}^K$. Changes in the illumination level can change the length of the spectral vector but not its, which is related to the shape of the spectrum. When targets are too small to be resolved spatially or when they are partially obscured or of an unknown shape, as shown in Winter (1999), then the detection has to rely on the available spectral information. Unfortunately, a perfect fixed spectrum for any given material does not exist.

In agreement with Winter (1999), spectra of the same material are probably never identical even in laboratory experiments. This is due to variations in the material surface. The variability amount is even more profound in remote sensing applications because of the variations in atmospheric conditions, sensor noise, material composition, location, surrounding materials and other contributing factors. As a result, the measured spectra, which correspond to pixels with the same surface type, exhibit an inherent spectral variability that prevents the characterization of homogeneous surface materials by unique spectral signatures.

Another significant complication arises from the interplay between the spatial resolution of the sensor and the spatial variability present in the observed ground scene. According to Winter (1999), a sensor integrates the radiance from all the materials within the ground surface that are "seen" by the sensor as a single image pixel. Therefore, depending on the spatial resolution of the sensor and the distribution of surface materials within each ground resolution cell, the result is a hyper-spectral data cube comprised of "pure" and "mixed" pixels, where a pure pixel contains a single surface material and a mixed pixel contains multiple (superposition of) materials.

A linear mixing model is the most widely used spectral mixing model. It assumes that the observed reflectance spectrum of a given pixel is generated by a linear combination of a small number of unique

constituent known as endmembers. This model is defined with constraints in the following way (Harsanyi & Chang, 1994):

$$x = \sum_{k=1}^{M} a_k s_k + w = Sa + w, \quad \sum_{k=1}^{M} a_k = 1, \text{ additivity constraint, } a_k \geq 0 \text{ positivity constraint} \tag{1}$$

where $s_1, \ldots, s_M$ are the M endmember spectra that assumed to be linearly independent, $a_1, \ldots, a_M$ are the corresponding abundances (cover material fractions) and w is an additive-noise vector.

1.2 Outline of the Algorithms to Identify Target with Known Spectra

The new methods in this paper achieve targets identification with known spectra. Target identification in hyper-spectral has the following consecutive steps:

1) Finding suspicious points: there are points whose spectra are different in any norm from the spectra of the points in its neighborhood. This is also called anomaly detection;

2) Extracting from the suspicious points the spectra of the independent components (unmixing) where one of them is the target that its spectrum fits the given (sought after) spectrum.

We assume that spectra of different materials are statistically dependent and the difference between them occurs from the behavior of the first and second derivatives in some sections in the spectrum. If they are statistically independent, then all the related work such as Maximum Likelihood (ML) and Geometrical (MVT, PPI and N-FINDR) work well.

The experiments in this paper were performed on three real hyper-spectral datasets, which were measured as reflectance, titled: “desert”, “city” and “field” which were acquired by the Specim camera SPECIM camera (2006) located on a plane. Their properties with a display of one waveband per dataset are given in Figures 1-3.

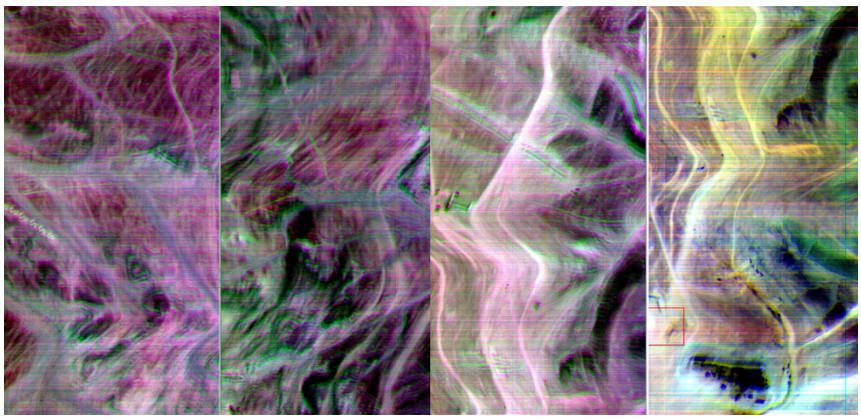

Figure 1. The dataset “desert” is a hyper-spectral image of a desert place taken from an airplane flying 10,000 feet above sea level. The resolution is 1.3 meter/pixel, 286×2640 pixels per waveband with 168 wavebands

Figure 2. The dataset “city” is a hyper-spectral image of a city taken from an airplane flying 10,000 feet above sea level. The resolution is 1.5 meter/pixel, 294 × 501 pixels per waveband with 28 wavebands

Figure 3. The dataset “field” is a hyper-spectral image of a field taken from an airplane flying 9,500 feet above sea level. The resolution is 1.2 meter/pixel, 286 × 300 pixels per waveband with 50 wavebands

The paper has the following structure: Section 2 describes the related work. The two algorithms, which are described in this paper, are compared with the performance of the orthogonal subspace projection (OSP) algorithm. Section 3 presents an algorithm that identifies the target's spectrum where the target occupies at least a whole pixel. This method assumes that the target's spectrum is distorted by atmospheric conditions and noised. Section 4 presents an unmixing method that is based on neighborhood analysis of each pixel. This method can also be used for detecting a subpixel target. This algorithm contains two parts. In the first part, suspicious points are discovered. The algorithm is based on the properties of neighborhood morphology and on the properties of the Diffusion Maps (DM) algorithm Coifman & Lafon (2006). The second part unmixes the suspicious point. It is based on the application of DM to the linear span of the neighboring background spectra. The appendix describes the Diffusion Maps algorithm for dimensionality reduction.

2. Related Work

Up-to-date overview on hyper-spectral unmixing is given in Bioucas-Dias & Plaza (2010; 2011). The challenges related to target detection, which is the main focus of this paper, are described in the survey papers Manolakis, Marden, & Shaw (2001), Manolakis & Shaw (2002). They provide tutorial review on state-of-the-art target detection algorithms for hyper-spectral imaging (HIS) applications. The main obstacles in having effective detection algorithms are the inherent variability target and background spectra. Adaptive algorithms are effective to solve some of these problems. The solution provided in this paper meets some of the challenges mentioned in Manolakis & Shaw (2002).

In the rest of this section, we divided the many existing algorithms into several groups. We wish to show some trends but do not attempt to cover the avalanche of related work on unmixing and target detection.

Linear approach: Under the linear mixing model, where the number of endmembers and their spectral signatures are known, hyper-spectral unmixing is a linear problem, which can be addressed, for example, by the ML setup Settle (1996) and by the constrained least squares approach Chang (2003). These methods do not supply sufficiently accurate estimates and do not reflect the physical behavior. Distinction between different material's spectra is conditioned generally by the distinction in the behavior of the first and second derivatives and not by a trend.

Independent component analysis (ICA) is an unsupervised source separation process that finds a linear decomposition of the observed data yielding statistically independent components Common (1994), Hyvarinen, Karhunen, & Oja (2001). It has been applied successfully to blind source separation, to feature extraction and to unsupervised recognition such as in Bayliss, Gualtieri, & Cromp (1997), where the endmember signatures are treated as sources and the mixing matrix is composed by the abundance fractions. Numerous works including Nascimento & Bioucas-Dias (2005) show that ICA cannot be used to unmix hyper-spectral data.

Geometric approach: Assume a linear mixing scenario where each observed spectral vector is given by $r = x + n = M\gamma a + n,\ \ \gamma a = s,$ where r is an L vector (L is the number of bands), $M = \left[m_1, \ldots, m_p \right]$ is the mixing matrix (m_i denotes the i th endmember signature and p is the number of endmembers present in the sensed area), $s = \gamma a$ (γ is a scale factor that models illumination variability due to a surface topography), $a = \left[a_1, \ldots, a_p \right]^T$ is the abundance vector that contains the fractions of each endmember (T denotes a transposed vector) and n is the system's additive noise. Owing to physical constraints, abundance fractions are nonnegative and satisfy the so-called positivity constraint $\sum_{k=1}^{p} a_k = 1$. Each pixel can be viewed as a vector in a L -dimensional Euclidean space, where each channel is assigned to one axis. Since the set $\left\{ a \in \mathbb{R}^p : \sum_{k=1}^{p} a_k = 1, a_k > 0, \forall k \right\}$ is a simplex, then the set $S_x = \left\{ x \in \mathbb{R}^L : x = Ma, \sum_{k=1}^{p} a_k = 1, a_k > 0, \forall k \right\}$ is also a simplex whose vertices correspond to endmembers.

Several approaches Ifarraguerri & Chang (1999), Boardman (1993), Craig (1994) exploited this geometric feature of hyper-spectral mixtures. The minimum volume transform (MVT) algorithm Craig (1994) determines the simplex of a minimal volume that contains the data. The method presented in Bateson, Asner, & Wessman (2000) is also of MVT type, but by introducing the notion of bundles, it takes into account the endmember variability that is usually present in hyper-spectral mixtures.

The MVT type approaches are complex from computational point of view. Usually, these algorithms first find the convex hull defined by the observed data and then fit a minimum volume simplex to it. Aiming at a lower computational complexity, some algorithms such as the pixel purity index (PPI) Boardman (1993) and the N-FINDR Winter (1999) still find the maximum volume simplex that contains the data cloud. They assume the presence of at least one pure pixel of each endmember in the data. This is a strong assumption that may not be true in general. In any case, these algorithms find the set of most of the pure pixels in the data.

Extending subspace approach: A fast unmixing algorithm, termed *vertex component analysis* (VCA), is described in Nascimento & Bioucas-Dias (2005). The algorithm is unsupervised and utilizes two facts: 1) The endmembers are the vertices of a simplex; 2) The affine transformation of a simplex is also a simplex. It works with projected and unprojected data. As PPI and N-FINDR algorithms, VCA also assumes the presence of pure pixels in the data. The algorithm iteratively projects data onto a direction orthogonal to the subspace spanned by the endmembers already detected. The new endmember's signature corresponds to the extreme projection. The algorithm iterates until all the endmembers are exhausted. VCA performs much better than PPI and better than or comparable to N-FINDR. Yet, its computational complexity is between one and two orders of magnitude lower than N-FINDR.

If the image is of size approximately 300×2000 pixels, then this method, which builds linear span in each step, is too computationally expensive. In addition, it relies on “pure” spectra which are not available all the time.

Statistical methods: In the statistical framework, spectral unmixing is formulated as a statistical inference problem by adopting a Bayesian methodology where the inference engine is the posterior density of the random objects to be estimated as described for example in Dobigeon, Moussaoui, Coulon, Tourneret, & Hero (2009), Moussaoui, Carteretb, Briea, & Mohammad-Djafaric (2006), Arngren, Schmidt, & Larsen (2009).

2.1 Orthogonal Subspace Projection (OSP)

The method of orthogonal subspace projection (OSP) for unmixing and target detection is described in Ahmad & Ul Haq (2011), Ahmad, Ul Haq, & Mushtaq (2011), Ren & Chang (2003). We will compare between our method and the method in Ahmad & Ul Haq (2011) that is currently considered to be very effective. According to the notation in Ahmad & Ul Haq (2011), we are given the dataset $X_i = SA + W$ where S is the set of pure signatures, A is the corresponding abundance fractions and W is a white noise matrix. According to the OSP method in Ahmad & Ul Haq (2011), the mixing matrix is found as $A = \left(I - U\left(\widehat{U^T U}\right)U^T\right)\left(U\Sigma U^T\right)$ where U, Σ are a singular matrix and an eigenvalues-matrix, respectively, of the projection matrix to the subspace L of the pure signatures and $\widehat{U^T U}$ is the pseudo inverse of U. The creation of the subspace L is described in Ren, H., & Chang, C. I. (2003), pp. 1236.

We present the results from target detection by the application of the OSP method with a given target signature s and compare them to our method. The targets in the scene are detected via the application of the OSP method on multipixels, which contain the dominant coefficient from the matrix A, corresponding to target signature s.

2.2 Linear Classification for Threshold Optimization

According to Cristianini & Shawe-Taylor (2000), a binary classification is frequently performed by using a real-valued function $f : X \subseteq \mathbb{R}^n \to \mathbb{R}$ in the following way: the input $x = \left(x_1, \ldots, x_n\right)^T$ is assigned to a positive class if $f\left(x\right) \geq 0$, otherwise, to a negative class. We consider the case where $f\left(x\right)$ is a linear function of x with the parameters w and b such that

$$f\left(x\right) = \langle w \cdot x \rangle + b = \sum_{i=1}^{n} w_i x_i + b \tag{2}$$

where $\left(w, b\right) \in \mathbb{R}^n \times \mathbb{R}$ are the parameters that control the function. The decision rule is given by $\operatorname{sgn}\left(f\left(x\right)\right)$. w is assumed to be the weight vector and b is the threshold.

Definition 2.1. (Cristianini & Shawe-Taylor, 2000)) *A training set is a collection of training examples (data)*

$$S = \left(\left(x_1, y_1\right), \ldots, \left(x_l, y_l\right)\right) \subseteq \left(X \times Y\right)^l \tag{3}$$

where l is the number of examples, $X \subseteq \mathbb{R}^n, Y = \{-1, 1\}$ is the output domain.

The Rosenblatt's Perceptron algorithm (Cristianini & Shawe-Taylor, 2000; Burges, 1998; pages 12 and 8, respectively) creates an hyperplane $\langle w \cdot x \rangle + b = 0$ with respect to a training set S. It creates the best linear separation between positive and negative examples via minimization of measurement function of "margin" distribution $\lambda_i = y_i\left(\langle w, x_i \rangle + b\right)$. $\lambda_i > 0$ that implies the correct classification for $\left(x_i, y_i\right)$.

The perceptron algorithm is guaranteed to converge only if the training data are linearly separable. A procedure that does not suffer from this limitation is the Linear Discriminant Analysis (LDA) via Fisher's discriminant functional Cristianini & Shawe-Taylor (2000). The aim is to find the hyperplane $\left(w, b\right)$ on which the projection of the data is maximally separated. The cost function (the Fisher's function) to be optimized is:

$$F = \frac{m_1 - m_{-1}}{\sigma_1^2 - \sigma_{-1}^2} \tag{4}$$

where m_i and σ_i are the mean and the standard deviation, respectively, of the function output values $P_i = \left\{\langle w \cdot x_j \rangle + b : y_j = i\right\}$ for the two classes $P_i, i = 1, -1$.

Definition 2.2. (Cristianini & Shawe-Taylor, 2000) *The dataset S from Equation 3 is linearly separable if the hyperplane $\langle w \cdot x \rangle + b = 0$, which is* obtained *via the LDA algorithm (*Cristianini & Shawe-Taylor, 2000*), correctly classifies the training data. It means that $\lambda_i = y_i\left(\langle w, x_i \rangle + b\right) > 0, i = 1, \ldots, l$. In this case, b is the separation threshold. If $\lambda_i < 0$ then the dataset is linearly inseparable.*

Definition 2.3. *The vector $x \in \mathbb{R}^n$ is isolated from the set $P = \{p_1, \ldots, p_k\} \subseteq \mathbb{R}^n$ if the training set $S = \left(\left(x, 1\right), \left(p_1, -1\right), \ldots \left(p_k, -1\right)\right)$ is linearly separable according to definition 2.2. In this case, the absolute value of b is the separation threshold.*

Suppose that we have a set $S=\{x_1,\ldots,x_n\}$ of n samples. First, we want to partition the data into exactly two disjoint subsets S_1 and S_{-1}. Each subset represents a cluster. The solution is based on the K-means algorithm (Duda, Hart, & Stork, 2001). K-means maximizes the function $J(e)$ where e is a partition. The value of $J(e)$ depends on how the samples are grouped into clusters and on the number of clusters (see Duda, Hart, & Stork, 2001)

$$J(e)=tr\left(S_W^{-1}S_B\right) \tag{5}$$

where $S_W=\sum_{i=1}^{l}\sum_{x\in S_i}(x-m_i)(x-m_i)^T$ is an "within-cluster scatter matrix" (Duda, Hart, & Stork, 2001), l is the classes, S_i are the classes and m_i are the center of each class. S_B is called "between-cluster scatter matrix" (Duda, Hart, & Stork, 2001), where $S_B=\sum_{i=1}^{l}n_i(m_i-m)(m_i-m)^T$, n_i is the cardinality of a class and m is the center for all the dataset.

Definition 2.4. *Let* (w,b) *be the best separation for the set* $S=\{x_1,\ldots,x_n\}\subseteq\mathbb{R}^n$ *via K-means and Fisher's discriminant analyzes* Cristianini and Shawe-Taylor (2000), Burges (1998). (w,b) *is called the Fisher's separation and* b *the Fisher's threshold for the data* P.

When a dataset is separable? One criterion is when $m_1-m_{-1}>\max\left(diam(P_1),diam(P_{-1})\right)$, where the notation in Equation 4 is used. *diam* is defined as $diam(P)=\max\left\{\|x-y\|_{L_2}:x,y\in P\right\}$.

Another criterion is:

Definition 2.5. (Duda, Hart, & Stork, 2001) *A dataset is separable if from Equation 5* $J(e_1)<J(e_2)$ *where* e_1 *is the partition and the number of classes is 1 and* e_2 *is the best partition into two classes. If* $J(e_1)\geq J(e_2)$ *then the dataset is inseparable and Fisher's separation is incorrect.*

3. Method I: Weak Dependency Recognition (WDR) of Targets That Occupy One or More Pixels

We assume that a target occupies one or more pixels. The process, which determines whether a given target's spectrum and the spectrum of the current pixel are dependent, is described next.

Definition 3.1. *Two discrete functions* Y_1 *and* Y_2 *are weakly dependent if there exists a permutation* σ *of the coordinates that provides monotonic order for the values of* $\sigma(Y_1)$ *and* $\sigma(Y_2)$.

Let T be a given target's spectrum and P is the pixel's spectrum. We assume that the spectra of T and P are discrete vectors. In general, we assume that T and P are normalized and centralized. The following hypotheses are assumed:

H_0: T and P are weakly dependent.

H_1: T and P are not weakly dependent.

3.1 Hypotheses Check

We find an orthogonal transformation Π that permutes the coordinates of T into a decreasing order. This permutation Π is applied to P and T. We get that $P_1=\Pi(P),T_1=\Pi(T)$ where T_1 is monotonic. If H_0 holds, which means that T and P are weakly dependent, then the values of P_1 are either monotonic decreasing or increasing and the first and second derivatives of P_1 are close to zero - see Figure 4 (left). Otherwise, H_1 holds and P_1 has an oscillatory behavior - see Figure 4 (right). In addition, P_1 has a subset of coordinates whose first and second derivatives have an oscillatory behavior - see Figure 4 (right).

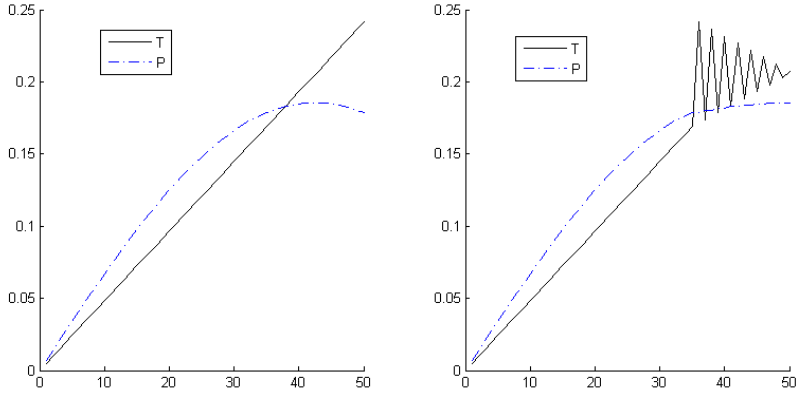

Figure 4. The x - and the y -axes are the wavebands and their reflectance values, respectively. The spectra are represented after the application of the permutation to the coordinates, which permutes T into a monotonic deceasing order. Left: Weak dependency between T and P, Right: No weak dependency between T and P

If the permutation of the coordinates of P provides that their values are either decreasing or increasing monotonically, then the first and second derivatives of P have a minimal norm. This is another criterion for deciding who has weak dependency.

Let $x=(x_1,\ldots,x_n)\in\mathbb{R}^n$. The norm is defined as $\|x\|_\infty=\max_i(|x_i|)$.

Definition 3.2. *Let π be an orthogonal transformation that permutes the coordinates of T into a decreasing order. Denote the second derivative of a vector X by X_2. Define the mapping $\Omega:\mathbb{R}^n\to\mathbb{R}^+$ such that $\Omega(x)=\|(\pi(X))_2\|_\infty$.*

Let $\{X_1,\ldots,X_\omega\}$ be a dataset of spectra from all the pixels in the scene. Denote $Y_i=\Omega(X_i)$. The dataset $\{Y_1,\ldots,Y_\omega\}$ can be classified as:

1) The set $\{Y_1,\ldots,Y_\omega\}$ is separable according to definition2.5.

2) The set $\{Y_1,\ldots,Y_\omega\}$ is inseparable according to definition 2.5.

In the first case, (w,b) is the best separation for the set $S=\{Y_1,\ldots,Y_\omega\}\subseteq\mathbb{R}^+$ according to definition 2.4 and b is the Fisher's threshold for this separation. Then, the set $\{i:Y_i<b\}$ is the set of targets. In the other case, there are no targets in the scene.

The flow of the WDR algorithm is given in Figure 5.

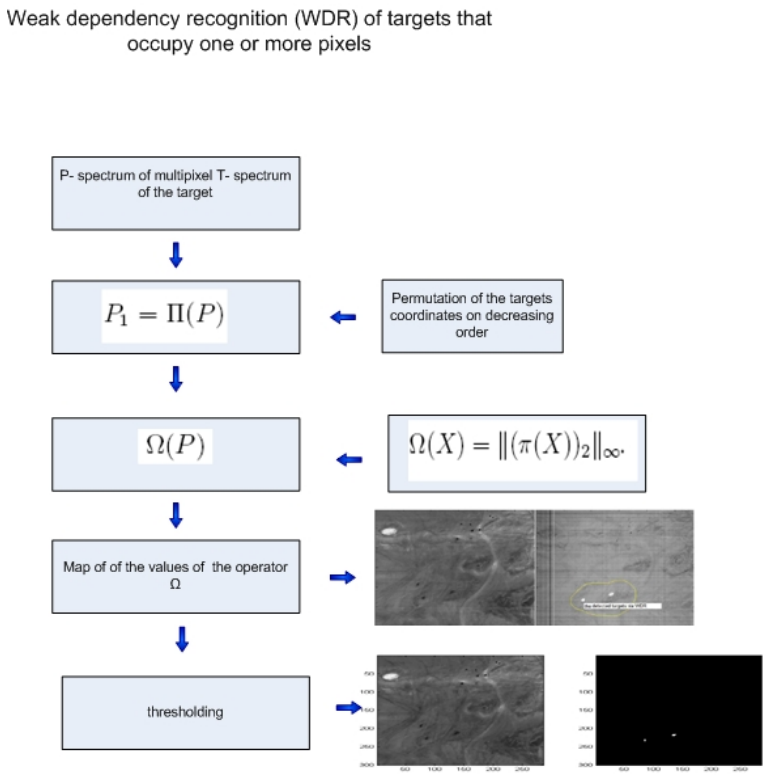

Figure 5. The flow of the WDR algorithm

3.2 Experimental Results

Figures 6-8 display the results after the application of the algorithm in section 3.1 to the "desert" image (Figure 1). The yellow lines mark the neighborhood of the detected targets.

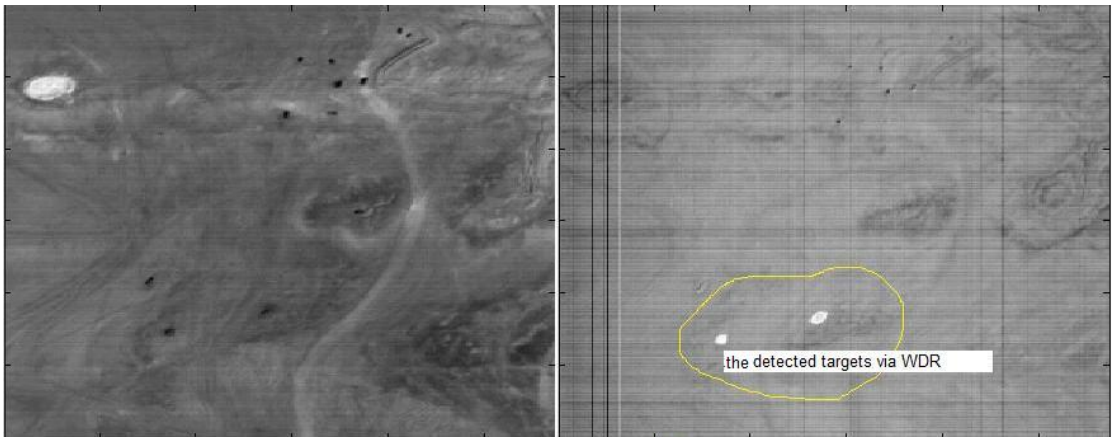

Figure 6. Left: One wavelength part from the original "desert" image (Figure 1). Right: The white points mark the detected targets. The intensity of each pixel in the right side corresponds to the value $-\Omega(X)$ where X the spectrum in the current pixel

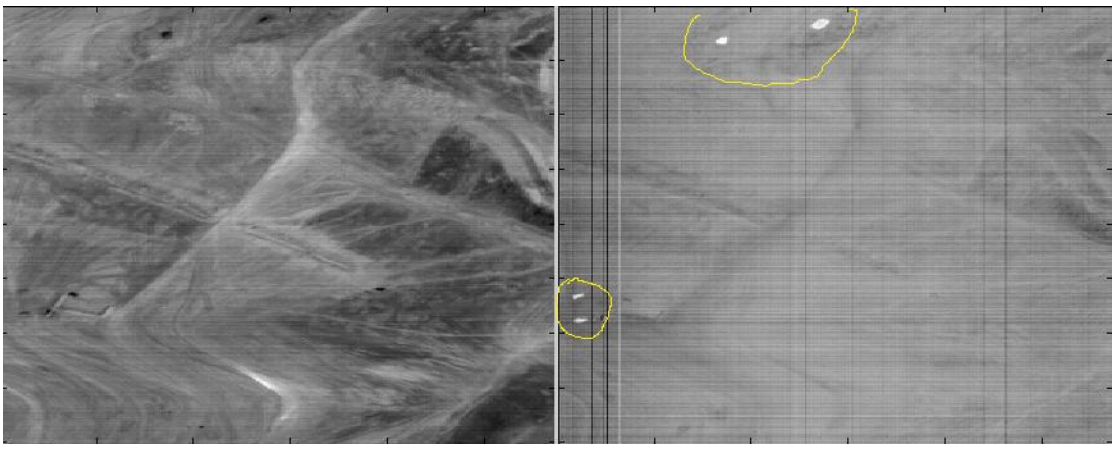

Figure 7. Left: One wavelength part from the original "desert" image (Figure 1). Right: The white points mark the detected targets. The intensity of each pixel in the right side corresponds to the value $-\Omega(X)$ where X is the spectrum in the current pixel

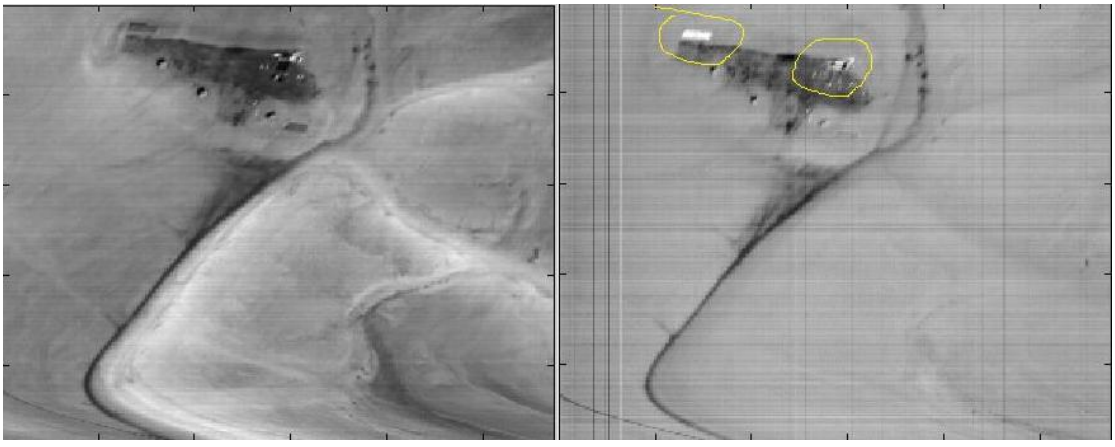

Figure 8. Left: One wavelength part from the original "desert" image (Figure 1). Right: The white points mark the detected targets. The intensity of each pixel in the right side corresponds to the value $-\Omega(X)$ where X is the spectrum in the current pixel

The desert image contains documented targets. The detection of the suspicious points in Figures 6-8 match exactly the known targets.

The point P_1 in Figure 8 is the pattern of the known target's material. Its spectrum is displayed in Figure 4 as a plot of the "target". Other spectra plots, which were detected by the WDR algorithm in the scenes of Figures 6-8, are classified as "spectra of suspicious points".

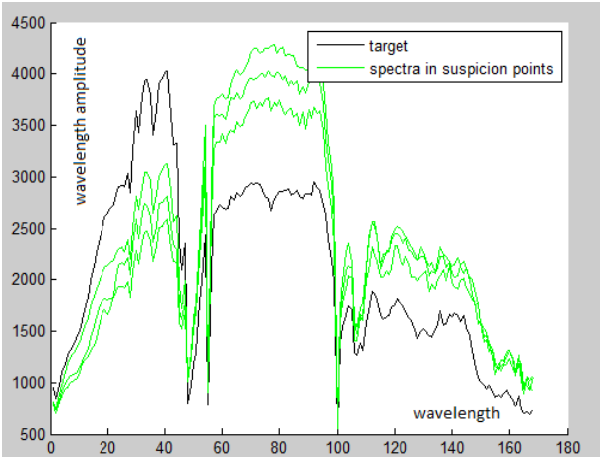

Figure 9. Comparison between the target's spectrum and the suspicious points' spectra in Figures 6-8. The x - and the y -axes are the wavebands and their reflectance values, respectively

The above results were compared next with the OSP algorithm.

3.2.1 Comparison between WDR and OSP Algorithms

In this section, we compare between the performance of WDR and OSP (Ahmad & Ul Haq, 2011) algorithms. The false alarm generated by the OSP algorithm is shown.

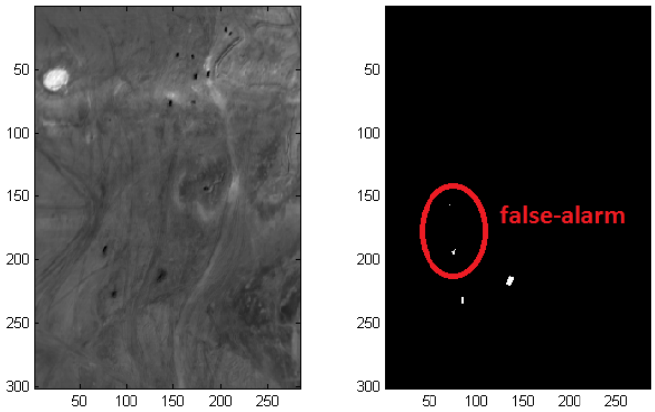

Figure 10. Left: Portion of one wavelength (multipixel) from the original "desert" image (Figure 1). Right: The white points mark the detected targets by the OSP algorithm Ahmad & Ul Haq (2011). The Red circle marks "false-alarm"

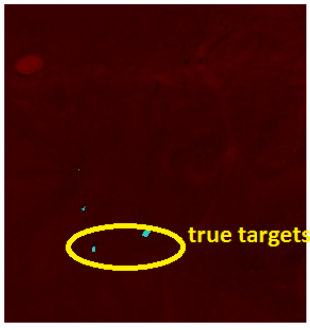

Figure 11. The detected targets by the OSP algorithm Ahmad & Ul Haq (2011) are marked on portion of one wavelength from the "desert" image. OSP generates false-alarm where WDR does not

Figure 12 shows the ROC-curves while comparing two methods for continuously varying the threshold.

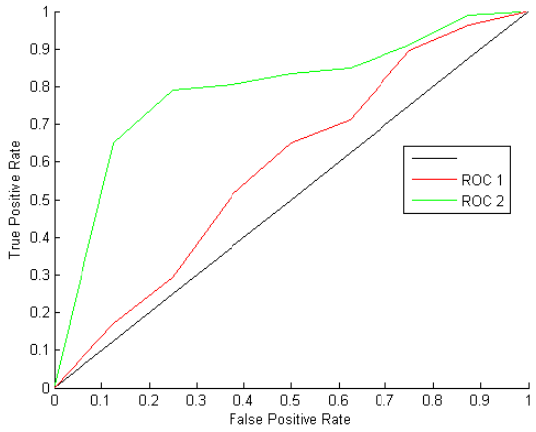

Figure 12. The "ROC-curve" for scene in Figure 11. The red line corresponds to OSP Ahmad & Ul Haq (2011) method. The green line corresponds to WDR method

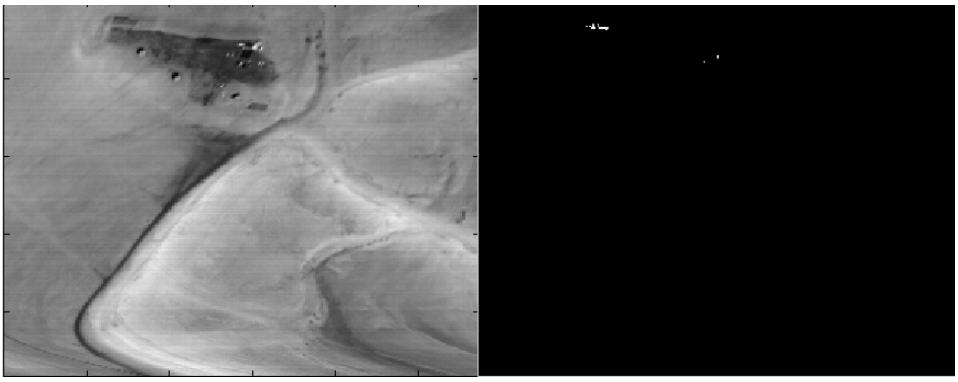

Figure 13. Left: Portion of one wavelength (multipixel) from the original "desert" image (Figure 1). Right: The white points mark the detected targets by the WDR algorithm. The intensity of each pixel in the right side corresponds to the value $-\Omega(X)$ where X is the spectrum in the current pixel

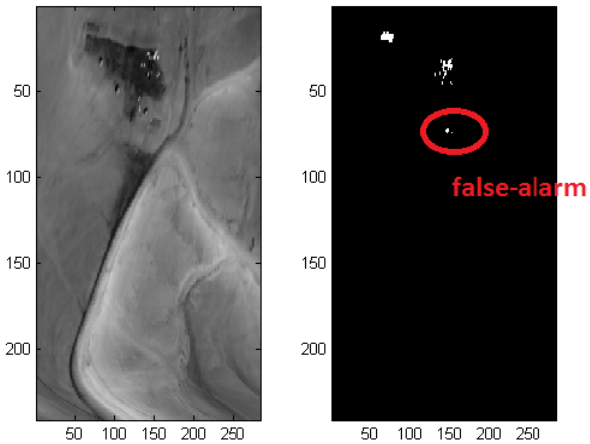

Figure 14. Left: Portion of one wavelength (multipixel) from the original "desert" image (Figure 1). Right: The white points mark the detected targets by the OSP algorithm Ahmad & Ul Haq (2011). The Red circle marks the "false-alarm"

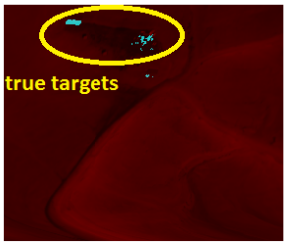

Figure 15. The detected targets by the OSP Ahmad & Ul Haq (2011) algorithm are marked on portion of one wavelength from the "desert" image. OSP produces more false-alarm than WDR

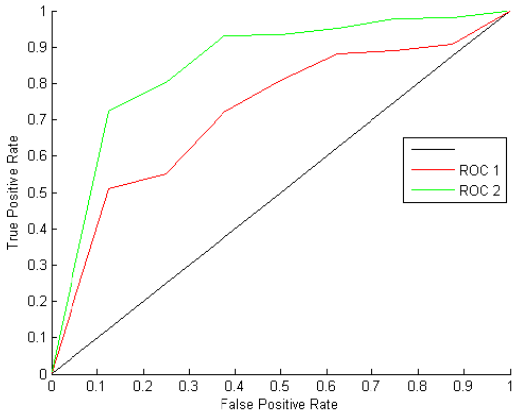

Figure 16. The "ROC-curve" for scene in Figure 15. The red line corresponds to OSP Ahmad & Ul Haq (2011) method. The green line corresponds to WDR method

4. Method II: Unmixing by Examining the Neighborhood of a Suspicious Point (UNSP)

In this section, we provide an algorithm that detects subpixel targets. The idea of the algorithm is close to Chang, Zhao, Althouse, & Pan (1998), Harsanyi & Chang, (1994). But in contrast to them, we construct a different projection. They project the data into linear subspace of the known targets. Our mapping projects the dataset into an orthogonal complement of the background of each pixel. The local model of the background is based on the morphological structure of the pixel's neighborhood. This yields better anomaly (suspicious point) detection.

The UNSP algorithm introduces the parameter m which is the neighborhood's size that we use in the processing. For ease of notation, a square of $m = 2m_1 + 1$ pixels on each side with a center at the pixel X is called the m -neighborhood of the pixel X, denoted by $\Omega_m(X)$, where m_1 is the radius of this neighborhood as displayed in Figure 17.

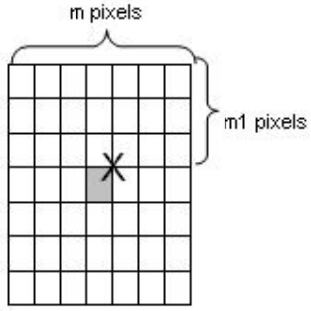

Figure 17. The m -neighborhood of the pixel X denoted by $\Omega_m(X)$

A connected component is a set of pixels in which any two pixels are connected to each other. This connection means that there exists a path between two pixels. The path is a sequence of pixels such that for each of its pixels the next pixel is adjacent to it either horizontally or vertically as we see in Figure 18.

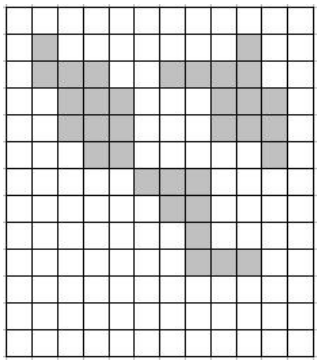

Figure 18. The morphological structure of the neighborhood is represented by three connected components

Consider the spectra from different materials which are present in a hyper-spectral image. Usually there is high correlation between these spectra in real situations. For example, Figure 19 displays the spectra from three different materials.

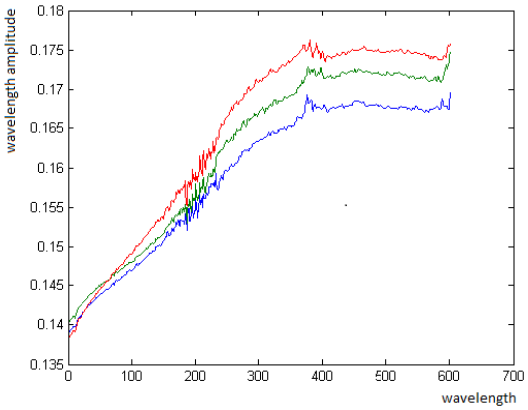

Figure 19. Spectra of three different materials

To reduce the correlation between spectra, we use the first derivative of the spectra. We denote the first derivative of the spectrum of the pixel X by $d(X)$ and it is called the d -spectrum of the pixel X.

We assume that the pixels, which contain a target (as a subpixel or as a whole pixel), represent one connected component that occupies less than half of the m -neighborhood of some pixel. T is the given target's spectrum.

The UNSP algorithm has two steps: Detection of suspicious points and extraction of the target spectrum from the suspicious point (unmixing).

4.1 The Morphology-Filter: Detection of Suspicious Points via Neighborhood Morphology

The following hypotheses are assumed:

H_0: Y is a suspicious point.

H_1: Y is not a suspicious point.

Hypotheses check: The indices of $\Omega_m(Y)$ are constructed in the following way. A pixel located in row i and column j is denoted by $p_{ij}, i, j = 1, \ldots, m$ - see Figure 20. For example, the central pixel is $Y = p_{m_1+1, m_1+1}$ where m_1 is the of the neighborhood's radius.

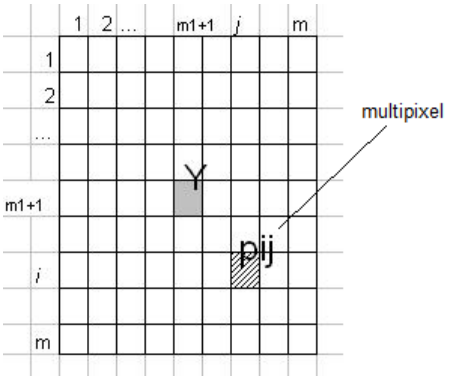

Figure 20. The indices of a pixel

Denote by $S=\{p_{ij}\}_{i,j=1,\ldots,m}$ the set of multipixels (multipixel means all the wavelengths that belong to this pixel) in the current neighborhood. Consider the mapping $\Omega: S \to \mathbb{R}$ such that $\Omega(p_{ij}) = corr(d(p_{ij}), d(Y))$ where $corr(d(p_{ij}), d(Y))$ is the correlation coefficient between the vectors $d(p_{ij})$ and $d(Y)$. Denote $\hat{S} = \Omega(S) = \{\Omega(p_{ij})\}_{i,j=1,\ldots,m} \subseteq [-1,1]$.

The set $\hat{S}$ can be in one of two cases:

1) $\hat{S}$ is inseparable according to definition 2.5. This means that the pixels, which are correlated with the target, are inseparable from the other pixels;
2) $\hat{S}$ is separable according to definition 2.5. This means that the pixels, which are correlated with the target, are separated from the other pixels.

If we are in case 1, then Y is not a suspicious point. If we are in case 2, assume that Ψ is the first cluster closest to 1. According to definition 2.4, (w,b) provides the best separation. It separates the set Ψ from the other points where b is the Fisher's threshold for this separation. Then, Ψ can be represented as $\Psi = \{p_{ij} : corr(d(p_{ij}), d(Y)) > b\}$.

If the set Ψ represents two or more connected components, then Y is also not a suspicious point. If $Y \notin \Psi$ then Y is also not a suspicious point. Therefore, H_1 holds. In other words, if Y is a suspicious point, then Ψ is a set of pixels that intersects with the target and this set of correlated points is concentrated around the central point Y. Here and below, we assume that a correlated point is a pixel whose d-spectrum and $d(Y)$ are correlated with the correlated coefficient that is greater than Fisher's threshold b.

Let N_1 be the neighborhood $\Omega_{m-2}(Y)$. N_1 is called the internal square. Let $N_2 = \Omega_m(Y) \setminus N_1$. N_2 is called the external square. They are visualized in Figure 21.

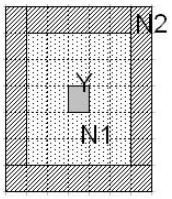

Figure 21. N_1 is the internal square and N_2 is the external square

Assume that Δ is the set of all pixels p_{ij}, which are bounded by the external square with correlation coefficients $corr(d(p_{ij}), d(Y))$, which are associated with the current neighborhood that are less than the Fisher's threshold b. Each pixel in Δ is treated as a vector (multipixel) where its entries are spread all over the wavelengths. The d-spectra of this vector is denoted by v_s where s is one of the $(i,j) \in \Delta$. The set of all these vectors is denoted by V. This is the set of all the d-spectra that belong to Δ. If $|\Delta| = s$ then $V = \{v_1, \ldots v_s\}$.

In order to derive the d-spectrum of some material in the central pixel, the background around the central pixel has to be removed. For that, we construct an orthogonal projection ρ, which projects all the d-spectra onto the

orthocomplement of the linear span where the background of the d -spectra is located. If the d -spectrum of the central pixel $d(Y)$ does not belong to this linear span, then this projection extracts an orthogonal component of $d(Y)$ which does not mix with the background of the d -spectrum. For example, if $d(Y) = d_1 + d_2$ where d_1 belongs to the linear span generated by the background of the d -spectrum and d_2 belongs to the orthocomplement of this span. Then, after projection we obtain $\rho(d(Y)) = \rho(d_2)$ which does not correlate with the background of the d -spectrum. Hence, the background influence is removed by this projection.

Now, we formalize the above. Assume the matrix E is associated with the vectors $v_1,\ldots,v_s$ where $E(i,j) = v_i \cdot v_j \in \Delta$. Assume that T_e is the Fisher's threshold, which separates between the big and small absolute values of the eigenvalues of the matrix E . In some cases, T_e can separate between zero and nonzero eigenvalues. The eigenvectors associated with the eigenvalues, which are smaller than T_e , generate the eigensubspace, which is the orthocomplement of the linear span of the principal directions of the set V . Denote this orthocomplement by C .

Throughout this paper, we assume that in our model the spectrum of any pixel X consists of three components:

1) The spectrum of the material M is different from its background;
2) The spectrum of the background was generated from a linear combination of spectra of pixels from the X -neighborhood;
3) Random noise is present.

The same model is true for the d-spectra $P' = \tau M' + L(v_1,\ldots,v_s) + N$ where $P' = d(Y)$, M' is the d -spectrum of the material $M, \tau \in [0,1]$ is the portion of the material M in Y , N is a random noise and $L(v_1,\ldots v_s)$ is a linear combination of the vectors $v_1,\ldots v_s$.

If the correlated points concentrate around Y , then these points consist of the same material as Y . If the uncorrelated points do not contain this material then they belong to the background. Consider the orthogonal projection operator ρ . This operator projects vectors onto the orthocomplement C . The vector $\rho(L(v_1,\ldots,v_s))$ is approximated to be a zero vector. Thus, this orthogonal projection removes from the d -spectrum of $d(Y)$ the influence of the background.

Let T' be the given d -spectrum of the target. If the correlation coefficient of $\rho(P')$ and $\rho(T')$ is greater than the correlation coefficient of P' and T', then Y is a suspicious point, M is the target, $T' = M'$ and H_0 holds.

4.2 Detection of Outliers *within a Single Testing Cube*

In section 4.1, we presented how to detect suspicious points. There is another way to do it. An alternative detection method uses dimensionality reduction by the application of the Diffusion Maps (DM) algorithm Coifman & Lafon (2006) and a nearest-neighbor scheme. The DM is a non-linear algorithm for dimensionality reduction.

Assume, we are given a data cube **D** of size $X \times Y \times Z$ where X and Y are the spatial dimensions and Z is the wavebands. We define a small testing cube **d** of size $v \times h \times Z, v \ll X, h \ll Y$ which is included in the hyper-spectral data cube **D**.

4.2.1 Dimensionality Reduction by DM Application

Assume that a sliding testing cube **d**, pointed by the arrows in Figure 22, is moving by ironing each time a different fragment in the data cube **D** described in Figure 2. Section 4.3 describes in details how the testing cube **d** moves.

Figure 22. An urban scene of size 294×501 (from the "city" in Figure 2) with different locations of the sliding testing cube **d.** The arrows point to these locations

The sliding testing cube **d** contains $N = vh$ multipixels each of which comprises Z wavebands. Typically, v and h are in the range 30-50, Z is in the range 30-100, $Y \approx 290$. Thus, each of the N data points is a vector $m_i, i = 1, \ldots, N,$ of length Z. We arrange these data points into a matrix **M** of size $N \times Z$.

The next step applies the DM (see the appendix for its description) algorithm to the matrix **M**. It reduces the dimensionality of the data vectors by embedding them into the main eigenvectors of the covariance matrix of the data **M**. This projection reveals the geometrical structure of the data and facilitates a search for singular (abnormal) data points. The data matrix **M** of size $N \times Z$ is mapped onto the eigenvectors of the matrix **P** of size $N \times R, R \ll Z$. Typically, R is in the range 3-5, which is determined by the magnitudes of the corresponding eigenvalues. R is the number of essential eigenvalues of the covariance matrix and it is determined as explained in Coifman & Lafon (2006). Figure 23 displays the embedding on three major eigenvectors of the data from four positions of the sliding testing cube. These are the embeddings onto three major eigenvectors of the covariance matrices.

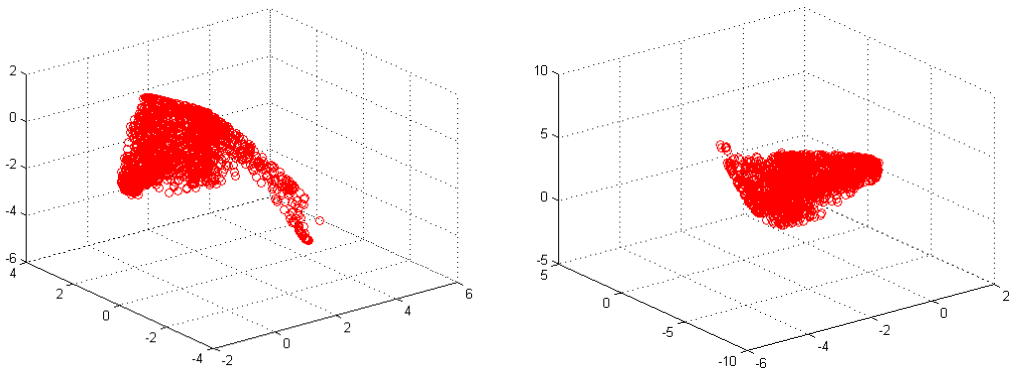

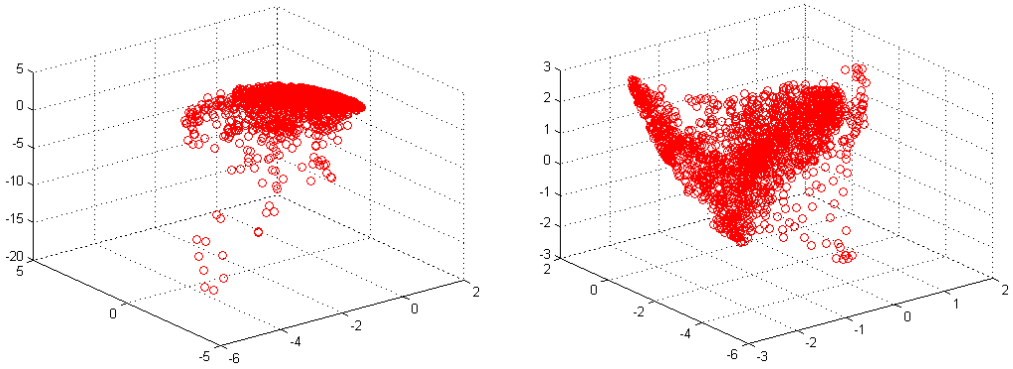

Figure 23. Embedding of the data from different positions of the sliding testing cube on the image in Figure 2 onto three major eigenvectors of the diffusion matrix

We observe that the overwhelming majority of the embedded data points form a dense cloud while a few outliers present. It can be a single point, which lies far away from the rest of points or, more frequently, there exists a small group of points, which are located close to each other but far away from the majority of the cloud. This reflects the situation when an optional target can occupy the area of size from one to several pixels (or even a subpixel). These single or grouped outliers are detected as explained in the next section on outliers detection.

4.2.2 Detection of Grouped Outliers

Assume we are looking for groups of outliers that consist of no more than K members. It is done by the following steps:

1) For each row $r_i, i = 1,\ldots,N,$ of the DM matrix $\tilde{P}$ (see Appendix), calculate its Euclidean distances $d_{i,j} = \|r_i - r_j\|$ to all other rows and sort them in ascending order $d_{i,j} \mapsto s_{i,j}$. Thus, $s_{i,1} = d_{i,j_{i,1}} \le s_{i,2} = d_{i,j_{i,2}} \le \ldots \le s_{i,N-1} = d_{i,j_{i,N-1}}$.

2) Form the matrix $S = \{s_{i,j}\}, i = 1,\ldots,N, j = 1,\ldots,N-1,$ of the sorted distances and the matrix $J = \{j_{i,k}\}, i = 1,\ldots,N, k = 1,\ldots,N-1,$ of the corresponding indices.

3) For each row $r_i, i = 1,\ldots,N,$ determine its K nearest neighbors. For this, take the first K columns $\{j_{i,1},\ldots,j_{i,K}\}, i = 1,\ldots,N,$ of the index matrix **J**. The corresponding distances are presented in the first K columns $\{s_{i,1},\ldots s_{i,K}\}, i = 1,\ldots,N,$ of the matrix **S**. Thus, we have the nearest neighbor index J_K and the distances matrices S_K where both are of size $N \times K$. First, the simplest case $K = 2$, which means that we are looking for groups of outliers consisting of no more than two points, is handled.

4) Assume that $\mu_2 = \max_i s_{i,2}$ is achieved by $i = i_2$. It means that the distance to the second in order for the nearest neighbor of the i_2-th data point p_{i_2} is the largest among the distances to their second nearest neighbors of all the data points. Restore the coordinates x_2 and y_2 of the data point p_{i_2} (multipixel m_{i_2}) in the data cube **D**. Store the point $P_2(x_2, y_2)$.

5) Find $\max_i s_{i,1}$. Two alternatives are possible:

   a) P_2 is an isolated outlier. It takes place when the maximum $\mu_1 = \max_i s_{i,1}$ is achieved by $i = i_2$. It means that the distances from the point P_2 to its first two nearest neighbors is greater than the respective distances of all the other points.

   b) However, it may happen that some point lies close to P_2 while all the others are far apart. It can be interpreted as a pairwise outlier. An indicator of this situation is the fact that the maximum $\mu_1 = \max_i s_{i,1}$ is achieved by $i = \tilde{i}_1 \ne i_2$. In this case, we add the point $P_1(x_1, y_1)$ closest to the point $P_2(x_2, y_2)$ and regard $\{P_1, P_2\}$ as a pairwise outlier. The index of the point $P_1(x_1, y_1)$ is $i_1 = j_{i_2,1}$.

6) While looking for grouped outliers that may contain up to $K > 2$ members, we find $i = i_K$, such that $\mu_K = \max_i s_{i,K}$ is achieved by $i = i_K$. Restore the coordinates x_K and y_K of the data point p_{i_K} (multipixel m_{i_K}) in the data cube **D**. Store the point $P_K(X_K, Y_K)$.

7) Find the maximal values in the first $K-1$ columns $\mu_k = \max_i s_{i,k}, k = 1,\ldots,K-1,$ of the distance matrix **S**. The following alternatives are possible:

a) P_K is an isolated outlier. It takes place when all the maxima $\mu_k, k=1,\ldots,K-1,$ are achieved $i=i_K$. It means that the distances from the point P_K to its first nearest neighbors are greater than the respective distances for all the other points.

b) Grouped outliers arrive when all the maxima $\mu_k, k=2,\ldots,K-1$, except μ_1 are achieved by $i=i_K$. In this case, we add the point $P_1(x_1,y_1)$ that is the closest to the point $P_2(x_2,y_2)$ and regard $\{P_1,P_2\}$ as a pairwise outlier. The index of the point $P_1(x_1,y_1)$ is $i_1=j_{i_2,1}$.

c) If the maxima in the columns $\mu_k, k=L+1,\ldots,K-1, L>1,$ are achieved by $i=i_K$, while μ_L is achieved by some other $\tilde{i}\neq i_K$, then we have grouped outliers. These outliers $\{P_1,\ldots,P_L,P_K\}$ consist of the point P_K and of the L points closest to P_K. The indices of the points $\{P_1,\ldots,P_L\}$ are $i_1=j_{i_K,1},\ldots i_1=j_{i_K,L}$, respectively.

We emphasize that, once the upper limit K is given, the number $L+1$ of group members is determined automatically depending on the data within the sliding testing cube **d**. Figure 24 illustrates the grouped detected outliers in the 3-dimensional space of eigenvectors of the data from four positions of the sliding testing cube.

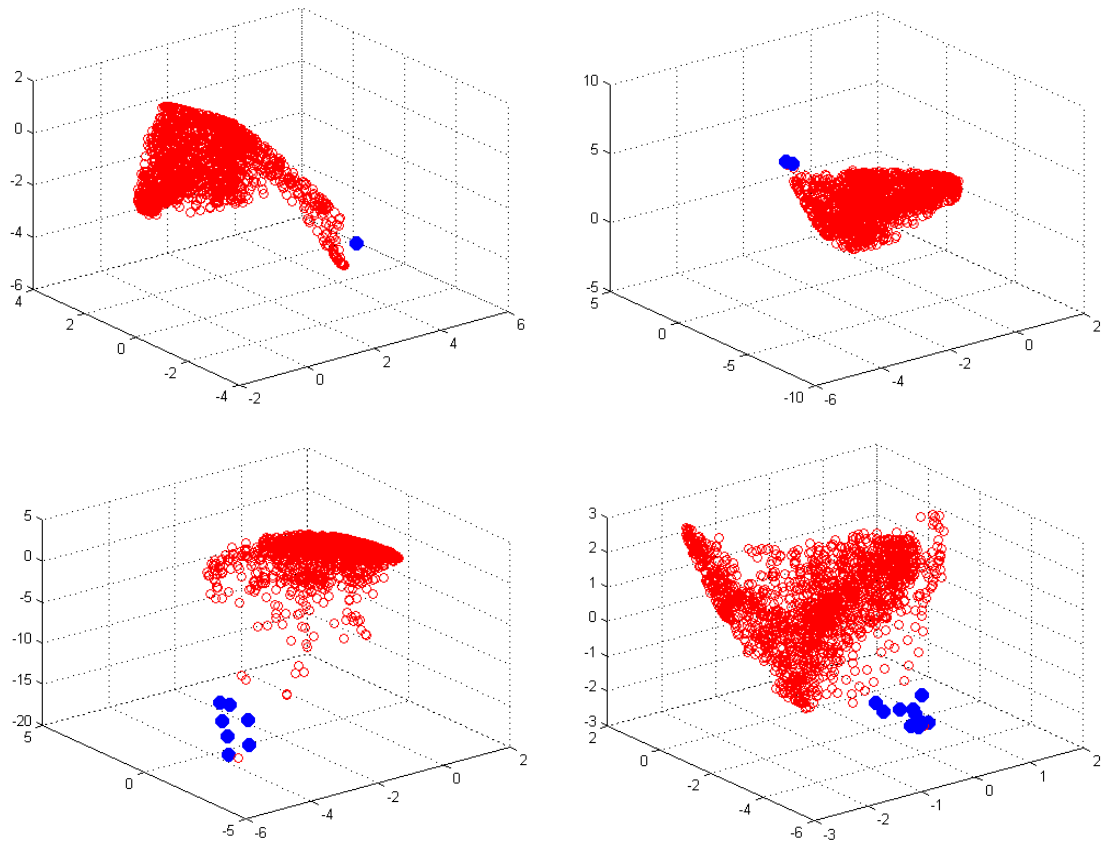

Figure 24. Detection of grouped outliers in data from different positions of the sliding testing cube embedded in the diffusion space

4.3 Detection of Singular Points within the Whole Data Cube

In the section on outliers detection, we described how to find a group of data points (multipixels) within one sliding testing cube, whose geometry differs from the geometry of the majority of the data points. Let $\Lambda^1=\{P_1^1,\ldots,P_{L^1}^1\}$ be the list of such data points in the sliding testing cube d^1 of size $v\times h\times Z$ located in the upper left corner of the sliding data cube **D** as illustrated by the arrow in Figure 22. The next testing cube d^2 is obtained by a right shift by $\eta\approx h/4$ of d^1. Let $\Lambda^2=\{P_1^2,\ldots,P_{L^2}^2\}$ be the list of outliers in the cube d^2. Append the list Λ^2 to Λ^1. Because of the vast overlap between the cubes d^2 and d^1, some outliers data points can be common for the lists Λ^2 and

Λ^1. In the united list, these points gain the weight 2. The next right shift produces the sliding testing cube d^3 outliers list Λ^3 s appended to the combined list $\Lambda^1 \cup \Lambda^2$. Again, the common gain weights. We proceed with the right shifts till the right edge of the data cube **D**. Then, the sliding testing cube slides down by $\nu = v/4$ and starts η-shifts to the left and so on. As a result, we get a combined list $\Lambda = \bigcup_1^R \Lambda^i$ of outliers, where R is the number of jumps of the testing cube **d** within the sliding data cube **D**. Figure 22 illustrates a route of the cube **d** on the data cube **D**.

It is important that each point P_i in the list Λ is supplied with the weight w_i, which can range from 1 to more than 40. The weight w_i can serve as a singularity measure for the point P_i. A large weight w_i reflects the fact that the point P_i is singular for a big number of overlaps between sliding testing cubes. Thus, it can be regarded as a strong singular point in the sliding data cube **D** and vice versa. Figure 25 illustrates the distribution of the weighted singular points around the data cube D_U of size $500 \times 294 \times 64$ from the urban scene displayed in Figure 22 whose source is Figure 2.

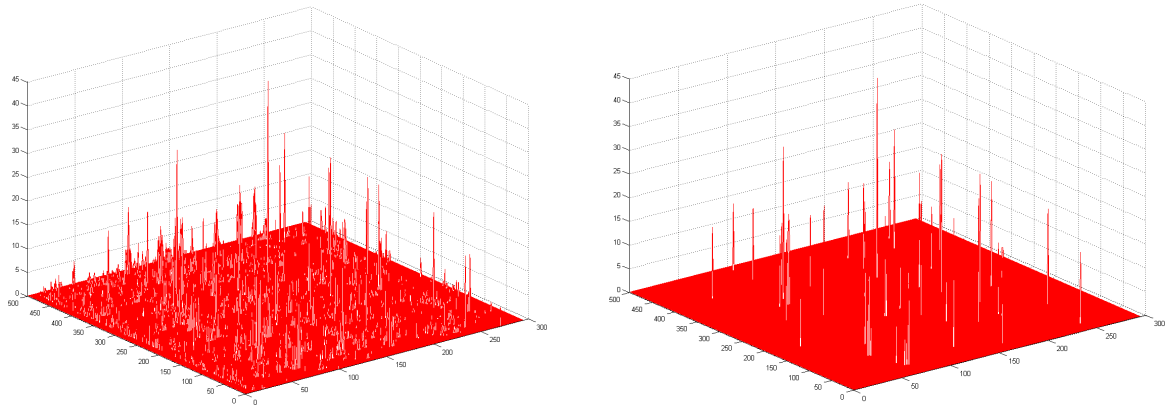

Figure 25. Distribution of the weighted singular points around the data cube D_U. Left: All the singular points. Right: Singular points whose weights exceed 12

4.3.1 Examples of Detected Singular Points

We applied the above algorithm to find singular points in different data cubes. The following figures display a few singular points detected in the data cube D_U.

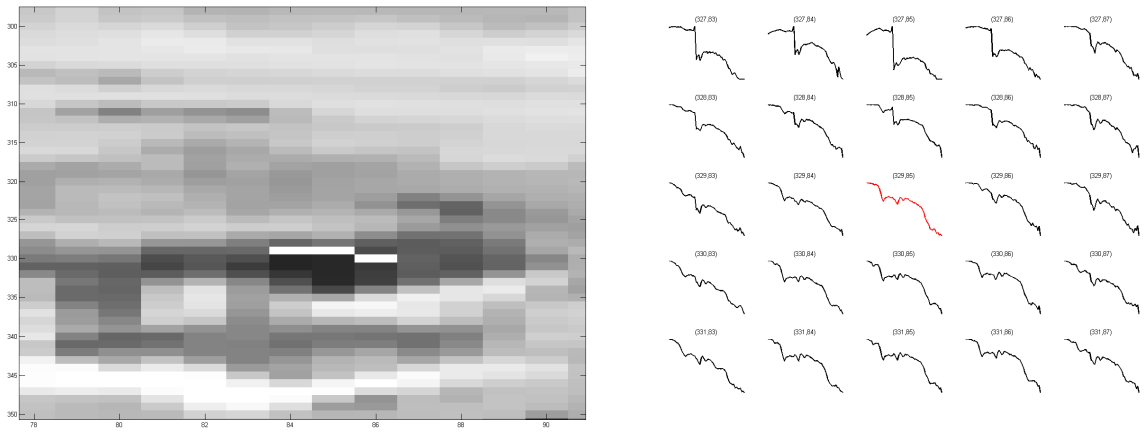

Figure 26. A group of singular points centered around the point $P(329,85)$. Left: Vicinity of the point **P**. Right: Multipixel spectra at the point $P(399,85)$ and the surrounding points. The weight of the data point **P** is 19

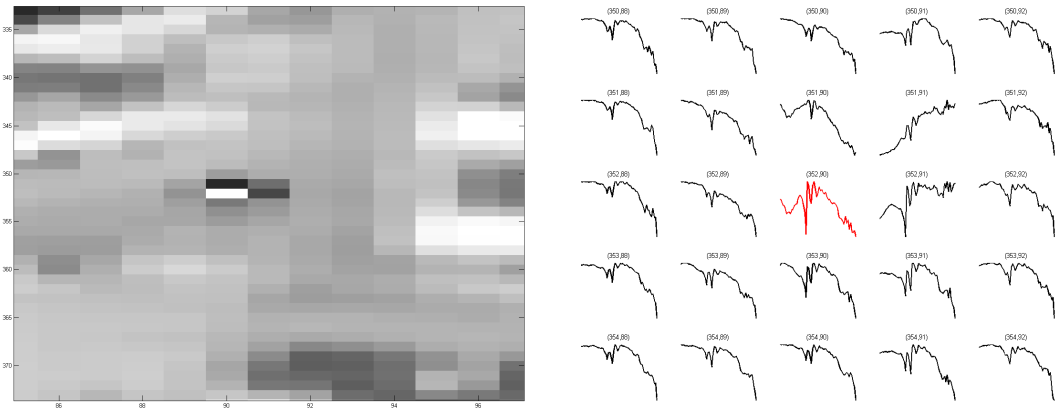

Figure 27. A strong singular point $P(352,90)$. Left: Vicinity of the point **P**. Right: Multipixel spectra of the point $P(352,90)$ and the surrounding points. The weight of the data point **P** is 32

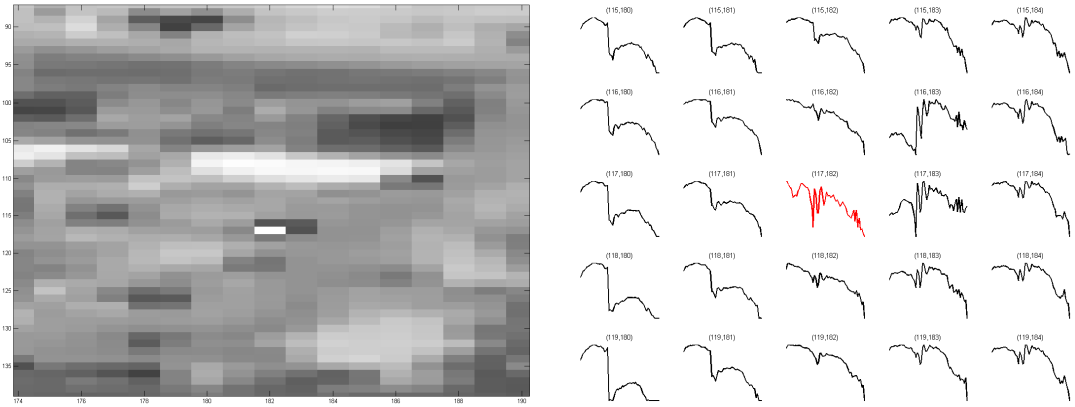

Figure 28. A strong singular point $P(117,182)$. Left: Vicinity of the point **P**. Right: Multipixel spectra at the point $P(117,182)$ and the surrounding points. The weight of the data point **P** is 32

By comparing between Figures 28 and 27 we observe that spectra of singular multipixels located at points $P(117,182)$ and $P(352,90)$ are similar to each other. Supposedly, they correspond to the same material. A different singular multipixel is displayed in Figure 29.

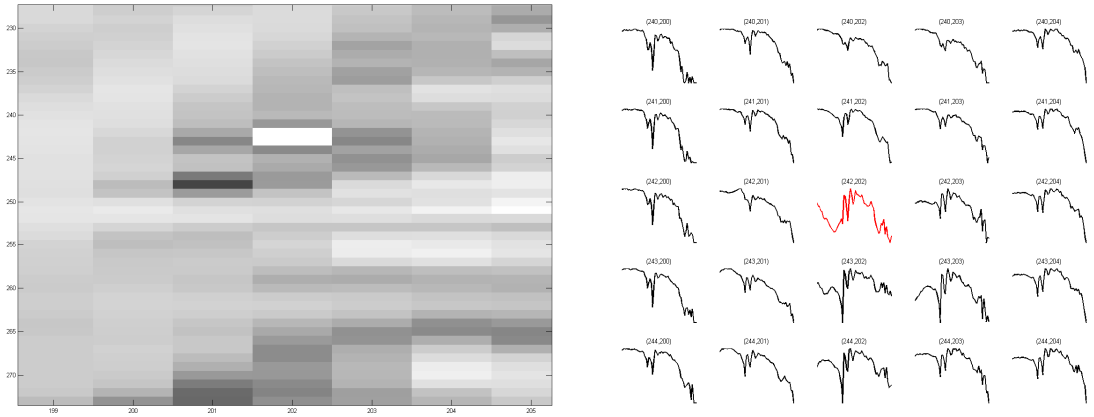

Figure 29. A singular point $P(242,202)$. Left: Vicinity of the point **P**. Right: Multipixel spectra at the point $P(242,202)$ and the surrounding points. The weight of the data point **P** is 32

4.4 Extraction of the *Target's Spectrum from a Suspicious Point*

Let Y be a suspicious point and let T be the given target's spectrum. What portion of the target is contained in Y?

We consider a simplified version of Equation 1 via the definition of a simple mixing model that describes the relation between a target and its background. Assume P is a pixel of mixed spectrum (a spectrum that contains background influence and the target) and T is the given target's spectrum. Consider three spectra: an average background spectrum $B=\sum_{k=1}^{M} a_k B_k$, a mixed pixel spectrum (spectrum of a suspicious point) P and the target's spectrum T. They are related by the following model

$$P = tB + (1-t)T = t\sum_{k=1}^{M} c_k B_k + (1-t)T \tag{6}$$

which is a modified version of Eq. 1, where $a_1 = t$ and $s_1 = T, t \in \mathbb{R}, t \in (0,1)$. $B_k, k = 1,\ldots,M$, was taken from the neighborhood pixel. Therefore, all of them are close to each other and have a similar feature.

We are given the target's spectrum T and the mixed pixel spectrum P. Our goal is to estimate t denoted by $\hat{t}$, which will satisfy Equation 6 provided that B and T have some independent features. Once $\hat{t}$ is found, the estimate of the unknown background spectrum B, denoted by $\hat{B}$, is calculated by $\hat{B} = (P - \hat{t}T)/(1-\hat{t})$. Estimating the parameter t in Equation 6 is called linear unmixing.

In Step 2 from Section 4.1, we calculated the following: V is the d-spectra set, which is uncorrelated with $d(Y)$ pixels from the m-neighborhood of Y and ρ, is the projection operator onto the orthocomplement of the linear span of V. Let $P_2 = \rho(d(Y)), T_2 = \rho(d(T))$, then $P_2 = t' T_2 + N$ where t' is an unknown parameter, N is a random noise that is independent of T_2. The parameter $t' \in [0,1]$ is estimated as the maximum of the independency between the two d spectra T_2 and $P_2 - t' T_2$.

The fact that two vectors X_1 and X_2 are independent is equivalent to $corr(\varphi(X_1), \varphi(X_2)) = 0$ for any analytical function φ (Hyvarinen, Karhunen, & Oja, 2001). An analytical function can be represented by a Taylor expansion of its argument's degrees. Then, the condition $corr(\varphi(X_1), \varphi(X_2)) = 0$ equals to $corr((X_1)^n, (X_2)^n) = 0$ for any positive integer n where n denotes a power. In our algorithm, we limit our self to $n = 1,2,3,4$. From the independency criterion between the two vectors X_1 and X_2 we can have

$$f = |corr(X_1, X_2)| + |corr((X_1)^2, (X_2)^2)| + |corr((X_1)^3, (X_2)^3)| + |corr((X_1)^4, (X_2)^4)| \tag{7}$$

which equals to zero in case X_1 and X_2 are independent. If t' is estimated, then $P = t'T + B$ where P is the spectrum of the suspicious point and B is a mix of the background's spectrum from the neighborhood that is affected by noise.

The flow of the UNSP algorithm is given in Figure 30.

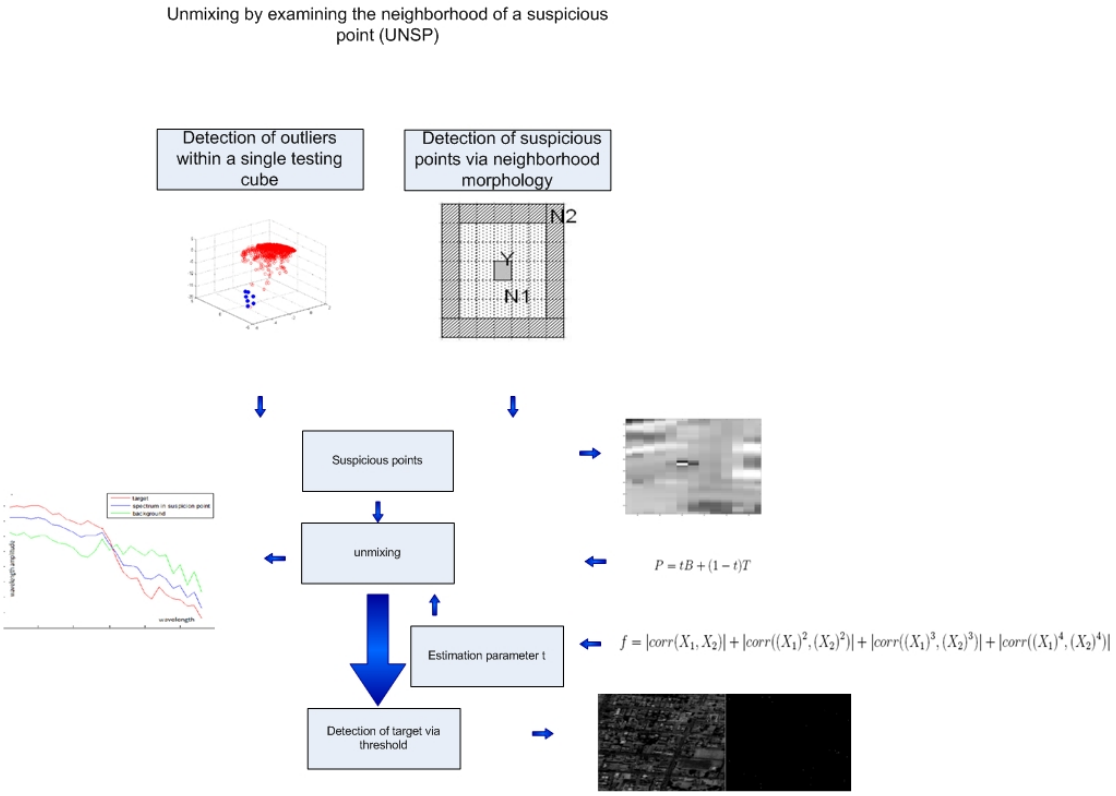

Figure 30. The flow of the UNSP algorithm

4.5 Experimental Results

In this section, we consider two scenes "field" (Figure 3) and "city" (Figure 2) that contain the subpixel's targets. As a first step, we find all the suspicious points via the application of anomaly detection process (section 4.2). The next step checks the anomaly by the "morphological-filter" which was described in section 4.1. If the pixel is passed via the application of the "morphological-filter" then the target is present in it.

Figures 31 and 32 present the outputs from the application of the "morphological-filter" algorithm to two different hyper-spectral scenarios.

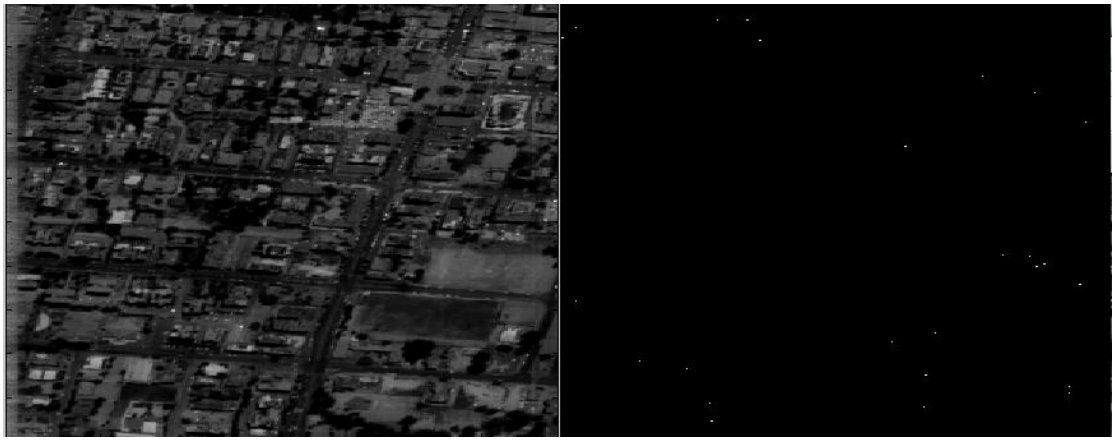

Figure 31. Left: The source image (Figure 2). Right: The white points are the suspicious points in the neighborhood of diameter $m = 10$

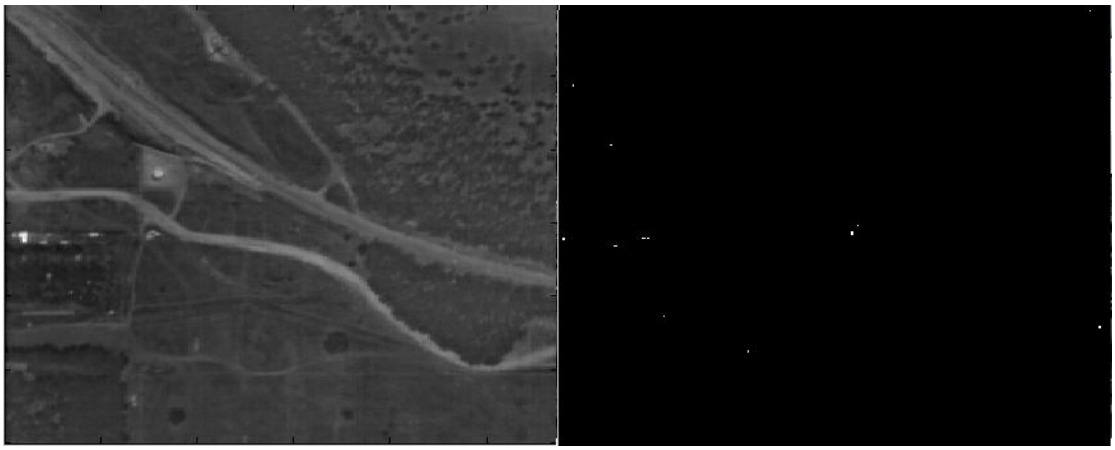

Figure 32. Left: The source image (Figure 2). Right: The white points are the suspicious points in the neighborhood of diameter $m = 10$

In Figures 33 and 34, the x - and y - axes are the wavebands and their values, respectively. The white points in Figures 31 and 32 are the anomalies that contain the known target. The next step performs the unmixing procedure. The unmixing estimates the parameter t from Equation 6 which means that this is a portion from the target that is present in the current suspicious pixel. The estimation of t is done via minimization of the functional f in Equation 7 for a pair of vectors T_2 and $P_2 - t^{'}T_2$ using the notations in section 4.4. Now we present an unmixing example in a pair of singular points detected as anomalies by the application of the "morphological-filter" (section 4.1).

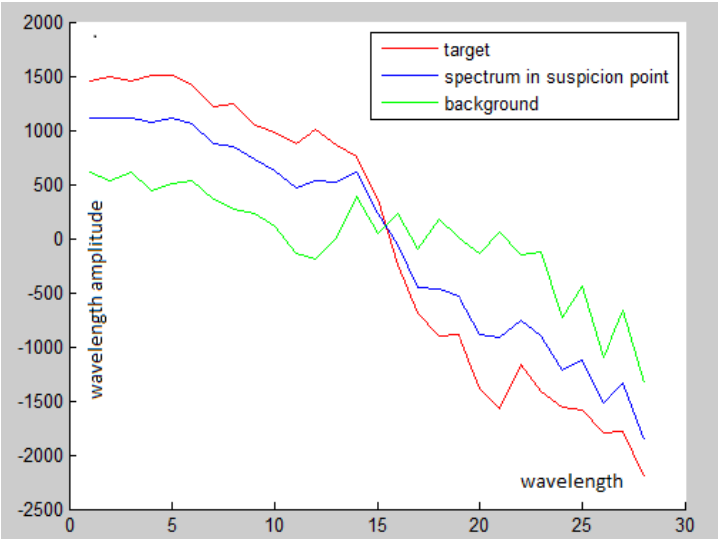

Figure 33. The output from the application of the UNSP unmixing algorithm to the suspicious point in Figure 31. This suspicious point is decomposed into a target and a background spectral portions

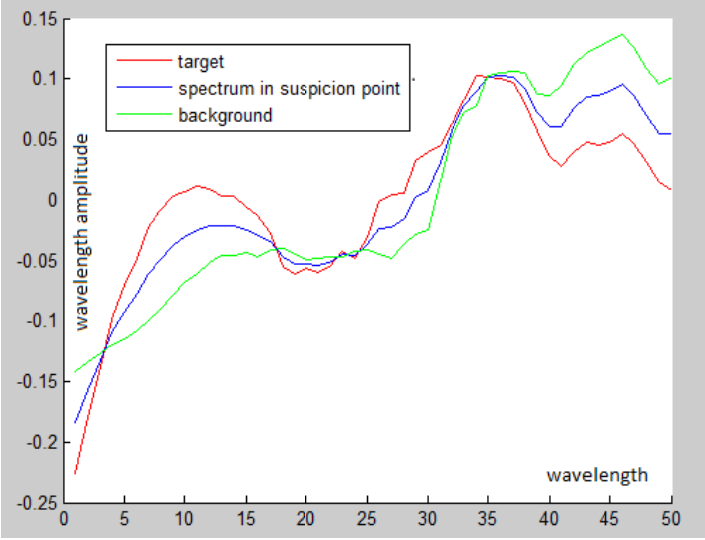

Figure 34. The output from the application of the UNSP unmixing algorithm to the suspicious point in Figure 32. This suspicious point is decomposed into a target and a background spectral portions

4.5.1 Comparison between UNSP and OSP Algorithms

In this section, we compare between the performances of UNSP and OSP (Ahmad & Ul Haq, 2011) algorithms. They are described in Figures 35-41.

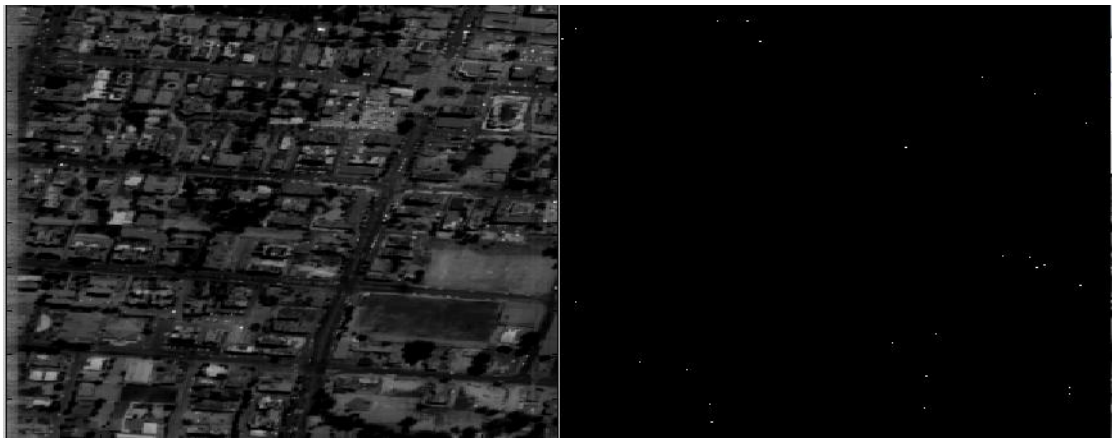

Figure 35. Left: The original “city” image. Right: The white points mark the detected targets by the UNSP algorithm

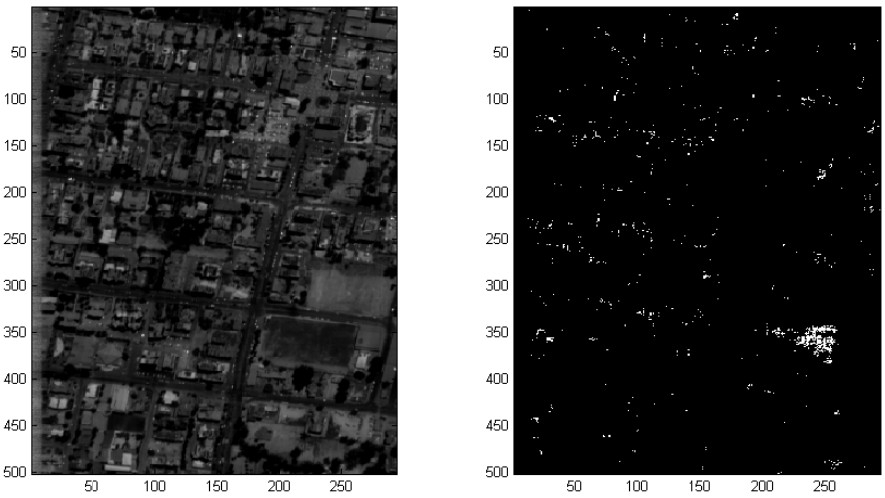

Figure 36. Left: The original “city” image. Right: The white points mark the detected targets by the OSP Ahmad, & Ul Haq (2011) algorithm

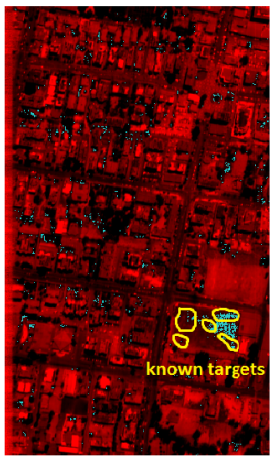

Figure 37. The detected targets by the OSP algorithm are marked over the original “city” image. The yellow circles mark known places that contain the targets. The other points are “false-alarm”". The OSP algorithm produces more “false-alarm” than our method

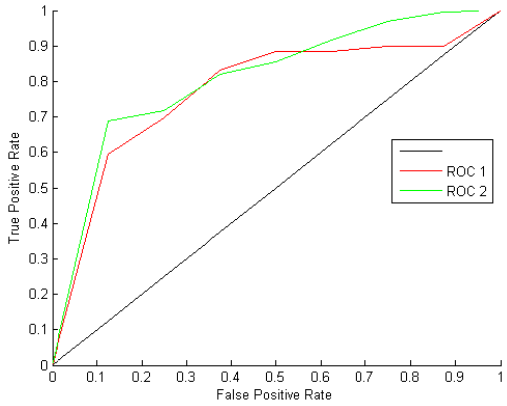

Figure 38. The “ROC-curve” for scene in Figure 37. The red line corresponds to OSP Ahmad & Ul Haq (2011) method. The green line corresponds to the WDR method

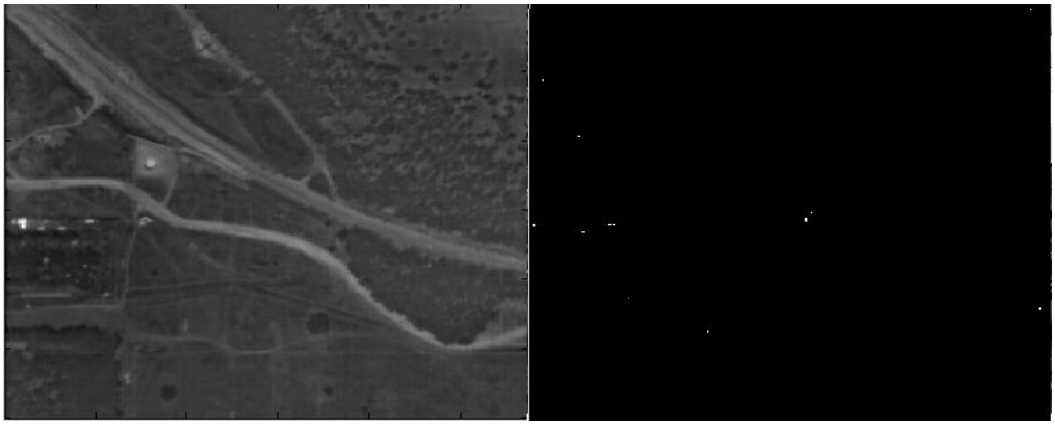

Figure 39. Left: The original "field" image. Right: The white points mark the detected targets by the UNSP algorithm

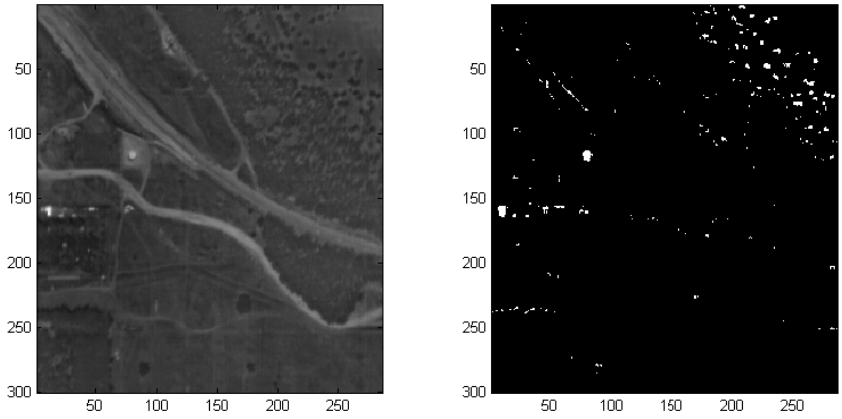

Figure 40. Left: The original "field" image. Right: The white points mark the detected targets found by the OSP Ahmad & Ul Haq (2011) algorithm

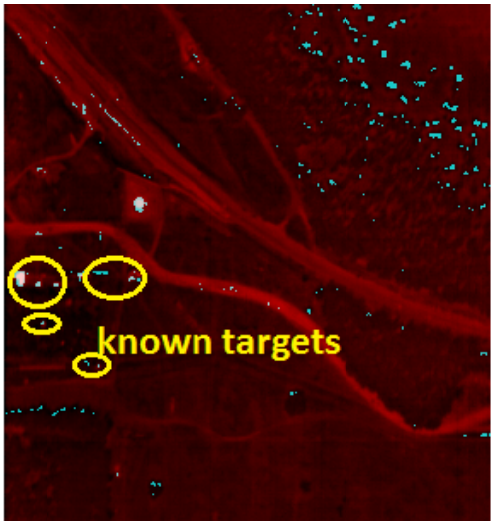

Figure 41. The detected targets by the OSP algorithm are marked over the original "field" image

The yellow circles mark known places containing the targets. Other points are "false-alarm". The OSP Ahmad & Ul Haq (2011) algorithm produces more "false-alarm" than our method.

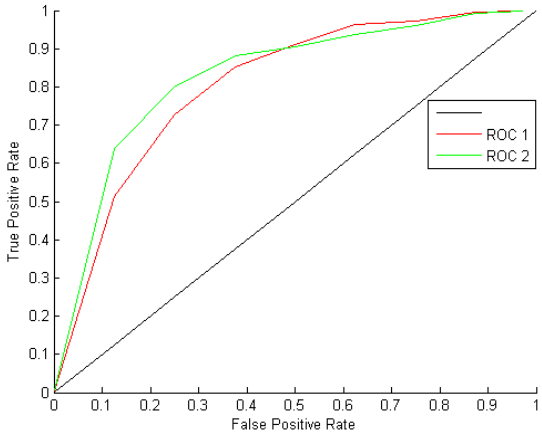

Figure 42. The "ROC-curve" for scene in Figure 41. The red line corresponds to OSP Ahmad, & Ul Haq (2011) method. The green line corresponds to the WDR method

5. Conclusions

We presented two algorithms for linear unmixing. The WDR algorithm detects well targets that occupy at least one pixel but fails to detect sub-pixel targets. The UNSP algorithm detects well sub-pixels targets but it is computational expensive due to the need to search for the spectral decomposition in each pixel's neighborhood by sliding the "morphology-filer". In the future, we plan to add to these algorithms a classification method with machine learning methodologies.

References

Ahmad, M., & Ul Haq, I. (2011). Linear Unmixing and Target Detection of Hyper-spectral Imagery. *2011 International Conference on Modeling, Simulation and Control IPCSIT, IACSIT Press, 10*, 179-183.

Ahmad, M., Ul Haq, I., & Mushtaq, Q. (2011). AIK Method for Band Clustering Using Statistics of Correlation and Dispersion Matrix. *2011 International Conference on Information Communication and Management, IACSIT Press, 10*, 114-118.

Arngren, M., Schmidt, M. N., & Larsen, J. (2009). Bayesian nonnegative matrix factorization with volume prior for unmixing of hyper-spectral images. *IEEE Workshop on Machine Learning for Signal Processing (MLSP), Grenoble*, 1-6. http://dx.doi.org/10.1109/MLSP.2009.5306262

Averbuch, A. Z., & Zheludev, M. V. (2012). Two Linear Unmixing Algorithms to Recognize Targets using Supervised Classification and Orthogonal Rotation in Airborne Hyper-spectral Images. *Remote Sensing, 4*, 532-560. http://dx.doi.org/10.3390/rs4020532

Bateson, C., Asner, G., & Wessman, C. (2000). Endmember bundles: A new approach to incorporating endmember variability into spectral mixture analysis. *IEEE Trans. Geoscience Remote Sensing, 38*, 1083-1094. http://dx.doi.org/10.1109/36.841987

Bayliss, J. D., Gualtieri, J. A., & Cromp, R. F. (1997). Analysing hyper-spectral data with independent component analysis. *Proceeding of the SPIE conference, 3240*, 133-143.

Bioucas-Dias, J., & Plaza, A. (2010). Hyper-spectral unmixing: Geometrical, statistical and sparse regression-based approaches. SPIE Remote Sensing Europe, Image and Signal Processing for Remote Sensing Conference, SPIE.

Bioucas-Dias, J., & Plaza, A. (2011). An overview on hyper-spectral unmixing: geometrical, statistical, and sparse regression based approaches. *Proceeding IEEE Int. Conf. Geosci. and Remote Sensing (IGARSS), IEEE International*, 1135-1138.

Boardman, J. (1993). Automating spectral unmixing of AVIRIS data using convex geometry concepts. *Summaries of the Fourth Annunl Airborne Gcoscicnce Workshop, TIMS Workshop, Jet Propulsion Laboratory, Pasadena, CA, 2*, 11-14.

Burges, J. C. (1998). A Tutorial on Support Vector Machines for Pattern Recognition. *Data Mining and Knowledge Discovery, 2*(2), 121-167. http://dx.doi.org/10.1023/A:1009715923555

Chang, C. I. (2003). *Hyper-spectral Imaging: Techniques for spectral detection and classification*. Kluwer Academic New York.

Chang, C. I., Zhao, X., Althouse, M. L. G., & Pan, J. J. (1998). Least squares subspace projection approach to mixed pixel classification for hyper-spectral images. *IEEE Trans. Geoscience Remote Sensing, 36*(3), 898-912. http://dx.doi.org/10.1109/36.673681

Coifman, R. R., &. Lafon, S. (2006). Diffusion Maps. *Applied and Computational Harmonic Analysis, 21*(1), 5-30. http://dx.doi.org/10.1016/j.acha.2006.04.006

Common, P. (1994). Independent component analysis: A new concept. *Signal Processing, 36*, 287-314. http://dx.doi.org/10.1016/0165-1684(94)90029-9

Craig, M. D. (1994). Minimum-volume transforms for remotely sensed data. *IEEE Trans. Geoscience Remote Sensing*, 99-109.

Cristianini, N., & Shawe-Taylor, J. (2000). *Support Vector Machines and other kernel-based learning methods*. Cambridge University Press.

Dobigeon, N., Moussaoui, S., Coulon, M., Tourneret, J. Y., & Hero, A. O. (2009). Joint Bayesian endmember extraction and linear unmixing for hyper-spectral imagery. *IEEE Trans. Signal Processing, 57*(11), 4355-4368. http://dx.doi.org/10.1109/TSP.2009.2025797

Duda, R. O., Hart, P. E., & Stork, D. G. (2001). *Pattern Classification*. John Wiley & Sons Inc.

Harsanyi, J. C., & Chang, C. I. (1994). Hyper-spectral image classification and dimensionality reduction: an orthogonal subspace projection approach. *IEEE Trans. Geosciencce Remote Sensing, 32*(4), 779-785. http://dx.doi.org/10.1109/36.298007

Hyvarinen, A., Karhunen, J., & Oja, E. (2001). *Independent Component Analysis*. John Wiley & Sons Inc1.

Ifarraguerri, A., & Chang, C. I. (1999). Multispectral and hyper-spectral image analysis with convex cones. IEEE Trans. *Geoscience Remote Sensing, 37*, 756-770. http://dx.doi.org/10.1109/36.752192

Manolakis, D., & Shaw, G. (2002). Detection algorithms for hyper-spectral imaging applications. *IEEE Signal Processing Magazine, 19*(1), 29-43. http://dx.doi.org/10.1109/79.974724

Manolakis, D., Marden, D., & Shaw, G. (2001). Hyper-spectral image processing for automatic target detection applications. *Lincoln Lab Journal, 14*(1), 79-114.

Moussaoui, S., Carteretb, C., Briea, D., & Mohammad-Djafaric, A. (2006). Bayesian analysis of spectral mixture data using markov chain monte carlo methods. *Chemometrics and Intelligent Laboratory Systems, 81*(2), 137-148. http://dx.doi.org/10.1016/j.chemolab.2005.11.004

Nascimento, M. P., & Bioucas-Dias, M. (2005a). Does independent component analysis play a role in unmixing hyper-spectral data? *IEEE Trans. Geoscience Remote Sensing, 43*(1), 175-187. http://dx.doi.org/10.1109/TGRS.2004.839806

Nascimento, M. P., & Bioucas-Dias, M. (2005b). Vertex component analysis: A fast algorithm to unmix hyper-spectral data. *IEEE Trans. Geoscience Remote Sensing, 43*(4), 898-910. http://dx.doi.org/10.1109/TGRS.2005.844293

Ren, H., & Chang, C. I. (2003). Automatic Spectral Target Recognition in Hyper-spectral imagery, *IEEE Trans, on Aerospace and electronic Systems, 39*(4), 1232-1249. http://dx.doi.org/10.1109/TAES.2003.1261124

Settle, J. J. (1996). On the relationship between spectral unmixing and subspace projection. *IEEE Trans. Geoscience Remote Sensing, 34*, 1045-1046. http://dx.doi.org/10.1109/36.508422

SPECIM camera. (2006). Retrieved from http://www.specim.fi/

Winter, M. E. (1999). N-findr: An algorithm for fast autonomous spectral end-member determination in hyper-spectral data. *Proceeding SPIE Conf. Imaging Spectrometry V, SPIE, 266-275*.

Appendix: Diffusion Maps

Diffusion Maps (DM) Coifman, R. R., &. Lafon, S. (2006) analyzes a dataset M by exploring the geometry of the manifold $\boldsymbol{M}$ from which it is sampled. It is based on defining an isotropic kernel $K \in \mathbb{R}^{n \times n}$ whose elements

are defined by $k(x,y)=e^{-\frac{\|x-y\|}{\varepsilon}}, x,y\in M$, ε is a meta-parameter of the algorithm. This kernel represents the affinities between data points in the manifold. The kernel can be viewed as a construction of a weighted graph over the dataset M. The data points in M are the vertices and the weights of the edges are defined by the kernel K. The degree of each data point (i.e., vertex) $x\in M$ in this graph is $q(x)=\sum_{y\in M}k(x,y)$. Normalization of the kernel by this degree produces an $n\times n$ row stochastic transition matrix P whose elements are $p(x,y)=k(x,y)/q(x), x,y\in M$, which defines a Markov process (i.e., a diffusion process) over the data points in M. A symmetric conjugate $\overline{P}$ of the transition operator P defines the diffusion affinities between data points by

$$\overline{p}(x,y)=\frac{k(x,y)}{\sqrt{q(x)q(y)}}=\sqrt{q(x)}p(x,y)\frac{1}{\sqrt{q(y)}},\quad x,y\in M.$$

DM embeds the manifold into an Euclidean space whose dimensionality is usually significantly lower than the original dimensionality. This embedding is a result from the spectral analysis of the diffusion affinity kernel $\overline{P}$. The eigenvalues $1\geq\sigma_0\geq\sigma_1\geq\ldots$ of $\overline{P}$ and their corresponding eigenvectors $\overline{\phi}_0,\overline{\phi}_1,\ldots$ are used to construct the desired map, which embeds each data point $x\in M$ into the data point $\overline{\Phi}(x)=\left(\sigma_i\overline{\phi}_i(x)\right)_{i=0}^{\delta}$ for a sufficiently small δ, which is the dimension of the embedded space. δ depends on the decay of the spectrum $\overline{P}$.

Earth Science Research; Vol. 1, No. 2; 2012
ISSN 1927-0542 E-ISSN 1927-0550
Published by Canadian Center of Science and Education

The Microelement Composition of the Soil-Plant Cover in the Basin of Lake Kotokel'

S. B. Sosorova[1], M. G. Merkusheva[1], A. B. Gyninova[2] & L. L. Ubugunov[1]

[1] Laboratory of Biogeochemistry and Experimental Agrochemistry, Institute of General and Experimental Biology Siberian Branch Russian Academy of Sciences, Ulan-Ude, Russia

[2] Laboratory of Geography and Ecology of Soils, Institute of General and Experimental Biology Siberian Branch Russian Academy of Sciences, Ulan-Ude, Russia

Correspondence: M. G. Merkusheva, Laboratory of Biogeochemistry and Experimental Agrochemistry, Institute of General and Experimental Biology, Siberian Branch, Russian Academy of Sciences, Sakh'yanovoi Str. 6, Ulan-Ude 670047, Russia. Tel: 8-3012-433-165. E-mail: merkusheva48@mail.ru

Received: July 4, 2012 Accepted: July 13, 2012 Online Published: July 23, 2012

doi:10.5539/esr.v1n2p229 URL: http://dx.doi.org/10.5539/esr.v1n2p229

Abstract

The content of microelements (Mn, Zn, Cu, Co, Ni, Cr, Pb, and Cd) and Fe is determined in the soils and plants of the Lake Kotokel' basin. Their content in the soils is proved not to exceed the regional background and the existing MPC and APC. The content of Cd is revealed to exceed its clarke value for the world soils, which is related to the natural origin of this element. The concentrations of Mn, Co, and Pb are close to their clarke values, and those of Zn, Cu, Ni, and Cr are lower than their clarkes. The studied soils are specified by the maximal amount of the mobile forms of microelements. The profile distribution of the microelements differs depending on the genetic soil type. For Mn, Zn, and Cu, a significant biogenic accumulation is pronounced in the organic soil horizons. The content of microelements in the aboveground phytomass exceeds the maximal permissible levels for Mn, Co, Cr, and Fe. The intensity of the microelements absorption by the plants varies widely, being specified by the high coefficient of the biological adsorption (except for Fe). Mn, Zn, and Cu are accumulated in the grass phytomass the most intensely.

Keywords: soils, vegetation, microelements, ecosystems, basin of Lake Kotokel'

1. Introduction

The necessity to analyze the microelement composition of the soil-plant cover in the basin of Lake Kotokel' included in the central ecological zone of the Baikal natural territory (Boundaries of the Baikal…, 2006) and to assess its present-day state is very important for the preservation of the natural complex and pure water of Lake Baikal as a part of our world heritage.

Lake Kotokel' is located 2 km to the east of Lake Baikal in its middle part (52°50' north latitude, 108°10' east longitude, and 460 m above the sea level). The lake is nearly 15 km long and about 5 km wide with its average depth being equal to 5-6 m with a maximal depth of 14 m. The lake's water runs off to Lake Baikal in the north via the Istok and Turka rivers. The climate is continental with a cold winter and a moderately warm summer (Bezrukova et al., 2008).

The soil-forming deposits in the investigated region are represented by the products of acidic rock weathering (Quaternary colluvial, colluvial-rubble loam, and sandy loam), layers of sands and rubble-sandy proluvium filling the intermountain depressions, and alluvial and alluvial-lacustrine sands of the low terraces (Baikal, 1996).

Larch and grass-shrub pine forests with birch prevail in the plant cover of the Lake Kotokel' basin. The dark coniferous taiga consisting of cedar, fir, and spruce occupies the middle-mountain taiga belt of ridges facing Lake Baikal. The low banks of the lake are often swamped and occupied by biocenoses with *Carex, Equisetum,* and *Typha* genera representatives.

The specifics of their accumulation and distribution in the soil-plant cover of the Lake Kotokel' basin have not been investigated.

The main aim was to estimate the present-day ecological and biogeochemical status of the soil-plant cover in the basin of Lake Kotokel'.

2. Objects and Methods

The soil-plant cover in the basin of Lake Kotokel' was the subject of our study. Samples for the physicochemical and chemical analyses and their subsequent treatment were taken according to the recommendations in (Agrochemical Methods…, 1975; Methods for Studying, 2002). The humus content was determined by the Tyurin method, the total nitrogen content was analyzed according to the Kjeldahl method, the exchangeable bases were determined by the complexometric method, the total (hydrolytic) acidity was determined by the Kappen method, and the content of mobile forms of potassium and phosphorus was analyzed according to the Kirsanov method.

The total content of microelements and iron in the soils was measured by atomic-absorption spectroscopy using an AAS Analyst 400 device produced by PerkinElmer after the preliminary decomposition of the samples by hydrofluoric acid (HF) in the presence of sulfuric acid with the subsequent decomposition of the precipitate with hydrochloric acid (HCl). The content of the mobile forms of the microelements was measured in an acetate-ammonium buffer extract (pH 4.8), and their content in the aboveground and underground phytomass of the herbs was analyzed after dry ignition. The data were treated statistically using Microsoft Excel 2000 software. The soils were classified according to (Classification & Diagnostics, 1977).The soil cover in the area is represented by various types of automorphic soils (soddy taiga, soddy forest, and gray forest soils), as well as by boggy and alluvial soils (Figure 1). Automorphic soils are formed under various arboreal and herb associations on the sandy loamy and loamy deposits.

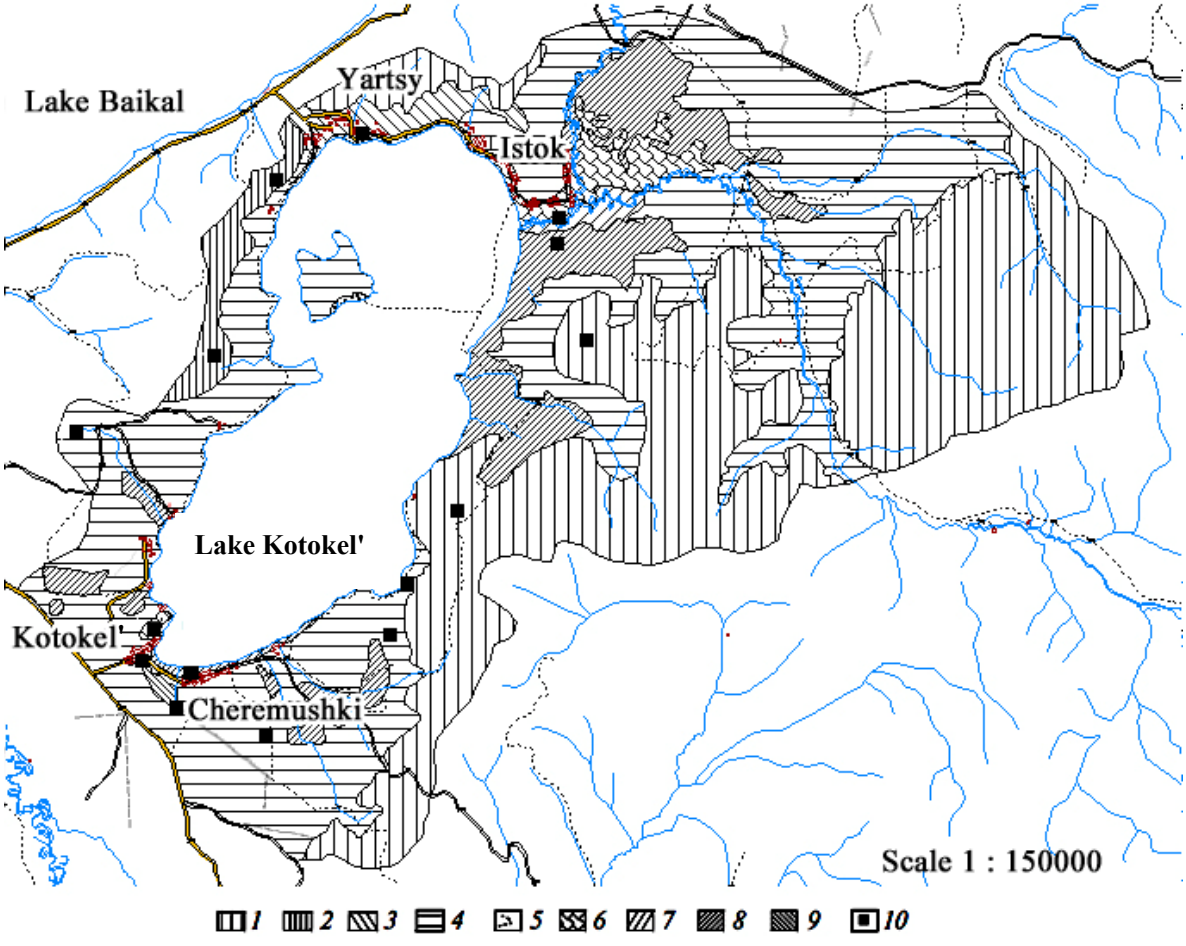

Figure 1. The soil map of the basin of Lake Kotokel' (authors: Gyninova, Tsybikdorzhiev, Balsanova, Gonchikov, & Beshentsev). Soils: (1) soddy-taiga unsaturated (raw-humus burozem); (2) soddy-taiga postcryogenic (dark burozem); (3) soddy forest; (4) gray forest; (5) soddy-gley; (6) alluvial meadow acid; (7) alluvial boggy clay-peat; (8) peat boggy low-moor; (9) peat boggy low-moor reclaimed; (10) position of the profiles

2.1 Forest Ecosystems

The profile of the soddy taiga unsaturated soils consists of the Ao–A1A2–AB–Bf–Bm–C horizons (profile 3). The zone of biogenic accumulation includes a thick weakly decomposed litter with fungal mycelium (3-12 cm) and a thin (4 cm) eluvial-accumulative A1A2 horizon. It is specified by the crumb structure, light-gray color, and the presence of lightened and *bleached* aggregates. The AB horizon is of grayish light brown color. All these features point to the eluvial processes with the insignificant accumulation of substances. The Bf horizon is stony, and the rock fragments have ferruginous ocherous coatings and fine weathering products of ocher color. The amount of stony fragments is lower in the Bm horizon with its color being reddish.

The soddy taiga unsaturated soils are characterized by their light loamy texture in the surface horizons and by their heavy loamy texture in the middle part of the profile (Table 1). The content of the clay fraction is insignificant in the upper horizons and in the soil-forming deposits; however, it reaches 12-16% in the middle part of the profile, which testifies to the metamorphism developed in the AB and Bf horizons. The soil's reaction is acidic, the humus content is low, the content of mobile forms of P_2O_5 is low, and that of K_2O is medium.

The profile of the gray forest soils is represented by the AO–A1–B1m–B2m–BCg–Cg horizons. The soils of this type are specified by the thick forest litter (6 cm) and the thick humus horizon (11 cm). The humus horizon is of dark gray and brownish color, it is underlain by a light brown horizon, and then by a brown one. The dove gray and ocherous mottles and bands in the lower part of the profile testify to the recurrent gleying. In the gray forest soils, the sandy loamy surface horizons are replaced by sandy horizons with the depth; the content of the clay fraction is maximal in the surface horizons (8.7–10.4%) while gradually decreasing to 3.6% down the profile. No signs of metamorphism and vertical migration of clay are revealed in these soils.

The soddy forest soils with the profile A0–A1–Bf–BC–C–D (profile 12) and A0–A1–AB–B1f–B2–BC (profile 7) are formed on the slopes of low hills up to 100 m high and on the northern part of the ridge spurs separating the basins of Lakes Kotokel' and Baikal. The thin humus horizon is replaced by the brown mineral Bf horizon in these soils. The soddy-forest soils are characterized by their sandy loamy texture with the maximal content of clay (3.5 and 6.2%) being found in the accumulative horizon and in the soil-forming rock, respectively. The soil's reaction is weakly acidic. The humus content is low. The upper organic horizons are characterized by a high amount of mobile K_2O.

Table 1. Physicochemical properties of forest soils in the basin of Lake Kotokel'

Horizon, depth, cm	Content of particles <0.01 mm, %	pH_{water}	Humus	N_{tot}	P_2O_5	K_2O	Exchangeable bases		Hydrolytic acidity
			%		mg/100 g of soil		Ca^{2+}	Mg^{2+}	
							mg-equiv./100 g of soil		
Profile 2. Gray forest soil under birch rhododendron – herb-green moss forest									
A0, 0–6	–	5.2	–	0.54	12.4	27.8	4.5	3.2	11.0
A1, 6–17	18.97	5.2	2.6	0.17	10.3	16.5	3.0	0.7	7.0
A1B, 17–36	18.33	5.5	1.2	0.12	11.8	4.7	1.0	0.7	3.3
B, 36–66	9.03	5.7	0.7	0.11	12.1	4.1	0.5	0.6	1.9
BCg, 66–108	4.50	6.0	0.2	0.00	19.1	3.5	0.6	0.6	1.3
Cg, 108–130	5.66	6.0	0.2	0.00	20.8	3.5	0.4	0.2	1.1
Profile 3. Soddy taiga unsaturated soil under herb–bilberry–green moss mixed forest									
Ao, 0–4	20.82	4.2	5.2	0.36	3.0	30.0	2.5	2.7	15.5
A1A2, 4–8	27.20	4.5	3.0	0.22	10.4	11.4	1.2	1.6	11.0
AB, 8–18	28.88	5.1	1.4	0.15	3.5	8.0	1.2	2.0	5.6
Bf, 18–32	19.57	5.5	1.2	0.11	2.3	10.7	1.4	0.6	3.7
Bm, 32–68	37.80	5.9	1.2	–	1.3	7.8	5.6	3.7	3.3
C, 68–118	12.36	6.2	0.7	–	39.6	3.5	6.9	4.0	2.2
Profile 7. Soddy forest soil under pine herb forest									
A1, 1.5–6	15.57	5.7	2.1	0.18	12.2	10.0	3.7	1.9	4.7
AB, 6–10	15.98	5.6	1.0	0.09	12.2	6.1	2.5	1.9	4.2
B1, 10–38	14.30	5.8	0.9	0.09	7.4	6.6	1.6	0.9	2.5
B2, 38–80	19.43	6.1	0.9	–	8.1	6.5	3.4	2.5	2.0
BC, 80–115	18.02	6.5	0.2	–	14.4	4.7	5.6	3.0	1.7
Profile 12. Soddy forest soil under pine rhododendron–cowberry forest									
Ao, 0–6	19.20	5.2	–	0.93	15.8	27.2	6.0	4.8	15.2
B1, 6–10	15.53	5.3	2.5	0.46	20.8	13.7	3.5	0.7	9.2
B, 10–16 (22)	12.86	5.8	1.0	0.26	19.3	4.0	1.7	0.3	3.7
BC, 16 (22)–32	11.07	5.9	0.9	–	9.4	4.2	2.6	0.6	2.7
C, 32–47	16.46	6.2	0.7	–	17.7	5.0	6.4	1.9	1.6
D, 47–100	8.71	6.6	0.2	–	35.4	2.5	4.6	0.9	1.2
Profile 17-07. Soddy gley soil under an herb association									
A_1 0–15	6.93	5.6	5.7	0.84	13.3	6.0	–	–	3.0
Bg 15(24)–57	1.92	6.9	0.3	–	10.3	2.4	7.1	2.4	0.5
Cg 57–75	3.36	6.9	0.4	–	9.0	2.4	6.0	2.0	0.7

2.2 Alluvial Ecosystems

Alluvial meadow soils are formed on the river floodplains in the basin of Lake Kotokel' (Table 2). The alluvial meadow soils are formed in the central flood-plain of the Kotochek River under the herb-cereal-sedge associations (Profile 13). The profile is represented by the following horizons: Ad–A1–Bg–BG–CG. The humus horizon's thickness does not exceed 18 cm. The illuvial horizons show gley features. The texture of the surface horizons is loamy sandy merging to loose sandy. The content of clay is 1.3-2.4%. The soil's reaction is acidic or weakly acidic. The humus content is high in the A1 horizon and it is much lower in the underlying horizons. The amount of mobile phosphorus is low in the organic horizons, and it is high and very high in the mineral horizons.

Table 2. Physicochemical properties of alluvial soils in the basin of Lake Kotokel'

Horizon, depth, cm	Content of particles < 0.01 mm, %	pH_{water}	Humus	N_{tot}	P_2O_5	K_2O	Exchangeable bases		Hydrolytic acidity
			%		mg/100 g of soil		Ca^{2+}	Mg^{2+}	
							mg-equiv./100 g of soil		
Profile 13. Alluvial meadow soil under herb–cereal association									
Asod, 1–2	14.38	5.5	–	0.77	2.3	15.5	7.6	1.4	16.6
A_1 2–18	15.31	5.2	7.1	0.80	2.8	5.4	4.7	0.9	11.2
Bg 18–29(33)	4.22	5.6	1.2	0.22	26.5	2.8	2.0	0.7	3.8
BG 29(33)–68(70)	7.27	5.8	1.4	–	15.5	0.6	2.5	0.5	2.9
CG 68(70) –95	1.78	6.0	0.2	–	26.1	0.6	0.5	0.6	1.6
Profile 14. Alluvial bog soil under cereal–horsetail association									
T_1d 0–7	–	5.7	14.8*	2.47	5.6	44.0	12.8	0.9	–
T2 7–14	–	5.6	13.6*	2.24	4.0	17.2	12.4	2.4	22.5
T3 14–74	–	5.7	16.5*	2.06	6.4	5.2	20.0	10.8	22.1
TG >74	–	5.8	14.9*	1.14	9.6	5.2	16.4	3.2	15.8

* Carbon content (according to Anstett).

Note: Hereinafter, dashes denote "not determined."

In the low floodplain, alluvial boggy soils are formed with a peat thickness of 74 cm (profile 14) and a T1d–T2–T3–TG profile. The soils manifest a weakly acidic reaction and a high adsorption capacity. The content of mobile phosphorus is medium, and that of potassium is very high in the surface horizons and low in the remaining part of profile.

2.3 Bog Ecosystems

The boggy low-moor peat soils are formed on sandy and loamy sandy deposits; they manifest an acidic soil reaction, are base-unsaturated, and have a high content of organic matter (Table 3). The clay content ranges from 1.7 (Profile 1) to 2.8-6.7% (Profile 10). The amount of mobile phosphorus changes from medium to elevated (7-27.5 mg/100 g of soil) in the surface horizons. The content of mobile K_2O is high in the organic horizons.

Table 3. Physicochemical properties of bog soils in the basin of Lake Kotokel'

Horizon, depth, cm	Content of particles <0.01 mm, %	pH_{water}	Humus	N_{tot}	P_2O_5	K_2O	Exchangeable bases		Hydrolytic acidity
			%		mg/100 g of soil		Ca^{2+}	Mg^{2+}	
							mg-equiv./100 g of soil		
Profile 1. Bog low-moor peat low-thickness soil under herb–sedge–moss association									
Td 0–4	–	5.5	16.1*	1.17	7.0	45.4	–	–	–
T_1 4–9	–	5.4	15.1*	1.28	8.0	66.5	–	–	22.7
T_2 9–48	–	5.4	16.6*	2.76	1.2	28.0	9.2	36.0	28.0
CG > 48	3.80	4.9	2.2	–	27.5	8.0	0.7	1.2	1.23
Profile 8. Bog low-moor peat soil under herb–cereal–orsetail–sphagnum association									
To 0–10	–	5.2	19.0*	1.17	21.8	14.0	–	–	–
T_1 10–24	–	5.1	14.2*	1.63	0.5	34.0	–	–	28.0
T_2 24–80	–	5.2	–	1.95	3.6	20.8	–	–	28.0
Profile 10. Bog lowland peaty–gley soil under sedge–shrubbery–sphagnum association									
T_1 0–9	–	5.2	15.3*	2.00	14.0	94.0	8.8	12.4	26.2
T_2 9–28	–	5.1	17.2*	3.79	1.6	28.0	20.0	8.8	28.6
G 28–32	11.44	5.0	9.5	0.14	6.8	0.9	1.2	2.6	5.0

* Carbon content (according to Anstett)

3. Results and Discussion

The soil-forming deposits in the basin of Lake Kotokel' are depleted in microelements as compared to the lithospheric clarke (Vinogradov, 1962) except for Cd, the content of which exceeds the clarke value. However, as compared to the clarke value for felsic rocks, the studied soil-forming deposits are depleted in Zn and Cu; however, the content of Mn, Co, and Pb is close to their clarkes and that of Ni, Cr, and Cd exceeds the clarke values.

The total content of microelements in the soils does not exceed the regional background value and the available maximal permissible concentration (MPC) and approximate permissible concentration (APC) (Table 4). The clarke value for the world soils is found to be exceeded for Cd, which is explained by its natural origin.

Table 4. Average total content of microelements in the soils (0–20 cm) in the basin of Lake Kotokel', mg/kg

Indices	Mn	Zn	Cu	Co	Ni	Pb	Cr	Cd
Forest ecosystems								
M±m, (n=7)	771±84.9	47.8±5.3	5.2±1.8	13.8±2.6	16.1±2.6	19.3±1.4	31.2±1.9	1.2±0.1
Lim	558-1156	33.0-75.7	2.6-15.6	9.3-27.8	10.9-30.7	15.4-25.4	5.5-38.3	0.9-1.7
V, %	29	29	89	49	43	19	16	25
Floodplain ecosystems								
M±m, (n=2)	203±3.2	24.9±2.7	3.9±0.2	7.8±2.2	10.1±1.9	16.3±1.4	19.5±3.3	1.05±0.05
Lim	200-207	22.2-27.6	3.7-4.1	5.5-10.0	8.3-12.0	14.9-17.6	16.2-22.8	1.0-1.1
V, %	2	15	7	41	26	12	24	7
Bog ecosystems								
M±m, (n=3)	239±11.6	25.7±3.9	6.0±2.5	3.7±0.9	6.5±2.5	7.5±0.8	8.8±2.3	0.9±0.03
Lim	218-258	20.1-33.4	1.0-9.1	2.5-5.4	3.6-11.5	5.9-8.5	5.9-13.4	0.8-0.9
V, %	8	27	73	40	67	19	45	7
MPC, APC (Ivanov, 1996)	1500	100*	55*	50	85*	32	100**	2.0*
Clarke in soils of the world (Requirements, 2002)	1000	90	30	8	50	12	70	0,35
Clarke in felsic rocks (Requirements, 2002)	540	58	25	10	8	20	14	0.17
Clarke in the lithosphere (Vinogradov, 1962)	1000	85	47	18	58	16	83	0.13
Southwestern Transbaikalia (Ubugunov & Kashin, 2004)	684***	76	23	–	27	34	54	–

Note: *M* is the mean content, *m* is the error of the mean, *n* is the replicate, *Lim* is the fluctuation limits, and *V* is the variation coefficients.

*Approximately permissible concentrations.

**According to (Mineev, 1988).

***Calculated by (Senichkina & Abasheeva, 1986).

The contents of Mn, Co, and Pb are close to their clarke values, and that of Zn, Cu, Ni, and the content of Cr is lower than the clarke.

According to the schedule of ecological standardization of heavy metals suggested in (Obukhov & Efremova, 1988), the soils are characterized by a low total content of Cu and Ni, by a medium content of Zn and Pb, and a very high content of Cd. The decreased concentrations of Zn, Cu, Ni, and Cr in the soils result from the removal of elements upon the acidic leaching prevailing over their biogenic accumulation.

The light-textured soils (profiles 1, 8, 10, and 16) are specified by the lower content of microelements than the relatively heavy-textured soils (profiles 3, 4, 5, 7, and 12).

According to their total content in the soils of the basin, the microelements form the following succession (in decreasing order): Mn > Zn > Cr > Pb > Ni > Co > Cu > Cd. This sequence corresponds to the distribution of the microelement clarkes in the regional soils. However, if compared to the distribution in the world soils (Mn > Zn > Cr > Ni > Cu > Pb > Co > Cd), an elevated concentration is noted for Pb (unlike Ni and Cu).

The soils of the different ecosystems form the following succession according to the decreasing content of microelements: forest > floodplain > boggy soils, which is related to the soil properties and the ecological conditions of their formation and functioning. The contents of Mn and Zn form another succession: forest > boggy > floodplain soils.

The mobile compounds of chemical elements is the most important group of chemical substances in the soil, which provide the main ecological function of soils as natural-historical bodies, the source of fertility, and contamination control for the environment (Motuzova, 2009). The content of the mobile forms of microelements in soil permits the determination of the soil's supply with chemical elements necessary for the normal growth and development of plants, as well as the levels of their tolerant and toxic concentrations.

The contents of mobile microelements in the upper layers (0-20 cm) of the investigated soils does not exceed 96 for Mn, 60 for Zn, 22 for Cu, 54 for Co, 23 for Ni, 23 for Pb, 51 for Cr, and 30% of the total content for Cd (Table 5, 6, 7). In the underlying horizons, the mobility of the microelements decreases and does not exceed the following (% of the total content): Mn–22, Zn–23, Cu–11, Co–17, Ni–20, Pb–165.7, Cr–4, Cd–24.

The mobility of heavy metals is higher in the low-moor boggy peat soils as compared to the other soils (Table 7). This is explained by the lower moisture of the automorphic soils, which limits the mobility of the chemical elements. According to schedule (Field Survey…, 1980), the studied soils are specified by the low and very low content of mobile forms of microelements except for Mn, the amount of which reaches average values in the boggy and soddy taiga soils.

The profile distribution of the total content of microelements in the soils depends on the soil's genetic type. The reason is the difference in the soil-forming processes developing in the soils. In the soils of the boggy soil-formation type (profiles 1, 8, 10, and 14) and in the soddy taiga unsaturated soils (profile 3), the total content of microelements increases with the depth. In the profile of the soddy forest (profile 2, 7, and 12) and soddy taiga post-cryogenic soil (profiles 4 and 5), no significant redistribution of the microelements is revealed as compared to the soil-forming deposits except for the biogenic accumulation of Mn and Zn and the distribution of Cu in the soddy forest soil, the content of which increases with the depth. In the soddy gley soil (profile 17-07), the accumulation of microelements is registered in the illuvial gley horizon, which is related to the soil's reaction varying from weakly acidic to neutral.

Table 5. Content of heavy metals (mobile form) in the soils of forest herb ecosystems (mg/kg of air-dry substance, AAB with pH 4.8 (% of the total content)

Horizon, depth, cm	Mn	Zn	Cu	Co	Ni	Pb	Cr	Cd
Profile 2. Gray forest soil under birch rhododendron-herb-green moss forest								
Ao, 0–6	193.6/31.1	2.89/5.9	0.19/6.3	0.37/3.9	0.40/3.2	1.20/5.8	0.34/1.3	0.06/4.6
A1, 6–17	113.6/23.0	0.85/1.6	0.18/7.2	0.33/2.7	0.23/1.7	0.77/3.1	0.64/2.3	0.08/8.0
A1B, 17–36	14.6/5.3	0.15/0.4	0.18/6.2	0.14/1.1	0.06/0.4	0.56/2.5	0.51/1.7	0.07/6.4
B, 36–66	4.0/1.2	2.60/8.0	0.14/4.4	0.04/0.3	0.13/0.9	0.26/1.1	0.41/1.4	0.06/5.5
BCg, 66–108	2.6/1.1	0.87/4.0	0.16/9.4	0.01/0.1	0.07/0.7	0.10/0.5	0.20/0.9	0.06/7.5
Cg, 108–130	1.7/0.7	0.79/4.2	0.13/5.6	0.02/0.2	0.04/0.4	0.02/0.1	0.23/1.1	0.06/8.6
Profile 3. Soddy taiga unsaturated soil under herb-bilberry-green moss mixed forest								
Ao, 0–4	400.2/43.6	6.43/17.6	0.21/4.5	0.50/4.8	0.32/3.2	1.05/4.2	0.77/3.3	0.11/12.2
A1A2, 4–8	128.3/20.6	1.76/4.7	0.17/3.7	0.47/4.2	0.19/1.7	0.62/2.3	0.73/2.3	0.09/12.9
AB, 8–18	50.0/18.7	1.05/2.0	0.18/3.8	0.40/3.5	0.15/1.3	0.57/2.3	0.45/1.5	0.07/7.8
Bf, 18–32	11.8/6.6	0.4/1.0	0.18/2.6	0.15/1.2	0.07/0.4	0.42/1.6	0.57/1.7	0.07/6.4
Bm, 32–68	3.8/1.2	0.54/0.9	0.21/2.4	0.21/1.5	0.17/1.0	0.69/2.8	0.14/0.3	0.07/7.0
C, 68–118	2.0/0.4	3.68/5.3	0.23/0.9	0.11/0.5	0.18/0.6	0.30/1.7	0.37/1.1	0.08/7.3
Profile 4. Soddy taiga postcryogenic soil under an herb pine forest								
Ao, 0–5	270.9/39.8	13.92/38.4	0.30/11.5	0.03/0.5	0.45/5.1	2.91/19.1	0.63/2.6	0.15/12.5
A1, 5–14	162.8/10.0	4.30/6.2	0.15/4.7	0.08/0.6	0.22/1.0	0.29/1.6	0.34/0.7	0.08/8.0
BF, 14–44	8.6/2.2	0.22/0.7	0.18/10.6	0.07/0.7	0.15/0.9	0.14/1.0	0.43/1.2	0.07/10.0
BC, 44–65	3.5/0.8	0.68/2.7	0.12/9.2	0.04/0.4	0.10/0.6	0.07/0.5	0.13/0.4	0.06/10.0
C, 65–95	2.4/0.5	0.31/1.4	0.09/4.3	0.01/0.1	0.08/0.5	0.04/0.3	0.21/0.6	0.06/6.0
Profile 5. Soddy taiga postcryogenic soil under an herb pine forest								
Ao, 0–10	505.5/80.4	15.12/49.7	0.30/6.7	0.03/0.3	0.54/4.7	1.59/8.6	0.75/2.3	0.12/10.0
A1, 10–19	118.8/18.8	1.12/3.1	0.16/6.9	0.16/1.7	0.05/0.4	0.36/2.4	0.42/1.3	0.08/8.9
BF, 19–39 (56)	7.70/2.2	0.36/1.0	0.47/10.7	0.24/2.0	0.21/1.1	0.24/1.6	0.16/0.4	0.06/5.5
BG, 39(56)–73	0.60/0.2	1.11/3.6	0.37/10.0	0.04/0.4	0.04/0.2	0.38/2.1	0.16/0.4	0.07/7.0
C, 73–120	1.00/0.4	0.38/1.3	0.18/7.5	0.01/0.1	0.04/0.3	0.15/1.0	0.25/0.8	0.06/6.7
Profile 7. Soddy forest soil under a pine herb forest								
A1, 1.5–6	61.5/6.6	0.70/1.5	0.06/2.1	0.03/0.3	0.19/1.5	0.22/1.1	0.16/0.6	0.04/4.0
AB, 6–10	33.5/5.1	0.43/1.2	0.08/3.2	0.16/1.7	0.09/0.7	0.12/0.6	0.17/0.7	0.01/1.0
B1, 10–38	10.5/3.0	0.38/1.3	0.12/4.6	0.02/6.7	0.12/1.1	0.15/1.5	0.20/0.8	0.01/1.0
B2, 38–80	6.70/2.0	0.13/0.5	0.19/4.5	0.05/0.5	0.10/0.8	0.35/1.7	0.59/2.0	0.01/1.1
BC, 80–115	4.20/1.2	0.45/1.6	0.17/3.8	0.01/0.1	0.26/1.5	0.31/1.6	0.46/1.5	0.02/2.0
Profile 12. Soddy forest soil under pine rhododendron-cowberry forest								
Ao, 0–6	218.1/26.2	6.98/9.3	0.15/1.2	0.40/1.5	0.18/0.6	1.17/16.4	0.39/0.9	0.07/4.7
A1, 6–10	61.0/5.7	27.40/34.7	0.10/0.9	0.30/1.0	0.13/0.4	0.88/6.2	0.33/0.8	0.05/3.3
B, 10–16(22)	11.7/1.1	0.19/0.3	0.25/1.1	0.06/0.2	0.09/0.3	0.30/1.9	0.31/0.9	0.02/1.3
BC, 16(22)–32	4.6/0.2	0.16/0.2	0.18/0.7	0.09/0.3	0.12/0.4	0.23/1.6	0.30/0.9	0.01/0.7
C, 32–47	3.6/0.1	0.14/0.3	0.45/1.6	0.21/0.9	0.16/3.9	0.42/3.8	0.19/0.9	0.02/1.7
D, 47–100	2.2/0.1	0.14/0.2	0.39/0.9	0.06/0.2	0.16/0.6	0.26/1.9	0.23/1.1	0.01/0.8
Profile 17–07. Soddy gley soil under herb association								
A1, 0–15	54.4/6.6	3.35/7.5	0.15/3.1	0.19/1.1	0.27/1.4	0.06/0.3	0.10/0.3	0.16/9.4
Bg, 15(24)–57	1.6/0.2	13.25/23.2	0.05/1.6	0.04/0.2	0.12/0.4	0.58/2.1	0.19/0.5	0.03/1.9
Cg, 57–75	2.1/0.4	3.14/9.0	0.10/1.9	0.06/0.4	0.11/0.6	0.06/0.3	0.16/0.4	0.02/1.4

Table 6. Content of heavy metals (mobile form) in the soils of alluvial ecosystems (mg/kg of air-dry substance, AAB with pH 4.8 (% of the total content)

Horizon, depth, cm	Mn	Zn	Cu	Co	Ni	Pb	Cr	Cd
Profile 13. Alluvial meadow soil under herb-cereal association								
Asod, 1–2	42.8/17.8	2.54/39.8	0.11/2.8.	0.36/3.8	0.25/2.1	0.89/5.1	0.65/2.9	0.05/5.0
A1, 2–18	7.1/4.1	0.78/3.8	0.07/1.9	0.34/3.2	0.23/1.8	0.51/2.9	1.03/4.4	0.05/5.0
Bg, 18–29(33)	0.9/0.4	0.29/0.7	0.07/3.7	0.02/0.1	0.01/0.1	0.07/0.3	0.19/0.8	0.03/2.7
BG, 29(33)–68(70)	0.6/0.1	0.15/0.4	0.17/6.5	0.10/0.6	0.15/1.0	0.17/1.0	0.35/1.3	0.03/3.0
CG, 68(70)–95	0.6/0.1	0.18/0.5	0.23/9.2	0.09/0.4	0.02/0.1	0.04/0.3	0.20/0.7	0.03/3.0
Profile 14. Alluvial boggy soil under cereal-horsetail association								
T1d, 0–7	146.0/82.5	9.54/28.8	0.18/4.6	0.84/18.3	0.69/9.8	3.06/21.0	0.30/2.3	0.21/17.5
T2, 7–14	64.3/28.7	2.31/10.4	0.24/5.6	0.90/14.3	0.66/7.0	1.50/9.8	0.54/2.8	0.24/21.8
T3, 14–74	100.1/47.9	1.35/6.1	0.27/5.4	0.39/7.5	0.24/2.7	0.45/3.7	1.11/5.6	0.18/16.4
TG, >74	92.6/34.5	2.37/6.5	0.18/2.9	0.30/3.8	0.39/3.3	0.69/4.9	1.50/5.9	0.06/5.4

Table 7. Content of heavy metals (mobile form) in the soils of bog ecosystems (mg/kg of air-dry substance, AAB with pH 4.8 (% of the total content)

Horizon, depth, cm	Mn	Zn	Cu	Co	Ni	Pb	Cr	Cd
Profile 1. Bog low-moor peat low-thickness soil under herb-sedge-moss association								
T2, 9–48	124.2/82.8	1.59/14.6	0.42/22.1	0.27/54.0	0.33/10.3	0.51/13.8	0.72/7.5	0.18/25.7
CG, >48	3.8/0.6	11.65/24.7	0.12/8.0	0.13/1.0	0.04/0.4	0.17/0.8	0.40/1.6	0.07/6.4
Profile 8. Bog low-moor peat soil under herb-cereal-horsetail-sphagnum association								
To, 0–10	304.5/95.8	13.56/37.3	0.69/11.9	2.19/43.8	2.58/23.2	1.56/2.4	1.47/26.3	0.27/30.0
T1, 10–24	82.9/70.0	6.75/22.1	0.75/6.0	1.32/22.4	2.73/22.9	2.25/21.6	1.80/8.4	0.21/23.3
T2, 24–80	57.3/64.4	9.57/23.3	1.26/6.1	0.90/16.7	2.70/19.7	1.95/15.7	0.42/1.6	0.24/24.0
Profile 10. Bog lowland peaty-gley soil under sedge-shrubbery-sphagnum association								
T1, 0–9	200.2/63.7	18.90/59.8	0.33/5.1	0.48/16.5	0.54/16.4	1.80/22.8	2.10/51.2	No data
T2, 9–28	104/62.3	5.19/33.9	0.18/1.9	0.39/10.5	0.27/6.7	0.39/4.5	0.33/3.2	0.18/22.5
G, 28–32	12.50/21.9	0.63/7.7	0.06/6.7	0.03/0.4	0.14/1.9	0.24/1.3	0.54/3.5	0.01/0.9
B_{other}, 32–59	9.10/11.4	0.23/2.2	0.08/8.0	0.07/0.9	0.23/2.8	0.33/1.7	0.65/4.0	0.01/0.8
BCG, 59–80	7.60/11.9	0.22/0.8	0.21/11.0	0.08/0.8	0.20/2.0	0.42/1.9	0.87/3.9	0.01/0.8
MPC (Hygienic Norms, 2006)	80	23	3.0	5.0	4.0	6.0	6.0	No data

The profile distribution of the mobile forms of the microelements does not always repeat the distribution of their total content by the soil profile. For the bulk of the microelements, it follows a certain regularity. In general, the content of mobile Mn, Co, Cr, and Cd decreases down the soil profile. Two maximums are revealed in the profile distribution of the mobile forms of Cu, Ni, and Pb: the first is caused by the biogenic accumulation, and the second is related to the adsorption accumulation in the illuvial soil horizons. An insignificant concentration of the mobile Zn forms is noted in the illuvial gley horizons. Zn's solubility grows noticeably in the neutral environment. This is caused by the amphoteric nature of this metal and its capacity to form hydrocomplexes. The substantial accumulation of the mobile forms of the microelements is typical for the upper organogenic soil layers.

Plants are the most important intermediate links for chemical elements passing from the soil, water, and air into humans and animals (Steblevskaya et al., 2006), and they represent a powerful biogeochemical barrier removing the excessive masses of elements from the migration flows to depositing media (Karel'skaya, 2008). The content of chemical elements in plants is mainly inherited from the soils on which they grow; however, it is not identical, as plants selectively consume the necessary elements according to their physiological and biochemical needs (El'chininova, 2009). As proceeds from the analysis of the microelement amount in the plants, despite the low content of mobile forms in the soil in the studied territory, the plants do not suffer from a physiological deficit in these elements, and the concentration of Mn, Co, Cr, and Fe in the aboveground phytomass exceeds their maximal permissible levels (Table 8). This is explained by the more intense consumption of the microelements by the plants in the acidic media as compared to neutral and alkaline media.

The coefficient of biological consumption is a quantitative measure of the intensity of the chemical elements accumulation by plants; it is calculated as the ratio of an element's content in the plant ash to its content in the soil

(Perel'man, 1975). Note that the intensity of the microelements accumulation in the aboveground phytomass in the investigated area varies widely and manifests high values of the biological consumption coefficient. The coefficient of the Mn consumption by the aboveground phytomass ranges from 1.7 to 53.4; Zn, 7.3-98.5; Cu, 3.5-37.4; Co, 1.2-16.6; Ni, 0.8-14.2; Cr, 1.2-24.0; Fe, 0.07-0.62; Pb, 1.5-15.3, and Cd, 0.9-7.3. The underground phytomass accumulates microelements less intensely. For example, the coefficient of the Mn consumption is equal to 3.910.7; Zn, 0.7-24.0; Cu, 2.5-15.1; Co, 0.7-16.1; Ni, 0.2-5.5; Cr, 0.4-6.5, Fe, 0.04-0.37; Pb, 0.7-21.0; and Cd, 0.5-4.5.

Table 8. Content of microelements in the phytomass (aboveground, above the dash; underground, below the dash) in the Lake Kotokel' basin, mg/kg of air-dry mass/coefficient of the biological consumption

Biocenosis; profile	Mn	Zn	Cu	Co	Ni	Pb	Cr	Cd	Fe
Forest ecosystems									
Herb, profile 2	355/10.7	24.1/8.1	3.6/21.0	1.6/2.5	2.2/2.8	2.5/1.9	4.8/3.1	0.14/2.1	204/0.22
	728/5.2	29.5/2.2	3.9/5.3	3.8/1.3	4.1/1.2	5.1/0.9	6.7/1.0	0.19/0.7	646/0.16
profile 3	1071/43.8	24.7/14.5	5.3/27.8	1.3/3.0	1.7/3.8	1.6/1.6	6.1/5.2	0.15/4.1	83/0.13
	732/10.7	35.8/7.5	4.5/8.5	4.5/3.6	2.2/1.8	4.6/1.6	5.7/1.8	0.24/2.3	648/0.37
profile 7	576/23.1	21.3/14.6	3.8/37.4	1.5/3.9	1.5/3.3	1.0/1.6	4.9/5.0	0.13/3.3	120/0.20
	2527/8.1	29.2/1.6	3.3/2.6	5.3/1.1	3.4/0.6	5.9/0.7	5.2/0.4	0.23/0.5	670/0.09
profile 12	1491/23.0	19.2/7.6	3.4/6.5	1.4/1.5	2.1/2.0	2.1/3.6	3.6/1.2	0.10/3.0	112/0.07
	1585/4.2	20.7/0.7	15.0/2.5	7.0/0.7	2.9/0.2	6.9/1.2	8.9/0.6	0.3/0.5	706/0.04
Cereal-herb, profile 17-	133/1.7	30.8/7.3	7.3/16.2	2.1/1.2	1.5/0.8	2.0/1.0	3.9/1.3	0.15/0.9	348/0.13
07	889/3.9	88.9/7.1	20.3/15.1	11.4/7.7	4.4/1.8	11.3/2.0	7.8/0.9	0.51/1.1	755/0.10
Floodplain ecosystems									
Herb-cereal, profile 13	260/23.1	32.8/27.3	6.5/14.6	1.6/2.7	2.2/3.2	2.5/2.6	4.3/3.3	0.14/2.6	145/0.18
	568/9.8	45.8/7.4	14.2/13.5	3.8/1.3	6.1/1.7	5.3/1.1	12.9/1.9	0.28/1.0	637/0.15
Herb-cereal-horsetail, profile 14	166/15.2	21.9/15.8	1.3/5.4	1.2/3.7	0.4/0.8	1.1/1.2	2.9/2.8	0.08/1.0	72/0.07
	157/7.1	13.4/4.8	4.1/8.5	3.1/5.3	0.9/0.9	4.8/2.9	5.7/3.0	0.26/1.7	674/0.37
Bog ecosystems									
Herb-sedge, profile 1	366/33.9	29.4/33.9	1.6/23.6	1.6/16.6	1.8/9.0	3.7/15.3	7.8/21.5	0.17/4.2	270/0.21
	190/105	35.0/24.0	1.1/10.1	2.6/16.1	1.0/2.8	8.6/21.0	4.0/6.5	0.31/4.5	811/0.37
Herb-cereal-horsetail, profile 8	233/11.6	26.6/7.5	3.4/3.5	2.0/3.4	1.0/2.0	1.2/1.5	5.5/3.4	0.17/1.8	173/0.15
	181/8.7	23.6/6.4	12.9/12.9	3.1/5.2	5.2/4.1	4.6/5.3	7.0/4.1	0.27/2.7	704/0.40
Herb-cereal, profile 10	477/53.4	98.9/98.5	4.6/13.3	1.8/12.6	2.2/14.2	2.6/7.3	7.4/24.0	0.25/7.3	213/0.62
	213/14.8	22.6/14.0	3.5/6.4	2.2/9.5	1.4/5.5	4.7/8.2	3.0/6.1	0.23/4.2	648/0.37
Limits of normal concentrations (Mineev, 1988)	no data	15-150	2.0-12.0	0.3-0.5	0.4-3.0	0.1-5.0	0.2-1.0	0.05-0.2	no data
Maximal permissible level in forage (Sanitary Rules …, 1996)	100	50	30	1.0	3.0	5.0	0.5	0.3	100
Rate of forage provision	40-50	30-50	6.0-10.0	0.8-1.0	0.4-3.0	0.1-5.0	0.4-0.6	no data	
Intensity of the biological consumption (Dobrovol'skii, 1997)	6.9	11.8	2.3	1.4	1.5	1.5	1.0	4.4	0.1
Mean content in the vegetation of the continents (Dobrovol'skii, 1997)	205	30	8.0	0.5	2.0	1.25	1.8	0.035	200

Note: The underground phytomass is determined in the soil layer of 0-20 cm, and the forest herb mowing consists of the following: profile 2 – *Rubus saxatilis*, *Pyrola asarifolia*, *Maianthemum bifolium*, *Galium boreale*, *Aegopodium alpastre*, *Diphasiastrum complanatum*, and sporadically *Calamagrostis sp.*, *Festuca ovina*; profile 3 –*Diphasiastrum complanatum*, *Vicia nervata*, *Maianthemum bifolium*, *Lathyrus humilis*, *Vaccinium myrtillus*, *Vaccinium vitis-idaea*, *Carex sp.*; profile 7 – *Festuca ovina*, *Pulsatilla flavescens*, *Orthilia secunda*, *Aegopodium alpastre*, *Galium boreale*, *Lathyrus humilis*, *Rubus saxatilis*, *Maianthemum bifolium*, *Hieracium ganeschinii*; profile 12 –*Aegopodium alpastre*, *Platanthera bifolia*, *Rubus saxatilis*, *Pyrola asarifolia*, *Festuca ovina*, *Maianthemum bifolium*, *Galium boreale*, *Geranium krylovii*, *Vaccinium myrtillus*, *Vaccinium vitis-idaea*; and profile 17-07 – *Poa supine*, *Carex ovalis*, *Plantago major*, *Trifolium repens*, *Prunella vulgaris*.

Mn, Zn, and Cu are accumulated in the phytomass most intensely, which is caused by their important biochemical function and points to the cationphilic character of the biogeochemical specialization of the forest landscape plants. The vegetation of bog ecosystems adsorbs microelements more intensely as compared to that of the forest ecosystems. The difference in the degree of the microelement consumption is caused both by the properties of the plant species and by the ecological conditions of their growth. For instance, in the boggy low-moor soils, the excessive moisture favors the low oxidation degree and the easily-soluble forms of chemical elements. The anaerobic conditions make the microelements more available to plants (Sadovnikova et al., 2006). In addition, the light texture of the boggy soils increases the mobility of the microelements.

4. Conclusions

Thus, the content of microelements in the soils of the Lake Kotokel' basin does not exceed the regional background as well as the existing MPC and APC. The profile distribution of the microelements is different and depends on the genetic type of the soils. The significant biogenic accumulation in the organic soil horizons is markedly pronounced for Mn, Zn, and Cu.

The amounts of microelements in the aboveground phytomass of the studied associations exceed the maximal permissible levels for Mn, Co, Cr, and Fe. The intensity of the microelements' consumption varies widely, being specified by the high values of the biological consumption coefficients, except for Fe.

References

Agrochemical Methods of Soil Study. (1975). Moscow: Nauka. (in Russian).

Baikal Atlas. (1996). Moscow: Feder. sluzhba geodez. kartogr. Rossii. (in Russian).

Bezrukova, E. V., Krivonogov, S. K., Takakhara, Kh., Letunova, P. P., Shichi, K., Abzaeva, A. A., … Zabelina, Yu. S. (2008). Lake Kotokel – A Reference Section of Sediments of the Late Glacial and Holocene Time in the South of East Siberia. *Dokl. Akad. Nauk, 420*(2), 248-253. (in Russian).

Boundaries of the Baikal Natural Territory and Its Environmental Zoning (Order of the Government of the Russian Federation No. R1641-p from November 27, 2006). (in Russian).

Classification and Diagnostics of Soils of the Soviet Union. (1977). Moscow: Kolos. (in Russian).

Dobrovol'skii, V. V. (1997). Biospheric Cycles of Heavy Metals and the Regulatory Role of Soil. *Pochvovedenie, 4*, 431-441. *Eur. Soil Sci., 30*(4), 371-380. (in Russian).

El'chininova, O. A. (2009). Extended Abstract of Doctoral Dissertation in Biology. Barnaul. (in Russian).

Field Survey and Mapping of the Soil Cover Contamination from Technogenic Aerial Pollution. (1980). Moscow: VASKhNIL, Pochv. inst. name of V. V. Dokuchaeva. (in Russian).

Hygienic Norms GN2.1.7.2041-06. (2006). *Maximum Permissible Concentrations (MPC) of Chemical Substances in Soil*. Moscow: IPK Izd. Standartov. (in Russian).

Ivanov, V. V. (1996). *Environmental Geochemistry of the Elements*. Moscow: Nedra. Vols. 1, 3 (in Russian).

Karel'skaya, T. A. (2008). Extended Abstract of Candidate's Dissertation in Chemistry. Ivanovo. (in Russian).

Lebedev, N. I. (1990). *The Use of Micronutirents for Improving the Productivity of Ruminants*. Leningrad: Agropromizdat. (in Russian).

Methods for Studying Forest Cenoses. (2002). St.-Peterburg: NIIKhim St-Peterb. Gos. Univ. (in Russian).

Mineev, V. G. (1988). *Ecological Problems of Agricultural Chemistry*. Moscow: Izd. Mosk. State Univ. (in Russian).

Motuzova, G. V. (2009). *Microelement Compounds in Soils. Systems Arrangement, Environmental Significance, and Monitoring*. Moscow: Kn. dom LIBROKOM. (in Russian).

Obukhov, A. I., & Efremova, L. L. (1988). *Conservation and Remediation of Soils Contaminated with Heavy Metals in Heavy Metals in the Environment and the Environmental Protection*. Moscow: NPO Medbioekonomika. (in Russian).

Perel'man, A. I. (1975). *Geochemistry of Landscape*. Moscow: Vyssh. Shkola. (in Russian).

Requirements for the Multipurpose Geochemical Mapping on a Scale of 1 : 200000 and Its Results. Appendices. (2002). Moscow: IMGRE. (in Russian).

Sadovnikova, L. K., Orlov, D. S., & Lazonovskaya, I. N. (2006). *Ecology and Environmental Protection upon the Chemical Contamination*. Moscow: Vyssh. Shkola. (in Russian).

Sanitary Rules and Norms 2.1.7.573-96. (1996). "Hygienic Requirements for the Use of Sewage Water and Sludge for Irrigation and Fertilization," (Approved by the State Sanitary Inspection of the Russian Federation on October 31, 1996, no. 46). (in Russian).

Senichkina, M. G., & Abasheeva, N. E. (1986). *Microelements in Soils of Siberia*. Novosibirsk: Nauka. (in Russian).

Steblevskaya, N. I., Medkov, M. A., Molchanov, V. P., Polyakova, N. V., Moiseenko, L. I., Zorikov, P. S., & Batyrbaeva, N. V. (2006). Studies of the Biogeochemical Accumulation of Microelements in Soils and Plants of the Far East. *Vest. DVO RAN, 2*, 57-63. (in Russian).

Ubugunov, V. L., & Kashin, V. K. (2004). *Heavy Metals in the Garden Soils and Plants of Ulan-Ude*. Ulan-Ude: Izd. BNTs SO RAN. (in Russian).

Vinogradov, A. P. (1962). Mean Contents of the Elements in Major Types of Rocks of the Earth Crust. *Geokhimiya, 7*, 555-571. (in Russian).

Earth Science Research; Vol. 1, No. 2; 2012
ISSN 1927-0542 E-ISSN 1927-0550
Published by Canadian Center of Science and Education

Research on the Relationship between Evolution of Urban Land Structure and Industrial Structure Transformation: A Case Study of Chengdu City

Qing Kang[1], Jian-Qiang Li[1] & Jie Ding[1]

[1] College of Economic and Management, Sichuan Agricultural University, Chengdu, China

Correspondence: Qing Kang, College of Economic and Management, Sichuan Agricultural University, Chengdu, China. Tel: 86-139-8171-4823. Email: kangqingchn@163.com

Received: May 14, 2012 Accepted: May 31, 2012 Online Published: July 23, 2012

doi:10.5539/esr.v1n2p241 URL: http://dx.doi.org/10.5539/esr.v1n2p241

Abstract

From lateral perspective, this paper analyzes the relationship between evolution of urban land structure and industrial structure transformation, through proportion change index and Granger method. The empirical study shows three points. First of all, Chengdu land structure change shows that city feature is not perfect, living environment and ecological environment construction needs to be strengthened. Moreover, the industrial structure optimization of Chengdu continues and the tertiary industry gradually occupied a dominant position. Ultimately, in short-term, urban land change drived industry structure transformation, then industry structure transformation feeded back urban land structure change; the synchronization action between urban land structure evolution and industrial structure change has not appeared, and the reciprocal causation of them will come true under the long-time adjusting.

Keywords: evolution of urban land structure, industry structure transformation, Chengdu city

1. Introduction

The urban land is the basis of social and economic development. The differences in quality and quantity of urban land, and its configuration between different industrial departments will bring different effects to urban development. Theoretical study shows that structure-orientated growth is the essential way of modern economic growth mode. In a certain sense, certain urban industrial structure is mapped through the corresponding urban land use structure, while the contradiction between industrial developments in demand for land growth and the scarcity of land resources has become the core issue of urban land use. Consequently, in the period of high index change, exploring the effect of reasonable evolution of urban land structure on industrial structure optimization is theoretically and realistically significant to macroeconomic control.

The theory about industrial distribution and land location can be traced back to "The Agricultural Location Theory" (Johann Heinrich Von Thunen, 1826), the largest contribution of which is revealing the formation mechanism of land use structure by introducing the location factors into land use study. Besides, anther famous theory was the urban land bid-rent modal of Alonso William, which reflected a basic principle that the growth of urban spatial structure was the result of industrial competition. Industrial economists believed that the most directly reflect of economic development is the change of industrial structure. The optimization of industrial structure was the key reason for the evolution of urban construction land and truly drives force of urban development. On the other hand, the reasonable evolution of urban construction land supplied the material basis for the optimization of industrial structure.

Zhang, Wang Q. and Wang W. (2007) used statistical analysis, exponential analysis and multiple index analysis method to reveal the variation rules between the industrial structure and the land structure from certain angle and to analyze the relationships between them. Lu, Yang and Wen (2010) made a verifying research on the coupling relationship between urban land structure and industrial structure in Chongqing by proportion change index and Granger method. The conclusion showed that, in short term, the coupling relationship did not appear. But in the long time harmony, it would come true. Meng and Zhang (2011) analyzed the relationship among the effectiveness, output value, and amount of land by the output value index for per area, and the odds ratio of value to area. This study area is an example of 18 districts in Beijing during stages of economic development. Authors

insisted that industrial structure adjustment was the main way to promote the level of intensive land utilization, and that intensive land use policy was also an important means to guide and restrict industrial structure adjustment.

As the evolution of urban land use structure and industrial structure transformation is a complex process, which appears to time-varying non-stationary characteristics. Thus, this paper selects Chengdu City as an example and uses proportion change index and Granger method to analyze and test the relationship between evolution of urban land structure and industrial structure transformation, in order to recommend suggestion for urban economic development.

2. Study Area, Research Methods and Data Sources

2.1 Study Area

Chengdu is a vice provincial level city, which is located in the central part of Sichuan province. It is an important center city in central and western China. And it is the technology centre, trade center, financial center and transportation hub. The economic aggregate of Chengdu ranked first in the long-term in the 12 western provincial capital cities. In promoting the economic and social development of central and western China, Chengdu plays an important role. As a consequence, there is a referential significance for cities in central and western China and other vice provincial level cities.

2.2 Research Methods

2.2.1 Proportion Change Index

The structure variation index is an indicator to measure the degree of quantitative structure change. The calculation formula is:

$$D_i = \sum_{i=1}^{n} | G_t - G_0 | \tag{1}$$

In which D_i is the structure variation index, G_t is the proportion of urban land use or industry proportion of period t, G_0 is the proportion of urban land use or industry proportion of base period, n is the number of type. Based on the formula, this paper calculates the variation degree of urban land use structure and industry structure over the calendar year in Chengdu, then analyzes the both of structure difference by the deviation factor. The deviation factor refers to the absolute value of the difference between the land use structure index and the urban land use structure change index. The larger the deviation factor, the greater gap between the land use structure and industry structure has changed, and vice versa.

2.2.2 Granger Method

For two time series X_t and Y_t, if Y_t plays role in the forecast; in other words, we use X_t forecast Y_t better than non-use of X_t, then X_t is the Granger cause for Y_t. Specifically, we need to establish the p-order lag equation to test whether X_t is the Granger cause for Y_t. The Granger causality model is as follow:

$$Y_t = \lambda + \sum_{i=1}^{p} \partial_i X_{t-i} + \sum_{j=1}^{p} \beta_i Y_{t-j} + \mu_i \tag{2}$$

$$Y_t = \lambda + \sum_{i=1}^{p} \partial_i X_{t-i} + \sum_{j=1}^{p} \beta_i Y_{t-j} + \mu_i \tag{3}$$

In the formulas (2) and (3), λ is constant term, ∂_i and β_i present the relevant regression coefficients respectively, i is lag number, p is maximum lag number, μ_i is error term. The former one aims to test whether X_t is the Granger reason of the Y_t change, and the latter formula is to test whether the Y_t Granger reason causes a X_t change. The null hypothesis is $H_0 : \partial_1 = \partial_2 = ... = \partial_k = 0$, k=1, 2 …p. Test the significance of ∂_1, $\partial_2 ... \partial_k$, if the significance is not 0, that means the null hypothesis $H_0 : X_t$ is not the Granger reason causing Y_t change. Then exchange place of X_t and Y_t, using the same method to test whether the Granger reason causing X_t change is $H_0 : Y_t$.

2.3 Urban Land Classification and Data Sources

According to "Statistical Yearbook of Chengdu" and "China City Statistical Yearbook" Chengdu will land into residential land, public facilities land, industrial land, warehouse space, external transport sites, roads and squares land, municipal facilities, green space and special land and urban land types 9, 1999-2009, the City and the towns of Chengdu, the land type data were derived from the "China urban Construction Statistical Yearbook" (2000-2010). The social and economic data of this paper comes from "Chengdu Statistical Yearbook" and "China City Statistical Yearbook" (2000-2010).

3. Chengdu City, the Dynamic Evolution of Urban Land Structure and Industrial Structure Transformation

3.1 The Dynamic Evolution of Urban Land Use Structure in Chengdu

Urban land use structure not only presented as a combination relationship of quantitative proportion and spatial layout, but also reflected on a timely evolution, which has necessarily been mapped by the industrial structure adjustment. The interaction between them is the basis and guarantee for the urban economic growth in space.

As can be seen from the Table 1, residential land accounts for the largest proportion of the whole urban land use structure at 35.96% in 2009. Although this proportion was higher by 4.82% than the upper limit of the domestic standard, compared to 45% of which in abroad, residential land in Chengdu was obviously insufficient, and the living environment needs to be further improved. Secondly, the proportion of industrial land reached at 20.57% in 2009, which was higher than that of 15% at a foreign standard. That is because Chengdu is an industrial city; the proportion of industrial land of Chengdu will be higher. Finally, the proportion of green land increased from 4.33% in 1999 to 6.57% in 2009, while there has some distance from the lowest limit of domestic standard.

From increment view from 1999 to 2009, a proportional decline appears in public facilities land, industrial land, warehousing and storage land, external traffic land and special land, among which the proportion of industrial land and special land decreased to the largest at 2.12% and 4.73% respectively. This is mainly due to Chengdu municipal government takes measures to strengthen the intensity of urban land use structure optimization by moving some heavy pollution and labor-intensive industry out from the inner city on the basis of building "world's ecological garden city". Thus, the tertiary industry of location-sensitive and strong capacity to pay are likely to acquire land use right in city center, which attributes to a decline in urban industrial and storage land perception. With speedy development of urban economy, urban agglomeration capacity is stronger, which attractive more people to live and work in the city, hence requiring a higher standard of the urban livability and suitability. Accordingly, the demand for residential land, road and squares land and green land would be increased.

Table 1. Evolution of urban land use structure proportion in Chengdu from 1999-2009

Year	Residential land (%)	Public facilities land (%)	Industrial land (%)	Warehouse space (%)	External transport sites (%)	Roads and squares land (%)	Municipal facilities land (%)	Green space (%)	Special land (%)
1999	32.36	14.17	22.69	2.65	4.22	11.56	2.64	4.33	5.39
2000	31.83	13.97	22.25	2.58	4.13	12.20	2.59	5.19	5.25
2001	30.59	13.37	24.53	2.48	3.94	12.57	2.5	5.16	4.86
2002	31.12	13.18	23.9	2.45	4.51	12.38	2.6	5.64	4.21
2003	30.54	16.24	25.15	2.33	2.12	12.19	3.35	4.37	3.62
2004	30.17	16.22	25.14	2.34	2.39	12.27	3.33	4.55	3.59
2005	30.53	16.5	24.81	2.24	2.23	12.3	3.06	4.88	3.46
2006	30.25	14.3	22.89	1.87	1.36	20.09	2.79	5.68	0.76
2007	33.73	13.69	21.14	1.85	1.3	18.81	2.95	5.74	0.8
2008	35.93	13.27	20.35	1.5	2.38	16.88	2.02	6.96	0.72
2009	35.96	13.44	20.57	1.57	2.81	15.72	2.71	6.57	0.66
increment	3.61	-0.73	-2.12	-1.09	-1.40	4.16	0.07	2.24	-4.73

Source: Chengdu Statistical Yearbook (1999-2010) and China City Statistical Yearbook (2000-2010)

3.2 The Dynamic Transformation of Industrial Structure in Chengdu

Industrial structure reveals the proportion constitutes of production factors among various sectors and the interdependence and mutual restriction relationship between them. Industrial structure can be divided into static and dynamic structure. The former one is in certain moment various industry resources allocation, transformation and output. The later one is the composition changing from one form to another form with time goes.

From Figure 1, industrial structure of Chengdu is in the continuous adjustment from 1999 to 2009. The proportion of primary industry decreased from 3.6% at 1999 to 2.1% at 2009, and the decrease amplitude is 41.76%. The whole growth amplitude of secondary industry is 6.34% that shows a characteristic of rise first then adjustment. The whole rise amplitude of the tertiary industry is 3.71% which shows the character firstly decreases then increases. Obviously, the overall scale of the tertiary industry has been continuous expansion. But its development speed significantly lags behind the secondary industry. It is thus clear that Chengdu is at the transformation stage from later stage of industrialization to post-industrialization, when the secondary industry and the tertiary industry are increasing and gradually turn to the tertiary industry-led industry pattern.

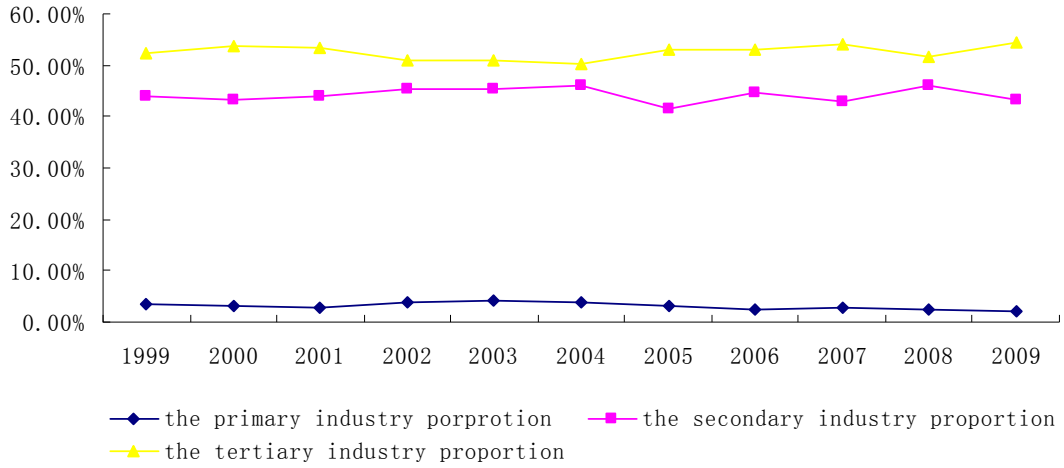

Figure 1. The conversion of industrial structure in Chengdu City from 1999 to 2009

4. The Relationship between Evolution of Urban Land Use Structure and Industrial Structure Transformation

4.1 The Proportion Relationship

Research on the relationship between urban land structure and industrial structure could be from the quantitative structure and the spatial structure effect in microscopic view. Because of the difficulty of spatial structure data obtained, this paper researches on the effect of evolution of urban use land structure on industrial structure transformation only from the difference of quantitative structure.

According to the formula (1), nearly 11years of Chengdu City, the proportion relationship of urban land use structure and industrial structure were calculated (Table 2). The conclusion shows that the urban land use structure change rate index is steady and presents an increasing trend on the whole, with a fluctuation in the middle. It went up from 3.01% in 2000 to 23.04% in 2009. Compared with the urban land use structure change rate index, the industrial structure change rate index has a larger fluctuation presenting a “W” pattern.

From the deviation coefficient of the urban land use structure change rate index and the industrial structure change rate index, on the whole, from 1999 to 2009, the urban land use structure change rate index is greater than the industrial structure change rate index. The deviation coefficient increases from 0.61% at 2000 to 8.97% at 2005 and reached its maximum of 18.80% at 2008. The overall tendency shows that the urban land use structure of Chengdu from 1999 to 2009 has large varied amplitude with fast change speed, and the industrial structure change lags behind the urban land use structure change. This is mainly due to the internal function division is not clear, which causes the industrial structure change lag behind.

Table 2. The change rate index of urban land structure and industrial structure and the deviation coefficient in Chengdu from 1999 -2009

Year	The urban land use structure change rate index (%) (1)	The industrial structure change rate index (%) (2)	The deviation coefficient (%) (1)-(2)
1999	-	-	-
2000	3.01	2.40	0.61
2001	7.38	1.68	5.70
2002	7.29	3.40	3.89
2003	11.85	3.35	8.50
2004	12.24	4.56	7.68
2005	12.31	3.34	8.97
2006	20.74	2.20	18.54
2007	20.69	3.46	17.23
2008	23.04	4.24	18.80
2009	20.15	4.04	16.11

4.2 Analyses on the Granger Method

In theory, if any city has all the statistical data of the urban land use structure and industrial structure and could make rational classification, the change tendency of the urban land use structure index will be roughly equal to the industrial structure index. That is the change of urban land use structure could influence the industrial structure change, vice versa.

This paper uses Granger method to analyze the effect of evolution of urban use land structure on industrial structure transformation. It uses the change rate index of urban land use structure (X) and the change rate index of industrial structure (Y) in 1999 as base period to analyze on the Granger method.

4.2.1 Data Stability Test

As time series data is not always stable, in order to ensure the reliability of conclusions, the research tries to make stable test selecting the extended ADF by the premise of error term exist serial correlation not determined. The level series of the urban land use structure change rate index and the industrial structure change rate index are expressed as Y and X. ⅠY and ⅠX represents the first-order difference, and ⅡY and ⅡX are their second-order difference respectively. The result of empirical analysis showed (Table 3) that all samples could not reject the existence of unit root null hypothesis at the 10% significance level, so the two sequences were not smooth. But the series of the urban land use structure change rate index (Y) and the industrial structure change rate index (X) showed their first-order difference stationary at the 10% significance level, I (1) process, by the unit root test.

Table 3. ADF test of the temporal variable

variables	ADF	Test types	critical values of 1%	critical values of 5%	critical values of 10%	Lag number
Y	-2.7353	Constant and trend	-5.8352	-4.2465	-3.5905	1
X	-3.2617	Constant and trend	-5.5201	-4.1078	-3.515	1
Ⅰy	-3.4004	Constant term	-4.5826	-3.3209	-2.8014	0
Ⅰx	-4.0879	Constant and trend	-5.8352	-4.2465	-3.5905	0
Ⅱy	-3.8496	Constant and trend	-6.292	-4.4504	-3.7015	0
Ⅱx	-2.8646	Constant and trend	-5.1198	-3.5195	-2.8984	1

4.2.2 Data Co-integration Test

On the basis of the result of unit root test, we had practiced whether the error term of regression equation can be smoothly to test and analyze the long-term equilibrium relation between the two series. If the error term is stable, the long-term equilibrium relation between the variable series can be defined, otherwise it does not exist.

Uses E-Views software as an analytical tool to obtain the regression equation of urban land use structure change rate index (Y) and industrial structure change rate index (X) is:

$$\ln Y = 0.5852 + 0.2247 \ln X \quad (4)$$

R^2 of regression model is 0.8056, while the F is 20.0705. Then the unit root test result of the error term showed that at the 10% significance level of first-order difference, the error term reject the existence of unit root null hypothesis. So that means the long-term equilibrium relation between the series of the urban land use structure change rate index (Y) and the industrial structure change rate index (X) can be defined. As shown in Table 4.

Table 4. ADF text of the error term

variable	ADF	Test types	critical values of 1%	critical values of 5%	critical values of 10%	Lag number
The error term	-3.5451	Constant term	-4.5826	-3.3209	-2.8014	0

4.2.3 Granger Causality Analysis

The result of co-integration test represented a the long-term equilibrium relation between the series of the urban land use structure change rate index (Y) and the industrial structure change rate index (X), so we can use Granger causality analysis directly.

As is showed in Table 5, when the lag number is 1 at the 10% significance level, the probability value of the Granger reason is 0.1653 that evolution of urban land structure does not cause industrial structure transformation. So when confidence level is 83.47%, it refuses the null hypothesis that evolution of urban land use structure does not cause industrial structure change. That means evolution of urban land use structure promotes industrial structure transformation. In contrast, the influence of industrial structure transformation on urban land use structure change was significantly weaker than the later on the former.

The explanation is in the process of implementing Western Development Strategy and constructing the World's Ecological Garden City by Chengdu government, the urban population and the income of urban residents continue to go up, hence demanding for an increasing amount of residential land, road and square land, Municipal utilities land and green land. In the process of optimization, evolution of urban land use structure is faster than industrial structure transformation.

When the lag number is 2 and at the 10% significance level, the probability value of the Granger reason is 0.3571 that industrial structure change does not cause evolution of urban land use structure. So when confidence level reaches 64.29%, it refused the null hypothesis that industrial structure change does not cause evolution of urban land use structure, which means industrial structure transformation reacts against evolution of urban land use structure, and evolution of urban land use structure does not lead to an industrial structure change.

This is because the Chengdu municipal government moves some heavy pollution and labor-intensive industry out from the city center, providing spaces for information industry and financial industry which need a good location condition and to pay a high government rent to develop. In this way, the proportion of industrial land and Warehousing and storage land were gradually reduced, and urban land use structure will be adjusted.

To sum up, in the short time, there is not the benign interactive relationship between the urban land use structure and the industrial structure, and the change of industrial structure lags behind the dynamic change of urban land use structure.

Table 5. The Granger test result of urban land use structure change rate index and industrial structure change rate index

Lag length	Granger causality	Freedom	F statistic	Adjoint probability
1	X does not Granger Cause Y	9	2.4955	0.1653
	Y does not Granger Cause X	9	0.0214	0.8886
2	X does not Granger Cause Y	8	0.4242	0.8674
	Y does not Granger Cause X	8	1.4803	0.3571

5. Conclusions and the Policy Suggestion

5.1 Conclusions

The article makes the empirical analysis on the time data of the change rate index of urban land use structure and the change rate index of industrial structure by using Granger method and explains the relationship between evolution of urban land use structure and industrial structure transformation. The result showed that:

1) The industrial structure optimization of Chengdu continues from 1999 to 2009. According to the theory of Chenery.H and Simon, it is thus clear that Chengdu is at the transformation stage from later stage of industrialization to post-industrialization, when the secondary industry and the tertiary industry are increasing and gradually turn to the tertiary industry-led industry pattern.
2) Chengdu urban land use structure has assumed a situation of a higher proportion of industrial land while a shortage of residential land and green space, which implies a city function to be perfect as well as much to do to strengthen the urban residential and ecological environment construction.
3) The large amplitude and fast speed appears in the industrial structure change, while the reason why the urban land structure lags behind of that is since the ambiguous of urban function partitioning in Chengdu.
4) In short-term, urban land use change promotes the industry structure transformation, then industry structure transformation feeds back the former. Since the influence of the length and lagtime of time series selected, it hasn't generated a reciprocal causation between them, which is an accordance view of the fact. As the interaction between them, the adjustment of urban land use structure hasn't reflected in the industrial structure optimization. Similarly, the two are unlikely to change in the meantime by the influence of land macro-control policies and land price. As a result, the reciprocal causation of them only comes out in a long lasting adjusting.

5.2 The Policy Suggestion

The results of study on the relationship between evolution of urban land use structure and industrial structure have important reference meaning to achieve sustainable development of western region economic. It is concluded that:

1) The industrial structure adjustment of Chengdu lags behind the urban construction land use structure change. There is no a reciprocal causation relationship between them, not a reciprocal causation relationship has generated between them. Therefore, Chengdu should guide the industrial location selection by imposing distinguished land taxes based on land price, as well as basing on the rule of industrial structuring evolution and the capital objective condition. All of which spurs to the heavily polluted and labor-intensive industries get far away from the central and residential regions, thus driving the tertiary industry development in the central city.
2) When formulating the land use planning, we must identify the urban function partitioning to promote a scale effect of the similar industries concentration by reducing the production cost. Moreover, we must think much of the effectiveness and feasibility of the planning. The planning should be appropriate advanced and left the flexible scope to adapt to market change and unforeseen factors impacted on land use.

References

Alonso William. (1965). *Location and Land Use*. Cambridge: Harvard University Press.

Chenery, H., & S. Robinson M. Syrquin. (1995). *Industrialization and Growth: A Comparative Study.* Shanghai: Renmin publishing company.

Clive W. J. Granger. (1969). Investigating causal relations by econometric models and cross-spectral methods.

Econometrica, 37, 424-459. http://dx.doi.org/10.2307/1912791

Han, X., Wu, P. L., & Dond, W. L. (2012). An analysis on interaction mechanism of urbanization and industrial structure evolution in Shandong China. Procedia *Environmental Sciences, 13*, 1291-1300. http://dx.doi.org/10.1016/j.proenv.2012.01.122

He Chunyag, Shi Peijun, & Chen Jin. (2001). A study on land use/cover change in Beijing area. *Geographical Research, 20*(6), 679-687.

Huang Xianjin, Peng Buzhuo, & Zhang Jianxin. (2002). Relationship between Regional Economic Sector Development and Sustainable Land use. *Economic Geography, 22*(4), 425-429.

Johann Heinrich Von Thunen, & Wu Hengkang. (1997). *The Isolated State*. Beijing: the Commercial Press.

Kong Xiangbin, Zhang Fengrong, & Li Yulan. (2005). Interactive Relationship between Land Use Change and Industrial Change. *Resources Science, 27*(2), 5-7.

Liu Yanjun, Li Chenggu, & Sun Di. (2006). Analysis on Process and Power Mechanism of Urbanization Response of Industrial Structure Evolvement in Northeast China. *Urban Studies, 13*(6), 58-64.

Liu Yansui, & Chen Baiming. (2002). The study framework of land use /cover change based on sustainable development in China. *Geographical Research, 21*(3), 324-330.

Lu Chunyang, Yang Qingyuan, & Wen Feng. (2010). Study on the Relationship between Urban Land Use Structure and Industry Structure---Chongqing as an Example. *Urban Studies, 17*(1), 102-107.

Wang Siyuan, Zhang Zengxiang, & Zhou Quangbin. (2002). Study on Spatial-Temporal Features of Land Use/ Land Cover Change Based on Technologies of RS and GIS. *Journal of Remote Sensing, 6*(3), 223-228.

White, R., & Engelen, G. (1993). Urban systems dynamic and cellular automata: Fractal structures between order and chaos. *Chao, Solitons & Fractals, 4*(4), 563-583. http://dx.doi.org/10.1016/0960-0779(94)90066-3

Xuebing Dong, Shunfeng Song, & Hui Zhu. (2011). Industrial structure and economic fluctuation--Evidence from China. *The Social Science Journal, 48*(3), 468-477. http://dx.doi.org/10.1016/j.soscij.2011.05.002

Zhang Ying, Wang Qun, & Wang Wanmao. (2007). Study on the Relationship between Industrial Structure and Land Structure in China. *China Land Science, 21*(2), 6-9.

Zhu Huiyi, Li Xiubin, & He Shujin. (2001). Spatio-temporal Change of Land Use in Bohai Rim. *Acta Geogarphica Sinica, 56*(3), 253-260.

Earth Science Research; Vol. 1, No. 2; 2012
ISSN 1927-0542 E-ISSN 1927-0550
Published by Canadian Center of Science and Education

Assessment of Quality and Pollution Potential of Groundwater around Dabhaura Area, Rewa District, Madhya Pradesh, India

U. K. Mishra[1], A. K. Tripathi[1], Saras Tiwari[2] & Ajay Mishra[3]

[1] Department of Geology, Shriyut P. G. College Gangeo Rewa, Madhya Pradesh, India

[2] Department of Chemistry, I. V. P. G. College Jawa Rewa, Madhya Pradesh, India

[3] Department of Geology, Govt. P. G. Science College Rewa, Madhya Pradesh, India

Correspondence: U. K. Mishra, Department of Geology, Shriyut P. G. College Gangeo Rewa, 486113, Madhya Pradesh, India. E-mail: umeshicvmmishra2007@rediffmail.com

Received: March 1, 2012 Accepted: March 26, 2012 Online Published: July 23, 2012

doi:10.5539/esr.v1n2p249 URL: http://dx.doi.org/10.5539/esr.v1n2p249

Abstract

The present paper deals with quality and pollution potential of Groundwater of Dabhaura area, Rewa District, Madhya Pradesh. The study area is mainly drained by Jatari river which finally meets to Tons river, a life line of Rewa region. Geologically, the area is occupied by shale and Govindgarh sandstone formations of Upper Vindhyan. A total of 22 groundwater samples from shallow aquifer zone collected in June 2011 and analyzed to see their suitability for drinking and irrigation purposes. The analysed data reflect that the groundwater of the area is moderately hard to very hard, higher amount of total dissolved solids as well as higher concentration of sulphate due to lithology of aquifers. A most of samples are within prescribed limits as suggested by World Health Organisation (WHO) and Indian Standard (ISI) for drinking purpose. The groundwater is mainly Ca-Mg-SO_4-Cl and Ca-Mg-HCO_3 type. The plot of electrical conductance (EC) vs sodium adsorption ratio (SAR) of analysed groundwater samples in U.S. salinity diagram indicating them to be of medium to high salinity and low sodium hazard type of groundwater. However, for the computation of vulnerability, the DRASTIC Index (DI) modelling has been adopted. The computed Drastic Index suggests that the area is moderate to high susceptible to pollution. Hence, proper attention and water quality monitoring programme has been suggested to check the groundwater pollution.

Keywords: groundwater pollution, DRASTIC index, Dabhaura, Madhya Pradesh India

1. Introduction

The Groundwater is a precious natural resource which plays a vital role to cater the demand of water supply arising due to inadequate surface water resources throughout the world. The changes are fairly rapid in shallow aquifers because of discharge recharge pattern as well as contaminated activities (Raghunath, 1987). The quality of groundwater is largely controlled by discharge-recharge pattern, nature of host and associated rocks as well as contaminated activities (Walton, 1970). The hydrogeochemical evolution of groundwater is a dynamics process undergoing constant change in space and time (Karanth, 1987). The quality of groundwater is of considerable importance in addition to its quantity for the management of groundwater resource. The study on groundwater quality of Vindhyan region has been performed by few researchers (Tiwari et al., 2009; Tiwari et al., 2010; Mishra, 2010). Hydrogeochemistry and classification of groundwater are carried out in order to evaluate its suitability for municipal, agricultural and industrial uses (Ahmed et al., 2002; Jasrotia & Singh, 2007; Suresh et al., 2010; Purushottam et al., 2011). Realizing the importance of groundwater quality delineation, the present work has been undertaken around Dabhaura area, a tehsil headquarter in Rewa district, Madhya Pradesh (Figure 1).

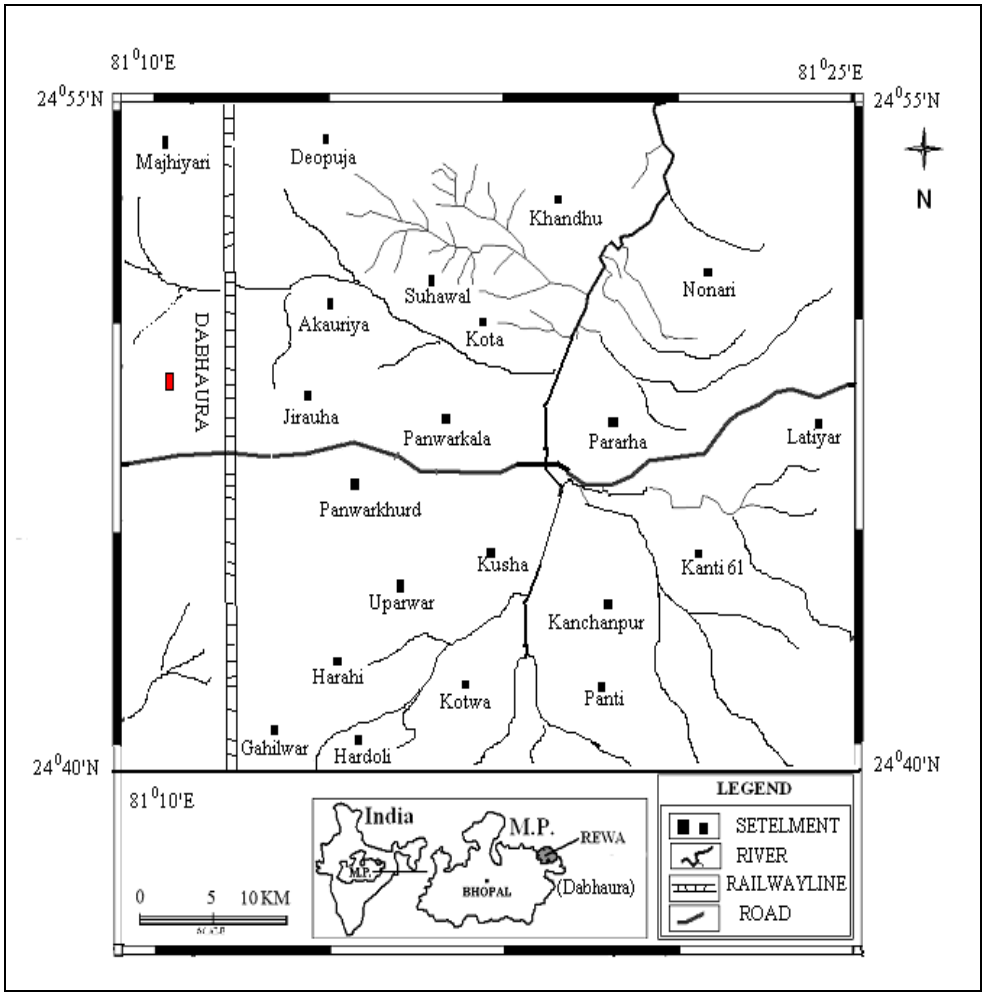

Figure 1. Location map of the Study Area

The study area is drained by Naina river and its tributaries and bounded by latitude $24^0$40' to $24^0$55'N and logitude 81°10' to 81°25'E covering an area of about 500 km^2. The climate is semi arid to humid type and average rainfall of the area is about 1000 mm however in the year 2010 it was recorded 549 mm. The temperature in summer months goes up to 46°C while as low as 2°C during peak winter month. The relative humidity is of about 75 percentage.

2. Geology and Hydrogeology

The study area is part of northern extension of Vindhyan sedimentary basin; one of the thickest sedimentary basins of India. The main rock types are Govindgarh sandstone and shale of Rewa Group of Vindhyan Supergroup. Besides these, recent alluviums also present in the area. Sandstone is medium to coarse grained, red and brown in colour and dominated by monocrystalline quartz. It is quartz arenite type (Tiwari & Dubey, 2007) and shows development of cross beds. The shale is thinly bedded and chocolate brown in colour with the development of polygonal mud cracks.

Hydrogeologically, the area is hard rock terrain, lying in Pre-Cambrian sedimentary province (Karanth, 1987). Due to high silica cementation in sandstone, the primary porosity is low. Secondary porosity in the form of joints, fractures, bedding planes and weathered pediments are favourable for the groundwater exploitation. The groundwater occurs in both semi confined and confined conditions.

3. Methodology

The present study is based on 22 groundwater samples which collected from Dugwells during June, 2011. The physico-chemical analysis was performed following standard methods (Ramteke & Moghe, 1986; APHA, 1998). The pH, electrical conductivity and total dissolved solids of the samples were determined in the field using

portable instruments. Calcium, magnesium, total hardness, sodium, potassium, chloride, bicarbonate, sulphate, and fluoride were determined in the laboratory by folowing standard analygtical technique (APHA, 1998).

The total hardness in groundwater in the study area has been calculated using the formula proposed by Raghunath (1987) as under:

$$TH \text{ as } CaCO_3 \text{ in mg/l} = (Ca + Mg) \text{ mg/l} \times 50$$

For the computation of DRASTIC Index, some hydrogeological parameters as outlined by Aller et al. (1987) have been used, which are given below:

i. Depth to water table (D)
ii. Net Recharge (R)
iii. Aquifer media (A)
iv. Soil media (S)
v. Topography (T)
vi. Impact of vadose zone and (I)
vii. Hydraulic conductivity of aquifer (C)

$$D.I. = D_R D_w + R_R R_W + A_R A_w + S_R S_w + T_R T_W + I_R I_W + C_R C_W$$

where R- rating; W- weightage

3.1 Classification of Groundwater

The classification of groundwater is essential to know the suitability of groundwater of an area for domestic, agricultural or industrial uses. In the study area, groundwater are classified based on the total dissolved constituents TDS, Cl^- SO_4^{-2}, HCO^-_3 etc. Wilcox (1955) classified groundwater on the basis of concentration of TDS as upto 500 mg/l; desirable for drinking, 500-1000 mg/l; permissible for drinking, upto 3000 mg/l; useful for irrigation and > 3000 mg/l; unfit for drinking and irrigation. Based on the above classification, about 45% of the samples are within the desirable limit and 55% are in permissible limit for drinking purpose.

The maximum sulphate concentration in the water samples is 315.30 mg/l (sandstone) while the concentration in shale formation is 612.00 mg/l in water sample (Table 1). This suggests that 65% of the water sample belong to the "normal sulphate" category (Schoeller, 1962). Based on this classification, the groundwater of the area has maximum concentration of chloride is 85.00 mg/l in sandstone and 212.00 in shale indicates that the groundwater is "normal chloride" water (Schoeller, 1962). The minimum total hardness concentration in groundwater in the study area is 100 mg/l and the maximum concentration is 802mg/l. According to classification based on hardness scale by USGS (Hem, 1985), the groundwater of the area is moderately hard to very hard. The minimum HCO^-_3 concentration in groundwater in the study area is 109.00 mg/l in while the maximum concentration is 365.00 mg/l observed in thus, most of the groundwater samples belong to the normal carbonate category (Schoeller, 1962).The analyzed data has been plotted on Chadha's (1999) diagram which is modified version of Piper's (1953) trilinear diagram. It has all the advantage on the diamond shaped field of the Piper's trilinear and can be also used to study various hydro-chemical processes such as base cation exchange, actual ion concentration, mixing of natural waters and sulphate reduction and other related hydro-chemical problems.

In the Chadha's scheme the difference in milliequivalent (epm) percent between alkaline earth (Calcium + Magnesium) and alkali (Sodium + Potassium) expressed as percentage reacting value is plotted on the X-axis and difference in milliequivalent (epm) percentage between weak acid anion (Carbonate +Bicarbonate) and strong acid anion (Chloride + Sulphate + Nitrate) is plotted on the Y-axis. The milliequivalent percentage difference between alkaline earth and alkaline metals and between weak acidic anions and strong acidic anions would plot in one of the four possible subfields of the diagram. In the study area, out of 22 groundwater samples, 12 sandstone samples and 07 shale samples fall in the subfield -5 of Ca-Mg-HCO_3 type whereas 02 sandstone samples and 01 shale samples fall in the subfield 6 indicating Ca-Mg-Cl-SO_4 type (Figure 2).

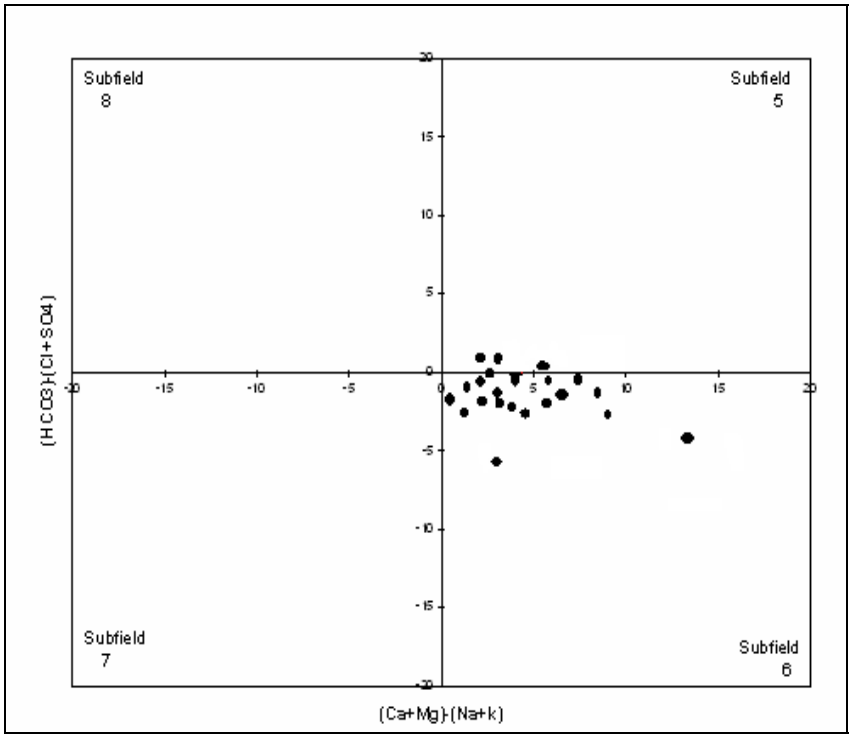

Figure 2. Classification of Groundwater samples as Per Chadha's (1999) Scheme

4. Results and Discussion

4.1 Drinking Water Quality

As evident from Table 1, pH ranges from 7.4 to 8.9 indicating alkaline nature of groundwater. The higher pH values observed in certain samples suggest that carbon dioxide, carbonate-bicarbonate equilibrium is affected more due to change in physico-chemical conditions (Karanth, 1987; Tiwari et al., 2010).

The conductivity of groundwater sample of the study area varies from 500 mg/l to 1867 mg/l in shale. Higher concentration of electrical conductance in shale may be due to the enough time for reaction between groundwater sample and impervious shale. The sandstone litho units have comparatively lesser amount of EC due to its hydrological characters. The total dissolved solids (TDS) varies between 321 mg/l to1197 mg/l. The water with TDS upto 1000 mg/l is considered to be suitable for drinking (Pophare & Dewalkar, 2007; Tiwari & Singh, 2010). The higher amount of TDS may cause gastrointestional irritation in human body.

The total hardness varies between 100 mg/l (Kanchanpur; moderately soft) to 802 mg/l (Pararha; very hard). The possibility of groundwater hardness in the area may be due to calcareous sandstone. The content of calcium in sandstone aquifers varies from 15 mg/l to 109 mg/l while in shale, the range of concentration varies from 30 mg/l to 99.2 mg/l. The magnesium concentration in water sample from sandstone ranges 11.5 mg/l to 75 mg/l while in shales, the concentration varies 16 mg/l to 177 mg/l. The concentration of sodium ranges from 5 mg/l to 104 mg/l in sandstone aquifers whereas it varies from 19.9 mg/l to 70 mg/l in shale lithounit. Similarly, concentration of potassium varies between 1.2 mg/l to 13.6 mg/l in sandstone and 1.1 mg/l to 11.24 mg/l in shale formations. It seems that the clay minerals present in sandstone and shales contributed these two constituents to the groundwater of the area. In the present study, the groundwater sample from sandstone have sulphate concentration ranging from 4.5 mg/l to 315.3 mg/l while in the case of water samples from shaly aquifers, the concentration range of sulphate varies from 20.20 mg/l to 612 mg/l. The higher concentration of sulphate is due to the gypsum and baryte nodules associated with shale.

The concentration of chloride in sandstone aquifer varying from 20.2 mg/l to 85 mg/l while the water samples from aquifer in shale have chloride concentration ranging between 36.66 mg/l to 212 mg/l. The water samples from sandstone aquifers have bicarbonate ions ranging between 125 mg/l to 309 mg/l while the shale formation have the range of bicarbonate ions between 109 mg/l to 365 mg/l. Potable water should have 0.6 to 1 mg/l of fluoride for substantial protection against tooth decay. If fluoride is totally absent in drinking water, it causes

dental caries. Continuous high intake of fluoride result in mottled teeth, skeletal fluorosis and sometimes severe osteosclerosis. In the study area, the concentration of fluoride ranges from 0.02 to 1.03 in sandstone aquifer whereas 0.01 to 2.7 in shale aquifers. The higher concentration of fluoride in shale formation is due to the presence of F^- bearing minerals (biotitic and clay minerals) in shale formation as well as leaching action from other sources. As evident from Table 1, higher concentration of fluoride is strongly related with pH indicating that higher alkalinity of the water promotes the leaching of F^- and thus affects the concentration of F^- in the groundwater (Chatterjee et al., 2008, Duraiswamy & Patankar, 2011; Saxena & Ahmed, 2001; Madhnure et al., 2007). To ascertain the suitability of groundwater for drinking purpose the geochemical parameters of the study area are compared with the guidelines as recommended by WHO (1984) and ISI (1991) which indicate that groundwater of the study area is more or less suitable for drinking purpose (Table 2).

Table 1. Geochemical analyses of groundwater samples of the study area

Lithology	Location	P^H	EC (μs/cm)	TDS	TH	Na	K	Ca	Mg	F	Cl	SO_4	HCO_3
1	2	3	4	5	6	7	8	9	10	11	12	13	14
SSt./1	DABHAURA	7.6	757	485	352	27.32	12.41	109.00	19.01	1.03	81.02	50.16	309.00
SSt./2	GAHILWAR	8.1	507	325	465	20.00	1.20	63.00	75.00	0.09	85.00	20.00	125.00
SSt./3	HARHAI	7.5	702	450	352	28.30	12.30	108.00	20.00	1.00	80.00	49.10	308.00
SSt./4	MAJHIYARI	7.6	863	553	293	11.50	8.40	98.30	11.50	0.30	20.20	315.30	179.00
SSt./5	KOTWA	8.2	607	389	123	5.00	13.40	27.49	27.49	1.00	27.60	56.90	242.80
SSt./6	KANCHANPUR	8.2	501	321	100	104.00	13.60	15.00	15.09	0.50	33.10	54.50	142.20
SSt./7	DEOPUJA	7.4	605	388	352	37.80	2.50	92.80	29.16	1.01	57.12	6.50	132.00
SSt./8	AKAURIYA	8.1	505	324	241	17.09	3.00	58.00	23.32	0.30	29.70	6.50	176.00
SSt./9	JIRAUHA	8.3	583	374	315	32.00	2.80	85.00	25.00	1.01	40.00	8.90	165.00
SSt./10	KOTA	8.5	1126	722	305	50.00	1.24	76.00	28.05	0.02	70.12	4.50	180.00
Sh/11	SUHAWAL	7.7	934	599	323	33.10	3.08	86.20	23.30	1.40	41.10	19.90	166.10
Sh/12	PANWARKALA	7.6	1026	658	372	51.20	2.10	96.10	57.11	0.06	56.20	21.80	182.10
Sh/13	KHANDHU	8.1	1025	657	388	56.10	2.12	99.20	28.18	0.01	60.10	22.40	156.20
Sh/14	UPARWAR	8.0	554	355	367	47.15	3.20	94.30	24.20	1.00	66.20	20.20	168.30
Sh/15	KUSHA	7.6	472	303	349	35.10	4.15	90.20	34.20	1.80	49.20	20.20	140.40
Sh/16	NONARI	7.8	1221	783	618	19.90	2.00	79.40	102.40	0.90	39.60	407.90	270.00
Sh/17	HARDOLI	8.9	1126	722	305	50.00	11.24	76.00	28.05	2.70	70.12	405.00	188.00
Sh/18	PANWARKHURD	7.7	1248	800	218	20.90	1.10	60.50	29.40	1.40	36.66	490.90	268.01
Sh/19	PANTI	8.2	906	581	271	70.00	11.00	82.10	16.00	1.50	64.00	159.10	365.00
Sh/20	KANTI 61	8.1	663	425	465	20.00	1.20	63.00	75.00	1.60	85.00	250.00	109.00
Sh/21	PARARHA	7.7	1867	1197	802	76.00	3.00	30.00	177.00	0.90	212.00	612.00	178.00
Sh/22	LATIYAR	7.6	1171	751	314	51.40	2.12	76.20	30.05	0.09	72.30	405.00	190.20

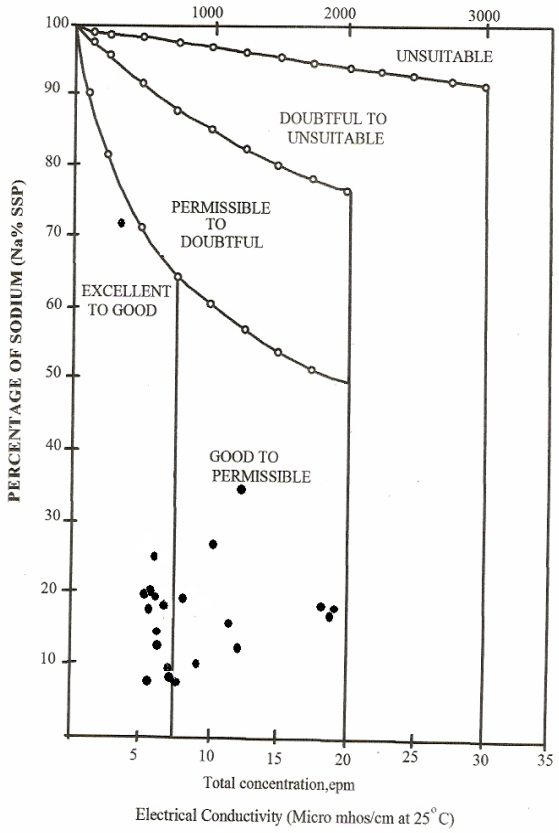

Figure 3. Plot of Sodium percent vs. Electrical conductivity (after Wilcox, 1955)

Table 2. Comparison of the quality parameters of groundwater of the study area with WHO and ISI for drinking purpose

S. No.	Water Quality Parameters	WHO (1984)		ISI (1991)		Concentration in Study Area	Undesirable Effect Produced Beyond Maximum Allowable Limit
		Highest Desirable	Max. Per missible	Highest Desirable	Max. Per missible		
1.	pH	7.0 to 8.5	6.5 to 9.2	6.5 to 8.5	No relaxation	7.4 to 8.9	Taste, effects mucus memberane and water supply system.
2.	TH mg/l	100	500	300	600	100 to 802	Encrustation in water supply and adverse effect on domestic use.
3.	TDS mg/l	500	1500	500	1000	321 to 1197	Gastrointestinal irritation.
4.	Ca mg/l	75	200	75	200	15 to 109	Encrustation in water supply, scale formation.
5.	Mg mg/l	30	150	30	100	11.5 to 177	Encrustation in water supply and adverse effect on domestic use.
6.	Na mg/l	-	200	-	200	5 to 104	--
7.	Cl mg/l	200	600	250	1000	20.2 to 212	Salty Taste
8.	SO_4 mg/l	200	400	150	400	4.5 to 612	Laxative effect
9.	F mg/l	0.6 to0.9	0.8 to1.7	1.00	1.5	0.01 to 2.70	Excessive fluoride causes skeletal and dental fluorosis in both children and adult

4.2 Irrigation Water Quality

In the present study the irrigation water quality has been evaluated on the basis of following criteria:

Sodium Percentage (Na%)

It is an important parameter to classify the groundwater samples for irrigation purpose. It is calculated by the formula proposed by Doneen (1962) as under:

$$\text{Na\%} = \frac{\text{Na}^{+} + K^{+}}{\text{Ca}^{++} + Mg^{++} + \text{Na}^{+} + K^{+}} \times 100$$

Sodium along with carbonate forms alkaline soil; while sodium with chloride forms saline soil; both of these are not suitable for the growth of plants (Pandian & Shankar, 2007). The quality classification of irrigation water based on the values of sodium percentage as proposed by Wilcox (1955) suggest that 55% samples are excellent to good category whereas 45% samples are good to permissible category.

4.2.1 Electrical Conductivity (EC)

It measures the capacity of substance or solution to conduct electric current. The EC of groundwater increases with the rise in temperature and varies with the amount of TDS. The conductivity in the groundwater samples of the area ranges from 472 to 1867 μs/cm at 25^0C indicating good category of irrigation water.

4.2.2 Sodium Adsorption Ratio (SAR)

The degree to which the irrigation water tends to enter into cation exchange reaction in soil can be indicated by the sodium adsorption ratio (U.S. Salinity, 1954). Since sodium replaces adsorbed calcium and magnesium in soil, hence it is expressed as:

$$\text{SAR} = \frac{\text{Na}^{+}}{\sqrt{\text{Ca}^{++} + Mg^{++}/2}}(epm)$$

Excess sodium in groundwater gets adsorbed on soil particles, thus change soil properties and also reduce soil permeability (Ayers & Bronson, 1975). U.S. Salinity Laboratory (1954) proposed to plot SAR against EC for rating irrigation water. The sixteen classes in the diagram indicate the extent that the waters can effect the soil in terms of salinity hazard. These classes are: low salinity (C_1), medium (C_2), high (C_3) and very high salinity (C_4) and similarly sodium hazard as low (S_1), medium (S_2), high (S_3) and very high (S_4). The groundwater samples of the study area fall in C_3S_1 (8 samples) and C_2S_1(14 samples) categories, hence suitable for irrigation purpose and indicate that most of the groundwater samples of the study area are medium to high saline and low sodium hazard zone. Hence high salinity water should be used only in those soils where adequate drainage is available to leach out the excessive water.

As per classification of Wilcox (1955), water with SAR ≤10 is considered as an excellent quality, between 10 to 18 is good; between 18 to 26 is fair and greater than 26 is said to be unsuitable for irrigation purpose in its natural form. As evident from Table 3, all groundwater samples possess ≤10 SAR; hence excellent for irrigation purpose.

4.2.3 Kelley's Ratio (KR)

It is the ratio of sodium ion to calcium and magnesium ion in epm (Kelley, 1951) and expressed as:

$$\text{K.R.} = \frac{Na^{+}}{\text{Ca}^{++} + Mg^{++}}(epm)$$

The Kelley's Ratio (KR) have been computed for all groundwater samples of the study area and presented in (Table 3). In the study area KR ranges from 0.06 to 2.28 indicating that water is suitable for irrigation purpose as the value is less than 2.5.

4.2.4 Permeability Index (PI)

The classification of irrigation waters has been attempted on the basis of permeability Index, as suggested by Doneen (1962). It is defined as:

$$\text{P.I.} = \frac{Na^{+} + \sqrt{\text{HCO}_3^{-}}}{\text{Ca}^{++} + Mg^{++} + Na^{+}} \times 100 \,(\text{epm})$$

The groundwater samples of the study area fall in class-I. As per Doneen chart (Domenico & Schwartz, 1990), the groundwater samples of the study area is of good quality for irrigation (Figure 5). The increased percentage of groundwater samples under class–I is due to dilution subsequent lower values of permeability index.

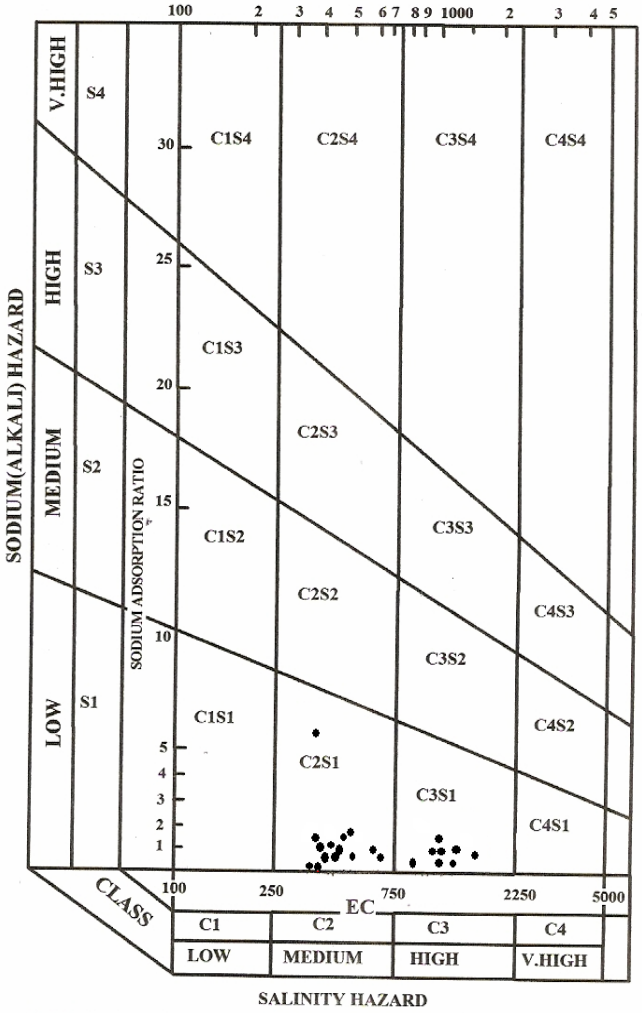

Figure 4. U.S. Salinity Diagram for classification of irrigation groundwater (after Richards, 1954)

Table 3. Ratio and indices of groundwater samples of the study Area

S.No.	No. of Location	SAR	KR	SSP	MR	CR	PI	RSC
1	2	3	4	5	6	7	8	9
1.	DABHAURA	0.90	0.17	17.70	22.33	0.06	42.00	-1.94
2.	GAHILWAR	0.57	0.09	8.82	66.24	0.07	22.59	-7.26
3.	HARHAI	0.93	0.18	18.01	23.39	1.06	42.04	-1.99
4.	MAJHIYARI	0.41	0.09	10.89	16.17	0.02	34.77	-2.92
5.	KOTWA	0.24	0.06	13.72	62.24	0.02	57.64	0.35
6.	KANCHANPUR	6.59	2.28	71.06	62.24	0.03	93.05	0.34
7.	DEOPUJA	1.24	0.23	19.55	34.12	0.05	24.91	-4.87

8.	AKAURIYA	0.67	0.15	14.56	39.86	0.02	90.93	-1.93
9.	JIRAUHA	1.11	0.22	18.86	32.65	0.03	39.44	-3.59
10.	KOTA	1.77	0.36	26.57	37.83	1.06	47.07	-3.15
11.	SUHAWAL	1.16	0.23	19.63	30.82	0.03	40.32	-3.50
12.	PANWARKALA	1.44	0.23	19.37	49.49	0.04	33.72	-6.51
13.	KHANDHU	1.82	0.34	25.55	31.89	0.05	41.60	-4.71
14.	UPARWAR	1.58	0.31	24.16	29.73	0.05	42.41	-3.94
15.	KUSHA	1.13	0.21	18.25	38.46	0.04	34.46	-5.01
16.	NONARI	0.49	0.07	6.89	68.01	0.04	22.45	-7.96
17.	HARDOLI	1.77	0.36	28.76	37.83	0.06	47.52	-3.02
18.	PANWARKHURD	0.78	0.17	14.70	44.48	0.03	47.32	-1.04
19.	PANTI	2.62	0.56	38.06	24.32	0.05	64.88	0.57
20.	KANTI 61	0.57	0.09	8.82	66.24	0.07	21.72	-7.51
21.	PARARHA	1.65	0.21	17.37	90.70	0.17	25.87	-13.17
22.	LATIYAR	1.79	0.36	26.74	39.40	1.06	47.07	-3.16

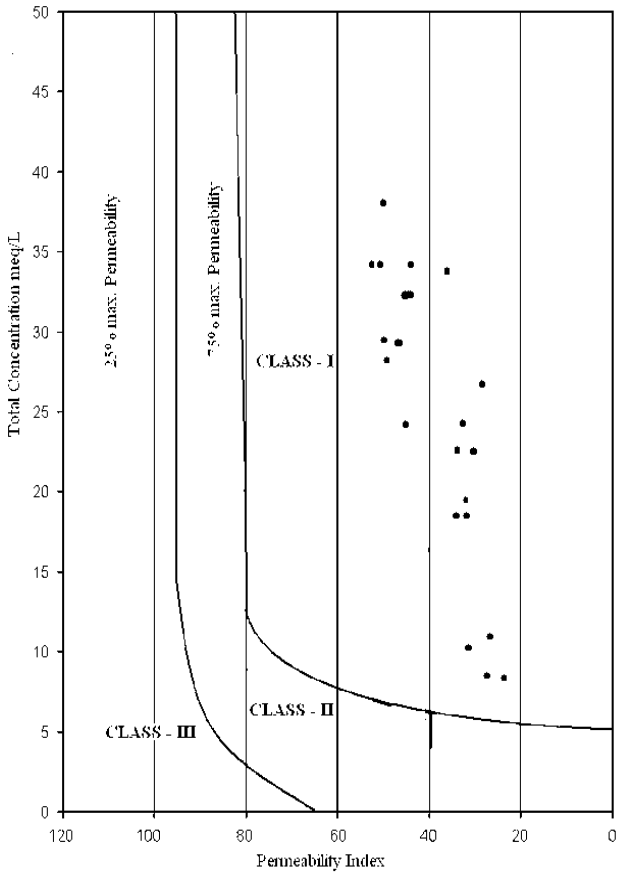

Figure 5. Classification of irrigation water (Doneen, 1962)

4.2.5 Magnesium Ratio (MR)

It is expressed as:

$$\text{M.R.}. = \frac{Mg^{+}}{\text{Ca}^{++} + Mg^{++}} \times 100(epm)$$

If the Magnesium Ratio is greater than 50%; it is considered as suitable for irrigation purpose (Palliwal, 1972). In the present study 70% samples are good for irrigation whereas 30% samples are unsuitable (Table 3).

4.2.6 Residual Sodium Carbonate (RSC)

It refers to the residual alkalinity and is calculated for irrigation water by the following formula:

$$RSC = (HCO_3^- + CO_3^{--}) - (Ca^{++} + Mg^{++}) \text{ (epm)}$$

The RSC values >1.25 mg/l are considered as safe for irrigation while those from 1.25 mg/l to 2.5 mg/l are marginally suitable for irrigation. If RSC values are > 2.5, the groundwater is unsuitable for irrigation (Eaton, 1950; Richards, 1954). The RSC values of groundwater samples of the study area ranges from -13.17 mg/l (Pararha) to +0.57 mg/l (Panti); hence suitable for irrigation purpose.

4.2.7 Corrosivity Ratio (CR)

It is defined as alkaline earth and alkalies and expressed as:

$$\text{C.R.} = \frac{Cl^- / 35.5 + 2\left(\frac{SO_4^{--}}{96}\right)}{2\left(\frac{HCO_3^- + CO_3^{--}}{100}\right)}$$

The groundwater with corrosivity ratio < 1 is considered to be safe for transport of water in any type of pipes, whereas >1 indicate corrosive nature and hence not to be transported through metal pipes (Ryner, 1944, Raman, 1985). The calculated values of groundwater samples of the study are presented in Table-1.3, which suggests that 19 samples are safe whereas 3 samples are corrosive in nature and need non-corrosive pipe for transporting and lifting of groundwater.

4.3 Pollution Susceptibility

For the estimation of pollution susceptibility, DRASTIC modelling proposed by Aller et al. (1987) has beed adopted. The DRASTIC approach takes into account seven hydrogeologic parameters which influence pollution of the area. The index of vulnerability is computed through multiplication of the value attributed to each parameter by its relative weight and adding up all seven products (Table 4).

$$\text{DRASTIC INDEX} = 5 \times D + 4 \times R + 3 \times A + 2 \times S + 1 \times T + 5 \times 1 + 3 \times C$$

Table 4. DRASTIC INDEX (pollution potential) of the study area

S.N.	Location Weightage	Depthto water table 5	Recharge 4	Aquifer Media 3	Soil Media 2	Topography 1	Impact of vadose zone 5	Hydraulic conductivity 3	Total Drastic Number
1.	DABHAURA	9x5=45	9x4=36	8x3=24	7x2=14	9x1=9	8x5=40	8x3=24	192
2.	GAHILWAR	8x5=40	6x4=24	6x3=18	6x2=12	10x1=10	3x5=15	6x3=18	137
3.	HARHAI	5x5=25	3x4=12	7x3=21	8x2=16	10x1=10	5x5=25	5x3=15	124
4.	MAJHIYARI	8x5=40	5x4=20	5x3=15	5x2=10	10x1=10	3x5=15	6x3=18	128
5.	KOTWA	6x5=30	3x4=12	6x3=18	8x2=16	10x1=10	6x5=30	6x3=18	134
6.	KANCHANPUR	8x5=40	7x4=28	8x3=24	7x2=14	10x1=10	6x5=30	8x3=24	170
7.	DEOPUJA	6x5=30	7x4=24	9x3=27	10x2=20	9x1=9	6x5=30	7x3=21	140
8.	AKAURIYA	10x5=50	6x4=24	9x3=27	6x2=12	10x1=10	4x5=20	8x3=24	167
9.	JIRAUHA	8x5=40	5x4=20	5x3=15	5x2=10	10x1=10	3x5=15	6x3=18	128
10.	KOTA	6x5=30	3x4=12	6x3=18	8x2=16	10x1=10	6x5=30	6x3=18	134
11.	SUHAWAL	10x5=50	6x4=24	9x3=27	6x2=12	10x1=10	4x5=20	8x3=24	167
12.	PANWARKALA	2x5=10	9x4=36	10x3=30	10x2=20	9x1=9	6x5=30	8x3=24	159
13.	KHANDHU	9x5=45	9x4=36	8x3=24	7x2=14	10x1=10	8x5=40	8x3=24	193
14.	UPARWAR	10x5=50	6x4=24	9x3=27	6x2=12	10x1=10	4x5=20	8x3=24	167
15.	KUSHA	8x5=40	7x4=28	8x3=24	6x2=12	10x1=10	6x5=30	8x3=24	168

16.	NONARI	3x5=15	6x4=24	4x3=27	7x2=14	10x1=10	6x5=30	8x3=24	144
17.	HARDOLI	10x5=50	6x4=24	9x3=27	6x2=12	10x1=10	4x5=20	8x3=24	167
18.	PANWARKHURD	9x5=45	9x4=36	10x3=30	8x2=16	10x1=10	6x5=30	10x3=30	197
19.	PANTI	8x5=40	7x4=28	8x3=24	6x2=12	10x1=10	6x5=30	8x3=24	168
20.	KANTI 61	5x5=25	3x4=12	7x3=21	8x2=16	9x1=9	5x5=25	5x3=15	123
21.	PARARHA	9x5=45	8x4=32	8x3=24	7x2=14	9x1=9	4x5=20	10x3=30	174
22.	LATIYAR	10x5=50	9x4=36	10x3=30	8x2=16	10x1=10	6x5=30	9x3=27	199

If D.I.>199; Very high, Between 160 and 199; High, Between 124 and 197; Intermediate, Lower than 124; Low pollution susceptibility.

The various parameters are discussed below:

In the area, the water table varies between 03 to 10 meters, hence the rating should be between 02 to 08 in sandstone and 08 to 10 in shale and the weight parameter is 05. It indicates the amount of water per unit area of land that penetrates the ground surface and reaches water table. The assigned weight for this parameter is 4. The net recharge in the area as determined by the water table fluctuation method is. The rating for this recharge is 3. The bedding planes, joint planes and fractures developed in sandstones and shale. Primary porosity and permeability are insignificant. The rating may be assigned a value of 2 to 5 in sandstone and 06 to 09 in shale. The ratings for aquifer media depend upon the type of consolidated and unconsolidated medium which serves as an aquifer.

In general, the less the clay shrinks and swells, and the smaller the grain-size, the less the pollution potential. The weight assigned to this grain-size, the less the pollution potential. The weight assigned to this parameter is 2. Thickness and types of soils in the area vary from place to place. There are areas where soil thickness is negligible while in others it goes up to 2 meters. The soil type varies from sandy loam to salty or clayey loam. Hence ratings may be taken as 10, 6, 5 and 4 for computing pollution index. The hilly tracts have slopes greater than 20 for which the rating is 01. However, in most places have slopes varying between 2 to 6 degrees for which the rating may be 10 in sandstone and shale and assigned weight for this parameter is 01.

The material present in this zone either facilitate pollution are helps in its attenuation. It also controls the time and distance taken by the pollutants to reach the zone of saturation. In the area, the vadose zone is mainly composed shales and sandstone. Jointing and fracturing are present in rocks. For this the rating may be 3 for shale and 6 for jointed sandstone and assigned weight is 5.It refers to the ability of the aquifer to transmit water under a given hydraulic gradient. The rate of flow within an aquifer controls the movement of contaminants from one place to another. From the computed values, it is observed that the DRASTIC Index varies between 124 to 192 in sandstone aquifer whereas 123 to 199 in shale aquifer. The values suggest the sandstone aquifer have intermediate pollution susceptibility whereas shale aquifer is highly susceptible to pollution.

5. Conclusion

The result of geochemical analyses of groundwater samples indicate overall alkaline nature of groundwater. The groundwater with pH above maximum desirable limit can affect the mucous membrane. The higher values of electrical conductance in shale aquifer may be due to enough time for reaction between groundwater and impervious shale whereas sandstone aquifer has comparatively lesser amount of EC are due to its hydrological characters. About 90% of samples have TDS less than 1000 mg/l; hence suitable for drinking. As per classification, most of the samples are normal chloride, normal carbonate, normal sulphate and moderate to very hard in nature. The samples plotted on Chadha's diagram indicate that 55% are Ca-Mg-HCO_3 type whereas 45% are Ca-Mg-Cl-SO_4 type. The concentration of sulphate associate with shale aquifer is high due to gypsum ($CaSO_4 \cdot 2H_2O$) and baryte ($BaSO_4$) nodules present in shale. The source of sodium and potassium ions may be the feldspar and clay minerals associate with aquifers. In few samples, concentration of fluoride is high due to presence of F^- bearing minerals (muscovite, biotite and clay). The deflouridation and ion exchange techniques may be adopted in high fluoride localities. The comparison of analysed data with WHO (1984) and ISI (1991) indicate that groundwater samples of the area are more or less suitable for drinking.

The groundwater samples have also been evaluated for their irrigation quality. The plot of sodium percentage vs electrical conductance of groundwater samples of the study area suggest that 55% samples are excellent to good category whereas 45% samples are in good to permissible category. The samples plotted in U.S. salinity diagram suggest medium to high saline and low alkaline nature. The water having high salinity should be used only in

those soils where adequate drainage is available. The calculated values of corrosivity ratio suggest that 84% samples are safe whereas 16% samples are corrosive in nature and need non-corrosive pipe for transporting and lifting of groundwater. The other parameters such as Kelley's Ratio, Residual sodium carbonate, Magnesium Ratio, Permeability Index suggest that groundwater of the study area are suitable for irrigation purpose.

The computed Drastic Index (Index of Vulnerability) varies between 124 to 192 in sandstone aquifer whereas 123to 199 in shale aquifer. The values suggest the sandstone aquifer have intermediate pollution susceptibility whereas shale aquifer is highly susceptible to pollution. In the high pollution susceptibility zone, the dug well need to have properly constructed which will present waste water from percolating into the well. The use of pesticides and insecticides in agriculture sector should be avoided. Besides these, proper attention and water quality monitoring programme is needed to check the groundwater pollution.

References

Ahmed, S. S., Mazumder, Q. H., Jahan, C. S., & Islam, A. (2002). Hydrogeochemistry and classification of groundwater, Rajshahi city, Bangladesh. *Jour. Geo. Soc. India, 60*(4), 411-418.

Aller, L., Lehar, J. H., Petty, & Benett, T. (1987). DRASTIC. A standardised system to Evaluate Groundwater Pollution Potential using Hydrogeological settings. *Jour. Geol. Soc. India, Special, 29*, 23-37.

APHA. (1998). *Standard methods for the examination of water and waste water* (14th ed.). Washington D.C.: American Public Health Association.

Ayers, R. S., & Bronson, R. L. (1975). Guidelines for Interpretation of Water quality for Agriculture, Univ. of California, Exension Mimeographed, 13p.

Chadha, D. K. (1999). A proposed new diagram for geochemical classification of natural waters and interpretation of chemical data. *Hydrogeology Journal, 7*, 431-439. http://dx.doi.org/10.1007/s100400050216

Chatterjee, A., Roy, R. K., Ghosh, U. C., Pramanik, T., Kabi, S. P., & Biswasm, K. (2008).Fluoride in water in parts of Raniganj Colfield, West Bengal. *Current Science, 94*, 309-311.

Domenico, D. A., & Schwartz, F. W. (1990). *Physical and chemical Hydrogeology*. NewYork: John wiley and sons. pp. 410-420.

Doneen, L. D. (1962). The influence of crop and soil on percolating water. *Proc. 1961 Biennial conference on Groundwater Recharge*, pp.156-163.

Duraiswamy, R. A., & Patankar, V. (2011). Occurrence of floride in the Drinking Water sources from Gad River, Basin, Maharashtra. *Geol. Soc. India, 77*, 167-174. http://dx.doi.org/10.1007/s12594-011-0020-9

Eaton, E. M. (1950). Significance of carbonate in irrigation water. *Soil Science, 69*, 123-133. http://dx.doi.org/10.1097/00010694-195002000-00004

Hem, J. D. (1985). Study and Interpretation of the Chemical characteristics of Natural Water. U.S. Geol. Surv. Water supply paper-2254, 264 p.

ISI. (1991). Indian standard specification for drinking water. IS: 10500, Indian Standard Institution, pp.1-5.

Jasrotia, A. S., & Singh, R. (2007). Hydrochemistry and groundwater quality around Devak and Rui watershed of Jammu Region, Jammu and Kashmir. *Jour. Geol. Soc. India, 69*, 1042-1054.

Karanth, K. R. (1987). Groundwater Assessment Development and Management. New Delhi: Tata McGraw Hill Publishing Company Ltd. 725p.

Kelley, W. P. (1951). *Alkali soils-their formation properties and reclamation*. New York: Reinold Publ. Corp.

Madhnure, P., Sirsikar, D. Y., Tiwari, A. N., Ranjan, B., & Malpe, D. B. (2007). Occurence of fluoride in the groundwaters Pandharkawada area, Yawatmal district, Maharastra, India. *Curr. Sci, 92*(5), 675-679.

Mishra, U. K. (2010). Hydrogeological Studies of Sirmour area, Rewa District, Madhya Pradesh.Unpubl. Ph.D. Thesis, A. P. S. Univ. Rewa, M.P., 173p.

Paliwal, K. V. (1972). Irrigation with Saline Water. LA.R.L Monograph, NO.02 (New Series), New Delhi, 198p.

Pandian, K., & Sankar, K. (2007). Hydrochemistry and groundwater quality in the Vaippar river basin, Tamil Nadu. *Jour. Geol.Soc. India, 69*, 970-982.

Piper, A. M. (1953). A graphic procedure in the Geochemical Interpretation of Water Analysis. U.S.G.S.

Ground Water. Note 12.

Pophare, A. M., & Dewalkar, M. S. (2007). Groundwater quality in Eastern and Southeastern parts of Rajura Tehsil, Chandrapur District, Maharastra. *Gond. Geol. Magz. Spec., 11*, 119-126.

Purushottam, D., Narsing Rao, A., Ravi Prakash, M., Ahmed, S., & Babu, A. G. (2011). Environmental impact on groundwater of Maheshwaram watershed, Ranga Reddy District, Andhra Pradesh. *Jour. Geol. Soc. India, 77*(6), 539-548. http://dx.doi.org/10.1007/s12594-011-0053-0

Raghunath, H. M. (1987). *Ground water*. New Delhi: Wiley Eastern Ltd. pp.59.

Raman, Y. (1985). Impact of corrosion in conveyance and distribution of water. *Jour. I. W. W. A., XV*(II), 115-12.

Ramteke, D. S., & Moghe, C. A. (1986). Manual on water and waste water analysis. NEERI, Nagpur, 340p.

Richard, L. A. (1954). Diagnosis and Improvement of Saline and alkaline soils, USDA. Handbook 160p. Sawyer, C. N., & McCarty, P. L. (1967). Chemistry for sanitary engineers (2nd ed.). New York: McGraw Hill. pp.518.

Ryner, J. W. (1944). A new index for determining amount of calcium carbonate scale formed by a water. *Jour. Amer. W. W. Assoc., 36*, A72-486.

Saxena, V. K., & Ahmed, S. (2001). Dissolution of fluoride in groundwater. A water-rock interaction study. *Environ. Ged., 40*, 1084-1087. http://dx.doi.org/10.1007/s002540100290

Schoeller, H. (1962). Les eaux Souterranies, Massow and cie Paris, 642p.

Suresh, M., Gurugnanam, B., Vasudevan, S., Dharanirajan, K., & Raj, J. N. (2010). Drinking and irrigational Feasibility of groundwater, GIS spatial mapping in upper Thirumanimuthar sub basin Cavery River,Tamil Nadu. *Jour. Geol.Soc. India, 75*(3), 518-526. http://dx.doi.org/10.1007/s12594-010-0045-5

Tiwari, R. N., & Dubey, D. P. (2007). Petrography, diagenesis and depositional environments of Govindgarh Sandstone of Rewa Group, Vindhyan Supergroup, Madhya Pradesh. *Gond. Geol. Magz., 22*(2), 11-16.

Tiwari, R. N., Bharti, S. L., & Mishra, Umesh. (2010). Hydrogeochemical Studies of Groundwater from Odda River Basin, Rewa District, Madhya Pradesh. *Gondwana Geological Magazine, Special*(12), 85-93.

Tiwari, R. N., Dubey, D. P., & Bharti, S. L. (2009). Hydrogeochemistry and groundwater quality in Beehar River Basin, Rewa district, Madhya Pradesh, India. *Inter. Jour. Earth Eng. Sci., 2*(4), 324-330.

U.S. Salinity Laboratory Staff. (1954). Diagnosis and Improvement of Saline and Alkali Soils. U.S. Deptt. Agriculture, Handbook, 160 p.

Walton, W. C. (1970). *Groundwater resources evaluation*. New York: Mc-Graw Hill Book Company. 664p.

WHO. (1984). *Guidelines to Drinking water quality*. World Organisation Geneva, 186p.

Wilcox, L. V. (1955). *Classification and use of irrigation waters*. U.S. Deptt. of Agriculture cire, 969, Washington, D.C., pp.19.

Earth Science Research; Vol. 1, No. 2; 2012
ISSN 1927-0542 E-ISSN 1927-0550
Published by Canadian Center of Science and Education

Geochemical Changes in the Caspian Salt Marshes Due to the Sea Level Fluctuations

Nicolay S. Kasimov[1], Alexandre N. Gennadiev[1], Maria S. Kasatenkova[1], Michail Y. Lychagin[1], Salomon B. Kroonenberg[2] & Peter Koltermann[3]

[1] Department of Landscape Geochemistry and Soil Geography, Faculty of Geography, Moscow State University, Moscow, Russia

[2] Delft University of Technology, Department of Geotechnology, Delft, Netherlands

[3] Natural Risk Assessment Lab, Faculty of Geography, Moscow State University, Moscow, Russia

Correspondence: Maria S. Kasatenkova, Department of Landscape Geochemistry and Soil Geography, Faculty of Geography, Moscow State University, Leninskiye Gory, 1, GSP-1, Moscow 119991, Russia. Tel: 7-495-939-4407. E-mail: kasatenkova2010@mail.ru

Received: June 12, 2012 Accepted: June 25, 2012 Online Published: July 23, 2012

doi:10.5539/esr.v1n2p262 URL: http://dx.doi.org/10.5539/esr.v1n2p262

Abstract

The Caspian Sea is subject to alternating transgressions and regressions that exert a strong impact on the topography, sediments, vegetation, and soils in coastal zones. The last transgression of the Caspian Sea (1978-1995) caused the development of a marsh-lagoon system along the accumulative seashore of the Central Dagestan. Salt marshes are complex and dynamic systems highly vulnerable to sea level fluctuations; therefore, they may be considered as a regional model of rapid environmental changes. Hazards in coastal zones may critically change the soil geochemistry affecting agricultural potential of large areas. Assessments of risks of the natural hazards in coastal zones are extremely difficult unless the end-to-end understanding of all natural factors. The research in the Caspian region shows the impact of extreme events in the coastal zones. Detailed landscape-geochemical investigations of the Caspian salt marshes were carried out in 1995-1996 (during the final stage of the transgression period) and in 2001-2003 (during the period of the sea level stabilization). These coastal areas are influenced by different landscape-geochemical processes, such as sulfidization, gleyzation, ferrugination, humus accumulation, halogenesis, and changes of alkali-acidic conditions. The development of the processes characterizes different stages of the Caspian Sea level fluctuations. This paper presents a discussion on stages and rates of landscape-geochemical processes, formation of geochemical barriers, and trace elements distribution in soils of the salt marshes.

Keywords: coastal zone, lagoon, trace elements, sea-level rise, risk assessment

1. Introduction

Global warming and the rise of the world's ocean level are among the most important present-day environmental problems. Many coastal areas experience inundation and water logging by sea water. At the same time, these dynamic regions are of immense ecological and economic importance. Therefore, studies of environmental consequences of sea level changes are of particular importance. Within the most of the world, the present sea level change proceeds rather slowly and it is almost imperceptible in human lifetime. The Caspian Sea offers a unique opportunity to study the impact of sea level change on the coastal zone during a short-term period, because the Caspian Sea level change is much more rapid than that of the world's ocean (Kroonenberg, Baduykova, Storms, Ignatov, & Kasimov, 2000). The Caspian Sea is well known for large and rapid sea level fluctuations (Figure 1).

The most recent cycle lasted only 65 years (Cazenave, Bonnefond, Dominh, & Schaeffer, 1997; Kaplin & Selivanov, 1995; Klige & Myagkov, 1992; Rychagov, 1993). The sea level fell by over 3 m between 1929 and 1977 and rose again by 2.4 m by 1995, when it started falling again. Today, it is stable at about –27 m, and there is no reliable forecast of its behavior even for the near future. The rate of the sea level rise averaged 150 mm/yr during the 1977-1995 transgression, and had its maximum of 340 mm in 1991. In this way, a one year of the Caspian Sea level rise equals to a century of the eustatic sea level rise in the oceans (Kroonenberg et al., 2000).

Many scientists believe that such short-term sea level fluctuations are related to climatic changes in the Caspian Sea basin (Rodionov, 1994; Kroonenberg, Rusakov, & Svitoch, 1997). Understanding consequences of the Caspian Sea level changes is very important as they threat large areas with inundation, water-logging, and other environmental changes (Kasimov, Gennadiev, Lychagin, Kroonenberg, & Kucheryaeva, 2000; TED Caspia, 1992).

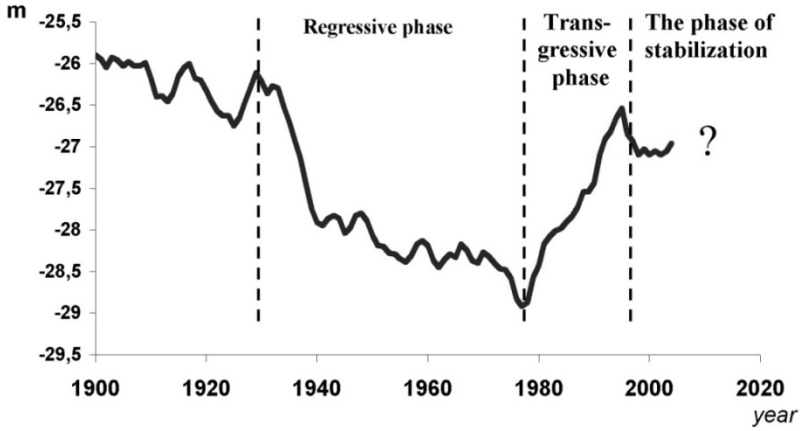

Figure 1. The Caspian Sea level fluctuations in the XX century

Different types of the Caspian littorals show various reactions to the sea level changes. The recent sea level rise generally did not cause qualitative changes at the abrasion shores and was manifested, first, in activation of abrasion processes and increase of their rate. Environmental effects of the sea level rise on the near-shore river mouth areas (Volga, Terek, Sulak, and other) were complicated by seasonal variations in river runoff, creation of artificial levees and channels, and use of river water for irrigation. The most dramatic consequences of the rapid marine transgression were found for accumulative shores. The width of the coastal zone affected by inundation and water-logging varied from hundreds meters to 10-20 km depending on the gradients of the submarine slope.

Along accumulative shores with intermediate (0.03°-0.3°) gradients of submarine slopes (Ignatov, Kaplin, Lukyanova, & Solovyova, 1993; Kaplin & Selivanov, 1995), a rapid sea level rise caused a formation of a barrier-lagoon system that moved landward with the sea transgression, with a corresponding rise of the groundwater table, and with simultaneous vigorous development of vegetation in newly-formed hydromorphic and semi-hydromorphic areas. On the contrary, the previous regression led mainly to the passive drainage of the shore zone. The formation of such barrier-lagoon systems is typical for the Caspian shore (Badyukova, Solovoyova, & Spolnikova, 1993; Kravtsova & Lukyanova, 1997) and for the world's oceanic shores (Recent global changes of the natural environment, 2006). The general domination of accumulative coasts on the global scale reflects the eustatic sea level rise in the postglacial period (Leontiev, Lukyanova, Nikiforov, Solovyova, & Holodilin, 1977).

Inundation and water-logging of accumulative shores due to the sea transgression caused formation of salt marshes in some coastal areas. Until recently, nobody considered such a type of landscapes in the Caspian region. Typical salt marshes are flat and poorly drained areas of land that are subject to periodic or occasional flooding by salt water and are usually covered by a thick mat of grassy halophytic (salt tolerant) plants (Bates & Jackson, 1980). They form important nutrient sources for estuarine and offshore fisheries and play an integral role in coastal defense (Allen & Pye, 1992).

Sea level and groundwater level are very unstable in the study area. This is caused by seasonal changes of the Caspian Sea level, wind and wave activity, seasonal rains, etc. That is why the marsh area adjacent to the lagoon is flooded often. Thus, its water regime is quite similar to that of the typical salt marshes that experience tidal effects.

Another important feature of salt-marshes is vegetation zonation. It was described by many authors (Bockelmann, Bakker, Neuhaus, & Lage, 2002; Myalo & Malkhazov, 2000; Rogel, Silla, & Ariza, 2001; Silvestri, Defina, & Marani, 2005) who evaluated environmental factors affecting the distribution of plants. Along the Caspian seashore, the vegetation cover develops under conditions of rapid environmental changes caused by the sea level fluctuations and, therefore, is highly dynamic. Grass vegetation is presented here by halophyte-hydrophytes' successive series that are common for low seashores (Myalo & Malkhazov, 2000). This fact also supports the

notion that these coastal landscapes can be considered as salt marshes.

Coastal soils are also affected by sea level changes. Soil morphology, organic matter content, salt composition, and other soil properties are influenced by salinity and the depth of the groundwater table. In our previous study, we have identified main stages of the regression–transgression cycle of the coastal soil development (Gennadiev, Kasimov, Golovanov, Lychagin, & Puzanova, 1998). During the last sea level cycle, the geochemical pattern within the coastal zone diversified, especially within the areas of the salt marshes (Kasimov et al., 2000). The regression phase was characterized by a relatively simple pattern, but the transgression phase resulted in a more complex soil-geochemical pattern differentiated into the zones of mobilization and accumulation of chemical elements.

Behavior of trace elements indicates the degree of development and the rate of geochemical processes in coastal soils where the sea level fluctuations caused changes in natural background values of chemical elements. Understanding such naturally occurring changes of the local geochemical background facilitates assessment of human-induced pollution in the coastal zone. Earlier (Kasimov et al., 2000), we have found that during the transgression phase, many heavy metals (Cu, Co, Zn, Ni, Cr, Fe, and Pb) accumulate at the geochemical barriers in the marsh zone.

There are many publications on geochemistry of salt marshes (Shaw, Gieskes, & Jahnke, 1990; Velde, Church, & Bauer, 2003; Zwolsman, Berger, & Van Eck, 1993). A special attention is paid to their pollution (Cundy et al., 2005; Williams, Bubb, & Lester, 1994) and to pollution sources (Cundy, Croudace, Thomson, & Lewis, 1997; Price, Winkle & Gehrels, 2005; Spencer, Cundy, & Croudace, 2003; Valette-Silver, 1993). A great number of studies have been conducted to investigate the impact of sea level rise on behavior of the coastal systems (Allen, 2000; Gornitz, Couch, & Hartig, 2002; Simas, Nunes, & Ferreira, 2001).

In our previous work (Gennadiev et al., 1998; Kasimov et al., 2000), we studied soil evolution and geochemical changes in the salt marshes along the western Caspian seashore for the regression and transgression phases. The subsequent stabilization of the sea level provided an excellent opportunity to continue the study and finally to report the effects and dynamics of soil-geochemical processes during the full cycle of the sea level changes including the stabilization phase.

2. Material and Methods

2.1 Study Area

Fieldwork was conducted on the semi-arid barrier coast of the Turali area in Dagestan Republic of Russia. The Turali site is located 30 km to the south of Makhachkala, the capital of Dagestan (Figure 2). This area has been intensively studied in 1995-1996 when the sea level was the highest (Gennadiev et al., 1998; Kasimov et al., 2000) and in 2001-2003 when it stabilized.

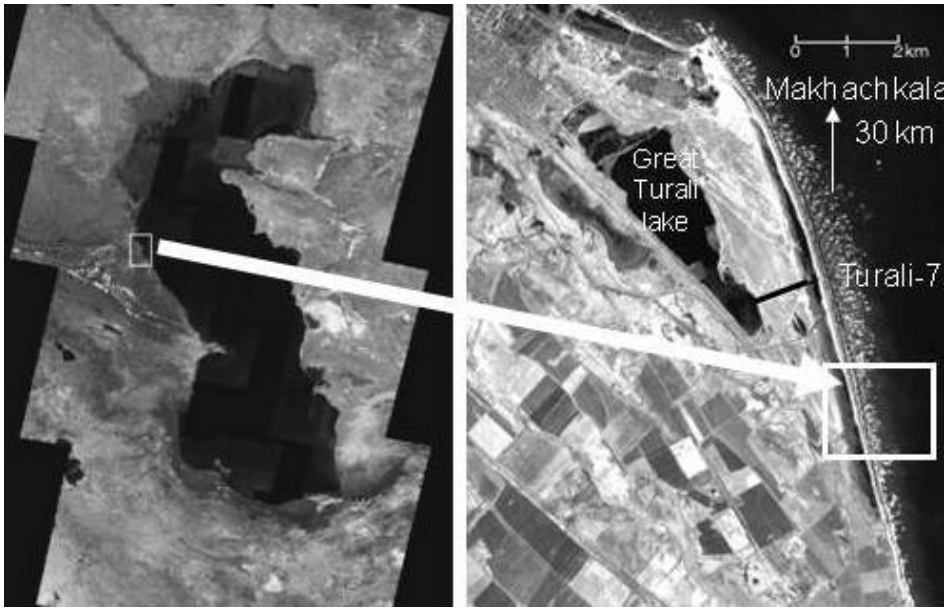

Figure 2. The study area (satellite image of the Dagestan coastal area)

The main part of the coastal plain is formed by a New-Caspian (Holocene) coastal terrace at about -22 m below ocean level (Kronstadt gauge). The terrace ends on its seaward side by a fossil cliff of about 3 m high, and is separated from the sea by a modern terrace which varies in width from 100 to 500 m. A series of low bars of 1929, 1941, and 1956 can be distinguished within its surface (Figure 3). They were formed during different phases of the Caspian Sea retreating in 1929-1978. In 1978-1995, a considerable part of the terrace was inundated. Presently, this part is occupied by a 0.8-1.0 m deep and a few hundreds of meters wide lagoon separated from the sea by a modern barrier beach with a height of 1.0-1.2 m and a width of 10-30 m (Figure 4).

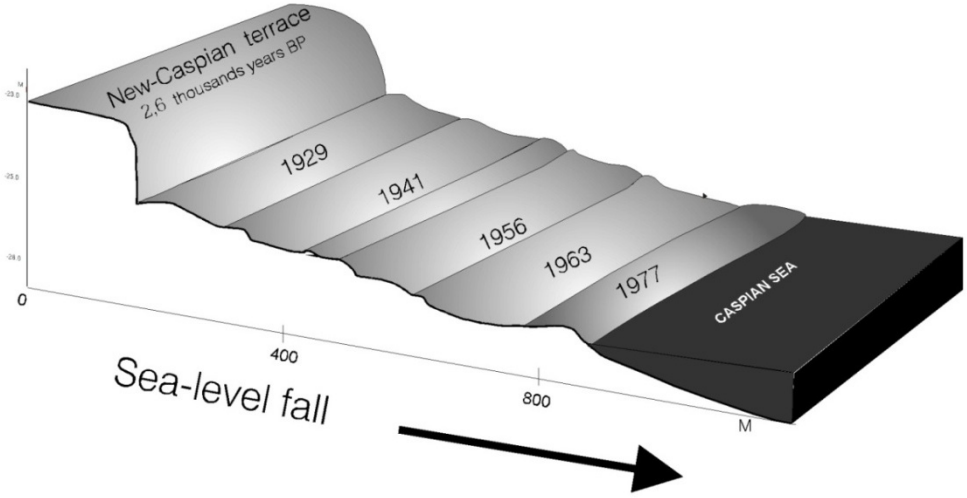

Figure 3. The formation of a series of the sea terraces during the regression cycle (1929-1978) (Badyukova et al., 1993; Kroonenberg et al., 2000)

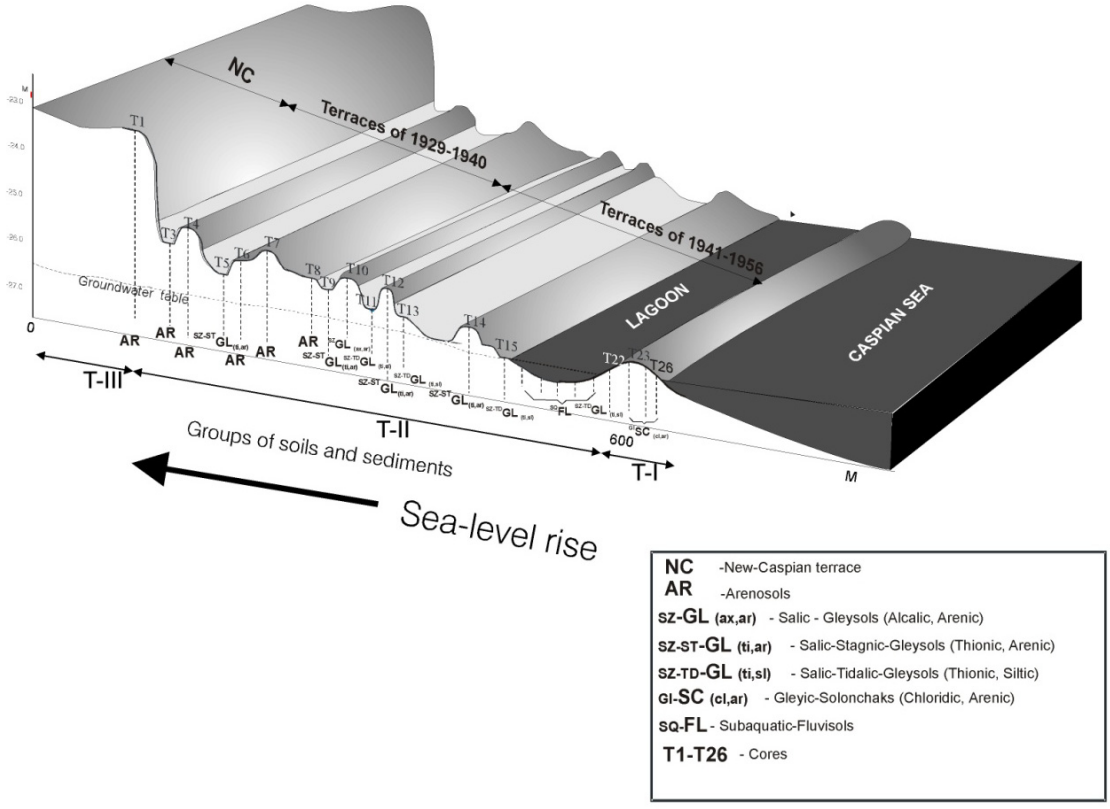

Figure 4. The distribution of soils and sediments in the profile T

2.2 Sampling Procedures

The fieldwork was carried out at a cross-section (150×400 m) stretched from the New-Caspian terrace towards the sea. The landscape-geochemical, geomorphologic, soil, and geobotanical investigations were conducted at four parallel transects (T, 2D, 2N, 2M) located across the coastal plain. The main transect is T. The study of soil pits along the main transect T was carried out both in 1995-1996 and 2001-2003. Transects 2D, 2N, and 2M were studied only in 1995-1996. During fieldwork, about 500 soil samples, 100 samples of bottom sediments, and 100 samples of natural water were collected.

A number of physical and chemical parameters of water and soils were defined immediately at the sampling points: pH, Eh, total dissolved salts (TDS), and the sodium content. The measurements were done with the portable devices (HANNA Instruments, Italy). For the lagoon sediments and soil horizons located below the groundwater table, the measurements were done directly under their natural moisture. For determination of physical-chemical parameters in dry soil horizons, distilled water was added to each soil sample at 1:1 ratio; the mixture was stirred by a plastic stick and measurements were made in the suspension obtained.

The cation content in the water samples, as well as the content of bulk and mobile forms of chemical elements in the soils, were analyzed by the atomic-absorption method using the spectrophotometer Hitachi 180 (Japan). The content of Na, K, Ca, and Mg was determined without background correction, since the content of Fe, Mn, Ni, Cr, Co, Zn, Pb, Cd, and Mo was defined with correction based on the Zeeman effect. In order to define the bulk values of heavy metals in soils and sediments, the samples were digested with a mixture of concentrated acids (HNO3 and HF). For analysis of mobile forms of elements, 1N (2N) HCl was used as the extraction agent. This extraction shows a general amount of water-soluble, exchangeable, and amorphous forms of elements (Solovyov, 1989).

3. Results

Morphometric studies of the topography of the coastal zone showed that, during the period from 1978 to 1995, the area of the modern terrace decreased by more than 200 m. The rise in the sea level by a centimeter led to the expansion of the lagoon by 4 m and the retreat of the coastline by 2-3 m (Badyukova et al., 1993). This reduction was the result of the movement of the bar-lagoon system. Finally the lowest part of the terrace formed in 1957-1977 was inundated by the sea. The adjacent part of the terrace was occupied by the coastal bar and the lagoon. Higher levels of the present terrace formed in 1929-1941 were subject to water-logging.

The coastal soils have close evolutionary links. They have undergone differently directed evolutionary stages. In their dependence on particular site conditions, the soils and sediments of the coastal zone can be subdivided into three evolutionary groups with respect to their response to the advances and retreats of the sea (Gennadiev et al., 1998).

The first group includes recent beach deposits (T-I). They occupy the most seaward position. The strand plain along the shoreline has a width 20-30 m. It is not covered by vegetation and consists of fine-grained sandy deposits of a yellow-gray color, with carbonates, and with darker interlayer of sand and shell detritus. It is a very dynamic zone and the processes of soil formation are periodically interrupted. The beach deposits represent the youngest evolutionary group of the site.

The oldest evolutionary group includes the soils of the New-Caspian terrace (T-III) that are not affected by modern water table fluctuations. The Arenosols of the New-Caspian terrace virtually have not changed since the 1930s. However, before that they had undergone all the previous stages of the soil cover development of the regression and transgression phases. The presence of buried ferruginous horizons is considered a specific soil feature that attests to the previous hydromorphic stage of soil development within the New-Caspian terrace (Gennadiev et al., 1998). The morphology of these soils is very close to the other soils of the site. The soils of the New-Caspian terrace are considered as the most developed stage of soil evolution in comparative analysis aimed at understanding the results of superimposed geochemical processes and at evaluating their duration.

The New-Caspian terrace is generally characterized by a deep groundwater table (> 3 m), low TDS values (20-40 mg/l), oxic environment (Eh>150 mV), and relatively high alkalinity (pH 8.3 to 8.5) in soils. Humus accumulation takes place here under the sparse grass-herbal semi-desert vegetation, so humus content is relatively low - 0.3-0.5 %. The Arenosols of the terrace show predominantly low content of chemical elements (Table 1).

Table 1. Concentration of elements in slightly affected soils and sediments of the site, mg/kg (n=5)

Concentration	Fe	Mn	Ni	Co	Cr	Cu	Zn	Pb	Cd	Sr	Mo
Bulk	10000	155	5.3	2.6	2.2	2.9	18.8	5.7	0.07	405	6.7
Mobile	1382	87.7	0.3	0.5	0.65	1.1	4.6	2.6	<0.01	225	---

The bulk Fe value varies from 0.9 to 1.2 % being about 1% on average, which is the same as in the sandstone (0.98 %) (Turekian & Wederpohl, 1961) and about 5 times less than the average content (clark) (Vinogradov, 1962) of this element in the Earth's crust (4.65 %). The concentration of mobile Fe in these sediments is the lowest (500-600 mg/kg), but they include ferruginous layers that are the former oxidized sulfide horizons with mobile iron content of 2000-3500 mg/kg. The bulk content of Fe in sediments of the present-day beach is very low – about 0.19 % with mobile Fe accounting for 0.17 %.

The average content of Mn, Zn, Pb, Cd, and Co is 3 to 5 times lower than that in the Earth's crust (clark) (Vinogradov, 1962), while Cu, Cr, and Ni contents are 15 to 25 times lower. In comparison with sandstone averages (Turekian & Wedepohl, 1961), the content of Ni is 2.5 times, Co – 8.6 times, and Mo – 33.5 times higher; the content of Zn and Pb is the same, and content of Cr is 17 times lower. Low geochemical background of the chemical elements is due to the light texture of marine sediments composed of pure sand and shell detritus. Only Mo shows increased background value, which corresponds to the boron-molybdenum geochemical specialization of the Caspian region. The average value of Sr is close to the clark, because this element is highly migratory and accumulates in soils under chloride-sulfate halogenesis.

The middle evolutionary group (T-II) includes different soils of the marsh-lagoon zone that were transformed variably by superimposed processes during the last transgression and the subsequent stabilization of the sea.

3.1 The Transgression Phase

The rise of the Caspian Sea level, started in 1978, has led to flooding and waterlogging of the coastal zone, which determined significant changes of the geochemical conditions and chemical composition of the modern soils and sediments.

The *Arenosols(1)* formed at the surface of 1929-1940 of the present terrace (cores T3, T4, T7) (Figure 4) are characterized by predominantly oxic alkaline environment in topsoil, and reduced alkaline conditions in the lower horizons (Table 2).

Table 2. Changes of geochemical properties in soils and sediments of salt marshes upon the fluctuation of the Caspian Sea level

Soils	Phase	Eh, mV	pH	TdS,mg/l
1	*transgression(23)Note 1*	+150…+200	8.2-8.6	20-100
	stabilization (30)Note 2	+150…+200	8.1-8.6	20-100
2	*transgression (32)*	-159..+150	8.4-9.2	100-1000
	stabilization (59)	-80…+120	8.3-8.7	200-5800
3	*transgression (22)*	-150…+100	8.1-8.5	500-2500
	stabilization (30)	-130…+150	6.1-7.4	1200-7100
4	*transgression (14)*	-50…-380	7.5-8.3	2000-6000
	stabilization (19)	-150…-300	6.1-7.3	3000-6000

Soils: 1- Arenosols, 2- Salic-Gleysols (Alcalic, Arenic) and Salic-Stagnic-Gleysols (Thionic, Arenic), 3- Salic-Tidalic-Gleysols (Thionic, Siltic), 4- Subaquatic Fluvisols.

They are confined to the most elevated positions within hydromorphic landscapes. The average content of trace elements in these soils is the same as in the New-Caspian sediments (Table 3). Thus, the chemical composition of these soils has not changed during the transgression.

Table 3. The concentrations of chemical elements in soils and sediments of salt marshes (Turali site), mg/kg

Soils	Phase	Forms	Fe	Mn	Ni	Co	Cu	Zn	Pb	Cr
1	*transgression (23)*	bulk	9500	152	4	1,7	2,5	15	5,8	2,5
		mobile	1500	101	0.4	0.4	0.8	4.1	2.4	0.05
	stabilization (30)	bulk	8700	144	3.7	1.5	2.4	13.5	6.3	2.3
		mobile	1850	121	0.6	0.5	0.7	2.9	1.8	0.05
2	*transgression (32)*	bulk	9300	163	3.8	2.0	2.0	14.8	4.1	2.8
		mobile	1200	109	0.5	0.6	1.0	5.6	2.6	0.14
	stabilization (59)	bulk	8900	189	4.3	1.7	2.2	15.2	4.5	2.5
		mobile	1500	118	0.9	0.8	0.7	4.1	2.4	0.09
3	*transgression (22)*	bulk	6500	227	3.9	2.2	1.9	15.6	4	3.7
		mobile	4200	131	0.7	0.9	1.2	7.3	3.2	0.15
	stabilization (30)	bulk	7600	248	6.2	2.4	2.5	17.1	5.7	4.4
		mobile	3100	161	1.4	1.5	1.8	9.2	2.7	0.12
4	*transgression (14)*	bulk	5950	136	3.2	2.2	3.0	13	3.5	8.8
		mobile	5400	102	2.6	1.2	2.9	12.1	3.2	0.9
	stabilization (19)	bulk	5200	176	6.5	2.6	3.3	14.2	4.5	6.6
		mobile	4400	110	1.6	1.6	2.7	13.0	3.0	0.11

The *Salic Gleysols (Alcalic, Arenic) and* the *Salic-Stagnic Gleysols (Thionic,Arenic)(2)* developed in more hydromorphic positions with rather close groundwater table (40-70 cm). They show higher salinity (TDS values up to 1000 mg/l), alternating redox regime, and higher alkalinity. The bulk content of the trace elements is up to 3 times higher than in the New-Caspian sediments. The Fe and trace elements accumulate in topsoil while the concentrations in the lower horizons fall down. The maximum content of the trace elements in topsoil is usually 2-3 times higher than in subsoil.

The *Salic-Tidalic Gleysols (Thionic, Siltic) (3)* are widespread in the marsh zone (T11, T12, T13, T15) which occupies a large part of the 1941-1956 surface within the present terrace. They are characterized by a rather high salt content, predominantly reducing environment, and lower pH values. The marsh soils form within micro-depressions adjacent to the lagoon. The depth of groundwater varies from 0 to 40 cm. The main feature of these soils is the horizon enriched with hydrotroilite (G_{FeS}). The bulk Fe content in the marsh zone falls to 6500 mg/kg, but the content of its migratory forms generally increases to 3200-5200 mg/kg. The maximum values of Fe in the marsh topsoil do not exceed 8075 mg/kg. The bulk amount of trace elements in these soils is similar to the other soils of the present terrace, but the content of the mobile forms increases; compared with the New-Caspian sediments, the coefficient of accumulation (Note 3) is as follows: $Ni_{2.3}\,Co_{2.0}\,Zn_{1.6}\,Mn_{1.5}\,Pb_{1.2}$.

The *Subaquatic Fluvisols (4)* show the highest salt content, mostly reducing environment and slightly alkali reaction. The mean bulk amount of Fe in such soils is rather low, however, the content of mobile Fe reaches its maximum. The bulk values of Mn, Ni, Zn, and Pb are lower in the lagoon sediments than in the soils, but higher for Cu, Cr, and Cd. The concentrations of the mobile forms of the trace elements increase dramatically in the lagoon sediments. The sulfide horizons are enriched with $Ni_{9.3}\,Zn_{3.5}\,Mn_{3.2}\,Co_{1.8}\,Cu_{1.7}\,Pb_{1.5}$.

3.2 The Phase of the Sea Level Stabilization

After the stabilization of the sea level, the movement of the bar-lagoon system has stopped and the lagoon has shoaled. The depth of the groundwater table has decreased in the marsh zone. That led to the transformation of the geochemical parameters and the trace elements content in the soils of the salt marshes.

The geochemical properties of the *Arenosols (1)* have practically not changed (Table 4).

Table 4. The coefficient of changes (Note 4) of chemical elements' contents in soils and sediments of salt marshes (Note 5)

Soils	Coefficient of changes	Fe	Mn	Ni	Co	Cu	Zn	Pb	Cr
1	bulk	0.9	0.95	0.93	0.88	0.96	0.9	1.1	0.92
	mobile	1.23	1.2	**1.5**	1.25	0.88	**0.7**	0.75	1.0
2	bulk	0.96	1.16	1.13	0.85	1.1	1.03	1.1	0.89
	mobile	1.25	1.08	**1.8**	**1.33**	**0.7**	0.73	0.92	**0.64**
3	bulk	1.17	1.1	**1.6**	1.09	**1.32**	1.1	1.4	1.19
	mobile	0.74	1.23	**2.0**	**1.67**	**1.5**	1.26	0.84	0.8
4	bulk	0.87	1.29	**2.03**	1.18	1.1	1.09	1.29	0.75
	mobile	0.81	1.08	**0.62**	**1.33**	0.93	1.07	0.94	**0.12**

The line of changes for the bulk values of elements during the stabilization phase is: Pb 1.1>Cu 0.96 >Mn 0.95 >Ni 0.93 >Cr 0.92 >Fe, Zn 0.9 >Co 0.88. The line of changes for the mobile forms looks different: Ni 1.5 >Co 1.25 >Fe 1.23 >Mn 1.2 >Cr 1.0 >Cu 0.88 >Pb 0.75 >Zn 0.7. The concentrations of bulk Pb and the mobile forms of Ni, Co, Fe, and Mn have increased slightly at the stabilization phase. Nevertheless, these distinctions are not essential because the measurement accuracy for the bulk and mobile values is 10 % and 5%, respectively.

During the period of the sea level stabilization, the salinity of the *Salic Gleysols (Alcalic, Arenic)* and the *Salic-Stagnic Gleysols (Thionic,Arenic) (2)* increased: in a depression within the 1930s surface (T5,T6), the TDS value rose up to 5800 mg/l; in other cases it varied from 200 to 850 mg/l. These soils are still characterized by alternating oxidizing-reducing regime and pH of about 8.5. At the stabilization phase, the bulk value of Fe slightly decreased, since the content of the mobile forms increased. The concentrations of the trace elements changed as well. For the bulk values of the chemical elements, the line of changes is: Mn 1.16 >Ni 1.13 >Cu, Pb 1.1>Zn 1.03 >Fe 0.96 >Cr 0.89 >Co 0.85; for the mobile forms: Ni 1.8 >Co 1.33 >Fe 1.25 >Mn 1.08 >Pb 0.92 >Zn 0.73 >Cu 0.7 >Cr 0.64.

The geochemical properties of the *Salic-Tidalic Gleysols (Thionic, Siltic) (3)* have changed more than in the other kinds of soils. The salinity of the upper horizons has increased. The high salt content was also found in the lower horizons – 1.2-3.5 g/l. This kind of soils is characterized by the predominantly reducing environments. The pH values decreased during the stabilization phase. The bulk Fe content increased, but the content of mobile Fe decreased. The maximum of Fe in the upper horizons reached 15000 mg/kg. The concentrations of trace elements increased also, especially in the upper horizons of the salt marsh soils. The coefficients of changes for the bulk contents of elements in *Salic-Tidalic Gleysols* are: Ni 1.6 >Pb 1.40 >Cu 1.32 >Cr 1.19 >Fe 1.17 >Mn,Zn 1.1 >Co 1.09. So, the concentrations of the bulk forms of the elements increase at the stabilization phase. The line for the mobile forms is: Ni 2 >Co 1.67 >Cu 1.5 >Zn 1.26 >Mn 1.23 >Pb 0.84 >Cr 0.8 >Fe 0.74.

The salinity of the reduced *Subaquatic Fluvisols (4)* has not changed; pH has decreased. The bulk content of Ni, Mn, Pb, Co, Cu, and Zn has increased compared to the transgression phase: Ni 2.03 >Mn 1.29 >Pb 1.29 >Co 1.18 >Cu 1.1 >Zn 1.09 >Fe 0.87 >Cr 0.75. The concentrations of the mobile forms of Pb, Cu, Fe, Ni, and Cr have become lower: Co 1.33 >Mn 1.08 >Zn 1.07 >Pb 0.94 >Cu 0.93 >Fe 0.81 >Ni 0.62 >Cr 0,12.

Thus, only the content of Mn has increased in all soils. The bulk values of Pb, Ni, Zn have increased during the stabilization phase in the *Salic Gleysols* (Alcalic, Arenic) and the *Salic-Stagnic Gleysols* (*Thionic,Arenic*) (2), the *Salic-Tidalic Gleysols* (*Thionic, Siltic*) (3), and the *Subaquatic Fluvisols* (4). The concentrations of Fe and Cr have decreased in all soils, except for the *Salic-Tidalic Gleysols* (*Thionic, Siltic*) (3).

The concentrations of the mobile forms have become higher for Co and lower for Cr and Pb, in all soils during the stabilization phase. The concentrations of Ni and Fe have increased in the *Arenosols* (1), the *Salic Gleysols* (*Alcalic, Arenic*) and the *Salic-Stagnic Gleysols* (*Thionic,Arenic*) (2) and decreased in the *Subaquatic Fluvisols* (4). The concentrations of Zn and Cu change in the opposite order – decreased in the *Arenosol*s (1), the *Salic Gleysols* (*Alcalic*, *Arenic*) and the *Salic-Stagnic Gleysols* (*Thionic,Arenic*) (2) and increased in the *Subaquatic Fluvisols* (4).

4. Discussion

The geochemical conditions in the salt marshes depend on the trend of the sea level fluctuations. The regression stages are associated with weak variability of the geochemical environment in the coastal soils and sediments. They are mainly characterized by alkaline oxidizing conditions. Geochemical diversity of the coastal zone landscapes is much higher during the transgression phase. The conditions vary from neutral to highly alkaline and from oxidizing to highly reducing. After the sea level stabilized, geochemical diversity changed – the salinity of the *Salic Gleysols* (*Alcalic, Arenic*) and the *Salic-Stagnic Gleysols* (*Thionic, Arenic*) and the *Salic-Tidalic Gleysols* (*Thionic, Siltic*) in marsh zone increased; the conditions in the *Salic-Tidalic Gleysols* became subacidic. Such changes of the geochemical parameters caused redistribution of the chemical elements.

The metal concentrations in the salt marsh sediments depend on a number of factors. These factors include parent material composition, particle size, organic loading, and sediment type, which are intrinsically linked to marsh morphology, estuarine circulation, frequency of flooding, type and extent of vegetation cover, suspended solid loads of incoming waters, and physical and chemical conditions in estuarine waters and marsh itself (Williams et al., 1994). Textural and geochemical characteristics influence the ability of marsh sediments to accumulate heavy metals. Early diagenesis has an important control on chemical element distribution in coastal zone (Zwolsman et al., 1993).

In our study, we use the concept of landscape-geochemical processes (Glazovskaya, 1988) and geochemical barriers (Perelman, 1975) for the explanation of the trace elements distribution in the soils and sediments of the Caspian salt marshes. Landscape-geochemical processes are the set of biogeochemical and physical-chemical processes that cause transport and accumulation of chemical elements. The development of different landscape-geochemical processes in soils leads to the formation of geochemical barriers. The geochemical barriers are places in soils or in the earth crust where a sharp decline in the rate of migration of chemical elements occurs over a short distance, so that they become concentrated (Perelman, 1975).

The development of biogenic and hydromorphic landscape-geochemical processes characterizes different phases of the Caspian sea level fluctuations. The main landscape-geochemical process of regression phase is the accumulation and leaching of soluble salts (halogenesis).

The Caspian Sea level rise caused the development of hydromorphic landscape-geochemical processes in the soils influenced by the sea water. The geochemical transformation of the coastal soils is related to a complex combination of landscape-geochemical processes, such as sulfidogenesis, gleyzation, iron accumulation (ferrugination), accumulation of humus and peat, halogenesis, and changes in redox conditions (Kasimov et al., 2000). These processes are accompanied by concentration of many trace elements, which is especially distinct against the low background content of these elements (except for Mo and Sr) in the sandy beach sediments.

4.1 Redox Changes

The transgression of the Caspian Sea caused flooding and waterlogging of the coastal zone which determined the development of anaerobic environment in the soils and sediments due to restricted atmospheric oxygen diffusion. Organic matter in the hydromorphic soils underwent biogenic decomposition in conditions of brackish groundwater, so sulfate reduction became the dominant reducing process. Black and dark-grey sulfide horizons were often found in the marsh soils of the coastal zone.

The process of sulfidization has characteristic features in different parts of the coastal marsh area. During the transgression stage, the process was the mostly pronounced in the bottom sediments of the newly-formed lagoon. The *Salic-Tidalic Gleysols* (*Thionic, Siltic*) in the area adjacent to lagoon underwent regular drying because of small-scale sea level oscillations during the transgression. The exposure of reduced sediment layers to oxygen decomposed metal sulfides to oxidized sulfate forms releasing associated counter ions and sulfuric acid to interstitial waters. This resulted in the pH values decrease from 7.0-7.6 to 6.1-7.3 and the Eh values increase from –120–0 to –90+30 mV during the 1995–2003 period.

Sulfidization is among the leading factors governing the distribution of a number of trace elements. Compared to the beach deposits, the sulfide horizons accumulate associations of elements, primarily Fe, which dictates the behavior of minor elements. On the hydrogen sulfide geochemical barrier, the accumulation of Co_{10-12}, Zn_4, $Cu_{2-2.5}$, $Ni_{2-2,5}$, $Cr_{2-2.5}$, $Pb_{1.5-2}$ takes place in the marsh soils (Figure 5) and the bottom sediments of the lagoon compared to the soils of the beach ridges.

The trace metal maxima are observed in the sulfide horizons (below 5 cm), which is caused by precipitation of metal sulfides (Williams et al., 1994). A number of trace metals including Cu, Pb, Zn, Ni, and Co commonly co-precipitate with sulfides below the redoxcline and, therefore, show enrichment at some depth. During the

Caspian Sea level stabilization period, the concentrations of these trace elements are also high in the sulfide horizons. However, in the *Salic-Tidalic Gleysols* (*Thionic, Siltic*), the capacity of the sulfide horizons decreased at the depth below 10-15 cm.

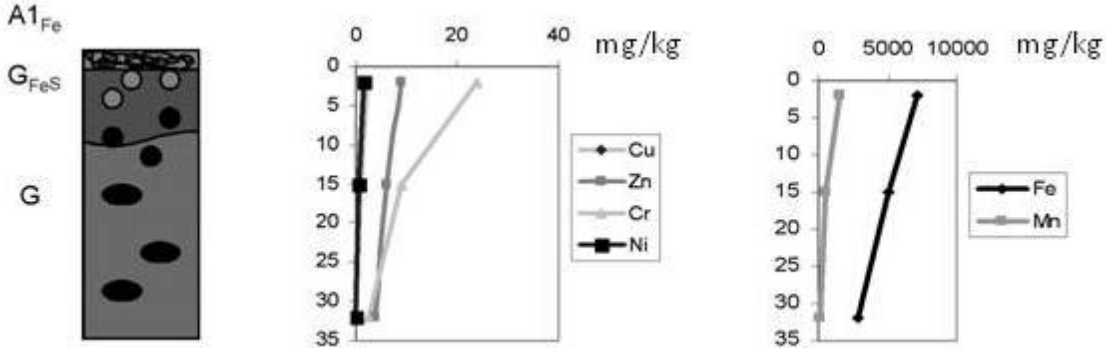

Figure 5. The distribution of the mobile forms of chemical elements in the Salic-Tidalic Gleysols (Thionic, Siltic) (sulfide geochemical barrier)

$A1_{Fe}$- humus ferruginous horizon; G_{FeS} – sulfide horizon (sulfide geochemical barrier); G – reduced gley horizon

Gleyzation includes the reducing processes in the absence of hydrogen sulfide which form sediments and soils of bluish-grey, green, blue, and ochric-bluish colors. Gleyzation is usually accompanied by the intensive migration of Fe due to its transfer from a less mobile form of Fe^{3+} to a more mobile Fe^{2+}. In such environment, Eh decreases from +200 to –100 mV. In marsh soils, the gleyic horizons lay under the sulfide horizons at 10-15 cm below the surface. In the upper 0-10 cm, there is enough organic matter for the sulfides formation. The pH values of the gleyic horizons were higher (7.8-8.6) during the transgression phase than after the sea level stabilization (7.3-7.5) because of acidification of the *Salic-Tidalic Gleysols* (*Thionic, Siltic*). In the *Salic-Stagnic Gleysols* (*Thionic,Arenic*), the gleyic horizons lie over the sulfide horizons and they are less subject to the influence of sulfate waters. In the transgression period, they appeared 20-30 cm below the surface. The sea level stabilization stopped the fluctuations of the groundwater table and, today, the gleyic horizons lie 40-50 cm below the surface. The process of gleyzation has a much smaller effect on the behavior of the trace elements than the associated processes of sulfidization and ferrugination. Therefore, it is rather difficult to describe the specific features of the trace elements behavior due to gleyzation.

4.2 Ferrugination

The lowest bulk Fe content was found in the sediments of the present beach. About 90% of the total Fe was presented by the mobile forms (Figure 6).

This is the result of a light texture and a high degree of washing of the sediments, while its high migration is due to the gleyzation process. As the distance from the beach grows, the total Fe content shows a sharp increase; the highest values are typical for the soils of the New-Caspian terrace. The concentration of the mobile Fe reaches its maximum in the lagoon bottom sediments because, in the anaerobic conditions, Fe exists in mobile form. With a growing distance from the lagoon, the share of the mobile forms of Fe decreases; within the New-Caspian terrace, they account for about 10% of the total.

During the transgression period, the content of Fe in the *Salic-Tidalic Gleysols* (*Thionic, Siltic*) near the lagoon showed minor profile differences because of the high groundwater table and reducing conditions. With increasing distance from the lagoon and lowering of the groundwater table, Fe was re-distributed: it accumulated in the upper horizons while the concentrations in the lower horizons fell down. The process was accompanied by a sharp decrease of the mobile Fe in the upper horizons due to its transfer from the mobile to the crystallized forms. Crystallization of Fe under arid conditions and lesser influence of groundwater go on rather rapidly; the process is of a reversible nature (Zonn, 1982).

The diagenetic enhancement of Fe and Mn in the surface sediments of lakes (Farmer & Lovell, 1984), estuaries (Valette-Silver, 1993; Zwolsman et al., 1993) and marine basins (Shaw et al., 1990) is well studied. With burial, microbial decomposition of organic material takes place resulting in the bacterial utilization of O_2 and other electron acceptors such as NO_3^-, MnO_2, $Fe(OH)_3$ and SO_4^{2-} (Buckley, Smith, & Winters, 1995). The reduction

of Fe^{3+} and Mn^{4+} forms results in mobilization of these metals and diffusion to oxic surface sediments where they are re-precipitated either as oxides or, occasionally, as carbonates (Farmer & Lovell, 1984).

After the sea level stabilization, the Fe content in the soils of the marsh zone has changed. The total amount of Fe is relatively higher in the upper horizons compared to the lower ones. The content of the mobile forms has decreased. This is the result of a lesser influence of groundwater and the drainage of the marsh zone. Thus, in the *Salic-Tidalic Gleysols* (*Thionic, Siltic*) under the alternating oxidizing-reducing conditions, Fe sulfides transform to oxide forms. This process goes on rather actively. Fe is accumulated on the oxygen barrier. Slight ferrugination occurs in the *Salic-Stagnic Gleysols* (*Thionic,Arenic*). The soils of ridges (the *Salic Gleysols* (*Alcalic, Arenic*)) are usually free of ferrugination. The signs of ancient oxide ferrugination, probably of a similar lagoon-marsh genesis, are preserved as ferruginous layers within the New-Caspian sediments (Figure 7).

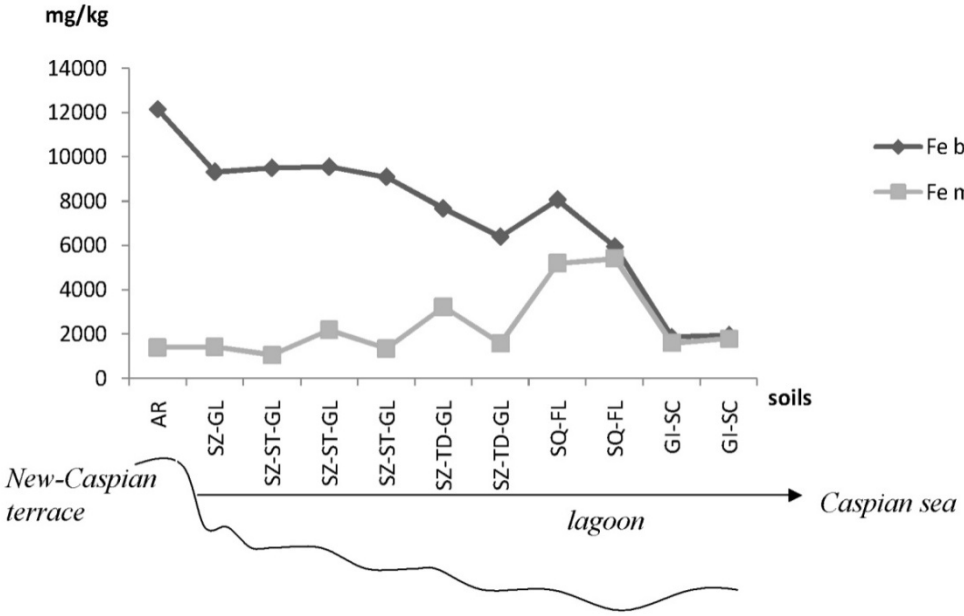

Figure 6. The distribution of the bulk and mobile forms of Fe in the soils of the Caspian salt marshes

AR- Arenosols, SZ-GL- Salic-Gleysols (Alcalic, Arenic), SZ-ST-GL- Salic-Stagnic-Gleysols (Thionic, Arenic), SZ-TD-GL- Salic-Tidalic-Gleysols (Thionic, Siltic), SQ-FL-Subaquatic Fluvisols, GI-SC- Gleic-Solonchaks (Chloridic, Arenic)

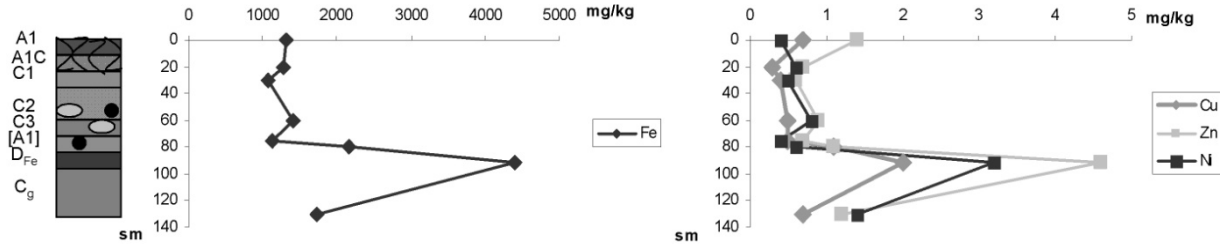

Figure 7. The accumulation of Fe, Cu, Zn, Ni in the ferruginous horizon of the New-Caspian sediments

A1 – humus horizon, A1C, C1-C3 – horizons, [A1] – buried humus horizon, D_{Fe} – ferruginous horizon, C_g – horizon

As shown in Figure 7 the Fe content in the ferruginous horizon is 4 to 7 times higher than in containing sediments, i.e. the intensity of this accumulation may be related to the process of recent ferrugination. Free metal ions may subsequently be co-precipitated and adsorbed to Fe and Mn oxides and hydroxides in aerobic zones

(Williams et al., 1994). Changes of Eh values control the distribution of trace elements.

In sediments, the transition between the aerobic and anaerobic zones is called the redoxcline or redox discontinuity and is identified by a visual change in color from red-brown oxidized surface deposits to dark grey-black of reduced sediment zones (Williams et al., 1994). This color change is synonymous with the presence of ferric oxide precipitates in surface layers and precipitation of insoluble FeS_2 (pyrite) at depth (Lyle, 1983). Consequently, the position of the redoxcline shifts from surface layers under saturated soil conditions to deeper sediment layers following soil water drainage. Salt marshes which are flooded frequently have a dynamic water table, leading to short-term fluctuations of the redox boundary. During the transgression of the Caspian Sea, the redoxcline in the marsh soils lay below 5-10 cm. After the sea level stabilization and partial drainage of the territory, it dropped to below 15-20 cm.

Cycling of Fe and Mn may partly control the vertical profile distribution of Cu, Pb, and Zn, with the maxima occurring in the zone of Fe and Mn enrichment (Cundy et al., 2005; Zwolsman et al., 1993). In the upper oxic horizons of the *Salic-Tidalic Gleysols* (*Thionic, Siltic*), the total Cu, Pb, and Zn show enrichment. This suggests that there has been significant re-mobilization of these metals associated with the diagenetic cycling of Fe and Mn. The subsurface maxima of Co, Cd, Cu, Ni, Cr, Pb, and Zn are located in the zone of diagenetic Fe and Mn enrichment, which may indicate re-adsorption by Mn and Fe oxyhydroxides (Tessier, Rapin, & Carignan, 1985). Compared to the containing sediments, the ferruginous horizon accumulates the following elements: Fe (the coefficient of the concentration is 4.6), Co (8.0), Cu (3.1), Mn (3.0), Ni (2.7), Zn (1.6), Cr (1.6), Pb (1.3). In the anoxic sediments, Fe and Mn oxyhydroxide phases are reduced leading to the release of the trace elements that were co-precipitated or adsorbed by them (Blasco, Saenz & Gomez-Parra, 2000). That leads to the trace element mobility in the coastal zone.

4.3 Organic Matter Accumulation

The process is closely related to the type of vegetation. The vegetation of the Caspian salt marshes is a successional system that worked out well in the process of evolution and adapted to the variable regime of the Caspian Sea level. The coastal succession series is presented by the following stages: A – shoal stage with the dominance of *Juncus species, Phragmites australis*; from the water edge – B – halophylous stage with the dominance of *Salicornia europea, Limonium gmelini*, *Puccinellia dolicholepis*; C – meadow stage with the dominance of *Cynodon dactylon*, *Elytrigia repens*; D – subzonal (pre-climatic) stage with the dominance of *Artemisia scoparia, Astragalus hircanicus.*

During the transgression phase, the plant associations change in the reverse order but excluding halophytic vegetation. Instead of halophytic vegetation, the coastal associations were replaced by meadow-solonchak vegetation. The development of hydromorphic vegetation leads to humus accumulation in the upper layers of soils.

According to specific features of humus accumulation in soils, two landscape situations can be identified. The first one includes the soils of higher surfaces where humus accumulates under sparse grass-herbal semi-desert vegetation. In 1995-1996, the humus content here was 0.3-0.5% increasing slightly to 0.7-1.3% in more hydromorphic soils. The process of slow humus accumulation continues at the phase of the sea level stabilization. In 2001-2003, the humus content increased to 0.6% in these soils and even to 2.9% in more hydromorphic soils of the depressions. Another landscape situation occurs within the marsh zone covered by abundant vegetation. The *Salic-Stagnic Gleysols* (*Thionic,Arenic*) and the *Salic-Tidalic Gleysols* (*Thionic, Siltic*) here show much more active humus accumulation. In 1995-1996, the average humus content in these soils was 2.4%; in several peaty horizons it grew to 9.0 %. The development of meadow vegetation in this zone increased the rate of humus accumulation in the soils. As a result in 2001-2003, the content of $C_{org.}$ was 5.5% and 22% in the *Salic-Tidalic Gleysols* (*Thionic, Siltic*) and in the peaty horizons, respectively.

Humus and peaty horizons of soils create biogeochemical (with biogenic accumulation) and sorption (adsorption by organic colloids) geochemical barriers accumulating a number of chemical elements. In soils of marsh-lagoon zone, Zn, Pb, and Cu have typically biogenic surface maxima; to a lesser extent, this is true for Ni and Cr. According to the correlation with the humus content, the mobile forms of chemical elements form the following sequence, from the most biogenic Zn up to Ni, which is least associated with organic matter of soils (in the values of correlation coefficient): Zn 0.95> Mn, Cu 0.8-0.9> Cd 0.7-0.8> Pb, Fe, Na, Co 0.6-0.7> Ni 0.3 (Kasimov et al., 2000). The content of metals usually reaches its maximum values in the horizons enriched with organic matter. At the stabilization phase, the concentrations of the mobile forms of Fe, Mn, Zn, and Cr increased in the upper layers of the marsh zone. However, for the *Salic-Tidalic Gleysols* (*Thionic, Siltic*), it is very hard to assess the leading role of humus accumulation in the distribution of the trace elements, because the upper

horizons of these soils are, at the same time, the biogeochemical and oxygen geochemical barriers.

The organic matter content is usually highly correlated with Pb, Cu, Zn, Ni, and Cd (Cundy et al., 2005; Di Giulio & Scanlon, 1985; Vestergaard, 1979). Metal enrichment normally occurs in organically rich silt-clay fractions which have high cation exchange capacities, large surface areas, and large surface charge, while sandy, organically poor sediments have low ability to retain metal ions. Organic material derived from decaying vegetation and detritus of marine and terrestrial origin may also lead to metal-organic complex formation which promotes pollutant retention within the sediment compartment.

4.4 Mobility of Trace Elements

The concentration of the mobile forms of chemical elements increases in the *Salic-Tidalic Gleysols* (*Thionic, Siltic*) and the bottom sediments of the lagoon. The mobility of trace elements is somewhat higher during the stabilization phase than at the transgression phase. A combination of factors that are unique for salt marsh sediments enhances trace metal mobilization. The principal reason for the mobilization process is the presence of a pronounced oxic sediment layer at the surface preventing precipitation of metals as sulfides. Instead, retention and mobility of the trace metals in the surface sediments are controlled by adsorption onto Fe and Mn oxyhydroxides, oxidation of sulfide and degradation of organic carbon. Moreover, periodic shifts from oxidizing to reducing conditions (during inundation) cause dissolution of the Fe and Mn carrier phases and release of associated trace metals. Metals released by dissolution of Fe and Mn oxides may also participate in reactions below the redoxcline (Zwolsman et al., 1993).

Thus, there are several factors of mobilization: (1) presence of a distinct oxic top layer; (2) acidification in the top layer due to oxidation of Fe sulfides and organic matter; (3) high pore water salinity near the surface due to sediment desiccation; (4) periodic shifts from oxidizing to reducing conditions during inundation; and (5) organic matter degradation (Zwolsman et al., 1993). The mechanisms tend to keep high trace metal concentrations in solution. These features have been recorded in salt marshes all over the world; it follows that trace metal mobilization from salt marsh sediments is a general phenomenon (Allen, Rae, & Zanin, 1990). Therefore, salt marshes are the sources of dissolved trace metals to the water column.

4.5 Assessment of the Vulnerability of Coastal Soils

Based on research in the Caspian region the assessment of the vulnerability of coastal soils to the sea-level fluctuations was made. Such assessment can be used as the methodical basis for zoning of the coastal soils according to their response to extreme weather events in coastal areas. The degree of vulnerability in soil was determined by a number of soil properties: 1) the position in the coastal catena, 2) oxidation-reduction and alkaline-acidic properties, and 3) soil texture.

The position in the catena of coastal soils is divided into four groups. The first group is presented by *Arenosols* on the New-Caspian terrace. These soils are not influenced by the modern sea level fluctuations. The second group includes *Salic-Gleysols* that are slightly affected by sea-level rise. The third group consists of *Salic-Stagnic-Gleysols* and *Salic-Tidalic-Gleysols* of the marsh zone. Flooding and waterlogging of these soils is directly related to sea level changes. The fourth group is *Gleyic-Solonchaks* of the modern beach ridge, experiencing the worst effects of the sea-level fluctuations.

The redox conditions of the coastal soils are divided into a number of oxidizing soils (*Arenosols*) and soil with variable redox conditions (*Salic-Gleysols, Salic-Stagnic-Gleysols, Salic-Tidalic-Gleysols, Gleyic-Solonchaks*). The coastal soils of the Turali site can be divided into three main groups (high, medium and low degree of the vulnerability) according to the sea-level fluctuations (Table 5).

Table 5. Assessment of the soil's vulnerability of Caspian salt marshes

The degree of vulnerability	*Coastal soils*
High	Salic-Tidalic-Gleysols
Medium	Gleyic-Solonchaks
Low	Arenosols, Salic-Gleysols, Salic-Stagnic-Gleysols

The high degree of the vulnerability of *Salic-Tidalic-Gleysols* are due to the developing of intensive processes of sulfidization and gleyzation, as well as acidification and redistribution of Fe and other elements in the upper peaty horizons of these soils as a result of sea-level fluctuations.

The medium degree of the vulnerability is typical for *Gleyic-Solonchaks* of the modern beach ridge. Strong storm surges lead to erosion of these soils. Because of the light texture and low organic matter the geochemical transformation of these soils is not very intensive. The rest coastal soils of the Caspian salt marshes have the low degree of vulnerability. In the present situation of the Caspian Sea level and frequency of occurrence and height of the surge, they are not influenced by the short-term sea-level fluctuations.

5. Conclusions

The long-term research of the coastal zone of the Central Dagestan (Turali site) made it possible to assess the environmental changes due to the complete cycle of the Caspian Sea level changes (regression-transgression-stabilization) (Figure 8).

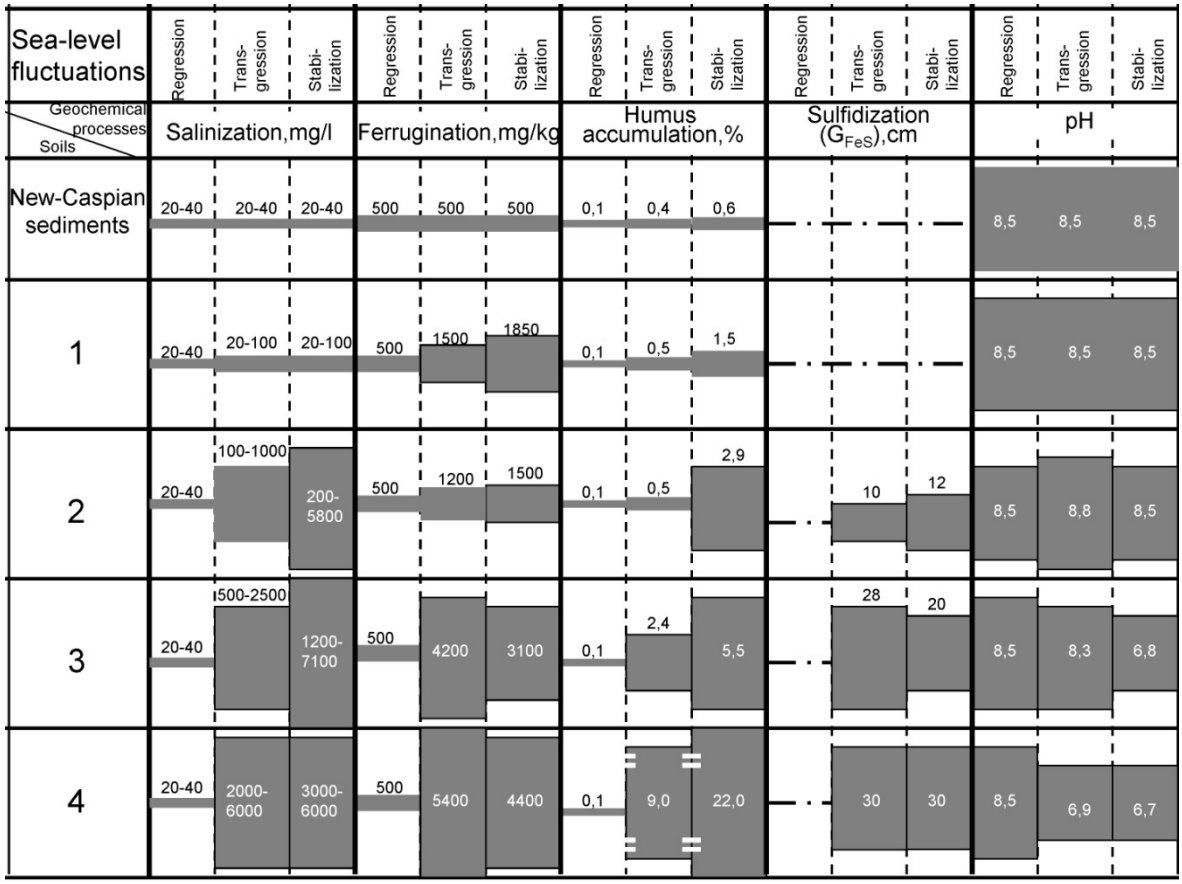

Figure 8. Geochemical changes of the Caspian salt marshes under the sea level fluctuations

Soils: 1- Arenosols, 2- Salic-Gleysols (Alcalic, Arenic) and Salic-Stagnic-Gleysols (Thionic, Arenic), 3- Salic-Tidalic-Gleysols (Thionic, Siltic), 4- Subaquatic Fluvisols; numbers – the average values.

The geochemical conditions in the coastal soils were not highly different during the regression phase. The concentrations of chemical elements were low and their spatial distribution was homogeneous. From the beginning of the transgression phase, the variety of geochemical conditions in the coastal soils increased. It affected the mobilization and availability of both major and minor metals. The distribution of trace metals in soils and sediments has been significantly modified by new landscape-geochemical processes leading to the formation of the geochemical barriers in the soils.

The formation and gradual inland movement of the bar-lagoon system has led to additional accumulation of organic matter in the marsh soils; the development of anaerobic processes in the presence of sulfate-rich water resulted in the precipitation of sulfides in the bottom sediments of the lagoon and in the soils of the marsh-lagoon zone. The co-precipitation of Fe and heavy metals together with sulfides and the accumulation of Fe at oxidizing barrier are the main processes of the transgression phase (Kasimov et al., 2000).

After the stabilization of the sea level, the geochemical conditions of the *Salic-Tidalic Gleysols* (*Thionic, Siltic*) began to change slowly. The shallowing of the lagoon has resulted in a partial oxidation of sulfides in the upper horizons of these soils and the formation of sulfuric acid. This was accompanied by the acidification of the coastal soils and increased the accumulation of Fe in the upper horizons of the soils. During the period of the sea level stabilization, the redoxcline in the *Salic-Tidalic Gleysols* (*Thionic, Siltic*) dropped below 10-15 cm enhancing mobility of the trace elements in the upper 5-15 cm and metal accumulation at the oxygen geochemical barrier. The development of meadow vegetation in the marsh zone increased the rate of humus accumulation in the coastal soils. As a result, in 2001-2003, the rate of humus accumulation in the peaty horizons was estimated at 1.9 % of $C_{org.}$ per year.

A new rise of the sea level may lead to the landward movement of the bar-lagoon system; the width of the lagoon may decrease. It may lead to water-logging of the *Salic Gleysols* (*Alcalic, Arenic*) and the *Salic-Stagnic Gleysols* (*Thionic,Arenic*). It may cause development of anaerobic processes, accumulation of sulfides and humus and concentration of chemical elements. Further stabilization or regression of the sea level may be accompanied by drainage of the marsh zone, oxidation of the sulfides in the upper horizons, acidification of soils, and accumulation of Fe in the soils. Accumulation of Fe oxides and hydroxides and humus can also cause accumulation of other trace elements. However, acidification of soils may enhance the mobility of heavy metals and their removal. The interaction of these two opposite processes should be studied in the future.

The salt marsh environment is a complex system. Even small changes to the surrounding environment can significantly affect the overall cycling of the metal forms. Salt marsh sediments provide a valuable tool for the study of trace metal behavior in different landscape-geochemical processes. Such study can be used in quantitative projections of risks to disastrous natural hazards (floods and droughts, degradation of soils) for different regions.

Acknowledgements

This research was performed under the INTAS project 94-3382 ("Geochemical changes in soils and sediments due to the rapid rise of the Caspian Sea level"), the NWO project 047-009-003 ("Holocene sea level change and mollusc biodiversity in the Caspian Sea: a proxy for the North Atlantic Oscillation"), and the projects of the Russian Foundation for Basic Research (№ 97-05-65731, 03-05-643060, 04-05-65073, and others), NRAL project (contract t G.34.31.0007).

References

Allen, J. R. L. & Pye, K. (1992). *Saltmarshes. Morphodynamics, Conservation and Engineering Significance*. Cambridge University Press. 184 p.

Allen, J. R. L. (2000). Morphodynamics of Holocene salt marshes: a review sketch from the Atlantic and Southern North Sea coasts of Europe. *Quaternary Science Reviews, 19*, 1155-1231. http://dx.doi.org/10.1016/S0277-3791(99)00034-7

Allen, J. R. L., Rae, J. E., & Zanin, P. E. (1990). Metal speciation (Cu, Zn, Pb) and organic matter in an oxic salt marsh, Severn estuary, southwest Britain. *Marine Pollution Bulletin, 21*, 574-580. http://dx.doi.org/10.1016/0025-326X(90)90606-9

Badyukova, E. N., Solovyova, G. D., & Spolnikova, L. N. (1993). Morpholithtodynamics of the Dagestan Coast of the Caspian Sea. *Moscow State University Bulletin, Ser.5: Geography, 4*, 56-64.

Bates, R. L., & Jackson, J. A. (1980). *Glossary of Geology*. American Geological Institute, Falls Church, Virginia, USA. 751 p.

Blasco, J., Saenz, V., & Gomez-Parra, A. (2000). Heavy metal fluxes at the sediment-water interface of three coastal ecosystems from south-west of the Iberian Peninsula. *The science of the total environment, 247*, 189-199. http://dx.doi.org/10.1016/S0048-9697(99)00490-8

Bockelmann, A. C., Bakker, J. P ., Neuhaus, R., & Lage, J. (2002). The relation between vegetation zonation, elevation and inundation frequency in a Wadden Sea Salt marsh. *Aquatic Botany, 73*, 211-221. http://dx.doi.org/10.1016/S0304-3770(02)00022-0

Buckley, D. E., Smith, J. N., & Winters, G. V. (1995). Accumulation of contaminant metals in the marine sediments of Halifax Harbour, Nova Scotia: environmental factors and historical trends. *Applied Geochemistry, 10*, 175-195. http://dx.doi.org/10.1016/0883-2927(94)00053-9

Cazenave, A., Bonnefond, P., Dominh, K., & Schaeffer, P. (1997). Caspian sea level from Topex-Poseidon altimetry: level now falling. *Geophysical Research Letter, 24*(8), 881-884.

http://dx.doi.org/10.1029/97GL00809

Cundy, A. B., Croudace, I. W., Thomson, J., & Lewis, J. T. (1997). Reliability of salt marshes as 'Geochemical Recorders' of pollution input: A case study from contrasting estuaries in southern England. *Environmental Science and Technology, 31*, 1093-1101. http://dx.doi.org/10.1021/es960622d

Cundy, A. B., Hopkinson, L., Lafite, R., Spencer, K., Taylor , J. A., Ouddane, B., … Ullyott, S. (2005). Heavy metal distribution and accumulation in two Spartina sp.-dominated macrotidal salt marshes from Seine estuary (France) and the Medway estuary (UK).*Applied Geochemistry, 20*, 1195-1208. http://dx.doi.org/10.1016/j.apgeochem.2005.01.010

Di Giulio, R. T. & Scanlon, P. E. (1985). Heavy metals in aquatic plants, clams and sediments from the Chesapeake Bay, USA. Implications for Waterfowl. *The Science of the total environment, 41*, 259-274. http://dx.doi.org/10.1016/0048-9697(85)90145-7

Farmer, J. G., & Lovell, M. A. (1984). Massive diagenetic enhancement of manganese in Loch Lomond sediments. *Environmental Technology Letters, 5*, 257-262. http://dx.doi.org/10.1080/09593338409384274

Gennadiev, A. N., Kasimov, N. S., Golovanov, D. L., Lychagin, M. Yu., & Puzanova, T. A. (1998). Soil evolution in the coastal zone under rapid changes in the Caspian sea level. *Eurasian soil science, 31*(9), 929-936.

Glazovskaya, M. A. (1988). *Geochemistry of natural and technogenic landscapes.* Moscow, High School.328p.

Gornitz, V., Couch, S., & Hartig, E. K. (2002). Impacts of sea level rise in the New York City metropolitan area. *Global and Planetary changes, 32*, 61-88.

Ignatov, E. I., Kaplin, P. A., Lukyanova, S. A., & Solovyova, G. D. (1993). Influence the recent transgression of the Caspian Sea on its coastal dynamics. *Journal of Coastal research, 9*(1), 104-111.

Kaplin, P. A. & Selivanov, A. O. (1995). Recent coastal evolution of the Caspian sea as a natural model for coastal responses to the possible acceleration of the global sea level rise. *Marine Geology, 124*, 161-175. http://dx.doi.org/10.1016/0025-3227(95)00038-Z

Kasimov, N. S., Gennadiev, A. N., Lychagin, M. Y., Kroonenberg, S. B., & Kucheryaeva, V. V. (2000). Geochemical transfomation of coastal soils in Central Dagestan upon the rise in the level of the Caspian Sea. *Eurasian soil science, 33*(1), 11-22.

Klige, R. K., & Myagkov, M. S. (1992). Changes in the water regime of the Caspian sea. *Geological Journal, 27*(3), 299-307.

Kravtsova, V. I., & Lukyanova, S. A. (1997). Transgressive changes of the Russian cost of the Caspian sea. *Geomorphology, 2*, 35-46.

Kroonenberg, S. B., Baduykova, E. N., Storms, J. E. A., Ignatov, E. I., & Kasimov, N. S. (2000). A full sea level cycle in 65 years: barrier dynamics along Caspian shores. *Sedimentary Geology, 134*, 257-274. http://dx.doi.org/10.1016/S0037-0738(00)00048-8

Kroonenberg, S. B., Rusakov, G. V., & Svitoch, A. A. (1997). The wandering of the Volga delta: a response to rapid Caspian sea level change. *Sedimentary Geology, 107*, 189-209. http://dx.doi.org/10.1016/S0037-0738(96)00028-0

Leontiev, O. K., Lukyanova, S. A., Nikiforov, L. G., Solovyova, G. D., & Holodilin, N. A. (1977). Map of type of the World Ocean coasts. *Relief and landscapes*. pp. 116-126.

Lyle, M. (1983). The brown-green colour transition in marine sediments: a marker of the Fe (III), Fe (II) redox boundary. Limnol. *Oceanography, 28*, 1026-1033. http://dx.doi.org/10.4319/lo.1983.28.5.1026

Myalo, E. G., & Malkhazov, M. Y. (2000). Dynamic of vegetation along the Dagestan coast upon fluctuations of the sea level. *Moscow State University Bulletin, Ser.5: Geography, 4*, 16-21.

Perelman, A. I. (1975). *Landscape geochemistry*. High school, Moscow. 342 p.

Price, G. D., Winkle, K., & Gehrels, W. R. (2005). A geochemical record of the mining history of the Erme Estuary, south Devon, UK. *Marine Pollution Bulletin, 50*, 1706-1712. http://dx.doi.org/10.1016/j.marpolbul.2005.07.016

Rodionov, S. (1994). *Global and regional interaction: the Caspian Sea experience.* Dordrecht: Kluwer.V.11, 241p. http://dx.doi.org/10.1007/978-94-011-1074-7

Rogel, J. A., Silla, R. O., & Ariza, F. A. (2001). Edaphic characterization and soil ionic composition influencing

plant zonation in a semiarid Mediterranean salt marsh. *Geoderma, 99*, 81-98. http://dx.doi.org/10.1016/S0016-7061(00)00067-7

Rychagov, G. I. (1993). The sea level regime of the Caspian sea during the last 10,000 years. *Moscow State University Bulletin, Ser.5: Geography, 2*, 38-49.

Shaw, T. J., Gieskes, J. M., & Jahnke, R. A. (1990). Early diagenesis in differing depositional environments: the response of transition metals in pore water. *Geochimica et Cosmochimica Acta, 54*, 1233-1246. http://dx.doi.org/10.1016/0016-7037(90)90149-F

Silvestri, S., Defina, A., & Marani, M. (2005). Tidal regime, salinity and salt marsh plant zonation . *Estuarine, coastal and shelf science, 62*, 119-130. http://dx.doi.org/10.1016/j.ecss.2004.08.010

Simas, T., Nunes, J. P., & Ferreira, J. G. (2001). Effects of global climate change on coastal salt marshes. *Ecological modeling, 139*, 1-15.

Solovyov, G. A. (1989). Use of complex extractions for definition of accessible forms of microelements in soils. *Monitoring of background pollution of natural environments, 5*, 216-228.

Spencer, K., Cundy, A. B., & Croudace, I. W. (2003). Heavy metal distribution and early diagenesis in salt marsh sediments from the Medway Estuary, Kent, UK. *Estuarine, Coastal and Shelf Science, 57*, 43-54. http://dx.doi.org/10.1016/S0272-7714(02)00324-4

TED Caspia. (2000). Main conclusions of the Technical Economical Report. Moscow. 49p.

Tessier, A., Rapin, F., & Carignan, R. (1985). Trace metals in oxic lake sediments: possible adsorption onto iron oxyhydroxides. *Geochimica et Cosmochimica Acta, 49*, 183-194. http://dx.doi.org/10.1016/0016-7037(85)90203-0

Turekian, K. K., & Wedepohl, K. H. (1961). Distribution of the elements in some major units of the Earth's crust. *Geological Society of America Bulletin, 72*, 175-192. http://dx.doi.org/10.1130/0016-7606(1961)72[175:DOTEIS]2.0.CO;2

Valette-Silver, N. J. (1993). The use of sediment cores to reconstruct historical trends in contamination of estuarine and coastal sediments. *Estuaries, 16*, 577-588. http://dx.doi.org/10.2307/1352796

Velde, B., Church, T., & Bauer, A. (2003). Contrasting trace element geochemistry in two American and French salt marshes. *Marine chemistry, 83*, 131-144. http://dx.doi.org/10.1016/S0304-4203(03)00107-5

Vestergaard, P. (1979). A study of indication of trace metal pollution of marine areas by analysis of salt marsh soils. *Marine environment research, 2*, 19-31. http://dx.doi.org/10.1016/0141-1136(79)90025-4

Vinogradov, A. P. (1962). Average content of chemical elements in the main types of igneous rocks of the Earth Crust. *Geochimiya, 7*, 555-572.

Williams, T. P., Bubb, J. M., & Lester, J. N. (1994). Metal accumulation within salt marsh environment: a review. *Marine pollution bulletin, 28*(5), 277-290. http://dx.doi.org/10.1016/0025-326X(94)90152-X

Zonn, S. V. (1982). *Iron in soils.* Moscow, Science.208p.

Zwolsman, J. J. G., Berger, G. W., & Van Eck, G. T. M. (1993). Sediment accumulation rates, historical input, post-depositional mobility and retention of major elements and trace elements in salt marsh sediments of the Scheldt estuary, SW Netherlands. *Marine Chemistry, 44*, 73-94. http://dx.doi.org/10.1016/0304-4203(93)90007-B

Notes

Note 1. Investigations: 1995-1996. (n) – number of samples.

Note 2. Investigations: 2001-2003. (n) – number of samples.

Note 3. The coefficient of accumulation was calculated as a ratio of the average content of the chemical element in soils of the marsh zone to that in the soils of the New-Caspian terrace.

Note 4. The coefficient of changes of chemical elements' contents – content of the chemical element in soils during the phase of stabilization/content of the chemical element in soils during the transgression phase.

Note 5. Coefficient of changes ≤0,7 and coefficient of changes ≥1,3 are shown in bold.

Earth Science Research; Vol. 1, No. 2; 2012
ISSN 1927-0542 E-ISSN 1927-0550
Published by Canadian Center of Science and Education

Characterizing Vegetation Response to Climatic Variations in Hovsgol, Mongolia Using Remotely Sensed Time Series Data

Thuan Chu[1] & Xulin Guo[1]

[1] Department of Geography and Planning, University of Saskatchewan, Saskatoon, Canada

Correspondence: Xulin Guo, Department of Geography and Planning, University of Saskatchewan, Kirk Hall, 117 Science Place, Saskatoon, SK S7N5C8, Canada. Tel: 1-306-966-5663. E-mail: xulinguo@gmail.com

Received: June 29, 2012 Accepted: July 9, 2012 Online Published: July 25, 2012

doi:10.5539/esr.v1n2p279 URL: http://dx.doi.org/10.5539/esr.v1n2p279

Abstract

One of the challenges faced by forest managers is the inability to quickly interpret forest ecosystem attributes and vegetation responses to climate change. This research aims to address this challenge by characterizing the phenological metrics and evaluating the temporal and spatial dynamics of vegetation over 12 years (2000-2011) under climate change effects in Hovsgol, Mongolia. Time series Normalized Difference Vegetation Index (NDVI) was used as an indicator to monitor vegetation response in the area. The effects of climatic variations on vegetation growth were considered through the relationship between climatic variables and NDVI. Results indicate that the growing season commonly starts in late April and ends in late October with full growth by July, and as a consequence of climate change in the area, the growing season in recent years seems to be beginning earlier. Plant stress caused by higher temperature was the most significant contributor to earlier vegetation green up since NDVI, length, and starting point of the growing season strongly depend on air temperature. Analysis of spatio-temporal heterogeneity indicates some areas with highly dynamic NDVI, particularly in the western part of the Hovsgol Lake, the high mountainous areas, and the Darhad valley. Our results suggest that temperature variations mainly determine the pattern of vegetation responses in the Hovsgol area.

Keywords: climatic variation, NDVI, phenological metrics, vegetation response

1. Introduction

The climate of Mongolia has undergone significant changes over the last few decades. Batima et al. (2005) reported that Mongolia's average temperature has increased by 1.7^{o}C since the 1940s, while the precipitation has tended to decrease slightly. The temperature is predicted to increase by 2^{o}C in summer and 1^{o}C in winter during the next 80 years (Sato et al., 2006). These changes are the likely causes of the summer droughts and directly affect vegetation growth, biodiversity, and human socioeconomics in Mongolia (Batima et al., 2005; James, 2011; Yu et al., 2003). The results of tree-ring analyses of single areas in Mongolia (Dulamsuren et al., 2010; James, 2011) suggest that forests generally respond to global warming with very high variations depending on the regional variations of temperature, precipitation, and land cover types.

Some recent studies in Mongolia have explored the use of time-series remotely sensed data to investigate vegetation response to climatic variation and other disturbances such as wildfires. Erdenesaikhan (2002) used National Oceanic and Atmospheric Administration (NOAA) Advanced Very High Resolution Radiometer (AVHRR) time series data from 1991 to 2001 to estimate vegetation greenness and variation based on Normalized Difference Vegetation Index (NDVI) for the entirety of Mongolia. The result showed that there were high spectral and greenness variations in the northern part of the country, including the high mountains and taiga forest during the maximum vegetation growing seasons in Mongolia (July to August). Yu et al. (2003, 2004) examined the seasonal vegetation response to climatic variations on the Mongolia steppes using time series analysis of AVHRR NDVI data, and proposed that the taiga forest of the northern Mongolia steppes experienced an earlier onset of green up. The authors assumed that the precipitation was the most significant factor determining the pattern of vegetation responses to global warming. Other studies in Mongolia related to active forest and steppe fires detection by using thermal infrared NOAA AVHRR bands (IFFN, 1999; Magsar Erdenetuya, 1999; Sanjaa Tuya, 2002).

There are a number of studies around the world which have successfully applied remote sensing techniques not only in identifying disturbance events, but also in vegetation trajectory responses in which NDVI is the most

common indicator to characterize vegetation responses (i.e. Zhang et al., 2008; Leon et al., 2012; Van Leeuwen, 2008; Van Leeuwen et al., 2010; Veraverbeke et al., 2011; Yang, 2011; Yu et al., 2003; 2004). Seasonal phenometrics of vegetation extracted from NDVI have been focused on to compare rates of change and length of growing season influenced by climate change or fire (Casady et al., 2009; Van Leeuwen et al., 2010). Additionally, a departure of NDVI from average (Erdenesaikhan, 2002; Van Leeuwen, 2008), standard deviation (SD), and coefficient of variation (COV) (Zhang et al., 2008; Guo, 2004; Van Leeuwen et al., 2010) have been widely used to estimate vegetation heterogeneity and dynamics caused by disturbances.

To date, however, very few studies in Mongolia and particularly in Hovsgol area have been conducted to identify seasonal phenology and detect both temporal and spatial changes of forest influenced by climate change using remote sensing. Under the assumption that NDVI is an effective surrogate for forest status, therefore, the objectives of this study are to: 1) extract phenological parameters and characterize the temporal and spatial variation of vegetation covers in the Hovsgol area from 2000 to 2011; and 2) evaluate the relationship between climate variations and vegetation responses in Hovsgol during the study period. More specifically, temporal and spatial vegetation dynamics and phenological metrics of vegetation growth were assessed based on time series NDVI data over 12 years (2000-2011). Air temperature and precipitation are two climatic variables to evaluate climate change effects on vegetation during the study period.

2. Data and Methods

2.1 Study Area

The study was conducted in Hovsgol province, the northern part of Mongolia (49°38'N, 100°10'E) (Figure 1). Hovsgol province is the most densely forested area in Mongolia with 31781 sq km of closed forest accounting for 30% of Mongolia's total closed forest area (James, 2011). The Siberian larch *(Larix Siberica)* dominantly contributes more than 90% to the forest composition in the area. The average temperatures during winter range from -16.5°C to -23.0°C with an extreme minimum of -47.7°C recorded in January 2000, while average summer temperatures range from 10.8°C to 11.8°C with the highest temperature of 31.6° recorded in July 2002 (Murray, 2004). The region is experiencing major climate change illustrated by the 1.8°C annual temperatures increase over the last 40 years (1963-2002) (Banzragch, 2007). Additionally, the forest area was heavily affected by wildfire in 1996 and 2000-2002 (Farukh et al., 2009; IFFN, 2007).

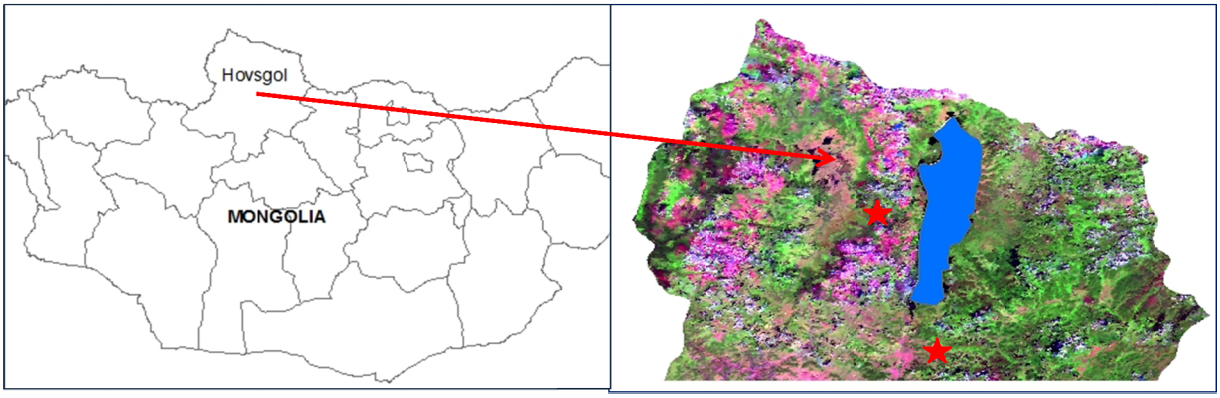

Figure 1. Study area in Hovsgol province, Mongolia; July, 2000 MODIS data in Hovsgol area (right); ★ weather station

2.2 MODIS Time Series Data and Climatic Variables

This study examined the use of 250 m spatial resolution, 16 day MODIS NDVI (MOD13Q1), and 1000 m spatial resolution, 8 day MODIS Land Surface Temperature (LST) (MOD11A2) time series data to evaluate vegetation dynamics and its response to climate variations using some of the methods in the literature. These MODIS time series data during the growing season (April to October) were obtained for the study area from the NASA website http://reverb.echo.nasa.gov. Statistical parameters (i.e. mean NDVI, LST, NDVI coefficient of variation) were calculated from these time series data.

For the purpose of extracting phenological metrics and in order to reduce calculation work, we only used subset of the 16 day MODIS NDVI data (100x100km; 51.52N, 98.92E) from January to December, 2000-2011, which

was downloaded from the website http://daac.ornl.gov/MODIS/modis.html. This resulted in 23 subsets of 250 m spatial resolution, 16 day MODIS NDVI images each year, except for the three missing NDVI images between January and February, 2000. The subset was selected as a representative for the entire area to extract phenological parameters.

Air temperature is commonly used to analyze climatic conditions within a geographic extent (Ravenscroft et al., 2010; Vancutsem et al., 2010). Monthly mean maximum air temperature and monthly sum precipitation in Hatgal (50.4N, 100.2E) and Rinchinlhumble (51.1N, 99.7E) weather stations in Hovsgol province were downloaded from the *Weather Underground* website http://www.wunderground.com. However, due to the insufficiency of these data from January 2000 to May, 2004, this study estimated missing monthly air temperature based on the Temperature Vegetation Index (TVX) method (Nieto et al., 2011; Prihodko et al., 1997). This approach derives air temperature based on the correlation between LST and NDVI.

2.3 Data Analysis Approach

2.3.1 Preprocessing

All downloaded MODIS LST and MODIS NDVI time series data in sinusoidal projection were reprojected into the UTM projection using MRTtools (USGS, 2011). 1km spatial 8 day MODIS LST was resampled to 250m 16 day MODIS LST data in order to be compatible with the 250m 16 day MODIS NDVI data. This preprocessing resulted in a time series of 336 MODIS images (168 NDVI and 168 LST) during the study area's growing season over 12 years. Following this preprocessing, 150 sample sites were then randomly selected in the time series images to collect LST and NDVI samples for the statistical descriptions and models calibration. For the subset MODIS data representing the study area, mean NDVI for each 16 day period from January to December over 12 years was extracted to derive phenological metrics.

2.3.2 Estimation of Air Temperature Using the TVX Method

Corresponding with observed air temperature from 2004 to 2011 at Rinchinlhumbe weather station, land surface temperature and NDVI were collected to derive the TVX regression model. Air temperature at pixel level for the entire area can be estimated using the equation below (2.1). The model was validated by the measured air temperature at Hatgal weather station with a mean absolute error of 2.2^{o}C (RMSE = 2.4^{o}C). Compared with the other studies from the literature review (i.e. Nieto et al., 2011; Vancutsem et al., 2010), this error is acceptable to estimate air temperature at any location based on land surface temperature and NDVI values.

$$Tair = 23.24*NDVI + 0.307*LST - 2.96 \quad (R^2 = 0.89,\ \text{Adjusted } R^2=0.88,\ p<0.001) \qquad (2.1)$$

The study used climatic variables including temperature and precipitation employed at Rinchinlhumbe weather station for the assessment of climate change effects since this station is located near Darhad valley in the centre of the study area. Missing air temperature from 2000 to 2004 in the Rinchinlhumbe station was estimated using the TVX equation above.

2.3.3 Extracting Phenological Metrics

Onset and end of growing season were decided by analyzing NDVI time series data based on curve derivative methods in the TIMESAT software (Jonsson et al., 2002; 2004). For the analysis of seasonal and interannual vegetation dynamics, this technique facilitates the evaluation of variability and trends of vegetation phenology in relation to climate change and disturbances (Jonsson & Eklundh, 2004). All monthly extracted mean NDVI data during January to December (2000-2011) from the subset MODIS data were imported into the software to identify the onset and end of the growing season each year. The Savitsky-Golay curve derivative method was used to describe vegetation phenometrics for the area (Figure 2). The start and end of the growing season was defined as the point in time for which the NDVI value had increased by 20% of the distance between the minimum NDVI value and the maximum NDVI value (Zhang et al., 2008; Van Leeuwen et al., 2010).

In addition to the graphical model (Figure 2), the seasonal phenometrics in Hovsgol were extracted including the start and end of the growing season, the time of peak growing season, the length of the growing season, the amplitude of the growing season, the large and small integral metric of NDVI values, the rate of green up (left derivative), and the rate of senescence (right derivative) (Table 1).

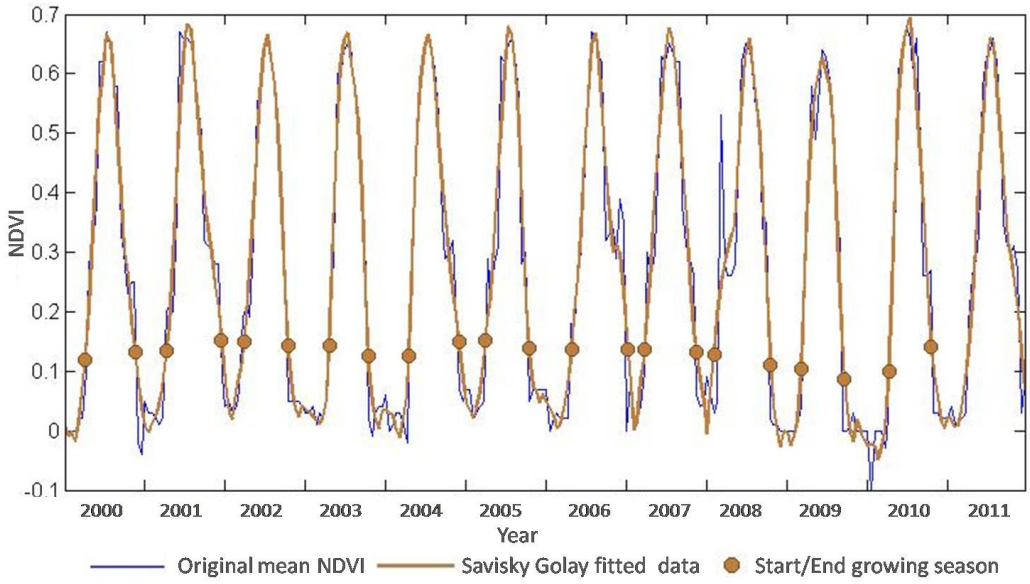

Figure 2. Graphical of the phenological metrics derived from NDVI time series; input NDVI time series data from January to December, 2000 to 2011; SG - Savitsky-Golay fitted curve with the points identifying the onset and end of growing season in Hovsgol, Mongolia

Table 1. Phenological metrics of vegetation growing in Hovsgol area extracted from NDVI time series data (January to December, 2000-2011)*

Year	Start	End	Length	Peak time	Peak NDVI	Ampl.	L.derive	R.derive
2000	113	295	182	193	0.66	0.63	0.15	0.10
2001	115	313	198	199	0.67	0.65	0.15	0.08
2002	113	292	179	195	0.65	0.61	0.16	0.12
2003	118	284	166	196	0.66	0.61	0.17	0.13
2004	116	299	182	199	0.66	0.62	0.15	0.09
2005	119	291	171	204	0.66	0.62	0.13	0.13
2006	129	306	177	206	0.67	0.63	0.14	0.09
2007	102	300	198	201	0.65	0.60	0.10	0.10
2008	105	294	189	201	0.65	0.61	0.11	0.11
2009	105	294	189	201	0.64	0.62	0.10	0.12
2010	123	302	179	204	0.68	0.65	0.18	0.10
Mean	114	297	183	200	0.66	0.62	0.14	0.11

* TIMESAT derives (n-1) result time series data from n input data; Start and End are the onset and end of growing season (in Julian date); Length: length of growing season (day); Peak time: Time of peak growing season – NDVI max (in Julian date); Peak NDVI: maximum NDVI during growing season; Ampl.: Amplitude of the growing season = NDVIpeak – NDVIbase, NDVIbase=(NDVIstart+NDVIend)/2; L.derive and R.derive: the rate of green up, and the rate of senescence respectively.

2.3.3 Analyzing of Spatial and Temporal Dynamics

The temporal dynamics of vegetation in the study area was assessed based on the extracted phenological parameters from the time series data in relation to climate change. The monthly mean of air temperature and NDVI during growing season of each year were calculated to analyze the relationship between climate variations and vegetation dynamics. Missing air temperature data in 2000-2003 were estimated using the TVX regression model calibrated in the Rinchinlhumbe weather station with validation by data from the Hatgal weather station.

The relationship between NDVI, air temperature, and precipitation was also derived using multiple linear regression models to explain the variation of NDVI caused by climatic variables.

To detect spatial heterogeneity due to climate change and other disturbances during 2000-2011, time series NDVI ($NDVI_i$) data of peak growing season (*in July*) were employed to estimate a 2000-2011 coefficient of variation map (COV_{NDVI}) (2.2) for which a Standard Deviation map (STD_{NDVI}) (2.4), derived from NDVI time series data (00-11), was divided by the average NDVI during the study period ($MEAN_{NDVI}$) (2.3). The COV_{NDVI} was calculated by each pixel over 12 year NDVI values (in July) for the entire area.

$$COV_{NDVI} = STD_{NDVI} / MEAN_{NDVI} \quad (2.2)$$

$$\text{In which: } MEAN_{NDVI} = \sum_{i=1}^{12} NDVI_i/12; \quad (2.3)$$

$$STD_{NDVI} = \sqrt{\sum_{i=1}^{12}(NDVI_i - MEAN_{NDVI})^2/11} \quad (2.4)$$

i – Year i_{th}.

To detect site-specific vegetation cover anomalies in each year, the departure from mean NDVI method was applied for which the difference between yearly mean NDVI ($MEAN_{NDVI}$) from 2000 to 2011 and July mean NDVI values for each year ($NDVI_{year\ ith}$) were calculated as (2.5).

$$dNDVI_{year\ ith,\ mean} = NDVI_{year\ ith} - MEAN_{NDVI} \quad (2.5)$$

3. Results and Discussions

3.1 Phenological Metrics and Climate Variation

The growing season in the area normally starts in late April (114 in Julian date) and ends in late October (297 in Julian date). The peak of the growing season is in the middle of July (200 in Julian date) (Table 1). The duration of the growing season in Hovsgol was unstable from 2000 to 2010 (Figure 3a). The longest growing seasons were witnessed in 2001 and 2007, 198 days each, while the 2003 growing season was the shortest with 166 days. However, the growing season in 2001 started and ended later than in 2007 and 2003. The fluctuation of the growing season length could be partially explained by the annual mean air temperature over 12 years as the length of the growing season was positively correlated with air temperature measured at the Rinchinlhumbe weather station ($R^2 = 0.5$) (Figure 3b). The timing of the earlier growing season start from 2007 to 2009 (105 in Julian date) revealed phenological trends that very likely reflect responses to recent climate change of vegetation in the area (Table 1). In general, higher annual mean temperature resulted in the earlier growing season in Hovsgol area ($Time_{start} = -7.7*T_{air} + 212.6$, $R^2 = 0.58$). According to results of Walther et al. (2002) and Yu et al. (2003), climate change studies in Europe, North America, and Central Asia revealed phenological trends that showed that the timing of the growing season is occurring earlier than ever before. A similar trend can be observed in the Hovsgol area including the earlier growth of plants in recent years (2007-2009).

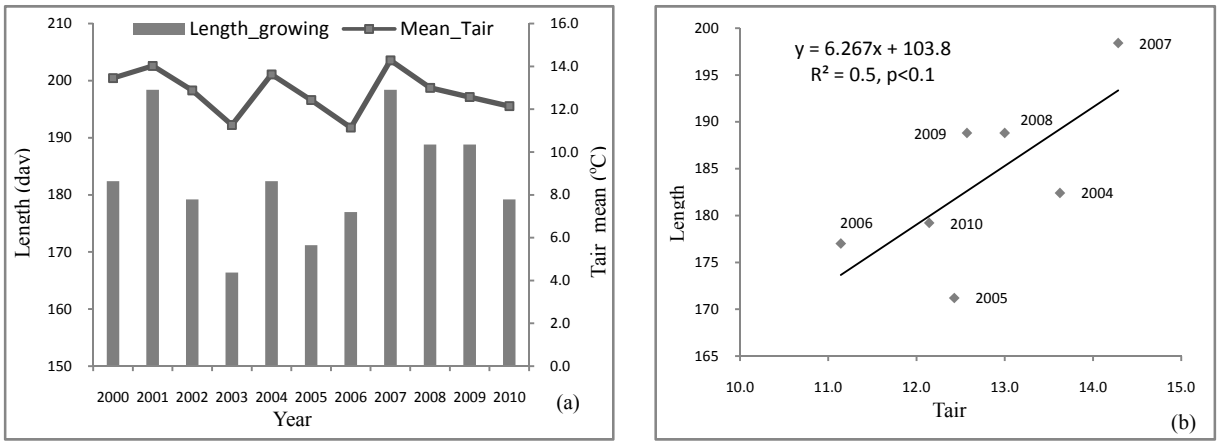

Figure 3. Length of growing season (day) and average air temperature (included the predicted T_{air} from January 2000- May 2004) (a); and correlation between length and mean air temperature of growing season (only available observed T_{air} data from 2004-2010 at Rinchinlhumbe) (b)

In terms of growing rate, the high rates of green up (L. derive) were witnessed in almost all years, except from 2007 to 2009. The rate of green up was much higher than that of senescence, average 0.14 and 0.1, respectively (Table 1). Compared to the length of growing season and air temperature, the lower rate of green up and senescence seems to be the longer growing season with higher temperature (R^2=0.12-0.34). There is no evidence of relationship between precipitation and phenological variables. This is probably because of the strong influence by permafrost and soil moisture coupled with temperature rather than precipitation in the area.

3.2 Seasonal NDVI and Climate Variation

Temperature and NDVI have illustrated strong yearly cyclic variation for the past 12 years (Figure 4). Furthermore, the lack of lag between air temperature and NDVI also revealed that temperature is the limiting factor influencing vegetation greenness in the area. Maximum average temperature values measured at the Rinchinlhumbe weather station (2000-2011) in April, May, June, July, August, September, and October were 5.5°C, 13.2°C, 19°C, 20.6°C, 17.8°C, 11.7°C, and 2.3°C respectively, with July being the highest. In relation to temperature, average NDVI values for the entire area in April, May, June, July, August, September, and October were 0.16, 0.32, 0.6, 0.67, 0.58, 0.34, and 0.2 respectively, with July being the highest as the full growing season. Compared with temperature and NDVI, precipitation values show a similar trend, but with larger variations. Total precipitation values in April, May, June, July, August, September, and October were 17, 34, 149, 222, 162, 100, and 23 mm respectively, and the highest amount of monthly precipitation for each year appeared in June and July.

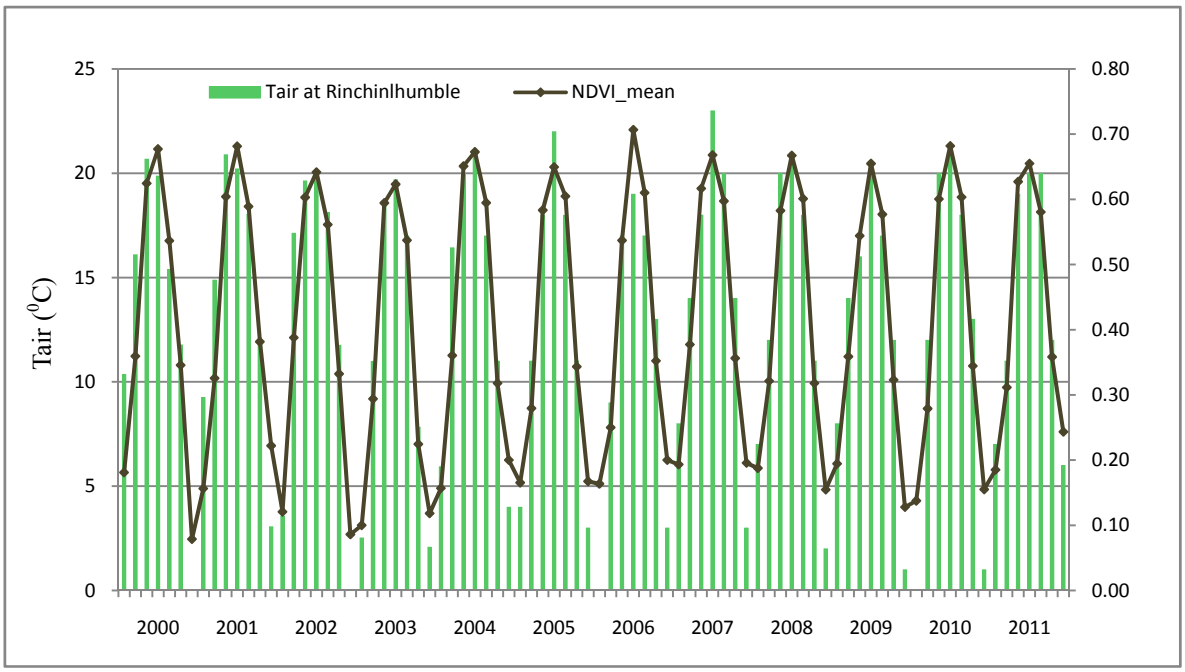

Figure 4. Monthly maximum mean air temperature measured (2004-2011) and estimated (January 2000- May 2004) at Rinchinlhumbe and mean NDVI for the entire area from April to October (2000-2011)

A positive high correlation between NDVI and independent temperature and precipitation variables (R^2 = 0.92, Adjusted R^2 = 0.91, p<0.0001, very low precipitation slope only significant at 0.001 level; no autocorrelation evidence between variables, p=0.1 with Durbin Watson test) was described using the equation below (3.1). This result is consistent with other published studies showing that *Larix* forest growing in the area responds positively with summer warming (James, 2011).

$$NDVI = 0.025*Temperature + 0.002*Precipitation + 0.062 \quad (3.1)$$

The result reveals that about 90% of the variation in NDVI can be explained by changes in temperature and precipitation which indicates their important influence on vegetation growth in the area. However, other factors such as soil moisture related to permafrost, land cover types, and fire events are also interrelated with vegetation growth and require further examining in the area.

3.3 NDVI Temporal Heterogeneity

The temporal forest heterogeneity in the study area showed a yearly variation. The high variation was witnessed in the onset of the growing season (late April) and the end of the growing season (late October) due to the green up and the senescence processes of vegetation, respectively, whereas the lowest variation occurred in July during the peak of the growing season (Figure 5). The high variation was also observed from late 2000 to 2003 and in late 2009, which may be due to the high frequency of fire occurrence reported during this period for which some locations were heavily affected (Farukh et al., 2009). In relation to climatic variables, however, there is evidence of the strong negative relationship between temperature during the growing season and NDVI heterogeneity (COV_{NDVI} = 0.001*Tair^2 – 0.065*Tair + 1.125, R^2 = 0.77). In other words, lower temperature in the early and late periods of the growing season is correlated with more vegetation dynamics.

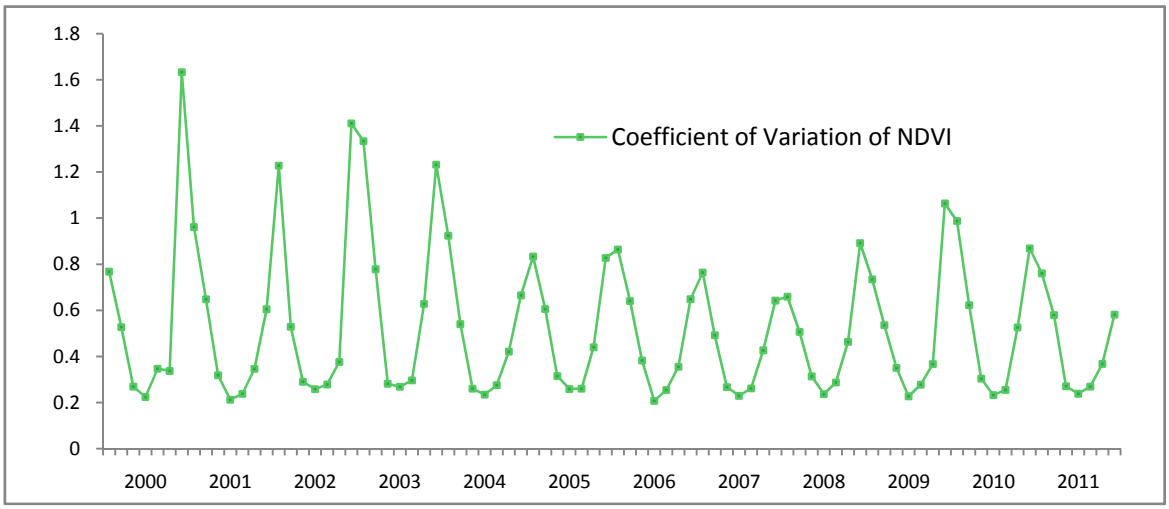

Figure 5. Temporal heterogeneity of NDVI in Hovsgol forest during the growing season from April to October (2000-2011) – COV was derived from NDVI values of 150 random samples within the area during the growing season over 12 years

3.4 Spatial Pattern of Annual NDVI Changes

Distribution of the high NDVI variation is shown in the western part of the Hovsgol Lake, including Darhad valley (Figure 6). According to the land cover map in 2005 (http://daac.ornl.gov/), the high variation areas are mainly covered by grassland and open shrublands. The result infers that these areas were highly affected by disturbances from 2000 to 2011.

In order to develop support for the findings of temporal heterogeneity in the area, the departure from average *July* NDVI images were derived (Figure 7). The below average values stand for negative changes, while above average values correspond to positive vegetation growth. Forest areas in 2002, 2003, 2005, 2007, 2008, 2009, and 2011 experienced severe growth conditions as illustrated by the large area of below average NDVI. On the other hand, a high proportion of positive changes were witnessed in 2000, 2001, 2004, 2006, and 2010 as a result of vegetation responses following a heavy disturbance event (i.e. severe condition in 2002, 2003 following by vegetation regrowth in 2004). Post disturbance landscapes caused by fire or climate change are typically characterized by a high degree of spatial variability immediately following the disturbance due to the response and distribution of biotic and abiotic factors (Liu et al., 2009; Van Leeuwen et al., 2010). This statement may be correct in this study. However, in order to fully understand the effects of climate change and other disturbances on spatial variation, land cover type, species components, and biophysical variables should be investigated and considered interrelated.

Finally, the average vegetation growth dynamics over 12 years was assessed based on the July 2000 NDVI image and July 2011 NDVI image. Overall, the large amount of vegetation negatively responds to growth conditions over 12 years, particularly in Darhad valley with 15-35% of losses being greenness (Figure 8).

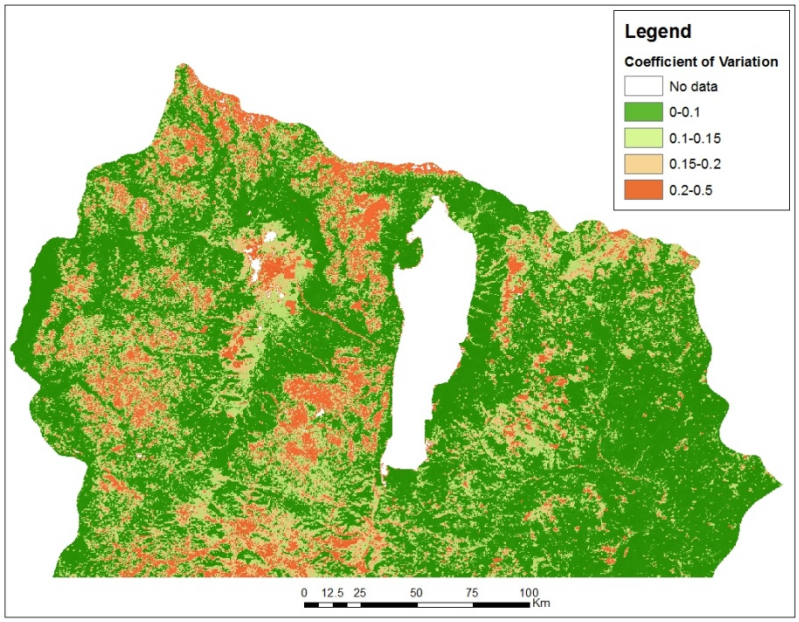

Figure 6. Coefficient of variation of NDVI values over 12 years (2000-2011) in Hovsgol area

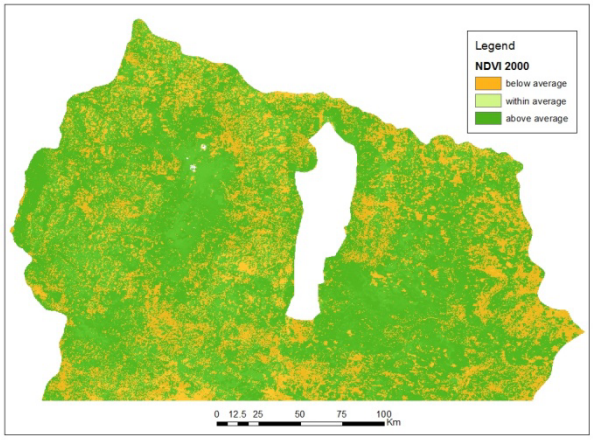

2000

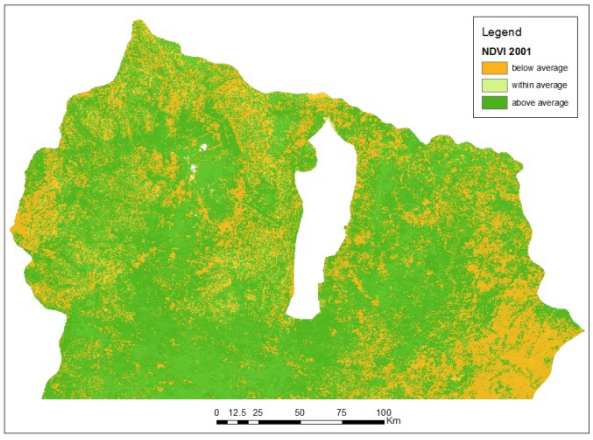

2001

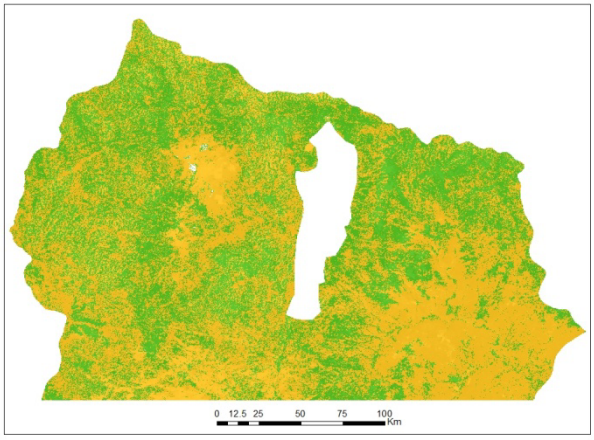

2002

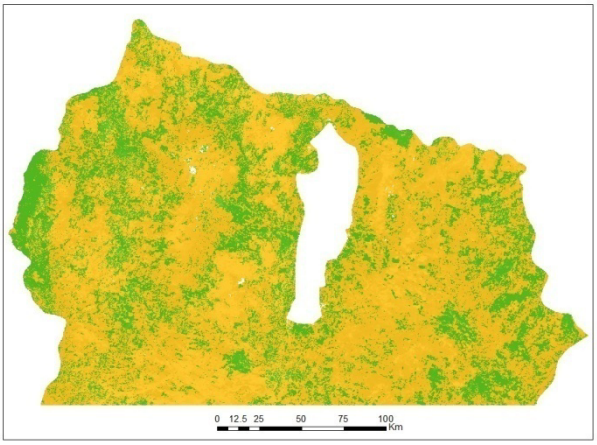

2003

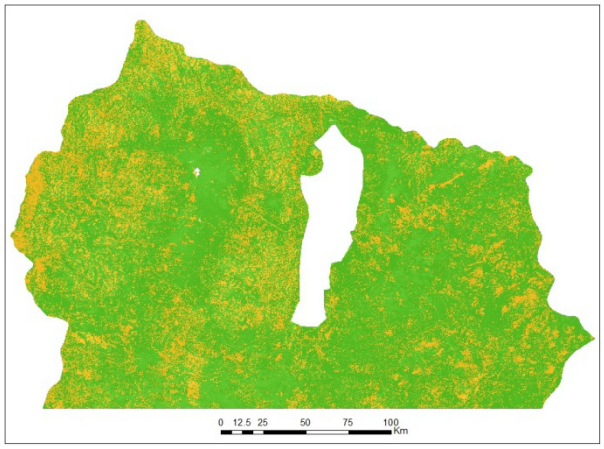

2004

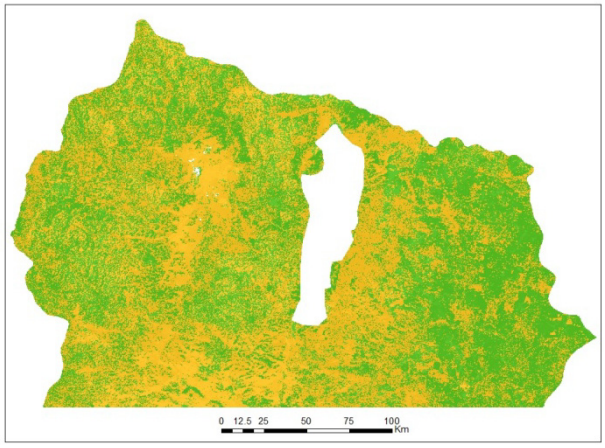

2005

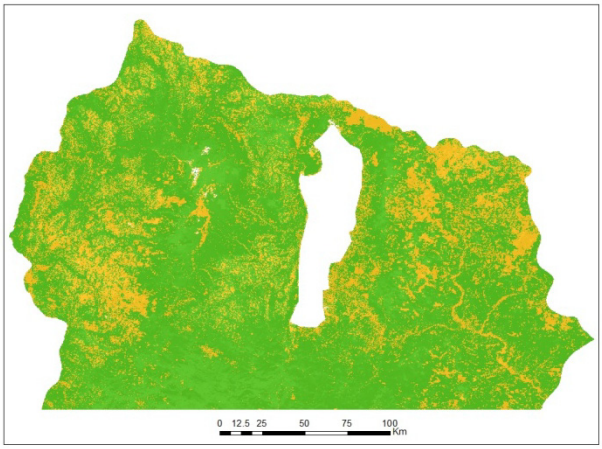

2006

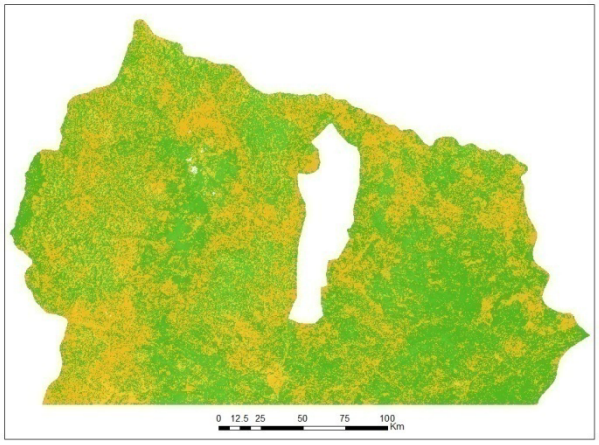

2007

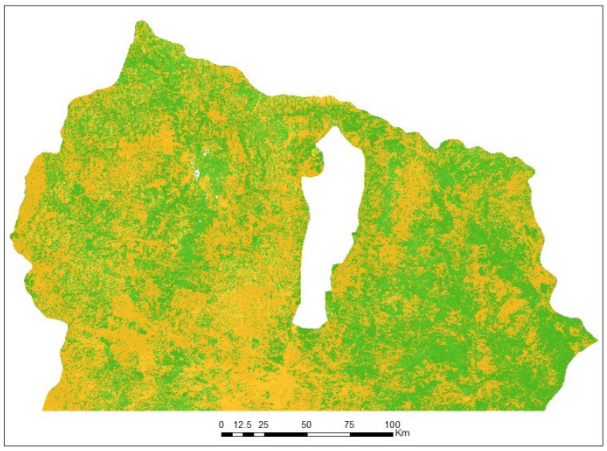

2008

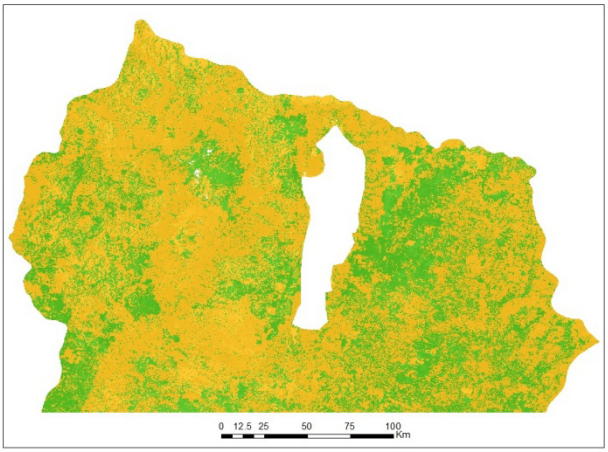

2009

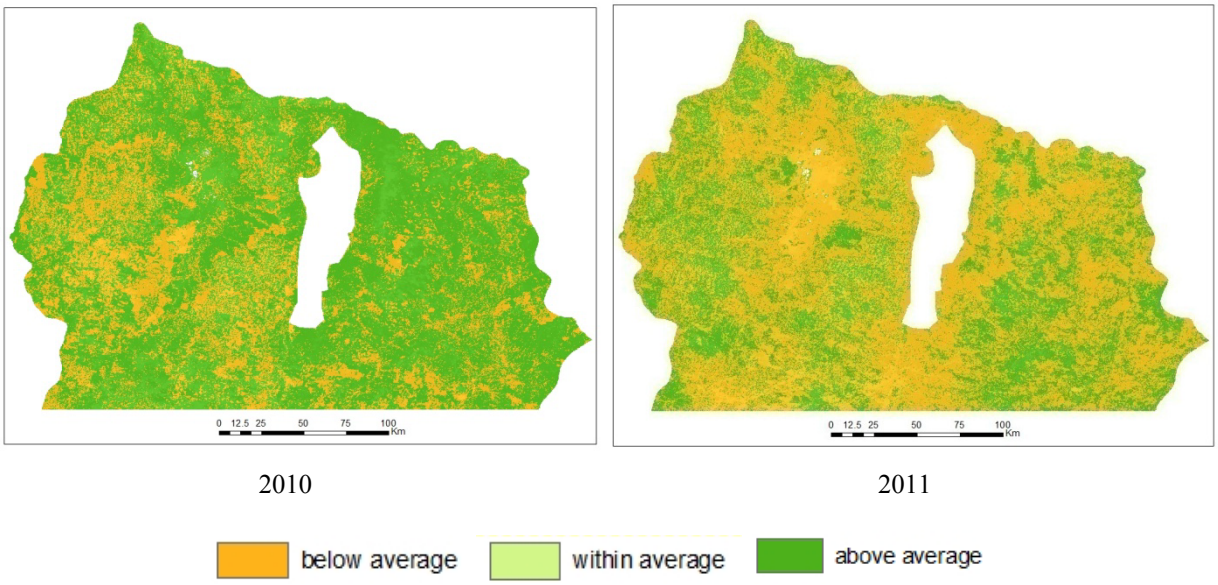

Figure 7. Departure from average July NDVI images (2000-2011), Hovsgol, Mongolia

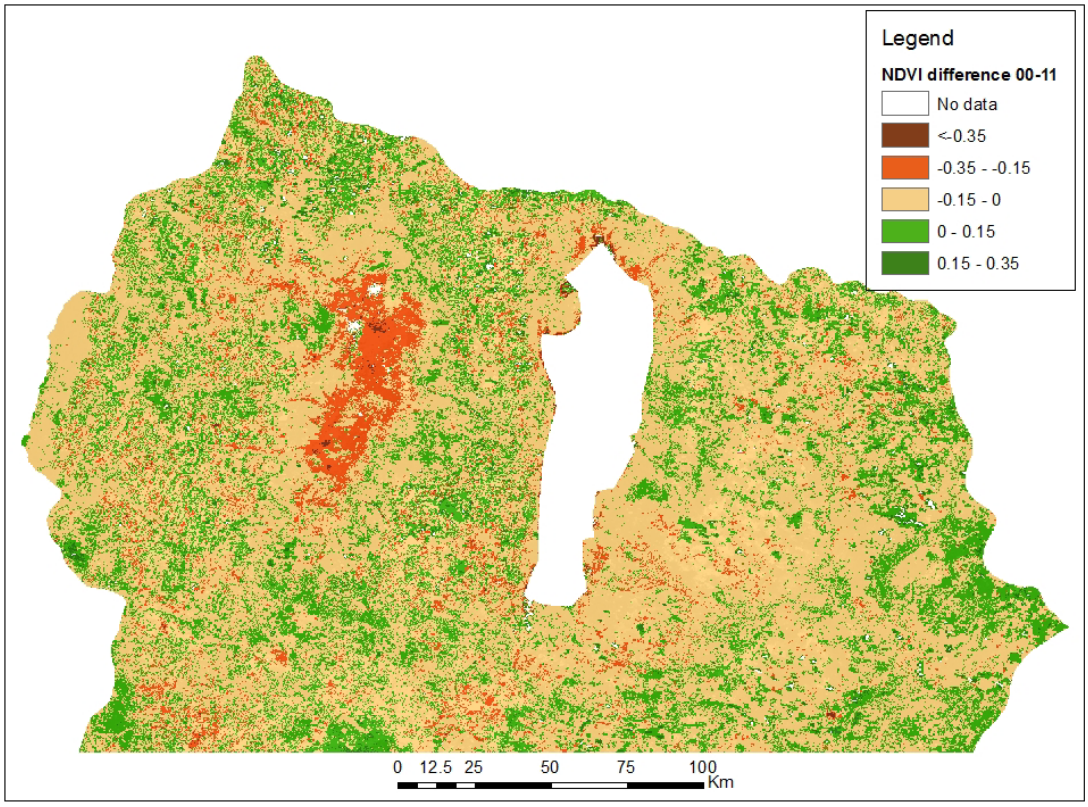

Figure 8. NDVI difference image of Hovsgol, Mongolia between 2000 and 2011

4. Conclusion and Future Work

Remotely sensed time series data from the MODIS sensor were used to estimate air temperature at the pixel level, extract the phenological metrics, characterize the temporal and spatial dynamics of vegetation, and evaluate the effects of climate change on vegetation in the Hovsgol area. Air temperature can be well estimated using the TVX regression model with a mean absolute error of 2.2^{o}C. The growing season in the area normally starts in

late April and ends in late October, and the peak of the growing season is reached in July. However, due to climate change and other disturbances, the length of the growing season among the observed years fluctuated between 166 and 198 days. The higher temperature results in a longer and earlier growing season (correlation between the length and temperature, the timing start and temperature with R^2 = 0.5 and 0.58 respectively). Precipitation, on the other hand, was insignificant with phenological variables dynamics.

Temperature and NDVI have illustrated strong yearly cyclic variation for the past 12 years. The highest mean air temperature during the growing season was witnessed in July at 20.6^{o}C and the lowest was in October at 2.3^{o}C. There was a strongly positive relationship between NDVI, air temperature, and precipitation during the growing season. Air temperature; however, seems to be the main factor contributing to NDVI variation in the area. In order to have strong evidence of climate change effects on vegetation growth, longer time series of satellite data such as NOAA AVHRR should be included to increase the observed timeframe probably up to 30 years. This is entirely possible as available daily NOAA AVHRR data can be downloaded for the area.

A high degree of NDVI variation was estimated in early April and late October of the growing seasons of 2000, 2001, 2002, 2003, and 2009. This may show the degree of vegetation response post disturbances in previous months and years, except for 2000 and 2001, as the spatial pattern of NDVI in July 2002, 2003, 2005, 2007, 2008, 2009, and 2011 illustrated the high level of degradation departing from average NDVI. However, identifying of disturbed areas by wildfire, logging, or climate change in specific and longer timeframes will be necessary to fully explain the interrelationship between disturbance events and vegetation responses. Finally, analysis of spatio-temporal heterogeneity using NDVI time series over 12 years also indicated that some areas with high variation of vegetation growth, particularly in the western part of the Hovsgol lake and Darhad valley.

Further explanations of climatic change and other disturbances such as wildfires and deforestation effects on vegetation dynamics and recovery will require the consideration of land use, land cover types, vegetation community, and structure for a certain time period. Because of remote sensing tool capabilities, these types of investigations can be conducted spatially and temporally by different sensors and scales, providing the opportunity to understand vegetation response after disturbances, especially following wildfires in Mongolia.

Acknowledgement

This study was funded by Vietnam International Education Development Program and Department of Geography and Planning, University of Saskatchewan scholarships. The authors acknowledge the anonymous reviewers, Jordon Steeg for their valuable comments and suggestions for improving this manuscript.

References

Banzragch, N., J. Scott Greene, & Clyde, E. Goulden. (2007). Trends in extreme daily precipitation and temperature near lake Hovsgol, Mongolia. *International Journal of Climatology, 27*, 341-347. http://dx.doi.org/10.1002/joc.1404

Batima, P., Natsagdorj, L., Gombluudev, P., & Erdenetsetseg, B. (2005). Observed climate change in Mongolia. *Assess Imp Adapt Clim Change Work Pap, 12*, 1-26.

Casady, G. M., van Leeuwen, W. J. D., & Marsh, S. E. (2009). Evaluating post-wildfire vegetation regeneration as a response to multiple environmental determinants. *Environmental Modeling and Assessment, 15*(5), 295-307. http://dx.doi.org/10.1007/s10666-009-9210-x

Dulamsuren, C., Hauck, M., & Leuschner, C. (2010). Recent drought stress leads to growth reductions in Larix sibirica in the western Khentey, Mongolia. *Global Change Biology, 16*(11), 3024-3035.

Erdenesaikhan, N. (2002). Time series satellite data analysis for assessment of vegetation cover of Mongolia. *ESRI's 22nd Annual User Conference*.

Farukh, M. A., Hayasaka, H., & Mishigdorj, O. (2009). Recent Tendency of Mongolian Wildland Fire Incidence: Analysis Using MODIS Hotspot and Weather Data. *Journal of Natural Disaster Science, 31*(1), 23-33. http://dx.doi.org/10.2328/jnds.31.23

Guo, X., Wilmshurst, J., McCanny, S., Fargey, P., & Richard, P. (2004). Measuring Spatial and Vertical Heterogeneity of Grasslands using Remote Sensing Techniques. *Journal of Environmental Informatics, 1726-2135*, 24-32.

IFFN. (1999). Forest and Steppe fire Monitoring in Mongolia using Satellite Remote sensing. *International Forest Fire News (IFFN), 21*, 71-74.

IFFN. (2007). The Forest Fire Situation in Mongolia. *International Forest Fire News (IFFN), 3*, 46-66.

James, T. M. (2011). Temperature sensitivity and recruitment dynamics of Siberian larch (Larix sibirica) and Siberian spruce (Picea obovata) in northern Mongolia's boreal forest. *Forest Ecology and Management*.

Jonsson, P., & Eklundh, L. (2002). Seasonality extraction by function fitting to time-series of satellite sensor data. *Geoscience and Remote Sensing, IEEE Transactions on, 40*(8), 1824-1832.

Jonsson, P., & Eklundh, L. (2004). TIMESAT--a program for analyzing time-series of satellite sensor data. *Computers & Geosciences, 30*(8), 833-845. http://dx.doi.org/10.1016/j.cageo.2004.05.006

Leon, J. R. R., van Leeuwen, W. J. D., & Casady, G. M. (2012). Using MODIS-NDVI for the Modeling of Post-Wildfire Vegetation Response as a Function of Environmental Conditions and Pre-Fire Restoration Treatments. *Remote Sensing, 4*(3), 598-621. http://dx.doi.org/10.3390/rs4030598

Liu, S., Mo, X., Zhao, W., Naeimi, V., Dai, D., Shu, C., & Mao, L. (2009). Temporal variation of soil moisture over the Wuding River basin assessed with an eco-hydrological model, in-situ observations and remote sensing. *Hydrology and Earth System Sciences, 13*(7), 1375-1398. http://dx.doi.org/10.5194/hess-13-1375-2009

Magsar Erdenetuya, S. K. (1999). Fire Monitoring in Mongolia. *GISdevelopment.net, ACRS, Poster Session 4*.

Murray, M. (2004). Dynamics of Biodiversity Loss and Permafrost Melt in Lake Hovsgol National Park, Mongolia. *Hovsgol GEF/WB Project TF028988, Geo-Ecology Institute 301, Mongolia*.

Nieto, H. C., Sandholt, I., Aguado, I., Chuvieco, E., & Stisen, S. (2011). Air temperature estimation with MSG-SEVIRI data: Calibration and validation of the TVX algorithm for the Iberian Peninsula. *Remote Sensing of Environment, 115*(1), 107-116. http://dx.doi.org/10.1016/j.rse.2010.08.010

Prihodko, L., & Goward, S. N. (1997). Estimation of air temperature from remotely sensed surface observations. *Remote Sensing of Environment, 60*(3), 335-346. http://dx.doi.org/10.1016/S0034-4257(96)00216-7

Ravenscroft, C., Scheller, R. M., Mladenoff, D. J., & White, M. A. (2010). Forest restoration in a mixed-ownership landscape under climate change. *Ecological Applications, 20*(2), 327-346. http://dx.doi.org/10.1890/08-1698.1

Sanjaa Tuya, C. P. G., & Yoshiaki Honda. (2002). Fire detection technology in Mongolia. *Hazard Mitigation and Disaster management*.

Sato, T., & Kimura, F. (2006). Regional climate simulations to diagnose environmental changes in Mongolia. *Bull Terr Environ Res Cent Univ Tsukuba, 7*, 59-69.

USGS. (2011). MODIS reprojection tool user's manual. *Land Processes DAAC, USGS Earth Resouces Observation and Science (EROS) Center, 4.1*.

Van Leeuwen, W. J. (2008). Monitoring the effects of forest restoration treatments on post-fire vegetation recovery with MODIS multitemporal data. *Sensors, 8*(3), 2017-2042. http://dx.doi.org/10.3390/s8032017

Van Leeuwen, W. J. D., Casady, G. M., Neary, D. G., Bautista, S., Alloza, J. A., Carmel, Y., … Barron J. O. (2010). Monitoring post-wildfire vegetation response with remotely sensed time-series data in Spain, USA and Israel. *International Journal of Wildland Fire, 19*(1), 75-93. http://dx.doi.org/10.1071/WF08078

Vancutsem, C., Ceccato, P., Dinku, T., & Connor, S. J. (2010). Evaluation of MODIS land surface temperature data to estimate air temperature in different ecosystems over Africa. *Remote Sensing of Environment, 114*(2), 449-465. http://dx.doi.org/10.1016/j.rse.2009.10.002

Veraverbeke, S., Gitas, I., Katagis, T., Polychronaki, A., Somers, B., & Goossens, R. (2011). Assessing post-fire vegetation recovery using red - near infrared vegetation indices: Accounting for background and vegetation variability. *ISPRS Journal of Photogrammetry and Remote Sensing, 68*, 28-39.

Walther, G. R., Post, E., Convey, P., Menzel, A., Parmesan, C., Beebee, T. J. C., et al. (2002). Ecological responses to recent climate change. *Nature, 416*(6879), 389-395. http://dx.doi.org/10.1038/416389a

Xiaohui Yang, X. G. (2011). Remote sensing of Vegetation Productivity in Northern Ecosystems: NDVI change figures and maps. *Report for Parks Canada*.

Yu, F., Price, K. P., Ellis, J., & Kastens, D. (2004). Satellite observations of the seasonal vegetation growth in central Asia: 1982-1990. *Photogrammetric engineering and remote sensing, 70*(4), 461-469.

Yu, F., Price, K. P., Ellis, J., & Shi, P. (2003). Response of seasonal vegetation development to climatic variations in eastern central Asia. *Remote Sensing of Environment, 87*(1), 42-54. http://dx.doi.org/10.1016/S0034-4257(03)00144-5

Zhang, C., Guo X., Wilmshurst, J. F., & Crump, S. (2008). Monitoring Temporal Heterogeneity in a Protected Mixed Prairie Ecosystem Using 10 day NDVI Composite. *Prairie Forum, 33*(1), 145-166.

Earth Science Research; Vol. 1, No. 2; 2012
ISSN 1927-0542 E-ISSN 1927-0550
Published by Canadian Center of Science and Education

Nonmetal and No Diameter Damage Borehole Wall Strengthening Technology

Lu Chunhua[1], Jiang Guosheng[1], Zhang Tao[1] & Fan Jiaxing[1]

[1] Engineering Faculty, China University of Geosciences, Wuhan, China

Correspondence: Lu Chunhua, Engineering Faculty, China University of Geosciences, No. 388 Lumo Road, Wuhan, China. Tel: 86-27-8748-1030. E-mail: cuglch@yahoo.cn

Received: June 14, 2012 Accepted: June 28, 2012 Online Published: July 30, 2012

doi:10.5539/esr.v1n2p291 URL: http://dx.doi.org/10.5539/esr.v1n2p291

Abstract

Instability of borehole wall is a common phenomenon when drilling in complex strata, which bring great difficulties to drilling. Traditional way of casing pipe can isolate unstable borehole wall reliably, however, there are some shortcomings: for example, reducing hole-diameter etc. In order to seek a simple, effective and no diameter damage way for supporting collapsed well section, the project team devotes to research hot-melt way used in dry hole and polyurethane way used in hole with water. The paper elaborates process principle and indoor tests of the two ways in detail. Study indicate, the two kinds of nonmetal borehole wall strengthening technology have many advantages, like simple to operate, effect is significant and no diameter to diameter of borehole, which have certain application prospect.

Keywords: borehole wall strengthening, hot-metal way, polyurethane

1. Introduction

When drilling, maintaining the stability of the sidewall is one of the basic conditions to ensure normal drilling. The collapses of sidewall can result in burying drilling tools, delaying construction period and even abandoning the borehole, which will make a huge economic loss (Shi & Liu, 2004; Peng & Dou, 2010). However, the sidewall instability is a prevalent technical challenge in the process of drilling and has been plagued for a long time (Chen, 1981; Yang & Su, 2008). For minor collapse in the drilling process, generally through using the high quality mud won't cause difficulties to drilling, but if drilling in broken and collapsed formation, in the short term, the sidewall will form a large-scale collapse and this situation is usually dealt with by supporting technologies of casing etc (Du & Hu, 1992; Chen & Sun, 2008). This paper will introduce two kinds of nonmetal sidewall strengthening technologies which have many advantages, like simple to operate, effect is significant and no damage to diameter of borehole.

2. Hot-melt Process Principle of Supporting the Sidewall

The basic principle of hot-melt method to reinforce the hole wall is shown in Figure 1, in the figure, 1 is to be reinforced sidewall, 2 is hot-melt granular materials, 3 is heating unit and 4 is reinforced sidewall. The heating element 3 produces a lot of heat and lifts slowly along the arrow of diagram, when encountering with the heating element, the hot-melt granular materials 2 (or hot melt pipe) will melt or soften quickly, and then part of the material will be squeezed into the cracks of sidewall to bond the broken rock together as a whole, in addition, the other part of the material will form casing support in the sidewall, so as to achieve the purpose of reinforcing sidewall.

The hot-melt method to reinforce sidewall can be divided into three processes: melting or softening, extrusion molding, cooling and solidifying.

1) Melting or softening: Through the heating element to produce a certain amount of heat to the melting point or softening point of the material, so make it in flow or semi-fluid state. For hot melt pipes, they will reach the softening state. For hot-melt granular materials, they will melt, reaching a flow or semi-fluid state.

2) Extrusion molding: After melting or softening material, in the extrusion of the heating element, part of the fluid material will be squeezed into the rock fractures to bond the broken rocks together, another part of the material is continuously adhere to the borewall to form the casing in order to achieve the purpose of supporting sidewall.

3) Cooling and solidifying: After molding, the physical and mechanical properties of the material only within a certain temperature range will be showed. After the extrusion stage, the material must have been solidified for a short time will reach a certain strength is qualified for the role of supporting and strengthening the sidewall.

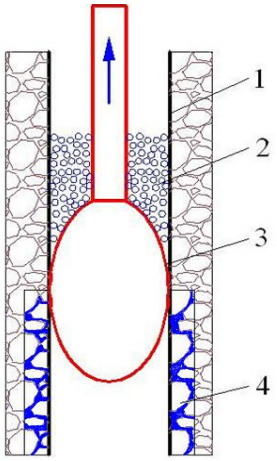

1-to be reinforced sidewall;

2-hot-melt granular materials;

3-heating unit;

4-reinforced sidewall

Figure 1. Hot-melt process principle of supporting the sidewall

3. Experiment of Hot-melt to Support Sidewall

After plenty of investigation and testing the properties of the material, the project team confirm two granular materials which are suitable for hot-melt sidewall reinforcement. The materials are TPU (Thermoplastic polyurethanes) hot melt adhesive and EVA (ethylene-vinyl acetate copo) hot melt adhesive.

TPU is a kind of hot plastic polyurethane adhesive, have excellent rubber characteristic, can adapt to different thermal expansion coefficient of adhesion base material, it has formed between the base material soft-hard transition layer, not only stick relay is strong, also excellent buffering, shock absorption function, have excellent flexibility characteristics, shear strength and impact resistance characteristics, it is suitable for various structural bonding field (Liu & Wu, 2008; Liu & Li, 2010). Its shape is granular, particle size is Φ 2-3 mm, basic performance parameters of the material is shown in Table 1.

Table 1. Basic performance parameters of TPU hot-melt adhesive

Product name	Melting temperature range ℃	Molten index g/10min @160℃	Viscosity Pa.s @160℃	Thermal bonding temperature ℃	Thermal bonding pressure kg/cm^2
TPU	95-115	50	300	135-150	0.2-0.5

EVA is a kind of translucent to opaque white wax-like material, soft and elastic rubber, can lengthen, non-toxic, tasteless. Cohesion of EVA is strong, melting surface tension is small. EVA can adhere to almost all materials, which have many advantages, like high solidifying speed, solified body with high strength and toughness. The basic properties parameters of the EVA in Table 2.

Table 2. Basic performance parameters of EVA hot-melt adhesive

Product name	Melting temperature range ℃	Molten index g/10min @160℃	Viscosity Pa.s @160℃	Thermal bonding temperature ℃	Thermal bonding pressure kg/cm^2
EVA	75-90	150	180	90-120	0.1-1.5

At the same time, carry out the indoor experiment, to simulate the sidewall, the project team designs the sidewall simulator as the Figure 2. The main part of the device was made of one cylinder, and the cylinder was cut open symmetry in axial. Outside of the main subject is equipped with the lathedog and the landing leg, in the bottom was equipped with the end cover. The landing leg is fixed with the ground through the rivet. The cylinder is perpendicular to the ground.

Figure 2. Sidewall simulator

Figure 3. The reinforcement sidewall effect by the EVA hot melt adhesive

When carry out the experiment, first to put another cylinder into the inner cylinder, then put some small stones or other materials into the clearance between the inside cylinder and the outside cylinder in order to simulate the different cranny sidewall. Connect the heat device well, operate the power head rig, at the meanwhile make the heat unit lie in the bottom of the artificial sidewall. Connect the electric power source of the heat device. Adjust the power to the proper quantity, and monitor the surface temperature of the heat unit constantly. When the temperature reach to the proper quantity, put the hot melt materials from the artificial wellhead. Operate the rig and make the heat unit move up slowly and with uniform velocity. Cooling and moldng in a short time, then open the simulating sidewall, observe and detect the reinforcement effect of the sidewall (Tan & Dai, 2006; Sun, Wu, & Tang, 2005).

The project team carried out plenty of experiments. Find out the reinforcing effects of the EVA and the TPU granular hot melt material good, especially the effect of the mixture of the two is the best.

The sidewall reinforcing effect of the EVA hot melt adhesive is showed as the Figure 3. This material have many advantages, such as low melting point, high speed molding, bonding with the sidewall firmly, after melting the material can be permeate into the fracture of the sidewall, formed pipe shape is regular. The disadvantage is that the material has a certain brittle after cooling and molding.

The characteristic of hole wall reinforcement by TPU hot melt adhesive is as follows: formed relatively complete casing pipe, granule melting completely, part of the molten hot melt adhesive can be well squeezed into the hole wall cracks and cemented, having nice toughness after Cooling molding but the hardness not as well as EVA hot melt adhesive.

Considering the advantages and disadvantages of EVA and TPU hot melt adhesive, mixed granular materials of EVA and TPU can obtain desired reinforcement effect: relatively high toughness and strength, part of the hot melt adhesive squeezed into the hole wall cracks and strongly cemented, then forming relatively complete casing pipe.

4. Process Principle of Polyurethane Reinforcing Borehole Wall

Polyurethane is a kind of synthetic polymer plugging material through polyisocyanate polyether polyol, which is commonly known as swelling rubber. The material can react with water and form consolidation body. It has the advantages of high molding strength, high curing speed, high chemical stability of consolidation body, adjustable molding speed, non-toxic and no pollution to environment, etc. The process principle of polyurethane reinforcing borehole wall is shown in Figure 4.

When strata need to be reinforced, take irrigator down into required reinforcing borehole section. The irrigator is full of liquid polyurethane. Once liquid polyurethane squeezed out of irrigator, it reacts violently with water in the hole. The volume rapidly expand and full of the hole section, and squeeze into hole wall cracks. The material

can achieve high consolidation strength in a short period of time. Then take sweep hole drilling with the same diameter drill bit.

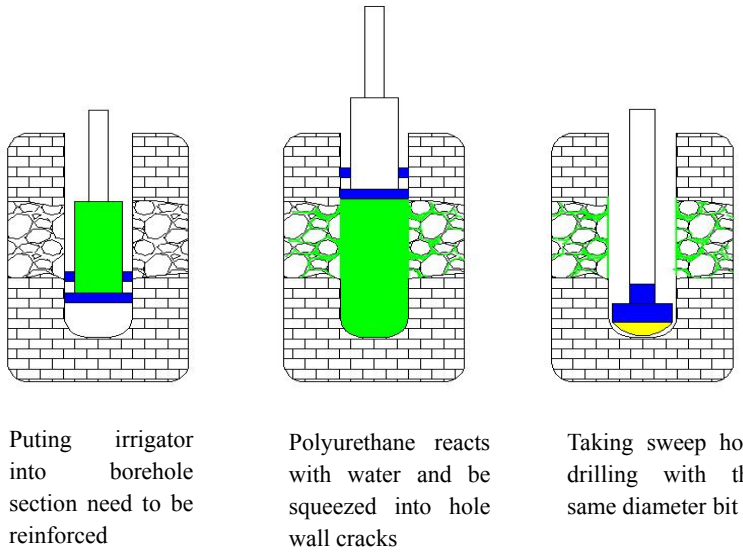

Figure 4. Schematic diagram of reinforcing borehole wall with polyurethane

5. Laboratory Test of Reinforcing Borehole Wall

5.1 Test 1: Seal Reinforcement Test

Test Method: taking a certain amount of gravel into the container, adding water until submerging gravel, then adding the liquid polyurethane material, sealing the container and observing experimental phenomenon.

Test Results: the reaction of polyurethane with water is violent. The multiple of material expansion is limited to about 3 times. The bond between gravel and polyurethane is strong. The consolidation body is relatively dense and itself has high strength. The result is as shown in Figure 5.

In addition, the team carried out several tests in the case of different multiples of material expansion. The result shows that with smaller multiples of polyurethane expansion, the consolidation body has higher strength and bond. With multiple of polyurethane expansion increasing, bond strength between polyurethane and gravel reduce. Therefore, it is essential to choose a reasonable multiple of polyurethane expansion. Through experiments can learn that when the multiple of polyurethane expansion is more than 10 times, the strength of cemented body reduce significantly. When the multiple of polyurethane expansion is 5 times, its strength and the other parameters are reasonable. Therefore recommend choosing multiple of polyurethane expansion at about five times in actual reinforcing borehole wall.

Figure 5. Formed concretion body of polyurethane and water

Figure 6. The artificial simulation sidewall which is made of the small stones

5.2 Test 2: Reinforcement Tests of Artificial Simulation Sidewall

Test method: Using the small stones to make the artificial simulation sidewall that is showed as the Fig 6, and the inner diameter of the artificial simulation sidewall is 30mm, the wall thickness is 25mm, the porosity is about 30% and the length of sidewall is 100mm. First fill up with water in the artificial simulation sidewall, then add 400ml liquid polyurethane, and take seal measures in the orifice, in the meantime control the expansion multiple of the polyurethane in about 5 times, watched experiment phenomenon.

Test results: After testing, the reinforcement effect of the artificial simulation sidewall is shown as the Fig 7, from which we can see the inner hole is full of the concretion that is generated by the chemical reaction between polyurethane and water. Meanwhile, under the inflation pressure, some concretion permeate into the gap of the artificial simulation sidewall, these concretions make the artificial simulation bond firmly into a whole, in a word the reinforcement effect of the sidewall is remarkable.

Figure 7. the reinforcement effect of the artificial simulation sidewall

6. Discussion

1) The Melt method is a new technology that is used to reinforce the sidewall by bonding the broken rock mass. Firstly, heating up the hot melt materials which are granular till melting down by the heating unit, then push the melted materials in the sidewall fracture. The process principle and the traditional sidewall reinforcement technique are completely different. It mainly used in the dry hole, and the key techniques are the properties of the hot melt materials and the design of the high power heating unit.

2) The method of the polyurethane supporting sidewall is using the properties that the polyurethane will solidify quickly after the chemical react with water. In the process of expanding, the polyurethane permeates into the sidewall fracture. After solidifying, the whole sidewall that is rupture and easy slump will bond firmly into a whole. Finally achieve the purpose of supporting sidewall. The method is mainly used in the hole with water, the key techniques is to control the distension rate and solidifying speed of polyurethane. The test shows that when the distension rate of the polyurethane is under the control of about 5 times, all of the technical indicators are good.

3) Compared with the traditional way of casing sidewall supporting, the hot melt method and the polyurethane sidewall reinforcement technology have many advantages, such as simple operation, low cost, at the same time not reduce the hole diameter etc.With the mineral exploration turn to the deep, when we drill the complex stratum, the problems that the sidewall destabilization will more and more. The nonmetal sidewall reinforcement technology provides a new choice, and it has a certain application prospect.

Acknowledgements

This research was supported by special funds used for central university basic scientific research and dig and drill research center of ministry of education, thank all person offer help to the project research.

References

Chen, J., & Sun, L. (2008). Techonlogy of well cementing with expandable tube and its application. *Exploration engineering, 8*, 19-21.

Chen, Z. C. (1981). Situation and prospect of supporting the hole walls and plugging the leaky zone with cement.

Du, H., & Hu, Z. Y. (1992). Practice and discussion on supporting the hole walls and plugging the leaky zone with common portland cement. *Coal Geology & Exploration, 20*(2), 63-65.

Liu, C. L., & Wu, D. (2008). Study on Toughening of POM by TPU. *Polyurethane industry, 23*(4), 12-15.

Liu, C., & Li, X. L. (2010). The modification of polyurethanefoam in coal mine. *Coal mine safety, 426*, 10-12.

Peng, Z. M., & Dou, S. B. (2010). Commentary development status of expandable casing technology at home and aboard. *Jointing pipe, 33*(6), 5-9.

Shi, D. Q., & Liu, G. (2004). Research and treatment of borehole walls' collapse and landslide accidents. *West-china Exploration Engineering, 7*, 124-25.

Sun, R. M., Wu, L. J., & Tang, F. L. (2005). Experimental research on hot melt drilling technology. *Geological Science and Technology Information, 24*(7), 23-26.

Tan, L. H., & Dai, Y. M. (2006). Progress in study on the reinforced rigid polyurethane. *Materials Review, 9*, 21-24.

Yang, Z. J., & Su, C. M. (2008). Advances in sidewall strengthening technology. *Fault-block oil & gas field, 15*(3), 99-102.

Earth Science Research; Vol. 1, No. 2; 2012
ISSN 1927-0542 E-ISSN 1927-0550
Published by Canadian Center of Science and Education

The Urban Land Ecosystem Health Evaluation in Chengdu City

Zhou Ting[1] & Yin Qi[1]

[1] College of Economics and Management, Sichuan Agricultural University, Wen'jiang, Sichuan, China

Correspondence: Yin Qi, College of Economics and Management, Sichuan Agricultural University, Wen'jiang 611130, Sichuan, China. E-mail: 25575670@qq.com

Receive: July 10, 2012 Accepted: July 23, 2012 Online Published: July 30, 2012

doi:10.5539/esr.v1n2p297 URL: http://dx.doi.org/10.5539/esr.v1n2p297

Abstract

This article declares the connotation of the Urban Land Ecosystem Health by ecological economics theory and method based on the study of ecosystem health. Besides, this paper constructs the evaluation system composed of "Vigor-Organization-Resilience-Ecosystem service function-Lifestyle" to analyse the urban land ecosystem healthy status in Chengdu city, and the evaluation results are calculated by parametric synthesis method. The results indicate that the system has been generally getting healthier from 2001 to 2009, ending up with a relative stable state in recent years, which is attributed to a series of policies. Thus, it is necessary for the government to take measures to spur the city vigor release, resilience and service enhancement, and a positive attitude towards the urban land ecosystem healthy protection should be established among the public.

Keywords: urban land ecosystem, health, evaluation, Chengdu

1. Introduction

Modern economic development has brought us better life of high quality with convenient lifestyle. However, humans' increasing demand for city resources makes the urban load capacity now close to saturation. We're suffering stresses such as environment containment, energy shortage, traffic congestion and restriction of raising living standard. As one of the most important resources for urban construction, land has become the bottleneck of regional development. Not only the construction land use change and its spatial pattern adjustment, but also the food safety threat resulting from a consistent amount of farm land transforming into a construction one, would play an important role in the social and economic region development. As a result, building a harmony and healthy urban land ecosystem is the internal demand for a sustainable land use, as well as the basic of keeping city prosperous. Therefore, this paper aims to evaluate the urban land ecosystem health in Chengdu city based on its urban development planning and function orientation, so as to supply a reasonable political suggestion for a sound development.

Up to the present, several researchers have studied health evaluation for different kinds of urban ecosystem . The evaluation system tends to be a richer and more practical one associating with the deeper connotation of the ecosystem as well as basing on the classical land health evaluation system called "pressure-state-response". For instance, Li Weihai chooses "vigor-organization-function-resilience" factors integrating into the "pressure" indicator in PSR system, so as to analyse the health state of ecosystem environment in Guiyang city, and the outcome reveals that the ecological security and service function in this region are declining, the ecological environment health is getting poorer. Guo Xiurui indicates that an urban ecosystem health evaluation should aim at a deeper study on human activities, environment change and their influences and threats on human and ecosystem health, rather than indicator system solely, thus she innovates the index system when analyzing urban ecosystem health by building "vigor-function-organization-ecosystem service function maintenance-public health" system. Ni Zhen adapts "vigor-vitality-resilience-ecosystem maintenance-ecosystem service-creativity" to evaluate realty industry ecosystem health in Chongqing city, and the outcome shows that the previous years are cooler sub-healthy, the latter years are developing into hotter sub-healthy and healthy.

2. The Connotation of Urban Land Ecosystem Health

The concept of "land health" could be traced back to the 1940s, when studies on ecosystem health had replaced that and developed into research focus. It was until 1980s that the program regarding land health firstly put forward in Canada, involving a general survey of soil through the whole country. Subsequently, some researchers spread out researches on several specific ecosystems, such as grassland ecosystem, lake basin

ecosystem, and wetland ecosystem. As for the more microcosmic urban land ecosystem, systematical health studies remain almost blank, and relevant theories need to be traced from the branch framework of "global ecosystem – land ecosystem – urban ecosystem – urban land ecosystem" to which this research subject was undertaken.

For example, Chen Meiqiu pointed out that, land health is a state that land remains its normal metabolism, and the system is capable of alleviating the harmful shock from external system by its own resilience, so as to achieve sustainable development through symbiosis, alternation and regeneration between the living body and inorganic environment. Besides, Cai Weimin holds that a healthy land utilize system is a healthy one composed of land utilize system structure, function and efficiency which aims to achieve sustainable development of human society, to spur to a harmonious unity among economy, society and ecology.

Based on the evidence from up to date literature, this paper summarizes that a healthy urban land ecosystem should be characterized by the following: 1 offering enough substance and energy needed by different groups of people; 2 a reasonable urban land structure, sustainable resources utilization and human lifestyle; 3 showing a certain flexibility to alleviate the outer harmful shock and sufficient resilience to keep the system stable. In terms of system efficiency, the service value of which supplies is unlikely to decline as time passing by; regarding the external force, the more natural or less amount a system depends on to keep itself steady, the healthier the system tends to be.

3. The Model Construction of Urban Land Ecosystem Health Evaluation in Chengdu City

Urban land ecosystem is a typical artificial system and composed by human willingness through city function realization. Therefore, the stability of system depends on human behaviors to a large extent, otherwise it couldn't be called a urban land ecosystem. In terms of Chengdu city, the landform of which appears to be plains, hills and mountains, it is likely to be replaced by desert ecosystem or forest ecosystem without human activities.

3.1 General Situation of Study Region

Chengdu is located in the hinterland of Sichuan Province, playing a role as political, economic and cultural center. It has a square of 12390 km^2 with fertile soil, and population of 140.5 million, subtropical monsoon climate, an average temperature of 16^oC, rich precipitation, cloudy and humid. The city stands on affluent biology resources and natural landscapes, with a view to modern economy construction, and has developed into the "western heart of China" – the core linkage of science, trade, finance, industry, transportation and communication in west regions through the country. The land resource configuration as well as land use regimes are closely related to the city construction, and especially the high urbanism rate and flourishing city strategies ask for an increasing amount of construction land. In recent years, the farm land remains steady with little decrease with the control of strict farm land policy, while the rise of construction land comes from mainly land consolidation, and a few amount of farm land collection. Besides, the utilize way tends to be more saving and intensive, such as metro and underground parking developing.

3.2 Methodology

3.2.1 The Evaluation System Construction

The evaluation system construction is the key element of ecosystem health evaluation. As the urban land ecosystem is a sub-system of urban ecosystem, the former one thereby owning the same characteristics as the urban ecosystem. Thus, we reserve the classical ecosystem evaluation system "vigor-organization-resilience" as a basic. In addition, since a healthy ecosystem should take individuals as the essential and tries to supply all kinds of services to meet city function, we take "ecosystem service function" to the evaluation system. Apart from that, as a humanistic system with a broader connotation, the health state of which is affected by human behaviours at every time, and the non-renewable resources consumed in daily life associated with the system sustainability, thereby the "lifestyle" is considered into the evaluation system. Therefore, this paper adapts "vigor-organization-resilience-ecosystem service function-lifestyle" to analyze the urban land ecosystem health in Chengdu city.

3.2.2 Indicators Selection

Generally, we select indicators by following the principle of data acquisition, regionality, scientific, representative, objectivity and early-warning.

Vigor is the direct expression of system health, which is represented by activity, metabolism and primary productivity. This can be reflected by macro economy development, resident purchasing power and real estate market activity.

Organization stands for the pattern and proportion of elements in the ecosystem, and the structure of which should stimulate to an efficient city function. As a result, we choose population density, science and education expenditure accounts for local finance, construction land area accounts for the urban area, factors contributing a lot to the indicator, to explain ecosystem organization.

Resilience reveals the capacity to keep system stable by restraining outer harmful shock. The way we dispose the discharge of waste water, gas and solid materials as well as the core resource--land, can be the best manifestation.

The ecosystem service function can be reflected by the closely related indicators concerning livelihood, such as medical treatment resource, transport capacity and job opportunities.

Lifestyle reveals the national quality directly, advocation of a low-carbon lifestyle helps the individuals build an awareness of ecosystem protection, which contributing to a sustainable resource utilize. By this way, we can select those absolutely necessary energy demand of citizens in daily life in an effective way, such as running water and household electricity consumption.

3.2.3 Index-weight Given

As various factors contribute differently to the ecosystem, we need to give proper weight to each index. To make sure the weight scientific and reasonable, we use entropy method--an objective method at the first, followed by analytic hierarchy process--a subjective method to revise the outcome according to the practical situation. Subsequently, we get parameter value of each factor in research years through dimensionless method (see Table 1).

3.2.4 Health value calculation

The comprehensive health score can be obtained by the weight sum of the weight and parameter value. The following step divides the score by the sum of maximum and minimum ones, so as to get G value--the urban land ecosystem health value (see Table 2) by the following formula:

$$G=\frac{X_i \times W_i}{[\max(X_i \times W_i)+\min(X_i \times W_i)]}(i=1,2,...,n) \quad (1)$$

Where, X_i and W_i stand for the parameter value and weight of each corresponding factor respectively; G represents the health value of urban land ecosystem.

According to the way of grading intensity in a land intensive use evaluation, we adapt cluster analysis method to grade the G value into groups with the help of software of SPSS 17.0, the principle of which is is to categorize data into groups basing on their similarity or difference. And the G values are finally divided into three grades as health, inferior healthy and poor health.

Table 1. The urban land ecosystem health evaluation index system and their proportions and values in Chengdu city

Evaluating indicator	Parameter factor	Weight	2009	2008	2007	2006	2005	2004	2003	2002	2001
Vigor	GDP growth (Gross domestic product growth) (%)	0.0423	61.91	0.00	100.00	40.48	33.33	35.71	21.43	23.81	35.71
	CPI (Consumer price index)	0.0709	100.00	16.11	68.12	6.04	78.31	0.00	61.49	43.45	4.58
	Housing investment accounts for real estate investment (RMB 10 000)	0.0907	100.00	93.27	92.61	49.46	22.85	6.54	7.27	3.20	0.00
Organiza-tion	Population density (person/km^2)	0.0732	4.41	0.00	12.05	20.48	21.60	43.22	58.10	91.76	100.00
	Science and education expenditure accounts for local finance (RMB 10 000)	0.0967	100.00	85.99	23.52	27.60	6.73	16.97	14.69	3.28	0.00
	Urban construction land accounts for the whole urban area (%)	0.1000	86.69	100.00	73.88	41.60	21.46	5.82	2.66	1.50	0.00
Resilience	Area of farmland increase by land consolidation (ha)	0.1103	78.34	94.11	100.00	50.64	11.84	0.00	4.71	2.80	0.32
	Comprehensive utilization of waste products (RMB 10 000)	0.1396	100.00	40.76	16.50	14.94	6.32	10.35	0.99	0.14	0.00
Ecosystem service function	Doctor numbers(person)	0.0693	100.00	73.06	49.26	25.82	16.47	13.55	0.00	14.02	15.52
	Urban road area per capita (m^2)	0.0419	100.00	72.48	58.81	55.58	81.48	62.77	65.83	3.24	0.00
	Registered urban unemployed number (person)	0.0600	13.19	0.00	38.97	11.97	69.74	75.14	22.52	27.61	100.00
Lifestyle	Urban living consumption of electricity (million kwh)	0.0595	46.16	100.00	99.35	83.858	94.36	84.57	0.00	7.13	5.04
	Residents water consumption (million tons)	0.0452	0.00	16.46	27.71	100.00	91.68	99.16	28.98	67.68	77.14

Data resources: <China city statistical yearbook>, <China land & resources almanac>, and <Sichuan statistical yearbook>.

Table 2. The evaluation results of urban land ecosystem health and their health grade in Chengdu city

Year	2006	2008	2005	2009	2004	2007	2003	2001	2002
G value	0.6953	0.6414	0.6160	0.6061	0.5965	0.5392	0.4663	0.3100	0.3047
Health grade	Health				Inferior health				Poor health

4. The Results of Urban Land Ecosystem Health Evaluation in Chengdu City

4.1 Outcomes

The data comes from related yearbooks and statistical sources, thus we can get corresponding parameter by dimensionless method (see Table 1), and calculate the G value for each year with formula 1, finally achieve the health grade (see Table 2).

4.2 Discussion

As is shown in Table 2, the average health value of urban land ecosystem in Chengdu is 0.5306, which is higher than that in the year of 2001, 2002 and 2003. The previous two years appear to be unhealthy while the other years are healthy and sub-healthy. The overall parameter values begin to climb sharply from 2002, and that of 2004 to 2009 rise smoothly, reaching the peak in 2006 and then fluctuating slightly. Generally speaking, the trend of urban land ecosystem health state in Chengdu city keeps optimistic.

During the study years, the Chengdu ecosystem suffered "5.12 Wenchuan earthquake" in 2008, the values of vigor indicator, especially relevant economic ones, were obviously impacted, GDP and CPI of that year were lower than that in the past years. However, after the disaster, the citizens' consumption ideas were no longer conservative generally, which spured to a new economy rise to some extent, hence the values of GDP and CPI had gone up again in 2009. Although facing the economy frustration, the government had tried best to keep the urban land ecosystem steady by taking several measures. Thus the value of medical treatment resources, science and education expenditure, disposal of waste discharge and urban road area per capita appeared to be relevantly stable.

The local government had also carried out positive policies to spur the healthy development of urban land ecosystem from the aspect of resilience and lifestyle indicators. For example, the implementation of environment protection regulations involving medical and electrical waste recycling regulation, taxation on pollution contributed to a certain extent of energy-saving and low carbon dioxide emission. Especially when the <Law of the People's Republic of China on Prevention of Environmental Pollution Caused by Solid Waste> came into force in 2005, the production value of waste goods multipurpose use rose greatly. All of those prove that various policy and regulations have come into the wind vane of industry developing, in turn, the rise and fall of parameter values reflect policy effectiveness as a barometer.

4.3 Conclusion and Suggestion

Human beings are not capable of dominating the natural law, but we need to comply with that and utilize the law reasonably as the first criterion to guide human behaviours. Besides, as the urban land ecosystem is a humanistic system, the prosperity of which still depends on the people's subjective initiative. As can be seen from the results illustrated above, several evaluation factors are affected by government policies. Therefore, it is wise for us to carry out sound plans not only to sustain the system vigor, but also to optimize its organization at the basis of economy development as well as science and technology innovation. In addition, we need develop a certain man-made ecological reconstruction when necessary, since it is not realistic to depend on the natural ecosystem resilience too much as it tends to be so long a term compared to a person's lifelong time. In summary, more efficient ways to build a healthier and more harmonious urban land ecosystem should be noticed, such as protection and utilization approaches on the natural landscape and resources, the advocation of low carbon dioxide lifestyle.

Researches on ecosystem health have been in a continuous hot discussion, as one branch study of that, urban land ecosystem is a forefront study comparatively. The progress not only needs to follow the general study framework, but also to show a view to the subject's attribute, involving the disciplines such as land economy, ecosystem health and so on. In addition, the adoption of modern geography technology like GIS, RS and GPS would do us a favor to get a easier way to achieve a healthy urban land ecosystem construction.

References

Cai Weimin, & Tang Huajun. (2004). The framework and indices selection of healthy land utilization system assessment. *China population, resources and environment*, 31-35.

Chen Meiqiu, & Huang Liang. (2004). The assessment of land health in Poyang Lake. *Journal of natural resources, 3*(2), 170-175. http://dx.doi.org/10.3321/j.issn:1000-3037.2004.02.005

Chen Meiqiu, & Wu Cifang. (2002). The progress of land health study. *Journal of Jiangxi Agricultural University (Journal of natural sciences)*, 324-329.

Chen Meiqiu, Liu Taoju, & Huang Liang. (2004). The main contents and obstacles confronted in a healthy land ecosystem study. *Ecology and environment, 12*(4), 698-701.

Cui Baoshan, & Yang Zhifeng. (2001). The study progress of wetland ecosystem health evaluation. *Ecology magazine, 20*(3), 31-36. http://dx.doi.org/10.3321/j.issn:1000-4890.2001.03.009

Guo Ruixiu, & Yang Jurong. (2002). An initial study urban ecosystem health evaluation. *China environment science, 22*(6), 525-529. http://dx.doi.org/10.3321/j.issn:1000-6923.2002.06.010

He Guangli. (2009). *The evaluation of typical grassland ecosystem service function and its health of Inner Mongolia city*. Inner Mongolia: Doctoral thesis of Inner Mongolia University.

Keynote Address. (1992). The Health of the World Lands: A Perspective. *7th International Soil Conservation Organization Conference, Sydney.*

Kong Hongmei, Zhao Jingzhu, & Ji Lanzhu. (2002). An initial study of ecosystem health evaluation method. *Journal of Applied Ecology, 13*(4), 486-490. http://dx.doi.org/10.3321/j.issn:1001-9332.2002.04.024

Leng Shuying, & Li Xiubin. (1999). New progress of International Study on Land Quality Indicators (LQIs). *Acta Geographica Sinica, 54*(1), 177-185. http://dx.doi.org/10.3321/j.issn:0375-5444.1999.02.010

Leopold, A. (1941). Wilderness as a land laboratory. *Living Wilderness.*

Li Jintao, & Tan Shukui. (2009). A case study on temporal-spatial diversity of urban land intensive utilization based on DPSIR model-take Hubei Province as an example. *China land science, 3*(3), 49-65.

Li Weihai. (2009). An analysis of urban spatial expansion and environment health. *Guiyang: Doctoral thesis of Guizhou Normal University*.

Ni Zhen. (2010). The study of realty industry ecosystem health evaluation system – Take Chongqing as an example. *Chongqing: Doctoral thesis of Xi'nan University.*

Xiao Fengjing, & Ouyang Hua. (2002). Healthy ecology system and its evaluated indices and method. *Journal of natural resources, 17*(2), 203-209. http://dx.doi.org/10.3321/j.issn:1000-3037.2002.02.012

Zhang Fengrong. (1996). *The theory and practice of land sustainable management*. Beijing: Peaking University Publisher.

Earth Science Research; Vol. 1, No. 2; 2012
ISSN 1927-0542 E-ISSN 1927-0550
Published by Canadian Center of Science and Education

Research on the Constitutive Model for Granular Material

Wei Zhen-hai[1,2], Wang Meng-shu[1] & Zhang Ding-li[1]

[1] School of Civil Engineering, Beijing Jiaotong University, Beijing, China

[2] School of Rear Professional Service, Logistics Command Academy, Beijing, China

Correspondence: Wei Zhen-hai, School of Civil Engineering, Beijing Jiaotong University, Beijing 100044, China. E-mail: wzhai@vip.sina.com

Received: June 29, 2012 Accepted: July 13, 2012 Online Published: July 30, 2012

doi:10.5539/esr.v1n2p303 URL: http://dx.doi.org/10.5539/esr.v1n2p303

Abstract

The constitutive relation of granular aggregate is one important aspect in solid mechanics research, since many problems involved are nothing like the ordinary mechanical problems. Using the energy method, this paper sets up the constitutive model for the granular material through the homogenization of granular material with structural characteristics. Several important factors that are influential to the characteristics of such material are fully considered by this model: performance of granular connector, its geometric position, directional distribution, morphology and size of statistical domain and the density of the connectors. The analysis of the model reveals that the mechanical properties of the granular material are not only related to the properties of the granular material but also to the arrangement of the granular aggregate, i.e. its fabric characteristics. In addition, the morphology of granules determines how the granules will be connected, which in turn modifies the mechanical performance of connection among granules and hence the performance of the granular aggregate. Besides, the couple stress is an important stress component, which makes classical theory no longer applicable to the granular material. Therefore, the constitutive model for the granular material is a generic model reflecting the granular material performance.

Keywords: granular material, structural characteristics, homogenization, constitutive model

1. Introduction

There is an agreement reached in recent years over the fact that the structural characteristics of granular materials are important factors affecting the macroscopic properties of the materials (Hu, 1999; He & Shen, 2003; Shi, 1996). Large amount of researches have dealt with the structural properties of soil composed of granules (Hu, 1999; He & Shen, 2003; Hu, 2000). The microstructure of the material will influence its macroscopic properties, which has also been generally accepted by many. The major problem is how to relate the microscopic properties of the material with its macroscopic properties and to decide what specific microscopic properties actually affect the macroscopic properties, especially the macroscopic mechanical properties. The theoretical study on these problems is still far from adequate, going blindly especially for the microstructure of granular materials. Despite much work done on microscopic parameters of the granular materials, the influence of these parameters on the macroscopic properties remains to be clarified (Zhang, 2008; Shi, 1996). What is important is to set up both micro- and macroscopic models for granular materials to be used in understanding the specific role that each parameter plays. Then we will be able to finally establish the methods for analysis and determination of these microscopic parameters. The paper attempts to establish the homogenization theory for granular structures by using the energy method based on the composition characteristics of the granular material. Next the constitutive model for granular structure on the macroscopic scale under static state is set up in the presence of external force. The static state here refers to that the granular system remains constant in terms of structure under the action of external force. That is to say, there is no slipping or separation (reconnection) among granules in the system, or the system is under elastic state (the dynamic problem is discussed in another paper).

2. Basic Assumptions

The performance of the granular system is mainly subject to the influence of connection and composition among the granules. Therefore, the connection among granules is a key factor affecting the macroscopic properties of granular material. In light of this, our discussion is based on the following assumptions:

1) When a stress is applied, the granules themselves will not be damaged, and their surfaces may deform only

to a negligible amount. The surface layer of the granules can be regarded as elastic, and the interaction among granules is mainly controlled by the performance of this layer;

2) When two granules act upon each other, there is only one point of action (plane or line) (Figure 1);

3) The contact between two granules can be simplified as a connector resembling an elastic beam, which may deform under external force (Figure 2).

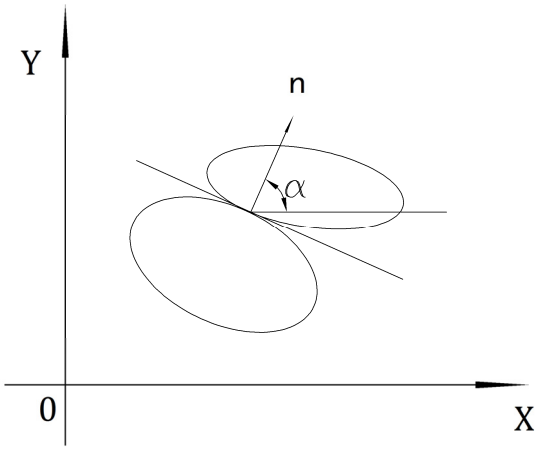

Figure 1. Connection among granules

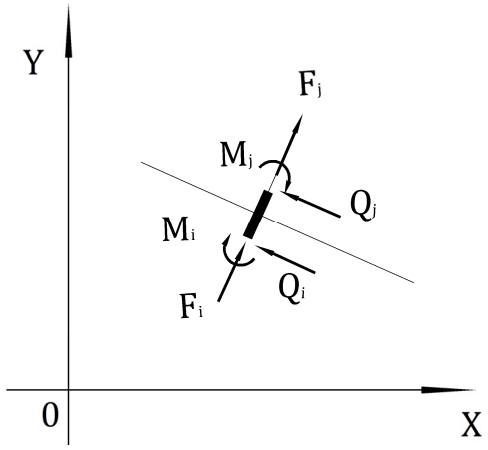

Figure 2. Simplified model of the connection

According to Assumption 3, the relation of the deformation of the two ends of the connection point with the external force can be written as:

$$[F]=[K][\delta] \tag{1}$$

Or in a component form:

$$\begin{bmatrix} F_i^1 \\ Q_i^1 \\ M_i^1 \\ F_i^2 \\ Q_i^2 \\ M_i^2 \end{bmatrix} = \left[K_i^{6\times 6}\right] \begin{bmatrix} u_i^1 \\ v_i^1 \\ \theta_i^1 \\ u_i^2 \\ v_i^2 \\ \theta_i^2 \end{bmatrix} \tag{2}$$

This corresponds to the case where the stress acts on the i^{th} connector, causing deformation, and can be transformed to a global coordinate system:

$$[F_i]=[K_i][\delta_i] \tag{3}$$

where

$$[F_i]=\left[F_i^{x1},F_i^{y1},M_i^{z1},F_i^{x2},F_i^{y2},M_i^{z2}\right],[\delta_i]=\left[u_i^{x1},u_i^{y1},\theta_i^{z1},u_i^{x2},u_i^{y2},\theta_i^{z2}\right]$$

$$[K_i]=\left[R_i^T\right]^T\left[K_i^e\right]\left[R_i^T\right]$$

$\left[R_i^T\right]$ is the coordinate transformation matrix for the i^{th} connector.

3. Equivalent Energy Homogenization in the Statistical Domain

The constitutive relation of granular system is subjected to the influence of granular morphology, granular connection and the fabric of granular system. It is a very complex static elastic problem, for which a solution is difficult to find. In order to simplify the problem, we can only estimate the constitutive relation on the macroscopic scale through homogenization. The essence of homogenization is taking an average, i.e. the mean values of parameters on mechanical properties such as stress and strain. The constitutive relation obtained on the macroscopic scale is an equivalent relation represented by the mean values.

Granular material is a highly heterogeneous material because it is composed of granules of variable sizes according to the arrangement in different sections of the material. The connection varies with the position, leading to discrepencies in granular size, gradation and also its performance. In order to get the characteristic parameters of a specific point on the macroscopic scale, the statistical values of the characteristic parameters including granular morphology and connection within a certain area near this point are taken as the representative values; and the area from which the values are taken is know as the statistical domain (Figure 3) (similar to representative unit RAV).

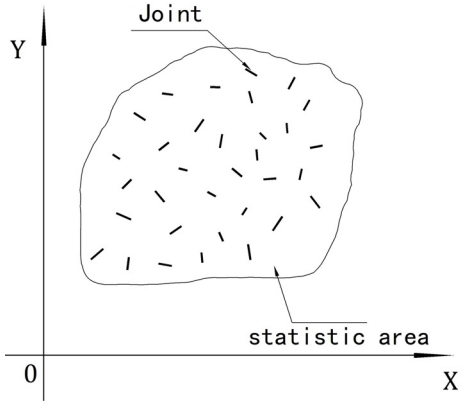

Figure 3. Connection distribution in statistic area

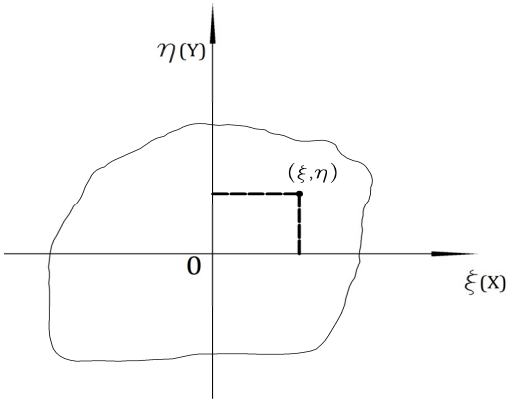

Figure 4. Local coordinates of the connection

There may be many methods to get the representative values of the statistical domain (Hassani & Hinton, 1998; Xie & Liao, 2001). But for any of these methods, the equivalent effect principle should be satisfied. Here according to the equivalent energy principle, the following equation is established with V as the volume of the statistical domain:

$$\begin{cases} \varepsilon_{ij} = \dfrac{1}{V}\displaystyle\int_V \varepsilon_{ij}^* dV^*, \\ \sigma_{ij} = \dfrac{1}{V}\displaystyle\int_V \sigma_{ij}^* dV^* \\ w_{ij}(\varepsilon_{ij}) = \dfrac{1}{V}\displaystyle\int_V w_{ij}^*(\varepsilon_{ij}^*) dV^* \end{cases} \tag{4}$$

And:

$$w_{ij} = \frac{1}{2}\sigma_{ij}\varepsilon_{ij} \tag{5}$$

where ε_{ij}, σ_{ij} and w_{ij} are respectively the average strain, average stress and average strain energy density in the statistical domain. And ε_{ij}^*, σ_{ij}^* and w_{ij}^* are respectively the strain, stress and strain energy density for each connection point in the statistical domain.

The strain energy of the i^{th} connector is:

$$w_i = \frac{1}{2}[\delta_i]^T [K_i][\delta_i] \tag{6}$$

If there are n connectors in the statistical domain, then the strain energy of the entire domain is given by:

$$W = \sum_{i=1}^{n} \frac{1}{2}[\delta_i]^T [K_i][\delta_i] \tag{7}$$

According to the principle of energy conservation, the strain energy (or the work done by the external force) generated from the overall deformation in the statistical domain under external force should be equal to the sum of the strain energy produced from all connectors of the statistical domain; or the average energy density calculated between the two should be equal.

4. Constitutive Model in the Statistical Domain

For elastic system composed of uniform medium, the following relation applies:

$$C_{ijkl} = \frac{\partial^2 w}{\partial \varepsilon_{ij} \partial \varepsilon_{kl}}, \sigma_{ij} = C_{ijkl} \varepsilon_{kl} \tag{8}$$

where w is the strain energy density.

Based on Formula (7) the strain density of the statistical domain can be obtained, and equivalent strain density is found by considering the size of the statiscal domain :

$$w = \frac{W}{V} = \frac{1}{2V} \sum_{i=1}^{n} [\delta_i]^T [K_i][\delta_i]$$

Thus, the above formula can be used to get C_{ijkl}, the parameter in equivalent stress-strain relation.

For 2D situation:

$$[\varepsilon] = \begin{bmatrix} \varepsilon_{11} \\ \varepsilon_{22} \\ \varepsilon_{12} \\ \varepsilon_{21} \\ \varepsilon_{13} \\ \varepsilon_{23} \end{bmatrix} = \begin{bmatrix} u_{1,1} \\ u_{2,2} \\ u_{2,1} - \theta \\ u_{1,2} + \theta \\ \theta_{,1} \\ \theta_{,2} \end{bmatrix}, \text{ and } : [\sigma] = \begin{bmatrix} \sigma_{11} \\ \sigma_{22} \\ \sigma_{12} \\ \sigma_{21} \\ m_{13} \\ m_{23} \end{bmatrix} \tag{9}$$

The stress-strain relation is represented by:

$$[\sigma] = [D][\varepsilon] \tag{10}$$

The strain energy density is known by:

$$w = w(\varepsilon_{11}, \varepsilon_{22}, \varepsilon_{12}, \varepsilon_{21}, \varepsilon_{13}, \varepsilon_{31}) = w(u_{1,1}, u_{2,2}, (u_{2,1} - \theta), (u_{1,2} + \theta), \theta_{,1}, \theta_{,2}) \tag{11}$$

Thus:

$$\begin{cases} \sigma_{11} = \dfrac{\partial w}{\partial \varepsilon_{11}} = \dfrac{\partial w}{\partial u_{1,1}}, \sigma_{22} = \dfrac{\partial w}{\partial \varepsilon_{22}} = \dfrac{\partial w}{\partial u_{2,2}} \\ \sigma_{12} = \dfrac{\partial w}{\partial \varepsilon_{12}} = \dfrac{\partial w}{\partial (u_{2,1} - \theta)}, \sigma_{21} = \dfrac{\partial w}{\partial \varepsilon_{21}} = \dfrac{\partial w}{\partial (u_{1,2} + \theta)} \\ m_{13} = \dfrac{\partial w}{\partial \varepsilon_{13}} = \dfrac{\partial w}{\partial \theta_{,1}}, m_{23} = \dfrac{\partial w}{\partial \varepsilon_{23}} = \dfrac{\partial w}{\partial \theta_{,2}} \end{cases} \tag{12}$$

That is to say, if the displacement of the two ends of the connections among all granules in the statistical domain is known, the corresponding deformation energy and deformation energy density can be calculated to obtain the equivalent stress-strain relation, i.e. the equivalent constitutive relation.

If the statistical domain is a relatively small domain in relation to the granular system, then the displacement of the central point of the statistical domain can be used to approximately represent the displacement of each point of the statistical domain by Taylor expansion:

$$\begin{cases} u^i \approx u_0 + L_\alpha \dfrac{\partial u}{\partial t_\alpha} + \dfrac{L_\alpha^2}{2}\dfrac{\partial^2 u}{\partial^2 t_\alpha} \\ \theta^i \approx \theta_0 + L_\alpha \dfrac{\partial \theta}{\partial t_\alpha} + \dfrac{L_\alpha^2}{2}\dfrac{\partial^2 \theta}{\partial^2 t_\alpha} \end{cases} \tag{13}$$

where u^i and θ^i are respectively the displacement of any point of the statiscal domain; u_0 and θ_0 are the macroscopic displacements of the central point of the statistical domain; L_α is the distance from the center of the statistical domain; t_α is directional derivative.

The expression above is in vector form. Its component form is written as:

$$\frac{\partial u}{\partial t_\alpha} = \frac{\partial}{\partial t_\alpha}(u_x\vec{i} + u_y\vec{j}) = (\frac{\partial u_x}{\partial x}\cos\alpha + \frac{\partial u_x}{\partial y}\cos\beta)\vec{i} + (\frac{\partial u_y}{\partial x}\cos\alpha + \frac{\partial u_y}{\partial y}\cos\beta)\vec{j}$$

$$\text{If: } L_\alpha\cos\alpha = \xi, L_\alpha\cos\beta = \eta, \text{ Then: } \begin{cases} u_\xi^i = u_x + \xi\dfrac{\partial u_x}{\partial \xi} + \eta\dfrac{\partial u_x}{\partial \eta} \\ \quad + \dfrac{1}{2}(\xi^2\dfrac{\partial^2 u_x}{\partial^2 \xi} + 2\xi\eta\dfrac{\partial^2 u_x}{\partial\xi\partial\eta} + \eta^2\dfrac{\partial^2 u_x}{\partial^2\eta}) \\ u_\eta^i = u_y + \eta\dfrac{\partial u_y}{\partial \eta} + \xi\dfrac{\partial u_y}{\partial \xi} \\ \quad + \dfrac{1}{2}(\eta^2\dfrac{\partial^2 u_y}{\partial^2 \eta} + 2\xi\eta\dfrac{\partial^2 u_y}{\partial\xi\partial\eta} + \xi^2\dfrac{\partial^2 u_y}{\partial^2\xi}) \\ \theta_\zeta^i = \theta_z + \eta\dfrac{\partial \theta_z}{\partial \eta} + \xi\dfrac{\partial \theta_z}{\partial \xi} \\ \quad + \dfrac{1}{2}(\eta^2\dfrac{\partial^2 \theta_z}{\partial^2 \eta} + 2\xi\eta\dfrac{\partial^2 \theta_z}{\partial\xi\partial\eta} + \xi^2\dfrac{\partial^2 \theta_z}{\partial^2\xi}) \end{cases} \tag{14}$$

where u_x, u_y and θ_z are respectively the displacement and angular displacement of the central point of the statistical domain in X, Y and Z direction:

When there is a big size difference between the statistical domain and the granular system with neglibile higher order terms, the displacement of the i^{th} connector in the statistical domain is given by:

$$[\delta_i] = \begin{bmatrix} u_{x1}^i \\ u_{y1}^i \\ \theta_{z1}^i \\ u_{x2}^i \\ u_{y2}^i \\ \theta_{z2}^i \end{bmatrix} = \begin{bmatrix} u_x + \xi_1^i\dfrac{\partial u_x}{\partial \xi} + \eta_1^i\dfrac{\partial u_x}{\partial \eta} \\ u_y + \eta_1^i\dfrac{\partial u_y}{\partial \eta} + \xi_1^i\dfrac{\partial u_y}{\partial \xi} \\ \theta_z + \eta_1^i\dfrac{\partial \theta_z}{\partial \eta} + \xi_1^i\dfrac{\partial \theta_z}{\partial \xi} \\ u_x + \xi_2^i\dfrac{\partial u_x}{\partial \xi} + \eta_2^i\dfrac{\partial u_x}{\partial \eta} \\ u_y + \eta_2^i\dfrac{\partial u_y}{\partial \eta} + \xi_2^i\dfrac{\partial u_y}{\partial \xi} \\ \theta_z + \eta_2^i\dfrac{\partial \theta_z}{\partial \eta} + \xi_2^i\dfrac{\partial \theta_z}{\partial \xi} \end{bmatrix} \tag{15}$$

After sorting out:

$$[\delta_i]=\begin{bmatrix}\begin{pmatrix}u_x\\u_y\\\theta_z\end{pmatrix}\\\begin{pmatrix}u_x\\u_y\\\theta_z\end{pmatrix}\end{bmatrix}+\begin{bmatrix}\xi_1^i & \eta_1^i\\\xi_2^i & \eta_2^i\end{bmatrix}\begin{bmatrix}\begin{pmatrix}\frac{\partial u_x}{\partial\xi}\\\frac{\partial u_y}{\partial\xi}\\\frac{\partial\theta_z}{\partial\xi}\end{pmatrix}\\\begin{pmatrix}\frac{\partial u_x}{\partial\eta}\\\frac{\partial u_y}{\partial\eta}\\\frac{\partial\theta_z}{\partial\eta}\end{pmatrix}\end{bmatrix} \tag{16}$$

If $\mathbf{u_0^T}=\begin{bmatrix}u_x & u_y & \theta_z\end{bmatrix}^T$, then: $\dfrac{\partial\mathbf{u}_0^{\mathbf{T}}}{\partial\xi}=\begin{bmatrix}\frac{\partial u_x}{\partial\xi} & \frac{\partial u_y}{\partial\xi} & \frac{\partial\theta_z}{\partial\xi}\end{bmatrix}^T$, $\dfrac{\partial\mathbf{u}_0^{\mathbf{T}}}{\partial\eta}=\begin{bmatrix}\frac{\partial u_x}{\partial\eta} & \frac{\partial u_y}{\partial\eta} & \frac{\partial\theta_z}{\partial\eta}\end{bmatrix}^T$

Formula (16) can be simplified as:

$$[\delta_i]=\begin{bmatrix}\mathbf{u_0}\\\mathbf{u_0}\end{bmatrix}+\begin{bmatrix}\xi_1^i & \eta_1^i\\\xi_2^i & \eta_2^i\end{bmatrix}\begin{bmatrix}\frac{\partial\mathbf{u_0}}{\partial\xi}\\\frac{\partial\mathbf{u_0}}{\partial\eta}\end{bmatrix} \tag{17}$$

Substitution into the expression of strain energy yields:

$$\begin{aligned}w_i&=\frac{1}{2}[\delta_i]^T[K_i][\delta_i]\\&=\frac{1}{2}\left\{\mathbf{u_0}\begin{bmatrix}1\\1\end{bmatrix}+\begin{bmatrix}\xi_1^i & \eta_1^i\\\xi_2^i & \eta_2^i\end{bmatrix}\begin{bmatrix}\frac{\partial\mathbf{u_0}}{\partial\xi}\\\frac{\partial\mathbf{u_0}}{\partial\eta}\end{bmatrix}\right\}^T\\&\quad[K_i]\left\{\mathbf{u_0}\begin{bmatrix}1\\1\end{bmatrix}+\begin{bmatrix}\xi_1^i & \eta_1^i\\\xi_2^i & \eta_2^i\end{bmatrix}\begin{bmatrix}\frac{\partial\mathbf{u_0}}{\partial\xi}\\\frac{\partial\mathbf{u_0}}{\partial\eta}\end{bmatrix}\right\}\end{aligned}$$

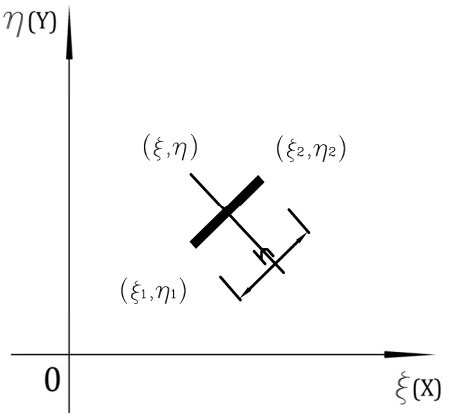

Figure 5. Connection parameters

In consideration that the size of the 2D statistical domain is A_c, the summation of strain energy of all connectors in statistical domain is given by:

$$w = \frac{1}{2A_c}\left\{\mathbf{u_0}^{\mathrm{T}}\bar{\mathbf{K}}_1\mathbf{u_0} + \mathbf{u_0}^{\mathrm{T}}\bar{\mathbf{K}}_2\boldsymbol{\varepsilon_0} + \boldsymbol{\varepsilon_0}^{\mathrm{T}}\bar{\mathbf{K}}_3\mathbf{u_0} + \boldsymbol{\varepsilon_0}^{\mathrm{T}}\bar{\mathbf{K}}_4\boldsymbol{\varepsilon_0}\right\} \tag{18}$$

where $\mathbf{u_0}$ is the same as $\boldsymbol{\varepsilon_0} = \begin{bmatrix} \frac{\partial \mathbf{u_0}}{\partial \xi} & \frac{\partial \mathbf{u_0}}{\partial \eta} \end{bmatrix}^T$

$$\begin{cases} \bar{\mathbf{K}}_1 = \begin{bmatrix} 1 & 1 \end{bmatrix} \sum_{i=1}^{n} \mathbf{K_i} \begin{bmatrix} 1 \\ 1 \end{bmatrix} \\ \bar{\mathbf{K}}_2 = \sum_{i=1}^{n} \begin{bmatrix} 1 & 1 \end{bmatrix} \mathbf{K_i} \begin{bmatrix} \xi_1^i & \eta_1^i \\ \xi_2^i & \eta_2^i \end{bmatrix} \\ \bar{\mathbf{K}}_3 = \sum_{i=1}^{n} \begin{bmatrix} \xi_1^i & \eta_1^i \\ \xi_2^i & \eta_2^i \end{bmatrix} \mathbf{K_i} \begin{bmatrix} 1 & 1 \end{bmatrix} \\ \bar{\mathbf{K}}_4 = \sum_{i=1}^{n} \begin{bmatrix} \xi_1^i & \eta_1^i \\ \xi_2^i & \eta_2^i \end{bmatrix} \mathbf{K_i} \begin{bmatrix} \xi_1^i & \eta_1^i \\ \xi_2^i & \eta_2^i \end{bmatrix} \end{cases}$$

$\mathbf{K_i}$ is the stiffness matrix after 3×3 segmentation:

$$\mathbf{K_i} = \begin{bmatrix} K_{11}^i & K_{12}^i \\ K_{21}^i & K_{22}^i \end{bmatrix}, K_{11}^i = \begin{bmatrix} k_{11} & k_{12} & k_{13} \\ k_{21} & k_{22} & k_{23} \\ k_{31} & k_{32} & k_{33} \end{bmatrix}$$

$$K_{12}^i = \begin{bmatrix} k_{14} & k_{15} & k_{16} \\ k_{24} & k_{25} & k_{26} \\ k_{34} & k_{35} & k_{36} \end{bmatrix}, K_{21}^i = \begin{bmatrix} k_{41} & k_{42} & k_{43} \\ k_{51} & k_{52} & k_{53} \\ k_{61} & k_{62} & k_{63} \end{bmatrix},$$

$$K_{22}^i = \begin{bmatrix} k_{44} & k_{45} & k_{46} \\ k_{54} & k_{55} & k_{56} \\ k_{64} & k_{65} & k_{66} \end{bmatrix}$$

From Formula (18) we can see that the strain energy density is related to the displacement and strain as well as to connector stiffness K_i, which depends on the morphology of granules and the action force among granules. $\bar{\mathbf{K}}_1$, $\bar{\mathbf{K}}_2$, $\bar{\mathbf{K}}_3$, $\bar{\mathbf{K}}_4$ represent not only the action among granular connectors but also the influence of the position on the granular connector. The constitutive relation of the granules varies according to the specific position.

The equivalent constitutive relation in the statistical domain can be derived based on strain energy density from Formula (12):

$$\begin{bmatrix} \sigma_{11} \\ \sigma_{21} \\ m_{13} \\ \sigma_{21} \\ \sigma_{22} \\ m_{23} \end{bmatrix} = \frac{1}{A_c}\left\{\bar{\mathbf{K}}_3\mathbf{u_0} + \bar{\mathbf{K}}_4\boldsymbol{\varepsilon_0}\right\} \tag{19}$$

The derivative of the composite function is taken with respect to σ_{12} and σ_{21}.

From formula (19) it can be seen that the stress and couple stress are not only related to the strain but also to the displacement. We can prove that when stiffness matrix K_i among granules can be simplified as a unit matrix of beam, the couple stress is independent of angle θ_z and other stress components are also not related to the displacement. However, if coordinate transformation is required for the unit matrix of beam, the expression of each stress component will include the displacement components.

Formula (19) shows that the equivalent constitutive relation in the statistical domain is determined by $\bar{\mathbf{K}}_3$ and $\bar{\mathbf{K}}_4$, which are in turn related to two factors: one is K_i, the stiffness matrix of granular connector, affected by the interaction among granules; another is the position of the connector in the statistical domain, affected by the position and direction of the connector in the statistical domain. Apparently, the constitutive relation of the

granular material is subjected to the influence of both the connection properties of granules and the distribution of the connectors among granules microscopically.

For the convenience of calculation, the coordinates of the midpoint of the connector is assumed as (ξ, η), its length h_i; and the angles with respect to X and Y axis are α and β respectively. Thus:

$$\begin{cases} \xi_1^i = \xi_i + \dfrac{h_i}{2}\cos\alpha_i \\ \xi_2^i = \xi_i - \dfrac{h_i}{2}\cos\alpha_i \end{cases} \text{ and } \begin{cases} \eta_1^i = \eta_i + \dfrac{h_i}{2}\cos\beta_i \\ \eta_2^i = \eta_i - \dfrac{h_i}{2}\cos\beta_i \end{cases}$$

If

$$\mathbf{G_i} = \begin{bmatrix} \xi_i + \dfrac{h_i}{2}\cos\alpha_i & \xi_i - \dfrac{h_i}{2}\cos\alpha_i \\ \eta_i + \dfrac{h_i}{2}\cos\beta_i & \eta_i - \dfrac{h_i}{2}\cos\beta_i \end{bmatrix} \tag{20}$$

Then:

$$\begin{cases} \bar{\mathbf{K}}_3 = \sum_{i=1}^{n} \mathbf{G_i}\mathbf{K_i}\mathbf{I} \\ \bar{\mathbf{K}}_4 = \sum_{i=1}^{n} \mathbf{G_i}\mathbf{K_i}\mathbf{G_i^T} \end{cases} \tag{21}$$

Here $\mathbf{I} = [1\ 1]^T$.

Obviously, $\mathbf{G_i}$ is the spatial characteristic matrix for the connector that includes three parameters: position, angle and length of the connector. Thus, statistical process is necessary for the three parameters when we analyze the distribution characteristics of the granular material.

5. Discussion

Formula (19) gives the equivalent constitutive relation of the granular material. In the following, the meaning of the parameters in this relation and their respective roles will be examined.

5.1 Meaning of the Parameters

Formula (20) can be decomposed into:

$$\begin{aligned} \mathbf{G_i} &= \begin{bmatrix} \xi_i & \xi_i \\ \eta_i & \eta_i \end{bmatrix} + \frac{h_i}{2}\begin{bmatrix} \cos\alpha_i & -\cos\alpha_i \\ \cos\beta_i & -\cos\beta_i \end{bmatrix} \\ &= \begin{bmatrix} \xi_i \\ \eta_i \end{bmatrix}\begin{bmatrix} 1 & 1 \end{bmatrix} + \frac{h_i}{2}\begin{bmatrix} \cos\alpha_i \\ \cos\beta_i \end{bmatrix}\begin{bmatrix} 1 & -1 \end{bmatrix} \end{aligned}$$

By substituting into Formula (21), $\bar{\mathbf{K}}_3 = \sum_{i=1}^{n}\left\{\begin{bmatrix} \xi_i \\ \eta_i \end{bmatrix} \otimes \mathbf{K}_1^i + \frac{h_i}{2}\begin{bmatrix} \cos\alpha_i \\ \cos\beta_i \end{bmatrix} \otimes \mathbf{K}_2^i\right\}$

$$\bar{\mathbf{K}}_4 = \sum_{i=1}^{n}\left\{\begin{array}{l} \begin{bmatrix} \xi_i \\ \eta_i \end{bmatrix}\begin{bmatrix} \xi_i & \eta_i \end{bmatrix} \otimes \mathbf{K}_1^i + \dfrac{h_i}{2}\begin{bmatrix} \cos\alpha_i \\ \cos\beta_i \end{bmatrix}\begin{bmatrix} \xi_i & \eta_i \end{bmatrix} \otimes \mathbf{K}_2^i \\ + \dfrac{h_i}{2}\begin{bmatrix} \xi_i \\ \eta_i \end{bmatrix}\begin{bmatrix} \cos\alpha_i & \cos\beta_i \end{bmatrix} \otimes \mathbf{K}_3^i \\ + \left(\dfrac{h_i}{2}\right)^2\begin{bmatrix} \cos\alpha_i \\ \cos\beta_i \end{bmatrix}\begin{bmatrix} \cos\alpha_i & \cos\beta_i \end{bmatrix} \otimes \mathbf{K}_4^i \end{array}\right\}$$

Where

$$\mathbf{K}_1^i = K_{11}^i + K_{12}^i + K_{21}^i + K_{22}^i;\quad \mathbf{K}_2^i = K_{11}^i + K_{12}^i - K_{21}^i - K_{22}^i;$$

$$\mathbf{K}_3^i = K_{11}^i - K_{12}^i + K_{21}^i - K_{22}^i \quad \text{and} \quad \mathbf{K}_4^i = K_{11}^i - K_{12}^i - K_{21}^i + K_{22}^i$$

Where K_{11}^i、K_{12}^i、K_{21}^i、K_{22}^i are the block submatrices of the stiffness matrix of the connector respectively. If the stiffness matrix of the connector is assumed to be similar to that of the elastic beam, then

$$K^{6\times 6} = \begin{bmatrix} K_{11}^{3\times 3} & K_{12}^{3\times 3} \\ K_{21}^{3\times 3} & K_{22}^{3\times 3} \end{bmatrix}$$

Where

$$K_{11} = \begin{bmatrix} k_{11} & k_{12} & k_{13} \\ k_{21} & k_{22} & k_{23} \\ k_{31} & k_{32} & k_{33} \end{bmatrix},$$

$$K_{12} = K_{21}^T = \begin{bmatrix} -k_{11} & -k_{12} & k_{13} \\ -k_{21} & -k_{22} & k_{23} \\ -k_{31} & -k_{32} & 1/2\,k_{33} \end{bmatrix},$$

$$K_{22} = \begin{bmatrix} k_{11} & k_{12} & -k_{13} \\ k_{21} & k_{22} & -k_{23} \\ -k_{31} & -k_{32} & k_{33} \end{bmatrix}$$

Thus,

$$\mathbf{K}_1^i = \begin{bmatrix} 0 & 0 & 0 \\ 0 & 0 & 0 \\ 0 & 0 & 3k_{33} \end{bmatrix}, \mathbf{K}_2^i = \begin{bmatrix} 0 & 0 & 4k_{13} \\ 0 & 0 & 4k_{23} \\ 0 & 0 & 0 \end{bmatrix},$$

$$\mathbf{K}_3^i = \begin{bmatrix} 0 & 0 & 0 \\ 0 & 0 & 0 \\ 4k_{13} & 4k_{13} & 0 \end{bmatrix}, \mathbf{K}_4^i = \begin{bmatrix} 4k_{11} & 4k_{12} & 0 \\ 4k_{21} & 4k_{22} & 0 \\ 0 & 0 & 0 \end{bmatrix}$$

By substituting into the expressions of $\bar{\mathbf{K}}_3$、$\bar{\mathbf{K}}_4$, it is found that for $\bar{\mathbf{K}}_3$ only the third column is non-zero; it is the angular displacement that corresponds to the displacement matrix. That is to say, what $\bar{\mathbf{K}}_3$ represents is the stress changes due to rotational displacement, since translational displacement will not cause stress changes. Then we examine the influence of the statistical domain. If the position of the connector with respect to the coordinate origin is symmetrical having the same stiffness matrix for each connector, then $\sum_{i=1}^{n}\xi_i = \sum_{i=1}^{n}\eta_i = 0$, which means rotational displacement will not cause the couple stress. Meanhile, $\sum_{i=1}^{n}\cos\alpha_i = \sum_{i=1}^{n}\cos\beta_i = 0$ will not lead to normal stress and shear stress components. Thus, $\bar{\mathbf{K}}_3$ represents the changes of stress components resulting from statistically eccentric and non-uniform action. The classical theory generally assumes that the material is uniform and continuous, and the material can be regarded as completely symmetrical, especially when the stress state of a point is considered. Therefore, the stress problems arising from the displacement of a non-uniform rigid body cannot be accounted for.

$\bar{\mathbf{K}}_4$ in the formula is composed of four terms. For the first term, only the subterm that is related to the angle gradient in the influence maxtirx of the connector is non-zero. So the term is the mean value of the couple stress components in the changing statistical domain of each point caused by angle gradient. For the influence matix in the second item, only the third column is non-zero, which is only related to the angle gradient when the arrangement of strain vector is considered. Therefore, the second term is in fact represents the contribution of angle gradient to other stress components. The contribution of strain to couple stress component can be found by examining the influence matix of the third term. For the influence matrix of the last term, only the four positions towards the upper left corner have values, while the rows and columns related to the angle have none. This indicates that the term represents the relation of other strain componments with the corresponding stress

components except the angle. In addition, if the morphology of the statistical domain and the stiffness matrix of the connector are symmetrical, we will find that the second and the third terms may be zero. This indicates that the two terms are related to the coordinates as well as the asymmetry of the system. This is an important feature of the constitutive relation of granular materials that is not represented in the classical theory.

5.2 Further Analysis of Influential Parameters

From the expressions of $\bar{\mathbf{K}}_3$ and $\bar{\mathbf{K}}_4$ it can be found that the influential parameters are basically related to the following three aspects:

1) The characteristics of granular connectors;
2) The geometric position, direction and distribution of granular connectors;
3) The morphology and size of the statistical domain, as well as the density of the connectors in the statistical domain.

The mechanical interaction among granules is influenced by the characteristics of granular connectors. The higher the stiffness of the connector, the higher the equivalent stiffness in the statistical domain will be. And the stiffness of the connector is also affected by the characteristics of the connection plane. For instance, the plane with friction action is very different from the plane with cementing action. Even the connection planes of the same type have variable stiffness characteristics due to the morphology of the connection plane. The plane with friction action has different impact for point-to-point contact and plane-to-plane contact. The anti-bending performance of the plane-to-plane contact is much higher than that of point-to-point contact.

The geometic position and directional distribution of granular connectors reflect the fabric relation of granules, which is an important aspect that affects the properties of granular materials. The geometic position and directional distribution are two important parameters that quantitatively describe the properties of granular materials. However, we have not yet understood how structural parameters of granular materials affect its macroscopic mechanical properties. Through the analysis of the constitutive relation of granular materials it can be found that the position of the granular connectors and the connection direction are two parameters that reflect the fabric characteristics of granular material.

The morphology and size of the statistical domain are also important influential parameters for the equivalent constitutive relation. The discrepancy in the morphology and size of the statistical domain may lead to different results. And this characteristic related to morphology and size of the statistical domain is also different from what is implied in the classical theory. That is, the characteristics of granular material have certain scale effect. Even given the same morphology and size of the statistical domain, the quantity of the connectors in the statistical domain or the density of the connectors may be greatly different due to different granular scale in the statistical domain. This explains the difference in the calculation results.

6. Conclusion

Through the above analysis we can see that the constitutive relation of the granular material is very complex and have much more influential factors compared to uniform and continuous materials. After the analysis of the model, conclusions that are very different from those obtained for uniform and continuous materials based on classical theory are reached:

1) Several important factors influencing the performance of granular material are fully considered in the constitutive model for the granular material: the performance of the connectors, geometic position and directional distribution, morphology and size of the statistical domain and the density of the connectors. The role of these factors can be analyzed quantitatively by this model;
2) The constitutive model for granular material is a generic model that reflects the material performance. The parameters in the model represent the properties of granular materials quite comprehensively. When some parameters degenerate to a homogenization state, the model is automatically adapted to the classical theory;
3) We have found out relevant parameters that can fully reflect the essential properties of granular structures by the model. This lays a theoretical foundation for validation tests of granular materials by reducing the blindness of parameter screening for the tests;
4) The equivalent stress-strain relation of granular material is directly related to the positon and directional distribution of granular connectors. This means that the non-uniform distribution of the connectors will influence the equivalent constitutive relation. If the properties of granular material are studied by assuming that the granules are continuous, then geometric position and directional distribution of the connectors will inevitably affect the constitutive relation;

5) Model analysis reveals that the couple stress in the equivalent constitutive relation of granular materials is an important stress component, which is not otherwise accounted for in classical theory. Therefore, the analysis method used in classical theory can not be directly borrowed for their applications in macroscopic study of granular materials. Cosserat theory is recommended for such cases since it considers the effect of the couple stress.

This paper has proposed and discussed the constitutive model for granular materials, but the research is still preliminary. Many problems need to be more thoroughly investigated, especially the description of the distribution of the connectors and the influence of granular morphology on the connection properties.

References

Cao Xiao-Qing, Wang Phi-Hua, Ma Honk-Wei, Zhao Long-Mao, & Yang Gui-Tong. (2006). The Effects of Micro-Structure on the Equivlent Elastic Constants of Cellular Materials. *Journal of Taiyuan University of Technology, 37*(1), 1-5.

Chen Huifa. (2004). *Elasticity and Plasticity*. China Architecture & Building Press July.

Hassani, B., & Hinton, E. (1998a). A review of homogenization and topology optimization I-homogenization theory for media with periodic structure. *Computers and Structures, 69*, 707-717. http://dx.doi.org/10.1016/S0045-7949(98)00131-X

Hassani, B., & Hinton, E. (1998b). A review of homogenization and topology optimization II-analytical and numerical solution of homogenization equations. *Computers and Structures, 69*, 719-738. http://dx.doi.org/10.1016/S0045-7949(98)00132-1

Hassani, B., & Hinton, E. (1998c). A review of homogenization and topology optimization III topology optimization using optimality criteria. *Computers and Structures, 69*, 739-756. http://dx.doi.org/10.1016/S0045-7949(98)00133-3

He Kai-Sheng, & Shen Zhu Jian. (2003). Study on Micro-Deformation and Mechanism of Structural Clay. *Journal of Hohai University, 31*(2), 161-165.

Hu Ruilin. (1999). Microstructure Effect on the Subsdnce of Loess. *Journal of Engineering Geology, 17*(2), 161-167.

Hu Ruilin. (2000). Approach to the Strength Behaviors and Microstructural Changes of Loess under Dynamic Load. *Chinese Journal of Geotechnical Engineering, 22*(2), 177-181.

Hu Xin, Sun Qiu, Hong Bao-Ning, & Zhou Yu-Quan. (2006). Correlations between Compressibility and Micro-structural Form of Cohesive Soils. *China Harbour Engineering, 145*(5), 16-19.

Jtang Hong-Ying, Lu Jin-Bu, & Miao Tian-De. (2008). An Experimental Analysis and the Establishment of Theoretical Models of the Granular Structures. *Journal of Gansu Sciences, 20*(1), 135-138.

Ju Hai-Yan, Huang Hong-Yuan, Li Jian-Hua, & Yang Wei-Zhong. (2006). The Study on the Structural Constitutive Models of Soil and Rock. *China Tungsten Industry, 21*(4), 21-24.

Kaneko, K., Terada, K., Kyoya, T., & Kishino, Y. (2003). Global–Local Analysis of Granular Media in Quasi-Static Equilibrium. *International Journal of Solids And Structures, 40*, 4043-4069. http://dx.doi.org/10.1016/S0020-7683(03)00209-9

Kang Xin, & Xi Zhanwen. (2007). Size Effect on the Dynamic Characteristic of a Micro Based on Cosserat Theory. *Journal of Mechanical Strength, 29*(1), 1-4.

Li Shun-Qun, Zheng Gang, Zhao Rui-Bin, & Wang Pei. (2009). Correlation Analysis and Principal Component Analysis on Microstructure Parameters of Clay. *Chinese Journal of Geotechnical Engineering, 31*(7), 1120-1126.

Li Xiang-Quan, Hu Rui-Lin, & Zhang Li. (2000). The Variation of Microstructure during Soft Soil Solidification. *Earth Science Frontiers (China University of Geosciences, Beijing), 7*(1), 147-152.

Liu Xu, Wang Lan-Min, Chen Long-Zhu, & Sun Jun-Jie. (2007). A Volumetric Model of Loess Based On Microstructure Instability and Generalized Suction Theories. *Rock and Soil Mechanics, 28*(12).

Patrice, C., & Tanguy, M. (2006). Computational Homogenization of Periodic Beam-Like Structures. *International Journal of Solids and Structures, 43*, 686-696. http://dx.doi.org/10.1016/j.ijsolstr.2005.03.063

Shi Bin. (1996). Review and Prospect on the Microstructure of Clayey Soil. *Journal of Engineering Geology, 4*, 39-45.

Sun Qiang, Zhang Xiao-Ke, & Li Hou-En. (2008). Research on Microstructural Catastrophe Model of Deformation of Collapsible Loess. *Rock and Soil Mechanics, 29*(3), 663-672.

Tang Liansheng, Liao Huarong, & Zhang Qinghua. (2006). Structural Entropy of Soil and Quantitative Research for Soil Structure Characteristics. *Chinese Journal of Rock Mechanics and Engineering, 25*(10), 1997-2002.

Wang Jun-Chao, Jia Yong-Gang, Shi Wen-Jun, Shan Hong-Xian, Xu Guo-Hui, & Fu Yuan-Bin. (2004). Case Study on the Fractal Characteristic Variations of Silty Soil Microstructure Due to Differential Hrodynamics in the Yellow River Estuarine Area. *Advances in Marine Science, 22*(2), 177-183.

Wang Wei, Feng Xiao-Ping, Chen Yan, & Wang Jian. (2006). Analysis of Intrinsic Correlation of Mechanical Strength with Microstructure Dynamic Environmental Energy Field of Clayey Soils. *Rock and Soil Mechanics, 27*(12), 2219-2224.

Wanga, J. G., Leungb, C. F., & Ichikawa, Y. (2002). A Simplified Homogenization Method for Composite Soils. *Computers and Geotechnics, 29*, 477-500. http://dx.doi.org/10.1016/S0266-352X(02)00004-6

Wei Lide. (2004). Study on Rock Mechanics Damage and Rheology Constitutive Models. *Chinese Journal of Rock Mechanics And Engineering, 23*(24), 4265-4265.

Weihong Zhang, Gaoming Dai, Fengwen Wang, Shiping Sun, & Hicham Bassir. (2007). Using Strain Energy-Based Prediction of Effective Elastic Properties in Topology Optimization of Material Microstructures. *Acta Mech Sin, 23*, 77-89. http://dx.doi.org/10.1007/s10409-006-0045-2

Xiao Qi-lin, Ling Zhong, Wu Yong-Li, & Yao Wen-hui. (2003). Incompatible Finite Element Analysis of Couple-stress Problems. *Journal of the Graduate School of the Chinese Academy of Sciences, 20*(2), 1-9.

Xie Xianhai, & Liao Daoxun. (2001). Computation Method of Equivalent Elastic Tensor in Homogenization Method.

Yasser, M., & Shabana, N. N. (2008). Numerical Evaluation of the Thermomechanical Effective Properties of a Functionally Graded Material Using the Homogenization Method. *International Journal of Solids And Structures, 45*, 3494-3506. http://dx.doi.org/10.1016/j.ijsolstr.2008.02.012

Yuan Zhen, Wu Changchun, & Li Hua. (2003). Homogenization-Based Topology Design for Pure Torsion of Composite Shafts. *Acta Mechanica Sinica, 19*(3), 0567-7718.

Zhang Hong Wu. (2001a). Hom Ogenization M Ethod for the Analysis of Assemblage of Elastic Contact Grains Part One: Local Rve Analysis. *Acta Materiae Compositae Sinicavol, 4*, 94-97.

Zhang Hong Wu. (2001b). Homogenisation Method for the Analysis of Assemblage of Elastic Contactgrains, Part II-Macro Homogenisation Analysis. *Acta Materiae Compositae Sinicavol, 4*, 99-102.

Zhang Hua Jiel, Sun Qiu, Hu Xin, & Hong Bao Ning. (2008). Summarizing Study on the Methods of Testing Microstructure of Geomaterials. *Soil Eng. and Foundation, 22*(4), 50-54.

Zhang Li-Zhong, Hu Rui-Lin, Li Xiang-Quan, & Zhanu Yong-Bo. (2008). Soil Microstructure Quantitative Analysis System and Its Application. *Geological Science and Technology Information, 27*, 108-112.

Zhang Min-Jiang, Yan Jing, & Chu Hong-Xia. (2005). The Quantitative Analysis of Microstructure Parameter of Soft Soil. *Journal of Shenyang Jianzhu University (Natural Science), 21*(5), 455-459.

Zhang Pei-Yuan, Zhang Xia-Min, & Tan Guan-Pu. (2002). A Difficulty of Symmetrical Stress Model. *Journal of Chongqing University (Natural Science Edition), 25*(4), 8-9.

Earth Science Research; Vol. 1, No. 2; 2012
ISSN 1927-0542 E-ISSN 1927-0550
Published by Canadian Center of Science and Education

Influence of Membrane Stress on Seafloor Spreading Driven by Tide-generating Force

Long Chen*[,1,2,3], Jianguo Chen*[,4], Qinghai Xu[2,5], Wei Guo[3,6], Dong Ma[4], Guoling Zhang[4], Jinsong Liu[2,5], Shuang Liang[3,6] & Lixue Wei[3,6]

[1] Hebei Normal University, Shijiazhuang, China

[2] Hebei Key Laboratory of Environmental Change and Ecological Construction, Shijiazhuang, China

[3] Hebei Key Laboratory of Computational Mathematics and Application, Shijiazhuang, China

[4] Research Centre for Analysis and Prediction, Earthquake Administration of Hebei Province, Shijiazhuang, China

[5] College of Resources and Environmental Sciences, Hebei Normal University, Shijiazhuang, China

[6] College of Mathematics and Information Science, Hebei Normal University, Shijiazhuang, China

* The two authors have contributed equally to the work.

Correspondence: Jianguo Chen, Research Centre for Analysis and Prediction, Earthquake Administration of Hebei Province, Shijiazhuang, China. Tel: 86-186-0321-6806. E-mail: zhuanjiatuijian@126.com

Received: July 10, 2012 Accepted: July 23, 2012 Online Published: July 31, 2012

doi:10.5539/esr.v1n2p315 URL: http://dx.doi.org/10.5539/esr.v1n2p315

Abstract

Although Alfred Lothar Wegener proposed his continental drift hypothesis more than 100 years ago, there has been constant contention regarding the driving source of plate motions. The current geodynamic theory is mainly based on traditional mechanics. The crust is extremely thin in comparison to the earth's radius, which may be caused by a more complex mechanical system: the mechanics of shells. The mechanics of shells reveals the mechanical effect of the tide-generating force on the earth's crust. We present a formula that can be used to calculate the membrane stress resulting from the fluctuation of the mantle tide wave in the crust and estimate its magnitude. Although the tidal force is small, the membrane stress is high. Our investigation suggests that the membrane stress is the fundamental reason for rifting and rupture processes at mid-ocean ridges. It is thus the dynamic source for seafloor spreading and plate motion, which offers a reasonable interpretation of various significant problems that are unexplained by mantle convection theory. And there must be the plate tectonics affected by the tidal force is in the terrestrial planets or other celestial bodies.

Keywords: tide-generating force, membrane stress, plate motion, dynamic source, terrestrial planets

1. Introduction

Since Alfred Lothar Wegener proposed the continental drift hypothesis (Evans, 1923; Hallam, 1975; Jordan, 1974; Meinesz, 1947; Minster, Jordan, Molnar, & Haines, 1974; Mobus, 1982; Ranalli, 2000; Scoppola, Boccaletti, Bevis, Carminati, & Doglioni, 2006), there has been disagreement regarding the formation mechanism, evolution law and the driving forces behind plate motions. No current hypothesis regarding driving mechanisms is proven or convincing (Bird, 1998; Conrad & Lithgow-Bertelloni, 2004; Forsyth & Uyeda, 1975; Lithgowbertelloni & Richards, 1995; Person & Garven, 1994; Plattner, Malservisi, & Govers, 2009; Royden, 1993; Vandecar, James, & Assumpcao, 1995; Wahr et al., 2009).

The present geodynamic theory is mainly based on traditional mechanics. However, the relatively thin crust in comparison to the earth's radius may have more complex source mechanism, and classical theory might be inapplicable here. Instead, the mechanics of shells and the effect of membrane stress(Belytschko, Stolarski, Liu, Carpenter, & Ong, 1985; Bitbol, Peliti, & Fournier, 2011; Capovilla & Guven, 2002; Springer et al., 2010) on the lithosphere system may cause a new revolution in geodynamics.

2. Data and Methods

After extensive investigation on the relation between 420747 Ms $\geq$ 4 global earthquakes and solid earth tides, earthquakes are concentrated around the 0°, 90°, 180° and 270° phases of the theoretical semidiurnal solid tide.

Moreover we propose a new method for the short-term forecasting of earthquakes (Chen, Chen, & Xu, 2012) .

It's found that *M*s ≥ 7 global earthquakes occur surrounding four earthquake-prone phases of the semidiurnal solid tide(Chen et al., 2012), providing strong evidence that the lunar-solar tidal force is an important factor for trigging earthquakes. As the origin times of earthquakes are controlled by the semidiurnal earth tides, and earthquakes themselves are caused by crustal fractures and plate motions, there must be an inherent relation between the tide-generating force and plate motions, which may provide insight into the driving forces of plate motions.

To describe this relation, we used principles of thin-shell mechanics to analyze the dynamics and influence of the tidal force on the crust. If there were no Moon or Sun, the earth would be stable due to gravity. However, the tidal force produces additional stress within the earth (Figure 1A) (i.e., pressure Pm as mentioned in the continuous incompressible elastic earth model proposed by Kelvin).

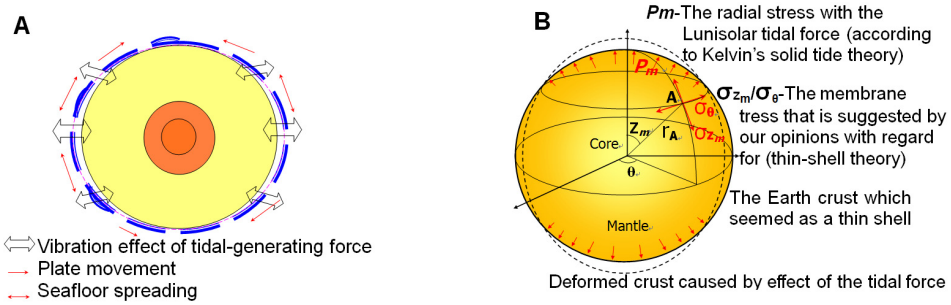

Figure 1. Driving forces of plate motions. (A) The lunisolar tidal force is an important factor for trigging earthquakes, which are caused by crustal fractures and plate motions, indicating that there might be an inherent relation between the tide-generating force and plate motions. (B) We propose that the radial stress causes the membrane stress in the crust through the tide-generating force within the earth

As the crust is extremely thin in comparison to the radius of the earth, the crust can be considered a thin shell and the theory of non-bending moment membrane stress (Belytschko et al., 1985; Bitbol et al., 2011; Capovilla & Guven, 2002; Springer et al., 2010) can be used to analyze the mechanical effect of the tidal force. Under the tidal force, the upward pressure Pm exerted by the viscoelastic mantle on the crust generates a horizontal distending membrane stress within the crust (Figure 1B), similar to wind causing tension of a boat's sail. Although the tidal force is small, the membrane stress may be large.

Therefore, we combined Kelvin's elastic earth model with thin-shell mechanics to establish a model of the tidal force on the crust and derive a relevant formula.

If there were no Moon or Sun, the earth should be statically balanced. There would exist only a compressive stress in the crust and earthquakes would not occur. However, the lunar and solar tidal forces cause additional stress within the elastic earth. In the theory of Kelvin's earth model, the earth is considered to be a continuous incompressible elastic ball and the tidal stress on any Point A within it by tidal force should be

$$P = \sum \rho V_n(A) + \sum P_n(A)$$

where

$$\sum \rho V_n(A) = \sum \rho T_n(A) + \rho T'(A)$$

$$\sum P_n(A) = -\sum \frac{\rho(2n^2+5n+3)\mu}{(2n^2+4n+3)\mu + n\rho gR} T_n(A)$$

where

$T_n(A)$ is the potential function of tidal force on Point A within the earth and $T'(A)$ is the additional gravitational potential resultant from the earth's deformation.

$$T^{'}(A)=\sum\frac{3g}{2n+1}\left(\frac{r(A)}{R}\right)^{n}\varepsilon_{n}S_{n}(A)$$

In this formula, $\varepsilon_{n}S_{n}(A)$ is the radial displacement of Point A, which can be calculated using

$$\varepsilon_{n}S_{n}(A)=\frac{n(2n+1)\rho R}{2[(2n^{2}+4n+3)\mu+n\rho gR](n-1)}T_{n}(A)$$

Therefore:

$$\rho T^{'}(A)=\sum\frac{3n\rho^{2}Rg}{2[(2n^{2}+4n+3)\mu+n\rho gR](n-1)}[\frac{r(A)}{R}]^{n}T_{n}(A)$$

$$\sum\rho V_{n}(A)=\sum\rho T_{n}(A)+\sum\frac{3n\rho^{2}Rg}{2[(2n^{2}+4n+3)\mu+n\rho gR](n-1)}[\frac{r(A)}{R}]^{n}T_{n}(A)$$

$$P=\sum\frac{3n\rho^{2}Rg}{2[(2n^{2}+4n+3)\mu+n\rho gR](n-1)}[\frac{r(A)}{R}]^{n}T_{n}(A)+\sum\rho T_{n}(A)-\sum\frac{(2n^{2}+5n+3)\rho\mu}{(2n^{2}+4n+3)\mu+n\rho gR}T_{n}(A)$$

When $n=0$ and $n=1$, P is small. $T_{n}(A)$ is small when $n>2$. We set $n=2$ so that we can calculate it approximately:

$$P=\sum\frac{3\rho^{2}Rg}{(19\mu+2\rho gR)}[\frac{r(A)}{R}]^{2}T_{n}(A)+\sum\rho T_{n}(A)-\sum\frac{21\rho\mu}{19\mu+2\rho gR}T_{n}(A) \quad (1)$$

The tidal force potential function $T_{n}(A)$ on Point A caused by the moon is

$$T_{n}(A)=G\frac{M}{r_{m}}[\frac{r(A)}{r_{m}}]^{2}P_{2}(\cos Z_{m})$$

where $P_{2}(\cos Z_{m})$ and $P_{2}(\cos Z_{S})$ are second-order Legendre polynomials. We conclude that

$$T_{n}(A)=G\frac{M}{2r_{m}^{3}}\left(r^{2}(A)\right)\left(3\cos^{2}Z_{m}-1\right) \quad (2)$$

By substituting (2) into (1), the equation for the radial stress on Point A exerted by the lunar tidal force in terms of zenith distance can be derived:

$$P_{m}=\frac{3\rho^{2}g}{(19\mu+2\rho gR)R}\frac{GM}{2r_{m}^{3}}r^{4}(A)(3\cos^{2}Z_{m}-1)+\left[\rho-\frac{21\mu\rho}{(19\mu+2\rho gR)}\right]\frac{GM}{2r_{m}^{3}}r^{2}(A)(3\cos^{2}Z_{m}-1) \quad (3)$$

Likewise, the radial stress on Point A exerted by the solar tidal force in terms of zenith distance can be described as:

$$P_{S}=\frac{3\rho^{2}g}{(19\mu+2\rho gR)R}\frac{GS}{2r_{S}^{3}}r^{4}(A)(3\cos^{2}Z_{S}-1)+\left[\rho-\frac{21\mu\rho}{(19\mu+2\rho gR)}\right]\frac{GS}{2r_{S}^{3}}r^{2}(A)(3\cos^{2}Z_{S}-1) \quad (4)$$

The coefficients are defined as follows:

$$C_{m1}=\frac{3\rho^{2}g}{(19\mu+2\rho gR)R}\frac{GM}{2r_{m}^{3}} \qquad C_{m2}=\left[\rho-\frac{21\mu\rho}{(19\mu+2\rho gR)}\right]\frac{GM}{2r_{m}^{3}}$$

$$C_{s1} = \frac{3\rho^2 g}{(19\mu + 2\rho g R)R}\frac{GS}{2r_s^3} \qquad C_{s2} = \left[\rho - \frac{21\mu\rho}{(19\mu + 2\rho g R)}\right]\frac{GS}{2r_s^3}$$

The upward radial stress P_m generated by the lunar tidal force on Point A in the mantle close to the surface can be determined via

$$P_m = [C_{m1} r^4(A) + C_{m2} r^2(A)](3\cos^2 Z_m - 1) \tag{5}$$

and the upward radial stress P_S generated by the solar tidal force on Point A in the mantle close to the surface can be determined via

$$P_S = [C_{s1} r^4(A) + C_{s2} r^2(A)](3\cos^2 Z_s - 1) \tag{6}$$

where

Z_m is the zenith distance between Point A and the moon,

Z_S is the zenith distance between Point A and the sun,

$r(A)$ is the distance between Point A and the earth's core,

R is the average radius of the earth and for crust close to the surface, $r(A) = R$,

ρ is the average density of the earth,

G is the constant of universal gravitation,

M is the mass of the moon,

S is the mass of the sun,

g is the mean acceleration of gravity,

r_m is the distance between the centers of the moon and the earth,

r_S is the distance between center of the solar and the earth,

μ is the average shear elasticity (rigidity modulus) of Kelvin's elastic earth model.

Let

$G = 6.67259 \times 10^{-11}\, N \cdot m^2 / kg^2$

$M = 7.350 \times 10^{22}\, kg,$

$S = 1.989 \times 10^{30}\, kg,$

$r_m = 3844 \times 10^5\, m,$

$r_s = 1496 \times 10^8\, m$

$\rho = 5520 kg / m^3,$

$g = 9.82 m / s^2,$

$R = 6371 \times 10^3\, m$

For the earth's surface at a geocentric distance of $r(A) = R$,

Because the thickness of the crust is trivial in comparison to the radius of the earth, the crust can be considered a thin shell, and thus the theory of non-bending moment membrane stress can be used to analyze the mechanical effect of tidal forcing on the crust. That is, under the tidal force, the upward inner pressure P_m exerted by the viscoelastic mantle on the crust generates a horizontal extensional membrane stress within the solid crust (Figure 1B), similar to the tension of a sail caused by the wind.

According to membrane stress theory, the formulas for calculating the membrane stress on the thin shell of an axially symmetric rotating ball under inner pressure should be

$$\sigma_{Zm} = \frac{1}{tR\sin^2 Z_m}\int_0^{Z_m}[R^2 \sin Z_m \cos Z_m \times P_m]dZ_m \tag{7}$$

$$\frac{\sigma_{Zm} + \sigma_{\theta m}}{R} = \frac{P_m}{t} \tag{8}$$

In (7) and (8),

t is the thickness of the crust,

σ_{Zm} is horizontal membrane stress in the direction of the zenith,

$\sigma_{\theta m}$ is horizontal membrane stress perpendicular to σ_{Zm}.

By substituting P_m from (5) into (7),

$$\sigma_{Zm} = \frac{C_{m1}R^5 + C_{m2}R^3}{t\sin^2 Z_m}\int_0^{Z_m}[3\sin Z_m \cos^3 Z_m - \sin Z_m \cos Z_m]dZ_m \tag{9}$$

By integrating (9), we obtain

$$\sigma_{Zm} = \frac{C_{m1}R^5 + C_{m2}R^3}{4t\sin^2 Z_m}(2\cos^2 Z_m - 3\cos^4 Z_m + 1) \tag{10}$$

By substituting (10) into (8), and using P_m from (5), we obtain

$$\sigma_{\theta m} = \frac{(C_{m1}R^5 + C_{m2}R^3)(3\cos^2 Z_m - 1)}{t} - \frac{C_{m1}R^5 + C_{m2}R^3}{4t\sin^2 Z_m}(2\cos^2 Z_m - 3\cos^4 Z_m + 1) \tag{11}$$

$$\text{Where } C_{m1} = \frac{3\rho^2 g}{(19\mu + 2\rho gR)R}\frac{GM}{2r_m^3}, \quad C_{m2} = \left[\rho - \frac{21\mu\rho}{(19\mu + 2\rho gR)}\right]\frac{GM}{2r_m^3} \tag{12}$$

Equations (10) and (11) are the final formulas for the extensional membrane stress on Point A in the crust caused by the lunar tidal forcing of the viscoelastic mantle, where σ_{Zm} is the horizontal membrane stress in the direction of the lunar zenith and $\sigma_{\theta m}$ is the horizontal membrane stress perpendicular to σ_{Zm}.

Similarly, the extensional membrane stress on Point A in the crust caused by the viscoelastic mantle driven by solar tidal forcing can be calculated via the following formulas:

$$\sigma_{Zs} = \frac{C_{s1}R^5 + C_{s2}R^3}{4t\sin^2 Z_s}(2\cos^2 Z_s - 3\cos^4 Z_s + 1) \tag{13}$$

$$\sigma_{\theta s} = \frac{(C_{s1}R^5 + C_{s2}R^3)(3\cos^2 Z_s - 1)}{t} - \frac{C_{s1}R^5 + C_{s2}R^3}{4t\sin^2 Z_s}(2\cos^2 Z_s - 3\cos^4 Z_s + 1) \tag{14}$$

$$\text{Where } C_{s1} = \frac{3\rho^2 g}{(19\mu + 2\rho gR)R}\frac{GS}{2r_s^3}, \quad C_{s2} = \left[\rho - \frac{21\mu\rho}{(19\mu + 2\rho gR)}\right]\frac{GS}{2r_s^3} \tag{15}$$

In formulas (13) and (14),

σ_{Zs} is the horizontal membrane stress in the direction of the solar zenith,

$\sigma_{\theta s}$ is the horizontal membrane stress in the direction of σ_{Zs}.

3. Results

Fig. 2 shows an earth model based on PREM. The magnitude of the shear modulus μ is hypothesized to vary from 1.0E10 to 5.0E11, and the crust membrane stress can be obtained from the above equations. From Figure 2, we can see that when the crustal thickness is less than 10 km, a seemingly insignificant tidal force would cause a horizontal tensile membrane stress within the crust, enabling tension fracturing (the tensile fracture strength for rocks is approximately 4-6 MPa).

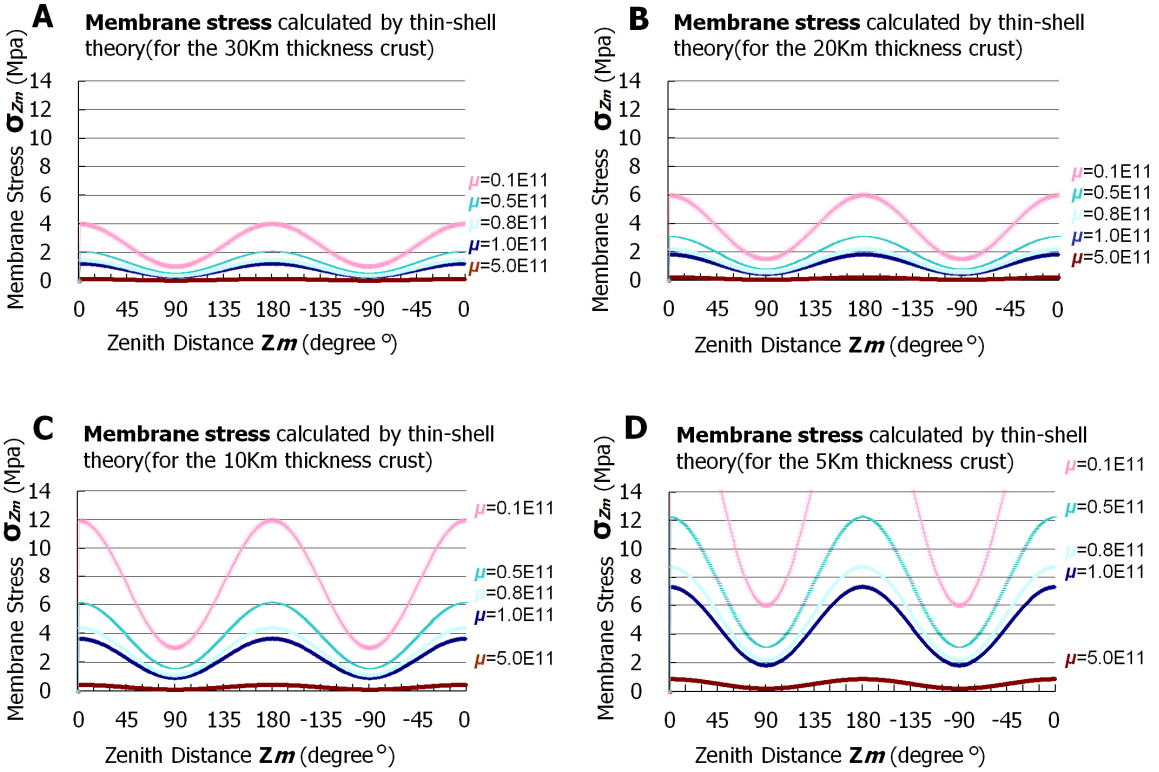

Figure 2. The membrane stresses on crust of various thicknesses are calculated using the thin-shell theory. Although the tide-generating force is seemingly insignificant, the horizontal tensile membrane stress caused by the solid tide in crust less than 10 km thick is powerful enough to cause tension fractures in rocks with strengths up to 5 MPa.

4. Discussion

We believe that fracturing of crust less than 10 km thick will be intensified and spread farther with the continued cyclic deformation caused by the tide-generating force. At mid-ocean ridges, lava is continuously erupted. Although the lava solidifies when it meets sea water, the broken crust does not have enough time to solidify completely due to the tensile effects of the semidiurnal solid tide. In other words, the crust has been ruptured since the existence of the moon and will continue to be in the future.

Therefore, we believe that both the rupturing of the crust and the formation of mid-ocean ridges are caused by the tensile membrane stress due to the tidal force (Figure 3A). In addition, under the periodic vibration of the solid tide, lava at mid-ocean ridges accumulates gradually and experiences repeated cycles of eruption and cooling. When a sufficient amount of solidified lava has accumulated, gravity causes the lava to thrust horizontally over the mid-ocean ridge and the oceanic plates on both sides of the ridge via wedging, giving rise to pressured seafloor spreading and plate motion due to the solid tide. This cycle of eruption and cooling, followed by wedging has a stable frequency in response to the cycle of earth tides, and thus the plate motion has become stable over time. Figure 3B depicts the breaking of a mid-ocean ridge and the consequent surging of

mantle materials caused by the tide-generating force, as well as the resulting plate motion and seafloor spreading. Due to the randomness of the horizontal component of the membrane stress, triple junctions may form. Transform fault perpendicular to mid-ocean ridges also form through this process.

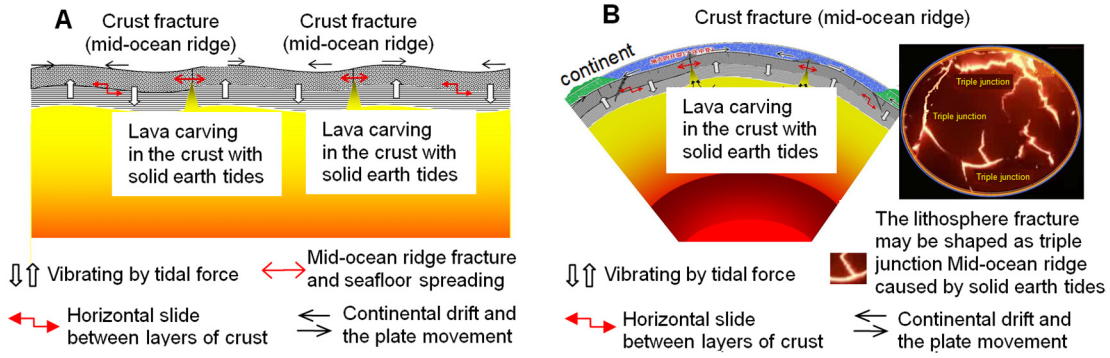

Figure 3. (A) While triggering numerous earthquakes, the tide-generating force can also result in fracturing at mid-ocean ridges and a surge in lava from the mantle. This causes plates to move and leads to seafloor spreading, causing plate motion. (B) The membrane stress in the crust is caused by the earth tides and is tensile in any horizontal direction. Due to membrane stress, transformation faults are perpendicular to the mid-ocean ridges and large fault zones or ridges may form triple junctions, which are not explained by mantle convection or mantle plume models

Therefore, we propose that the thin-shell theory can be used to analyze the dynamic effect of the tidal force on the crust. Our findings are not only a theoretical support of the proposition that mid-ocean ridge fracturing and plate motions originate from the lunar-solar tidal force, but they are also a possible solution to certain geological problems, including the long-term stabilization of plate motions, the formation of triple junctions, large transform faults and why only the earth has tectonic plates. These explanations make the present theory more rational than mantle convection models and other previous geodynamical theories.

Although other terrestrial planets in our solar system have concentric layers such as the core, mantle and crust, and they may have mantle convection similar to the earth, they do not have seafloor spreading or tectonic plates.

We believe that the earth has three specific conditions that make it possible for it to have tectonic plates and the capacity for life, arising from the existence of the moon. These three conditions are as follows:

1) Among all the terrestrial planets, the moon has a relatively large mass relative to the earth and is relatively close to the earth, which causes a strong tide-generating force.

2) Affected by the tidal force, the earth has a viscoelastic mantle capable of exerting a radial stress and a membrane stress on the solid crust.

3) The thickness of the earth's crust relative to its radius is very small and the membrane stress is strong enough to cause crust thinner than 10 km to rupture, leading to large-scale mid-ocean ridges and tectonic plates.

For the first time, the thin-shell mechanism is used to analyze the response of the crust under the tide-generating force and to speculate about the driving source of plate motions. And we may discover the plate tectonics effected by the tidal force is in the terrestrial planets or other celestial bodies in future.

The conclusions of our analysis are:

1) Although the tidal force is small, the membrane stress is large. A theoretical formula is given for the crust membrane stress model. Calculations show that the horizontal tensile membrane stress is capable of causing tensile rupture in oceanic crust.

2) We speculate that the tide-generating force drives plate motions. We believe that the solid tide triggers numerous earthquakes, and the membrane stress within the crust makes possible for triple junctions and large transform faults to form in the thinner parts of the oceanic crust. Seafloor spreading and plate motions arise from the membrane stress and are formed by lava that has erupted due to the tide-generating force. The existence of the moon is the reason why the earth become the only planet in our solar system to have tectonic plates and plate

motions. The analysis of shell mechanics may cause new breakthroughs in geodynamics.

3) We infer that there must be the plate tectonics effected by the tidal force is in the terrestrial planets or other celestial bodies.

Acknowledgements

This research was supported by the Key National Science Foundation of China (Grant No. 40730103), the National Science Foundation of China (Grant No. 40571166, 40672107), and the National Science and Technology Support Program (Grant No. 2006BAC01B02-02-05)

References

Belytschko, T., Stolarski, H., Liu, W. K., Carpenter, N., & Ong, J. S. J. (1985). Stress projection for membrane and shear locking in shell finite-elements. *Computer Methods In Applied Mechanics and Engineering, 51*(1-3), 221-258. http://dx.doi.org/10.1016/0045-7825(85)90035-0

Bird, P. (1998). Testing hypotheses on plate-driving mechanisms with global lithosphere models including topography, thermal structure, and faults. *Journal of Geophysical Research-Solid Earth, 103*(B5), 10115-10129. http://dx.doi.org/10.1029/98JB00198

Bitbol, A. F., Peliti, L., & Fournier, J. B. (2011). Membrane stress tensor in the presence of lipid density and composition inhomogeneities. *European Physical Journal E, 34*(5). http://dx.doi.org/10.1140/epje/i2011-11053-4

Capovilla, R., & Guven, J. (2002). Stresses in lipid membranes. *Journal Of Physics A-mathematical and General, 35*(30), 6233-6247. http://dx.doi.org/10.1088/0305-4470/35/30/302

Chen, L., Chen, J. G., & Xu, Q. H. (2012). Correlations between solid tides and worldwide earthquakes ms ≥ 7.0 since 1900. *Nat. Hazards Earth Syst. Sci., 12*(3), 587-590. http://dx.doi.org/10.5194/nhess-12-587-2012

Conrad, C. P., & Lithgow-Bertelloni, C. (2004). The temporal evolution of plate driving forces: Importance of "slab suction" versus "slab pull" during the cenozoic. *Journal of Geophysical Research-Solid Earth, 109*(B10).

Evans, J. W. (1923). The wegener hypothesis of continental drift. *Nature, 111*, 393-394. http://dx.doi.org/10.1038/111393a0

Forsyth, D., & Uyeda, S. (1975). Relative importance of driving forces of plate motion. [Review]. *Geophysical Journal of the Royal Astronomical Society, 43*(1), 163-200. http://dx.doi.org/10.1111/j.1365-246X.1975.tb00631.x

Hallam, A. (1975). Wegener,a and hypothesis of continental-drift. *Scientific American, 232*(2), 88-&. http://dx.doi.org/10.1038/scientificamerican0275-88

Jordan, T. H. (1974). Some comments on tidal drag as a mechanism for driving plate motions. *Journal Of Geophysical Research, 79*(14), 2141-2142. http://dx.doi.org/10.1029/JB079i014p02141

Lithgowbertelloni, C., & Richards, M. A. (1995). Cenozoic plate driving forces. *Geophysical Research Letters, 22*(11), 1317-1320. http://dx.doi.org/10.1029/95GL01325

Meinesz, F. A. V. (1947). Shear patterns of the earth's crust. *Transactions of the American Geophysical Union, 28*, 1-61.

Minster, J. B., Jordan, T. H., Molnar, P., & Haines, E. (1974). Numerical modeling of instantaneous plate tectonics. *Geophysical Journal of the Royal Astronomical Society, 36*(3), 541-576. http://dx.doi.org/10.1111/j.1365-246X.1974.tb00613.x

Mobus, G. (1982). In memory of wegener,alfred - on the occasion of the 70th anniversary of his 1st publication on his continental-drift hypothesis. *Petermanns Geographische Mitteilungen, 126*(3), 137-148.

Person, M., & Garven, G. (1994). A sensitivity study of the driving forces on fluid-flow during continental-drift basin evolution. *Geological Society Of America Bulletin, 106*(4), 461-475. http://dx.doi.org/10.1130/0016-7606(1994)106<0461:ASSOTD>2.3.CO;2

Plattner, C., Malservisi, R., & Govers, R. (2009). On the plate boundary forces that drive and resist baja california motion. *Geology, 37*(4), 359-362. http://dx.doi.org/10.1130/G25360A.1

Ranalli, G. (2000). Westward drift of the lithosphere: Not a result of rotational drag. *Geophysical Journal International, 141*(2), 535-537. http://dx.doi.org/10.1046/j.1365-246x.2000.00091.x

Royden, L. H. (1993). The tectonic expression slab pull at continental convergent boundaries. *Tectonics, 12*(2), 303-325. http://dx.doi.org/10.1029/92TC02248

Scoppola, B., Boccaletti, D., Bevis, A., Carminati, E., & Doglioni, C. (2006). The westward drift of the lithosphere: A rotational drag? (vol 118, pg 199, 2006). *Geological Society Of America Bulletin, 118*(3-4), 511-511.

Springer, F., Ghidossi, R., Carretier, E., Veyret, D., Dhaler, D., & Moulin, P. (2010). Study of the effect of geometry on wall shear stress and permeate flux for ceramic membranes: Cfd and experimental approaches. *Engineering Applications of Computational Fluid Mechanics, 4*(1), 17-28.

Vandecar, J. C., James, D. E., & Assumpcao, M. (1995). Seismic evidence for a fossil mantle plume beneath south-america and implications for plate driving forces. *Nature, 378*(6552), 25-31. http://dx.doi.org/10.1038/378025a0

Wahr, J., Selvans, Z. A., Mullen, M. E., Barr, A. C., Collins, G. C., Selvans, M. M., & Pappalardo, R. T. (2009). Modeling stresses on satellites due to nonsynchronous rotation and orbital eccentricity using gravitational potential theory. *Icarus, 200*(1), 188-206. http://dx.doi.org/10.1016/j.icarus.2008.11.002

Call for Manuscripts

Earth Science Research is a peer-reviewed journal, published by Canadian Center of Science and Education. The journal publishes research papers in the fields of geology, geophysics, oceanography, planetary sciences, geodesy, geodynamics, earthquake engineering, meteorology and atmospheric sciences, seismology engineering and geological engineering. The journal is available in electronic form in conjunction with its print edition. All articles and issues are available for free download online.

We are seeking submissions for forthcoming issues. All manuscripts should be written in English. Manuscripts from 3000–8000 words in length are preferred. All manuscripts should be prepared in MS-Word format, and submitted online, or sent to: esr@ccsenet.org

Paper Selection and Publishing Process

a) Upon receipt of a submission, the editor sends an e-mail of confirmation to the submission's author within one to three working days. If you fail to receive this confirmation, your submission e-mail may have been missed.

b) Peer review. We use a double-blind system for peer review; both reviewers' and authors' identities remain anonymous. The paper will be reviewed by at least two experts: one editorial staff member and at least one external reviewer. The review process may take two to three weeks.

c) Notification of the result of review by e-mail.

d) If the submission is accepted, the authors revise paper and pay the publication fee.

e) After publication, the corresponding author will receive two hard copies of the journal, free of charge. If you want to keep more copies, please contact the editor before making an order.

f) A PDF version of the journal is available for download on the journal's website, free of charge.

Requirements and Copyrights

Submission of an article implies that the work described has not been published previously (except in the form of an abstract or as part of a published lecture or academic thesis), that it is not under consideration for publication elsewhere, that its publication is approved by all authors and tacitly or explicitly by the authorities responsible where the work was carried out, and that, if accepted, the article will not be published elsewhere in the same form, in English or in any other language, without the written consent of the publisher. The editors reserve the right to edit or otherwise alter all contributions, but authors will receive proofs for approval before publication.

Copyrights for articles are retained by the authors, with first publication rights granted to the journal. The journal/publisher is not responsible for subsequent uses of the work. It is the author's responsibility to bring an infringement action if so desired by the author.

More Information

E-mail: esr@ccsenet.org

Website: www.ccsenet.org/esr

Paper Submission Guide: www.ccsenet.org/submission

Recruitment for Reviewers: www.ccsenet.org/reviewer

The journal is peer-reviewed
The journal is open-access to the full text
The journal is included in:

AMICUS
Canadiana
EBSCOhost
Gale's Academic Databases
Google Scholar
Library and Archives Canada
PKP Open Archives Harvester
ProQuest
Standard Periokical Directory
Ulrich's

Earth Science Research

Semiannual

Publisher Canadian Center of Science and Education
Address 1120 Finch Avenue West, Suite 701-309, Toronto, ON., M3J 3H7, Canada
Telephone 1-416-642-2606
Fax 1-416-642-2608
E-mail esr@ccsenet.org
Website www.ccsenet.org/esr

ISSN 1927-0542